Sedimentary rocks of the Internal Hellenides, Greece: age, source, and depositional setting

Dissertation
zur Erlangung des Grades
"Doktor der Naturwissenschaften"
im Promotionsfach Geologie/Paläontologie

am Fachbereich Chemie, Pharmazie und Geowissenschaften
der Johannes Gutenberg-Universität in Mainz

Guido Meinhold
geb. in Schleiz

Mainz, 2007

Erklärung

Ich versichere hiermit, die vorliegende Arbeit selbstständig und nur unter Verwendung der angegebenen Quellen und Hilfsmittel verfasst zu haben.

Mainz, Dezember 2007

Summary

In this PhD thesis the provenance and depositional setting of sedimentary rocks from selected areas of the Internal Hellenides, Greece, are examined in detail. The main sedimentary successions studied on the mainland Greece belong to the Pirgadikia and Vertiskos Units of the Serbo-Macedonian Massif, to the Examili, Melissochori and Prinochori Formations of the eastern Vardar Zone and to the Makri Unit and the Melia Formation of the Thrace area. In the eastern Aegean Sea special emphasis was placed on sedimentary successions cropping out on Chios Island. The rocks investigated range from virtually non-metamorphosed to amphibolite facies; their ages span from Ordovician to Cretaceous. Provenance characterisation was achieved using whole-rock major- and trace-element geochemistry, mineral chemistry and U–Pb zircon geochronology. Depositional ages of selected samples were additionally constrained using biostratigraphic analysis. Identifying ancient source areas and depositional settings is of fundamental importance for palaeogeographic reconstructions in the Tethyan realm. The most significant results obtained are outlined below:

The oldest sedimentary rocks in the Internal Hellenides belong to the Pirgadikia Unit of the Serbo-Macedonian Massif. They are very mature quartz-rich siliciclastic sediments, which are correlated with Ordovician overlap sequences deposited at the northern margin of Gondwana on the basis of maturity and zircon age spectra. Metasedimentary rocks from the Vertiskos Unit are nearly coeval but of different depositional facies. Detrital zircon ages suggest a NW African source (Hun superterrane). The rocks are interpreted to have been deposited at an ancient active-margin setting.

The oldest biostratigraphically dated sedimentary rocks of Greece are Silurian to Carboniferous olistoliths from a Late Palaeozoic turbidite-olistostrome succession on Chios Island. The analysis of fossiliferous olistoliths, in conjunction with detrital zircon ages suggest that the Late Palaeozoic siliciclastic succession of Chios received its detritus from basement rocks of the Sakarya Zone in western Turkey and time and facies equivalents of Palaeozoic units from the Istanbul Zone in northern Turkey and the Balkan region.

During the Permo-Triassic the Examili Formation of the eastern Vardar Zone was deposited in an intracontinental basin in proximity to the Vertiskos Unit. Minor input came from Carboniferous basement rocks.

The Early–Middle Jurassic Melissochori Formation (formerly Svoula flysch) of the eastern Vardar Zone was deposited at the slope of a carbonate platform and received large amounts of detritus from a Permo-Carboniferous basement unit, probably the Pelagonian Zone and/or the Lower Tectonic Unit of the Rhodope Massif. The Makri Unit of the Thrace area is probably of the same age. Its sedimentary succession resembles that of the Melissochori Formation, and it received large amounts of detritus from Permo-Carboniferous basement rocks of the Pelagonian Zone or equivalent rocks.

During the Early Cretaceous the Prinochori Formation of the eastern Vardar Zone was deposited in front of a nappe pile comprising ophiolitic rocks of the Vardar Ocean and basement rocks of the Vertiskos Unit. The Melia Formation of the Thrace area was deposited in front of a metamorphic nappe pile with Rhodope affinities in Cretaceous times.

The data of this study clearly show that subduction of a branch of the Palaeotethys Ocean in the Late Palaeozoic and the subsequent accretion of North Gondwana-derived terranes close to the southern active margin of Eurasia supplied detritus to sedimentary successions of the Internal Hellenides. Early Mesozoic rifting marks the birth of Neotethyan oceans in Greece. Intraoceanic subduction and ophiolite obduction characterise the Jurassic. The Late Jurassic and Early Cretaceous phase of nappe tectonics was sealed by Mid-Cretaceous carbonate deposition. In the Internal Hellenides the final closure of Neotethyan oceanic basins occurred during the Late Cretaceous and Tertiary.

Kurzfassung

Ziel der vorliegenden Dissertation war die Untersuchung der Liefergebiete und Ablagerungsräume sedimentärer Gesteine aus ausgewählten Gebieten der inneren Helleniden Griechenlands. Die untersuchten Sedimente Nordgriechenlands gehören zu den Pirgadikia und Vertiskos Einheiten des Serbo-Makedonische Massifs, zu den Examili, Melissochori und Prinochori Formationen der östlichen Vardar Zone und zur Makri Einheit und Melia Formation des östlichen Zirkum-Rhodope-Gürtels in Thrakien. In der östlichen Ägäis lag der Schwerpunkt bei den Sedimenten der Insel Chios. Der Metamorphosegrad der untersuchten Gesteine variiert von der untersten Grünschieferfazies bis hin zur Amphibolitfazies. Das stratigraphische Alter reicht vom Ordovizium bis zur Kreide. Zur Charakterisierung der Gesteine und ihrer Liefgebiete wurden Haupt- und Spurenelementgehalte der Gesamtgesteine bestimmt, mineralchemische Analysen durchgeführt und detritische Zirkone mit U–Pb datiert. An ausgewählten Proben wurden außerdem biostratigraphische Untersuchungen zur Bestimmung des Sedimentationsalters durchgeführt. Die Untersuchungsergebnisse dieser Arbeit sind von großer Bedeutung für paläogeographische Rekonstruktionen der Tethys. Die wichtigsten Ergebnisse lassen sich wie folgt zusammenfassen:

Die ältesten Sedimente Nordgriechenlands gehören zur Pirgadikia Einheit des Serbo-Makedonischen Massifs. Es sind sehr reife, quarzreiche, siliziklastische Metasedimente, die auf Grund ihrer Maturität und ihrer detritischen Zirkone mit ordovizischen overlap-Sequenzen vom Nordrand Gondwanas korreliert werden können. Die Metasedimente der Vertiskos Einheit besitzen ein ähnliches stratigraphisches Alter, haben aber einen anderen Ablagerungsraum. Das Altersspektrum detritischer Zirkone lässt auf ein Liefergebiet im Raum NW Afrikas (Hun Superterrane) schließen. Die Gesteinsassoziation der Vertiskos Einheit wird als Teil einer aktiven Kontinentalrandabfolge gesehen.

Die ältesten biostratigraphisch datierten Sedimente Griechenlands sind silurische bis karbonische Olistolithe aus einer spätpaläozoischen Turbidit-Olistostrom Einheit auf der Insel Chios. Die Alter detritischer Zirkone und die Liefergebietsanalyse der fossilführenden Olistolithe lassen den Schluss zu, dass die klastischen Sedimente von Chios Material vom Sakarya Mikrokontinent in der West-Türkei und faziellen Äquivalenten zu paläozoischen Gesteinen der Istanbul Zone in der Nord-Türkei und der Balkan Region erhalten haben.

Während der Permotrias wurde die Examili Formation der östlichen Vardar Zone in einem intrakontinentalen, sedimentären Becken, nahe der Vertiskos Einheit abgelagert. Untergeordnet wurde auch karbonisches Grundgebirgsmaterial eingetragen.

Im frühen bis mittleren Jura wurde die Melissochori Formation der östlichen Vardar Zone am Abhang eines karbonatführenden Kontinentalrandes abgelagert. Der Großteil des detritischen Materials kam von permokarbonischem Grundgebirge vulkanischen Ursprungs, vermutlich von der Pelagonischen Zone und/oder der unteren tektonischen Einheit des Rhodope Massifs. Die Makri Einheit in Thrakien besitzt vermutlich ein ähnliches Alter wie die Melissochori Formation. Beide sedimentären Abfolgen ähneln sich sehr. Der Großteil des detritischen Materials für die Makri Einheit kam vom Grundgebirge der Pelagonischen Zone oder äquivalenten Gesteinen.

Während der frühen Kreide wurde die Prinochori Formation der östlichen Vardar Zone im Vorfeld eines heterogenen Deckenstapels abgelagert, der ophiolitisches Material sowie Grundgebirge ähnlich zu dem der Vertiskos Einheit enthielt. Ebenfalls während der Kreidezeit wurde in Thrakien, vermutlich im Vorfeld eines metamorphen Deckenstapels mit Affinitäten zum Grundgebirge der Rhodopen die Melia Formation abgelagert.

Zusammenfassend kann festgehalten werden, dass die Subduktion eines Teiles der Paläotethys und die anschließende Akkretion vom Nordrand Gondwanas stammender Mikrokontinente (Terranes) nahe dem südlichen aktiven Kontinentalrand Eurasiens den geodynamischen Rahmen für die Schüttung des detritischen Materials der Sedimente der inneren Helleniden im späten Paläozoikum bildeten. Die darauf folgenden frühmesozoischen Riftprozesse leiteten die Bildung von Ozeanbecken der Neotethys ein. Intraozeanische Subduktion und die Obduzierung von Ophioliten prägten die Zeit des Jura. Die spät-jurassische und frühkretazische tektonische Phase wurde durch die Ablagerung von mittel-kretazischen Kalksteinen besiegelt. Die endgültige Schließung von Ozeanbecken der Neotethys im Bereich der inneren Helleniden erfolgte schließlich in der späten Kreide und im Tertiär.

Table of Contents

Summary ..... **iii**
Kurzfassung ..... **v**
Preface **1**

Chapter 1 Geochemical constraints on the provenance and depositional setting of sedimentary rocks from the islands of Chios, Inousses and Psara, Aegean Sea, Greece: implications for the evolution of Palaeotethys

Abstract 5
1. Introduction 6
2. Geological setting 8
2.1. Chios 8
2.2. Inousses 14
2.3. Psara 15
3. Sample description and methods 17
3.1. Sample description 17
3.2. Whole-rock geochemistry 18
3.3. Mineral chemistry 20
4. Geochemical results 21
4.1. Chemical classification 21
4.2. Mineral controls on whole-rock geochemistry 22
4.3. Weathering and sediment recycling 24
4.4. Provenance 25
4.5. Tectonic setting 31
5. Discussion 32
5.1. Chios 32
5.2. Inousses 34
5.3. Psara 34
5.4. Implications for Palaeotethyan evolution 35
6. Conclusions 40

Chapter 2 Rutile chemistry and thermometry as provenance indicator: An example from Chios Island, Greece

Abstract 42
1. Introduction 43
2. Geological setting 43

3. Sample description 46
4. Rutile chemistry and thermometry 47
5. Analytical methods 51
6. Results 52
7. Discussion and conclusions 58

Chapter 3 Provenance of sediments during subduction of Palaeotethys: detrital zircon ages and olistolith analysis in Palaeozoic sediments from Chios Island, Greece

Abstract 61
1. Introduction 62
2. Geological setting 64
3. Geochronological method 68
4. Sample description and results 68
4.1. Carboniferous sample CH52 68
4.2. Permo-Triassic sample CH11 72
5. Discussion 73
5.1. Possible source areas according to zircon data 73
5.2. Source of zircons 80
5.3. Source of olistoliths 82
6. Implications for Palaeotethys 92
7. Conclusions 96

Chapter 4 U-Pb LA-ICPMS zircon geochronology of the Serbo-Macedonian Massif, Greece: Palaeotectonic constraints for Gondwana-derived terranes in the Eastern Mediterranean

Abstract 97
1. Introduction 98
2. Geological setting 100
3. Analytical methods 104
4. Sample description and geochemistry 106
4.1. Pirgadikia Unit 106
4.2. Vertiskos Unit 108
5. Geochronological results 109
5.1. Pirgadikia Unit 109
5.2. Vertiskos Unit 114
6. Discussion and conclusions 118
6.1. Pirgadikia Unit 118
6.2. Vertiskos Unit 122

Chapter 5 Geochemistry, provenance and stratigraphic age of metasedimentary rocks from the eastern Vardar suture zone, northern Greece

Abstract 124
1. Introduction 125
2. Geological setting 127
2.1. Examili Formation 129
2.2. Pirghoto Formation 131
2.3. Melissochori Formation 132
2.4. Aspro Vrisi Serie and Chortiatis Unit 134
2.5. Oreokastro-Chalkidiki ophiolite complexes 137
2.6. Prinochori Formation 138
2.7. Neochorouda Unit 141
3. Methods 142
3.1. Whole-rock geochemistry 143
3.2. Mineral chemistry 144
3.3. Zircon geochronology 144
3.4. Biostratigraphy 145
4. Results 145
4.1. Whole-rock geochemistry 145
4.2. Mineral chemistry 153
4.3. Zircon geochronology 154
4.4. Biostratigraphy 162
5. Discussion and conclusions....165
5.1. Examili Formation 165
5.2. Melissochori Formation 167
5.3. Prinochori Formation 170
5.4. Oreokastro area 171
5.5. Palaeogeographic model 172

Chapter 6 Geochemistry and provenance of metasedimentary rocks from the eastern Circum-Rhodope Belt, Thrace, NE Greece

Abstract 176
1. Introduction 177
2. Geological setting 180
2.1. Makri Unit 181
2.2. Melia Formation 184
3. Samples and methods 186
3.1. Whole-rock geochemistry 187
3.2. Mineral chemistry 188

3.3. Zircon geochronology 188
3.4. Palynology 189
4. Results 189
4.1. Whole-rock geochemistry 189
4.2. Mineral chemistry 196
4.3. Zircon geochronology 199
5. Discussion and conclusions 206
5.1. Makri Unit 206
5.2. Melia Formation 207
5.3. Palaeotectonic implications 210

Synthesis 214
References 218

Appendix

Preface

The Hellenides of Greece constitute a major segment of the Alpine-Himalayan mountain chain in the Eastern Mediterranean. They have traditionally been subdivided into the Internal (hinterland) and the External (foreland) Hellenides. Recent studies have shown that several distinct crustal units can be recognized by geochronological data representing a tectonic collage of exotic terranes, forming nowadays the Internal Hellenides. In pre-Cenozoic time their position in relation to each other and to the neighbouring units in Bulgaria and Turkey was quite different from today. Simplified, the Internal Hellenides are composed in varying amounts of Neoproterozoic, Palaeozoic and minor Mesozoic igneous basement rocks overlain by or intercalated with sedimentary successions. The rocks record various plate tectonic processes such as rifting, subduction and collision. Most of them experienced quite complex tectonism and metamorphism, which gave rise to equivocal palaeotectonic models and interpretations.

In this PhD study the provenance and depositional setting of clastic sedimentary rocks from several key areas of the Internal Hellenides are examined in detail. This is crucial for palaeotectonic reconstructions because clastic sedimentary rocks can provide information about rock lithologies in the source area that have often been destroyed and recycled during ancient plate tectonic processes. Besides provenance studies, additional palaeontological, stratigraphical and tectonic evidence in combination with an in-depth analysis of literature are used because it becomes more and more evident that only a multidisciplinary approach can provide reliable constraints for palaeotectonic reconstructions. The studied areas are in the eastern Aegean Sea, the islands of Chios, Inousses and Psara, and in northern Greece, the Serbo-Macedonian Massif, the Vardar Zone and the Circum-Rhodope Belt. The results are presented and discussed in six chapters. Sample list, including geographic coordinates, and associated analytical data are given in the Appendix.

Chapter 1 discusses the provenance and depositional setting of Late Palaeozoic–Early Mesozoic metasedimentary rocks from the islands of Chios, Inousses and Psara, based on whole-rock geochemistry and mineral chemistry of detrital chrome spinel. Previous tectonostratigraphic concepts are evaluated and new ones are proposed. The chapter is largely identical with the manuscript “Geochemical constraints on the provenance and depositional

setting of sedimentary rocks from the islands of Chios, Inousses and Psara, Aegean Sea, Greece: implications for the evolution of Palaeotethys", which was published in the *Journal of the Geological Society of London* in November 2007. Co-authors are D. Kostopoulos (Department of Mineralogy and Petrology, National and Kapodistrian University of Athens, Greece) and T. Reischmann (Max Planck Institute for Chemistry, Mainz, Germany). Data interpretation and preparation of the manuscript were done by G. Meinhold.

Chapter 2 discusses the application of rutile chemistry, including Zr-in-rutile thermometry, for quantitative single-mineral provenance analysis on samples from Chios Island. The chapter is largely identical with the manuscript "Rutile chemistry and thermometry as provenance indicator: An example from Chios Island, Greece", which has been accepted for publication in *Sedimentary Geology* in November 2007. Co-authors are B. Anders (Institute of Geosciences, University of Mainz, Germany), D. Kostopoulos (Department of Mineralogy and Petrology, National and Kapodistrian University of Athens, Greece) and T. Reischmann (Max Planck Institute for Chemistry, Mainz, Germany). The mineral chemical analyses were carried out in collaboration with B. Anders. Data interpretation and preparation of the manuscript were done by G. Meinhold.

Chapter 3 discusses possible sources of detrital zircons and fossiliferous olistoliths from Palaeozoic sediments of Chios Island. The chapter is largely identical with the manuscript "Provenance of Palaeozoic sediments during subduction of Palaeotethys: detrital zircon ages and olistolith analysis from Chios Island, Greece", which has been reviewed for publication in *Palaeogeography, Palaeoclimatology, Palaeoecology* with positive advice. The revised version will be submitted with some additional figures in the near future. Co-authors are T. Reischmann (Max Planck Institute for Chemistry, Mainz, Germany), D. Kostopoulos (Department of Mineralogy and Petrology, National and Kapodistrian University of Athens, Greece), O. Lehnert (Institute for Geology and Mineralogy, Erlangen University, Germany), D. Matukov and S. Sergeev (Centre of Isotopic Research, St. Petersburg, Russia). The geochronological analyses were carried out by G. Meinhold and T. Reischmann at VSEGEI in St. Petersburg. Conodont determination and preparation of the Figures 12 and 13 were performed by O. Lehnert. Data interpretation and preparation of the manuscript were done by G. Meinhold.

Chapter 4 discusses possible sources of detrital zircons from metasedimentary rock of previously unknown stratigraphic age from the Serbo-Macedonian Massif. Furthermore, zircons from one meta-igneous rock give hints for magmatic events through Ordovician and Silurian times. The chapter is under consideration to be submitted as manuscript "U–Pb LA-ICPMS zircon geochronology of the Serbo-Macedonian Massif, Greece: Palaeotectonic constraints for Gondwanan-derived terranes in the Eastern Mediterranean" for publication to an international journal in the near future. Co-authors are D. Kostopoulos (Department of Mineralogy and Petrology, National and Kapodistrian University of Athens, Greece), F. Himmerkus (Forschungszentrum Karlsruhe, Eggenstein-Leopoldshafen, Germany), D. Frei (Geological Survey of Denmark and Greenland, Copenhagen, Denmark) and T. Reischmann (Max Planck Institute for Chemistry, Mainz, Germany). The geochronological analyses were carried out by G. Meinhold in collaboration with D. Frei at GEUS in Copenhagen. Data interpretation and preparation of the manuscript were done by G. Meinhold.

Chapter 5 discusses the age and provenance of Mesozoic metasedimentary rocks from the eastern Vardar Zone based on whole-rock geochemistry, mineral chemistry, detrital zircon ages and biostratigraphic data. The chapter is under consideration to be prepared as manuscript "Geochemistry, provenance and stratigraphic age of metasedimentary rocks from the eastern Vardar suture zone, northern Greece" that it can be submitted for publication to an international journal in the near future. Co-authors are D. Kostopoulos (Department of Mineralogy and Petrology, National and Kapodistrian University of Athens, Greece), T. Reischmann (Max Planck Institute for Chemistry, Mainz, Germany) and D. Frei (Geological Survey of Denmark and Greenland, Copenhagen, Denmark). The geochronological analyses were carried out by G. Meinhold in collaboration with D. Frei at GEUS in Copenhagen. Data interpretation and preparation of the manuscript were done by G. Meinhold.

Chapter 6 discusses the age and provenance of Mesozoic metasedimentary rocks from the eastern Circum-Rhodope Belt, Thrace, based on whole-rock geochemical, mineral chemical and detrital zircon age data. The chapter is is under consideration to be prepared as manuscript "Geochemistry and provenance of metasedimentary rocks from the eastern Circum-Rhodope Belt, Thrace, NE Greece" that is can be submitted for publication to an international journal in the near future. Co-authors are D. Kostopoulos (Department of Mineralogy and Petrology, National and Kapodistrian University of Athens, Greece), T. Reischmann (Max Planck Institute for Chemistry, Mainz, Germany) and D. Frei (Geological

Survey of Denmark and Greenland, Copenhagen, Denmark). The geochronological analyses were carried out by G. Meinhold in collaboration with D. Frei at GEUS in Copenhagen. Data interpretation and preparation of the manuscript were done by G. Meinhold.

Chapter 1

Geochemical constraints on the provenance and depositional setting of sedimentary rocks from the islands of Chios, Inousses and Psara, Aegean Sea, Greece: implications for the evolution of Palaeotethys

Abstract

The provenance and depositional setting of Late Palaeozoic and Early Mesozoic clastic sediments from the eastern Aegean archipelago are examined here for the first time using whole-rock geochemistry and composition of detrital chrome spinel. Major- and trace-element data of Late Palaeozoic and Permo-Triassic clastic sediments from the Lower and Upper Units of Chios are compatible with an acidic to intermediate source, minor input of (ultra)basic detritus and recycling of older sedimentary components. Chondrite-normalized REE profiles are uniform with light REE enrichments (La_N/Yb_N ca. 7.7), negative Eu anomalies (Eu/Eu* ca. 0.67) and flat heavy REE patterns (Gd_N/Yb_N ca. 1.5), indicating an upper-continental crustal source and/or young differentiated arc material. Detrital chrome spinel from the clastic sediments of Chios has Cr-number (Cr/(Cr+Al)) values between 0.29 and 0.89 and Mg-number ($Mg/(Mg+Fe^{2+})$) values between 0.24 and 0.70, suggesting a probably mixed (ultra)basic source involving ridge peridotites (mid-ocean ridge type), fore-arc peridotites and island-arc basalts. The metasediments from the islands of Inousses and Psara have similar whole-rock chemical signatures to those of Chios, although no evidence was found for an (ultra)basic source. We conclude that both the Late Palaeozoic sediments from the Lower and Upper Units of Chios and the metasediments from Inousses and Psara were deposited in a continental island-arc setting until at least Late Permian times, probably at a single Palaeotethyan margin. They are interpreted to be allochthonous, tectonically transported to their present position by Late Mesozoic to Cenozoic orogenic processes.

1. Introduction

In the eastern Mediterranean, the Hellenides of Greece and the Pontides, Anatolides and Taurides of Turkey are an integral part of the Alpine-Himalayan orogenic system and have traditionally been subdivided into several geotectonic zones (Fig. 1). Late Palaeozoic and Mesozoic palaeogeographic reconstructions show the existence of two major oceanic realms in the eastern Mediterranean area: the Palaeotethys and the Neotethys (e.g. Stampfli 2000, and references therein). Following Stampfli & Borel (2002), the term Palaeotethys is used here to denote a seaway that separated Gondwana from fragments thereof in a time period from the Silurian to early Late Triassic, during which the same fragments drifted northward and accreted to Laurussia in a stepwise fashion. Palaeotethys was closed by the northward drift of the Cimmerian terranes in response to the opening of Neotethys in the south. Despite the accumulation of new data over recent decades, the Palaeozoic to early Mesozoic history of Palaeotethys is strongly debated (see Robertson et al. 1996; Stampfli 2000; Robertson et al. 2004) because evidence for subduction, in terms of accretionary complexes, blueschists and magmatic arcs, is scarce. Moreover, the complex Mesozoic to Cenozoic structural and metamorphic overprint gave rise to equivocal palaeotectonic models and interpretations.

Chios is a key area for understanding the closure of the Palaeotethys Ocean because it is one of the rare localities where very low-grade to virtually unmetamorphosed fossil-bearing Palaeozoic to Mesozoic sequences are preserved (see Besenecker et al. 1968). A similar succession of Late Palaeozoic age can be found in western Turkey east of Chios in the Karaburun peninsula (Kozur 1998; Robertson & Pickett 2000, and references therein), and in the Tavas nappe (Lycian nappes) further south (Kozur et al. 1998).

Identifying ancient source areas and depositional settings is of fundamental importance for palaeogeographic reconstructions in the Tethyan realm. As far as clastic sediments are concerned, several well-established discriminant diagrams exist based on their petrography, heavy-mineral assemblage and geochemistry (e.g. Dickinson & Suczek 1979; Bhatia 1985; Morton 1985; Bhatia & Crook 1986; McLennan 1989; McLennan et al. 1990, 1993). The Palaeozoic clastic sediments of Chios have already been studied using petrographical and heavy-mineral analyses (Neubauer & Stattegger 1995; Zanchi et al. 2003). These data indicate a recycled-orogen provenance, specifically of an alpine-type continent–

continent collision zone, with minor influence from magmatic-arc sources. The presence of detrital chrome spinel also suggests an ultrabasic source (Stattegger 1984; Neubauer & Stattegger 1995). Compared with Chios, little attention has been paid to its neighbouring islands of Inousses and Psara, where predominantly metasedimentary rocks of previously unknown stratigraphic age and uncertain affiliation occur.

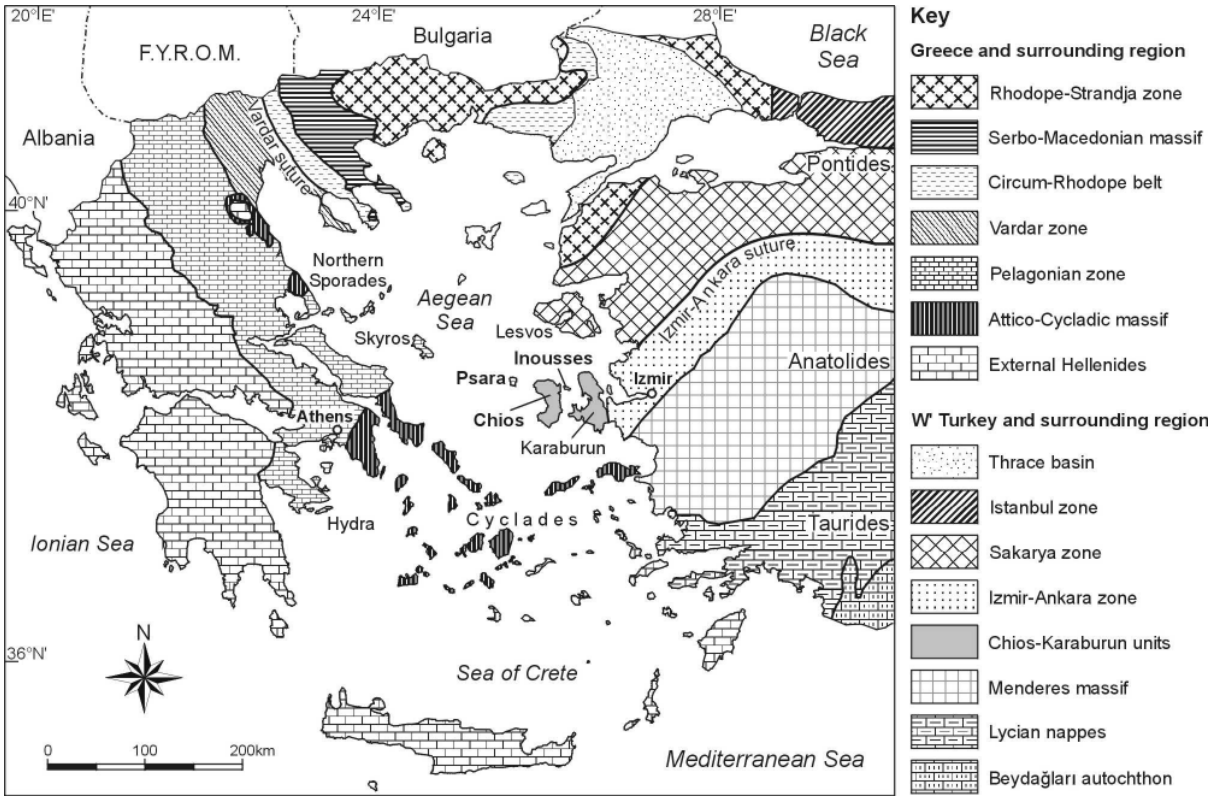

Fig. 1. Simplified map of Greece and western Turkey showing the main geotectonic zones (modified after Jacobshagen 1986; Okay et al. 1994, 2001).

This study focuses on the geochemistry of Late Palaeozoic and Early Mesozoic clastic sediments from the islands of Chios, Inousses and Psara. We present, for the first time, major- and trace-element whole-rock data, supplemented by detrital chrome spinel chemistry, to evaluate their source-rock lithologies and depositional settings. Elements useful for studying marine deposits are those with a short residence time in the ocean water, such as REE, Y, Sc, Th, Ti, Zr, Hf and Nb (Holland 1978; Taylor & McLennan 1985). These elements are transferred quantitatively into clastic sediments without significant interaction with seawater and can preserve the chemical record of their source (e.g. Bhatia & Crook 1986; McLennan 1989; McLennan et al. 1990, 1993). The geochemical data of this study can be used as a base for chemostratigraphic correlations with adjacent areas in Greece and

Turkey. Based on previous publications and our own field and laboratory work we propose new tectonostratigraphic and facies concepts for the sedimentary units of Chios, Inousses, and Psara, which can help to improve our understanding of the Palaeotethyan realm in the eastern Mediterranean region.

2. Geological setting

2.1. Chios

Late Palaeozoic rocks of the Lower Unit. The island of Chios is located in the eastern Aegean Sea, only a few kilometres west of the Karaburun peninsula on the Turkish mainland (Fig. 1). A detailed description of the geology of Chios was given by Besenecker et al. (1968) and Robertson & Pickett (2000). Simplified, Chios can be subdivided into two tectonostratigraphic units (Fig. 2): an 'autochthonous' Lower Unit and a tectonically overlying 'allochthonous' Upper Unit (Herget & Roth 1968; Besenecker et al. 1968). The nappe style of Chios is illustrated in Figure 3. The Lower Unit is commonly assumed to consist of clastic rocks of Late Palaeozoic age containing blocks of up to 100 m in diameter of massive and well-bedded limestones, cherty limestones, radiolarites and volcanic rocks. This succession was variably named 'Chios mélange', 'Chios (wild)flysch' or 'Volissos turbidites' (e.g. Robertson & Pickett 2000; Groves et al. 2003; Zanchi et al. 2003). Here we use the non-descriptive term Late Palaeozoic rocks of the Lower Unit. The major rock types of this unit are greywackes, minor sandstones and siltstones as well as intercalated quartz-bearing conglomerates. The latter mainly contain clasts of quartz, black chert and quartzite embedded in a coarse-grained quartzose matrix. Limestone clasts are very rare. Erosional contacts at the base of greywacke and conglomerate beds and upward reduction in grain size can often be observed. In some outcrops, ripples and well-developed sole marks can be seen at the base of turbidite units. The facies of the turbidite–olistostrome succession resulted mainly from turbidity currents, debris flows and submarine slides. Layers rich in plant fragments can locally be found on bedding surfaces (e.g. at sample localities CH63, CH65 and CH66; see Fig. 2). A biostratigraphic age for these plant fragments has not be obtained as yet because of lack of characteristic features necessary for an accurate age determination (V. Wilde, pers. comm.). However, Broutin (cited by Groves et al. 2003) suggested a Middle–

Late Viséan age for macrofloras from turbidites that occur along Papalia Beach, SW of Sidirounta village (see Fig. 2). Furthermore, Groves et al. (2003) reported Mississippian microfossils from calcareous clasts of a breccia lying within the turbidite-olistostrome succession and suggested that the Late Palaeozoic rocks of the Lower Unit are most probably Late Viséan or Early Serpukhovian in age.

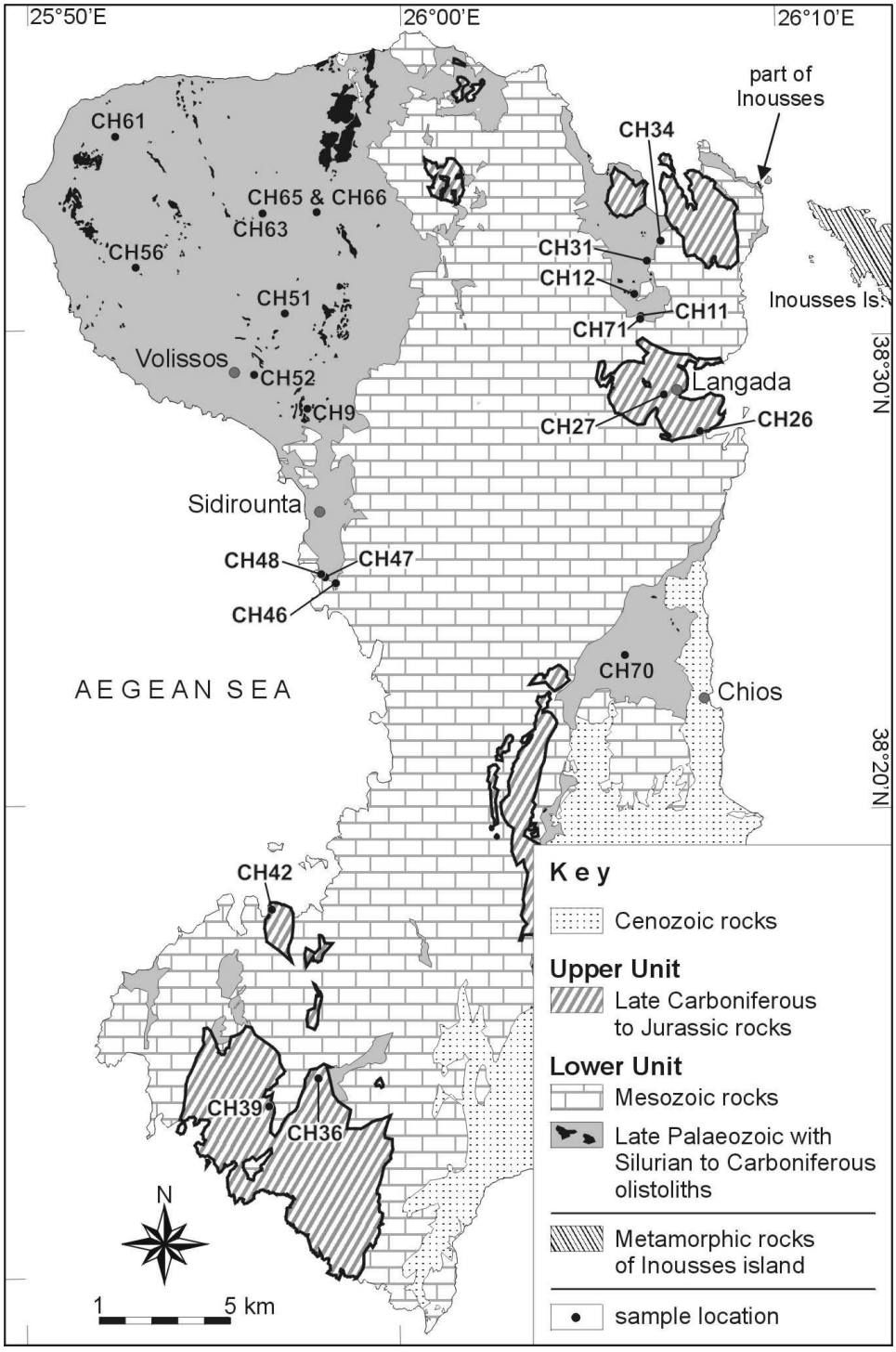

Fig. 2. Geological map of Chios with sample locations (modified after Besenecker et al. 1968, 1971).

The exotic limestone blocks that occur as olistoliths within the Late Palaeozoic rocks of the Lower Unit have been dated as Silurian to Carboniferous in age (Kauffmann 1965; Besenecker et al. 1968; Herget & Roth 1968). Recently, the chert olistoliths (ribbon radiolarites) were examined biostratigraphically by Larghi *et al.* (2005), who found age-diagnostic radiolarians and conodonts in two samples, which allowed them to establish Late Silurian (probably Přidolian) and Late Devonian (Famennian) ages, whereas only a more general age range from Devonian to Early(?) Carboniferous could be proposed for the remainder. The olistoliths essentially define four olistostrome formations with a very clear predominance of younger blocks (Early Carboniferous) in the lower formation and of older blocks (Silurian) in the upper formation (Papanikolaou & Sideris 1983; Sideris 1989).

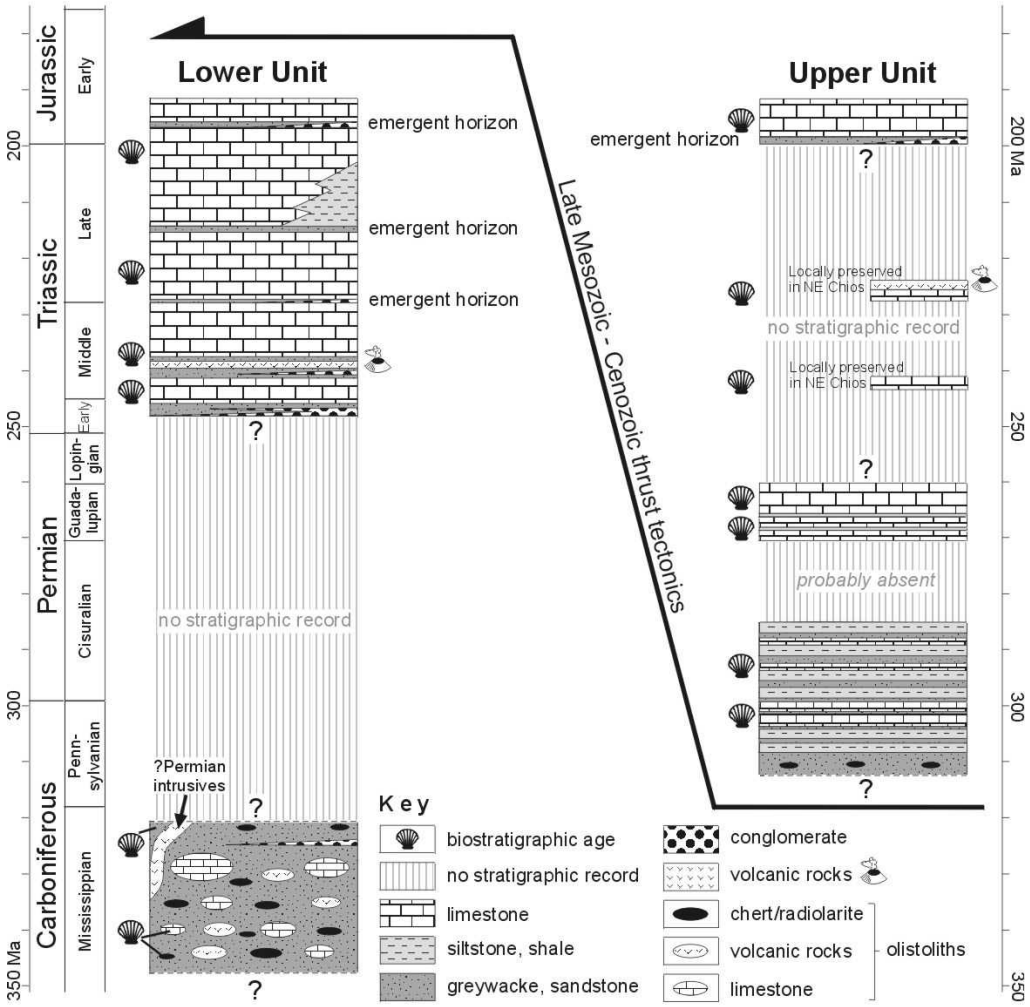

Fig. 3. Tectonostratigraphic columns for Palaeozoic and Mesozoic rocks of Chios. Compiled using data from Besenecker et al. (1968), Kauffmann (1969), Pe-Piper & Kotopouli (1994), Groves et al. (2003) and Zanchi et al. (2003). Geological time scale according to Gradstein et al. (2004).

The volcanic rocks (basic, intermediate and acid in composition) were studied in detail by Pe-Piper & Kotopouli (1994), who found clear evidence that at least some of the volcanic rocks intruded the deformed Palaeozoic clastic succession and therefore cannot be olistoliths. They suggested that these volcanic rocks probably formed in a back-arc setting above a subducting Palaeotethyan oceanic slab and correlated them with Early Permian granodiorites of the Karakaya Complex in Turkey.

Several tectonic models have been proposed for the origin of the Late Palaeozoic rocks of the Lower Unit. Papanikolaou & Sideris (1983) interpreted this unit as a post-Middle Carboniferous to pre-Scythian wildflysch bearing Silurian to Carboniferous olistoliths, and compared it with the Late Permian to Scythian rocks of Attica. Stampfli et al. (1991) proposed that the wildflysch represents a mainly Permian accretionary wedge that can be correlated with the Karakaya Complex of Turkey, which they considered to mark a Palaeotethyan suture. Robertson & Pickett (2000) maintained that the Late Palaeozoic rocks of the Lower Unit are a Late Carboniferous to ?Early Permian subduction–accretionary complex that developed near the southern margin of the Palaeotethys Ocean. Models invoking a rift setting or a long-lived, deep marine basin receiving olistoliths are also discussed by Robertson & Pickett (2000). Recently, Stampfli et al. (2003) and Zanchi et al. (2003) proposed a tectonic model of an arc–trench system that formed along the Palaeotethyan subduction zone in Carboniferous times.

Permo-Triassic and younger rocks of the Lower Unit. The Late Palaeozoic rocks of the Lower Unit are overlain by non-fossiliferous conglomerates and sandstones (Besenecker *et al.* 1968) (Fig. 3). The conglomerates mainly contain clasts of quartz and black chert embedded in a coarse-grained quartzose matrix. Zanchi et al. (2003) described an angular unconformity at the base of this clastic succession, interpreted as a Variscan unconformity. However, the stratigraphic age of these possibly Early Triassic conglomerates and sandstones is uncertain because no biostratigraphic and only few geochronological ages exist so far. The youngest detrital zircon age is 326 Ma (Meinhold et al. 2006), thus giving a maximum age for deposition. Although a Pennsylvanian sedimentation age cannot be excluded, the rounded shape of the youngest detrital zircon rather indicates a Permian sedimentation age for the conglomerates and sandstones, as has already been mentioned by Besenecker et al. (1968). Therefore, in the following discussion we use the term Permo-Triassic instead of Early

Triassic. The conglomerates and sandstones pass upwards into well-bedded limestones of late Early Triassic age, followed by massive limestones that themselves interfinger with reddish ammonoid-bearing limestones of Hallstatt type in their upper parts (Besenecker et al. 1968). This sequence is overlain by a Middle Triassic (Anisian–?Carnian) volcano-sedimentary succession consisting of red to purple shales, radiolarites and tuffitic horizons (Besenecker et al. 1968; Gaetani et al. 1992), followed by well-bedded marly limestones of probably Late Anisian age and limestones of Ladinian to Rhaetian–Liassic age that are more than 1000 m thick (Besenecker et al. 1968). Few clastic intercalations (emergent horizons, Fig. 3) occur within the Ladinian–Liassic limestones. The latest Triassic–earliest Jurassic is marked by non-marine clastic deposits followed by well-bedded dolomites and limestones. Late Jurassic limestones (Cladocoropsis limestones) are only known from Venetiko near the southernmost cape of Chios (Besenecker et al. 1968). The youngest rocks on Chios are Cenozoic sediments and volcanic rocks cropping out mainly in the south-eastern part of the island.

Permo-Carboniferous and younger rocks of the Upper Unit. The Upper Unit of Chios (Figs. 2 and 3) belongs to the allochthonous nappe *sensu* Besenecker et al. (1968). Lithostratigraphically, its lowermost part consists of quartzose greywackes, sandstones and minor siltstones of Late Carboniferous age occasionally containing lenses of black and greenish chert a few meters in size. One of these lenses, sampled near Mesta village in SW Chios (38°14’49’’N, 25°54’48’’E), yielded poorly preserved radiolaria (Entactinaria; A. Braun, pers. comm.) which are of only low stratigraphic significance. Layers rich in plant fossils can be found on the bedding surfaces of siltstones and fine-grained sandstones (e.g. near Langada village; see Fig. 2). Unfortunately, no biostratigrapic age could be obtained for these plant fragments because of the lack of characteristic features for an accurate determination (V. Wilde, pers. comm.). Fossil-bearing limestones of Late Carboniferous age are overlain by a clastic carbonaceous succession of Early Permian age (Kauffmann 1969). The Middle Permian is represented by fossiliferous carbonate sequences containing numerous Gymnocodiacae algae and fusulinid foraminifera of genus *Verbeekina* (e.g. Besenecker et al. 1968; Flajs et al. 1996; Angiolini et al. 2005). Rocks of Late Permian age are absent. Recently, Angiolini et al. (2005) carried out a palaeobiogeographical analysis of limestones from the Middle Permian succession. On the basis of the brachiopod fauna identified, Angiolini et al. (2005) suggested that the Middle Permian rocks of the Upper Unit have a

Gondwanan affinity, in marked contrast to the interpretation of Zanchi et al. (2003), who proposed a Laurasian affinity for the Late Palaeozoic rocks of the Lower Unit. Nevertheless, a Middle Permian fossil assemblage similar to that found on Chios was described by Altiner et al. (2000) from the northern Taurides and ascribed to a distinct 'Northern Biofacies Belt'.

Papanikolaou & Sideris (1983; cited by Sideris 1989) advocated that the Late Carboniferous to Early Permian flysch-type sequence changed to a shallow-water marine carbonate platform during Middle to Late Permian times. The Permian limestones are overlain by transgressive sediments of Early Jurassic age, starting with red conglomerates, sandstones and siltstones and passing upwards into thick-bedded limestones (Dachstein-type with bivalvia Megalodontidae) and minor dolomites (Besenecker et al. 1968). This sequence is locally overlain by transgressive Upper Cretaceous sediments. Within the Upper Unit, Triassic rocks are only locally preserved in the northeastern part of Chios, where red Anisian limestones, Carnian limestones and volcanic tuffs occur (Besenecker et al. 1968).

Besenecker et al. (1968) and Robertson & Pickett (2000) have mentioned that the stratigraphy of the Lower Unit differs markedly from that of the Upper Unit of Chios. The Upper Unit was considered by Robertson & Pickett (2000) to be 'exotic'. However, a characteristic feature in both units is a (?Late Triassic–)Early Jurassic unconformity. The Chios and Karaburun Units show strong affinities with the Pelagonian domain from Carboniferous to Late Triassic times; they also show strong affinities with the western Taurides during Late Triassic–Early Jurassic times (Rosselet & Stampfli 2003). This might explain the ongoing controversy on whether Chios is tectonostratigraphically affiliated to units in Greece or in Turkey.

For example, Chios has been correlated with the Vardar (Axios) Zone and the Circum-Rhodope Belt of northern Greece (Papanikolaou 1984, fig. 1) but it has also been shown to be part of the Lycian nappes of Turkey (e.g. Ring et al. 1999b, fig. 1). However, the thick succession of Triassic rocks of the Lower Unit shows clear affinities to the Pelagonian Zone of mainland Greece (Besenecker et al. 1968; Gaetani et al. 1992), whereas the Upper Unit can be correlated with the autochthonous 'basement' of Lesvos to the north (e.g. Papanikolaou 1997; Robertson & Pickett 2000) that was assigned to the Paikon Unit of the Vardar Zone (Papanikolaou 1997). The Mesozoic platform of Chios and Karaburun was interpreted by Robertson & Pickett (2000) as part of a Mesozoic, northerly Neotethyan,

oceanic basin bordering the Tauride–Anatolide Platform and the Menderes Metamorphic Massif to the south. All these equivocal interpretations illustrate the need to revisit Chios.

2.2. Inousses

Inousses (Figs. 1 and 4) and its surrounding islets are located between Chios to the west and the Karaburun peninsula to the east. In NE Chios, metamorphic rocks crop out in a small area (ca. 250 m × 280 m) which supposedly belongs to the metamorphic complex of Inousses (Kauffmann 1965; Besenecker et al. 1968, 1971). The contact between the metamorphic rocks and their overlying very low-grade to unmetamorphosed rocks is marked by a moderately steep, SW-dipping fault (Kauffmann 1965). Inousses itself consists of a flysch-like sequence comprising light grey quartzose metaconglomerates, fine-grained grey metapsammites, grey to dark grey pyrite-bearing metapelites (phyllites), pyrite-bearing greyish quartz-micaschists, and grey to dark grey platy marble layers or lenses (Kilias 1987).

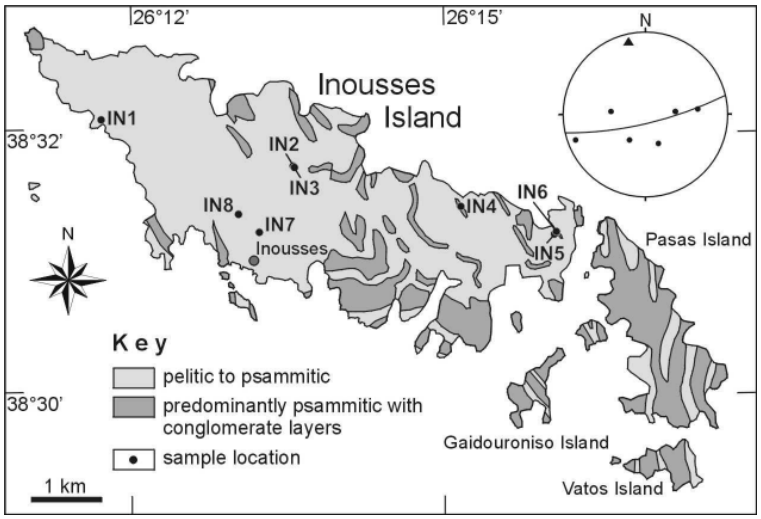

Fig. 4. Geological map of Inousses with sample locations (modified after Besenecker et al. 1971). The inset (upper right) shows poles of bedding planes (black dots) lying on a great circle defining a mean fold axis (triangle).

Within the metasandstones and metagreywackes pyrite cubes with a crystal size ranging from a few millimetres to 1.5 cm can frequently be found. According to Besenecker et al. (1968, 1971) and our own field observations, the metasedimentary succession of Inousses can be lithostratigraphically subdivided into a lower and an upper part. The lower part is exposed in the centre and the south of the island, where medium- to coarse-grained metasediments including light grey metasandstones and metagreywackes with intercalations of light grey to greenish grey conglomerate layers predominantly occur; these pass upwards

into medium- to very fine-grained metasediments including argillaceous metagreywackes and dark grey to black metapelites (phyllites). This lithostratigraphically upper part crops out mainly in the north and NW part of the island. The main structural feature on Inousses is multiple folding with two axial trends (Kilias 1987; see Zanchi et al. 2003). The major foliation is folded with gently to NNW-dipping fold axes.

In general, the monotonous character of the sedimentary succession, the lack of fossils and radiometric data and the greenschist-facies metamorphic overprint complicate its stratigraphic affiliation. Besenecker et al. (1968) assumed that the epimetamorphic flysch sequence of Inousses is older than the Palaeozoic of the autochthonous Lower Unit of Chios and thus forms its metamorphic basement. Mountrakis et al. (1983) correlated the Inousses metamorphic rocks with the Permian–Early Triassic metasediments of the western margin of the Pelagonian Zone of continental Greece and those of the Sporades. Kilias (1987) also assumed an affiliation of the Inousses metamorphic rocks to the Pelagonian nappes. All this contradicts the interpretation of Kozur (1998), who compared the metasediments of Inousses with the monotonous siliciclastic Küçükbahçe Formation of the Karaburun peninsula of probable Ordovician (or Cambro-Ordovician) age (Kozur 1998).

2.3. Psara

Psara is located ca. 20 km west of Chios in the Aegean Sea (Fig. 1). Wallbrecher (cited by Dürr & Jacobshagen 1986) distinguished three units on Psara. In the southern and central part of the island very low-grade metamorphic slates, phyllites and greenschists interlayered with quartzites and metagreywackes occur. They are tectonically overlain by garnet-bearing micaschists and gneisses, in turn tectonically overlain by a marble unit ca. 300 m thick. However, our field analysis showed only a Lower Unit and a tectonically overlying Upper Unit (Fig. 5a). The nappe style of Psara is illustrated in Figure 5b. The Lower Unit consists of dark grey metapelites (phyllites), metasandstones and metagreywackes that were intruded by basic rocks (now greenschists). An intrusive contact with the country rocks could be observed along a fresh road cut north of Agios Ioannis (Fig. 5a). Some metasediments have minor carbonate content. The major foliation strikes approximately north–south and dips steeply either towards the east or the west (Fig. 5a). The Upper Unit of Psara mainly comprises mica schists (with garnets up to 0.8 cm in diameter) intercalated with calcschists

and marble layers that pass up into pure marbles at the top. The predominant foliation dips mostly to the south and is folded with fold axes dipping gently to the east or west. Unfortunately, in both units neither fossils nor radiometric data are yet available, thus complicating their stratigraphic affiliation. Cenozoic volcanic rocks crop out in the northwestern and central part of Psara.

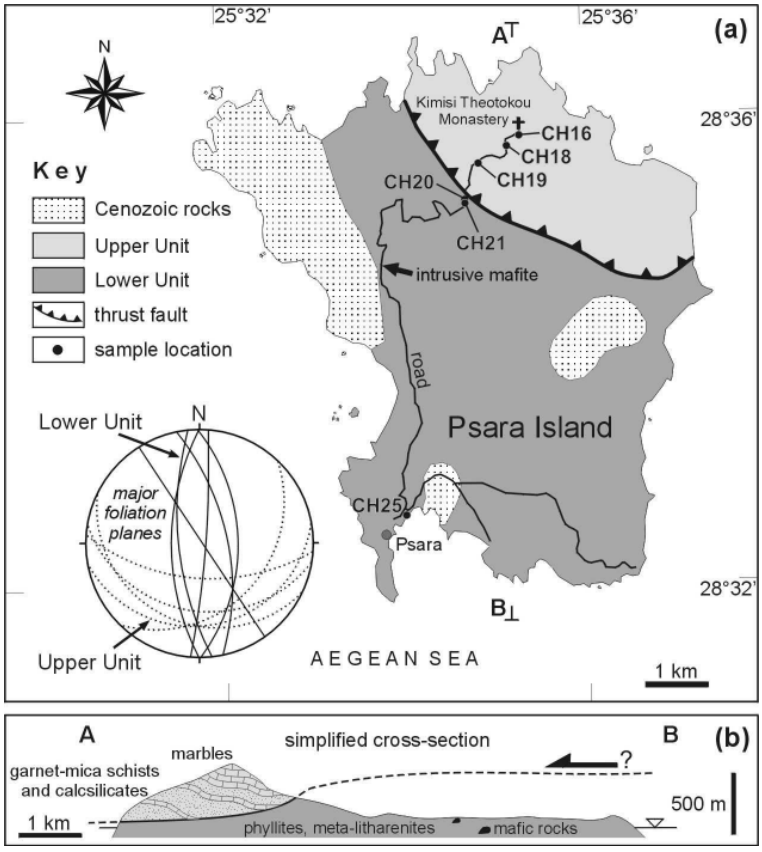

Fig. 5. (a) Geological map of Psara with sample locations, adapted after the IGME geological map of Greece (IGME 1983). The inset (lower left) shows a stereographic equal area plot of the major foliation planes. **(b)** The simplified cross-section illustrates the nappe pile of Psara (this study).

The tectonostratigraphic affiliation of Psara to units in Greece is undecided. Mountrakis et al. (1983) correlated both units of Psara with the Subpelagonian Zone of continental Greece, whereas Wallbrecher (cited by Dürr & Jacobshagen 1986) favoured an affiliation to successions from the southern Pelion peninsula and the northern Sporades of the Pelagonian Zone. Taken together with Chios and Inousses, all these equivocal interpretations suggested that a reinvestigation of the (meta)sedimentary successions in the eastern Aegean Sea would be worthwhile.

3. Sample description and methods

A total of 35 siliciclastic sediments including greywackes and sandstones, minor siltstones, phyllites and micaschists were collected from Chios, Inousses and Psara for whole-rock geochemical analyses (major and trace elements) and detrital chrome spinel microprobe analyses. The stratigraphic affiliation of the samples from Chios is based on work by Besenecker et al. (1968, 1971). Sample localities for Chios, Inousses and Psara are shown in Figures 2, 4 and 5a, respectively. Ages, lithologies, localities (including geographic coordinates), whole-rock chemical data and the mineral chemical data for the detrital chrome spinels referred to in this chapter are included in the Appendix.

3.1. Sample description

Chios. Petrographically, the clastic sediments of Late Palaeozoic age from the Lower and Upper Units of Chios have similar framework grains in varying amounts, consisting of monocrystalline and polycrystalline quartz, sedimentary and volcanic lithoclasts. Feldspar grains are common and always present. Plagioclase (mainly albite) is by far the most abundant feldspar, whereas K-feldspar is rare. Plagioclase grains often display patchy sericitization and replacement by calcite. Single muscovite flakes and minor detrital biotite also occur. Interestingly, few grains showing myrmekitic texture were found in the Late Palaeozoic greywacke sample CH39. The polycrystalline quartz grains have irregular subgrain boundaries typical of their metamorphic origin. The sedimentary lithoclasts consist of phyllites, radiolarian chert and quartz-rich, low-grade metasedimentary rock fragments. Calcite clasts are rare in the Late Palaeozoic greywackes from the Lower Unit but common in the Permo-Carboniferous from the Upper Unit. The volcanic lithoclasts are mainly acidic in composition. The few basic lithoclasts are often strongly altered (e.g. in sample CH26). All psammites are poorly sorted by size and dominated by angular to subangular clasts. This feature, together with the abundant unstable lithoclasts, indicate that the clasts were rapidly eroded and deposited without significant rounding or sorting, which is one of the characteristics of many greywackes transported by turbidity currents (see Pettijohn et al. 1972). The occurrence of iron hydroxides in some samples indicates secondary alteration

processes. Accessory minerals include clay minerals, micas, opaque minerals, chlorite and heavy minerals, dominantly zircon, tourmaline and rutile, minor chrome spinel and epidote.

Inousses. The framework grains of the psammites from Inousses are mainly monocrystalline and polycrystalline quartz, sedimentary and altered volcanic lithoclasts, minor muscovite flakes, feldspar and detrital biotite. The latter is commonly strongly altered. In some samples the quartz grains are almost elongated and sigmoid-shaped, indicating that they were deformed at a temperature higher than ca. 300°C depending on strain rate, differential stress and the presence of water (Passchier & Trouw 2005). Feldspar grains often display patchy sericitization. All psammites are poorly sorted by size and dominated by angular to subangular clasts. A few grains are also subrounded to rounded. The psammites are clast-supported with a quartzose–sericitic matrix. Accessory minerals include clay minerals and micas but also heavy minerals, such as zircon, tourmaline, opaque minerals and epidote.

Psara. The framework grains of psammite sample CH25 from the Lower Unit of Psara are mainly monocrystalline and polycrystalline quartz, minor muscovite and twinned plagioclase grains. The psammite is poorly sorted by size and dominated by angular to subangular clasts. Iron hydroxides are common, indicating secondary alteration processes. The mica schists from the Upper Unit are mainly composed of quartz, muscovite, biotite, garnet and chlorite. Altered plagioclase grains ($Ab_{70-86}An_{13-30}Or_{0-2}$) have also been found in small amounts. Aluminosilicates were not observed. Garnet ($Alm_{63-65}Grs_{21-26}Prp_{6-11}Sps_{2-6}$) forms porphyroblasts, up to 0.8 cm in diameter, which are strongly fractured. Biotite is often replaced by chlorite. Zircon, tourmaline and ilmenite are accessory minerals. The assemblage quartz–muscovite–chlorite–garnet–biotite suggests mid-upper greenschist facies metamorphic conditions (garnet-zone metapelites; ca. 450°C at low pressures).

3.2. Whole-rock geochemistry

The composition of clastic sediments is controlled by the lithology of their source area(s), weathering, transport and sorting, redox environment and diagenesis (Johnsson 1993). Commonly, the original composition and mineralogy of a rock is changed during

metamorphism by metamorphic mineral reactions. Petrographical analysis for provenance studies of metamorphosed sediments is therefore not applicable. However, if the whole-rock geochemistry is not significantly modified by secondary processes it can be used to fingerprint the provenance and depositional setting of metasedimentary rocks. In general, the alkali and alkaline-earth elements can be strongly fractionated by weathering and diagenesis (e.g. Nesbitt et al. 1980), making them liable to movement and redistribution, and thus influencing the geochemical composition of the sediment. Therefore, discrimination diagrams using such elements must be treated with caution. Immobile trace elements are expected to be more useful in studying sedimentary provenance and depositional setting than major elements (e.g. Bhatia & Crook 1986; McLennan 1989; McLennan et al. 1990, 1993). The REE in particular are best suited for such studies, because of their relative immobility during weathering, transport, diagenesis and metamorphism (e.g. McLennan 1989). In some cases, however, fractionation and mobilisation may occur as a result of source-rock weathering and diagenesis (e.g. Nesbitt 1979; Nesbitt et al. 1990; Milodowski & Zalasiewicz 1991).

The studied samples from Chios, Inousses and the Lower Unit of Psara are virtually unmetamorphosed or have undergone only a very low-grade metamorphic overprint. Significant element mobilisation can be excluded (apart from volatile phases). The mica schists from the Upper Unit of Psara, however, show evidence of Barrovian-type, low-grade metamorphism which might have influenced their primary geochemical signature. In this study, with the exception of a few major-element fingerprints, we have used only relatively immobile trace elements and REE for the characterization of sedimentary provenance and depositional setting.

Analytical procedures. For geochemical analyses, the samples were crushed into small pieces and then powdered using an agate mill. Sample powder was mixed with lithium tetraborate (1:7) and fused in platinum crucibles at ca. 1200°C to prepare fused discs. Major-element data were determined by X-ray fluorescence (XRF) on fused discs at the Institut für Geowissenschaften, Mainz, Germany, using a Philips MagiX Pro X-ray spectrometer equipped with an Rh-anode tube. Selected trace elements were analysed using the same analytical equipment but measured on pressed powder pellets. Relative errors on major and trace elements are usually <2% and <5%, respectively. Loss on ignition (LOI) was

determined gravimetrically by heating the samples to 1000°C. Total iron is expressed as Fe_2O_3.

REE, Hf, Ta, Th, and U were analysed at the Department of Afdeling Fysico-Chemische Geologie, Katholieke Universiteit Leuven, Belgium. The analytical procedures followed are those described in Mareels (2004). Sample powder (0.2 g) was mixed with 1 g of lithium metaborate, homogenized and fused in a graphite crucible for 10 min at 1050 °C in a laboratory furnace. The molten samples were dissolved in HNO_3 and homogenised. After homogenization, quantitative REE hydroxide precipitation by Fe(III)-hydroxide scavenging was performed for each sample. After finishing the precipitation steps, 1 ml of each of In and Re mono-elemental solutions were added to the sample solutions to serve as internal monitors during measurements. Samples, blanks and standards (USGS rocks) were analysed using a Hewlett-Packard 4500 quadrupole inductively-coupled plasma mass spectrometer (ICP-MS) coupled to a Cetac 500SX sample changer. All measurements were corrected for instrumental drift using the peak intensities of the ^{115}In and ^{185}Re internal monitors. Accuracy was better than 10% for all analysed elements.

The REE data were normalized against both PAAS (Post-Archaean Australian Shale; values from McLennan 1989) and C1-chondrite (values from Taylor & McLennan 1985). In addition to the PAAS- and chondrite-normalized REE patterns, the normalized Eu anomaly (Eu/Eu*) also serves as a useful discriminant between samples and between plate-tectonic settings (e.g. Bhatia 1985; McLennan 1989; McLennan et al. 1990), where Eu* is a theoretical Eu concentration calculated by interpolation between Sm and Gd. The Eu anomaly was calculated according to McLennan (1989): $Eu/Eu^* = Eu_N/(Sm_N \times Gd_N)^{0.5}$, where the subscript N denotes chondrite-normalized values. Values of Eu/Eu*>1 are considered to be positive, whereas values <1 are considered to be negative (McLennan et al. 1990).

3.3. Mineral chemistry

Detrital chrome spinel compositions were determined on polished thin sections and on polished heavy mineral separates. To prepare the latter, samples were crushed using a hydraulic press and a rotary mill, then processed using a Wilfley table, a Frantz isodynamic magnetic separator and heavy liquids (methylene iodide). The heavy mineral fractions thus

obtained were mounted in epoxy resin, sectioned and polished. Mineral analyses were carried out using a Jeol JXA 8900 RL electron microprobe at the University of Mainz, Germany, operated at an accelerating voltage of 20 kV and a beam current of 12 nA, with a beam diameter of 2 µm. Following common practice for chrome spinel interpretation, the Cr-number (Cr – number = Cr/(Cr+Al)) and Mg-number (Mg – number = Mg/(Mg+Fe^{2+})) for each analysis were calculated assuming stoichiometry (e.g. Dick & Bullen 1984; Cookenboo et al. 1997; Barnes & Roeder 2001; Kamenetsky et al. 2001).

4. Geochemical results

4.1. Chemical classification

Because many discrimination diagrams for identifying source-area lithologies and tectonic settings of sedimentary rocks yield different results for psammitic and pelitic protoliths (as a result of, e.g. sorting effects), a differentiation between psammitic and pelitic sediments was deemed necessary. In this study, pelites include very fine-grained sediments such as shales and siltstones, whereas psammites include medium- to coarse-grained clastic sediments like litharenites, sublitharenites and sandstones. Various classification schemes for clastic sediments based on whole-rock chemical data have been established (e.g. Pettijohn et al. 1972; Herron 1988, and references therein). Figure 6 shows the classification diagram of Herron (1988), which distinguishes between different lithologies according to their logarithmic ratios of SiO_2/Al_2O_3 vs. Fe_2O_3/K_2O. The SiO_2/Al_2O_3 ratio distinguishes between quartz-rich (high ratios) and clay-rich (low ratios) sediments. SiO_2 reflects the content of quartz and Al_2O_3 that of clay minerals. With an increasing SiO_2/Al_2O_3 ratio the grain size also increases, as do the grade of recycling and the maturity of the sediment. The Fe_2O_3/K_2O ratio is used as an indicator of mineralogical stability and distinguishes lithic fragments from feldspar (Herron 1988). Most of the analysed sediments are classified as unstable immature wackes (i.e. greywackes) and litharenites because of their quartz and lithic contents; two samples are classified as sublitharenites and nine as shales (Fig. 6). The geochemical classification is broadly coincident with the petrographical observations.

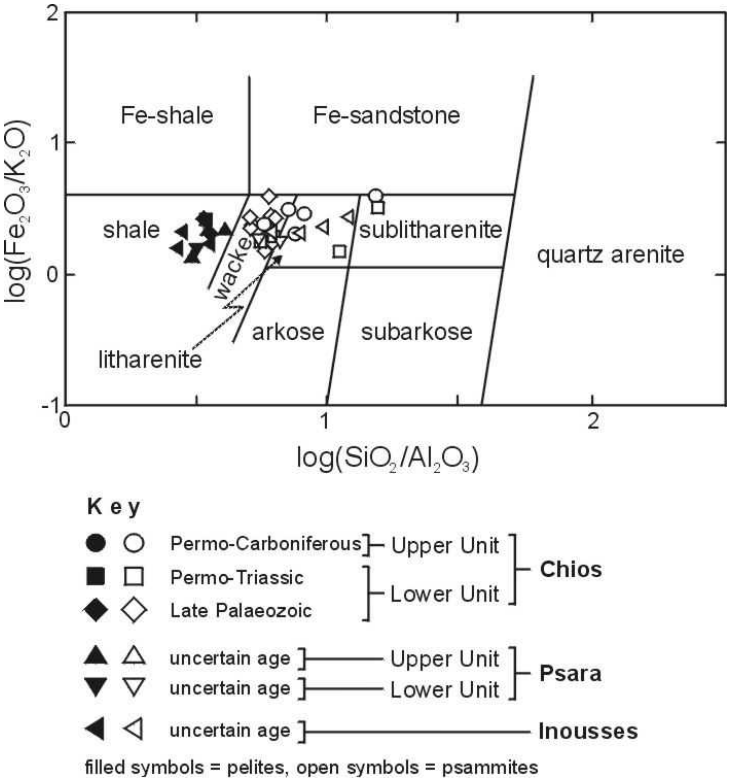

Fig. 6. Chemical classification scheme for terrigenous clastic sediments after Herron (1988).

4.2. Mineral controls on whole-rock geochemistry

Figure 7 shows some bivariate diagrams to identify mineral controls on whole-rock geochemistry. The strong positive linear correlations between K_2O and Rb with Al_2O_3 (Fig. 7a and b) suggest that both K and Rb reside in phyllosilicates. Inasmuch as pelites are more enriched in clay minerals and/or micas than psammites, they occupy distinct fields in Figure 7a and b, except for two pelite samples with a high carbonate content that plot in the field of psammites. The clastic sediments from the Late Palaeozoic rocks of the Lower Unit of Chios and from Inousses are characterized by very low CaO contents (<1.7 wt.%), whereas samples from the Upper Unit and the Permo-Triassic of Chios, as well as the garnet–mica schists of Psara generally have much higher CaO contents (Fig. 7c). CaO is mainly bound in carbonates as indicated by the positive correlation between CaO and LOI (Fig. 7d). Most samples show a positive linear correlation between Cr and Al_2O_3 (Fig. 7e), suggesting that the Cr content is controlled by Cr-bearing aluminous phases such as clay minerals. A lack of correlation might be indicative of the presence of Cr-bearing accessory oxide minerals such as chrome spinel. Total REE contents correlate negatively with SiO_2 and positively with Al_2O_3, K_2O, TiO_2, and

Nb (diagrams not shown), indicating that the REE are controlled by various amounts of phyllosilicate minerals and rutile (as carrier of Ti and Nb). The less pronounced positive correlation between total REE and Zr suggests that the heavy mineral zircon has minor influence on total REE contents, probably because it is largely controlled by irregular distribution during sedimentation.

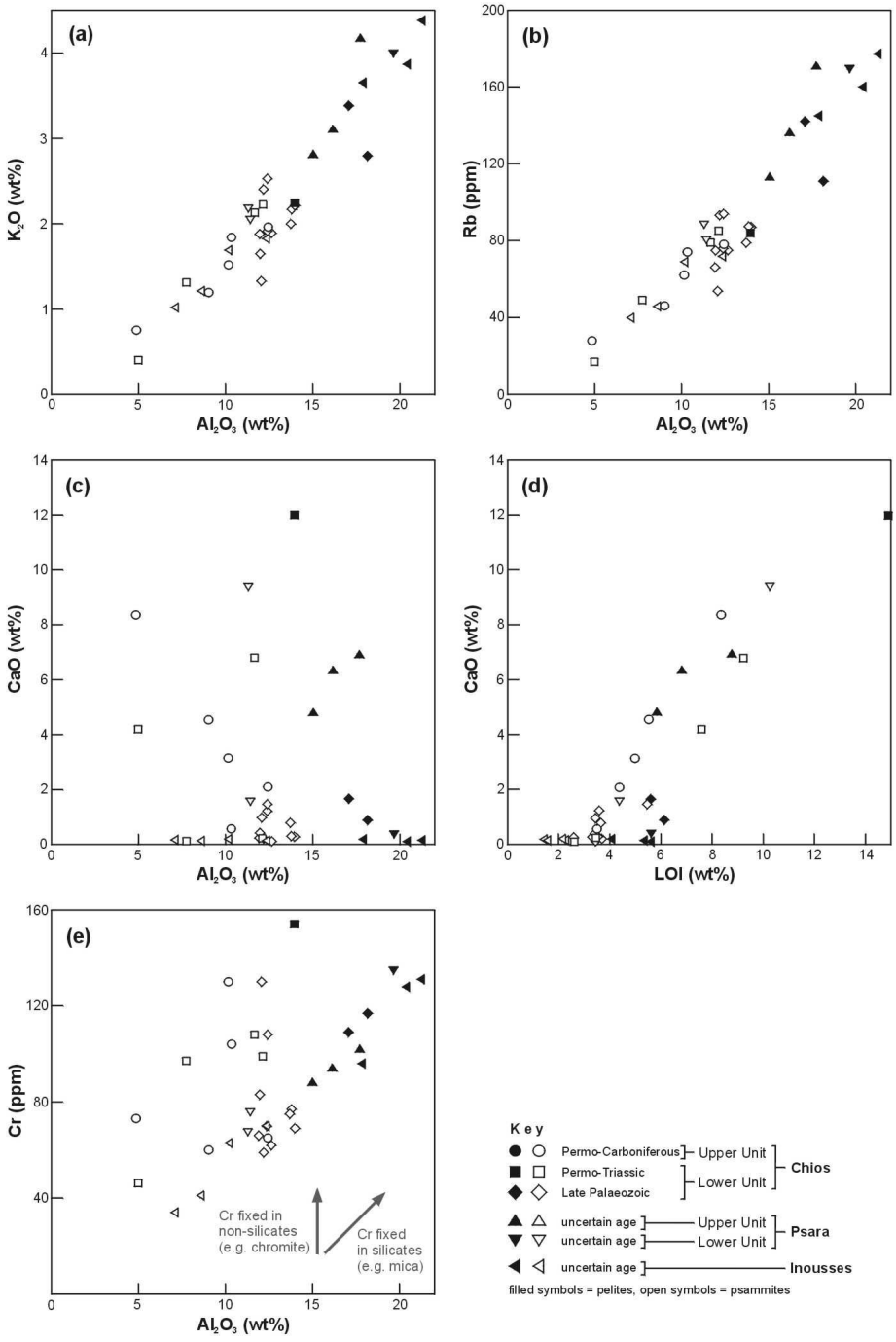

Fig. 7. Correlation diagrams of K, Rb, Ca and Cr vs. Al_2O_3 and Ca vs. LOI for clastic sediments of Chios, Inousses and Psara.

4.3. Weathering and sediment recycling

Figure 8a shows the Th/U vs. Th plot of McLennan et al. (1993). In contrast to Th, U is easily mobilized during weathering and sedimentary recycling, resulting in an increase of the Th/U ratio. Although highly reduced sedimentary environments can be enriched in U leading to low Th/U ratios, weathering favours the oxidation of insoluble U^{4+} to soluble U^{6+} with subsequent loss of U to solution and elevation of Th/U ratios (McLennan & Taylor 1980, 1991; McLennan et al. 1990). Upper crustal rocks have a Th/U ratio averaging around 3.8 (Taylor & McLennan 1985). The Th/U ratios of all studied sediments are ca. 2–6, with the exception of one garnet–mica schist from the Upper Unit of Psara (Fig. 8a).

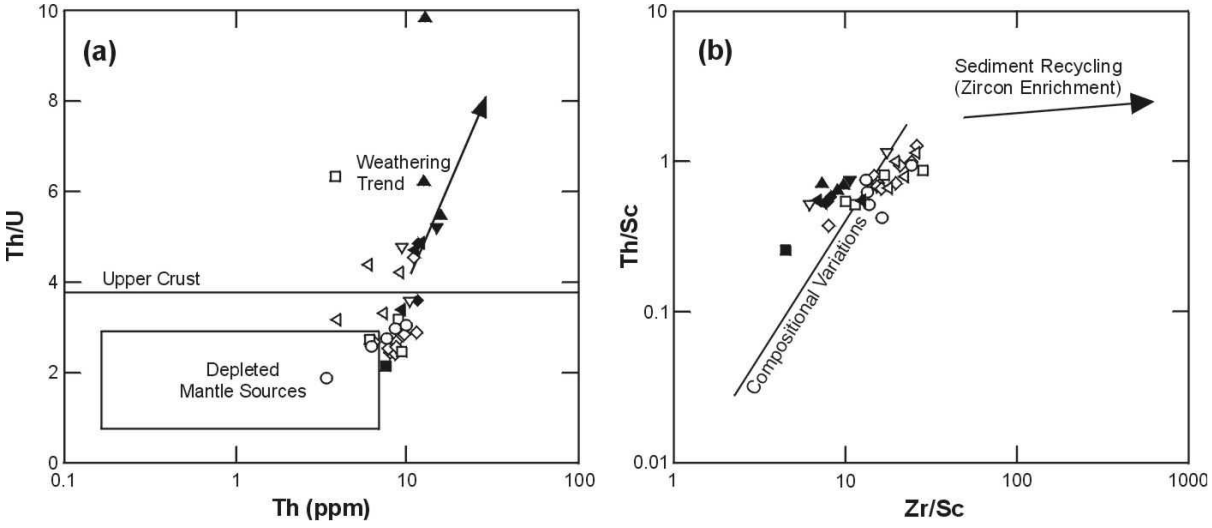

Fig. 8. Discrimination diagrams illustrating weathering and sediment recycling. **(a)** Th/U vs. Th diagram after McLennan et al. (1993). **(b)** Th/Sc vs. Zr/Sc diagram after McLennan *et al.* (1993).

Considering that, on average, the Th/U ratio of most psammites here lies below the value for the upper continental crust (UCC), it is likely that these sediments were derived from source rocks with the least weathering and/or from material with the least recycling. In contrast, the pelites (and very few psammites) follow the normal weathering trend. One psammite from the Late Palaeozoic rocks of the Lower Unit, two Permo-Triassic psammites and one psammite from the Upper Unit of Chios lie in the field of depleted mantle sources. Their source rocks were probably non-recycled arc magmatic rocks that have undergone a minimal degree of weathering.

The compositional variation and the degree of sediment reworking and heavy mineral sorting can be illustrated in a plot of Th/Sc vs. Zr/Sc (McLennan et al. 1993). A positive linear correlation between the two ratios expresses the igneous differentiation trend. The Th/Sc ratio of sedimentary rocks characterizes the average provenance, whereas an increase in the Zr/Sc ratio alone indicates significant sediment reworking, consistent with zircon enrichment (McLennan et al. 1993). The Zr/Sc ratios are smaller for pelites than for psammites (Fig. 8b), suggesting concentration of zircon in the coarser fraction. All sediments have undergone minor degree of weathering and no significant sediment recycling.

4.4. Provenance

Figure 9 summarises various diagrams for sedimentary provenance. Roser & Korsch (1988) reported discriminant functions (DFs) for sedimentary provenance using major-element ratios (Fig. 9a). In one sample (CH34), the Al_2O_3 content is very low, resulting in a DF2 value of about 19. For illustration purposes, this sample has been plotted at 10 on the *y*-axis of Figure 9a. All data lie mainly in the field of quartzose sedimentary provenance and close to or in the field of intermediate igneous provenance. Only one sample from the Upper Unit of Chios lies in the field of basic igneous provenance.

Floyd & Leveridge (1987) established a discrimination diagram using the La/Th ratio vs. Hf to determine different arc compositions and sources (Fig. 9b). Apart from one metapsammite from Inousses that plots near the andesitic arc source field, uniform low La/Th ratios (<5) and Hf contents of about 3.2–7.8 ppm for all the sediments studied here suggest derivation predominantly from an acidic arc source and the minor influence of an old sediment component.

Figure 9c is a plot of Cr/V vs. Y/Ni that illustrates the importance of ophiolitic provenance (McLennan et al. 1993). The Cr/V ratio monitors the enrichment of Cr over other ferromagnesian trace elements, whereas the Y/Ni ratio shows the general level of ferromagnesian trace elements (Ni) compared with Y, which is used as a proxy for the heavy REE (McLennan et al. 1993). Basic–ultrabasic sources tend to have higher Cr/V and lower Y/Ni ratios. Only one Permo-Triassic psammite from the Lower Unit and one Permo-Carboniferous psammite from the Upper Unit of Chios tend towards an ophiolitic source (Fig. 9c).

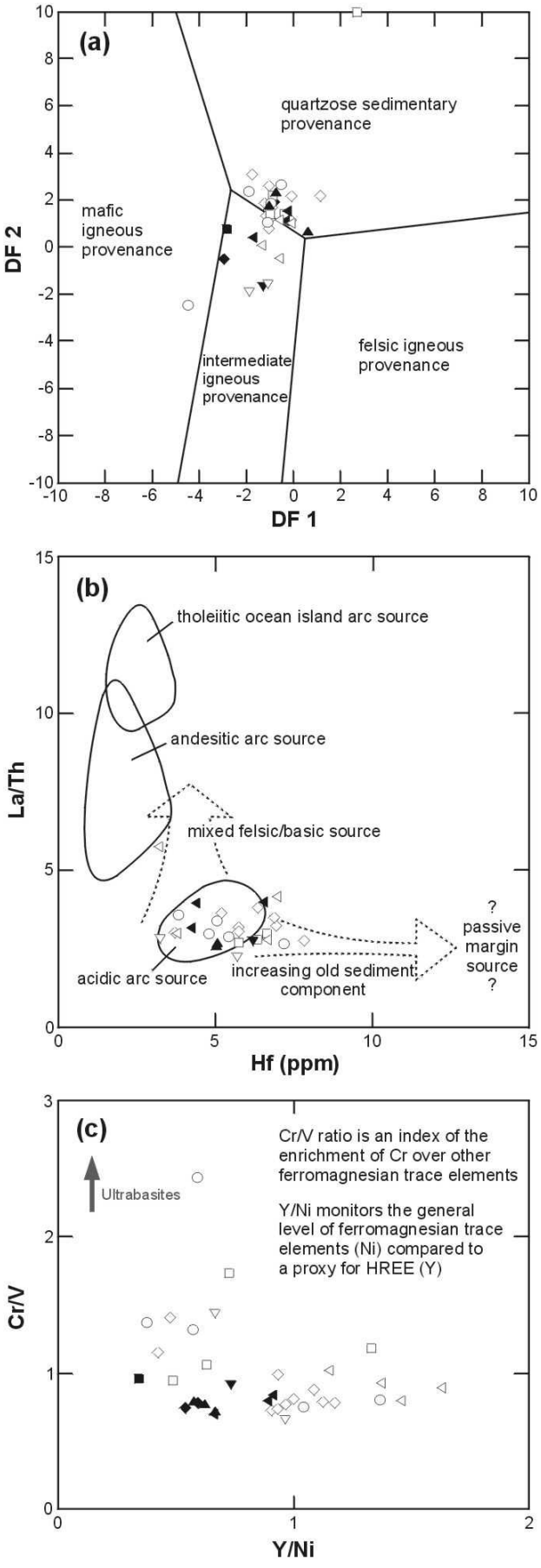

Garver et al. (1994) used Cr and Ni whole-rock geochemistry to identify ophiolitic rock sources. They suggested that values of Cr >150 ppm, Ni >100 ppm, Cr/Ni ca. 1.3–1.5 and a high correlation coefficient between Cr and Ni are diagnostic of ultrabasic rocks in the source area, whereas higher Cr/Ni ratios (around 2.0 and higher) indicate basic volcanic detritus. Cr/Ni ratios of >3.0 for sandstones suggest significant sedimentary fractionation (Garver *et al.* 1994). The siliciclastic sediments from Chios have Cr/Ni ratios of 2.2–4.4 (Cr 59–154 ppm, Ni 12–61 ppm), Cr/Ni ratios of 2.2–4.4 (Cr 59–154 ppm, Ni 12–61 ppm), those from Inousses 2.5–3.7 (Cr 34–128 ppm, Ni 11–48 ppm) and those from Psara 2.0–2.8 (Cr 68–135 ppm, Ni 27–45 ppm). The Cr–Ni signatures typify an input of basic volcanic rocks rather than ultrabasic rocks from the source area. Some psammites (e.g. samples CH11, CH34, CH39 and CH70) have been affected by sedimentary fractionation.

Fig. 9. Discrimination diagrams illustrating sedimentary provenance. **(a)** Discriminant function (DF) analysis using major elements after Roser & Korsch (1988). **(b)** La/Th vs. Hf diagram after Floyd & Leveridge (1987). **(c)** Cr/V vs. Y/Ni diagram after McLennan et al. (1993).

To identify the input of basic and/or ultrabasic rocks, the chemical compositions of detrital chrome spinel grains were analysed. Detrital chrome spinels are known as provenance indicators of basic and ultrabasic rocks and their chemistry reflects the tectonic setting of source rocks from which they were derived (e.g. Dick & Bullen 1984; Pober & Faupl 1988; Cookenboo et al. 1997; Barnes & Roeder 2001; Kamenetsky et al. 2001, and references therein). The detrital chrome spinel grains analysed here are light brown to dark reddish brown and black with quite variable major-element concentrations. The observed spread in Cr-number (0.29 and 0.89) and Mg-number (0.24 and 0.70) typifies a mixed (ultra)basic source of highly depleted peridotites of mainly harzburgite and minor lherzolite composition (Fig. 10a). Except two grains, all spinels are characterized by low contents of TiO_2 (<1.0 wt.%) and and Al_2O_3 values between 4.9 and 40.7 wt.%, indicating an origin from mid-ocean ridge (MOR)-type peridotites, supra-subducation zone (SSZ) peridotites and island-arc basalts (Fig. 10b). For illustration purposes, five samples with a TiO_2 value below the detection limit have been plotted at 0.01 on the *y*-axis of Figure 10b.

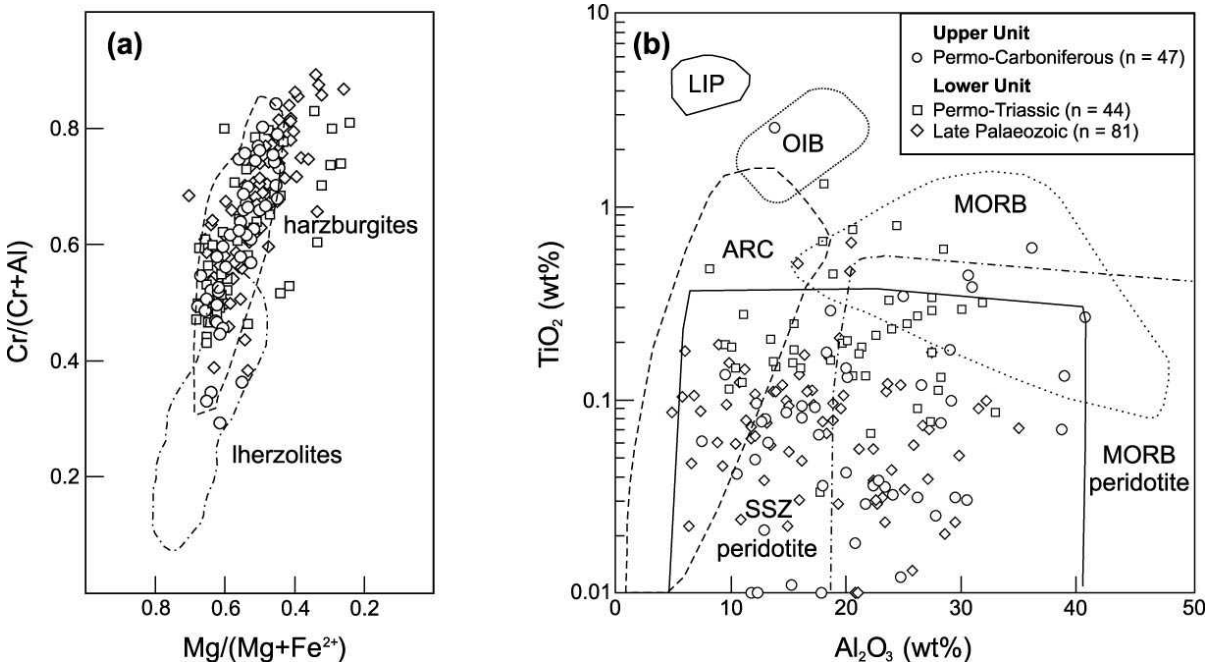

Fig. 10. Compositional data of detrital chrome spinel from Late Palaeozoic and Early Mesozoic clastic sediments of Chios. **(a)** Cr/(Cr + Al) vs. Mg/(Mg + Fe^{2+}) diagram showing the discrimination fields of chrome spinel derived from the two major peridotite subtypes after Pober & Faupl (1988). **(b)** TiO_2 vs. Al_2O_3 diagram showing the discrimination fields of chrome spinel derived from various types of basic and ultrabasic rocks after Kamenetsky et al. (2001). MORB, mid-ocean ridge basalt; OIB, ocean-island basalt; LIP, large igneous province; ARC, island-arc magmas; SSZ, supra-subduction zone.

Few detrital chrome spinel grains have Cr-number >0.8, which might be taken to indicate an input of boninitic material (see Dick & Bullen 1984; Barnes & Roeder 2001). Boninites are typical second-stage melts formed in fore-arc regions during the earliest stages of intraoceanic subduction (Bloomer & Hawkins 1987; Duncan & Green 1987; Kostopoulos & Murton 1992) and their presence is indicative of this special tectonic setting.

Figure 11 illustrates the fractionation within the REE in relation to the Eu anomaly. For comparison, the average value for the UCC (data from Taylor & McLennan 1985) is also included. The Eu anomaly in clastic sediments is a good fingerprint for source rock characterization. This parameter reflects changes in a mixture between juvenile crustal influx, without Eu anomaly, characterizing active continental-margin settings, and recycled crustal material, with significant Eu anomaly, characterizing evolved stable cratons (Gao & Wedepohl 1995).

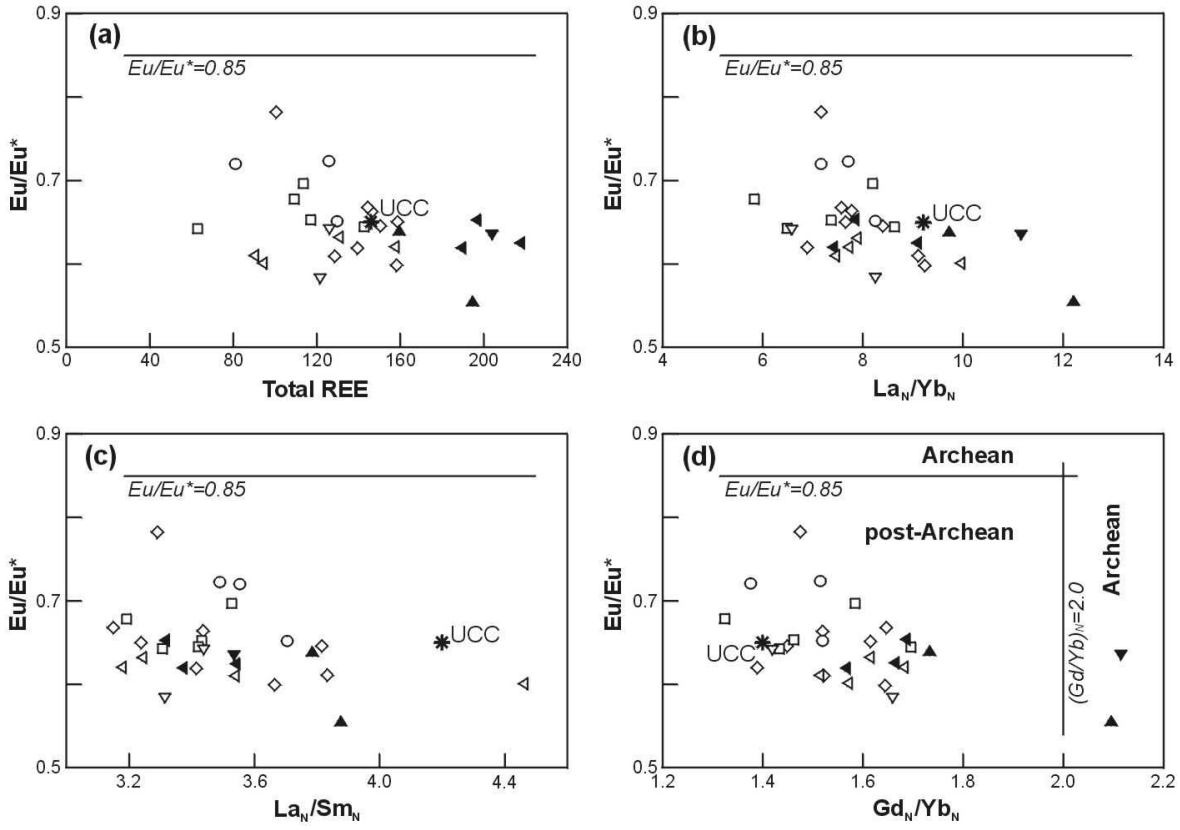

Fig. 11. (a) Total REE content in relation to the Eu anomaly (Eu/Eu*). **(b)** Fractionation of LREE and HREE in relation to Eu/Eu*. **(c)** Fractionation within the LREE in relation to Eu/Eu*. **(d)** Fractionation within the HREE in relation to Eu/Eu*. Fields are after McLennan (1989). The average upper continental crust (UCC, values from Taylor & McLennan 1985) is also included. Symbols are the same as in Figure 7.

The sediments studied here display variable negative Eu anomalies with values in the range of 0.60–0.78 (mean 0.67) for Chios, 0.60–0.65 (mean 0.62) for Inousses and 0.55–0.64 (mean 0.60) for Psara. These values suggest that intracrustal differentiation processes such as partial melting or fractional crystallization had affected the source rocks (see McLennan 1989, for discussion).

The degree of light REE (LREE: La–Sm) vs. heavy REE (HREE: Gd–Lu) enrichment is assessed in Figure 11b through the ratio of chondrite-normalized La and Yb values (La_N/Yb_N). Fractionation within the LREE and the HREE is illustrated in Figures 11c and 11d, respectively. All samples reveal significant LREE enrichment with La_N/Yb_N ca. 7.7 for sediments from Chios, ca. 8.2 for sediments from Inousses and ca. 9.5 for sediments from Psara. With regard to La_N/Sm_N ratios, they all fall within a narrow range from 3.1 to 3.8, with the exception of one psammite from Inousses. As for the Gd_N/Yb_N ratios, all but two samples from Psara range from 1.3 to 1.7, indicating nearly flat chondrite-normalized HREE patterns. Both Gd_N/Yb_N ratios and Eu/Eu* ratios are similar to the mean values for the UCC. Two pelites from Psara show HREE-depleted patterns (Gd_N/Yb_N ca. 2.1), reflecting fractionation of garnet from the source rocks (e.g. McLennan et al. 1993, for discussion).

Figure 12 shows REE patterns for the analysed sediments normalized both to PAAS (Fig. 12a–e) and chondrite (Fig. 12f–j). The PAAS-normalized patterns are similar for all psammites, with depleted (<1) LREE and relatively flat HREE. The Early Carboniferous greywackes from the Lower Unit of Chios have HREE concentrations closely matching those of PAAS (Fig. 12c) because of their higher content of phyllosilicate minerals in the matrix. Pelites from Inousses have similar PAAS-normalized patterns to the psammites from the island, and they are enriched in absolute REE abundances relative to PAAS. The patterns of pelites from Psara are more variable, but on the whole similar to PAAS. The depletion of total REE in some psammites (samples CH11, CH27, CH31, IN5, IN6) can be attributed to quartz dilution (Taylor & McLennan 1985), consistent with their high SiO_2 contents (71–85 wt.%). The chondrite-normalized patterns in all samples show strong LREE enrichment, negative Eu anomalies and flat HREE, the exception being one psammite from the Late Palaeozoic rocks of the Lower Unit (sample CH31) with an indistinct Eu anomaly (Fig. 12h). This sample also has higher contents of Na_2O and Sr. A higher Na_2O content suggests plagioclase enrichment. Given the fact that Eu^{2+} and Sr^{2+} have comparable ionic sizes and that both partly substitute for Ca^{2+} in plagioclase, a higher Sr content with no concomitant Eu

anomaly may reflect input of juvenile crustal material (McLennan 1989; Gao & Wedepohl 1995). The lack of a Eu anomaly probably resulted from concentration of plagioclase in the sand-size fraction during sorting (e.g. McLennan et al. 1990). In general, according to Bhatia (1985), McLennan et al. (1990, 1993) and McLennan & Taylor (1991), the PAAS- and chondrite-normalized patterns in Figure 12 suggest a derivation from predominantly upper continental crust and/or young differentiated arc material.

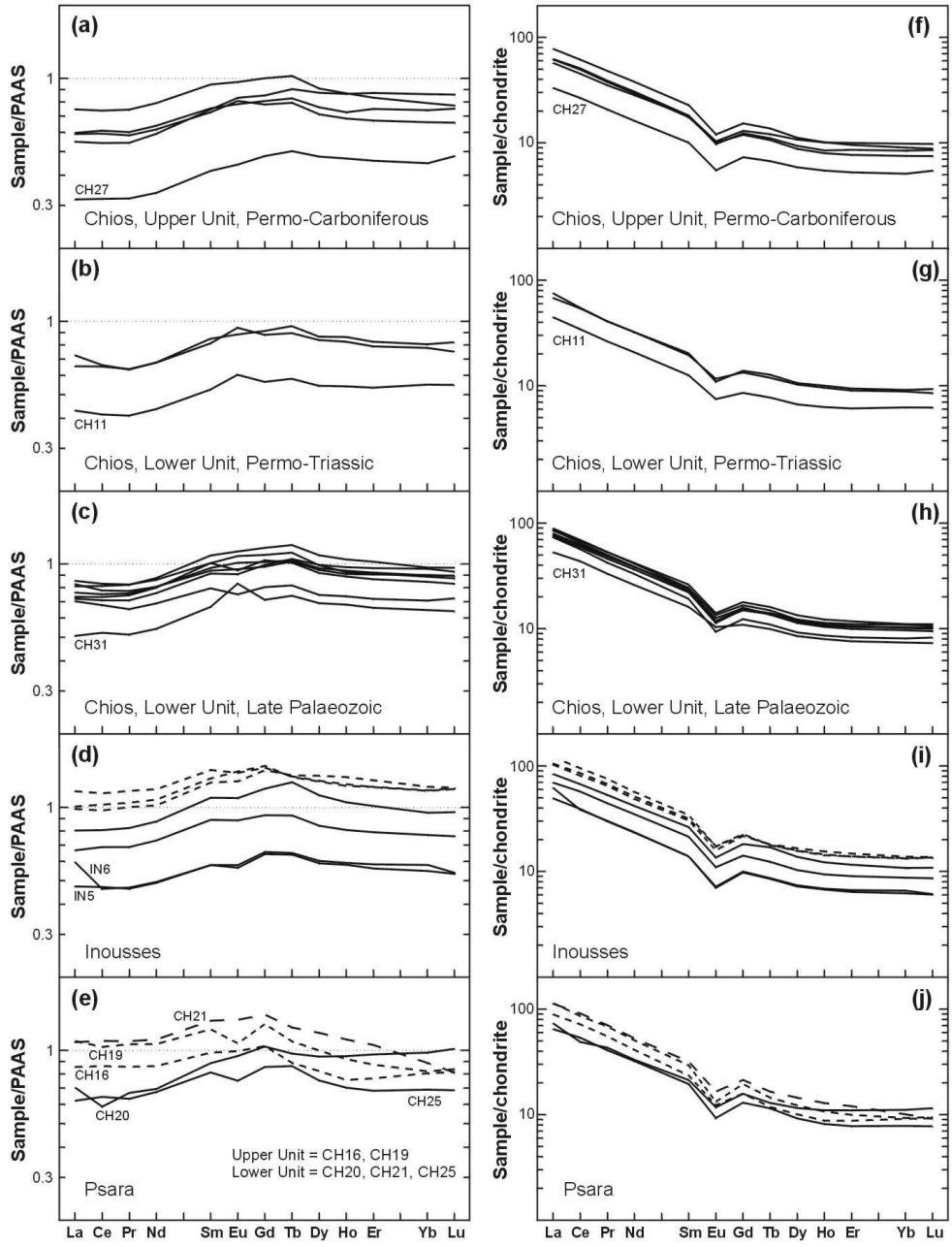

Fig. 12. (a–e) PAAS-normalized REE diagrams. Normalising values from McLennan (1989). **(f–j)** Chondrite-normalized REE diagrams. Normalising values from Taylor & McLennan (1985). Continuous lines indicate psammitic sediments; dashed lines, pelitic sediments.

4.5. Tectonic setting

Trace elements with relatively low mobility and low residence time in ocean water, such as La, Th, Zr and Sc, are transferred quantitatively into clastic sediments during primary weathering and transportation, and are thus useful fingerprints for chemical discrimination of plate-tectonic settings (e.g. Bhatia & Crook 1986). The following settings are generally distinguished: oceanic island arc (OIA), continental island arc (CIA), active continental margin (ACM), and passive margin (PM). In the ternary diagrams of Bhatia & Crook (1986) all psammites plot in the continental island-arc field (Fig. 13a and b), except for one psammite from the Lower Unit of Psara that lies in the active continental-margin field (Fig. 13a) and one psammite from Inousses that plots outside the discriminant fields but close to the continental island-arc field (Fig. 13b). Whereas a continental island arc is by definition an "island arc formed on well-developed continental crust or on thin continental margin" with a provenance of a "dissected magmatic arc-recycled orogen", an active continental margin is formed on a "thick continental margin" and on "crystalline basement" with a provenance of "uplifted basement" and comprises both Andean-type margin and strike-slip type settings (for further details, see Bhatia 1983; Bhatia & Crook 1986). The overall geochemical fingerprints for all analysed psammites suggest a continental island arc as depositional setting. Thus, based on trace-element signatures, a passive-margin setting and an oceanic island-arc setting can be excluded.

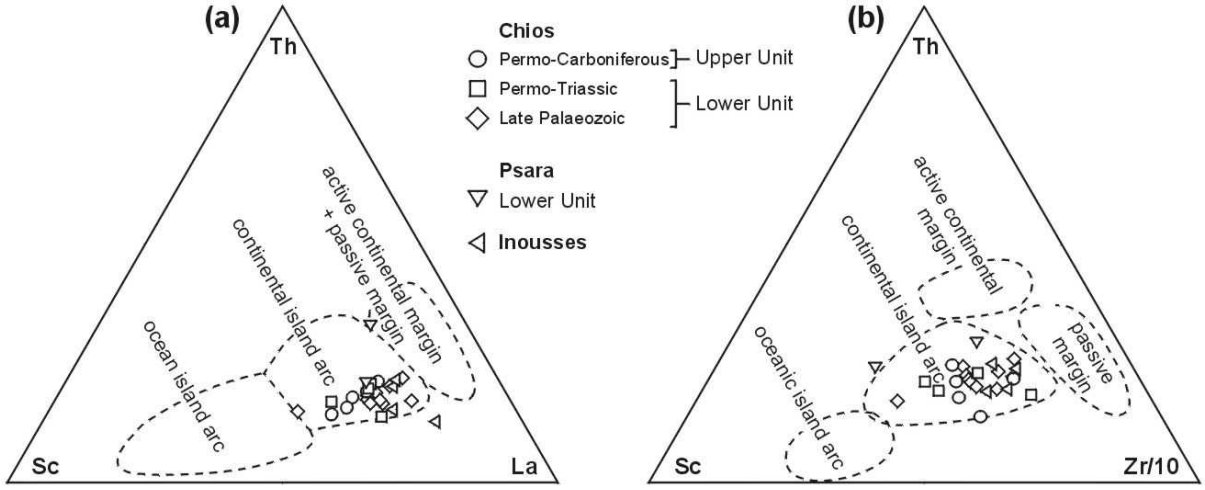

Fig. 13. (a–b) Discrimination diagrams after Bhatia & Crook (1986) illustrating tectonic setting. Only psammites are plotted.

However, sediment geochemistry does not indicate the age of the continental island arc. Remains of an older continental island-arc basement exposed to erosion at a passive margin environment could impart its signature to the whole-rock chemistry of the deposited sediments. Nevertheless, a continental island-arc setting seems the most plausible alternative for the Late Palaeozoic, as geochronological studies of orthogneisses from the Aegean and the surrounding area document a major igneous event between ca. 290 and 325 Ma (e.g. Engel & Reischmann 1998, 1999; Reischmann 1998; Özmen & Reischmann 1999; Vavassis et al. 2000; Reischmann et al. 2001; Anders et al. 2006a, b; Xypolias et al. 2006). Geochemical analyses indicate a volcanic-arc or active continental-margin setting at this time (e.g. Pe-Piper & Piper 2002, and references therein), as a result of northward subduction of (a branch of) Palaeotethys beneath Pelagonia (e.g. Stampfli 2000; Vavassis et al. 2000; Stampfli et al. 2003).

Bhatia (1985) established several REE-related parameters to distinguish the tectonic settings of terrigenous sedimentary rocks. (1) for passive continental margins: ΣREE ca. 210 ppm, La_N/Yb_N ca. 10.8, Eu/Eu* ca. 0.56; (2) for Andean-type continental margins (i.e. active continental margins): ΣREE ca. 186 ppm, La_N/Yb_N ca. 8.5, Eu/Eu* ca. 0.6; (3) for continental island arcs: ΣREE ca. 146 ± 20 ppm, La_N/Yb_N ca. 7.5 ± 2.5, Eu/Eu* ca. 0.79 ± 0.13 and (4) for oceanic island arcs: ΣREE ca. 58 ± 10 ppm, La_N/Yb_N ca. 2.8 ± 0.9, Eu/Eu* ca. 1.04 ± 0.11. Taking into account the above parameters (see Fig. 11), a continental island-arc setting is the most probable setting for all psammites.

5. Discussion

5.1. Chios

The sedimentary record of the Late Palaeozoic rocks of the Lower Unit from Chios is the key to understanding the closure of the Palaeotethys Ocean in space and time. These consist of greywackes, minor sandstones and siltstones as well as intercalated quartz-bearing conglomerates containing blocks of massive and well-bedded limestones, cherty limestones, radiolarites and volcanic rocks. Petrographical and geochemical analyses reveal no clear differences between Late Palaeozoic clastic sediments from the Lower and the Upper Units of Chios. The Permo-Triassic clastic sediments from the Lower Unit are similar to the Late

Palaeozoic clastic sediments. Only the carbonate content of the clastic sediments can provide some means of discrimination. Permo-Triassic clastic sediments from the Lower Unit and Permo-Carboniferous clastic sediments from the Upper Unit commonly have a higher carbonate content than Late Palaeozoic clastic sediments from the Lower Unit, probably because of deposition above the calcite compensation depth (CCD).

For most psammites, high SiO_2 contents (>70 wt.%) and low trace-element concentrations indicate typical quartz-rich sources. The significant enrichment in LREE, the negative Eu anomalies and the flat HREE patterns suggest derivation chiefly from old upper continental crust and/or young differentiated arc material. The negative Eu anomalies also indicate that intracrustal differentiation processes such as partial melting or fractional crystallization, involving separation of plagioclase, had affected the source rocks (e.g. McLennan 1989; McLennan et al. 1990). The nature of a mainly acidic (magmatic and sedimentary) source is consistent with petrographical and heavy mineral analyses presented by Neubauer & Stattegger (1995) and Zanchi et al. (2003). Petrography indicates that the source was composed of three main constituents: volcanic and plutonic acidic rocks, low-grade metamorphosed sedimentary rocks and minor (ultra)basic rocks. According to the discriminant diagrams of Bhatia & Crook (1986), all psammites appear to have been deposited predominantly in a continental island-arc setting. The source rocks were slightly affected by weathering and sediment recycling, indicated by low to moderate Th/U and Zr/Sc ratios and also by high proportions of angular to subangular framework clasts. These observations indicate that (1) the depositional environment was relatively close to the source rocks and (2) the source rocks may be of two types, a continental source (responsible for the quartz and low-grade metamorphic fragments) and a volcanic-arc source (responsible for the amounts of plagioclase and volcanic fragments).

Our new field observations suggest that it might be possible to divide the Late Palaeozoic rocks of the Lower Unit into at least two formations: a lower formation equivalent to the ‘Chios mélange’, consisting of siliciclastic matrix sediments including the olistoliths, and a conformably overlying upper formation consisting mainly of quartzose greywackes and sandstones. Both formations together with the Late Palaeozoic of the Upper Unit may be correlated to the Late Palaeozoic formations on the Turkish Karaburun peninsula described by Stampfli et al. (2003). It appears that remapping of the Late Palaeozoic of Chios is necessary to clarify the tectonostratigraphy of the island.

5.2. Inousses

The metasedimentary sequence of Inousses consists of light grey quartzose metaconglomerates, fine-grained grey metapsammites, pyrite-bearing metapelites and platy marble layers or lenses (e.g. Kilias 1987). The metapsammites have high SiO_2 contents (>75 wt.%), and low trace-element concentrations typical of quartz-rich sources. The significant enrichment in LREE, the negative Eu anomalies and the flat HREE patterns suggest chief derivation from an old upper continental crust and/or young differentiated arc material. The negative Eu anomalies also indicate that intracrustal differentiation processes, such as partial melting leaving residual plagioclase or fractional crystallization involving removal of plagioclase, had affected the source rocks (e.g. McLennan 1989; McLennan et al. 1990). Generally, the geochemical signature of the metasedimentary succession of Inousses is similar to that of Late Palaeozoic sediments of Chios. The protoliths of this succession derived from acidic magmatic and sedimentary source rocks and were deposited in a continental island-arc setting. The conglomerates probably represent proximal-facies deposits, presumably in a submarine canyon or feeder channel. The crystalline dark limestones (Kilias 1987) may have been primarily transported into a deeper marine environment, probably from the edge of a carbonate platform.

Rock successions similar to those of Inousses crop out on the northern Sporades Islands and Pelion peninsula in central Greece (e.g. Jacobshagen & Wallbrecher 1984). At the present state of knowledge, we agree with the interpretation of Kilias (1987) and correlate the metasedimentary rocks of Inousses with Late Palaeozoic rocks of the Pelagonian nappes in mainland Greece.

5.3. Psara

Psara can be divided into two metasedimentary units. The Lower Unit consists of turbidite-type dark grey metapelites and phyllites, metasandstones and metagreywackes that were locally intruded by basic rocks. Some metasediments are slightly carbonate-bearing. The geochemical signature of this unit is similar to that of clastic sediments from Chios and Inousses, indicating a quartzose sedimentary to intermediate igneous provenance. The significant enrichment in LREE, the negative Eu anomalies and the flat HREE patterns

suggest derivation predominantly from an old upper continental crust and/or young differentiated arc material. The tectonic setting varies between that of an active continental margin and a continental island arc.

The tectonically overlying Upper Unit consists of garnet-bearing mica schists, calcschists and marbles. The geochemical signature of the mica schists is similar to that of clastic sediments from Chios and Inousses, indicating a quartzose sedimentary to intermediate igneous provenance. The significant enrichment in LREE, the negative Eu anomalies and the flat HREE patterns suggest chief derivation from an old upper continental crust and/or young differentiated arc material. The protoliths of the calcschists and marbles have been chalky sand- and siltstones and limestones, respectively, probably deposited under shallow water conditions above the CCD.

The metasedimentary units of Psara are most probably an eastern extension of the Pelagonian nappes *sensu* Jacobshagen et al. (1978). We follow the assumption of Wallbrecher (in Dürr & Jacobshagen 1986) and correlate the clastic sequences of the Lower Unit with the Skiathos Unit of the northern Sporades and Pelion peninsula, whereas the tectonically overlying Upper Unit most likely represents a fragment of the Pelagonian marbles.

5.4. Implications for Palaeotethyan evolution

Our petrographical and geochemical analysis presented here reveals no significant differences in provenance and tectonic setting between Late Palaeozoic and Early Mesozoic clastic sediments from the Lower and the Upper Units of Chios. Furthermore, the metasedimentary rocks of Inousses and Psara have similar petrographical and geochemical characteristics, although lacking evidence for an (ultra)basic source. It seems that the source area of all sediments remained unchanged from Late Palaeozoic to Early Mesozoic times. We interpret the Late Palaeozoic sediments from both the Lower and Upper Units of Chios as having been deposited along the same Palaeotethyan margin but at some distance from each other, which gave rise to the observed facies variations. The Late Palaeozoic turbidite-olistostrome sedimentation is proposed to have taken place in a continental island-arc environment as a result of subduction of a branch of the Palaeotethys Ocean beneath either Pelagonia (e.g. Stampfli et al. 2003) or Sakarya; detrital zircon ages indicate that basement

rocks from the latter supplied detritus to the clastic sediments of Chios (Meinhold et al. 2006). Pelagonia itself is regarded as a Carboniferous magmatic arc formed in an active continental-margin environment (e.g. Vavassis et al. 2000; Reischmann et al. 2001) with the Palaeotethyan suture located at its southern margin (e.g. Vavassis et al. 2000; Stampfli et al. 2003). Sakarya consists of several tectonostratigraphic units of pre-Jurassic age (e.g. Okay et al. 1996; Özmen & Reischmann 1999) forming the Sakarya Composite Terrane (Göncüoğlu et al. 1997) with the Palaeotethys suture also located at its southern margin (e.g. Vavassis et al. 2000; Stampfli et al. 2003).

The source rocks of the detrital chrome spinels in the Palaeozoic sediments of Chios Island must be sought in the Late Neoproterozoic ophiolitic successions of both MORB and SSZ affinities that occur in NW Turkey (Çele ophiolite; Yiğitbaş et al. 2004) and western Bulgaria–eastern Serbia (Balkan–Carpathian ophiolite; Savov et al. 2001) or equivalents to those which are not preserved. They represent Prototethyan oceanic crust that was accreted to the northern Gondwana margin during the late stages of the Pan-African collisional event. Prototethys represents a peri-Gondwana ocean, the southward subduction of which under the northern Gondwana margin resulted in the diachronous fragmentation of this margin and the opening of back-arc basins from Late Neoproterozoic to Silurian times (Stampfli & Borel 2002). The rifted fragments (Avalonian terranes, Hun superterrane) were eventually transported northward to be accreted to the southern margin of Laurussia. In the case of the Palaeotethys Ocean, ocean-floor spreading resulted in northward drifting of the Hun superterrane and its final amalgamation with the southern Laurussian margin by the Late Carboniferous (Stampfli & Borel 2002; von Raumer et al. 2003). It should be noted that northward subduction of Palaeotethys under the Hun superterrane had already started by Early Carboniferous (Stampfli & Borel 2002). Clearly then, we favour a scenario of northward-directed subduction of a branch of the Palaeotethys Ocean beneath the Sakarya microcontinent (terrane) in close proximity to the southern active margin of Eurasia in Late Palaeozoic times. This is in contradiction to Robertson & Pickett (2000), who placed the Chios–Karaburun units at the southern margin of the Palaeotethys Ocean; that is, at the northern margin of Gondwana. However, the Carboniferous foraminiferal fauna of the Chios–Karaburun units shows rather distinct biogeographic affinities to the southern Laurussian shelf (Kalvoda 2003). In general, the accretion of Gondwana-derived terranes to the southeastern margin of Eurasia was probably a common feature throughout Tethys history,

consolidating, for example, the pre-Alpine basement of the Internal Hellenides (e.g. Anders et al. 2006a; Himmerkus et al. 2006, 2007).

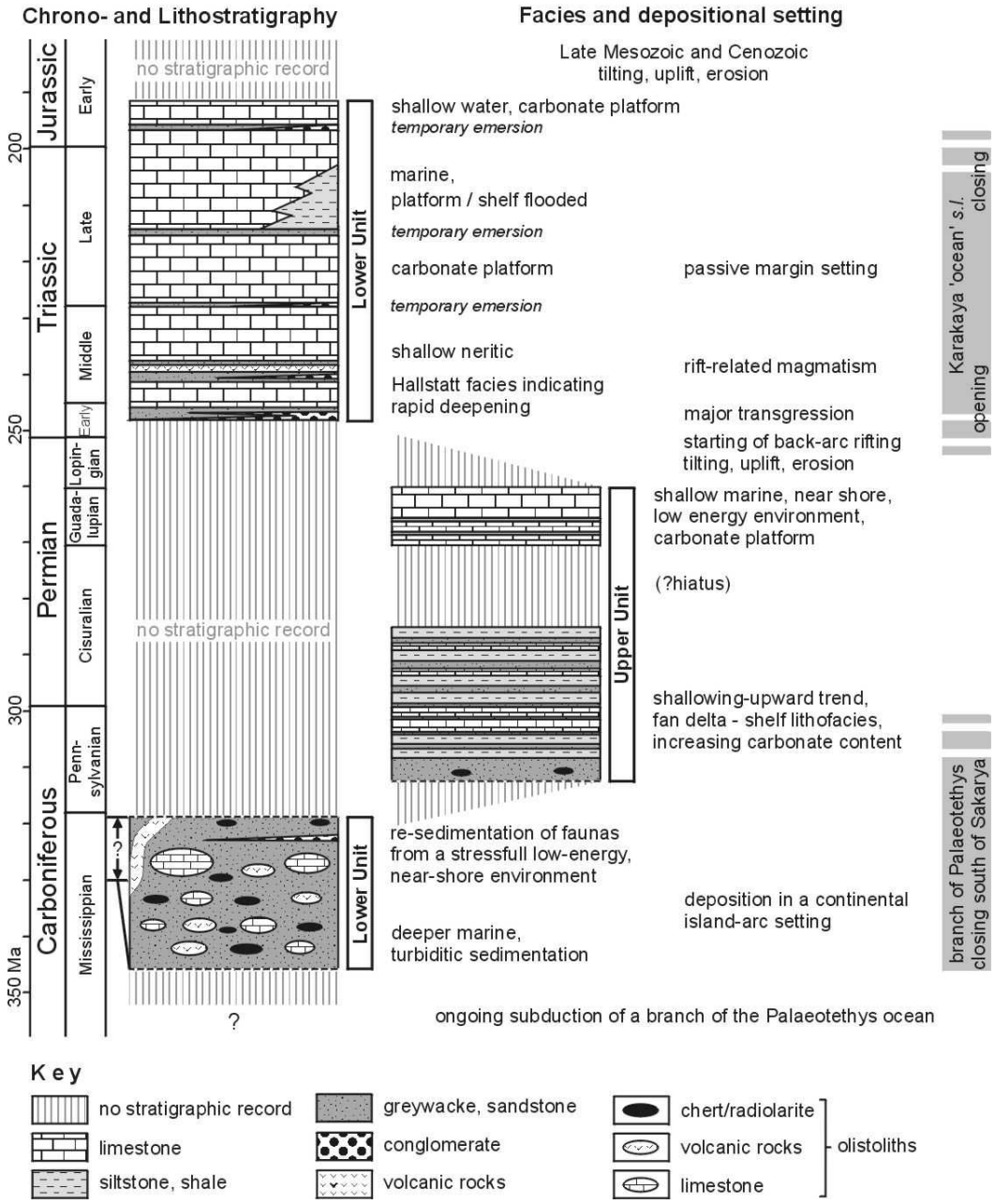

Fig. 14. Variation of facies and depositional setting of sedimentary rocks from Chios in Late Palaeozoic to Mesozoic times. Because the Mesozoic cover of the Upper Unit is mostly missing, its facies variation is not shown in the schematic column. Compiled using data from Besenecker et al. (1968), Kauffmann (1969), Sideris (1989), Gaetani et al. (1992), Flajs et al. (1996); Robertson & Pickett (2000), Groves et al. (2003), Stampfli et al. (2003); Zanchi et al. (2003) and own field observations (this study). Geological time scale according to Gradstein et al. (2004).

The sedimentological record indicates an upward transition of the Carboniferous turbiditic fan system to more proximal quartz-rich greywackes and sandstones, followed by carbonate-bearing sandstones with increasing intercalations of limestone beds through to thick limestones; it marks a shallowing-upward trend above the CCD and the initiation of a carbonate platform in Permian times (Fig. 14). The sedimentary input of plant fragments indicates proximity to a hinterland with vegetation. The fossil assemblage of the Permian limestones (e.g. Besenecker et al. 1968; Flajs et al. 1996) can be assigned to the 'Northern Biofacies Belt' of Altiner et al. (2000), which would indicate an affinity of Chios to the Late Palaeozoic cover sequences of the Northern Taurides (Altiner et al. 2000). Benthic Foraminifera and calcareous algae associations suggest that Chios must have been situated at the southern margin of the Sakarya microcontinent in the late Early Permian (Jenny & Stampfli 2000).

Figure 15 illustrates the location of Chios in close proximity to the Sakarya microcontinent in a Late Palaeozoic palaeogeographical reconstruction. During the Late Permian parts of the northern Anatolide–Tauride Block and the basement of the Sakarya microcontinent were covered by the same extensive carbonate platform and the two units were possibly attached to each other prior to the opening of the İzmir–Ankara branch of the Neotethys (Turhan et al. 2004). Furthermore, bearing in mind that the Permian succession of Chios can be correlated with Permian sediments from Pelagonia (e.g. Hydra, see Baud et al. 1991), a novel terrane assemblage emerges at the northern margin of Palaeotethys during the Late Palaeozoic including parts of the northern Anatolide–Tauride Block, the Sakarya microcontinent and Pelagonia (or parts of them) (see Kalvoda 2003, fig. 3; Stampfli et al. 2003, fig. 9a and b). This is in contradiction with palaeogeographical models that suggest a southward subduction of Palaeotethys beneath the above-mentioned fragments located at the northern margin of Gondwana during the Late Palaeozoic (e.g. Şengör et al. 1984; Okay et al. 1996; Xypolias et al. 2006). However, an in-depth analysis of the palaeotectonic and palaeogeographic reconstructions of the eastern Mediterranean region is beyond the scope of the present paper.

In the late Permian (Fig. 15), rifting and extension became dominant, forming, for example, the Karakaya basin (e.g. Turhan et al. 2004, and references therein). This extensional setting was probably accompanied by the development of horst and graben structures. The Late Palaeozoic sedimentary succession of the Lower Unit of Chios was

probably situated on a horst structure and therefore partly eroded and redeposited as olistoliths (blocks) in the Karakaya basin. This could explain the absence of Permian rocks in this unit. The Permian of the Upper Unit, however, probably survived in a graben structure. After uplift and erosion, the Palaeozoic successions were unconformably overlain by transgressive Permo-Triassic clastic and late Early Triassic carbonaceous sequences followed by increasing subsidence and volcanism. The Permo-Triassic clastic sediments originated from input of *in situ* reworked Late Palaeozoic detritus. Detrital zircon ages clearly show an input from the Sakarya basement (Meinhold et al. 2006).

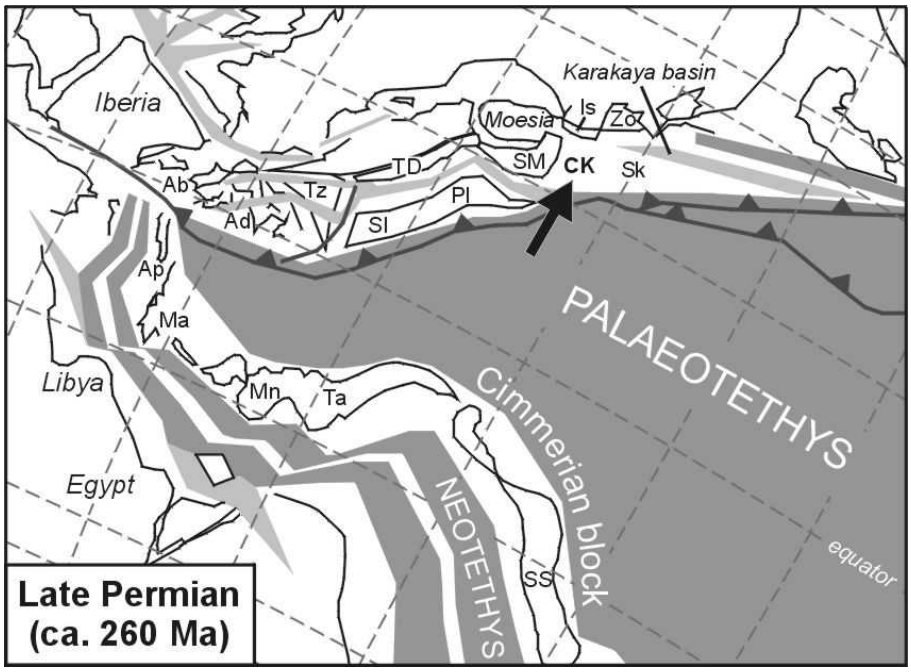

Fig. 15. Palaeotectonic reconstruction for the Late Permian (after Stampfli et al. 2001). At this time, the opening of Neotethys in the south and the detachment of the Cimmerian blocks from the Gondwana mainland probably took place through the increased slab-pull forces incurred when Palaeotethys subducted beneath the Eurasian margin (Stampfli & Borel 2002). The light grey areas are initial rift basin systems. The arrow shows the position of the Chios–Karaburun units. Ab, Albora; Ad, Adria; Ap, Apulia; CK, Chios–Karaburun; Is, Istanbul; Ma, Mani; Mn, Menderes; Pl, Pelagonia; SI, Slavonia; Sk, Sakarya; SM, Serbo-Macedonian; SS, Sanandaj–Sirjan; Ta, Taurus; TD, Trans-Danubian; Tz, Tizia; Zo, Zonguldak.

Crustal extension continued to the Middle Triassic (see Gaetani et al. 1992) and initiated the formation of new Tethyan back-arc oceans (see Stampfli et al. 2003). The Hallstatt facies of the Early Triassic limestones indicates this rapid deepening (e.g. Baud et al. 1991; Stampfli et al. 1991; Gaetani et al. 1992). However, Chios must always have occupied

an external (distal) position to these new oceans because very few tuffitic horizons occur on the island. The Triassic cover sequence of Chios clearly has a Pelagonian affinity (e.g. Besenecker et al. 1968; Gaetani et al. 1992), whereas the Late Triassic–Early Jurassic succession shows strong affinities to the western Taurides (Rosselet & Stampfli 2003). The latest Triassic–earliest Jurassic emergent horizon of both the Lower and Upper Units of Chios can also be found in the Karaburun peninsula succession (e.g. Robertson & Pickett 2000), in the cover sequences of the Sakarya microcontinent (e.g. Okay et al. 1996; Göncüoğlu et al. 1997) and in the Tauride autochthon (e.g. Robertson et al. 2004); it could either be related to a Cimmerian collision (Robertson & Pickett 2000) or document the opening of a new Neotethyan branch.

We conclude that in Triassic times Chios was probably situated at the passive margin of a microcontinent consisting of Pelagonia and an attached fragment of Sakarya. The latter can be considered as the southernmost or southwesternmost margin of the present-day Karakaya basin. In the Early Jurassic this microcontinent was located close to or became attached to the western Taurides. The metasedimentary sequences of Inousses and of the Lower Unit of Psara are lithologically comparable to the Skiathos Unit and are interpreted as time equivalent deposits to the Late Palaeozoic of Chios, albeit from different facies areas. During the Cenozoic, some areas experienced low-grade metamorphism (e.g. the islands of Skiathos, Psara, and Inousses), whereas others have remained virtually unmetamorphosed (upper plate position, e.g. Chios). The units of Chios together with the metasedimentary rocks of Inousses and Psara are interpreted to be allochthonous, tectonically transported to their present-day location by late Mesozoic to Cenozoic orogenic processes.

6. Conlusions

The new field work and geochemical data presented in this study have led us to the following conclusions about the provenance, depositional setting and stratigraphic affiliation of sedimentary units from the East Aegean region of Greece:

(1) Geochemical fingerprints of Late Palaeozoic and Permo-Triassic clastic sediments of Chios are similar and consistent with sediment petrography suggesting a derivation predominantly from acidic magmatic and sedimentary rocks and minor (ultra)basic input. Detrital chrome spinel chemistry suggests a probably mixed (ultra)basic source of MOR-type

peridotites, fore-arc peridotites, island-arc basalts and possibly boninites. Generally, the sedimentary geochemistry indicates a continental island arc as depositional setting, probably formed as a result of subduction of a branch of Palaeotethys beneath the Sakarya microcontinent in Late Palaeozoic time.

(2) The protoliths of the metasedimentary succession of Inousses were deposited in a continental island-arc setting probably in Late Palaeozoic or Triassic times and originated from acidic magmatic and sedimentary sources. This succession is assigned to the Pelagonian nappes of mainland Greece.

(3) The protoliths of the metasediments from the Lower and Upper Units of Psara Island were deposited in a continental island-arc setting and mainly originated from acidic magmatic and sedimentary sources. The high amount of carbonate in the Upper Unit indicates a shallow marine environment. The very low-grade metasediments of the Lower Unit are correlated with the Skiathos Unit, whereas the more carbonate-dominated Upper Unit is assigned to the Pelagonian marble nappe of the northern Sporades and the nearby Pelion peninsula.

To summarise, the combined analysis of provenance, depositional setting and stratigraphic affiliation of (meta)sedimentary units in the Aegean region indicates turbidite–olistostrome sedimentation in a continental island-arc setting due to subduction of a branch of Palaeotethys beneath Pelagonia and/or Sakarya in Carboniferous times. The final closure of this branch is marked by a shallowing-upward trend in sedimentation in Late Carboniferous and Permian times. Early Triassic rifting marks the formation of the Neotethyan ocean(s). Chios and its surrounding islands of Inousses and Psara most probably represent a link between Pelagonian units in Greece and Sakarya–Anatolide–Tauride units in Turkey.

Chapter 2

Rutile chemistry and thermometry as provenance indicator: An example from Chios Island, Greece

Abstract

In the present study we focused on detrital rutile separated from 12 psammitic samples that belong to three different sedimentary successions (Carboniferous, Permo-Carboniferous, Permo-Triassic) occuring on Chios Island, Greece. The Ti, Cr, Al, Fe, Nb, Zr, Si, and V contents of the rutiles were obtained by electron-microprobe analyses to trace their provenance. The Cr and Nb concentrations of the analysed rutile grains show a wide range and indicate that this mineral in the Carboniferous succession is mainly derived from metamafic rocks, whereas in the Permo-Carboniferous and Permo-Triassic successions stem from a metapelitic source. The calculated formation temperatures using the Zr-in-rutile thermometer range from ca. 520 to 850 °C with "hotter" rutile being encountered in the Permo-Carboniferous and Permo-Triassic successions. This feature together with the rutile chemistry indicate a change in source rock lithology through time, which could either reflect an increasing depth of erosion of an exhumed 'Variscan' nappe pile of heterogeneous composition in the hinterland or a change in the style of accretion and erosion of different terranes at the southern margin of Laurussia during the subduction of a branch of the Palaeotethys Ocean in the Late Palaeozoic. In general, this study underscores the importance of rutile chemistry and thermometry in quantitative single-mineral provenance analysis and in chemostratigraphic analysis of clastic sedimentary rocks.

1. Introduction

Knowledge of the provenance of ancient clastic sedimentary rocks is important for exploration of mineral resources, for basin analysis as well as for palaeotectonic reconstructions. Clastic sedimentary rocks are commonly composed of quartz, feldspar and mica as major constituents, and of minor amounts of heavy minerals such as zircon, rutile, tourmaline, garnet, epidote, and chrome spinel. Sediment composition is primarily affected by the composition of the initial source rock but also by a complex set of parameters such as weathering, transport, deposition and diagenesis that modify the sediment during the sedimentation cycle (e.g. Morton 1985; Johnsson 1993; Morton & Hallsworth 1999). In addition to whole-rock petrography and heavy-mineral analysis, geochemical discrimination studies of whole rock and specific detrital minerals are a powerful tool in provenance characterization, especially in deciphering tectonic processes like timing of erosion or the tectonic setting of source terrains. Most of the heavy minerals mentioned above have been used as provenance indicators for a long time by virtue of their major-, trace- and isotope-element signatures (e.g. Pober & Faupl 1988; Morton 1991; von Eynatten & Gaupp 1999; Sircombe 1999; Spiegel et al. 2002; Faupl et al. 2002), one exception being rutile (see Zack et al. 2004b) which is the focus of this study.

Here we present the results of electron-microprobe analyses and laser micro-Raman spectroscopic investigations on detrital rutiles from sedimentary rocks of Chios Island, Greece. The samples studied were taken from three different rocks units ranging in age from Late Palaeozoic to Early Mesozoic. We will discuss the application of rutile chemistry and thermometry to single-mineral provenance analysis and compare the results obtained by using the Zr-in-rutile thermometers of Zack et al. (2004a) and Watson et al. (2006). We will furthermore evaluate the power of rutile chemistry in unravelling specific source characteristics and its use as chemostratigraphic indicator.

2. Geological setting

The island of Chios is situated in the eastern Aegean Sea (Fig. 1); tectono-stratigraphically it belongs to the Hellenides, which are an integral part of the Alpine-Himalayan orogenic system in the south-eastern Mediterranean region. The Hellenides have traditionally been subdivided into Internal (hinterland) and External (foreland) zones. The

Internal Hellenides comprise, from SW to NE, the Pelagonian Zone (including the Attic-Cycladic Massif), the Vardar Zone, the Serbo-Macedonian Massif and the Rhodope Massif (e.g. Jacobshagen 1986; and references therein). All these units consist predominantly of Palaeozoic (but also Neoproterozoic and Mesozoic) basement rocks (e.g. Vavassis et al. 2000; Anders et al. 2005, 2006a, b; Turpaud & Reischmann 2005; Himmerkus et al. 2006a, 2007) overlain by or intercalated with sedimentary successions. They experienced quite complex Mesozoic to Cenozoic tectonism, which gave rise to equivocal palinspastic models and interpretations.

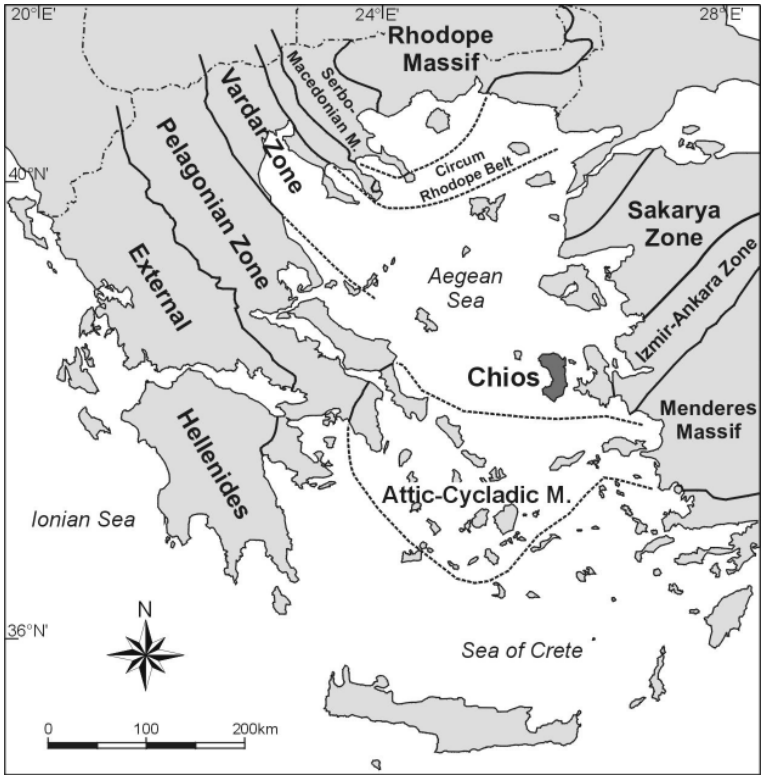

Fig. 1. Map showing the location of Chios within the Aegean region, including the main geotectonic zones (modified after Jacobshagen 1986; Okay et al. 2001).

Chios is generally assigned to the easternmost part of the Pelagonian Zone (e.g. Jacobshagen 1986; see also discussion in Meinhold et al. 2007). It basically comprises two tectonostratigraphic units (Fig. 2): an 'autochthonous' Lower Unit and a tectonically overlying 'allochthonous' Upper Unit (Herget & Roth 1968; Besenecker et al. 1968). A large part of the Lower Unit consists of Late Palaeozoic clastic sedimentary rocks containing blocks (of up to 100 m in diameter) of limestones, radiolarites and volcanic rocks. This succession was variably named 'Chios mélange', 'Chios (wild)flysch' or 'Volissos turbidites' (e.g. Robertson & Pickett 2000; Groves et al. 2003; Zanchi et al. 2003). Here we use the non-genetic term Late Palaeozoic of the Lower Unit (Meinhold et al. 2007). The major rock types

of this unit are greywackes, minor sandstones and siltstones as well as intercalated quartz-bearing conglomerates. The latter mainly contain clasts of quartz, black chert and quartzite, embedded in a coarse-grained quartzose matrix. Erosional contacts at the base of greywacke and conglomerate beds and upward reduction in grain size can often be observed. In some outcrops, well-developed sole marks and ripples can be seen at the base of turbidite beds. The facies of the turbidite-olistostrome succession resulted mainly from turbidity currents, debris flows and submarine slides. Groves et al. (2003) reported Mississippian microfossils from calcareous clasts of a breccia lying within the turbidite-olistostrome succession and suggested that the Late Palaeozoic rocks of the Lower Unit are most probably Late Visean or Early Serpukhovian in age. According to Stampfli et al. (2003) and Zanchi et al. (2003) Chios fits a geotectonic model of an arc-trench system formed along the Palaeotethyan subduction zone in Carboniferous times (cf. Robertson & Pickett 2000, and references therein). Meinhold et al. (2007) specified a tectonic setting of a continental volcanic arc, involving upper-continental crustal rocks and/or young differentiated arc material as well as a mixed source of (ultra)mafic rocks.

The Late Palaeozoic rocks of the Lower Unit are overlain by non-fossiliferous Early Triassic conglomerates and sandstones (Besenecker et al. 1968). The conglomerates mainly contain clasts of quartz and black chert embedded in a coarse-grained quartzose matrix. Zanchi et al. (2003) described an angular unconformity at the base of this clastic succession, interpreted as a Variscan unconformity. However, the stratigraphic age of these conglomerates and sandstones is uncertain because no biostratigraphic and only few radiometric ages exist so far (Meinhold et al. 2006). The youngest detrital zircon grain found in the Permo-Triassic sandstone so far has a rounded shape and a concordant $^{206}Pb/^{238}U$ age of ca. 326 Ma, thus giving a maximum age of deposition for this rock. Here we use the more comprehensive term Permo-Triassic instead of Early Triassic (Meinhold et al. 2007). The conglomerates and sandstones pass upwards into limestones of late Early to Late Triassic–Early Jurassic age (Besenecker et al. 1968). A Middle Triassic volcano-sedimentary succession is intercalated with the limestones (Besenecker et al. 1968; Gaetani et al. 1992). The Triassic–Jurassic transition is marked by non-marine clastic deposits followed by dolomites and limestones.

The Upper Unit of Chios belongs to the allochthonous nappe *sensu* Besenecker et al. (1968). Lithostratigraphically, its lowermost part consists of Late Carboniferous quartzose

greywackes, sandstones and minor siltstones, and occasionally contains lenses of black and greenish chert a few meters in size. Layers rich in plant fossils can be found on the bedding surfaces of siltstones and fine-grained sandstones. Fossil-bearing limestones of Late Carboniferous age are overlain by an Early Permian clastic carbonaceous succession (Kauffmann 1969). The Middle Permian is represented by fossiliferous carbonate sequences (e.g. Besenecker et al. 1968). Late Permian rocks are absent. The Permo-Carboniferous is overlain by transgressive Early Jurassic sediments which are themselves locally overlain by transgressive Upper Cretaceous deposits. The youngest rocks on Chios are Cenozoic sediments and volcanic rocks cropping out mainly in the southeastern part of the island.

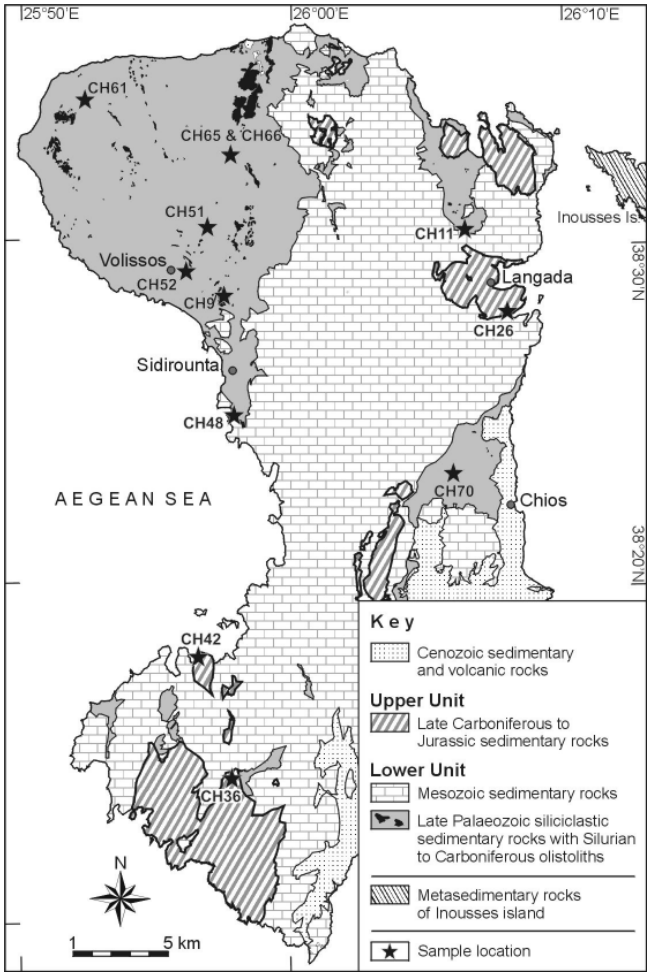

Fig. 2. Simplified geological map of Chios (after Besenecker et al. 1968, 1971). *Stars* indicate sample localities.

3. Sample description

A total of 12 psammitic samples were chosen for rutile chemical analyses. Of these, seven come from the Carboniferous and two from the Permo-Triassic part of the Lower Unit.

Three Permo-Carboniferous samples were also taken from the Upper Unit of Chios. Sample locations are shown in Figure 2; their geographic coordinates are listed in the Appendix.

All samples have framework grains consisting of monocrystalline and polycrystalline quartz as well as sedimentary and volcanic lithoclasts in varying amounts. Feldspar grains are common and always present. Plagioclase (mainly albite) is by far the most abundant feldspar mineral, whereas K-feldspar is rare. Plagioclase grains often display patchy sericitisation and replacement by calcite. Single muscovite flakes and minor detrital biotite also occur. All psammites are poorly sorted by size and dominated by angular to subangular clasts. The occurrence of iron hydroxides in some samples indicates secondary alteration processes. Accessory minerals include clay minerals, opaque minerals, chlorite and heavy minerals, predominantly zircon, rutile, chrome spinel, epidote and tourmaline. The analysed sedimentary rocks are virtually non-metamorphosed or have experienced only very low-grade metamorphism, as indicated by petrology (Zanchi et al. 2003) and conodont colour alteration index data (Groves et al. 2003; Larghi et al. 2005).

The samples used here have already been investigated for their whole-rock major-, trace- and rare-earth element (REE) contents, whereas a number of them have been additionally investigated for the chemistry of detrital chrome spinel (Meinhold et al. 2007). Major- and trace-element values are compatible with a felsic to intermediate source, minor input of (ultra)mafic detritus and recycling of older sedimentary components. Chondrite-normalized REE profiles are uniform showing light REE enrichment, negative Eu anomalies and flat heavy REE patterns, indicating an upper-continental crustal source and/or young differentiated arc material. The chemistry of detrital chrome spinel suggests a mixed (ultra)mafic source involving ridge peridotites (MOR-type), fore-arc peridotites and island-arc basalts.

4. Rutile chemistry and thermometry

Rutile mainly consists of titanium dioxide (TiO_2) and is the dominant carrier (>90% of the whole-rock content) of Ti, Nb, Sb, Ta and W as well as an important carrier (5–45% of the whole-rock content) of V, Cr, Mo and Sn (Rudnick et al. 2000; Zack et al. 2002). Analyses of rutiles can nowadays be routinely performed by electron microprobe (EMP) so that differences in chemical composition can easily be identified. Rutile is mainly formed

during medium- to high-grade metamorphic processes and is usually absent in igneous and low-grade metamorphic rocks (Force 1980). Therefore, medium- to high-grade metamorphic rocks are considered to be the chief primary source of detrital rutile (Force 1980). Additional, but minor, sources of rutile are alpine quartz veins, alkaline magmatic rocks, pegmatites, kimberlites and porphyry copper deposits (Force 1980). Inasmuch as rutile is chemically and physically stable and not prone to destruction during the sedimentation cycle, it can provide important information about source area lithologies, and therefore, it can be used for sedimentary provenance analysis.

Few papers have been published dealing with the chemistry of detrital rutile and its application to provenance studies (e.g. Götze 1996; Preston et al. 2002). More recently, however, rutile has attracted a lot of interest as new studies have demonstrated the high potential of the trace-element signature of rutile, including rutile thermometry, for source-rock characterization and hence for quantitative provenance analysis (Zack et al. 2004a, b; Triebold et al. 2005, 2007; Stendal et al. 2006). The trace-element content of detrital rutile grains can discriminate between possible source rocks, for example, high-grade metamorphic rocks such as eclogites and high-pressure granulites from hydrothermal ore deposits and kimberlites (Zack et al. 2002). Moreover, Cr and Nb abundances (Fig. 3) can effectively distinguish between metamafic and metapelitic lithologies (Zack et al. 2002, 2004b), whereas the Fe content can be used as an indicator of metamorphic origin since metamorphic rutile contains mostly >1000 ppm Fe (Zack et al. 2004a).

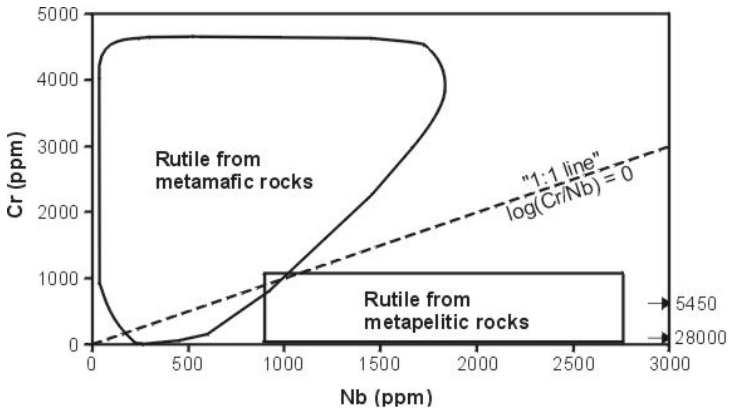

Fig. 3. Plot of Nb v. Cr contents of rutile from different metamorphic lithologies (after Zack et al. 2004b). Arrows indicate exceptionally high Nb contents of felsic granulite-facies rocks. The "1:1 line" is taken from Triebold et al. (2005); positive log(Cr/Nb) values mostly indicate a metamafic source for rutile while negative values suggest derivation from metapelitic rocks.

Triebold et al. (2005, 2007) introduced log(Cr/Nb) values to discriminate between metamafic and metapelitic source lithologies ("1:1" line; Fig. 3). This method is applicable, except for very low Cr and very low Nb contents. Based on literature data of Nb/TiO_2 ratios of whole rock for pelites, Zack et al. (2002, 2004b) calculated the Nb content of rutile in metapelites with 900–2700 ppm (see Fig. 3). Combined with reference data, we herein propose that the lower limit of Nb in metapelitic rutiles should be set at 800 ppm and that the discriminant boundaries between metamafic and metapelitic rocks should therefore be modified accordingly (see Fig. 4). Rutiles with negative log(Cr/Nb) values and accompanied Nb >800 ppm are interpreted to be derived from metapelitic rocks (e.g., mica-schists, paragneisses, felsic granulites) whereas positive and negative log(Cr/Nb) values, the latter however accompanied with Nb <800 ppm, suggest derivation from metamafic rocks (e.g., eclogites, mafic granulites). Rutiles from amphibolites plot in both fields because the protoliths of amphibolites are of either sedimentary or mafic igneous origin.

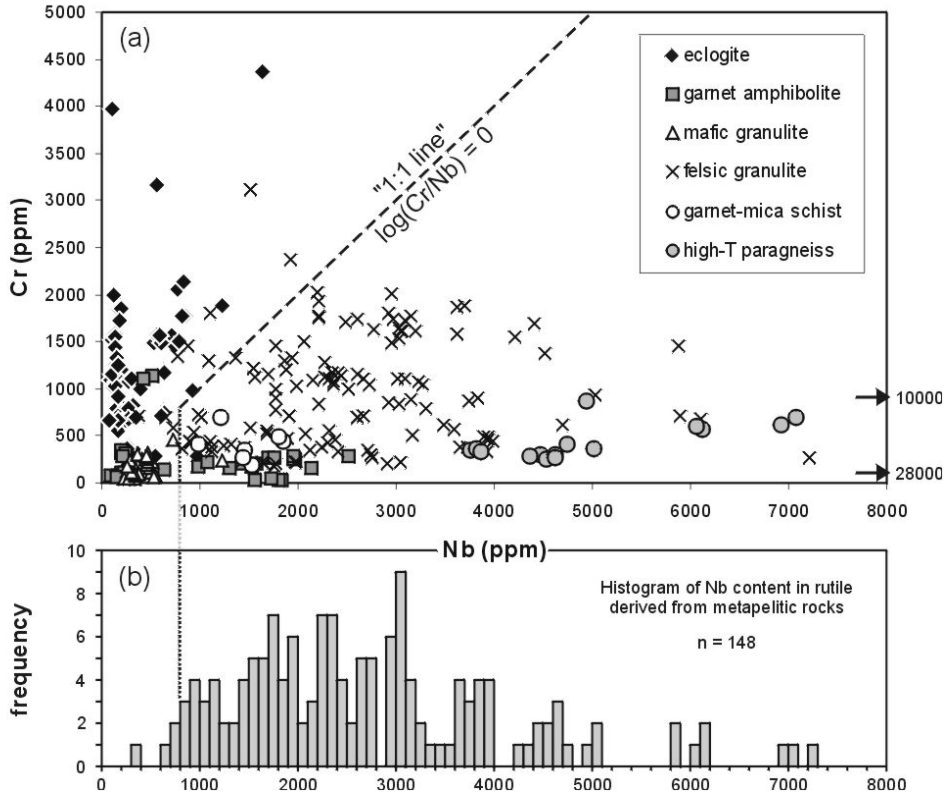

Fig. 4. (a) Plot of Nb v. Cr contents of rutile from different metamorphic lithologies (compiled after data from Fett 1995; Zack et al. 2002, 2004a). Arrows indicate exceptionally high Nb contents of felsic granulite-facies rocks. The "1:1 line" is according to Triebold et al. (2005). The lower limit for rutile derived from a metapelitic rock was set at 800 ppm (see Fig. 4b). **(b)** Histogram of Nb content in rutile derived from metapelitic rocks.

Zack et al. (2004a) demonstrated that the Zr concentration in rutile coexisting with quartz and zircon is strongly temperature dependent. They presented an empirically calibrated Zr-in-rutile thermometer (Fig. 5), expressing temperature as:

$$T(°C) = 127.8 \times \ln(Zr\ ppm) - 10$$

with an error of ± 50 °C. The calibration of Zack et al. (2004a) was based on analyses of rutile grains from 31 metamorphic rocks with rutile–quartz–zircon assemblages spanning a temperature range from 430 to 1100 °C. The reliability of this rutile thermometer for a wide variety of eclogites was demonstrated by Zack & Luvizotto (2006). Recently, Watson et al. (2006) presented a revised Zr-in-rutile thermometer based on experimental data and constrained by natural rutiles from metamorphic rocks (Fig. 5), expressing temperature as:

$$T(°C) = \frac{4470}{7.36 - \log_{10}(Zr\ ppm)} - 273$$

with an error of ± 20 °C. The two thermometers intersect at a temperature of ~540 °C but diverge significantly both at lower and higher temperatures (Fig. 5). Watson et al. (2006) considered this behaviour to indicate a possible pressure dependence and emphasised the need for further investigation. The successful application of the Watson et al. (2006) calibration was recently shown by Spear et al. (2006) on blueschist-facies rocks from Sifnos Island, Greece.

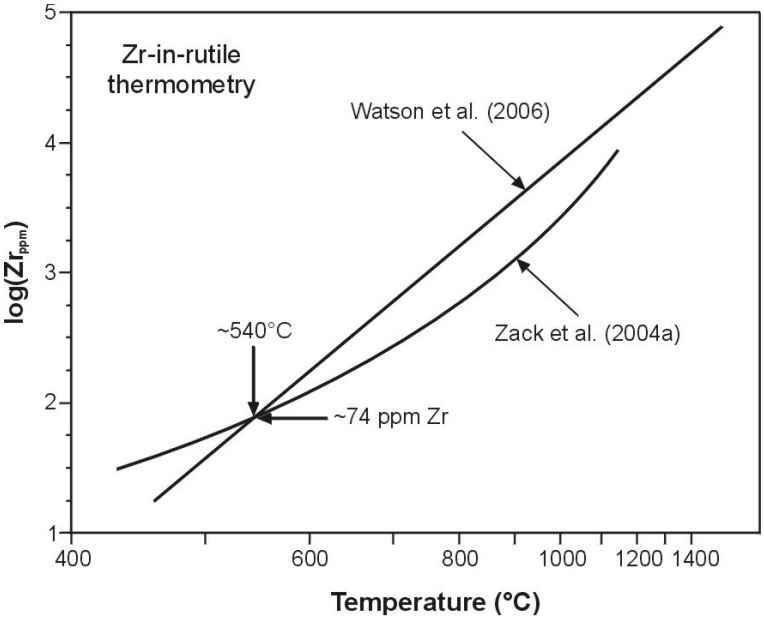

Fig. 5. Comparison of Zr-in-rutile thermometers (modified after Watson et al. 2006).

The combined use of detrital rutile chemistry and thermometry for quantitative provenance analysis was first applied by Zack et al. (2004b). Subsequent studies by Triebold et al. (2005, 2007) and von Eynatten et al. (2005) have demonstrated that the trace-element composition of detrital rutile is unrelated to the grain size of the host sediment and revealed that high-grade metamorphic rutile may preserve its chemical signature to much lower temperatures, meaning that rutile may survives metamorphic conditions on a retrograde path below 550 °C. Stendal et al. (2006) have also shown that relic rutile can retain its original composition during low- to medium-grade metamorphism, indicating that it can survive temperatures as high as 620 °C. Thus, the generally accepted views of rutile breakdown during low-grade metamorphic overprint (greenschist facies) and formation during medium-grade metamorphic conditions (e.g. Force 1980; Zack et al. 2004b) may not be strictly valid.

5. Analytical methods

Rutiles were separated following standard procedures (hydraulic press, rotary mill, Wilfley table, Frantz isodynamic magnetic separator and heavy liquids [methylene iodide]). Rutile grains were hand-picked under a binocular microscope and mounted in epoxy resin, sectioned and polished. For each sample electron-microprobe analyses of randomly selected rutile grains were performed with a JEOL JXA 8900RL instrument at the University of Mainz, equipped with 5 wavelength-dispersive spectrometers. The analytical conditions of the EMP were similar to those described by Zack et al. (2004a) on a similar instrument. Each rutile grain was analysed for Ti, Cr, Al, Fe, Nb, Zr, Si and V. Operating conditions were 20 kV acceleration voltage with a beam current of 120 nA and a beam diameter of 5 µm. Detailed conditions for the spectrometers and standards used can be found in the Table 1.

Areas devoid of cracks or inclusions were chosen for spot analyses. Besides single measurements (one spot per grain) multiple analyses of selected grains were also performed to check for chemical homogeneity. The formation temperature of each rutile grain was calculated by applying the Zr-in-rutile thermometers of both Zack et al. (2004a) and Watson et al. (2006) [abbreviated as T_Z and T_W respectively]. Since the Zr detection limit of the EMP employed is 20 ppm, the Zr-in-rutile thermometer is applicable for rutiles crystallised above ~470 °C (T_W). A complete set of mineral analyses is given in the Appendix.

Table 1. Conditions of the electron microprobe for rutile trace-element analyses

Spectrometer	**1 TAP**	**2 PETJ**	**3 LIF**	**4 LIF**	**5 PETH**
Element (Line)	Al (Kα)	Nb (Lα)	Cr (Kα)	Ti (Kβ)	Zr (Lα)
Count time	240	300	130	15	300
Bckg time	60	80	80	12	150
Standard	Al_2O_3, synthetic	Nb_2O_5, synthetic	Cr_2O_3, synthetic	TiO_2, synthetic	$ZrSiO_4$, natural
DL	15	70	20	650	20
Element (Line)	Si (Kα)		Fe (Kα)	V (Kα)	
Count time	60		150	260	
Bckg time	30		75	75	
Standard	$CaSiO_3$, natural		Fe_2O_3, synthetic	V-metal, synthetic	
DL	20		20	30	

Count time counting time on the peak (in sec), *Bckg time* counting time on background position (in sec), *DL* detection limit (in ppm)

In addition to EMP analyses, laser micro-Raman spectroscopy was applied to randomly selected rutile grains with variable Zr and Si contents to identify the TiO_2 structure type. Raman spectra were obtained using a Horiba Jobin Yvon HR800 spectrometer system at the University of Mainz, equipped with an Olympus BX41 optical microscope. The Raman system was operated at room temperature with an excitation wavelength of 632.8 nm. Titanium dioxide occurs in nature in three structural states. The most common is rutile (tetragonal) which is the high-temperature polymorph. The low-temperature polymorphs are anatase (tetragonal) and brookite (orthorhombic). Rutile was identified by Raman bands at 143, 247, 447, and 612 cm^{-1} (Porto et al. 1967; Tompsett et al. 1995) and anatase by bands at 144, 197, 400, 516, and 640 cm^{-1} (Ohsaka et al. 1978). Brookite is characterized by several bands; strong ones are at 153, 247, 322, and 636 cm^{-1} (Tompsett et al. 1995). The grains analysed by laser micro-Raman spectroscopy are indicated in the Supplementary data.

6. Results

The analysed rutiles from Chios vary in size from a few μm to 0.4 mm and are yellowish to reddish-brown in colour. The results of 399 single and 151 multiple (16 grains) EMP spot measurements are summarised in the Appendix. There is a large variation in the trace-element composition of rutile in all samples analysed: Cr: <20–8703 ppm, Al: 53–1784 ppm, Fe: 194–5853 ppm, Nb: <70–8794 ppm, Zr: <20–5256 ppm, Si: 70–1744 ppm and V:

<30–6036 ppm. Those grains with abnormally low or high Zr and Si contents (23 in all) were additionally analysed by laser micro-Raman spectroscopy. All Raman spectra are characteristic of rutile with the exception of one grain which is clearly anatase (Fig. 6). Brookite was not found in the analysed samples. The EMP analysis of the anatase grain is also included in the Supplementary data; this grain, however, was not considered any further in provenance analysis.

The chemical variability of rutile was tested by multiple measurements on single grains. An example is shown in Fig. 7. Eleven spot measurements on grain 1 from sample CH70 demonstrate that the chemical variability of the Zr content (141–185 ppm) is within the range of the error of the applied Zr-in-rutile thermometer. The variability of the contents in Cr (246–335 ppm) and Nb (1964–2174 ppm) is negligible relative to the overall variability considered here (see Fig. 8), taking into account the analytical error. The Zr-in-rutile thermometer (T_W formalism) yielded temperatures within a narrow range (585–605 °C). Combined with the data in the Appendix, it suggests that for our case study one spot measurement per grain is enough for quantitative single-mineral provenance analysis to distinguish different rutile generations according to their formation temperature.

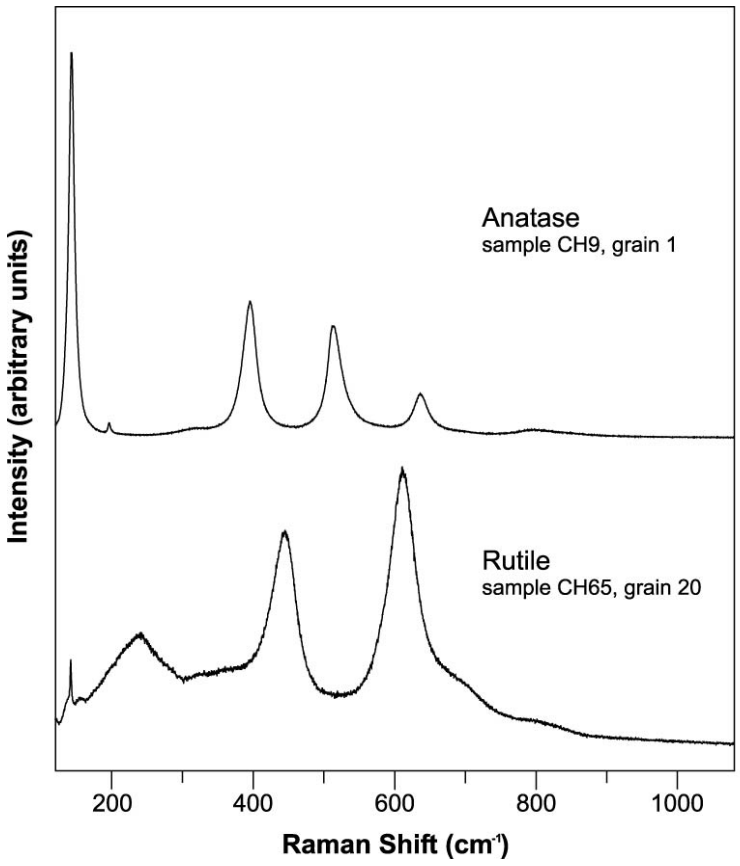

Fig. 6. Laser Raman spectrum of rutile from sample CH65 (grain no. 20) compared with the spectrum of anatase from sample CH9 (grain no. 1).

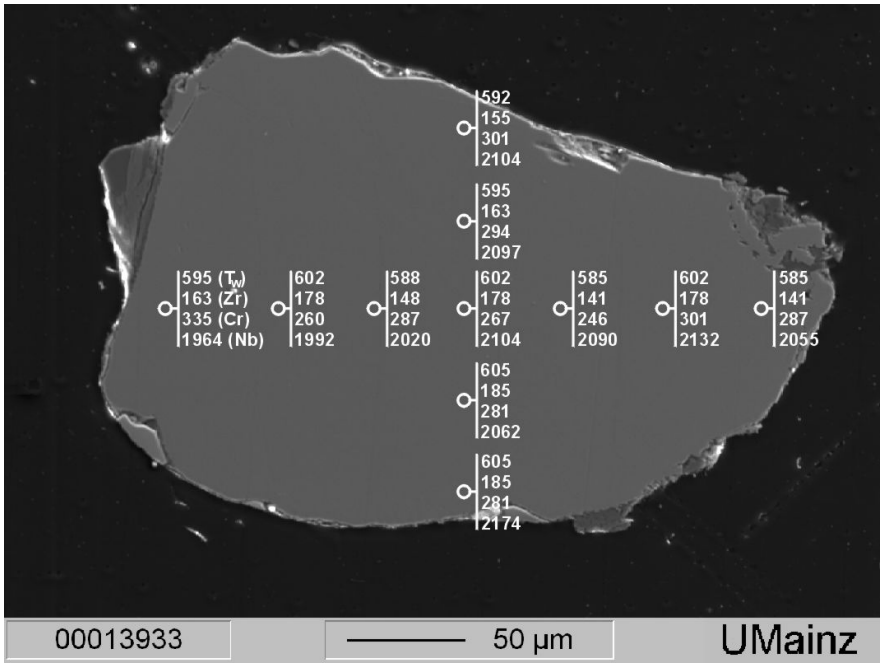

Fig. 7. Secondary electron image of rutile from sample CH70 (grain no. 1) used for multiple measurements. Circles mark the location of the spots analysed. The numbers give T_W in °C and the concentrations of Zr, Cr and Nb in ppm for the indicated spots. Calculated temperatures range between 585 and 605 °C indicating a homogenous distribution of Zr in rutile (see text for discussion).

According to the Nb v. Cr diagram and pie charts (Fig. 8) our data indicate a mixed rutile source for all three Chios successions, with a more pronounced metamafic source in Carboniferous times (especially for the Lower Unit) and a more pronounced metapelitic source in Permo-Triassic times. The low Fe contents (<1000 ppm) of the few Cr-rich rutiles (Cr >3000 ppm) probably hint at their magmatic origin since metamorphic rutile generally contains >1000 ppm Fe (Zack et al. 2004a).

The results of Zr-in-rutile thermometry are shown as histograms in Figure 9 (all rutiles) and as pie charts in Figure 10 (metapelitic rutiles only). Here it is noteworthy that the application of Zr-in-rutile thermometry to detrital rutile is based on the assumption that the source rocks for the rutile had a stable rutile–quartz–zircon assemblage (Zack et al. 2004a, b). Because quartz and zircon are characteristically common in metapelitic rocks, Zr-in-rutile thermometry is applicable for those rocks (Zack et al. 2004a, b). The presence of rutile coexisting with quartz and zircon, however, is not always given in a mafic rock that seems to restrict the application of Zr-in-rutile thermometry. But meanwhile there is some evidence that the Zr-in-rutile thermometer may also work with more mafic lithologies (H. von Eynatten, pers. comm. 2007).

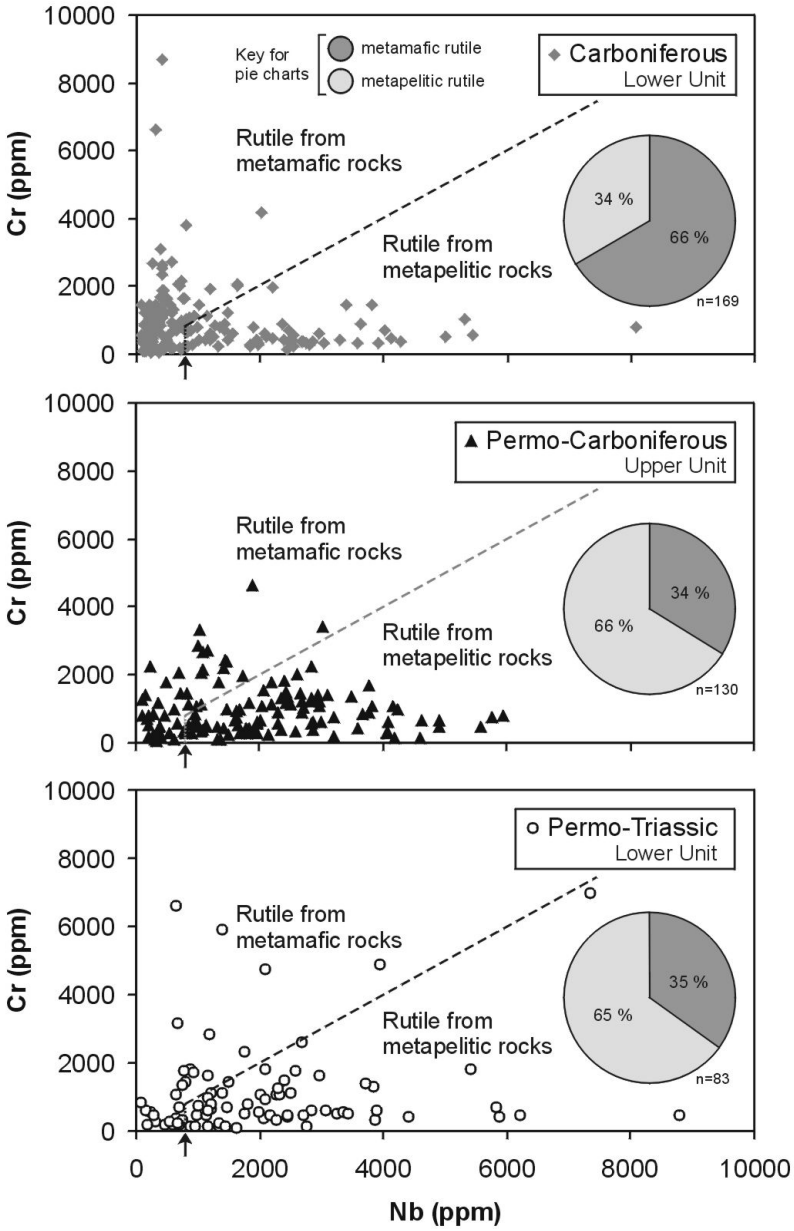

Fig. 8. Plot of Nb v. Cr contents of detrital rutiles. The fields for rutile derived from metamafic and metapelitic rocks are according to Triebold et al. (2005) whereas the lower limit for rutile derived from a metapelitic source rock is set at 800 ppm, marked by an arrow. The discrimination between metamafic and metapelitic rutiles is additionally shown in pie charts (insets).

In this case study, calculated temperatures range between ca. 495–1000 °C (T_Z formalism) and ca. 520–850 °C (T_W formalism) respectively (Fig. 9). In general, the thermometer of Zack et al. (2004a) gives a wider spread and higher formation temperatures for the same rutile grain than the thermometer of Watson et al. (2006), except for grains with <74 ppm Zr (see Fig. 5).

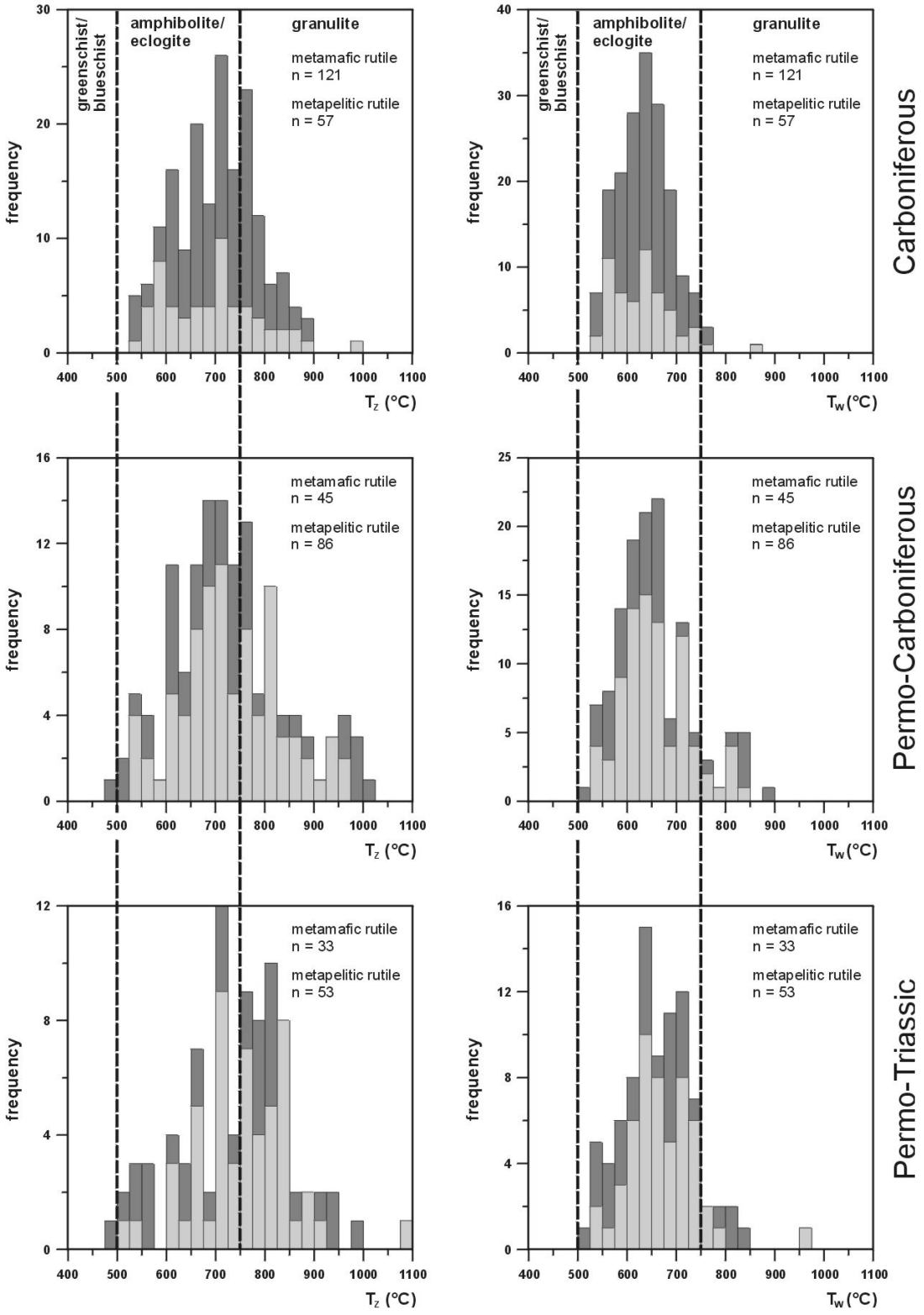

Fig. 9. Histograms of calculated formation temperatures for metamafic and metapelitic rutiles analysed from each unit. On the *left side* the equation of Zack et al. (2004a) was used, on the *right side* the equation of Watson et al. (2006) was applied. Approximate temperature boundaries of metamorphic facies for metapelitic rutile are shown for comparison following Zack et al. (2004b).

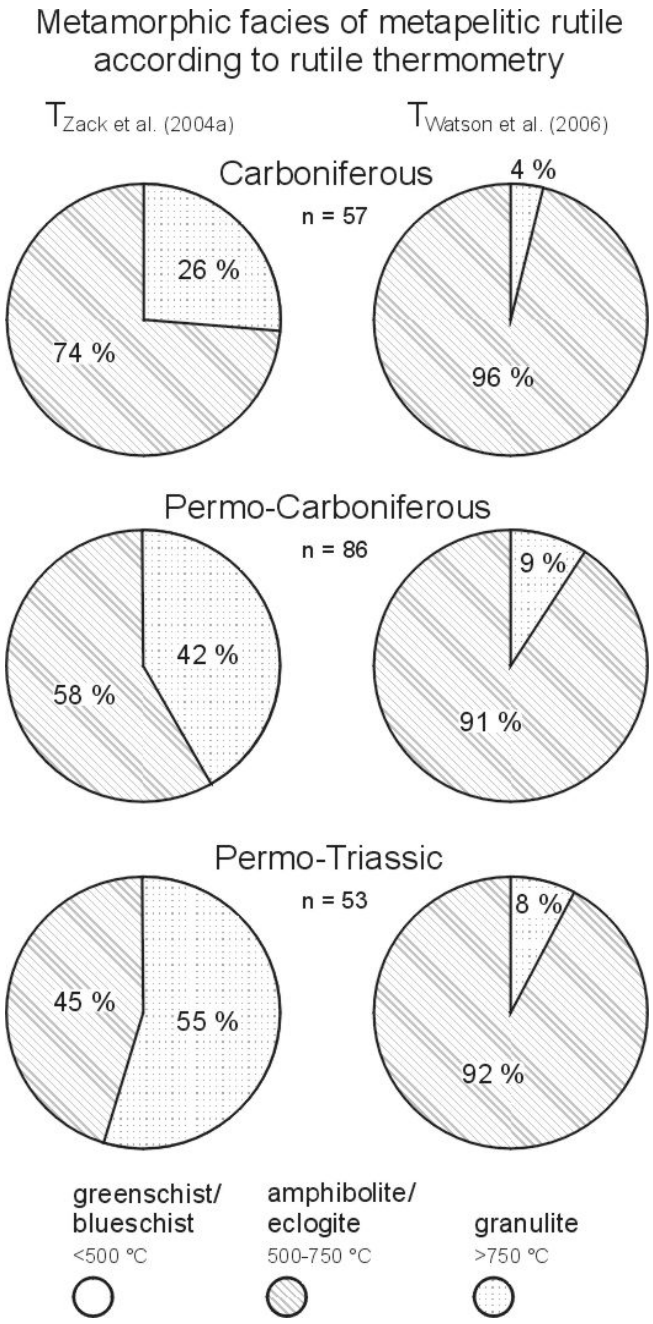

Fig. 10. Pie charts showing the percentage of different metamorphic facies for the source rocks of metapelitic rutile according to calculated formation temperatures in Figure 9.

Nevertheless, both thermometers show a shift towards "hotter" rutiles in both the Permo-Carboniferous and the Permo-Triassic samples. High Zr concentrations in our rutiles are not accompanied by high Si values; we therefore interpret the high temperatures calculated for these grains as real formation temperatures and not due to submicroscopic zircon inclusions. It is interesting to note that the highest Zr contents (>1000 ppm) and, by implication, the highest calculated formation temperatures (e.g. T_W >750 °C) are restricted to

rutiles with Nb <2500 ppm and Cr <3500 ppm. Moreover, the highest calculated temperatures belong to metapelitic rutiles.

As Fig. 9 indicates there is no input of metapelitic rutile from greenschist- or blueschist-facies rocks, instead, amphibolite- and eclogite-facies lithologies are the most plausible candidates for this type of rutile, whereas the contribution of granulite-facies rocks depends critically on the thermometer adopted. Granulite-facies sources become important only in the Permo-Carboniferous and Permo-Triassic samples, as can be clearly seen from Fig. 10. However, the T_Z formalism requires that about 50% of the rutiles from the Permo-Carboniferous and Permo-Triassic samples be derived from granulite-facies sources for which we find no solid geological evidence so far. For this reason we will adhere, in this paper, to the thermometer of Watson et al. (2006). It is nonetheless significant that even using the latter thermometer at least ca. 8% of the detrital rutile in Permo-Carboniferous and Permo-Triassic times seems to have originated from high-grade metamorphic gneiss terranes.

7. Discussion and conclusions

The chemistry and thermometry of detrital rutile from clastic sedimentary rocks of Chios have provided important information about the lithology of their source rocks and allow a chemostratigraphic distinction to be made between the Carboniferous samples on the one hand and the Permo-Carboniferous and Permo-Triassic samples on the other. Rutile Cr-Nb systematic indicates a major input from metamafic lithologies in the Carboniferous succession and a major input from metapelitic lithologies in the Permo-Carboniferous and Permo-Triassic successions. The presence of detrital chrome spinel in the clastic sedimentary successions of Chios confirms an input from (ultra)mafic rocks (e.g. Meinhold et al. 2007). The calculated rutile formation temperatures (T_W formalism) range between ca. 520 and 850 °C with “hotter” rutile being encountered in the Permo-Carboniferous and Permo-Triassic successions. The source of rutiles derived from amphibolite- and eclogite-facies rocks could be sought in basement rocks of Pelagonia (which comprises the Pelagonian Zone and the Attic-Cycladic Massif), Sakarya, the Balkan region and the Menderes Massif since amphibolite- and eclogite-facies rocks of pre-Triassic age have been reported there (e.g. Candan et al. 2001; Mposkos et al. 2001; Anders et al. 2006b; Carrigan et al. 2006; Okay et al. 2006, and references therein). Another potential source for the detrital rutiles of Chios

could be pre-Triassic syenites, diorites, pegmatites and quartz veins. The latter two, although volumetrically minor, show a wide range in chemical composition (e.g. Uher et al. 1998; Rudnick et al. 2000; Zack et al. 2002; Okrusch et al. 2003). The source of rutile derived from high-grade metamorphic gneiss terranes (T >750 °C) cannot yet be identified with confidence. To our knowledge, there are only few localities in the neighbouring Aegean region where granulite-facies rocks of pre-Triassic age have been recognised. The closest locality to Chios is the core series of the Menderes Massif in western Turkey (e.g. Candan et al. 2001, and references therein) where late Pan-African (583.0 ± 5.7 Ma) pelitic granulites have been dated (Koralay et al. 2006). A sediment supply from the Menderes Massif into the clastic sediments of Chios in Late Palaeozoic and Early Triassic times would have an impact on palinspastic reconstructions of the Eastern Mediterranean. However, such an in-depth analysis is beyond the scope of the present paper. High-grade metamorphic gneisses have also been documented from the Balkan region. Carrigan et al. (2006) reported Early Carboniferous (Viséan) high-grade metamorphism from the Sredna Gora Zone of Bulgaria. Pre-Alpine (latest Carboniferous) high-T low-P metamorphism with maximum temperatures exceeding 640 °C was reported for high-alumina metapelitic rocks from the Vernon Massif in the Pelagonian Zone (Mposkos et al. 2001). Furthermore, Early Carboniferous (Viséan–Serpukhovian) high-T medium-P metamorphism and anatexis have been documented for gneisses and pegmatites of the Pulur Massif in the Eastern Pontides (Topuz et al. 2004). If we consider fast exhumation of such 'Variscan' units to the surface and erosion in Permo-Carboniferous times, high-grade metamorphic rocks similar to those exposed nowadays in the Balkan region, in parts of Pelagonia and Sakarya as well as in the Pontides could well have been a source of granulite-facies rutile. Another explanation for the source of granulite-facies rutiles might be recycling of older rutile grains (see Zack et al. 2004b). Geochronological studies indicate an input of Grenvillian (ca. 1 Ga) and Eburnean (ca. 2 Ga) zircons into the Permo-Triassic succession of Chios for which a heterogeneous northern Gondwana-derived source was proposed (Meinhold et al. 2006). Because zircon and rutile behave similarly during the sedimentation cycle, it seems reasonable to assume a minor input of Grenvillian and Eburnean rutile as well.

In general, rutile chemistry in combination with rutile thermometry indicate a change in source rock lithology through time, with more metamafic rocks of low to medium grade eroding in Carboniferous times and more metapelitic rocks of medium to high grade eroding

in Late Carboniferous to Early Triassic times. However, the question arises as to what caused this shift in source composition from the Carboniferous to the Early Triassic. Present palaeotectonic models (e.g. Stampfli et al. 2003) suggest a fore-arc basin setting for the Chios successions in Carboniferous times with northward subduction of the Palaeotethys Ocean beneath the southern margin of Laurussia that switched to a back-arc setting during the Permian and Triassic. This switch in setting probably caused a change in source lithology attested to by a concomitant change in rutile chemistry. It could reflect either an increasing erosion depth of an exhumed 'Variscan' nappe pile of heterogeneous composition in the hinterland (collapsing 'Variscan cordillera': Stampfli et al. 2003, fig. 8) or a change in the style of accretion and erosion of different terranes, probably accompanied by large-scale transcurrent movements (e.g. Stampfli et al. 2002, fig. 4), placing very different oceanic or continental fragments next to each other during the subduction of a branch of the Palaeotethys Ocean in the Late Palaeozoic.

Chapter 3

Provenance of sediments during subduction of Palaeotethys: detrital zircon ages and olistolith analysis in Palaeozoic sediments from Chios Island, Greece

Abstract

Detrital zircon geochronology and analysis of fossiliferous olistoliths from Chios Island, Greece, are used here to constrain terrane accretion processes and the provenance of crustal sources for sediments during the subduction of (a branch of) the Palaeotethys Ocean. U/Pb ages obtained by ion microprobe (SHRIMP-II) analyses of detrital zircons from a Carboniferous greywacke belonging to the tectonostratigraphic Lower Unit of Chios gave major age groups of 2150–1890 Ma, 640–540 Ma, 505–475 Ma and 365–322 Ma. Detrital zircons from a Permo-Triassic sandstone yielded prominent age clusters of 2200–1840 Ma, 1100–910 Ma, 625–560 Ma and 385–370 Ma. The lack of zircon ages between 1.8–1.1 Ga in both samples, coupled with the occurrence of ca. 2 Ga-old zircons, imply a northern Gondwana (NW Africa) source. The recovered conodont fauna from an '*Orthoceras*'-bearing limestone lens from the Carboniferous succession of the Lower Unit indicates a Late Silurian age. The fauna is typical of the Ludfordian *Polygnathoides siluricus* conodont zone. The material has a conodont colour alteration index (CAI) of about 1–2, indicating very low-grade thermal alteration of less than 100 °C. The closest localities with similar conodont-bearing limestones are to be found in the Balkan region and in the Istanbul Zone of northern Turkey. The occurrence of '*Orthoceras* Limestone' can be used as an indicator of palaeo-source reconstruction. Our new zircon ages in conjunction with provenance analysis of Silurian to Early Carboniferous olistoliths strongly suggest that the clastic succession of Chios received its detritus from basement rocks of the Sakarya microcontinent in western Turkey and time

and facies equivalents of Palaeozoic units from the Istanbul Zone in northern Turkey and the Balkan region due to subduction of a branch of Palaeotethys close to the southern active margin of Eurasia in Late Paleozoic times. The multidisciplinary approach of this study underlines the importance of terrane accretion during stepwise closure of Palaeotethys.

1. Introduction

Palaeogeographical reconstructions show the existence of two major oceanic realms in the eastern Mediterranean area: the Palaeotethys and the Neotethys (e.g. Şengör et al. 1984; Stampfli 2000, and references therein). Following Stampfli & Borel (2002), the term Palaeotethys is used here to denote a seaway that separated Gondwana from fragments thereof in a period from the Silurian to early Late Triassic, during which these same fragments drifted northward and accreted to Laurussia in a stepwise fashion. Palaeotethys was closed by the northward drift of the Cimmerian terranes in response to the opening of Neotethys in the south. Despite the accumulation of new data over recent years, the Palaeozoic to early Mesozoic history of Palaeotethys is strongly debated (see Robertson et al. 1996, 2004; Stampfli 2000; Stampfli & Borel 2002) because evidence for subduction, in terms of accretionary complexes, blueschists and magmatic arcs, is scarce. Moreover, the complex Mesozoic to Cenozoic structural and metamorphic overprint gave rise to equivocal palaeotectonic models and interpretations. Two of the most controversial topics are (i) the location of peri-Gondwana fragments such as Pelagonia, Sakarya and the Anatolide–Tauride Block within the Palaeotethyan frame and (ii) the precise location and polarity of subduction of Palaeotethys under those fragments in late Palaeozoic times; it could have been either northward (e.g. Stampfli et al. 1991, 2003; Eren et al. 2004) or southward (e.g. Şengör et al. 1984; Okay et al. 1996; Romano et al. 2006; Xypolias et al. 2006).

The island of Chios in the eastern Aegean Sea (Fig. 1) is a key area for understanding the closure of Palaeotethys (e.g. Stampfli et al. 2003) because it is one of the rare localities where very low-grade to virtually unmetamorphosed fossil-bearing Palaeozoic to Mesozoic sequences are preserved (e.g. Besenecker et al. 1968). A similar succession of late Palaeozoic age can be found in western Turkey opposite Chios in the Karaburun peninsula (Kozur 1998; Robertson & Pickett 2000, and references therein), in the Tavas nappe (Lycian nappes) further south (Kozur et al. 1998) and in the Konya region at the northern margin of the

Menderes–Tauride Platform (Eren et al. 2004). Several tectonic models have been proposed for the origin of the Chios–Karaburun units, including that of an accretionary complex or a rift setting (see Stampfli et al. 1991, 2003; Robertson & Pickett 2000; Zanchi et al. 2003).

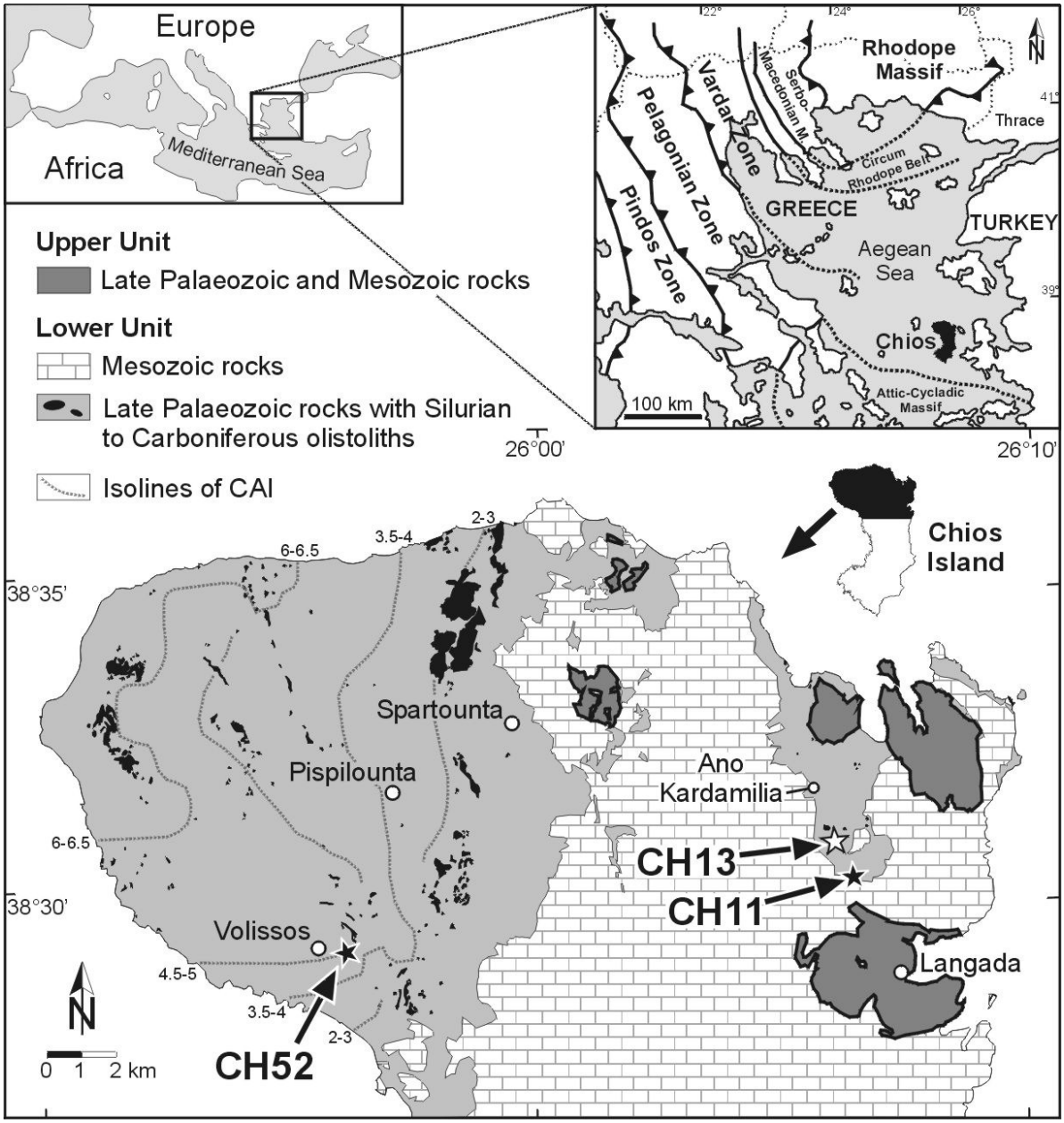

Fig. 1. Simplified geological map showing the northern part of Chios (modified after Besenecker et al. 1968, 1971). The position of Chios in relation to the geotectonic zones of the Hellenic orogen is shown in the upper right inset (after Jacobshagen 1986). Isolines of the conodont colour alteration index (CAI) are according to Larghi et al. (2005). In NW Chios, the CAI values decrease from 6–6.5 in the west to 2–3 in the east. *Black stars* indicate the position of the samples for SHRIMP-II U–Pb zircon dating. *White star* indicates the position of the cephalopod-bearing limestone lens used for micropalaentological investigations.

In the present study, special emphasis has been placed on constraining the provenance of Carboniferous and Permo-Triassic clastic sediments from the Lower Unit of Chios by investigating the age spectra of detrital zircons using the sensitive high-resolution ion microprobe (SHRIMP-II) U–Pb dating method. SHRIMP is a powerful tool in sedimentary provenance analysis to glean information regarding ancient source areas and major magmatic events, crucial for Tethyan plate-tectonic and palaeogeographic reconstructions. The provenance of olistoliths found within the Carboniferous succession is also discussed in order to better constrain the possible sources identified by zircon dating. Our data provide new information about crustal sources and terrane accretion during diachronous closure of Palaeotethys and help clarify the palaeotectonic position of Chios during subduction of this ocean.

2. Geological setting

In the eastern Mediterranean, the Hellenides are an integral part of the Alpine-Himalayan orogenic system and have traditionally been subdivided into the internal (hinterland) and the external (foreland) Hellenides. The internal Hellenides comprise, from SW to NE, the Pelagonian Zone (including the Attic-Cycladic Massif), the Vardar Zone, the Serbo-Macedonian Massif and the Rhodope Massif (e.g. Jacobshagen 1986, and references therein). All these units consist predominantly of Palaeozoic (but also Neoproterozoic and Mesozoic) basement rocks (e.g. Vavassis et al. 2000; Anders et al. 2005, 2006a, b; Turpaud & Reischmann 2005; Turpaud 2006; Himmerkus et al. 2004a, b, 2006a, b, 2007) overlain by or intercalated with sedimentary successions. They experienced quite complex Mesozoic to Cenozoic tectonism, which gave rise to equivocal palinspastic models and interpretations. Chios is generally assigned to the easternmost part of the Pelagonian Zone (e.g. Jacobshagen 1986; see Meinhold et al. 2007, for discussion). Basically, it comprises two tectonostratigraphic units (Figs. 1 and 2): an ‘autochthonous’ Lower Unit and a tectonically overlying ‘allochthonous’ Upper Unit (Herget & Roth 1968; Besenecker et al. 1968). The Lower Unit consists of clastic sediments of Late Palaeozoic age containing blocks (of up to 100 m in diameter) of limestones, radiolarites and volcanic rocks. This succession was variably named ‘Chios mélange’, ‘Chios (wild)flysch’ or ‘Volissos turbidites’ (e.g. Robertson & Pickett 2000; Groves et al. 2003; Zanchi et al. 2003). Here, we use the non-genetic term

Late Palaeozoic rocks of the Lower Unit (Meinhold et al. 2007). The major rock types of this unit are greywackes, minor sandstones and siltstones as well as intercalated quartz-bearing conglomerates (Fig. 3). The latter mainly contain clasts of quartz, black chert and quartzite embedded in a coarse-grained quartzose matrix. Erosional contacts at the base of greywacke and conglomerate beds and upward reduction in grain size can often be observed. In some outcrops, well developed sole marks and ripples can be seen at the base of turbidite beds (Fig. 3). The facies of the turbidite-olistostrome succession resulted mainly from turbidity currents, debris flows and submarine slides. Groves et al. (2003) reported Mississippian microfossils from calcareous clasts of a breccia lying within the turbidite-olistostrome succession and suggested that the Late Palaeozoic rocks of the Lower Unit are most probably Late Visean or Early Serpukhovian in age.

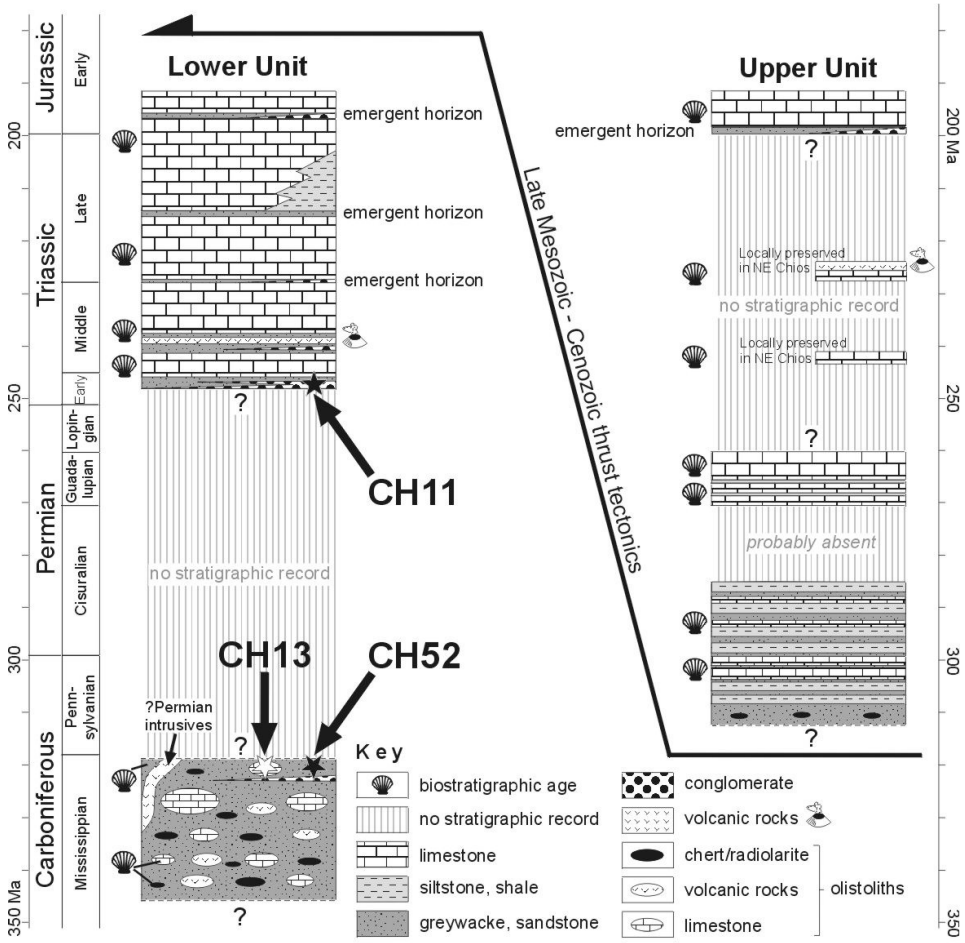

Fig. 2. Tectonostratigaphic columns for Late Palaeozoic and Mesozoic rocks of Chios (taken from Meinhold et al. 2007), including stratigraphic position of analysed samples (*star*). Geological time scale is according to Gradstein et al. (2004).

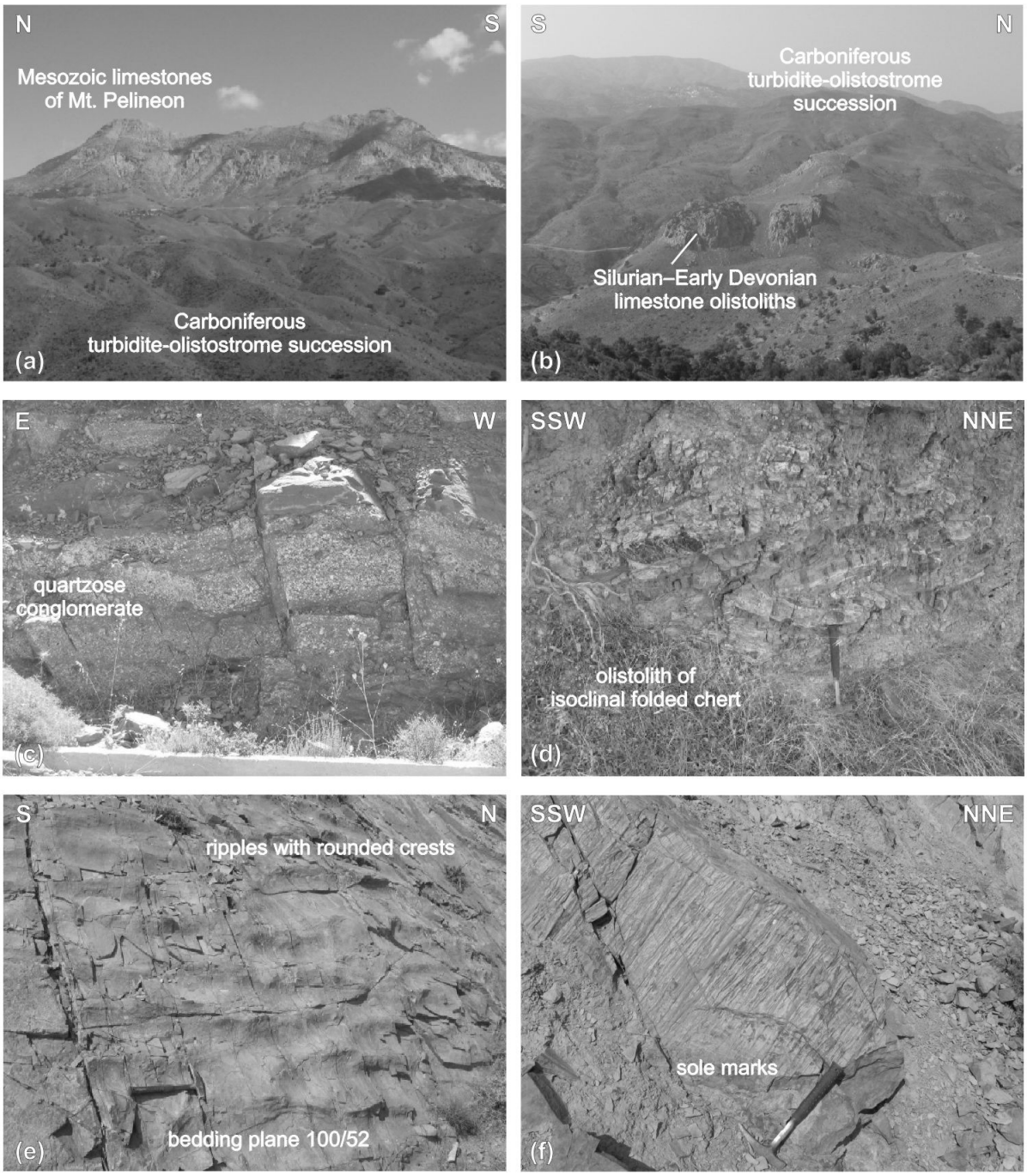

Fig. 3. (a) Photograph showing the Late Palaeozoic rocks of the Lower Unit overlain by Mesozoic limestones. **(b)** Silurian–Early Devonian limestone olistoliths; SSW of Spartounta village. **(c)** Quartzose conglomerate within the Late Palaeozoic rocks of the Lower Unit. Channel deposit with erosive base, graded bedding and fining upward; SE of Volissos town. **(d)** Olistolith of isoclinal folded chert; E of Ano Kardamilia town. **(e)** Ripples at the base of fine-grained quartzose litharenite beds within the Late Palaeozoic rocks of the Lower Unit; NW of Pispilounta village. **(f)** Sole marks at the base of a litharenite bed within the Late Palaeozoic rocks of the Lower Unit; NW of Pispilounta village. For scale in (d), (e) and (f): The hammer is ca. 30 cm long.

The Late Palaeozoic rocks of the Lower Unit were interpreted by Papanikolaou & Sideris (1983) as a post-Middle Carboniferous to pre-Scythian wildflysch bearing Silurian to Carboniferous olistoliths. Stampfli et al. (1991) proposed that the wildflysch represents a predominantly Permian accretionary wedge that can be correlated with the Karakaya Complex of Turkey, which they considered to mark a Palaeotethyan suture. Robertson & Pickett (2000) maintained that the Late Palaeozoic rocks of the Lower Unit are a Late Carboniferous to ?Early Permian subduction–accretionary complex that developed near the southern margin of the Palaeotethys Ocean. Models invoking a rift setting or a long-lived, deep marine basin receiving olistoliths are also discussed in Robertson & Pickett (2000). Recently, Stampfli et al. (2003) and Zanchi et al. (2003) proposed a tectonic model of an arc–trench system, which formed along the Palaeotethyan subduction zone in Carboniferous times. Meinhold et al. (2007) suggested a tectonic setting of a continental volcanic arc, involving upper-continental crustal rocks and/or young differentiated arc material as well as a mixed source of (ultra)basic rocks.

Non-fossiliferous conglomerates and sandstones overlie the Late Palaeozoic rocks of the Lower Unit (Fig. 2). The conglomerates mainly contain clasts of quartz and black chert embedded in a coarse-grained quartzose matrix. Zanchi et al. (2003) described an angular unconformity at the base of this clastic succession, interpreted as a Variscan unconformity. However, the stratigraphic age of these possibly Early Triassic conglomerates and sandstones is uncertain because neither biostratigraphic nor geochronological ages exist so far. Following Meinhold et al. (2007) we use the term Permo-Triassic instead of Early Triassic. The conglomerates and sandstones pass upwards into limestones of late Early to Late Triassic–Early Jurassic age (Besenecker et al. 1968). A Middle Triassic volcano-sedimentary succession is intercalated with the limestones (Besenecker et al. 1968; Gaetani et al. 1992). Non-marine clastic deposits followed by dolomites and limestones mark the latest Triassic–earliest Jurassic.

The Upper Unit of Chios predominantly comprises siliciclastic and carbonaceous rocks of Late Carboniferous and Permian ages (e.g. Besenecker et al. 1968), overlain by transgressive sediments of Early Jurassic age, which are locally overlain themselves by transgressive deposits of Late Cretaceous age. The youngest rocks on Chios are Cenozoic sediments and volcanic rocks cropping out mainly in the southeastern part of the island.

3. Geochronological method

Zircon separation was carried out using standard techniques. The samples were crushed with a hydraulic press and a rotary mill. Zircon enrichment was achieved through hydro-gravimetric (Wilfley table), magnetic (Frantz isodynamic separator) and density (methylene iodide) separation techniques followed by handpicking under a binocular microscope. Zircon grains were mounted in epoxy resin, sectioned and polished together with grains of zircon standard 91500 (ID-TIMS age = 1065.4 ± 0.3 Ma; Wiedenbeck et al., 1995) for calibration of the U concentrations and TEMORA 1 (ID-TIMS age = 416.75 ± 0.24 Ma; Black et al. 2003) for calibration of the U–Pb ratios. Prior to the analyses the mounts were gold-coated, photographed under the microscope using both reflected and transmitted light and CL-imaged to reveal the internal structure of the zircons and target specific areas within single crystals, e.g. growth zones, inherited cores, etc. (Fig. 4). Measurements were carried out on the SHRIMP-II mass spectrometer using a secondary electron multiplier operated in a mass-scanning mode at the Centre of Isotopic Research in St. Petersburg, Russia. During U–Pb–Th analysis, the spot size of the O_2^- primary ion beam was set at about 25 μm. The primary beam intensity was about 4 nA. Data reduction and presentation were processed with SQUID (Ludwig 2001) and Isoplot/Ex (Ludwig 2003), using decay constants recommended by IUGS (Steiger & Jäger 1977). The common lead correction was done by using the measured ^{204}Pb and the model of Stacey & Kramers (1975). Unless otherwise stated $^{206}Pb/^{238}U$ ages are quoted for analyses younger than 1.2 Ga whereas $^{207}Pb/^{206}Pb$ ages are quoted for analyses older than 1.2 Ga. The latter are generally considered as being minimum ages. The analytical data are given in the Appendix.

4. Sample description and results

4.1. Carboniferous sample CH52

Sample CH52 was collected from a Carboniferous bluish-grey, medium-grained litharenite (greywacke) cropping out east of Volissos town (Fig. 1). The framework grains are monocrystalline and polycrystalline quartz, and sedimentary and volcanic lithoclasts. Plagioclase grains often display patchy sericitisation and calcite replacement. Single

muscovite flakes and minor detrital biotite also occur. The greywacke is poorly sorted by size and dominated by angular to subangular clasts. Accessory minerals include predominantly zircon, rutile, tourmaline and opaque minerals as well as minor chrome spinel and epidote.

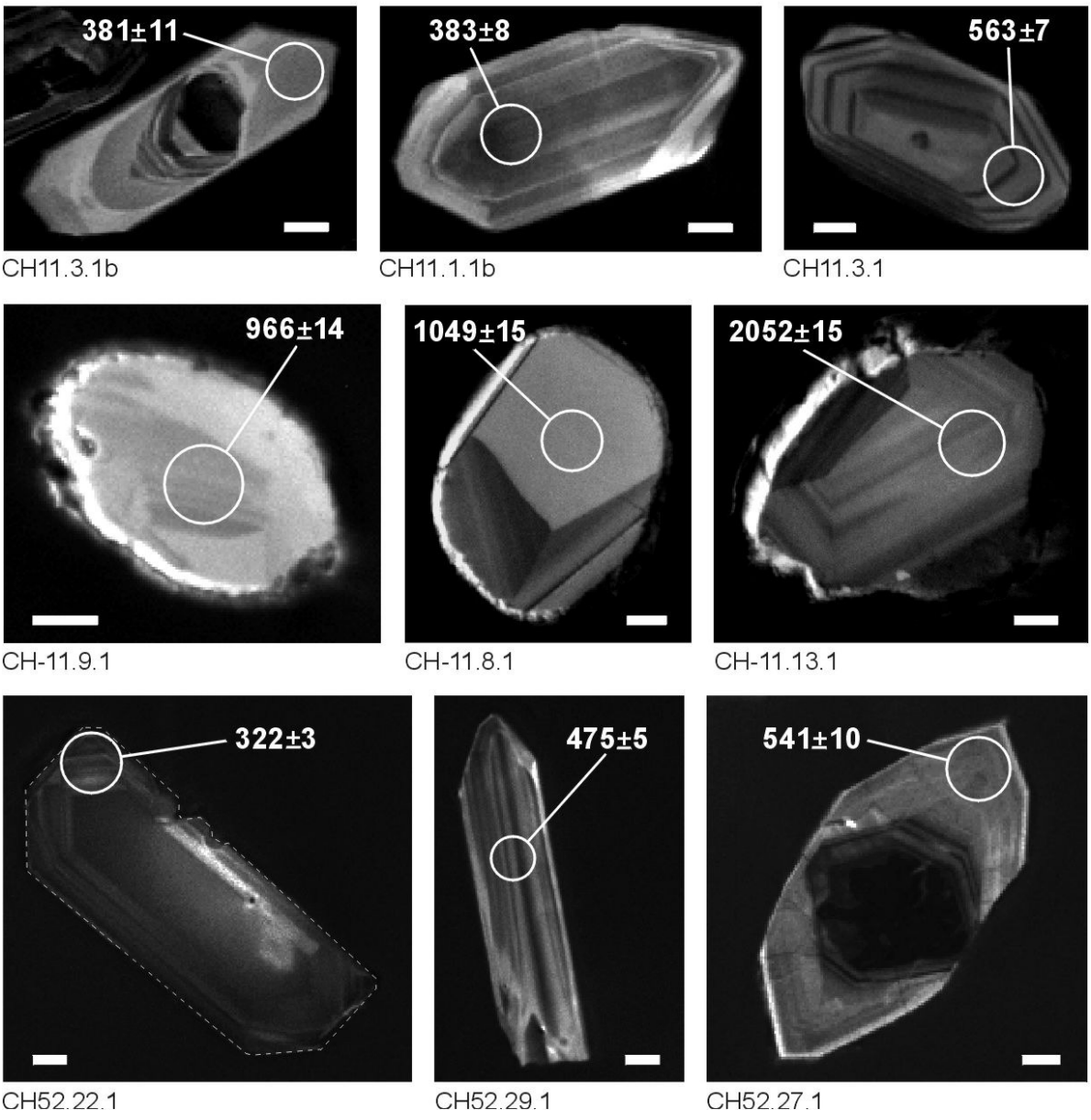

Fig. 4. CL images of representative zircon grains from Chios with location of the SHRIMP-II analysis spot and corresponding $^{206}U/^{238}Pb$ age (±1σ); for grain CH-11.13.1 the $^{207}Pb/^{206}Pb$ age (±1σ) is shown. Letter–number code below the images: sample-grain-spot. The scale bar represents 20 μm in all images.

Most of the analysed zircons have clear oscillatory growth zoning and appear to be magmatic in origin whereas few are structureless. Inherited cores are rare. The length of single zircon crystals varies between ca. 80 and 290 μm, and their morphology ranges from

long prismatic to isometric. Around 65% of the detrital zircon grains have an aspect ratio (length/width) of between 1 and 2. The Palaeoproterozoic to Neoproterozoic zircons have a well-rounded to rounded shape; the Cambro-Ordovician to Carboniferous zircons are slightly rounded, subhedral to euhedral. Euhedral zircons are clear. The (110) prism generally dominates over the (100) prism, as does the (221) bipyramid over the (101) bipyramid, corresponding to the S1, S6, S12 and S17 zircon types of Pupin (1980). Such a morphology is typical of an igneous origin and suggests crystallisation temperatures of about 650–700 °C in a magma of crustal origin. The presence of euhedral detrital zircons may be taken to indicate the last input of magmatic zircons. These zircons are of first-order cycle. Some well-rounded zircons have a pitted surface, which clearly indicates long-distance sedimentary transport.

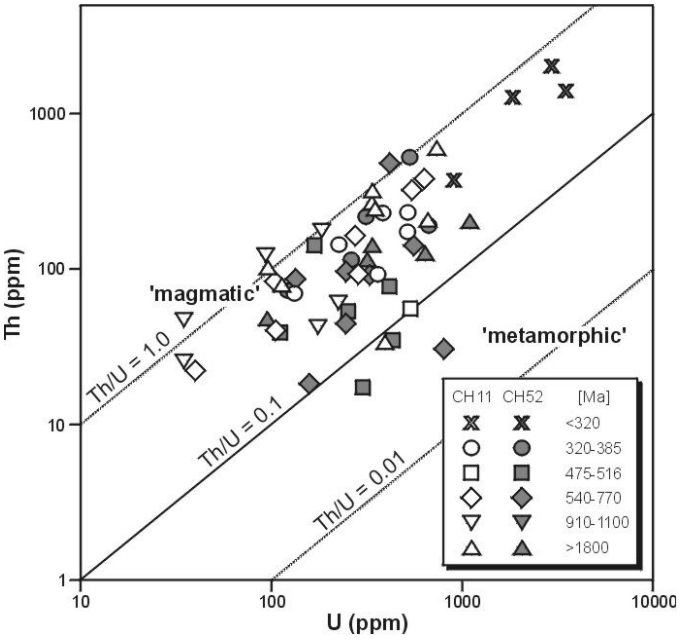

Fig. 5. Th and U concentrations of different zircon age groups. Relevant Th/U ratios are included for comparison: 1.0 – lower limit for magmatic zircon from basic rocks; 0.1 – upper limit for metamorphic zircon (diagram modified after Teipel et al. 2004)

With the exception of a few grains, the analysed zircons have low to medium U contents (94–661 ppm) and moderate Th/U ratios (0.12–1.19). These values are typical of zircons from acidic igneous rocks (Fig. 5). Three grains seem to be of metamorphic origin with Th/U ratios <0.1. Analysed grains gave four prominent zircon populations that range in age from Early Proterozoic to Phanerozoic. Sample CH52 contains zircon clusters of ca. 2150–1890, 640–540, 505–475 and 365–322 Ma (Figs. 6 and 8). Grain CH52.1.1 has a concordant age of 2542 ± 11 Ma, which indicates the presence of a minor Archaean component. The $^{206}Pb/^{238}U$ age of 1422 ± 8 Ma of grain CH52.20.1 is strongly discordant and thus may not be geologically meaningful since the time of Pb loss cannot be determined. By

contrast, its $^{207}Pb/^{206}Pb$ age of 1890 ± 18 Ma appears to be geologically significant. Grain CH52.22.1 has a concordant $^{206}Pb/^{238}U$ age of 322 ± 3 Ma. This zircon crystal is euhedral, clear and has oscillatory growth zoning (Fig. 4) with U and Th values typical of magmatic origin. It is characterized by the dominance of the (100) prism over the (110) prism. Only the (101) pyramid is present. This type of morphology corresponds to the P5 zircon type of Pupin (1980) and indicates crystallisation temperatures of about 800–850 °C in an alkaline magma. Grain CH52.22.1 can therefore be considered as representing the youngest detrital input, thus giving a maximum age of deposition for the Carboniferous greywacke. Four zircon grains (CH52.2.1, CH52.4.1, CH52.10.1, and CH52.21.1) have $^{206}Pb/^{238}U$ ages of ca. 273 to 206 Ma much younger than the age of the host sediment. These zircons also have very high concentrations of U (909–3453 ppm), Th (370–2016 pm) and common Pb (3.95–24.99%). Their ages are therefore interpreted as the result of radiogenic lead loss probably caused by radiation damage (see Kolodner et al. 2006) and as soiled with common Pb, and were consequently not considered in provenance analysis.

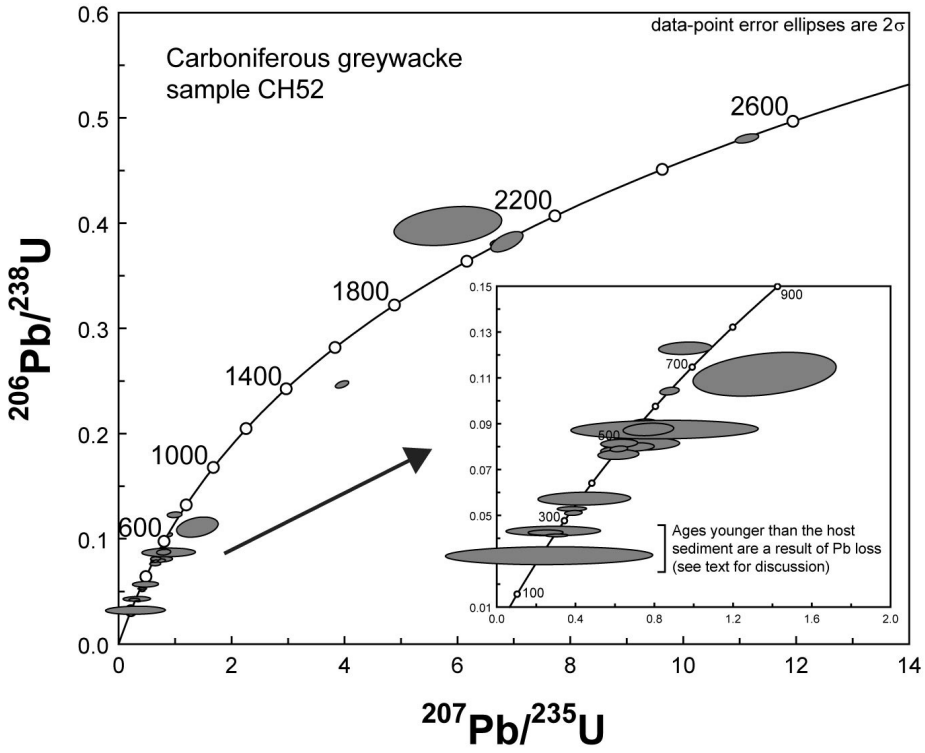

Fig. 6. Concordia diagrams showing the results of SHRIMP-II U–Pb zircon analyses for sample CH52. Error ellipses are drawn at the 2-sigma level. The inset shows the enlarged concordia plot for $^{206}U/^{238}Pb$ ages younger than 800 Ma.

4.2. Permo-Triassic sample CH11

Sample CH11 is a Permo-Triassic, yellowish-grey, medium-grained quartz arenite (sandstone) collected from a quartzose conglomerate layer cropping out northwest of Langada village (Fig. 1). Monocrystalline and polycrystalline quartz are the major framework components. The heavy minerals observed are characterized by the stable assemblage zircon+rutile+tourmaline, indicating sediment maturity. Chrome spinel grains were also found with Cr-number (Cr/(Cr+Al)) values between 0.43 and 0.83 and Mg-number ($Mg/(Mg+Fe^{2+})$) values between 0.24 and 0.68, suggesting a probably mixed (ultra)basic source involving ridge peridotites, fore-arc peridotites and island-arc basalts (Meinhold et al., 2007). The occurrence of iron-hydroxy-oxides indicates secondary alteration processes. Description of zircon structure morphology fits that of sample CH52 above. However, the length of single zircon crystals varies between ca. 80 and 230 µm with only a few long prismatic grains. Around 70% of the detrital zircon grains have an aspect ratio of between 1 and 2. Only a few crystals are euhedral that could be used for determining type. The (100) prism of the euhedral zircons dominates over the (110) prism, as does the (101) bipyramid over the (221) bipyramid, corresponding to the S19, S20 and S24 zircon types of Pupin (1980). Such a morphology is typical of an igneous origin and suggests crystallisation temperatures of about 800–850 °C in a calc-alkaline to sub-alkaline granitic magma.

In this sample, the analysed zircons have low to medium U contents (35–745 ppm) and, except one grain, moderate Th/U ratios (0.11–1.45). These values are typical of zircons from acidic igneous rocks (Fig. 5). The zircon ages gave populations of ca. 2200–1840, 1100–910, 625–560 and 385–370 Ma (Figs. 7 and 8). Grain CH-11.6 has an inherited core with a magmatic rim of ca. 475 Ma. In a concordia diagram, a regression of the core and the rim yields a discordia with a concordant lower intercept at 477 ± 6 Ma and an upper intercept at 1922 ± 21 Ma (Fig. 7). In effect, lower-intercept ages do not necessarily have a geological meaning and should therefore be handled with care (Mezger & Krogstad 1997). In this case, however, the lower intercept of the zircon rim at 477 ± 6 Ma is a concordant age and can be interpreted as the time of secondary zircon crystallisation (magmatic or metamorphic). The upper intercept reflects the time of primary zircon crystallisation, and is interpreted as the age of formation of the magmatic protolith that survived as the inherited core. The $^{206}Pb/^{238}U$ age of around 1.6 Ga of grain CH-11.6.1 is the result of lead loss and was therefore excluded

from the age histogram of Figure 8 and from further discussion. Lead loss in zircons is a common phenomenon and mostly attributed to metamictisation and later recrystallisation during which Pb is removed from the zircon crystals (Williams, 1992; Mezger and Krogstad, 1997). Grain CH11.9.1 has a rounded shape and a concordant $^{206}Pb/^{238}U$ age of 326 ± 2 Ma, which is the youngest age found in the Permo-Triassic sandstone so far, giving a maximum age of deposition for this rock.

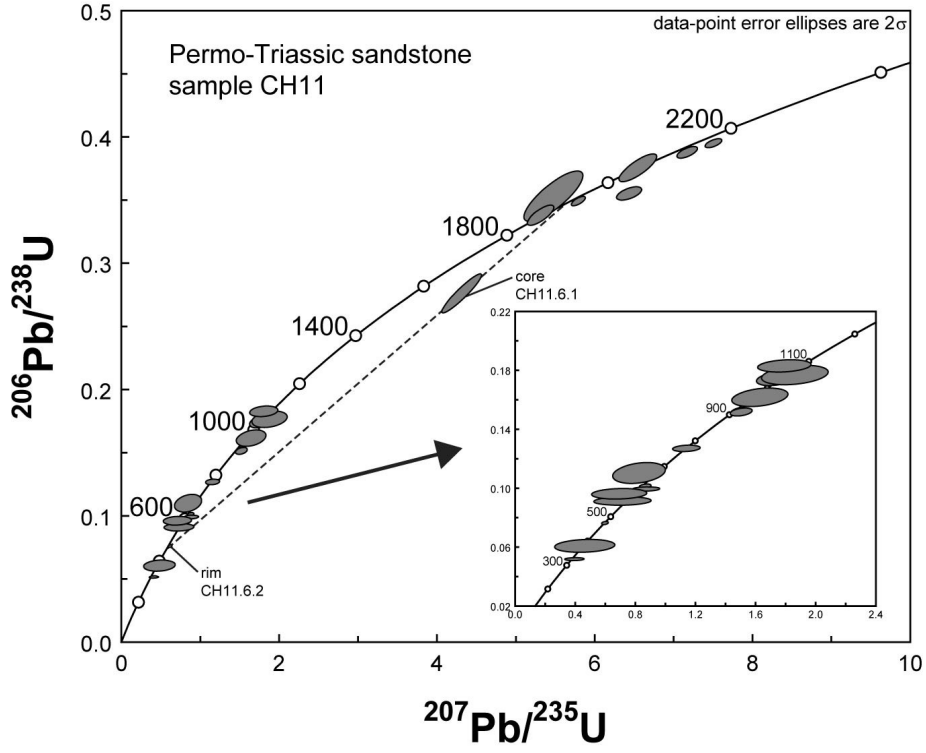

Fig. 7. Concordia diagrams showing the results of SHRIMP-II U–Pb zircon analyses for sample CH11. Error ellipses are drawn at the 2-sigma level. The inset shows the enlarged concordia plot for $^{206}U/^{238}Pb$ ages younger than 1.2 Ga.

5. Discussion

5.1. Possible source areas according to zircon data

The U/Pb data for detrital zircons from Chios indicate the presence of at least three Proterozoic and a number of Palaeozoic crustal sources. The period between ca. 1.8 and 1.1 Ga is characterized by a total absence of tectonomagmatic activities in the source area of the analysed zircons (Fig. 8). The oscillatory zoning pattern of most of the zircons and the Th/U

ratios between 0.1 and 1.2 indicate a source of mainly magmatic origin. To facilitate identification of possible source areas for the Chios samples presented herein we have compiled the distribution of Late Neoproterozoic and Palaeozoic zircon age data from Greece and the surrounding region (Fig. 9 and Appendix E). In the ensuing discussion, we make inferences as to possible source areas for the detrital zircon age clusters recorded in the analysed sediments from Chios.

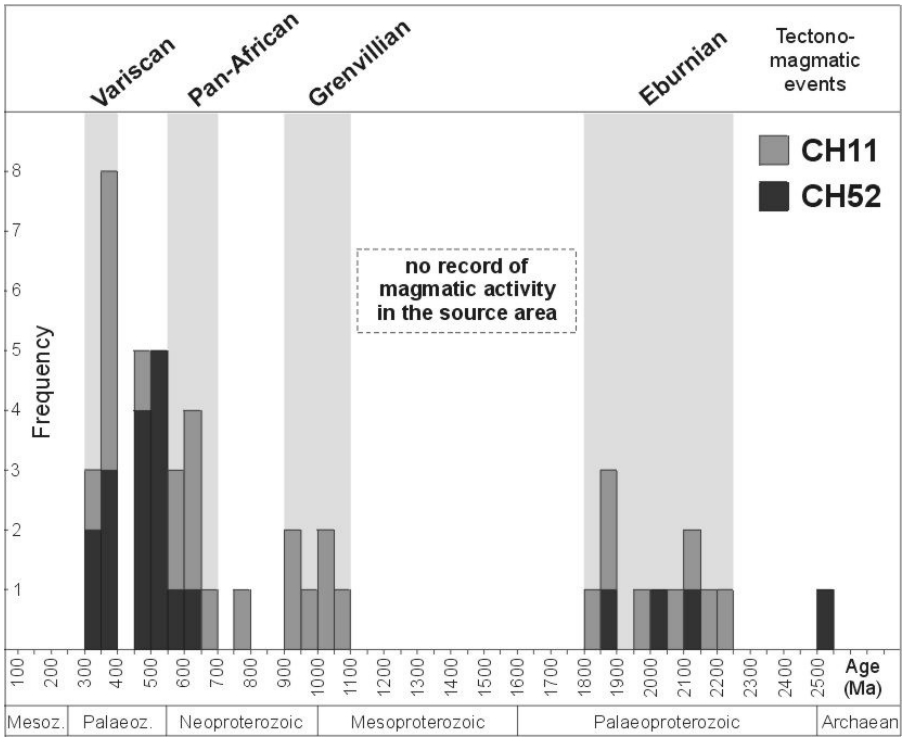

Fig. 8. Distribution of SHRIMP-II U/Pb ages for analysed detrital zircons from Chios. Ages younger than 320 Ma (see paragraph 4 for discussion) and the highly discordant grains CH52.12.1, CH52.13.1 and CH52.24.1 (see Fig. 6) were excluded from the frequency diagram. $^{206}Pb/^{238}U$ ages are quoted for analyses younger than 1.2 Ga whereas $^{207}Pb/^{206}Pb$ ages are quoted for analyses older than 1.2 Ga.

Ca. 2.2–1.9 zircon ages

Early Proterozoic (ca. 2 Ga) ages are commonly present among zircons in terranes derived from northern Gondwana (e.g. Zeh et al. 2001; Linnemann et al. 2004, and references therein) as the result of the Icartian–Eburnian crust formation event that is known from the West African Craton (e.g. Ennih & Liégeois 2001; Egal et al. 2002; Walsh et al. 2002), from South America (Keppie et al. 1998, and references therein) and also from Brittany and the Channel Islands in western Europe (Calvez & Vidal 1978; Samson & D'Lemos 1998). The

lack of late Palaeoproterozoic and Mesoproterozoic zircon ages has often been used as a strong argument in favour of a NW African provenance of Precambrian peri-Gondwanan basement terranes (e.g. Zeh et al. 2001; Friedl et al. 2004; Linnemann et al. 2004; Samson et al. 2005). In the case of the Chios sediments then, the lack of detrital zircons with ages between 1.8 and 1.1 Ga, combined with the high abundance of grains aged around 2 Ga can be interpreted as pointing towards a NW African provenance. Moreover, the total absence of zircons with ages of between ca. 1.5 and 1.7 Ga (Rapakivi events: Gorbatschev & Bogdanova 1993) indicates that a detrital input from Baltica can safely be excluded.

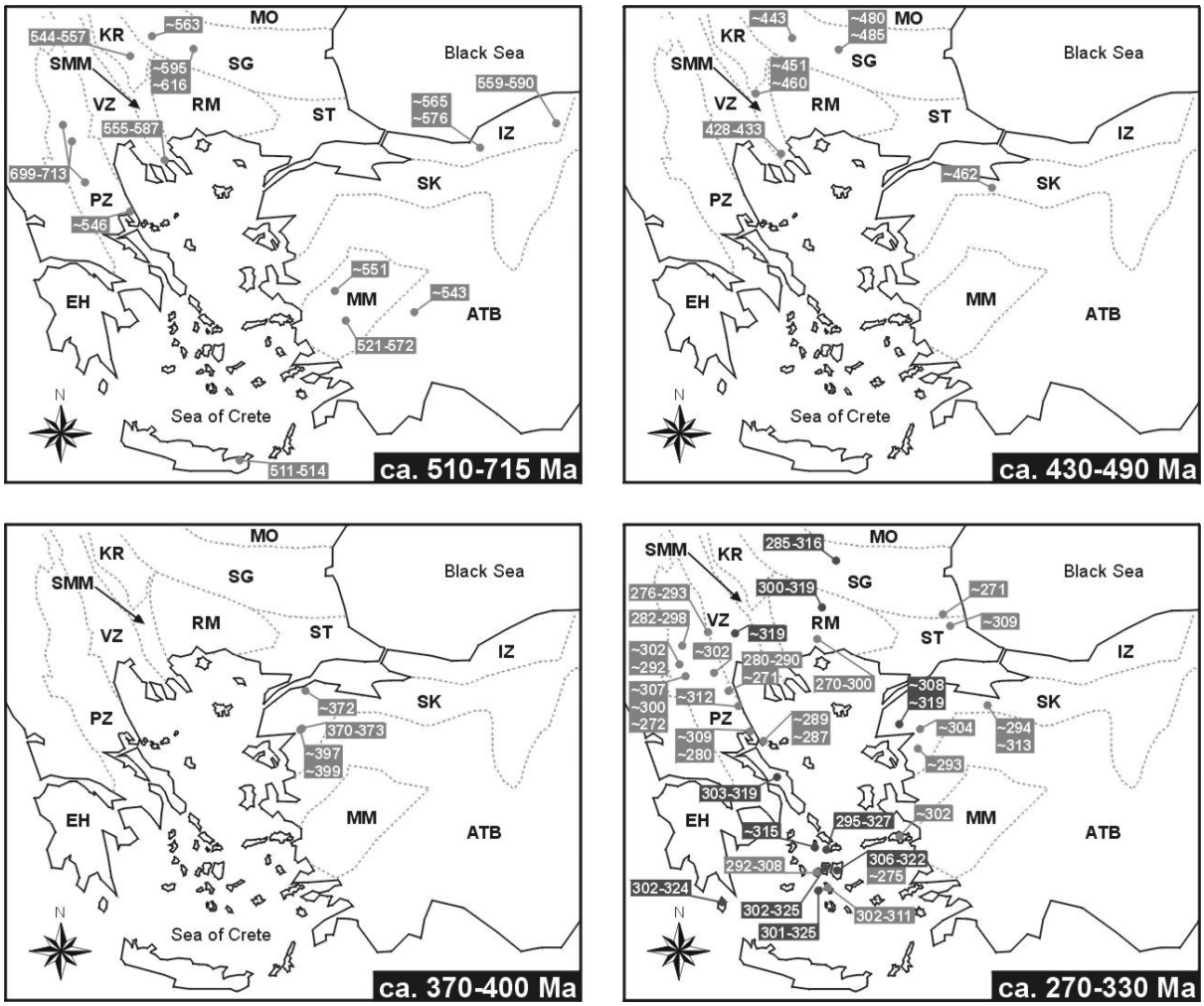

Fig. 9. Compilation of Late Neoproterozoic and Palaeozoic zircon age distribution data from Greece and the surrounding region; based on references (see Appendix E); see also discussion in the text. For better visualisation, the dark grey fillings in the map lower right mark localities with Early to earliest Late Carboniferous ages (≥315–330 Ma) reported. ATB: Anatolide-Tauride Block, EH: External Hellenides, IZ: Istanbul Zone, KR: Kraište, MM: Menderes Massif, MO: Moesia, PZ: Pelagonian Zone, RM: Rhodope Massif, SG: Sredna Gora Zone, SK: Sakarya, SMM: Serbo-Macedonian Massif, ST: Strandja, VZ: Vardar Zone.

Ca. 1.1–0.9 Ga zircon ages

Ages around 1 Ga are generally restricted to the Grenvillian–Kibaran orogenic belts that resulted from the amalgamation of the Rodinia supercontinent (e.g. Dalziel 1997). Kemp et al. (2006) have recently shown that remelting of old supracrustal rocks was significant during that period. The Grenvillian orogenic belt can be traced from SW Baltica and eastern Greenland over to western Amazonia and the southern part of North America during the Neoproterozoic (Dalziel 1992). A branch of this belt also extends along the Africa–Antarctica margin and into eastern India and western Australia. In the West African Craton and the "Saharan Metacraton" ages around 1.1–0.9 Ga have not been hitherto reported (e.g. Nance & Murphy 1996; Ennih & Liégeois 2001; Egal et al. 2002; Abdelsalam et al. 2002). They are however known from numerous peri-Gondwanan terranes in Europe (e.g. Moldanubia: Gebauer et al. 1989; Friedl et al. 2004; Mid-German Crystalline Rise: Zeh et al. 2001; Iberia: Fernández-Suárez et al. 2000, 2002). Detrital zircon ages of ca. 1 Ga have been reported from metasedimentary rocks from the Cyclades Islands (Keay & Lister 2002) and from Crete (Romano et al. 2005). Infra-Cambrian and Carboniferous metasedimentary rocks in the Karacahisar and Sandıklı areas of the Menderes–Taurus block contain ca. 990 Ma zircons (Kröner & Şengör 1990). Avigad et al. (2003) and Kolodner et al. (2006) described 1.1–0.9 Ga zircons in Cambro-Ordovician sandstones from Israel and Jordan. Inherited zircons of comparable ages have recently been reported for orthogneisses from the Sredna Gora Zone in Bulgaria (Carrigan et al. 2006). The presence of ca. 1 Ga zircons in European peri-Gondwanan crustal fragments and in the northern part of the Arabian-Nubian Shield, thousands of kilometres away from any known source, is still a matter of discussion (see Zeh et al. 2001; Avigad et al. 2003; Gutiérrez-Alonso et al. 2005; Kolodner et al. 2006). Avigad et al. (2003) suggested that they were derived from the Kibaran Belt of central Africa. They proposed that Neoproterozoic glaciers might have transported a large quantity of detritus toward the Gondwana margins where it was later reworked and deposited in the Early Palaeozoic siliciclastic cover sequences. Keppie et al. (1998) noted that river systems can travel across several cratons, suggesting that the provenance of the zircons might be sought farther afield. Therefore, it might also be possible that the Grenvillian detritus was transported by continental rivers similar to the present-day Amazon or Nile, towards the northern margin of Gondwana, maybe prior to the Cadomian event (Zeh et al. 2001). An alternative scenario was recently suggested by Gutiérrez-Alonso et al. (2005), proposing that

Grenvillian zircons in both Iberia and the northern Congo Craton have an ultimate South American (Amazonian & Oaxaquian) source that was widely dispersed after the amalgamation of northern Gondwana. Generally, it seems that Grenvillian–Kibaran zircons have accumulated in post-Cadomian (Ediacaran–Cambro-Ordovician) cover sequences at the northern margin of Gondwana (Fernández-Suárez et al. 2000, 2002; Avigad et al. 2003; Gutiérrez-Alonso et al. 2005; Kolodner et al. 2006). These sequences may have been reworked during younger orogenic processes, then re-sedimented, thus supplying inherited zircons to younger sediments. In this way, the ca. 1 Ga-old, well-rounded zircons in the Chios sediments studied here probably have a secondary source due to polyphase recycling.

Ca. 640–540 Ma zircon ages

Zircons yielding 640–540 Ma ages are probably related to late Pan-African orogenic processes, i.e. to the so-called Avalonian–Cadomian belt (Nance & Murphy 1994). Magmatic rocks of this event are generally interpreted as proof of a Neoproterozoic to earliest Palaeozoic Andean-type subduction-zone setting at the northern margin of Gondwana (Nance & Murphy 1994). Cadomian ages are known from orthogneisses in the Menderes Massif of western Turkey (ca. 521–590 Ma, Pb–Pb and U–Pb on zircon: Kröner & Şengör 1990; Hetzel & Reischmann 1996; Loos & Reischmann 1999; Gessner et al. 2004), from units in the Serbo-Macedonian Massif of northern Greece (ca. 540–587 Ma, Pb–Pb on zircon: Himmerkus et al. 2004a, 2006a, 2007) and of SW Bulgaria (ca. 544–569 Ma, U–Pb on zircon: von Quadt et al. 2000; Graf 2001; Kounov 2002) and from the Istanbul Zone of NW Turkey (ca. 560–590 Ma, Pb–Pb and U–Pb on zircon: Chen et al. 2002; Ustaömer et al. 2005). Recently, Carrigan et al. (2006) reported concordia ages of 616.9 ± 9.5 Ma and 595 ± 23 Ma for zircons in orthogneisses from the Sredna Gora Zone of Bulgaria. With regard to the latter sample, however, Carrigan et al. (2006) cautioned that its Late Neoproterozoic age of ~600 Ma is not precise because of its widely varying U concentrations and Th/U values. Using all data available at present, it can be concluded that the 640–540 Ma zircons were probably derived from the Avalonian-Cadomian belt and that their source can actually be sought in the terranes mentioned above. An input from the Arabian-Nubian Shield is highly unlikely since this terrane, besides containing 650–550 Ma igneous rocks, is also largely characterized by 900–700 Ma basement rocks (e.g. Kröner et al. 1987, 1990), and zircon ages in the latter range are absent from our Chios data set.

Ca. 505–460 Ma zircon ages

Late Cambrian to Early Ordovician magmatic rocks are widespread in the pre-Variscan basement of Europe, and have been attributed to rifting processes and the opening of the Rheic ocean, separating Avalonia from the northern margin of Gondwana (e.g. Crowley et al. 2000; von Raumer et al. 2002). Some Early Ordovician calc-alkaline metaluminous granites of arc origin are probably related to a Cambro-Ordovician active-margin setting (von Raumer et al. 2003). Relatively younger (~450 Ma) magmatic rocks characterize a late- to post-orogenic evolution (von Raumer et al. 2003). Basement rocks with zircon ages of 490–460 Ma are not known so far from the Hellenides of Greece. However, the involvement of an Ordovician crustal source during Permo-Carboniferous magma genesis was recently shown by Anders et al. (2006b) for orthogneisses from the Pelagonian Zone and is also documented in orthogneisses from the Eastern Rhodope of Greece (N. Cornelius, pers. comm. 2007). Furthermore, two inherited zircons of 472.4 ± 5 Ma and 481.5 ± 4.8 Ma were reported for a Middle Jurassic gabbro from the Vourinos ophiolite (Liati et al. 2004). This implies that basement or older sedimentary rocks containing Early–Middle Ordovician zircons were reworked during Neotethyan magmatic activity in Jurassic times. Zircons in basement gneisses from the Sredna Gora Zone in central Bulgaria yielded ages of 480 ± 30 Ma and 485 ± 50 Ma (Arnaudov et al. 1989, cited by Peytcheva & von Quadt 2004). Furthermore, Carrigan et al. (2005) reported Ordovician ages (~445–467 Ma) from inherited cores of Variscan zircons in metagranites of the Sredna Gora Zone. Zircons in metagranites from the Serbo-Macedonian Massif in SW Bulgaria yielded an upper-intercept age of 459.9 ± 7.6 Ma, which was interpreted as the intrusion age (Titorenkova et al. 2003). A Pb/Pb single-zircon evaporation age of around 462 Ma was documented from orthogneisses from the Biga Peninsula in NW Turkey (Özmen & Reischmann 1999). The Biga Peninsula belongs to the Sakarya microcontinent and constitutes part of the Sakarya Composite Terrane (Göncüoğlu et al. 1997). It should also be noted here that earlier K–Ar mineral and Rb–Sr whole-rock dating provides evidence that a magmatic or metamorphic event around 460 Ma affected basement rocks in the Pelagonian Zone of Greece (ca. 461 Ma and 465 Ma, K–Ar: Marakis 1970; ca. 460 Ma, Rb–Sr: Henjes-Kunst & Kreuzer 1982). However, further work is required to establish the significance of these ages. According to the data available, the source of Early–Middle Ordovician zircons in the Chios sediments should probably be sought in basement rocks of the Sakarya microcontinent or in basement units of Bulgaria.

Ca. 385–370 Ma zircon ages

Devonian ages between 385–370 Ma have been reported from several parts of Central and Eastern Europe. Such ages reflect either accretion of Gondwana-derived terranes to Baltica, resulting in HT–MP metamorphism and partial melting during a single-cycle Variscan orogeny (e.g. Góry Sowie, Sudetes: Timmermann et al. 2000) or the timing of Variscan exhumation and associated decompression melting under upper amphibolite-facies to granulite-facies conditions (e.g. Mariánské Lázne Complex: Timmermann et al. 2004). The accretion of Gondwana-derived terranes to Laurussia marks the onset of Variscan orogeny. The spatial distribution and temporal variation of Devonian ages in the eastern Mediterranean realm is not yet accurately known. Crystalline basement rocks of Devonian age have only been reported from one locality in the Hellenides (Andriessen et al. 1987). These authors documented an upper-intercept age of 372 Ma +28/-24 Ma (U–Pb method) on zircons from the core gneisses of Naxos that they interpreted to approximate the crystallisation age of the main zircon generation. This however has to be revised since Reischmann (1998) found a more precise age of 316 ± 4 Ma (Pb–Pb method) for the Naxos gneisses. By contrast, Devonian ages are well known from the Biga peninsula in NW Turkey. Zircons from the Çamlık metagranodiorite gave a Pb/Pb single zircon age of 397.5 ± 1.4 Ma (Okay et al. 2006), confirming an earlier Pb/Pb age of 399 ± 13 Ma by Okay et al. (1996). Pb/Pb single-zircon evaporation ages around 372 Ma were obtained from granitic-granodioritic gneisses cropping out in the northern part of the Biga peninsula close to the Sea of Marmara and in the south near Edremit town (Özmen & Reischmann 1999). Taking into account the data available, we suggest that basement rocks from the Sakarya microcontinent were probably the source rocks of the 370–385 Ma-old detrital zircons of the Chios clastic successions.

Ca. 350–320 Ma zircon ages

Early Carboniferous magmatic rocks are widespread in the Central European Variscides. They reflect ongoing Variscan exhumation and associated decompression melting under upper-amphibolite to granulite-facies conditions at around 340 Ma (e.g. Kröner et al. 2000, and references therein) and regional low pressure–high temperature metamorphism, migmatisation and granitic magmatism between 330 and 320 Ma (e.g. Anthes & Reischmann 2001, and references therein). By contrast, Early Carboniferous magmatic rocks are rare in the Hellenides. They have been documented for basement rocks of the Lower Tectonic Unit

of the western Rhodope Massif (357 ± 20 Ma, U–Pb on zircon: Wawrzenitz 1997 cited by Liati & Gebauer 1999; 345 ± 40 Ma, Pb–Pb on zircon: Kokkinakis 1978 cited by Vavassis et al. 2000). This however has to be revised since Turpaud & Reischmann (2005) and Turpaud (2006) found latest Carboniferous–Early Permian ages in those regions. Recent geochronological studies in the Lower Tectonic Unit of the eastern Rhodope Massif show minor evidence of Early Carboniferous magmatic rocks (ca. 325 Ma, U–Pb on zircon: N. Cornelius, pers. comm. 2007). Early Carboniferous ages, however, are well documented for basement rocks from the Pelagonian Zone (Evia Island, 319 ± 0.7, U–Pb on zircon: Vavassis et al. 2000), the Attic-Cycladic Massif (Paros Island, 325 ± 4 Ma, Pb–Pb on zircon: Engel & Reischmann 1998; Naxos Island, 316 ± 4 Ma, Pb–Pb on zircon: Reischmann 1998; 319 ± 1 Ma, 322 ± 2 Ma, U–Pb on zircon: Keay et al. 2001; Sikinos Island, 325 ± 4 Ma, Pb–Pb on zircon: Engel & Reischmann 1999; Delos Island, 327 ± 4 Ma, Pb–Pb on zircon: Engel & Reischmann 1999) and recently for orthogneisses from Kithira Island, External Hellenides (324 ± 2 Ma, 323 ± 3 Ma and 320 ± 1.2 Ma, U–Pb on zircon: Xypolias et al. 2006). Carrigan et al. (2006) reported a concordia age of 336.5 ± 5.4 Ma for metamorphic rims of a migmatite leucosome from the Sredna Gora Zone in Bulgaria that they interpret as the age of zircon recrystallisation during high-grade metamorphism. Recently, Pb/Pb single-zircon evaporation analyses of zircons from a gneiss sample of the Kazdağ Massif on the Biga Peninsula in NW Turkey gave a relatively precise age of 319.2 ± 1.5 Ma (Okay et al., 2006). Thus, the Early Carboniferous zircons found in the clastic sediments of Chios (322 ± 3 Ma from sample CH52 and 326 ± 2 Ma from sample CH11) could have been derived from basement rocks of the Pelagonian Zone / Attic-Cycladic Massif, from Sakarya or the Lower Tectonic Unit of the Rhodope Massif.

5.2. Source of zircons

The analysis of magmatic, inherited and detrital zircon ages from different parts of the Eastern Mediterranean helps to indentify possible sources for the clastic sediments of Chios. The occurrence of ca. 2 Ga-old zircons, in conjunction with the lack of detrital zircons with ages between 1.8 and 1.1 Ga in our studied sediments from Chios, characterize a northern Gondwana source, especially one from NW Africa. Zircons of Late Neoproterozoic (~540–650 Ma) and Palaeozoic (~280–330 Ma, ~370 Ma, ~430–460 Ma, ~480 Ma) ages are

important time-markers for palaeotectonic reconstructions in the Eastern Mediterranean (Fig. 9; Appendix).

Permo-Carboniferous zircons (ca. 280–320 Ma) were not found in the analysed sediments from Chios, implying that rocks of such an age were either never present or not yet exposed in the source area at the time of sedimentation. The youngest detrital zircon grains in samples CH11 and CH52 are 326 ± 2 Ma and 322 ± 3 Ma respectively. These zircons are slightly younger than 330–335 Ma-old detrital zircons from the Küçükbahçe formation of the Karaburun peninsula (Rosselet & Stampfli 2003). Both late Carboniferous and earliest Permian zircons (ca. 280–330 Ma) document a major igneous event in the Aegean and the surrounding area (e.g. Reischmann 1998; Engel & Reischmann 1998, 1999; Vavassis et al. 2000; Reischmann et al. 2001; Anders et al. 2006b). Geochemical analyses indicate a volcanic-arc or active continental-margin setting at this time (e.g. Pe-Piper & Piper 2002, and references therein), due to northward subduction of (a branch of) Palaeotethys beneath Pelagonia and Sakarya (e.g. Vavassis et al. 2000; Stampfli et al. 2003). Hence, the provenance of the analysed detrital zircons from Chios can be constrained as follows:

Sample CH52 yielded abundant magmatic zircons of Late Neoproterozoic–Cambrian, Ordovician and minor Devonian ages, in addition to very old (>2 Ga) grains. The External Hellenides, the Pelagonian Zone and the Attic-Cycladic Massif consist of Permo-Carboniferous (ca. 280–330 Ma) basement with only rare evidence for older magmatic rocks (see references above), if one excludes the Florina terrane of Anders et al. (2006a). The latter terrane most probably belonged to East Avalonia and formed the continental basement (ca. 699–713 Ma) onto which the Pelagonian Permo-Carboniferous magmatic arc was founded (Anders et al. 2006a). The data available suggest that the Pelagonian Zone and the Attic-Cycladic Massif cannot be considered as a possible source of zircons during Carboniferous times. Detrital input from the Florina terrane is also not documented by the Chios clastic sediments. The source should rather be sought in areas lying to the north or northeast of present-day Chios such as NW Turkey or the Balkan region. Detrital zircons of around 540–640 Ma were probably derived from basement rocks of the Avalonian-Cadomian belt. Terrane fragments of these are preserved in northern Greece, Bulgaria and northern Turkey (Fig. 9). Detrital zircons with Ordovician ages could be derived from basement gneisses of southern Bulgaria and NW Turkey (Fig. 9).

The Permo-Triassic sample CH11 shows a similar detrital zircon age spectrum to the Carboniferous sample CH52 with two exceptions: (I) Grenvillian ages are present and (II) the amount of Devonian zircons is higher. The source of Grenvillian zircons seems difficult to identify. Grenvillian zircons could be inherited components in magmatic zircons, as already described above for zircons from Cadomian orthogneisses of the Sredna Gora Zone in Bulgaria (Carrigan et al. 2006). The Grenvillian zircons from the Chios sediments, however, are well rounded and homogeneous without evidence of magmatic or metamorphic overgrowth. Nevertheless, younger magmatic or metamorphic rims on zircons can be removed by abrasion during long-distance river transport, in which case only the inherited components survive. A more plausible scenario is that of recycling of older sedimentary Grenvillian detritus. As already discussed before (see paragraph 5.1.), zircons aged around 1 Ga have accumulated in post-Cadomian (Ediacaran–Cambro-Ordovician) cover sequences at the northern margin of Gondwana (Fernández-Suárez et al. 2000, 2002; Avigad et al. 2003; Gutiérrez-Alonso et al. 2005; Kolodner et al. 2006). Outcrops with biostratigraphically dated post-Cadomian clastic cover sequences can be found, for example, in southern Turkey (SE Anatolia and the Taurides: e.g. Göncüoğlu & Kozlu 2000) and in northern Turkey (Istanbul Zone: e.g. Görür et al. 1997; Dean et al. 2000; Yanev et al. 2006).

We propose that the best source candidate for the Chios sediments studied here was the Sakarya microcontinent because of the occurrence there of Ordovician and Devonian basement rocks. Time and facies equivalents of the Early Palaeozoic sediments from the Istanbul Zone were probably re-worked at the southern margin of Laurussia during the Variscan orogeny (see paragraph 5.3.) thus supplying Grenvillian zircon detritus. It becomes then apparent that the ca. 1 Ga-old zircons in the Chios sediments have a secondary source due to polyphase recycling. We infer that the basement of the Sakarya microcontinent was probably exposed at the surface on a regional scale in Permo-Triassic times, thus supplying Devonian detritus.

5.3. Source of olistoliths

The analysis of olistoliths found within the turbidite-olistostrome succession of Chios provides additional evidence for possible source areas. Figure 10 shows a compilation of lithology and fossil content for olistoliths from Chios, including an interpretation for their

depositional setting. The Silurian to Carboniferous olistoliths are mainly characterized by a variety of chert, carbonate and fine-grained siliciclastic rocks which were mainly dated by graptolites, conodonts, corals, brachiopods, algae and foraminifers (see Kauffmann 1965; Besenecker et al. 1968; Herget 1968; Herget & Roth 1968; Fenninger 1983; Groves et al. 2003; Larghi et al. 2005). Furthermore, volcanic rocks basic, intermediate and acidic in composition mentioned by previous researchers were studied in detail by Pe-Piper & Kotopouli (1994) who found clear evidence that at least some of them intruded the deformed Palaeozoic clastic succession and therefore cannot be olistoliths. Based on geochemical data, they suggested that these volcanic rocks probably formed in a back-arc setting above a subducting Palaeotethyan oceanic slab and correlated them with Early Permian granodiorites from the Karakaya Complex in Turkey. Robertson & Pickett (2000) assumed a Silurian age for some of the volcanic rocks based on the close spacial association of Silurian limestone olistoliths with volcanic rocks north of Spartounta. An in-depth analysis of the provenance of the volcanic rocks, however, is beyond the scope of the present paper. Here, we will only focus on the fossil-bearing sedimentary olistoliths.

The olistoliths essentially define four olistostrome formations with a very clear predominance of younger blocks (Early Carboniferous) in the lower formation and of older blocks (Silurian) in the upper formation (Papanikolaou & Sideris 1983; Sideris 1989). This implies a down-stratigraphy continuous erosion of lithologies in the source area. The limestones and cherts were thermally and tectonically overprinted before they were deposited as olistoliths. Most of the chert and radiolaria-bearing olistoliths found on Chios are strongly fractured and penetrated by veins. At least two generations of veins can be identified in cherty samples. The first generation is characterized by quartz veins and the second by calcite veins. The thermal metamorphic overprint is documented by the conodont colour alteration index (CAI: Epstein et al. 1977; Rejeban et al. 1987). Conodonts from a late Visean (?early Serpukhovian) limestone breccia cropping out in the Kourounia-Nenitouria area, NW Chios, have a CAI of 5, indicating heating temperatures of 300–480°C (Groves et al. 2003). In general, a decrease of the CAI from west (CAI of 6–6.5) to east (CAI of 2–3) can be observed in NW Chios (Fig. 1). Detailed investigations by Kozur (1998) on the Karaburun peninsula, opposite Chios, have shown that the Variscan structural and metamorphic overprint cannot be younger than Late Visean because pre-Late Visean rocks show cleavage and have experienced very low-grade metamorphism (CAI of 4–5), whereas Late Visean and Triassic

rocks lack cleavage and display only very low-grade thermal alteration with a CAI of 2–3 and 1–1.5 respectively. This provides evidence that the Variscan metamorphic overprint affecting the olistoliths is older than ca. 330 Ma.

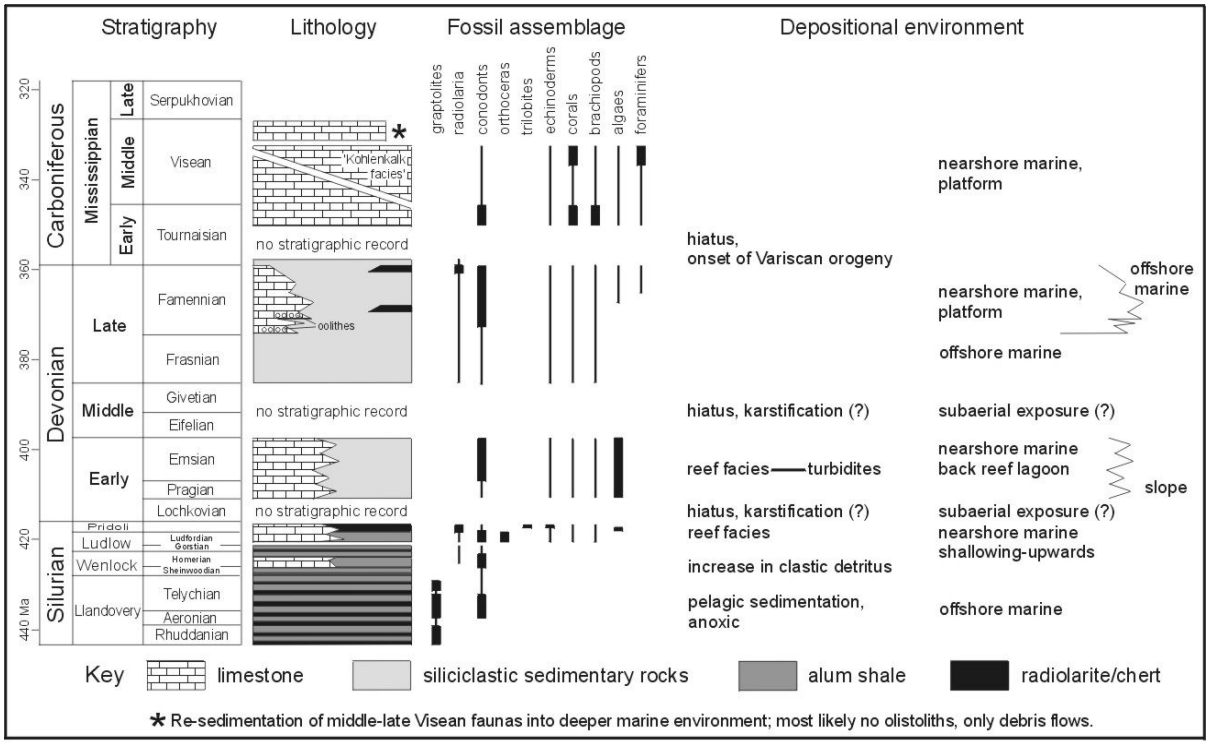

Fig. 10. Compilation of lithology and fossil content for sedimentary olistoliths from the Late Palaeozoic rocks of the Lower Unit and their interpretation in terms of depositional environment. Data sources: Kauffmann (1965), Besenecker et al. (1968), Herget (1968), Herget & Roth (1968), Fenninger (1983); Robertson & Pickett (2000), Groves et al. (2003), Larghi et al. (2005). Geological time scale according to Gradstein et al. (2004).

Recently, the chert olistoliths (ribbon radiolarites) were examined biostratigraphically by Larghi et al. (2005), who found age-diagnostic radiolarians and conodonts in two samples thus allowing them to establish Late Silurian (probably Přídolían) and Late Devonian (Famennian) ages, whereas only a more general age range from Devonian to Early(?) Carboniferous could be proposed for the remainder. Based on graptolite fauna, Herget (1968) noted that the Silurian of northern Chios shows similarities to that of Stara Planina and the Kraište area in Bulgaria.

The exotic limestone blocks and breccias have been dated as Silurian to Carboniferous (Kauffmann 1965; Besenecker et al. 1968; Herget 1968; Herget & Roth 1968; Fenninger 1983; Groves et al. 2003). In the course of this study, a small limestone lens, ca. 25

cm in diameter, was found in a fine-grained siliciclastic succession south of Ano Kardamila town (Figs. 1 and 11). The lens consists of light-grey fossiliferous limestone and is cut by calcite veins, stylolites and fractures filled with siliciclastic material from the host sediment. The limestone is surrounded by a weathered crust that itself is covered by a thin layer of the host sediment, indicating that weathering occurred before deposition in the siliciclastic host succession. According to Holland (1992), the lens contains orthoconic nautiloid cephalopods known as '*Orthoceras*'. In order to precisely define the age of the '*Orthoceras* Limestone', part of the sample was processed for conodonts according to standard procedures using acetic acid. After sieving the residue, the fraction of particles ranging in size from 112 μm to 2 mm was handpicked under a binocular microscope. Besides conodonts, small brachiopods, a trilobite pygidium and several spines were also found. The fauna is well preserved, thermally almost unaltered (CAI of 1–2), indicating that no pre-Late Visean Variscan metamorphic overprint affected the reworked limestone olistolith. However, it also shows that the material was derived from a provenance area which had not been heated before the limestone was transported into the post-Late Visean (based on the low thermal alteration) Carboniferous succession investigated here. The low CAI of the studied limestone olistolith further confirms the general observation of decreasing CAI from west to east on Chios (Fig. 1) and, according to observations on the Karaburun peninsula (see above), indicates that the host succession cannot be older than Late Visean.

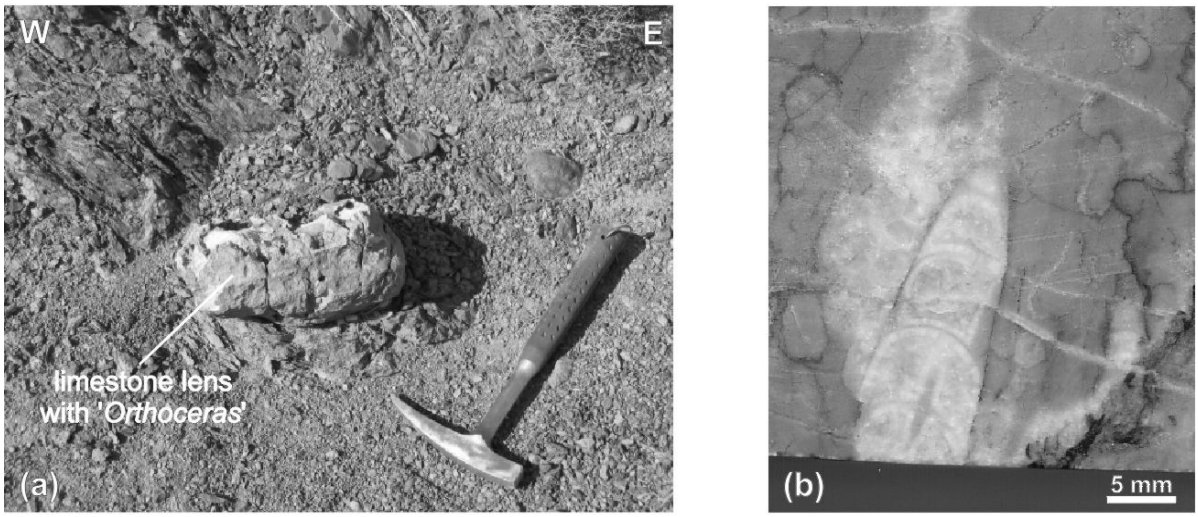

Fig. 11. (a) Limestone olistolith, sample CH13, floating in fine-grained siliciclastic sediments, Late Palaeozoic succession of the Lower Unit; S of Ano Kardamilia town (38°30´48.5´´N, 26°06´04.0´´E). **(b)** Polished specimen of sample CH13 shows an orthoconic nautiloid cephalopod.

Scanning electron microscope (SEM) images of conodont elements were produced at the Institute of Palaeontology in Erlangen; the illustrated specimens (Plate I) are deposited in the Senckenberg Museum Frankfurt/Main (SFM numbers in caption to Plate I). The conodont fauna is dominated by elements of the *Ozarkodina excavata* group (Plate I, a to e). This subspecies of *O. excavata* is abundant and similar to *O. excavata excavata* (Branson and Mehl), but seems to represent an older ssp. (Lennart Jeppsson, pers. comm. to O. Lehnert). This *Ozarkodina excavata* ssp. aff. *excavata* (Branson and Mehl) (Figs. 12-a, c to e), occurs together with species of *Panderodus* (*P. recurvatus* (Rhodes), Figs. 12-k, m, n; *P. gracilis* (Branson and Mehl), Fig. 12-j) as well as with elements of *Oulodus siluricus siluricus* (Fig. 12) and *Oulodus* cf. *siluricus siluricus* (Figs. 12g, h). The zonal index *Polygnathoides siluricus* Branson and Mehl (Fig. 12-i) and *Kockelella variabilis ichnusae* Serpagli and Corradini (Fig. 12-l) in conjunction with the overall diverse assemblage allow correlation with the lower *P. siluricus* zone (pre-Lau event; Fig. 13). In the uppermost *P. siluricus* zone and the overlying Icriodontid zone, a successive extinction of taxa is observed during the Ludfordian Lau event (e.g. Jeppsson 1993, 1998; Jeppsson & Aldridge 2000). Some of the taxa occurring in the Chios assemblage (e.g. *P. siluricus*, *Ou. siluricus*, *P. gracilis*) are common in the När Formation of Gotland and, together with several platform-bearing taxa, become extinct in its uppermost part (Botvide Member) during the early phase of the Lau event in the uppermost *siluricus* zone (Jeppsson et al. 2005b). The presence of such taxa in the Chios assemblage fits with a correlation of the fauna with the lower part of the zone.

Similar "*siluricus*" fauna with occurrence of the zonal index together with *K. variabilis ichnusae*, and dominated by *O. excavata excavata*, are reported from different sections on Sardinia (compiled in Corradini & Serpagli 1999). On Sardinia, *K. variabilis ichnusae* occurs in the basal *O. excavate hamata* zone (for the first time) throughout the *A. ploeckensis* zone and in the lower part of the *siluricus* zone only (Serpagli & Corradini 1999), thus justifying the assignment of the new Chios fauna to the lower *siluricus* zone.

Conodont fauna of an equivalent age (*P. siluricus* zone) are also known from many other peri-Gondwana areas (e.g. Carnic Alps: Walliser 1964; Bohemia: Chlupáč et al. 1980; Western Europe and Northern Africa locations: compiled in García-López et al. 1994; Morocco: Sarmiento et al. 1997; Turkey: Kozur 1998; Poland: Männik & Małkowski 1998; Sardinia: Corradini & Serpagli 1998, 1999; Australia: Talent & Mawson 1999;

Frankenwald/Germany: Blumenstengel et al. 2006), from Laurentia (e.g. Klapper & Murphy 1975; Uyeno 1980) and from Baltica (references in Jeppsson et al. 1994a, b, 2006).

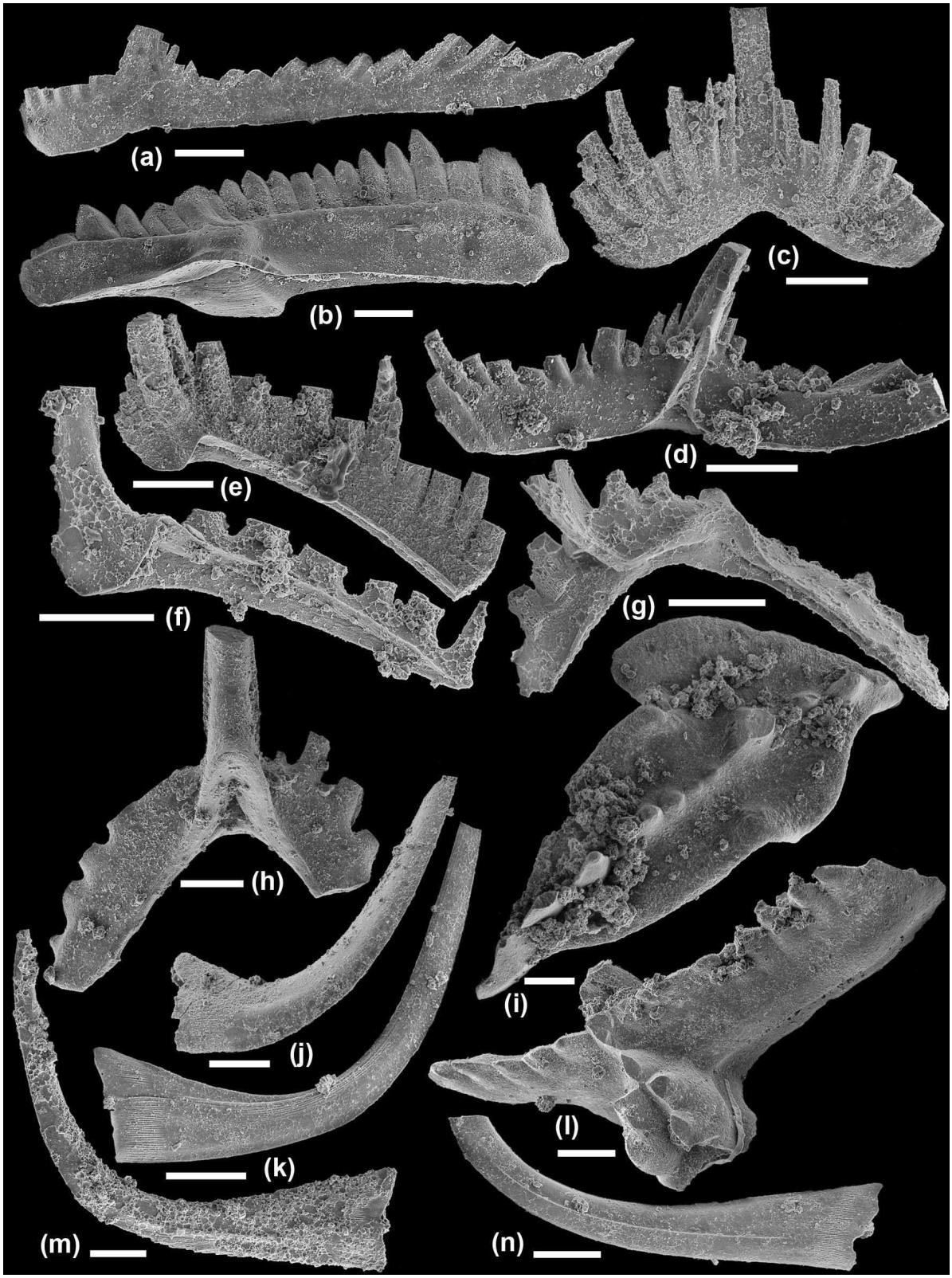

(*caption on page 88*)

Kauffmann (1965) has already reported occurrences of conodonts in cephalopod limestones lenses found in northeastern Chios. The recovered conodont faunas from these lenses have not been illustrated or described, but taxa have been listed in the form sense and assigned by Kauffmann (1965) to the Late Silurian (Ludlow) *K. crassa* and *P. siluricus* conodont zones. The faunal lists from locations no. 5 to 7 in the region around Kardamila (Kauffmann 1965: 653–654, fig. 2) reflect similar faunal compositions; the material is comparable in age and may tentatively also be placed in the *Polygnathoides siluricus* zone.

The closest potential source localities of '*Orthoceras* Limestone' similar in lithology to the reworked lenses on Chios are located in Turkey and in the Balkan region; the locations are summarised in Figure 14. Paeckelmann & Sieverts (1932) mentioned '*Orthoceras*' from Sedef Island (Antirovitha) in the Sea of Marmara and from Kartal and Pendik districts on the mainland SE of Istanbul town. Based on litho- and biostratigraphic correlations, Haas (1968) assumed a Ludlow age for the '*Orthoceras*'-bearing limestones from Sedef Island; those from Kartal and Pendik districts were assigned to the 'Obere Soğanlı-Schichten' for which he proposed an Early Emsian age. Recently, Kozlu et al. (2002) described '*Orthoceras* Limestone' from the Çamdağ area, dated by conodonts, as being Přídolí in age.

'*Orthoceras* Limestone' was also reported from the Yukarı Yayla Formation of the eastern Taurides and is according to conodont data, of latest Llandovery to earliest Wenlock age (Göncüoğlu & Kozlu 2000; Göncüoğlu et al. 2004). In contrast to the low CAI (1–2) of the new fauna reported in this paper, Silurian conodonts from the Çamdağ area and the eastern Taurides have a CAI value of 5 (Kozlu et al. 2002; Göncüoğlu et al. 2004).

Fig. 12. Representative conodont elements recovered from the cephalopod-bearing limestone lens of Chios. Scale bars equal 100 µm. The figured conodont specimens are deposited in the Senckenberg Museum Frankfurt/M. (SFM numbers). **(a–e)** Elements of the *Ozarkodina excavata* group: **(a–e)** *Ozarkodina excavata* ssp. aff. *excavata*; **(a)** SMF-78114, Sc element, lateral view; **(b)** SMF-78115, lower-lateral view; **(c)** SMF-78116, Sa element, anterior view; **(d)** SMF-78117, Sb element, lateral view; **(e)** SMF-78118, M element, lateral view; **(f)** *Oulodus siluricus* (Branson and Mehl), SMF-78119, M element, postero-lateral view; **(g–h)** *Oulodus siluricus* cf. *siluricus* (Branson and Mehl); **(g)** SMF-78120, Pb element, postero-lateral view; **(h)** SMF-78121, Sa element, posterior view; **(i)** *Polygnathoides siluricus* Branson and Mehl, SMF-78122, Pa element, upper view; **(j)** *Panderodus gracilis* (Branson and Mehl), SMF-78123; **(k, m, n)** *Panderodus recurvatus* (Rhodes), **(k)** SMF-78124, lateral view, **(m)** SMF-78126, lateral view, **(n)** SMF-78127, lateral view; **(l)** *Kockelella variabilis ichnusae* Serpagli and Corradini, SMF-78125, Pa element, upper-lateral view.

In the northern Central Taurides of the Konya area '*Orthoceras* Limestone' from the Ayı Tepesi Formation yielded upper Lochkovian–Pragian conodonts (Göncüoğlu et al. 2004). As far as the Balkan region is concerned, '*Orthoceras* Limestone' has been reported from the Suva Planina Mountains in eastern Serbia and from the Bistra Mountains in western F.Y.R.O.M (Gnoli 2003). Geologically, the Suva Planina Mountains are part of the Kraište area and the Bistra Mountains belong to the internal zone of the Dinarides. Silurian–Early Devonian cephalopod limestone biofacies is furthermore documented from NW Africa, the Pyrenees, SW Sardinia, the Armorican Massif, the Prague Basin, the Carnic Alps, the Uppony Mountains in NE Hungary and from the continental platform in Ukraine (Gnoli 2003). The Early Palaeozoic '*Orthoceras* Limestone' may therefore become an important marker for palaeobiogeographic reconstructions of northern Gondwana-derived terranes (e.g. Kozlu et al. 2002; Gnoli 2003).

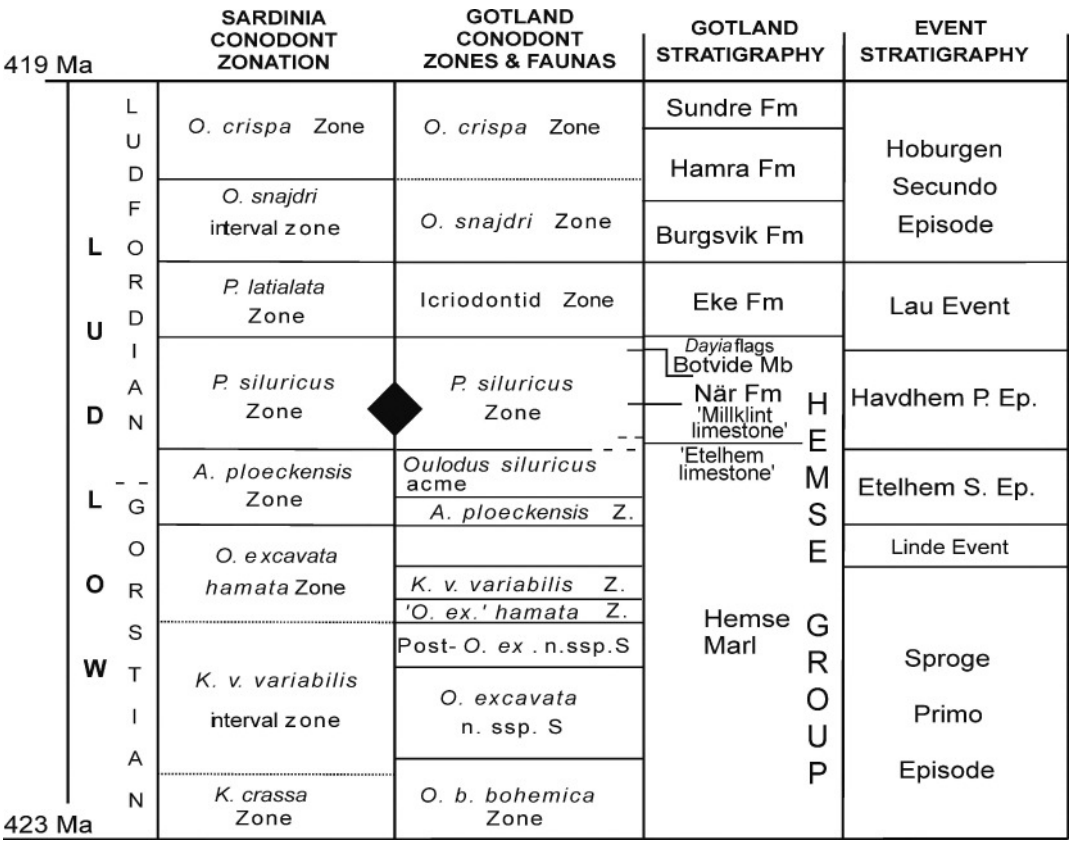

Fig. 13. Ludlow conodont zonation on Sardinia by Corradini & Serpagli (1999), and conodont succession and event stratigraphy on Gotland modified from Jeppsson et al. (2005a). The age of the Ludfordian conodont fauna from the Chios olistolith is indicated by a black quadrangle.

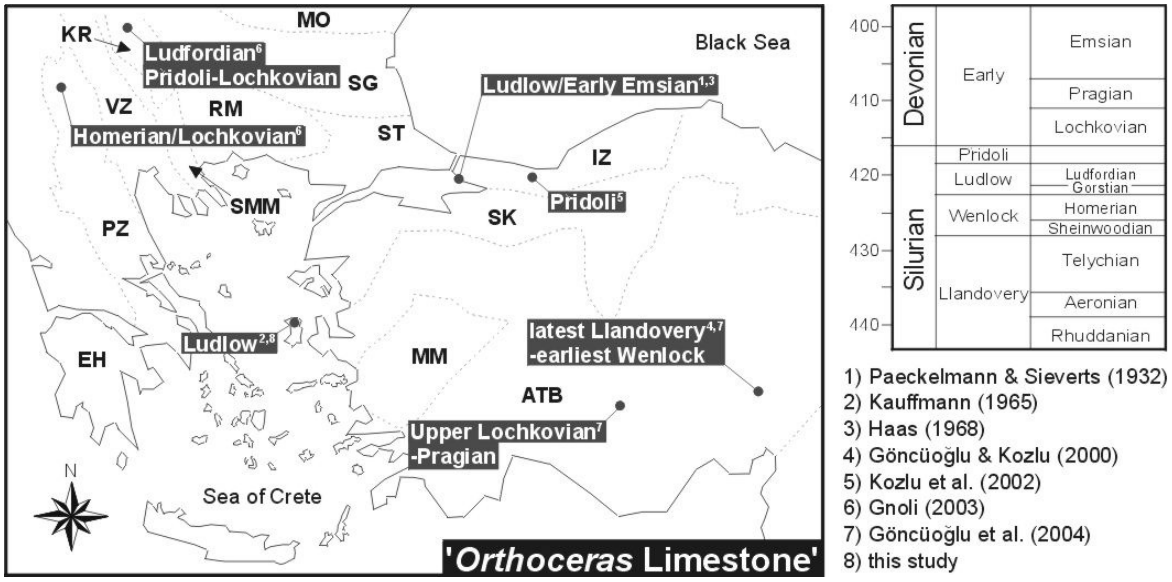

Fig. 14. Occurrences of '*Orthoceras* Limestone' in the Eastern Mediterranean. For abbreviations see Figure 9.

With regard to the weathered limestone crust mentioned above, Robertson & Pickett (2000) noted that some limestone olistoliths are locally karstified and cut by laterite-filled fissures, whereas the host sediment is not. The palaeokarst must be younger than the lithification of the limestones (post-Silurian) but older than their age of deposition as olistoliths (pre-Serpukhovian). The palaeokarst marks a hiatus in sedimentation and suggests subaerial exposure somewhere in the Palaeotethyan realm at some point in the Devonian. According to the olistolith data available (Fig. 10), there seem to be two gaps in sedimentation in pre-Carboniferous times, suggesting that karstification could have occurred in the Early Devonian (Lochkovian) and/or in the Middle Devonian (Eifelian and Givetian). Interestingly, in the Çamdağ, the Safranbolu-Araç and the Karadere-Zirze areas of the Zonguldak Terrane, NW Turkey, an unconformity exists between the Silurian and Devonian sequences (Gürör et al. 1997; Dean et al. 2000). The stratigraphic gap between the graptolite-bearing upper Wenlock and the unconformably overlying Emsian successions, together with an accompanying late Early Devonian thermal event, are characteristic features of the Zonguldak Terrane (Lakova & Göncüoğlu 2005; Yanev et al. 2006) and are in sharp contrast with the continuous platform-type sedimentation seen in the Istanbul Terrane during the same time period (Yanev et al. 2006). The Early Devonian unconformity and accompanying thermal event were probably due to the docking of the Zonguldak Terrane to Baltica (Yanev et al. 2006). The Istanbul and Balkan Terranes, however, were accreted to the southern margin of Laurussia in Carboniferous times (Yanev et al. 2006). Moreover, a regional

unconformity between the Upper Silurian and the Lower Devonian (Middle Lochkovian) also exists in the southern and eastern Taurides and in SE Anatolia (Göncüoğlu & Kozlu 2000; Göncüoğlu et al. 2004). In the southern Taurides and SE Anatolia this is probably related to the closure of a branch of the Palaeotethys to the north of the peri-Gondwana terranes (Göncüoğlu & Kozlu 2000), whereas in the eastern Taurides it could be related to a stepwise detachment of terranes from the northern margin of Gondwana (Göncüoğlu et al. 2004). The sedimentation gap between the latest Silurian and early Devonian in the Zonguldak Terrane and in the Tauride-Anatolide block most probably represents the time of karstification of the Silurian limestones of Chios.

It is important to note that fossil assemblages of Early Palaeozoic rocks from the Istanbul, Zonguldak and Balkan Terranes are similar to those from the Avalonian and Armorican Terranes of Central and Western Europe (e.g. Yanev et al. 2006, and references therein). For example, in a palaeogeographic reconstruction for Ordovician times (Dean et al. 2000) trilobite fauna were used to place the Zirze unit of the Zonguldak Terrane in the vicinity of successions from central Europe (Bohemia) and the Anglo-Welsh Basin (Avalonia). The Devonian benthic fauna of this terrane is typical of that of the Rhenohercynian Zone (Yanev et al. 2006). The Zonguldak Terrane may have been located in the eastern continuation of the Avalonian and Moravo-Silesian Terranes (Yanev et al. 2006). Ordovician and Silurian benthic fauna from the Istanbul Terrane are of Avalonian and Podolian affinity, whereas Devonian brachiopods and trilobites are clearly of Bohemian and North African affinity (Yanev et al. 2006). Emsian ostracodes indicate an open marine connection between the Istanbul Terrane, Thuringia and Morocco (Dojen et al. 2004). The Balkan and NW Anatolian Terranes were part of northern Gondwana but not of Baltica (Yanev et al. 2006, and references therein).

To summarise, taken collectively (lithology, fossil content, age and metamorphic overprint together with depositional environment) all data suggest that an input from the Pelagonian Zone or the Attic-Cycladic Massif can be safely excluded because neither Silurian nor Devonian sediments have been reported from these areas so far. We propose that the source area of the olistoliths is located north of present-day Chios, most likely in NW Turkey or southern Bulgaria–Serbia. Alternatively, the source rocks could have been time and facies equivalents of Palaeozoic units in NW Turkey or southern Bulgaria–Serbia, which have not been preserved.

The Visean 'Thracian flysch' of the Istanbul Zone probably indicates the onset of Variscan orogeny in this part of the Eastern Mediterranean (Görür et al. 1997) and may represent a time and facies equivalent of the Carboniferous turbidite-olistostrome succession of Chios. The time of deposition of the latter was constrained by biostratigraphic data from calcareous clasts of a breccia lying within the turbidite-olistostrome succession and was proposed to be older than Pennsylvanian, probably Late Visean or Early Serpukhovian (Groves et al. 2003). The youngest detrital zircon (grain CH52.22.1) found in this succession is 322 ± 3 Ma-old (this study). According to the Geological Time Scale (GTS) of Gradstein et al. (2004), the Serpukhovian ranges from 326.4 to 318.1 Ma; this range is virtually identical to the age of zircon grain CH52.1.1 if the (1σ) error is included (325–319 Ma). We therefore suggest that the time of deposition of the Chios turbidite-olistostrome succession is younger than Visean, probably Serpukhovian, whereas an even younger age (e.g. Bashkirian) cannot be excluded insofar as no further biostratigraphic or geochronological data are available. Late Carboniferous and Early-Middle Permian shallow marine siliciclastic-calcareous sedimentation, however, set the upper time limit of deposition.

6. Implications for Palaeotethys

Stampfli & Borel (2002) have presented palaeogeographic maps for the Palaeozoic showing an assemblage of terranes at the northern margin of Gondwana, termed the European Hunic terranes, bordered by the Rheic Ocean to the north and by the Palaeotethys Ocean to the south. According to Stampfli & Borel (2002), the term Palaeotethys is used to denote a seaway that separated Gondwana from Gondwana-derived fragments between the Silurian to early Late Triassic, a time in which these fragments drifted northward and accreted to Laurussia in a stepwise fashion. The Palaeotethys Ocean was closed by the northward drift of the Cimmerian terranes in response to the opening of Neotethys in the south. One of the most controversial topics over the last three decades has been the time of closure of Palaeotethys and the location of its suture zone (e.g. Şengör et al. 1984; Stampfli et al. 1991; Robertson et al. 2004). As already discussed by previous authors (e.g. Stampfli et al. 2003) and shown in the present work, Chios is a key area for understanding the closure of Palaeotethys because it is one of the rare localities where very low-grade to virtually unmetamorphosed fossil-bearing Palaeozoic to Mesozoic sequences are preserved (e.g. Besenecker et al. 1968). Detrital zircon

ages and olistolith provenance (this study) imply sediment supply from terranes north of present-day Chios, most probably the Sakarya microcontinent in western Turkey and the Istanbul Zone in northern Turkey, or from time and facies equivalent successions such as those found in southern and central Bulgaria and Serbia. Below we compiled new and pre-existing data regarding Late Palaeozoic magmatic activity, metamorphism, depositional environment and fossil content in clastic successions of Chios and in similar formations in the surrounding region and put forward the following scenario for the geotectonic evolution of the Eastern Mediterranean in Late Palaeozoic to earliest Triassic times:

Variscan orogenic processes were already underway at the southern margin of Laurussia by at least Early Carboniferous times. Carrigan et al. (2006) reported a concordia age of 336.5 ± 5.4 Ma for metamorphic rims of a migmatite leucosome from the Sredna Gora Zone in Bulgaria, which they interpret as the age of zircon recrystallisation during high-grade metamorphism. Subduction of (a northern branch of) Palaeotethys beneath terranes accreted to the southern margin of Laurussia probably ended around 325–320 Ma, testified to by the end of turbidite-olistostrome sedimentation on Chios and Karaburun. The upward transition of the Carboniferous turbiditic fan system to more proximal quartz-rich greywackes and sandstones, followed by carbonate-bearing sandstones with increasing intercalations of limestone beds through to thick limestones marks a shallowing-upward trend above the CCD (calcite compensation depth) and the initiation of a carbonate platform in Late Carboniferous and Permian times (Meinhold et al. 2007). Carboniferous foraminiferal fauna of the Chios–Karaburun units show distinct biogeographic affinities to the southern Laurussian shelf (Kalvoda 2003). Benthic foraminifera and calcareous algae associations suggest that Chios must have been situated at the southern margin of the Sakarya microcontinent in the late Early Permian (Jenny & Stampfli 2000). Figure 15 illustrates the location of Chios in close proximity to the Sakarya microcontinent in a Carboniferous palaeogeographic reconstruction.

Subduction of a more southern or south-western branch of Palaeotethys beneath what was to become the Pelagonian–Cycladic Zone probably started around 330 Ma, producing a voluminous amount of arc-type granitoids between ca. 325 and 300 Ma (e.g. Reischmann 1998; Vavassis et al. 2000; Reischmann et al. 2001; Anders et al. 2006b; Xypolias et al. 2006). Most of the Carboniferous basement rocks from the External Hellenides, the Attic-Cycladic Massif and the Pelagonian Zone in Greece and the Sakarya microcontinent in NW Turkey have similar geochemical and isotopic signatures (Pe-Piper & Piper 2002), suggesting

their close proximity in Late Palaeozoic times (Xypolias et al. 2006). They are commonly interpreted as being the product of northward subduction of (a branch of) Palaeotethys beneath the above-mentioned areas (e.g. Vavassis et al. 2000; Stampfli et al. 2003).

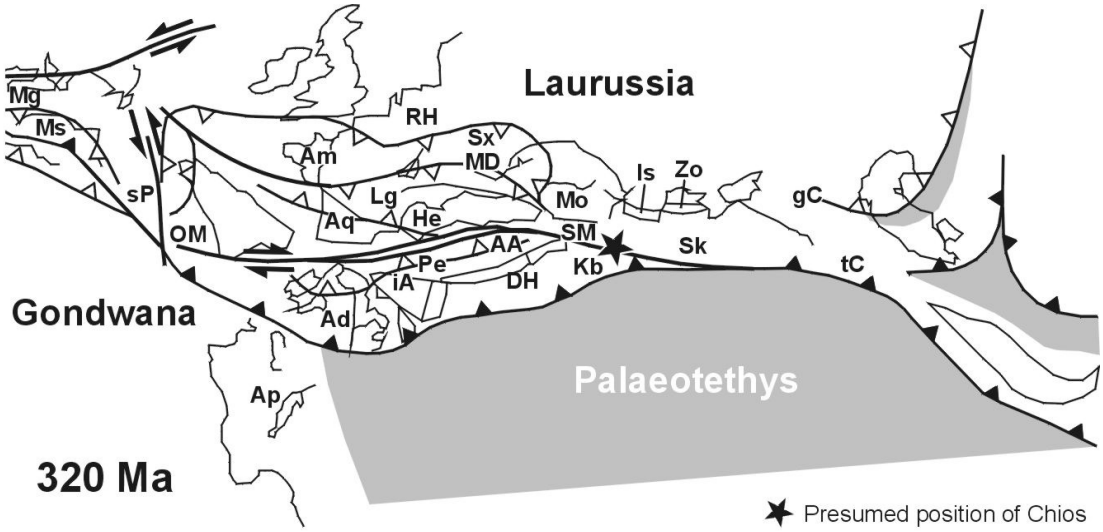

Fig. 15. Palaeotectonic reconstruction for the Carboniferous (after Stampfli et al. 2002). The *black star* shows the presumed position of Chios. AA: Austro-Alpine, Ad: Adria–south Alpine, Am: Armorica, Ap: Apulia, Aq: Aquitaine, DH: Dinarides-Hellenides, gC: great Caucasus, He: Helvetic, iA: intra-Alpine, Is: Istanbul, Kb: Karaburun, Lg: Ligerian, MD: Moldanubian, Mg: Meguma, Mo: Moesia, Ms: Meseta, OM: Ossa-Morena, Pe: Penninic, RH: Rheno-Hercynian, Sk: Sakarya, SM: Serbo-Macedonian, Sp: south Portuguese, tC: trans-Caucasus, Zo: Zonguldak.

However, southward subduction of Palaeotethys beneath the Cimmerian terranes during the Late Palaeozoic has also been proposed (e.g. Sengör et al. 1984; Robertson & Pickett 2000; Romano et al. 2006; Xypolias et al. 2006). To solve the problem of subduction polarity of Palaeotethys is beyond the scope of the present paper. Rather, several branches of this ocean were subducted, a process that eventually led to multiple terrane accretion. Furthermore, as was the case in other parts of Europe (e.g. Matte 1986; von Raumer et al. 2003), orogeny in the Eastern Mediterranean during the Late Palaeozoic was probably accompanied by large-scale transcurrent movements (e.g. Stampfli et al. 2002: fig. 4), juxtaposing very different oceanic or continental fragments and hence giving rise to equivocal palaeotectonic models and interpretations.

Remnants of one of the Palaeotethyan sutures can be traced from Chios north into the Pontides. Such remnants can also be traced on the Karaburun peninsula in western Turkey

(Kozur 1998; Robertson & Pickett 2000, and references therein), in the Tavas nappe (Lycian nappes) further southeast (Kozur et al. 1998) and near Konya in central Turkey (Eren et al. 2004). The present-day position of these units, so far south from their possible source is still a matter of discussion. Gessner et al. (2001) noted that the tectonic position of the Lycian Allochthon above the ophiolitic Selçuk mélange implies that the lower units of the Lycian Allochthon were deposited either on a promontory of Adria or Sakarya or on a separate continental fragment, and were not part of Anatolia as has been generally assumed by previous workers. We have shown here that the Late Palaeozoic–Early Mesozoic clastic successions of Chios were probably deposited on or close to the Sakarya microcontinent during Permo-Triassic times. If, then, the correlation of units from Chios with similar units from the Karaburun peninsula, the Konya region and the Lycian nappes (e.g. Tavas nappe) is correct, the latter must also have been deposited on or close to Sakarya, which would be in agreement with the model of Gessner et al. (2001).

In order to gain a more regional perspective, we would like to note here that the Late Palaeozoic Chios olistostrome-turbidite succession may correlate to metamorphic rocks cropping out on Sakarya. Göncüoğlu et al. (2000) described the Tepeköy unit which they interpreted as an accretionary complex formed in an intra-oceanic fore-arc setting due to southward subduction of a branch of the Palaeotethys beneath an arc complex (future Söğüt unit). The Tepeköy and Söğüt units were attached to the northern margin of the Tauride-Anatolide Platform during Middle–Late Carboniferous times. Göncüoğlu et al. (2000) proposed that a back-arc basin developed at the northern margin of the Tauride-Anatolide Platform in the Late Carboniferous, as evidenced by the rocks of the Göktepe Metamorphics. The olistostrome-turbidite unit on the Karaburun peninsula and the Halıcı Formation at Konya are interpreted by Göncüoğlu et al. (2000) as possible tectonic slices of the Göktepe Metamorphics. If this is the case, the Chios units can also be compared to the latter since they have already been correlated with the Karaburun units (see above).

Which model is correct for the Chios olistostrome-turbidite succession discussed will certainly be the subject of further studies, but it seems clear that Chios was located close to the Sakarya microcontinent in Late Palaeozoic times and received detritus from north Gondwana-derived terranes with similarities to terranes preserved in northern Turkey and the Balkan region. Furthermore, the virtually unmetamorphosed nature of Chios means that it must have always been in an upper plate position.

7. Conclusions

The presence of ca. 2 Ga-old detrital zircons in the Carboniferous and Permo-Triassic successions of Chios coupled with the lack of ages between 1.8 and 1.1 Ga is a characteristic feature of NW Africa-derived terranes. Zircons aged around 1 Ga almost certainly have a secondary source due to polyphase recycling. Detrital zircon ages of ca. 640–540, 505–475 and 385–370 Ma can be assigned to terranes in western and northern Turkey (e.g. Sakarya microcontinent, Istanbul Zone) and to units in Bulgaria. The analysis of fossiliferous olistoliths (Silurian cephalopod limestones) from the Carboniferous olistostrome-turbidite succession indicates a source area similar to that of Palaeozoic sequences exposed nowadays in northern Turkey and the Balkan region.

In summary, the results stemming from the new data presented here establish that NW African-derived terranes were involved in Palaeotethyan subduction-accretion processes in the Aegean region during Late Palaeozoic times. The relationships however between these terranes at the southern margin of Laurussia are now masked by younger (Mesozoic to Cenozoic) complex structural and metamorphic events. Our study demonstrates that the combined use of detrital zircon U/Pb ages and provenance analysis of olistoliths can impose tight constraints on terrane accretion processes and the provenance of crustal sources for sediments during the subduction of Tethyan oceans.

Chapter 4

U–Pb LA-ICPMS zircon geochronology of the Serbo-Macedonian Massif, Greece: Palaeotectonic constraints for Gondwana-derived terranes in the Eastern Mediterranean

Abstract

The Pirgadikia Unit in northern Greece forms tectonic inliers within the Vardar suture zone bordering the Serbo-Macedonian Massif to the southwest. It comprises Cadomian basement rocks of volcanic-arc origin and very mature quartz-rich metasedimentary rocks. U–Pb LA-ICPMS analyses of detrital zircons from the latter reveal a marked input from a Cadomian–Pan-African source with minor contribution from Mesoproterozoic, Palaeoproterozoic and Archaean sources. The metasedimentary rocks are correlated with Ordovician overlap sequences deposited at the northern margin of Gondwana on the basis of their maturity and zircon age spectra. The Pirgadikia Unit can be best interpreted as a peri-Gondwana terrane of Avalonian origin, which was situated in close proximity to the Cadomian terranes by the Late Neoproterozoic–Early Palaeozoic, very much like the Istanbul Terrane. U–Pb analyses of detrital zircons from a garnetiferous micaschist of the Vertiskos Unit indicate derivation from 550–1150 Ma-old source rocks with a major Cadomian peak. This, combined with minor input of >1950 Ma-old zircons and the absence of ages between ca. 1.2 and 1.7 Ga suggests a NW African source. The protolith age of the garnetiferous micaschist is presumably Early Ordovician. One sample of garnet-biotite gneiss, interpreted as orthogneiss, comprises predominantly subhedral zircons of igneous origin with late Middle Ordovician to Silurian ages. We suggest that the rock association of the Vertiskos Unit is part of an ancient active-margin succession of the Hun superterrane, comparable to successions of the Intra-Alpine terranes. The new data of this study provide proof of the occurrences of

Avalonia- and Armorica-derived terranes in the Eastern Mediterranean and moreover help to clarify palaeogeographic reconstructions for the peri-Gondwana realm in the Early Palaeozoic.

1. Introduction

Understanding ancient plate tectonic processes in space and time is strongly dependent on the accessibility and preservation of old crustal or oceanic fragments. Major tectonic and thermal events commonly lead to destruction and recycling of continental and oceanic crust, especially during orogenic processes at active continental margins. A prime example is the so-called Avalonian–Cadomian belt (Nance & Murphy 1994), which Late Neoproterozoic to Early Palaeozoic evolution had an important bearing on the geological development of Europe (e.g. Neubauer 2002). The Avalonian–Cadomian belt was formed during late Neoproterozoic Andean-type subduction of the Prototethys Ocean under the northern margin of Gondwana (Nance & Murphy 1994; Stampfli & Borel 2002) and subsequently dismembered in Cambrian to Silurian times with the diachronous opening of back-arc basins, giving birth to the Rheic Ocean and later on to the Palaeotethys Ocean (e.g. Stampfli & Borel 2002; Stampfli et al. 2002). It is widely agreed that the rifted fragments (Avalonian terranes, Hun superterrane including the Armorican terranes) were transported northward to be accreted to the southern margin of Laurussia (e.g. Stampfli & Borel 2002; Stampfli et al. 2002; von Raumer et al. 2002, 2003). They became involved in the late Palaeozoic Variscan orogeny and some of them were also overprinted by the Alpine–Himalayan orogeny in the Late Mesozoic to Cenozoic. The Alps, the Bohemian Massif, and the Carpathians are prominent areas in Central and Eastern Europe (Fig. 1) which comprise fragments of the Avalonian–Cadomian belt (e.g. Neubauer 2002). In the Eastern Mediterranean the relationships between different pre-Alpine crustal fragments are now masked by younger (Mesozoic to Cenozoic) complex structural and metamorphic events. This, together with the scarcity of biostratigraphic, geochronological and palaeomagnetic data, has given rise to equivocal palaeotectonic models and interpretations. Notwithstanding, one of the main innovative topics in recent years has been the identification of Avalonia- and Armorica-derived terranes in the Eastern Mediterranean (e.g. Anders et al. 2006a; Himmerkus et al. 2006a, 2007; Yanev et al. 2006; Winchester et al. 2006).

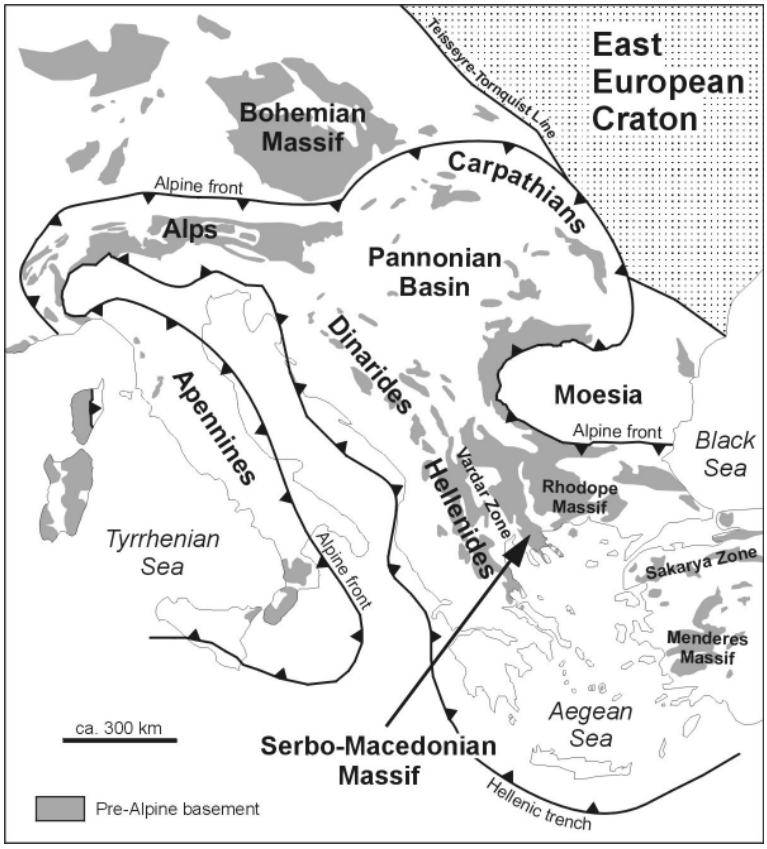

Fig. 1. Present-day location of the Serbo-Macedonian Massif within the Alpine–Mediterranean mountain belt (modified after Neubauer 2002).

The Serbo-Macedonian Massif (SMM) of northern Greece (Figs. 1 and 2) is a case in point. Late Neoproterozoic and Silurian rocks of magmatic-arc origin have recently been discovered there (Himmerkus et al. 2006a, 2007), but their affiliation with surrounding basement units in Turkey and Bulgaria is still speculative. In recent palaeotectonic reconstructions for the Cambro-Ordovician (~ 490 Ma), for instance, the SMM is assigned to the Cadomian terranes in proximity to Saxothuringia and Ligerian (Stampfli et al. 2002). Later during the Carboniferous (~ 320 Ma) it is proposed to have become sandwiched between the Austro-Alpine unit to the southwest and the Sakarya terrane to the east (Stampfli et al. 2002). The data base for such reconstructions, however, is still wanting. No fossil data are available for the intercalated siliciclastic metasedimentary rocks of the SMM due to polyphase deformation and upper amphibolite-facies metamorphism (e.g. Kockel et al. 1971; Kilias et al. 1999). Their stratigraphic age is questionable and their provenance is unknown: they could have derived from the Avalonian or the Armorican terranes, or from elsewhere. Hence, the age and origin of basement units of the Greece may well provide further insight into the configuration of North Gondwana-derived terranes in the Eastern Mediterranean.

In recent years, in situ U–Pb dating of detrital zircons by laser ablation inductively-coupled plasma mass spectrometry (LA-ICPMS) has proven to be a powerful tool in sedimentary provenance studies (e.g. Fernández-Suárez et al. 2002; Košler et al. 2002; Murphy et al. 2004; Gerdes & Zeh 2006). Here we present for the first time high-spatial resolution U–Pb dating by laser ablation sector-field inductively-coupled plasma mass spectrometry (LA-ICPMS) of detrital and igneous zircon grains from basement rocks of the Serbo-Macedonian Massif and adjacent basement slivers to evaluate potential source regions and ancient major magmatic events.

The study of clastic sedimentary rocks is crucial for palaeotectonic reconstructions because they can provide information about rock lithologies in the source area which have often been destroyed and recycled during ancient plate tectonic processes. Furthermore, in the absence of fossil and other stratigraphic data, the youngest grain (e.g. zircon) in a sedimentary rock can indicate a maximum limit for the age of deposition (e.g. Fedo et al. 2003). The age and origin of pre-Alpine basement units in the Internal Hellenides has important implications in our understanding the evolution of North Gondwana-derived terranes in more detail and consequently in alternative plate-tectonic reconstruction for the Early Palaeozoic.

2. Geological setting

The Serbo-Macedonian Massif in northern Greece is an elongated, structurally complicated basement complex between the relatively homogeneous basement complexes of the Pelagonian Zone to the west and the Rhodope Massif to the east. It extends north into western Bulgaria and eastern F.Y.R.O.M. Its boundary with the Pelagonian Zone marks the Vardar strike-slip zone and its border with the Rhodope Massif is camouflaged by Tertiary sediments of the Strimon River valley. Early workers suggested that the SMM was thrust over the Rhodope Massif along the Strimon River valley fault in the Tertiary (Kockel & Walther 1965; Kockel et al. 1971). Later on, this fault was reinterpreted as a large-scale, southwest-dipping, extensional detachment (e.g. Dinter & Royden 1993; Kilias et al. 1999). Recently, however, Brun & Sokoutis (2007) have demonstrated that the Strimon fault is in fact a décollement within the upper brittle crust that operated during Pliocene–Pleistocene times and that the boundary between the SMM and the Rhodope Massif is represented by the

WSW-dipping extensional Kerdillion detachment that separates the Kerdillion from the Vertiskos Series of the SMM (see below).

The Serbo-Macedonian Massif is mainly composed of amphibolite-facies schists and gneisses, in places migmatitic, amphibolites and marbles. Its subdivision and age have been a matter of controversy and lengthy discussion. It has conventionally been subdivided into two 'series', the underlying (older) Kerdillion Series to the east and the overlying (younger) Vertiskos Series to the west (Kockel et al. 1971, 1977). The rocks were thought to represent a Palaeozoic or older stable basement that was only superficially involved in the complex Mesozoic and Cenozoic evolution of the Hellenides (e.g. Aleksić et al. 1988; Kockel et al. 1971, 1977). Burg et al. (1995) demonstrated that the Vertiskos Group is a composite unit comprising a lower metaturbiditic and orthogneissic sequence, with few amphibolites and distinct marble layers, and an upper migmatitic para- and orthogneissic sequence, separated by a metaophiolite-bearing mylonite zone. Ricou et al. (1998) suggested that the Serbo-Macedonian Massif represents the western extension of thrust units belonging to the Rhodope Massif, the latter commonly interpreted as a nappe complex characterized by south to southwestward stacking and associated with both coeval and subsequent extension in an Alpine active-margin setting (Burg et al. 1996).

Geochronological and geochemical studies carried out over the last few years have provided us with new insights regarding the Serbo-Macedonian Massif (Himmerkus et al. 2006a, b, 2007). Its western and central parts are formed by the Vertiskos Unit. This unit consists dominantly of very coarse-grained augengneisses of granitic composition which originated in a magmatic-arc environment (Himmerkus et al. 2006a). Minor micaschists and paragneisses occur. Pb–Pb and U–Pb zircon geochronology has shown a Silurian age for the augengneisses (Himmerkus et al. 2006a). The basement rocks of the Vertiskos Unit were intruded by Triassic (ca. 222–241 Ma) A-type granitoids (Arnea suite) in a within-plate rift setting together with a number of basic intrusives, interpreted as less evolved magmas (Himmerkus et al. 2004b, in preparation). The rocks of the Vertiskos Unit underwent amphibolite-facies metamorphism and a retrograde greenschist-facies overprint in Middle–Late Cretaceous and Cenozoic times, respectively (e.g. Dixon & Dimitriadis 1984; Kilias et al. 1999). Because all contacts are tectonic, there is no clear relationship with the surrounding country rocks.

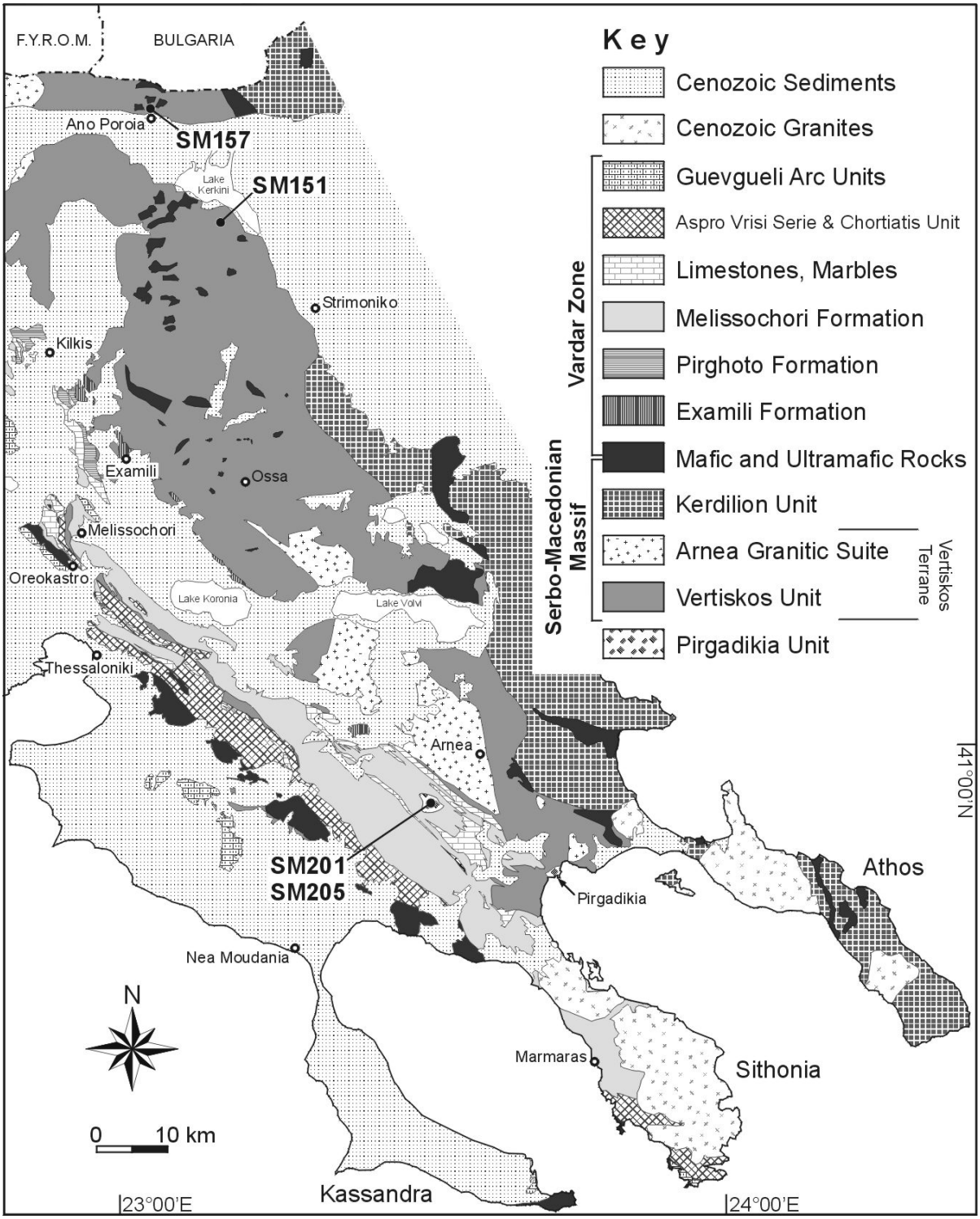

Fig. 2. Geological map of the Serbo-Macedonian Massif and the bordering Vardar Zone (modified after Kockel & Mollat 1977; IGME 1983) showing the sampling locations used for zircon geochronology. The occurrences of the Kerdilion Unit are after Himmerkus et al. (2006a).

The eastern and southeastern part of the Serbo-Macedonian Massif is formed by the Kerdillion Unit. This unit is very homogeneous, consisting of strongly deformed biotite-

gneisses, which are intruded by a plethora of leucocratic dykes. Permo-Carboniferous, Late Jurassic and Early Tertiary magmatic events have been identified by zircon geochronology (Himmerkus et al. 2006b). The Kerdilion Unit can be seen as the western promontory of the adjacent Rhodope Massif where similar intrusion ages have also been found (Turpaud & Reischmann 2003; Turpaud 2006). The boundary between the Kerdillion and the Vertiskos Units is interpreted as a suture (e.g. Şengör et al. 1984; Himmerkus et al. 2006a), consisting of a mélange of marble, amphibolite and metagabbro bodies, several tens of metres thick, floating in a metasedimentary succession. The basic–ultrabasic rocks have generally been assigned to the so-called Therma–Volvi–Gomati (TVG) Complex (e.g. Dixon & Dimitriadis 1984) and commonly been interpreted as either a remnant of the Palaeotethys Ocean that closed in the Early Jurassic (Şengör et al. 1984) or, in contradiction, as a rift-related intrusive complex of Mesozoic age (Dixon & Dimitriadis 1984).

Recently, Neoproterozoic basement rocks have been identified as tectonic inliers within the Circum-Rhodope Belt (part of the Vardar Zone *sensu* Jacobshagen 1986) bordering the Serbo-Macedonian Massif to the southwest (Himmerkus et al. 2006a). Main outcrops occur near the villages of Pirgadikia and Taxiarchis. Himmerkus et al. (2006a) introduced the Pirgadikia Unit based on lithological, geochronological and structural features that differ strongly from those units belonging to the Serbo-Macedonian Massif and the adjacent basement rocks of the Pelagonian Zone and the Rhodope Massif. The Pirgadikia Unit near Pirgadikia village consists of mylonitic orthogneisses. Their geochemistry and zircon ages point to volcanic-arc magmatism during late Precambrian times (Himmerkus et al. 2006a).

In the course of this study, the area near Taxiarchis village was revisited. The basement rocks there are of sedimentary origin, consisting mainly of fine- to coarse-grained, well sorted, and light coloured to greenish-grey metaquartzites intercalated with greenish grey metasiltstones; conglomerate horizons up to one metre thick occur sporadically. The metaquartzites in places show a strong mylonitic fabric. The conglomerates are predominantly composed of milky-white quartz pebbles embedded in a coarse-grained quartzose matrix. The width of the pebbles ranges from a few mm to 1.5 cm. Inasmuch no fossils have yet been discovered, the age of the metasedimentary succession is open to question. Preliminary single-zircon Pb–Pb age determinations for a mylonitic metaquartzite range between ca. 530 and 590 Ma, probably indicating proximity to a Cadomian basement

(Himmerkus et al. 2006a). The circa 530 Ma age can be considered as representing the youngest detrital input thus giving a maximum age of deposition for the metasedimentary rocks of the Pirgadikia Unit.

3. Analytical methods

Major and trace elements of whole-rock samples were analysed by X-ray fluorescence (XRF) spectrometry on fused glass discs and pressed powder pellets respectively, using a Philips MagiX Pro X-ray spectrometer at the University of Mainz, following procedures outlined in Meinhold et al. (2007). Rare-earth elements (REE), Hf, Ta, Th and U of selected samples were analysed on fused discs by LA-ICPMS using an Agilent 7500ce equipped with a Merchantek NewWave 213 nm Nd-YAG laser at the University of Mainz, following procedures described in Nehring et al. (2007). Whole-rock geochemical data are listed in the Appendix.

For U–Pb geochronology zircons were separated from the bulk samples using standard techniques (hydraulic press, rotary mill, Wilfley table, Frantz isodynamic magnetic separator and heavy liquids [methylene iodide]). Final purification was carried out by hand-picking under a binocular microscope. Zircon grains were set in epoxy resin mounts, sectioned and polished to approximately half their original thickness. Prior to the analyses, cathodoluminescence (CL) images were obtained for all grains in order to study their internal structure and to target specific areas within them, e.g. growth structures and inherited cores.
The U–Pb isotopic analyses of individual zircon grains were performed using a Thermo-Finnigan Element II sector-field ICPMS system coupled to a Merchantek/NewWave 213 nm Nd-YAG laser system at the Geological Survey of Denmark and Greenland (GEUS), Copenhagen, Denmark. The zircon mounts were rigorously cleaned in an ultrasonic bath before introducing them into the sample cell to remove surface lead contamination. The methodology applied essentially followed that described by Gerdes & Zeh (2006) and Frei et al. (2006). The nominal pulse width of the laser was 5 ns with a pulse-to-pulse stability of 2% RSD. The laser was operated at a repetition rate of 10 Hz and a nominal energy output of 40%, corresponding to a laser energy of ~0.006 mJ and a laser fluency of ~0.8 J cm^{-2}. All data were acquired with single-spot analyses on individual zircon grains using a 30 µm spot size. Samples and standards were held in a low-volume ablation cell specially developed for U–

Pb-dating (Horstwood et al. 2003). Helium gas was used to flush the sample cell and was mixed downstream with the Ar sample gas of the mass-spectrometer. The washout time for this configuration is <15 s. The total acquisition time for each analysis was 60 s with the first 30 s used to measure the gas blank. The instrument was tuned to give large, stable signals for the ^{206}Pb and ^{238}U peaks, low background count rates (typically around 150 counts per second for ^{207}Pb) and low oxide production rates ($^{238}U^{16}O/^{238}U$ generally below <0.2%). All measurements were performed in low resolution mode using electrostatic scanning (E-scan) with the magnetic field resting at mass ^{202}Hg. The following masses were measured: ^{202}Hg, $^{204}(Pb + Hg)$, ^{206}Pb, ^{207}Pb, ^{208}Pb, ^{232}Th, ^{235}U, and ^{238}U. All data were acquired on four samples per peak with a sampling and settling time of 1 ms for each isotope. Mass ^{202}Hg was measured to monitor the ^{204}Hg interference on ^{204}Pb (using a $^{202}Hg/^{204}Hg$-ratio of 4.36). Only if the net intensities for mass ^{204}Pb, corrected for ^{204}Hg, were significantly above the limit of detection a correction for common Pb was applied (see Janoušek et al. 2006). The laser-induced elemental fractionation and instrumental mass biases on measured isotopic ratios were corrected by matrix-matched external standardisation using the GJ-1 zircon standard (Jackson et al. 2004). Samples were analysed in sequences with three standards analysed initially, followed by ten samples, then three standards, followed once again by ten samples, and so on. Raw data were processed off-line in an in-house Excel® spreadsheet program. Long-term precision (2σ) of the used facility used at the GEUS based on 109 analyses of the Plešovice zircon standard (provided by Jan Košler, University of Bergen, Norway) by two different operators is 2%, 2.3% and 1.1% for the $^{206}Pb/^{238}U$, $^{207}Pb/^{235}U$ and $^{207}Pb/^{206}Pb$ ratios respectively (Frei et al. 2006).

For the interpretation of the zircon data, analyses with 95–105% concordance (calculated from 100 × ($^{206}Pb/^{238}U$ age)/($^{207}Pb/^{235}U$ age)) are considered to be concordant. Analyses with a discordance >10% were rejected and consequently not considered for data interpretation. Such high discordance arises when the laser penetrates domains with distinct Pb/U ratios (Janoušek et al. 2006), the epoxy resin, mineral inclusions and/or cracks in zircon, and/or zircon zones affected by radiogenic Pb loss. The latter is a common phenomenon and mostly attributed to metamictization and later recrystallisation during which Pb is removed from the zircon crystals (Williams 1992; Mezger & Krogstad 1997). Unless stated otherwise, $^{206}Pb/^{238}U$ ages are used for zircon grains <1.2 Ga whereas older grains are quoted using their $^{207}Pb/^{206}Pb$ ages. This is because the $^{207}Pb/^{206}Pb$ ages become increasingly

imprecise below <1.2 Ga due to small amounts of ^{207}Pb. The $^{207}Pb/^{206}Pb$ ages are generally considered as minimum ages due to the effect of possible Pb loss. Concordia diagrams and probability density distribution and histogram plots were produced using the programs Isoplot/Ex (Ludwig 2003) and AgeDisplay (Sircombe 2004) respectively. Unless stated otherwise, ages reported in the text are given at the 2-sigma level. The isotopic data of 226 analyses on 219 single zircon grains referred to in this manuscript are included in the accompanying Appendix. The Geological Time Scale (GTS) of Gradstein et al. (2004) was used as stratigraphic reference for data interpretation.

4. Sample description and geochemistry

To constrain the age and provenance of basement rocks from the Serbo-Macedonian Massif and adjacent basement slivers, we have collected two metaquartzites from the Pirgadikia Unit and one garnetiferous micaschist and one garnet-biotite gneiss from the Vertiskos Unit for zircon geochronology (Fig. 3). These samples as well as additional ones from the Pirgadikia Unit were also analysed for their whole-rock major- and trace-element content.

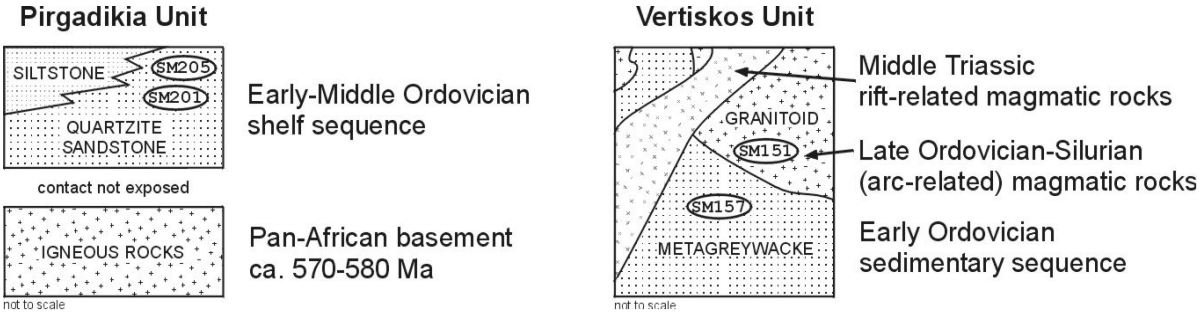

Fig. 3. Interpretive tectonostratigraphic columns for the Pirgadikia and Vertiskos Units (see text for references). The stratigraphic positions of samples used for U–Pb zircon geochronology are indicated.

4.1. Pirgadikia Unit

Sample SM201 was collected from a metaquartzite succession cropping out along a minor road northeast of Taxiarchis village (40°26´00.7´´N, 23°30´58.1´´E; Figs. 2 and 4); sample SM205 comes from a small metaquartzite outcrop along a new road southwest of Taxiarchis (40°25´39.1´´N, 23°30´51.8´´E; Fig. 2). The samples are almost feldspar-free

quartz arenites with chlorite and accessory zircon, apatite and opaque minerals (Fe-oxides). All quartz grains are single crystals with almost no undulose extinction. Some larger grains show undulose extinction and subgrain formation. The quartz grain boundaries are almost straight, only a few are sutured. In general, the textures indicate that the quartz grains underwent dynamically recrystallisation (Passchier & Trouw 2005), probably at upper greenschist-facies conditions. The zircons in both samples have a predominantly well-rounded to rounded shape, only a few are subhedral. The length of single zircon crystals varies between 50 and 220 µm in sample SM201 and between 80 and 320 µm in sample SM205. Their colour ranges from pink and yellowish to whitish.

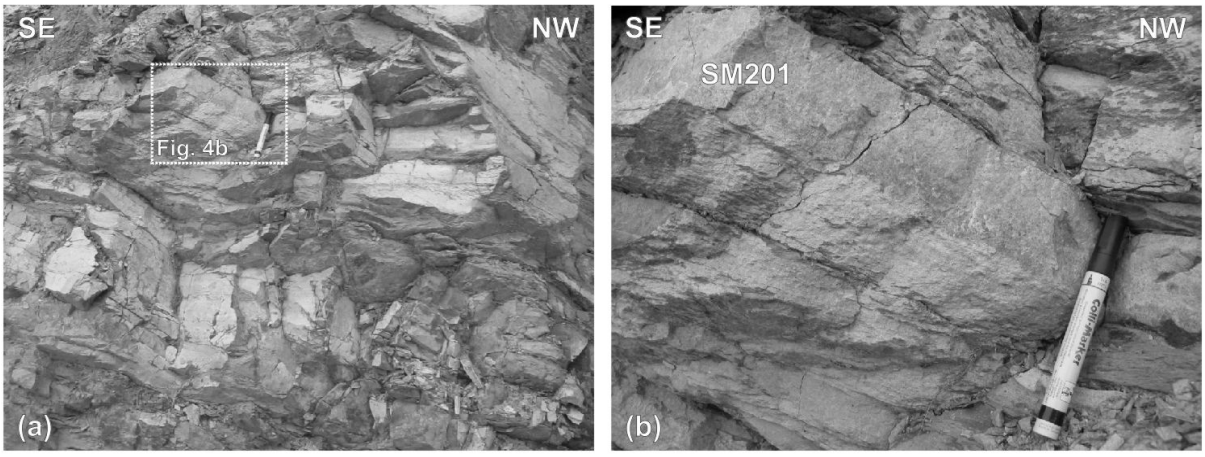

Fig. 4. Photographs showing mature metaquartzites of the Pirgadikia Unit at Taxiarchis village. Location of sample SM201 used for zircon geochronology is indicated.

Geochemically, the metasedimentary rocks from the Pirgadikia Unit are very mature sediments. A low to medium SiO_2 group (SiO_2: 60–73 wt.%, Na_2O+K_2O+CaO: 3.4–5.7 wt.%, Al_2O_3: 11–18 wt.%) can be assigned to metapelites, whereas the high SiO_2 group (SiO_2: 84–96 wt.%, Na_2O+K_2O+CaO: up to 2.2 wt.%, Al_2O_3: ≤6 wt.%) are interpreted as metapsammites (Fig. 5a). According to the classification scheme of Herron (1988), the metapelites are shales and the metapsammites are iron-bearing sandstones and quartz arenites. Compared to average upper continental crust the high-SiO_2 group samples show a strong depletion in Rb, Ba, K, Sr and P, whereas those of the low-SiO_2 group have an almost flat profile with a characteristic depletion in Sr and P (Fig. 5a). Chondrite-normalized rare-earth element (REE) patterns of two metaquartzite samples used for zircon geochronology (Fig. 5b) show light rare-earth element (LREE) enriched and flat to slightly depleted heavy

rare-earth element (HREE) patterns with a negative Eu anomaly (Eu/Eu* ~ 0.68 for SM201 and ~ 0.64 for SM206). The negative Ce anomaly of sample SM205 might be a result of quartz dilution since this sample has the highest SiO_2 content but very low trace- and rare-earth element concentrations.

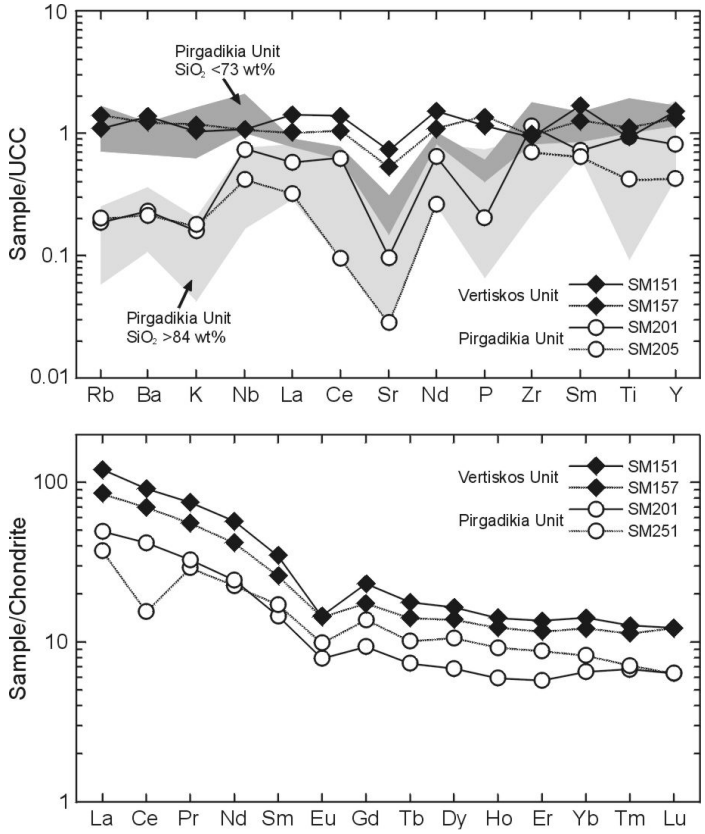

Fig. 5. (a) Multi-element diagram normalized to upper continental crust (UCC) composition of samples used for zircon geochronology. Normalizing values are from Rudnick & Gao (2003). For comparison purposes, the remaining metasedimentary samples of the Pirgadikia Unit are shown as light and dark greyish fields, respectively, according to their SiO_2 concentrations. **(b)** Chondrite-normalized rare-earth element (REE) diagram of selected samples. Normalizing values are from Taylor & McLennan (1985).

4.2. Vertiskos Unit

Sample SM157 was collected from an outcrop north of Ano Poroia village ca. 4 km south of the border with Bulgaria (41°17´27.3´´N, 23°02´00.0´´E; Fig. 2), where garnetiferous micaschists are exposed. Augengneisses with large feldspar porphyroblasts measuring up to 5 cm across and migmatitic gneisses occur nearby. The main fabric in the area is an almost flat-lying foliation. Sample SM157 contains quartz, biotite, white mica, plagioclase, and minor garnet and corundum. The main accessory minerals are zircon, rutile and opaque minerals. The zircon crystals are predominantly subhedral to rounded, yellowish to clear colourless. The length of single zircon crystals varies between 60 and 360 µm. According to the classification scheme of Herron (1988), the protolith of the garnetiferous micaschist is a wacke (i.e. greywacke). The SiO_2 content of ~ 70 wt.%, Na_2O+K_2O+CaO content of ~ 7 wt.%

and relatively high Al_2O_3 content of ~ 14 wt.% suggest a peraluminous composition. When normalized to average upper-continental crust this rock shows an almost flat multi-element profile with a minor depletion in Sr (Fig. 5a). The chondrite-normalized REE pattern (Fig. 5b) shows a strong LREE enrichment and an almost flat HREE region with a negative Eu anomaly (Eu/Eu* ~ 0.67).

Sample SM151 was collected from a small outcrop along a stream south of Lake Kerkini (41°07´44.4´´N, 23°12´13.7´´E; Fig. 2), in which garnet-biotite gneiss, interpreted here as orthogneiss, is exposed. Amphibolites and tourmaline-bearing pegmatites crop out in the vicinity. The main fabric here is an almost flat-lying foliation accompanied by a strong ENE-trending biotite mineral lineation. Sample SM151 contains quartz, plagioclase, biotite, white mica, K-feldspar, garnet, zoisite and epidote. The garnet crystals are almandine and grossular rich (see Appendix; Alm ~ 50 mol.%, Grs ~ 40 mol.%). Accessory minerals are zircon, rutile and opaque minerals. The long-prismatic zircon crystals are euhedral with rounded edges to subhedral, clear colourless. The length of single zircon crystals varies between 100 and 300 µm. The chemical signature of the garnet-biotite gneiss (SiO_2: ~ 67 wt.%, Na_2O+K_2O+CaO: ~ 9 wt.%, Al_2O_3: ~ 15 wt.%) suggests a calcalkaline, peraluminous and granodioritic composition with I-type affinities. Geochemical discrimination diagrams for granitoid rocks (e.g. Yb vs. Ta, [Y + Nb] vs. Rb; see Pearce et al. 1984) reveal a volcanic-arc signature with affinities with within-plate granites. The multi-element pattern of sample SM151 is almost flat with a minor depletion of Sr, compared to average upper-continental crust composition (Fig. 5a). The chondrite-normalized REE pattern (Fig. 5b) shows a strong LREE enrichment and almost flat HREE region with a well-developed negative Eu anomaly (Eu/Eu* ~ 0.52).

5. Geochronological results

5.1. Pirgadikia Unit

The majority of the analysed zircons from metaquartzites of the Pirgadikia Unit have clear oscillatory zonation patterns in CL images and appear to be magmatic in origin (Fig. 6); few exhibit no zoning or patchy zoning.

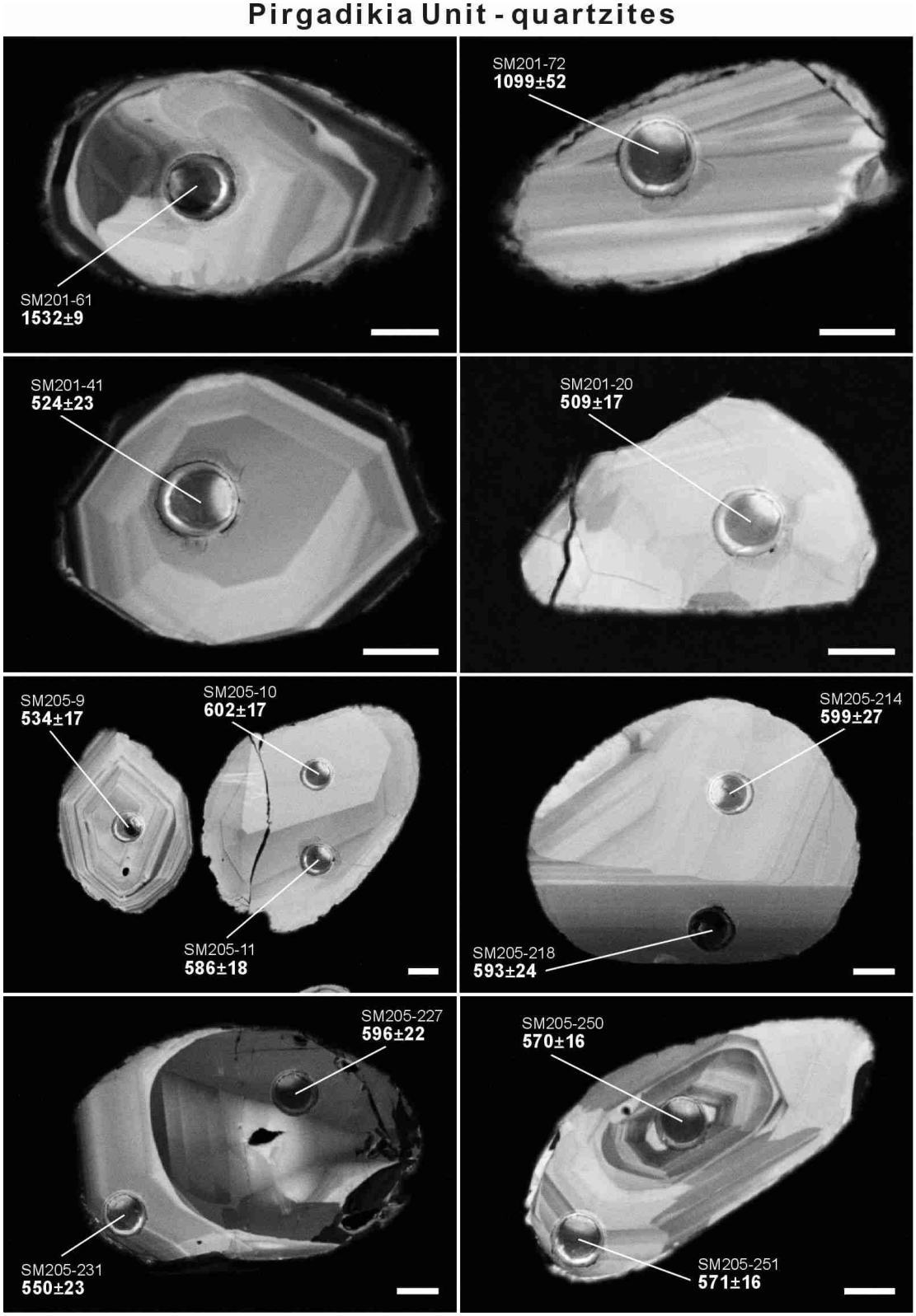

Fig. 6. CL images of representative zircon grains from analysed samples of the Pirgadikia Unit with location of the LA-ICPMS analysis spot and corresponding $^{206}U/^{238}Pb$ age (±2σ) for grains <1.2 Ga and $^{207}Pb/^{206}Pb$ age (±2σ) for grains >1.2 Ga, respectively. Letter–number code above the ages: sample-spot. The scale bar represents 30 μm in all images.

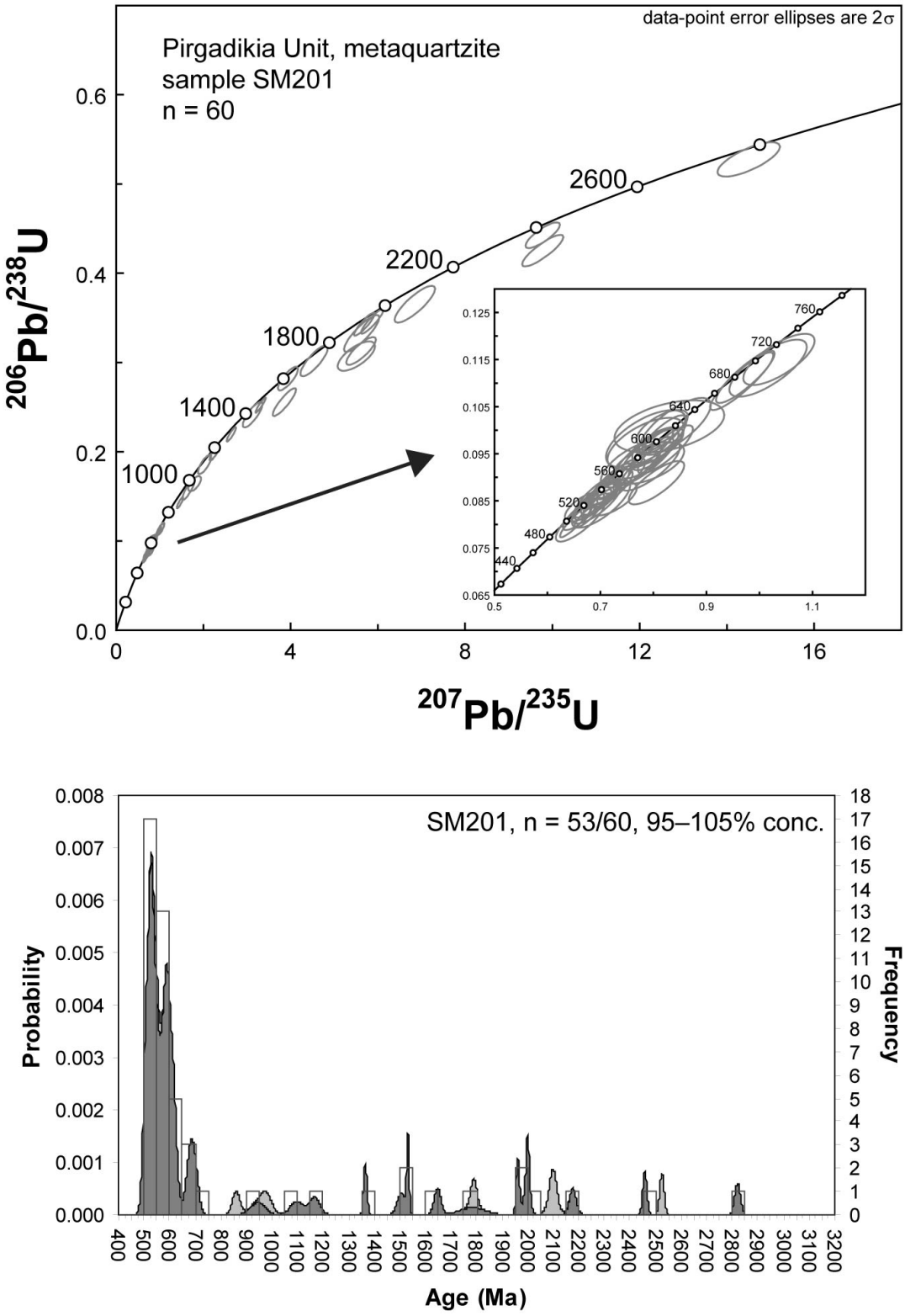

Fig. 7. Concordia diagrams (*upper*) and combined probability density distribution and histogram plots (*lower*) for the set of U–Pb analytical zircon data from samples SM201. Error ellipses in concordia plots represent 2σ uncertainties. 1.2 Ga limit is used to switch between $^{206}Pb/^{238}U$ and $^{207}Pb/^{206}Pb$ ages for the probability and histogram plots. Dark grey shaded – zircon ages with 95–105% concordance, light grey shaded – zircon ages with >5 % discordance (see text for explanation). Abbreviation: n = number of analyses.

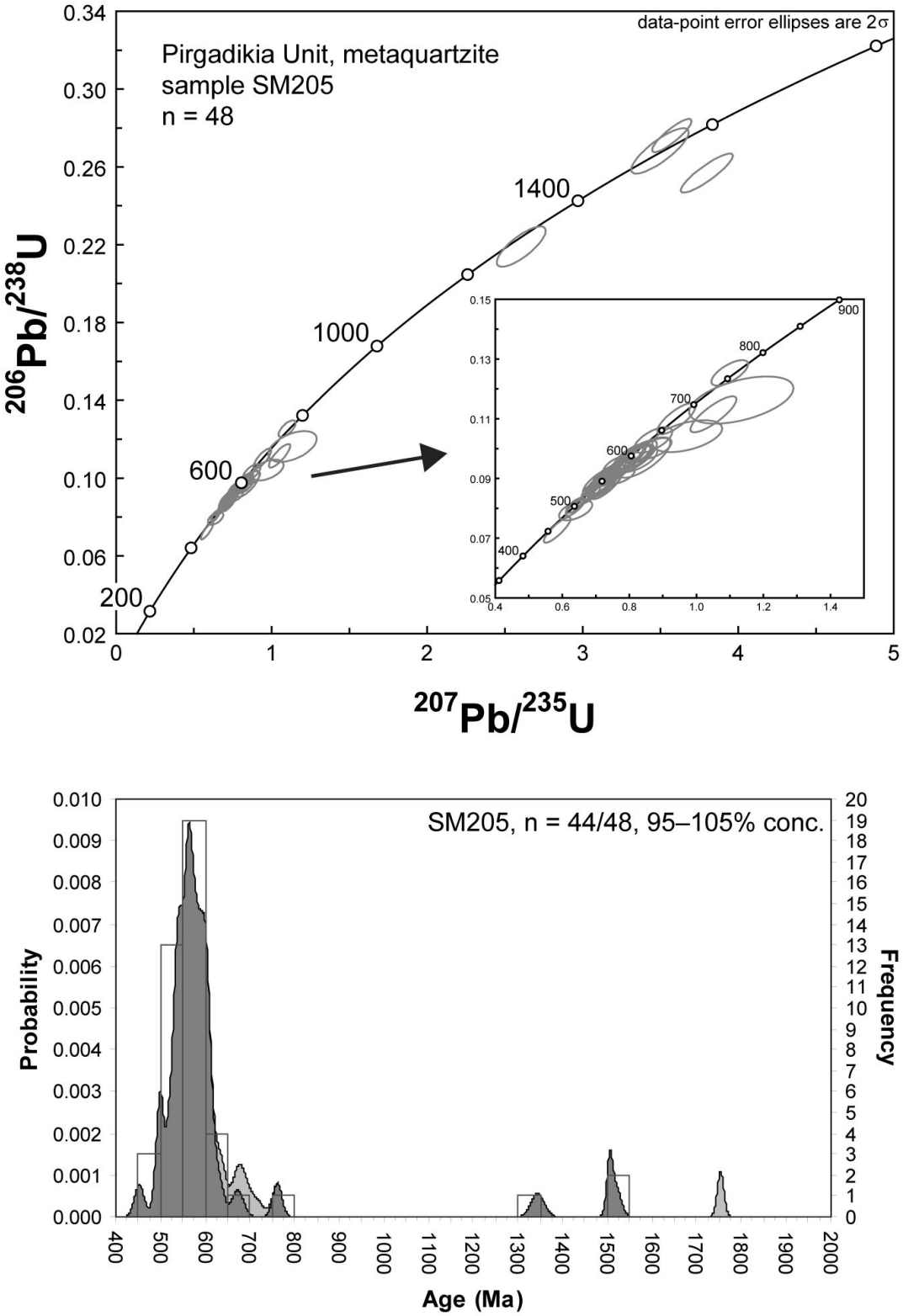

Fig. 8. Concordia diagrams (*upper*) and combined probability density distribution and histogram plots (*lower*) for the set of U–Pb analytical zircon data from samples SM205. Error ellipses in concordia plot represent 2σ uncertainties. 1.2 Ga limit is used to switch between $^{206}Pb/^{238}U$ and $^{207}Pb/^{206}Pb$ ages for the probability and histogram plots. Dark grey shaded – zircon ages with 95–105% concordance, light grey shaded – zircon ages with >5 % discordance (see text for explanation). Abbreviation: n = number of analyses.

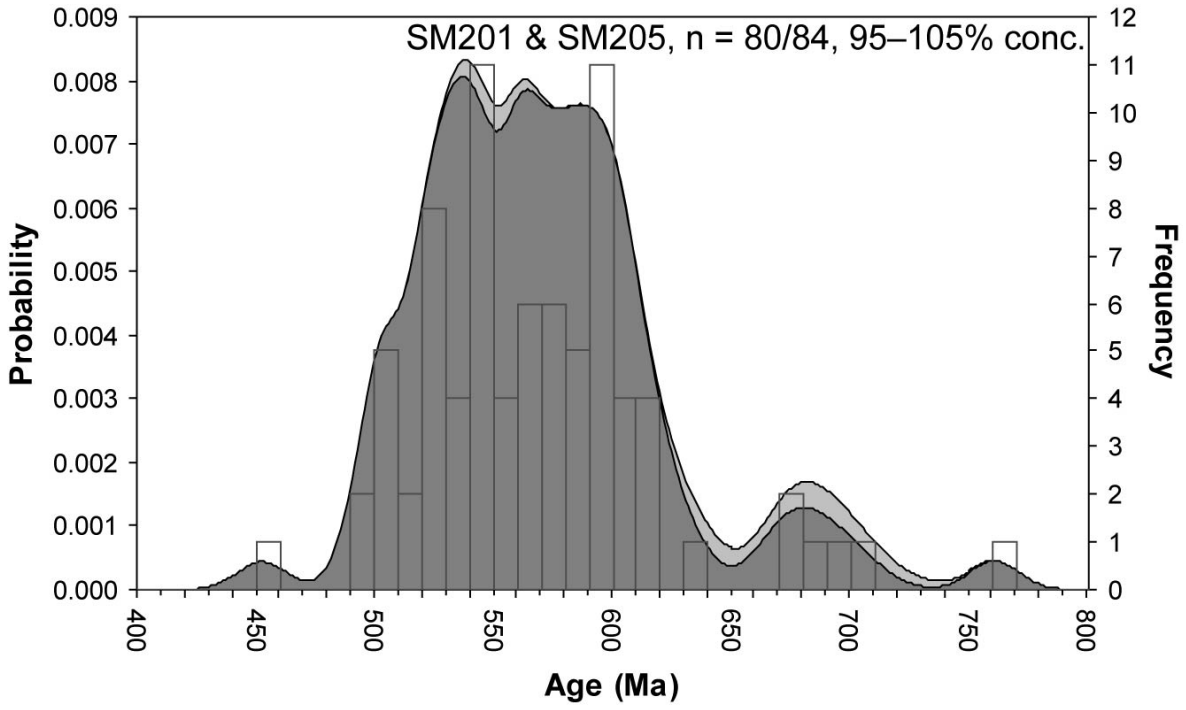

Fig. 9. Combined probability density distribution and histogram plots for the set of U–Pb analytical zircon data from samples SM201 and SM205 for the time range between 400 and 800 Ma. Dark grey shaded – zircon ages with 95–105% concordance, light grey shaded – zircon ages with >5 % discordance (see text for explanation). Abbreviation: n = number of analyses.

Inherited cores are present to a minor degree in sample SM201 and almost absent in sample SM205. The concordance-filtered zircon ages of 60 analyses on 59 single grains from sample SM201 show a polymodal age distribution with major peaks at ca. 530, 590 and 690 Ma, a subordinate cluster at ca. 950–1200, and a scatter of ages between ca. 1370 and 2820 Ma (Fig. 7). The youngest nearly concordant grain is 501 ± 18 Ma old and belongs to a group of four detrital zircons with a rounded shape and $^{206}Pb/^{238}U$ ages ranging between 501 ± 18 and 509 ± 17 Ma. The presence of Mesoproterozoic (~ 1000 Ma), Palaeoproterozoic (1800–2200 Ma) and Archaean (~2500 Ma) sources is also demonstrated by discordant grains that probably suffered radiogenic lead loss. The oldest grain has a $^{207}Pb/^{206}Pb$ age of 2821 ± 22 Ma.

The concordance-filtered zircon ages of 48 analyses on 42 single grains from sample SM205 show a similar pattern to that of sample SM201, with a polymodal age distribution between 500 and 700 Ma but a virtual absence of older ages, with only three peaks at ca. 760, 1350 and 1500 Ma (Fig. 8). Major peaks occur at ca. 500 Ma, 545 Ma and 565 Ma; a less prominent peak appears at ca. 675 Ma. The youngest nearly concordant grain is well rounded

and has a $^{206}Pb/^{238}U$ age of 453 ± 22 Ma. The youngest group of zircons includes three concordant grains with $^{206}Pb/^{238}U$ ages of 492 ± 17 Ma, 499 ± 15 Ma and 502 ± 13 Ma. The presence of Mesoproterozoic (~ 1000 Ma) and Palaeoproterozoic (~ 1750 Ma) sources may be documented by few discordant grains that probably suffered radiogenic lead loss. The oldest concordant grain has a $^{207}Pb/^{206}Pb$ age of 1519 ± 23 Ma.

The analyses of both samples from the Pirgadikia Unit are combined in Figure 9, with focus on the age spectrum between 400 and 800 Ma. Four distinct periods, at ca. 490–510, 520–550, 560–620 and 670–710 Ma, can be identified which may represent distinct periods of zircon growth in Neoproterozoic and Cambrian times.

5.2. Vertiskos Unit

The majority of the zircons analysed from garnetiferous micaschist SM157 have clear oscillatory zonation patterns in CL images and appear to be magmatic in origin (Fig. 10); only a few exhibit no zoning. Inherited cores are present to a minor degree.

The concordance-filtered zircon ages of 60 single-grain analyses show a predominance of zircons in the 550–1050 Ma range with major peaks at ca. 570, 620, 670 and 770 Ma, and a cluster at ca. 900–1050 Ma. The two youngest grains in sample SM157 are rounded and have $^{206}Pb/^{238}U$ ages of 459 ± 20 Ma and 493 ± 17 Ma, respectively. The first of the two grains, however, has a Th/U value <0.1 and its age cannot therefore be considered as magmatic; it rather suggests post-depositional metamorphic re-crystallisation. The gap that exists in ages between 1100 and 1760 Ma should also be noted. A second zircon population shows Palaeoproterozoic and Archaean ages with single peaks at ca. 1760, 1950, 2050, 2080, 2430 and 3130 Ma (Fig. 11). These peaks, however, are based on a very limited number of analyses only and stand out because of the relatively small errors in their $^{207}Pb/^{206}Pb$ ratios. The presence of Palaeoproterozoic (~ 2000 Ma) and Archaean (~ 2600 Ma) sources is also demonstrated by discordant grains (see also Fig. 11) that probably suffered radiogenic lead loss. The oldest concordant grain has a $^{207}Pb/^{206}Pb$ age of 3134 ± 13 Ma.

Zircons from garnet-biotite gneiss SM151 are very homogeneous. They display clear oscillatory zonation patterns in CL images and appear to be magmatic in origin. Inherited cores are almost absent. The concordance-filtered zircon ages of 58 single-grain analyses show a uniform age distribution between ca. 400 and 500 Ma, with major peaks at ca. 435

and 455 Ma and minor ones at ca. 405 and 480 Ma (Fig. 12). The presence of Palaeoproterozoic (ca. 1.8 Ga) and Late Archaean (ca. 2.7 Ga) sources may be documented by two highly discordant zircon grains that probably suffered radiogenic lead loss.

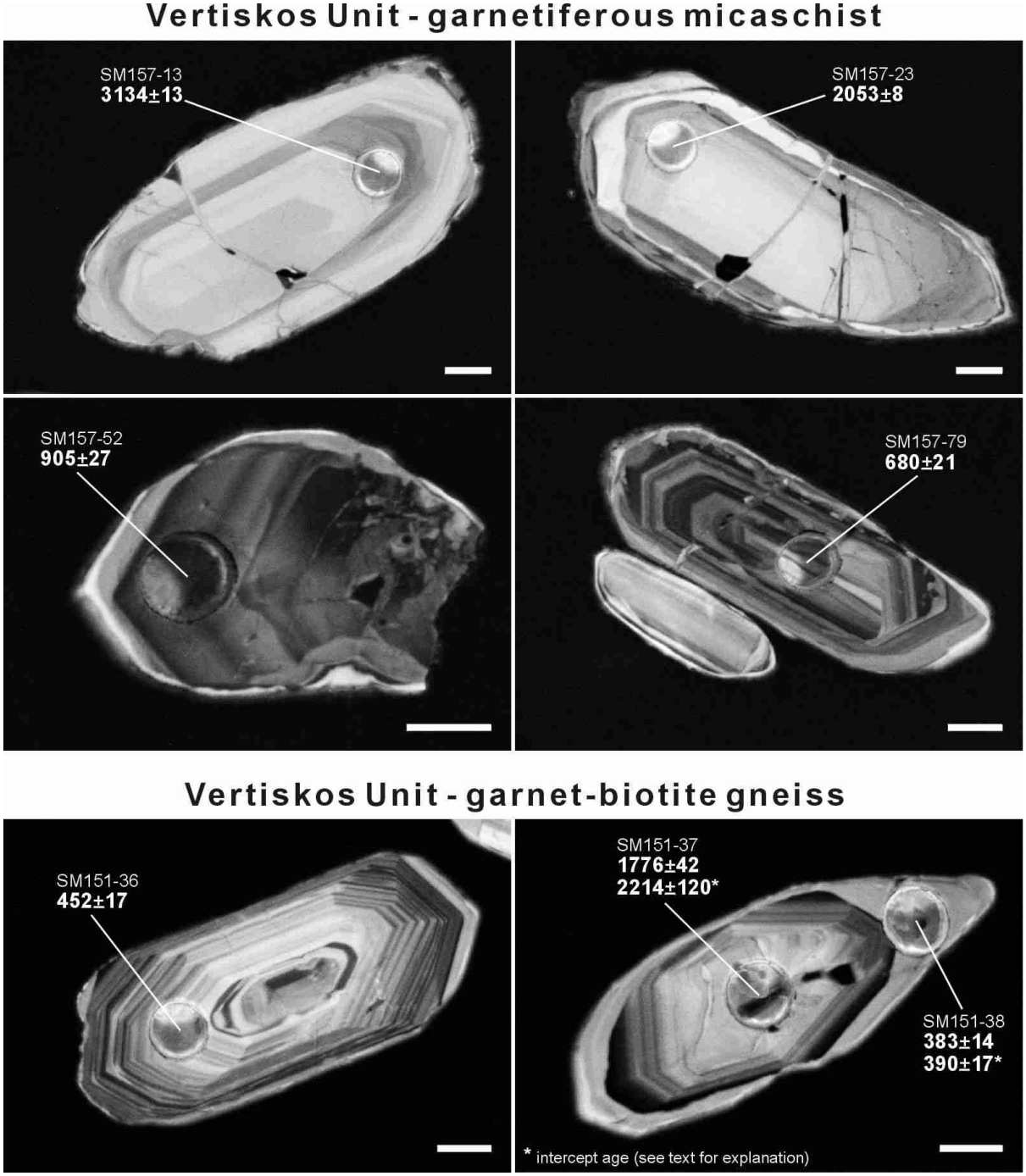

Fig. 10. CL images of representative zircon grains from analysed samples of the Vertiskos Unit with location of the LA-ICPMS analysis spot and corresponding $^{206}U/^{238}Pb$ age (±2σ) for grains <1.2 Ga and $^{207}Pb/^{206}Pb$ age (±2σ) for grains >1.2 Ga, respectively. Letter–number code above the ages: sample-spot. The scale bar represents 30 μm in all images.

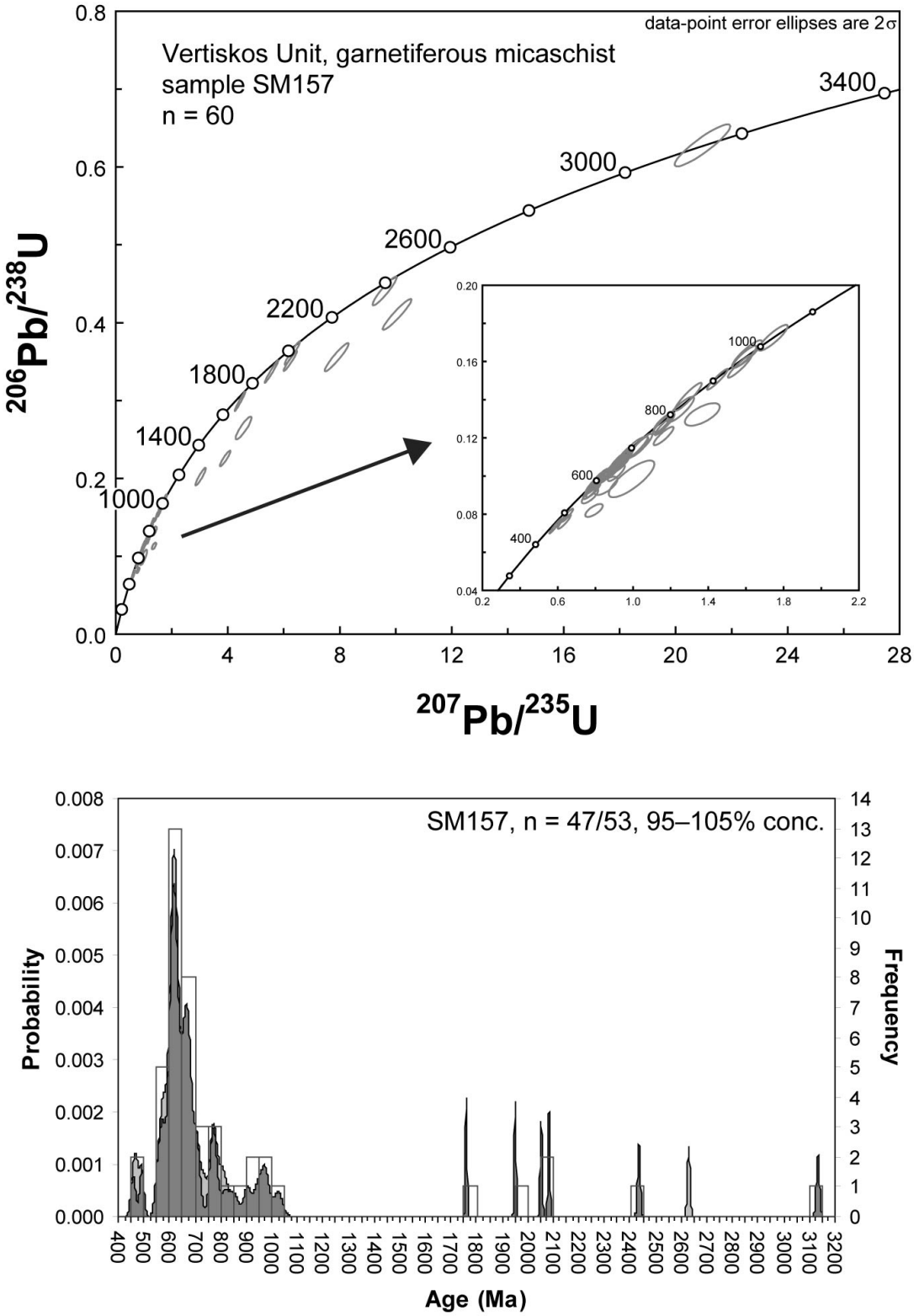

Fig. 11. Concordia diagrams (*upper*) and combined probability density distribution and histogram plots (*lower*) for the set of U–Pb analytical zircon data from sample SM157. Error ellipses in concordia plots represent 2σ uncertainties. 1.2 Ga limit is used to switch between $^{206}Pb/^{238}U$ and $^{207}Pb/^{206}Pb$ ages for the probability and histogram plots. Dark grey shaded – zircon ages with 95–105% concordance, light grey shaded – zircon ages with >5 % discordance (see text for explanation). Abbreviation: n = number of analyses.

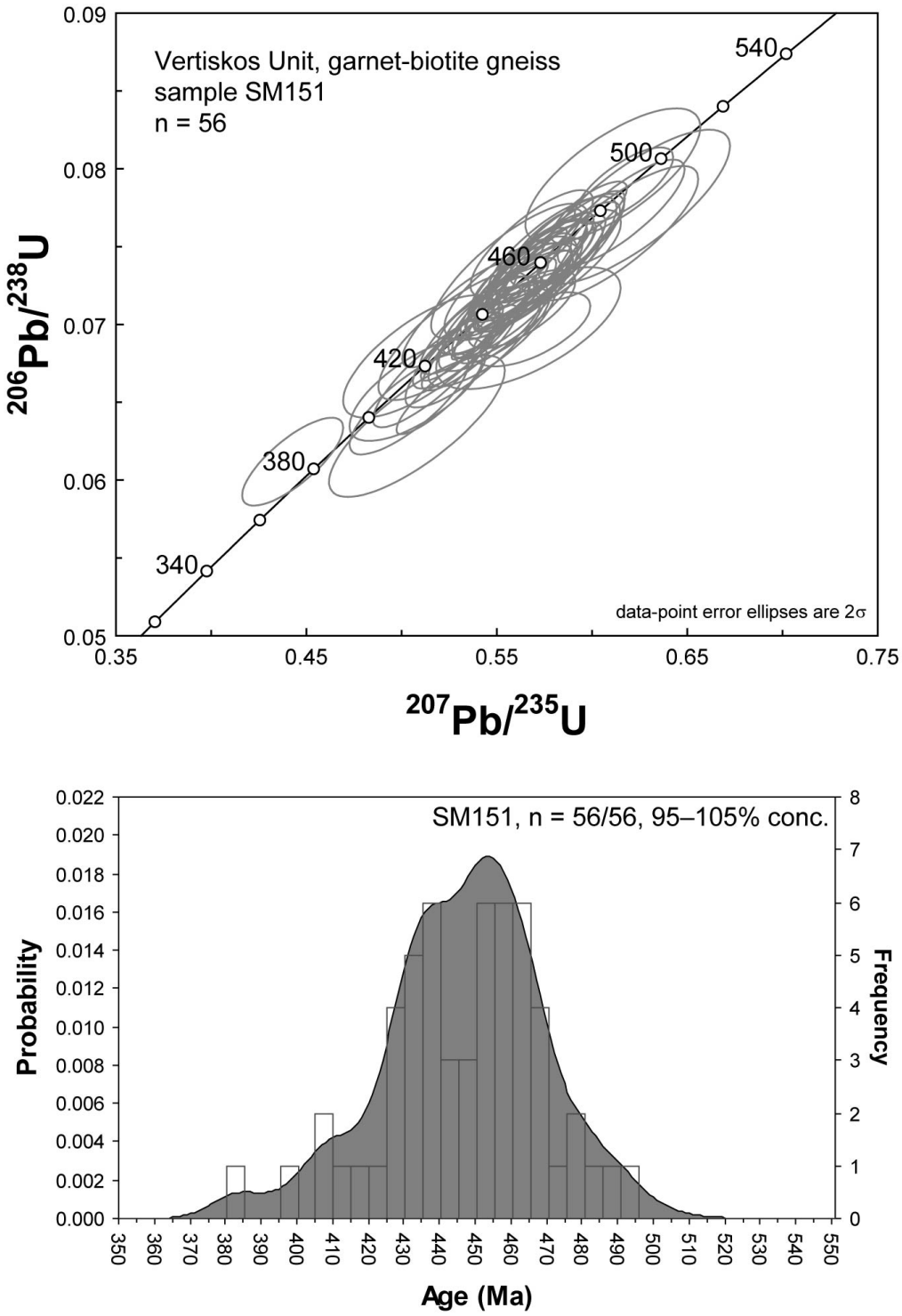

Fig. 12. Concordia diagram (*upper*) and combined probability density distribution and histogram plots (*lower*) for the set of U–Pb analytical zircon data from sample SM155. Two highly discordant grains with $^{207}Pb/^{206}Pb$ ages of 1776 ± 21 Ma and 2715 ± 8 Ma, respectively, are not shown (see text for discussion). Error ellipses in concordia plots represent 2σ uncertainties. 1.2 Ga limit is used to switch between $^{206}Pb/^{238}U$ and $^{207}Pb/^{206}Pb$ ages for the probability and histogram plots. Dark grey shaded – zircon ages with 95–105% concordance, light grey shaded – zircon ages with >5 % discordance (see text for explanation). Abbreviation: n = number of analyses.

One analysis of a zircon overgrowth yielded a slightly reverse discordant $^{206}Pb/^{238}U$ age of 383 ± 14 Ma which is the youngest age determined in this sample. In a concordia diagram, a regression of the core and the overgrowth yields a discordia with a lower intercept at 390 ± 17 Ma and an upper intercept at 2214 ± 120 Ma. In effect, lower-intercept ages do not necessarily have a geological meaning and should therefore be handled with care (Mezger & Krogstad 1997). However, the lower intercept of the zircon overgrowth at 390 ± 17 Ma is interpreted here as the time of secondary zircon crystallisation (magmatic or metamorphic). The upper intercept reflects the time of primary zircon crystallisation, and is interpreted as the age of formation of the magmatic protolith that survived as the inherited core. The $^{207}Pb/^{206}Pb$ age of around 1776 ± 21 Ma (Fig. 10) is the result of lead loss and was excluded from further discussion. Lead loss in zircons is a common phenomenon and mostly attributed to metamictisation and later recrystallisation during which Pb is removed from the zircon crystals (Williams 1992; Mezger & Krogstad 1997). The oldest concordant grain in sample SM151 has a $^{206}Pb/^{238}U$ age of 493 ± 22 Ma.

6. Discussion and conclusions

6.1. Pirgadikia Unit

Petrology and geochemistry indicate that the metasedimentary rocks of the Pirgadikia Unit are characterized by very mature sandstones, siltstones and minor conglomerates, mainly composed of weathering-resistant quartz clasts. Detrital zircon age spectra from samples SM201 and SM205 differ slightly but both show a prominent age cluster between 490 and 710 Ma that indicates denudation of Pan-African basement. The interval between 490 and 710 Ma comprises four distinct events, at ca. 490–510, 520–550, 560–620 and 670–710 Ma. Interestingly, a similar spectrum was obtained by Gerdes & Zeh (2006) for a high-grade metasediment from the Mid-German Crystalline Rise that was interpreted as indicating distinct periods of magma formation during the Neoproterozoic to Cambrian, at ca. 500–515, 545, 575–595 and 640–720 Ma. Following Gerdes & Zeh (2006), the 670–710 and 560–620 Ma-old zircons from the Pirgadikia Unit might have formed in an island-arc or continental-arc setting related to the formation of the Avalonian-Cadomian orogenic belt, whereas zircons at ca. 520–550 Ma were most probably formed during late-orogenic magmatism related to the

Cadomian orogeny. Zircons ca. 490–510 Ma old can be related to rifting processes and back-arc opening of the Rheic Ocean, separating Avalonian and later on Armorican terranes from the northern margin of Gondwana (e.g. von Raumer et al. 2002, 2003, and references therein). The maximum depositional age of the metasedimentary rocks from the Pirgadikia Unit can be constrained by the youngest detrital zircons: 501 ± 18 Ma for sample SM201 and 453 ± 22 Ma for sample SM205. The former age seems geologically meaningful since it belongs to a group of ages that cluster between ca. 501 and 509 Ma. The latter, however, is a single age determination and should therefore be interpreted with care. The youngest age group in sample SM205 comprises zircons between ca. 492 and 502 Ma. The roundness of the zircon grains suggests prolonged reworking, due to either long-distance transport by river systems or long-lasting abrasion in a coastal environment. Keeping in mind both the geological frame and time necessary for uplift and erosion of plutonic rocks and that necessary for weathering, transport and abrasion, we propose that the sedimentary rocks of the Pirgadikia Unit are younger than Cambrian, probably Early–Middle Ordovician, whereas an even younger age cannot be excluded insofar as no biostratigraphic or other geochronological data are available. The upper time limit for deposition, however, is set by the structural and upper greenschist-facies metamorphic overprint that took place in the latest Jurassic–Early Cretaceous. Nevertheless, an Ordovician age seems quite reasonable since, on a regional scale, the sedimentary rocks of the Pirgadikia Unit share many similarities with those of the widespread Ordovician Armorican Quartzite Formation (Grès Armorican Formation and its equivalents), a succession of continental or marine, very mature quartzitic sandstones sometimes associated with conglomerates and arkosic sandstones (e.g. Noblet & Lefort 1990). In many places of North Africa and Europe the Armorican Quartzite Formation conformably or unconformably overlies the Pan-African basement or Cambrian sedimentary rocks (e.g. Noblet & Lefort 1990). Its deposition was constrained by a lower-intercept age of ca. 465 Ma on zircons from an intercalated rhyolitic tuff (Bonjour et al. 1988) and provides a minimum age for the amalgamation of West Africa- and Amazonia-derived terranes by strike-slip motion along the northern margin of Gondwana that resulted in the Armorican Terrane Collage (Fernández-Suárez et al. 2002). The formation of very mature quartzose sediments of Cambro-Ordovician age along the entire northern margin of Gondwana (Noblet & Lefort 1990; Avigad et al. 2005) reflects intense chemical weathering processes, particularly in a warm and humid climate, accompanied by low relief and low sedimentation

rates, which led to the destruction of unstable fragments during erosion of the source rocks before final deposition.

Besides zircon grains that range in age between 490 and 710 Ma, Mesoproterozoic, Palaeoproterozoic and Late Archaean zircons are also present although in minor amounts. The older ones (≥1.6 Ga) probably represent recycled zircons than have been directly derived from Palaeoproterozoic or Late Archaean rocks. Zircons of such ages match the spread of orogenic events recorded in the West African and eastern Amazonian cratons (e.g. Nance & Murphy 1994, 1996). Palaeoproterozoic (ca. 1.8–2.1 Ga) basement is also known from Brittany and the Channel Islands in Western Europe (Calvez & Vidal 1978; Samson & D'Lemos 1998). The Mesoproterozoic concordant zircon grains are of palaeotectonic significance, especially those with ages around 1.5 Ga (Gothian–Rondonian–Rio Negro events) in combination with grains around 1.0 Ga old (Sveconorwegian–Grenvillian events). Similar ages were reported from NW Iberia (Fernández-Suárez et al. 2002), the NE Bohemian Massif (Hegner & Kröner 2000; Mingram et al. 2004), the Moravo-Silesian Unit (Friedl et al. 2000; 2004), West Avalonia (Nance & Murphy 1994, 1996), the Małopolska Unit (Belka et al. 2002) and the Polish East European Platform (Belka et al. 2002). Such ages, however, are not known from the Meguma Terrane (Nance & Murphy 1996), Saxothuringia (e.g. Linnemann et al. 2004), SW Iberia and Brittany (Fernández-Suárez et al. 2002), meaning that they are absent in rocks which have their source in the West African Craton. In north-western Greece, Anders et al. (2006a) obtained $^{206}Pb/^{207}Pb$ ages ranging between ca. 800 and 1340 Ma and a concordant $^{206}Pb/^{238}U$ SHRIMP-II age of 1500 ± 18 Ma from inherited zircons in Neoproterozoic orthogneisses (ca. 700 Ma) from the Florina Terrane. The Florina Terrane constitutes the basement of the NW Pelagonian Zone and has affinities with East Avalonia (Anders et al. 2006a). In general, inherited and detrital zircon ages of ca. 1 Ga and 1.5 Ga are well known from Avalonia supporting a position adjacent to the Amazonian Craton at the end of the Neoproterozoic whereas Armorican terranes lack such a component, suggesting closer affinities with the West African Craton (Nance & Murphy 1996; Winchester et al. 2006).

In the Eastern Mediterranean, the closest localities with quartz-rich sediments similar to those of the Pirgadikia Unit can be found in the Istanbul and Zonguldak Terranes of northern Turkey (see Yanev et al. 2006). In the latter terrane, for instance, pre-Cambrian basement rocks are unconformably overlain by Early Ordovician sediments consisting of

sandstones and conglomerates (Dean et al. 2000). Ordovician trilobite fauna from the Zonguldak Terrane indicate a close relation to Ordovician successions from central Europe (Bohemia) and the Anglo-Welsh Basin (Avalonia) (Dean et al. 2000). The Zonguldak Terrane may have been located along the eastern continuation of Avalonia and the Moravo-Silesian Terrane (Yanev et al. 2006). Ordovician and Silurian benthic fauna from the Istanbul Terrane are of Avalonian and Podolian affinity, whereas Devonian brachiopods and trilobites are clearly of Bohemian and North African affinity (Yanev et al. 2006). The Balkan and NW Anatolian Terranes were part of northern Gondwana but not of Baltica (Yanev et al. 2006, and references therein).

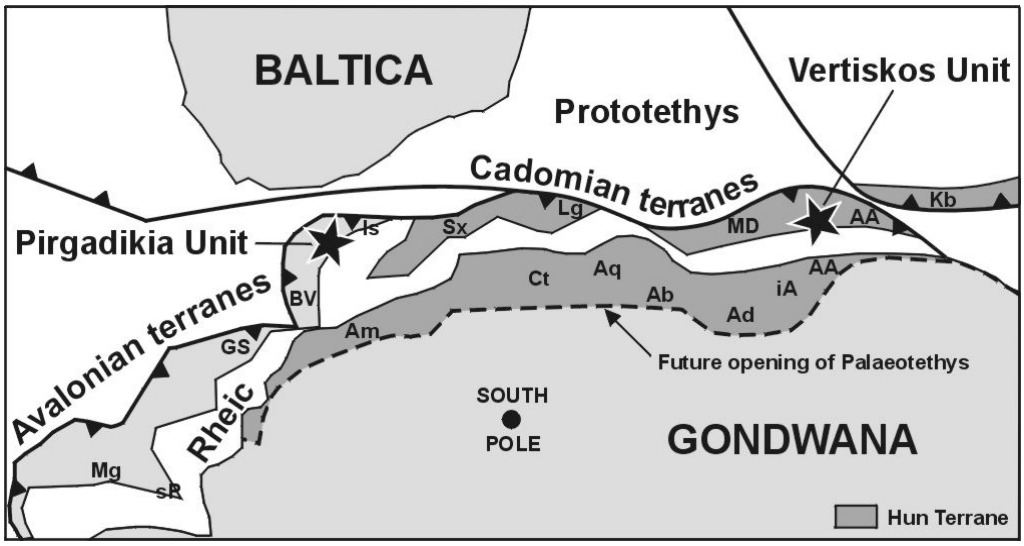

Fig. 13. Early Ordovician (~ 490 Ma) plate-tectonic reconstruction showing presumed location of the Pirgadikia and the Vertiskos Units (*black stars*) in the peri-Gondwana realm (modified from von Raumer et al. 2003). Abbreviations: AA, Austro-Alpine; Ab, Alboran plate; Ad, Adria sensu stricto; Am, Armorica; Aq, Aquitaine; Ct, Cantabria; iA, Intra-Alpine terrane; GS, Gory Sowie; Kb, Karaburun; Mg, Meguma; sP, South Portuguese; BV, Bruno-Vistulikum; Is, Istanbul terrane; Lg, Ligerian; MD, Moldanubia; Sx, Saxothuringia.

To conclude, the Pirgadikia Unit comprises island-arc basement (ca. 570–580 Ma: Himmerkus et al. 2006a, 2007) of the Avalonian-Cadomian orogenic belt and very mature quartzose sediments of probably Early–Middle Ordovician age (this study). Detrital zircon ages reflect derivation of these sediments from at least three distinct crustal sources, i.e. the Avalonian-Cadomian belt, the West African and/or Amazonian cratons and the Grenvillian belt, which may be taken as evidence for an Avalonian origin of the Pirgadikia Unit. The 490–510 Ma-old detrital zircons can be related to Late Cambrian igneous rocks probably

emplaced in a transtensional setting. Thus, in the Late Neoproterozoic–Early Palaeozoic, the Pirgadikia Unit can be best interpreted as a peri-Gondwana terrane, situated in the Avalonian realm north of the evolving Rheic Ocean but in proximity to Cadomian terranes (Fig. 13), very much like the "Avalonian satellites" of von Raumer et al. (2003). The history of the Pirgadikia Unit throughout the Palaeozoic and Mesozoic, however, is still enigmatic because of the lack of palaeogeographic constraints (e.g. palaeomagnetic data and fauna) for that time. Today, the rocks of the Pirgadikia Unit occur in isolated fault-bounded inliers within the Vardar zone bordering the Serbo-Macedonian Massif to the west.

6.2. Vertiskos Unit

The detrital zircon age spectrum from the garnetiferous micaschist shows a prominent age cluster between 550 and 800 Ma, indicating denudation of the Cadomian and Pan-African basement. The gap in zircon ages between 500 and 550 Ma suggests that there was no input of rocks from the source area related to late-orogenic tectonothermal events of the Cadomian orogeny. On the basis of the $^{206}Pb/^{238}U$ age of 493 ± 17 Ma, the maximum age of deposition is suggested to be Early Ordovician with an upper time limit for deposition given by the intrusion of the Late Ordovician–Silurian magmatic rocks into the metasedimentary succession. The ca. 900–1050 Ma-old zircons are assumed to be derived from the Grenvillian orogenic belt and might have been transported by large river systems to the northern margin of Gondwana (Zeh et al. 2001). The few Palaeoproterozoic (>1.7 Ga) and Archaean zircons probably represent recycled zircons, rather than zircons directly derived from Palaeoproterozoic and Archaean rocks. Zircons of such ages match the spread of orogenic events recorded in the West African and eastern Amazonian cratons (e.g. Nance & Murphy 1994, 1996). Taking all data collectively, the Pan-African (550–800 Ma), Grenvillian (900–1050 Ma), Icartian–Eburnean (1950–2100 Ma) and minor Archaean (>2.5 Ga) ages, together with the gap in ages between 1050 and 1760 Ma found in the garnetiferous micaschist studied clearly indicate a North Gondwana signature. At this point we suggest that the sedimentary protolith of the garnetiferous micaschist, and on a larger scale, most of the metasedimentary rocks of the Vertiskos Unit, were deposited in a Cadomian realm (future Hun superterrane), probably prior to the final break-off from the northern margin of Gondwana (Fig. 13). Their palaeotectonic position within the Cadomian realm can be further constrained by analysis of

the intrusive rocks. The zircon ages from the garnet-biotite gneiss cover a wide time span from ca. 405 to 490 Ma with major peaks around 435 and 455 Ma. They fit to Ordovician and Silurian ages of acidic meta-magmatites from the Vertiskos Unit (see Himmerkus et al. 2006a, 2007) and presumably those of equivalent rocks from SW Bulgaria (e.g. Titorenkova et al. 2003), and are interpreted here to be typical of the older part of the Serbo-Macedonian Massif. The extension of these basement rocks into western Turkey can also be anticipated since a $^{207}Pb/^{206}Pb$ single-zircon evaporation age of around 462 Ma was documented for orthogneisses from the Biga Peninsula in NW Turkey (Özmen & Reischmann 1999). Bright overgrowths of some zircons observed in CL images indicate reheating of the Vertiskos basement and new zircon growth during a late Early Devonian event (ca. 390 Ma). The age information, in conjunction with the geochemical signature of the orthogneisses (volcanic-arc granites showing within-plate affinities) suggest that Vertiskos Unit most probably originated in the eastern Hun superterrane, as did the Austro- and Intra-Alpine terranes (Fig. 13) where Ordovician and Silurian magmatic episodes are well documented and related to an active-margin setting (e.g. Neubauer 2002; von Raumer et al. 2002). The final break-off of these terranes from the northern margin of Gondwana was accompanied by the opening of the Palaeotethys Ocean to the south.

Inasmuch as Carboniferous magmatic and metamorphic events have not yet been reported from the Vertiskos Unit we suggest following possibility for the location of the Vertiskos Unit at the northern margin of Gondwana and its evolution through time. The model centres on the affiliation of Vertiskos to units of the eastern Hun superterrane, which in our opinion best fits the data. The Vertiskos Unit (along with Moldanubia and the Austro- and Intra-Alpine terranes) rifted away from the northern margin of Gondwana, leading to the opening of the Palaeotethys Ocean to the south. Later, it was “softly” accreted by transcurrent movements to the southern margin of Laurussia in the Devonian–Carboniferous, where it rifted in Early–Middle Triassic (intrusion of the within-plate Arnea suite) and was again involved in subduction-accretion processes during the Late Jurassic to Early Cretaceous, when a branch of the Vardar Ocean closed.

Chapter 5

Geochemistry, provenance and stratigraphic age of metasedimentary rocks in the eastern Vardar suture zone, northern Greece

Abstract

In this study, whole-rock geochemistry, detrital chrome spinel chemistry, and detrital zircon and biostratigraphic data provide constraints on the age, provenance and depositional setting of latest Palaeozoic and Mesozoic metasedimentary rocks in the eastern Vardar suture zone of northern Greece. This is important for understanding the palaeotectonic history of the Vardar Zone since the sediments here record a Neotethyan cycle of oceanic basin opening and closure. The oldest post-Carboniferous sedimentary unit in the study area is the Examili Formation, comprising mainly metaarkoses and metaquartzites. This clastic sedimentary succession was deposited in an intra-continental rift-related sedimentary basin in proximity to the Vertiskos Unit in the Permo–Triassic. The Melissochori Formation (formerly Svoula flysch) comprises predominantly metasandstones with significant carbonate content. Their major- and trace-element concentrations reveal the relative homogeneity of their source. The Melissochori Formation was deposited in front of a Permo-Carboniferous basement unit of volcanic-arc origin with minor input of older basement rocks, probably at the slope of a carbonate platform in the Early–Middle Jurassic. In contrast, the sedimentary rocks of the Prinochori Formation are characterised by chrome spinel as major accessory phase. Petrography and whole-rock geochemistry point to a source area dominated by intermediate and pronounced basic and ultrabasic composition, supposedly granodiorites or equivalents and ophiolitic rocks. The observed spread in Cr-number (Cr/(Cr+Al)) values between 0.40 and 0.90 and Mg-number (Mg/(Mg+Fe^{2+})) values between 0.25 and 0.70 suggest a mixed (ultra)basic source of highly depleted peridotites of mainly harzburgite and minor lherzolite

composition. Most of the detrital chrome spinels were derived from MOR-type peridotites and supra-subduction zone (SSZ) peridotites, whereas only a small fraction comes from volcanic rocks, supposedly island-arc basalts and MORB-type rocks. The Prinochori Formation was probably deposited in front of a nappe complex in the Early Cretaceous, comprising ophiolitic rocks and basement slivers of the Vertiskos Unit or equivalent rocks. Furthermore, a microfauna assemblage of *Ovalveolina* sp., *Pseudonummuloculina* sp. and dasycladacea algae of genus *Thaumatoporella* sp. was found in a calcareous clastic succession cropping out in the Oreokastro area, which was so far thought to be of Late Triassic–Middle Jurassic age. These data clearly indicate an Albian–Cenomanian age of deposition for this sedimentary succession. Taken collectively, the eastern Vardar Zone is a complex imbricated belt (suture zone) comprising various types of metasedimentary and meta-igneous rocks which were tectonically juxtaposed. The rocks record earliest Mesozoic intracontinental rifting, related to the opening of Neotethyan oceans in Greece, Jurassic intraoceanic subduction, volcanic-arc magmatism and ophiolite obduction, and finally the closure of Neotethyan oceanic basins. Polyphase tectonics and metamorphism obstruct palinspastic reconstructions.

1. Introduction

The Vardar Zone (Kossmat 1924) is a prominent suture within the Alpine-Mediterranean orogenic belt extending from the Hellenides in northern Greece to the Dinarides in former Yugoslavia. This zone is characteristed by numerous ophiolitic bodies, which were originating from the Vardar Ocean *sensu lato*. The palaeotectonic evolution of the Vardar Ocean is controversially discussed as it is evident in numerous alternative palinspastic models (e.g. Ricou et al. 1998; Stampfli & Borel 2002; Brown & Robertson 2003, 2004, and references therein). In northern Greece, the Vardar Zone forms a 60–80 km wide NNW–SSE-trending zone between the Serbo-Macedonian Massif to the east and the Pelagonian Zone to the west (Fig. 1). Here, the Vardar Zone has traditionally been subdivided into three elongated stripes (from west to east): the Almopias subzone, the Paikon subzone and the Peonias subzone (Mercier 1968). The latter has the most complex organization and is the focus of this study. The Peonias subzone is a complex imbricated belt, involving various types of metamorphic rocks (in some parts also blueschists), Mesozoic sedimentary and

plutonic and volcanic rocks, and ophiolites. The rocks were juxtaposed to each other by ophiolite obduction and nappe stacking during the Late Jurassic to Cretaceous, with later overprinting by dextral strike slip and block rotation during the Cenozoic (e.g. Kiriakidis & Brooks 1989; Ricou & Godfriaux 1994; Michard et al. 1998; Ricou et al. 1998; Brun & Sokoutis 2007). Kauffmann et al. (1976) introduced the term Circum-Rhodope Belt to describe the Triassic and Jurassic metasedimentary rocks bordering the Serbo-Macedonian Massif to the west and thought they built the original Mesozoic sedimentary cover of the crystalline basement of the Serbo-Macedonian Massif. Similar rock assemblages cropping out on Samothraki Island and in Thrace were interpreted as an extension of the Circum-Rhodope Belt to the east (e.g. Kockel et al. 1971; Kauffmann et al. 1976). That concept, however, was rejected by Ricou et al. (1998) who suggested the existence of two distinct greenschist-facies belts. This is critical to palaeotectonic interpretations of the Neotethys, especially to the geodynamic evolution of the Vardar Ocean *sensu lato*.

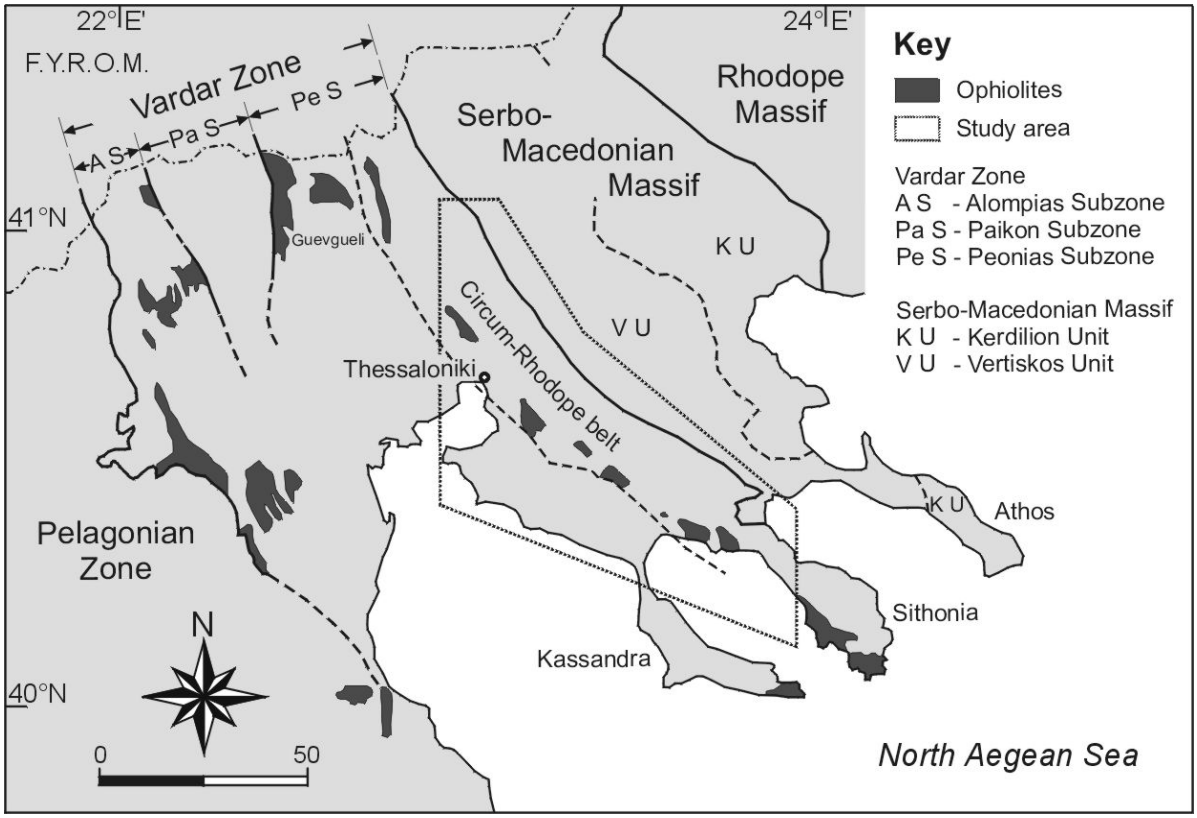

Fig. 1. Map showing the location of the study area in the Vardar Zone of northern Greece, including the neighbouring main geotectonic zones (modified after Kockel et al. 1977). The Kerdilion and Vertiskos Units are after Himmerkus et al. (2006a). F.Y.R.O.M., Former Yugoslav Republic of Macedonia.

The ophiolite complexes of the eastern Vardar Zone have been subject of intensive research over the last decades including structural, geochemical and geophysical studies, whereas the sedimentary rocks received only minor attention, one exception being the fossiliferous limestones (e.g. Kauffmann et al. 1976; Carras & Geogala 1988). Identifying ancient source areas and depositional settings is of fundamental importance for palaeogeographic reconstructions in the Tethyan realm. This study therefore focuses on the provenance of presumably latest Palaeozoic and Mesozoic metasedimentary rocks in the western Circum-Rhodope Belt and adjacent units, including sedimentary rocks from the Examili, Melissochori (formerly Svoula flysch) and Prinochori Formations, and from the Neochorouda Unit (formerly Oreokastro Limestone breccia). We present for the first time data of major- and trace-element whole-rock geochemistry, detrital chrome spinel chemistry, and detrital zircon ages in order to evaluate source-rock lithologies and ancient depositional settings. Furthermore, we present new biostratigraphic results from the Oreokastro area that let to a revision of previous stratigraphic concepts. Our new data contribute significantly to palaeotectonic reconstructions of the Tethyan realm in the eastern Mediterranean in latest Palaeozoic and Mesozoic times.

2. Geological setting

Geologists of the Federal Institute for Geosciences and Natural Resources (BGR), Germany, and the Institute of Geology and Mineral Exploration (IGME), Greece, have mapped the Chalkidiki peninsula and the adjacent area to the north in detail over several years. This finally resulted in a detailed map of scale 1 : 100 000 (Kockel & Mollat 1977) and an accompanying memoir (Kockel et al. 1977). In the following paragraphs, we give a brief geological overview about the major units of the areas mentioned above with special emphasis on the clastic sedimentary rocks of the Circum-Rhodope Belt and the Upper Jurassic–Lower Cretaceous successions of the Petralona and Oreokastro areas. According to previous studies (e.g. Kauffmann et al. 1976; Kockel et al. 1977), the Circum-Rhodope Belt includes the Examili Formation, the Pirghoto Formation, the Svoula Limestones and Marbles, the Melissochori Formation (formerly Svoula flysch), the Aspro Vrisi Serie and the Chortiatis Unit (e.g. Figs. 2 and 3). We have to note that we almost neglect the prefix “meta” for the rocks described, although they experienced at least one metamorphic overprint.

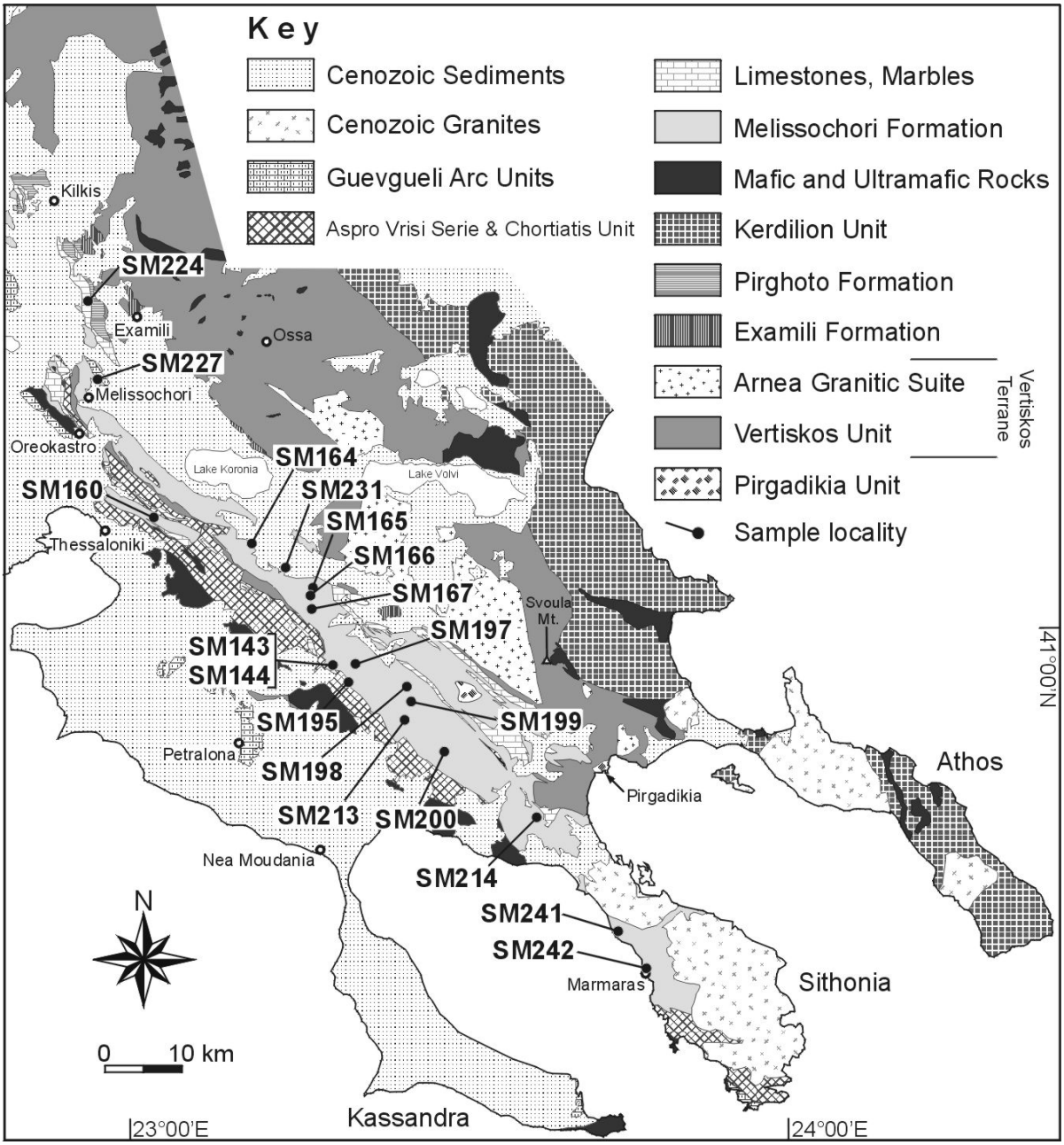

Fig. 2. Geological map of the Chalkidiki peninsula and surrounding region (modified after Kockel & Mollat 1977). The Pirghoto Formation includes the Volcano-sedimentary Series and the Melissochori Formation the Svoula flysch of Kockel et al. (1977), respectively. The Guevgueli Arc Unit includes the Monopigadon granitoid, the Petralona limestone and the Prinochori Formation as well as the Neochorouda Unit (see text for explanation). The sampling locations for samples of the Melissochori Formation as well as one sample from the Svoula Limestone (sample SM224, see paragraphs for biostratigraphy) are indicated. All other sampling locations are shown in Figures 4, 8 and 10.

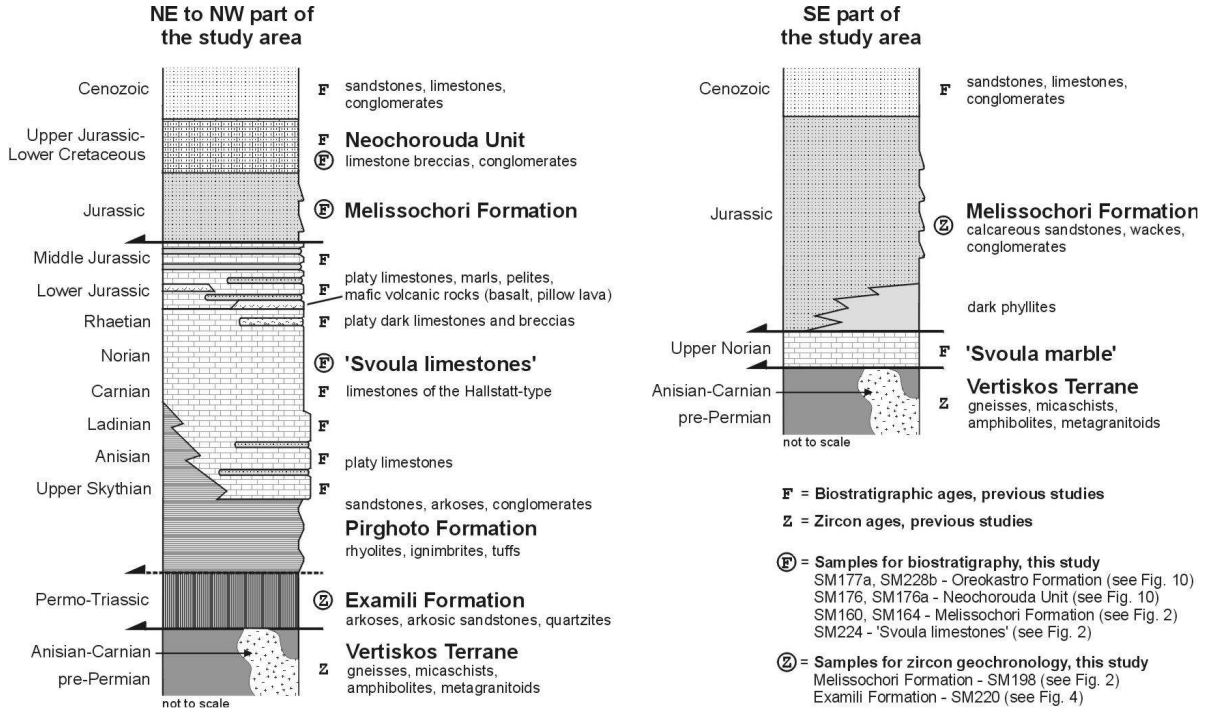

Fig. 3. Interpretive tectonostratigraphic columns for the Circum-Rhodope Belt of the eastern Vardar suture zone (see text for references). Stratigraphic positions of samples used for biostratigraphy and zircon geochronology are indicated. Note: The stratigraphic column for the Prinochori Formation is shown in Figure 9.

2.1. Examili Formation

The Examili Formation is generally seen as the stratigraphically lowermost unit of the Circum Rhodope Belt, cropping out in dispatched small areas along the western border of the Serbo-Macedonian Massif, forming its first sedimentary cover (e.g. Kauffmann et al. 1976; Kockel et al. 1977; Dixon & Dimitriadis 1984). The Examili Formation is mainly composed of K-feldspar-bearing arkoses and quartzites (Fig. 5) with minor conglomerate horizons, varying in colour from white-grey to greenish. Although these rocks are unfossiliferous, they are generally thought of being Permian to Early Triassic age because of the time constraints imposed by the overlying Pirghoto Formation (see below). Dimitriadis & Asvesta (1993) described cross bedding, planar cross stratification and coarse debris flow channel fillings with a NE to SW direction of transport (present-day orientation), meaning sediment supply from the Serbo-Macedonian Massif. They interpreted the Examili Formation as a fan-delta deposit during the initital stage of continental rifting west of the Serbo-Macedonian Massif. In direct contact to the latter, the rocks of Examili Formation show a strong mylonitic fabric.

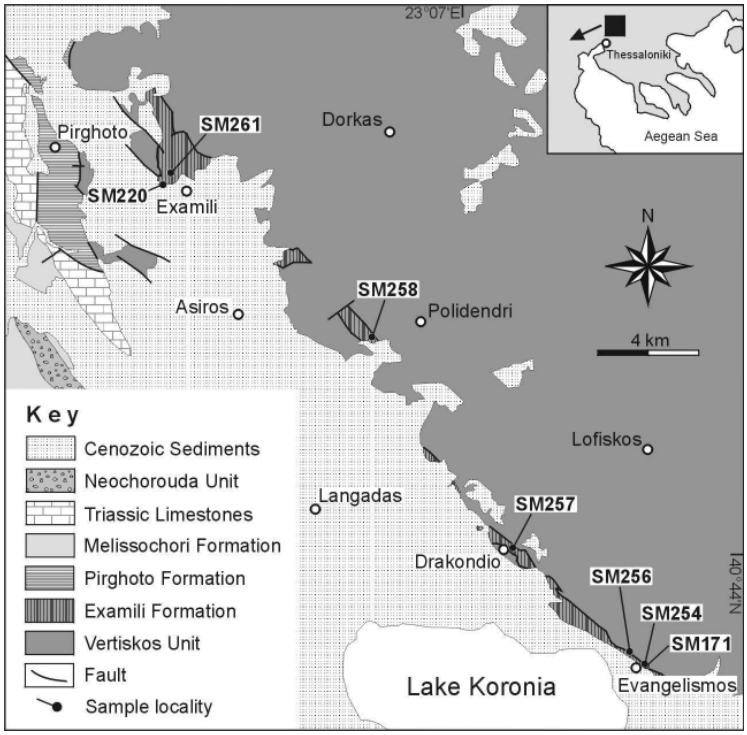

Fig. 4. Geological map showing the occurrences of the Examili Formation after Kockel & Mollat (1977) and the sampling locations for samples of the Examili Formation.

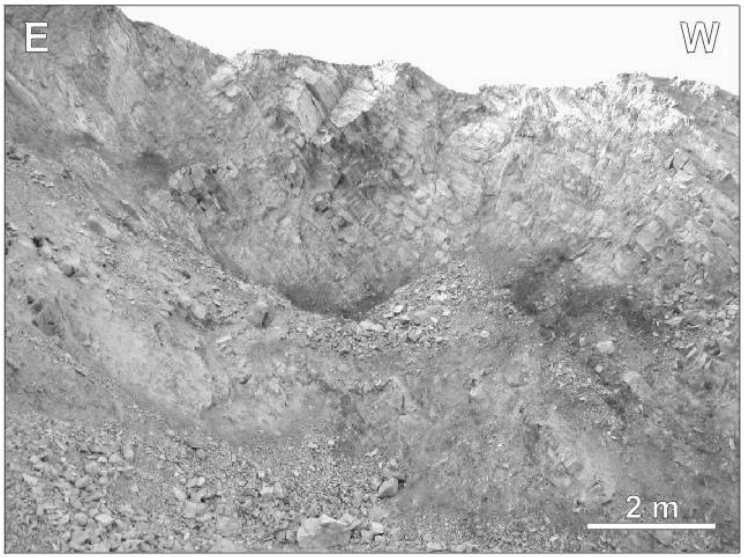

Fig. 5. Photograph showing arkosic metaquartzite of the Examili Formation cropping out in a quarry NW Examili (40°52´26.7´´N, 22°59´44.7´´E). Sampling location of sample SM220 used for zircon geochronology.

In general, all contacts to the underlying basement as well as to the overlying Pirghoto Formation are tectonically. One exception might be an outcrop west of Kato Potamia village where Kockel et al. (1977) suggested that the contact between the Examili Formation and the Pirghoto Formation is only slightly tectonically overprinted. Metapelitic rocks of the Examili Formation yielded chloritoid in association with quartz, low-Si phengite (Si = 3.15 p.f.u.) and chlorite that is not critical for high pressure–low temperature metamorphism (Michard et al. 1994a, b). According to the latter and Kockel et al. (1977), the sedimentary succession of the Examili Formation experienced only a greenschist-facies metamorphic overprint.

2.2. Pirghoto Formation

The Examili Formation underlies the so-called "Volcanosedimentary Serie" of supposed Early Triassic age (Mercier 1968; Kockel et al. 1977). Here, we follow Ferrière & Stais (1995) and use the term Pirghoto Formation what they consider to be of Permian to earliest Triassic age. Massive rhyolites, lavas and pyroclastites mainly build up its lower part. Some of the latter may represent ignimbrites (Kockel et al. 1977; Dimitriadis & Asvesta 1993). The volcanic rocks, petrographically and geochemically studied by Kelepertsis et al. (1985) and Kougoulis et al. (1990), show a porphyritic texture with phenocrysts of plagioclase feldspar, K-feldspar, zircon, magnetite and apatite in a groundmass of fine quartz and potassic feldspar (orthoclase). They have high K_2O contents (ultrapotassic rocks) and belong to alkali feldspar-rhyolites to quartz-alkalifeldspar trachytes. The occurrences of accretionary lapilli suggest phreatomagmatic eruptions (Dimitriadis & Asvesta 1993). The volcanic rocks of the Pirghoto Formation have probably an Early–Middle Triassic age, based on the occurrences of micro- and macrofauna in the overlying and interbedded limestones (e.g. Dimitriadis & Asvesta 1993; Ferrière & Stais 1995) and on U–Pb of rhyolitic zircon (ca. 240 Ma; R. Frei cited by Kostopoulos et al. 2001). This is in contradiction to Kelepertsis et al. (1985) who supposed a Cenozoic age, based on geochemical similarities with Paleogene and Early Neogene volcanic rocks from the Chalkidiki and the Aegean Sea that is, however, according to the facts mentioned before, not maintainable. Phyllitic sandstones of reddish, whitish or greyish colour with intercalated conglomerates, arkoses and violet reddish schists mainly build up the upper part of the Pirghoto Formation. Limestones and rhyolitic megaclasts can be interbedded (Dimitriadis & Asvesta 1993). For a long time, the rocks of the Pirghoto Formation have been accepted of being only overprinted by greenschist-facies metamorphism (e.g. Kockel et al. 1977). Michard et al. (1994a, b) however found high-Si phengite (Si ~ 3.5 p.f.u.) in metapelitic and metavolcanic rocks of the Nea Santa area that shows evidence for high pressure–low temperature metamorphism.

The Pirghoto Formation is overlain by the fossiliferous Svoula Limestones (e.g. Kockel et al. 1977); basic and intermediate rocks are intercalated with Middle and Upper Triassic pelagic sediments (e.g. Mercier 1968; Dimitriadis & Asvesta 1993). Some of the basic rocks show pillow structures; evidence of contact metamorphism has also been found (Dimitriadis & Asvesta 1993). Zoisite and garnet formed during the contact metamorphism

are evidence for intrusion in formerly hydrated sediment (Dimitriadis & Asvesta 1993). Geochemically, the metabasalts (olivine tholeiites) show mid-ocean ridge basalt (MORB) to within-plate basalt (WPB) signatures (Dimitriadis & Asvesta 1993) and were interpreted as volcanic rocks of a Triassic rift-related tholeiitic suite.

2.3. Melissochori Formation

The term Melissochori Formation is used here as synonym for almost the entire upper member of the Svoula Formation of Kauffmann et al. (1976) and the Svoula flysch of Kockel et al. (1977), respectively. It was previously proposed that this succession is of Permo–Triassic age (see Mercier 1968; Kockel et al. 1971) but a Mesozoic age is nowadays generally accepted since the discovery of Triassic fauna in limestone olistoliths and breccias (e.g. Kauffmann et al. 1976; Kockel et al. 1977). The Melissochori Formation is Early–Middle Jurassic (e.g. Kockel et al. 1977) or Late Triassic–early Late Jurassic in age (e.g. Dimitriadis & Asvesta 1993), although biostratigraphic constraints are very scarce and geochronological data are still lacking. The unconformably overlying Neochorouda Unit gives the maximum age of deposition as being latest Jurassic (e.g. Kockel et al. 1977).

The Melissochori Formation forms a prominent part of the Chalkidiki peninsula. Major outcrops occur between Melissochori village in the NW and Marmaras town on the Sithonia peninsula in the SE (Fig. 2). The marble, phyllite and mica schist horizons in the southwesternmost part of the Serbo-Macedonian Massif, which were interpreted by Kockel et al. (1977) as a cover sequence of the massif belonging to the Svoula flysch, are not included here in the Melissochori Formation. They are assigned to a mélange zone, forming the border between the Vertiskos Terrane and the Kerdilion Terrane (see Himmerkus et al. 2006a, 2007). In general, the Melissochori Formation is a turbiditic succession. Its lower part consists either of dark phyllites (metapelites), which pass upwards into calcareous siltstones and sandstones or it starts with a basal clastic succession of conglomeratic sandstones and limestone olistoliths and breccias containing Middle–Upper Triassic fauna (Kockel et al. 1977). The former facies is widespread in the southeastern part of the study area, whereas the latter one has only been described by Kockel et al. (1977) from the northwestern part of the study area around the villages of Petroto, Melissochori and Filiro.

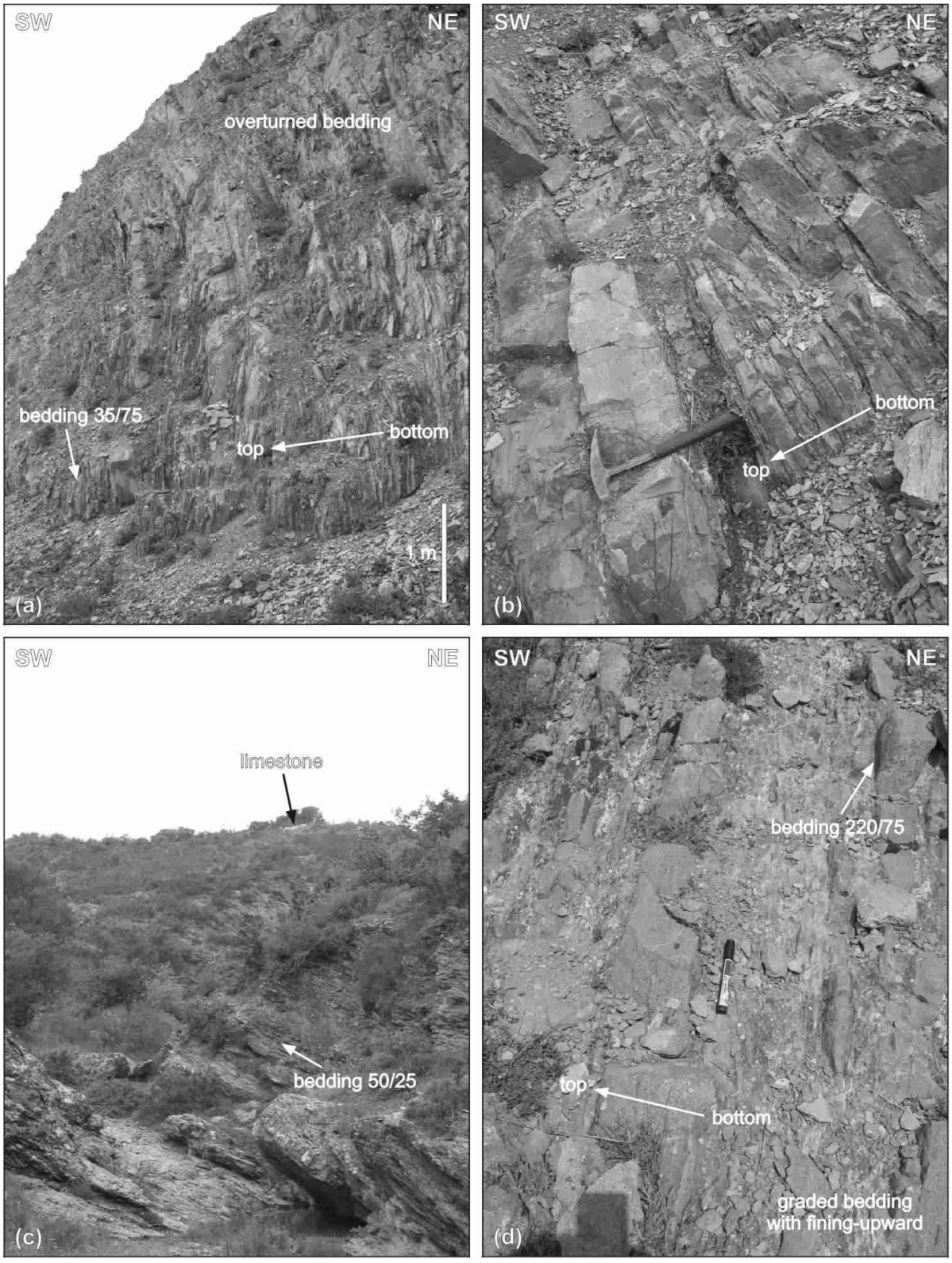

Fig. 6. Photographs illustrating outcrop situation. **(a–b)** Melissochori Formation west of Paleokastro north of Poligiros (40°26´27.6´´N, 23°25´31.5´´E), locality of sample SM198 used for zircon geochronology. **(c)** Prinochori Formation cropping out in a canyon north of Prinochori village (40°24´00.3´´N, 23°11´35.3´´E), locality of sample SM181 used for zircon geochronology. **(d)** Neochorouda Unit east of Neochorouda village (40°44´53.3´´N, 22°52´39.0´´E), sampling location of sample SM176b (see Fig. 10).

The major part of the Melissochori Formation is mainly built up by platy to massive calcareous sandstones and wackes and minor of quartzites varying in colour between light grey to dark greyish and brownish (Fig. 6a, b). The sandstone banks can reach up to 1.2 m in thickness. Dimitriadis & Asvesta (1993) interpreted the Melissochori Formation as a slope and rise sequence developed at a passive margin after Late Triassic continental rifting. Mussalam (1991) discussed deposition in a fore-arc setting due to westward subduction beneath the Chortiatis Volcanic Arc in Middle–Late Jurassic times. The bedding, especially in the fine-grained succession, shows strong folding. Tight to isoclinal, sometimes recumbent folds are a general feature. One characteristic of the Melissochori Formation is the occurrences of pyrite cubes varying in size from few millimetres up to 1 cm across. It is worth mentioning that in some outcrops, in vicinity to the Chortiatis Unit, pyrites with quartz pressure shadows were observed, indicating a top-to-the-SE tectonic transport (Fig. 7a). In general, Kockel et al. (1971) interpreted the western border of the Melissochori Formation as a SW-directed thrust onto the Chortiatis Unit. The latter is also involved in this southwestward thrusting, where in parts slivers of basement gneisses are tectonically intercalated. Close to the tectonic contacts, quartz mobilisation becomes a characteristic feature in the rock successions.

2.4. Aspro Vrisi Serie and Chortiatis Unit

2.4.1. Aspro Vrisi Serie

The Aspro Vrisi Serie of Kockel et al. (1977) crops out in an elongated stripe between Oreokastro in the NW and the Sithonia peninsula in the SE (Fig. 2). It predominantly comprises greenish–grey to dark grey sandy phyllites and sandstones with numerous black chert horizons (Fig. 7b) as well as dolerite and altered basalt (diabase). The phyllites and sandstones are underlain and partly intercalated in their lower part by Triassic (Rhaetian) limestones (Kockel et al. 1977). The sedimentary succession was intruded by the intermediate to basic rocks. From the northwestern part of the study area, Kauffmann et al. (1976) and Kockel et al. (1977) described turbiditic sandstones and quartzites of the Melissochori Formation intercalating with the chert-bearing sedimentary succession of the Aspro Vrisi Serie.

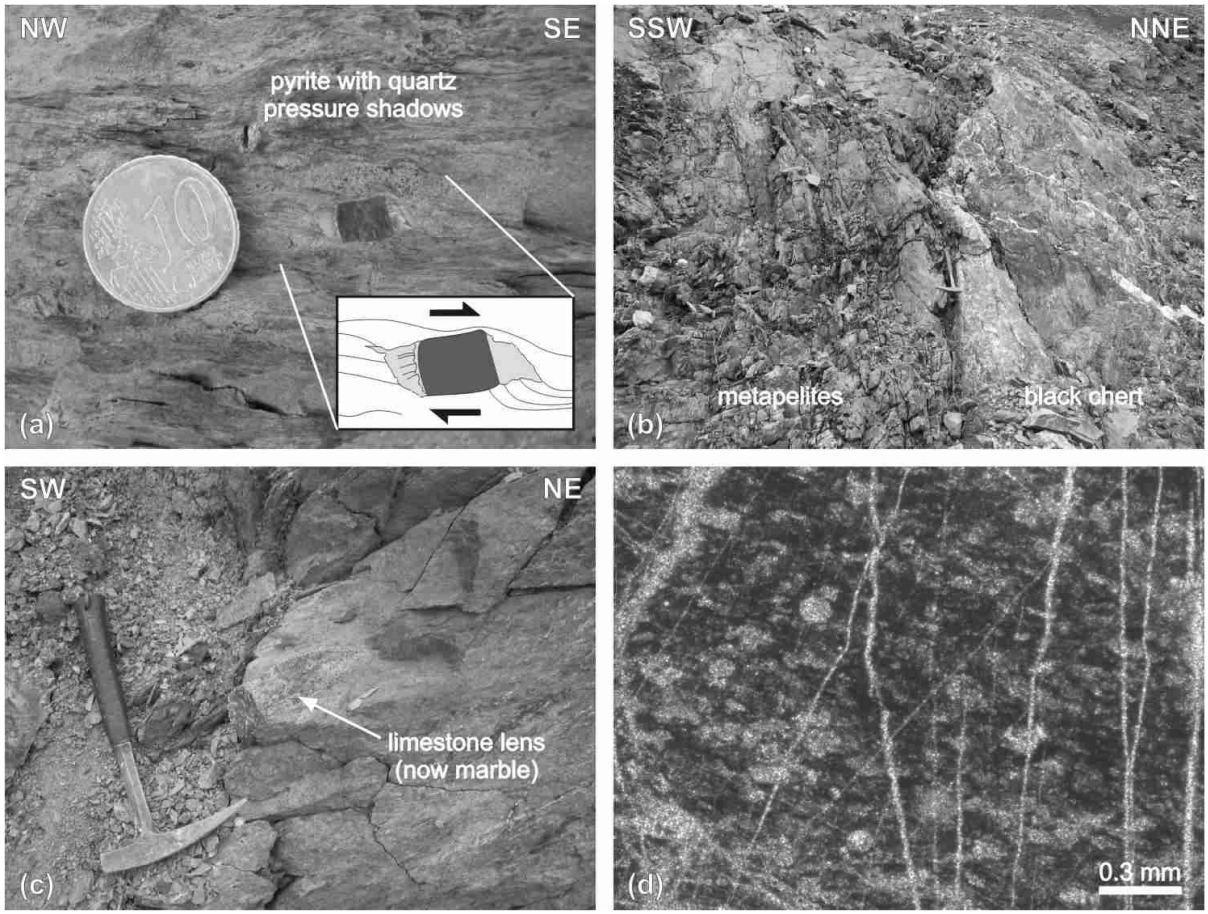

Fig. 7. (**a)** Pyrite with quartz pressure shadows in pelitic rocks of the Melissochori Formation near Petrokerase village (40°31´44.0´´N, 23°16´38.5´´E); (**b)** Metapelites (phyllites) and black chert from the Aspro-Vrisi Serie along the main road south of Galatista village (40°27´22.3´´N, 23°19´06.0´´E); **(c)** Limestone lens (now marble) within metasedimentary rocks of the Chortiatis Unit along the main road south of Vavdos village (40°24´41.7´´N, 23°19´42.2´´E); **(d)** Black chert of the Aspro-Vrisi Serie with radiolaria-like structures southwest of Monolofo village (40°47´50.6´´N, 22°54´29.4´´E).

Although no biostratigraphic data from the latter have been reported so far, Kockel et al. (1977) suggested a Jurassic age based on the underlying Upper Triassic limestones and the intercalations of sedimentary rocks of Melissochori Formation observed. Because of this Kockel et al. (1977) interpreted the Aspro Vrisi Serie as facies equivalent to the Melissochori Formation (see Dimitriadis & Asvesta 1993 for further discussion). However, Ferrière & Stais (1995) suggested that the Aspro Vrisi Serie is Permo-Carboniferous in age, based on lithostratigraphic correlations with other chert-bearing succession of the Hellenides. Here, we would like to note that one sample of black chert, collected during the course of this study south of Monolofo village, shows quartz-filled roundish structures in thin section that resemble in their morphology recrystallized radiolaria (Fig. 7d). The bad preservation of the

sample, however, limits further investigation. The Aspro Vrisi Serie was overprinted under up to upper greenschist-facies metamorphic conditions, whereas the grade of metamorphism increases towards the southeast (Kockel et al. 1977).

2.4.2. Chortiatis Unit

The Chortiatis Unit of Kockel et al. (1977) crops out parallel to the Aspro Vrisi Serie in an elongated stripe between Oreokastro village in the NW and the Sithonia peninsula in the SE (Fig. 2). The Chortiatis Unit is often also descripted as the Chortiatis Magmatic Suite, which includes metaquartzdiorites, metagranitoids, metagabbros and diorites (e.g. Kockel et al. 1977). Tonalitic to trondhjemitic rock types have also been reported (Mussallam & Jung 1986). Amphibolites, greenschists, garnet-mica schists, phyllites, metacherts, and layers and lenses of marble are minor present. The marbles were partly affected by contact metamorphism because of the intrusive diorites (Ricou & Godfriaux 1994). Marble lenses several cm in size floating in a metasedimentary succession have been found ca. 1 km south of Vavdos village along the main road to Simandra village (Fig. 7c). At the same locality oblique slickenside striations were observed on a small, steeply-deeping NNW-striking shear fault plane that indicate dextral strike slip and may be related to Early Cenozoic transcurrent movements described by Ricou et al. (1998). Kockel et al. (1977) interpreted the rock assemblage of garnet-mica schist, phyllite and metachert as facies equivalent to the Aspro Vrisi Serie, whereas the marbles represent the Triassic limestones. Based on fieldwork and lithostratigraphic correlations, the age of the various rock types of the Chortiatis Unit was narrowed by Kockel et al. (1977) between Late Liassic and Kimmeridgian–Tithonian. Zircons from a diorite of the Chortiatis Magmatic Suite collected in the Livadi area yielded a concordia age of ca. 159 ± 4 Ma (U–Pb on zircon, SHRIMP-II: Zachariadis 2007), which confirms a Jurassic age for these rocks and probably also for the adjacent chert-horizons and metapelites. Studies by Kockel et al. (1977) indicate a mid-upper greenschist-facies metamorphic overprint for rocks of the Chortiatis Unit. Michard et al. (1994a, b) found at one locality near Livadi also blueschist-facies rocks. Ricou & Godfriaux (1994) favoured an amphibolite-facies regional metamorphism with later overprinting under greenschist-facies conditions. Both events are younger than Jurassic (Ricou et al. 1998). However, since almost all contacts are tectonic it seems plausible to suggest that the different rock types of the

Chortiatis Unit experienced quite different metamorphic conditions before they were juxtaposed to their present location.

2.5. Oreokastro–Chalkidiki ophiolite complexes

The Oreokastro–Chalkidiki ophiolite complexes (term as used here) include the ophiolite complexes of Oreokastro and of Thessaloniki–Chalkidiki. They constitute together with the Guevgueli ophiolite complex the Innermost Hellenic Ophiolite Belt of Bébien et al. (1986); for a detailed description see Zachariadis (2007). Mafic and ultrabasic rocks mainly build up the Thessaloniki–Chalkidiki ophiolite complex. Rocks of this complex crop out for approximately 70 km, within a NW–SE-trending stripe on the Chalkidiki peninsula, from Thessaloniki town in the NW to Metamorphosis village in the SE. Geophysical data from the area northwest of Metamorphosis village indicate a flat base for the ophiolites in ca. 1–2.5 km below surface (Kiriakidis & Brooks 1989). Their southwestern margin dips ca. 25–35° to the northeast, whereas the northeastern margin dips in the same direction but with a steeper angle of ca. 60–80° (Kiriakidis & Brooks 1989). The contact between the ophiolites and the overlying rocks of the Aspro Vrisi–Chortiatis Unit is interpreted by Kiriakidis & Brooks (1989) as a thrust plane dipping northeast with a variable angle of 20° to 60°. The ultrabasic rocks predominantly comprise dunites, serpentinized to varying degrees, harzburgites and chromitites (e.g. Mussallam et al. 1981). Varying types of gabbro are the predominating basic rocks. The most widespread petrographical types are normal gabbro, gabbronorite and olivine gabbro (e.g. Kockel et al. 1977; Christofides et al. 1994). Diorites and plagiogranites are present to a minor degree. The ophiolite complexes experienced a greenschist-facies metamorphic overprint. Recent geochronological studies by Zachariadis et al. (2006) indicate a Middle Jurassic age (ca. 169 ± 1 Ma) for the Thessaloniki complex, based on U–Pb SHRIMP-II ages on zircons from a plagiogranite sample. Further south, zircons from a diorite sample collected near Metamorphosis village gave an age of ca. 160 ± 4 Ma, using the Pb–Pb single-zircon evaporation method, and zircons from a diorite sample collected on the Sithonia peninsula yielded an U–Pb SHRIMP-II age of ca. 160 ± 10 Ma (Zachariadis et al. 2006). Taking all data collectively, the subduction zone-related magmatism observed in the ophiolite complexes of the eastern Vardar Zone took place during Middle to Late Jurassic times (Spray et al. 1984; Zachariadis et al. 2006; Zachariadis 2007).

The Oreokastro ophiolite complex crops out north of Oreokastro town. It is mainly built up by gabbros and dolerites with, in some places, pillow lavas and highly serpentinized ultrabasic rocks (Haenel-Remy & Bebien 1985). The age of the Oreokastro ophiolite complex is not known. But the transgressively overlying breccia conglomerates of the Neochorouda Unit (see below) suggest that the Oreokastro ophiolite complex can not be younger than earliest Cretaceous. Similar ophiolitic formations including gabbros, sheeted dykes, pillow basalts and breccias occur in E Kassandra and in SW Sithonia (e.g. Kockel et al. 1977; Mussallam & Jung 1986; Michard et al. 1998). Here, we refer to Zachariadis (2007) who presented an evolutionary model for the Oreokastro–Chalkidiki ophiolite complexes, including geochemical, isotopic and geochronological data.

2.6. Prinochori Formation

The term Prinochori Formation is used here as synonym for the Prinochori beds of Kockel et al. (1977). Major outcrops occur in the southern part of Kassandra and Sithonia as well as in the southwestern part of Chalkidiki east of Petralona village. The latter area is the focus of this study (Fig. 8 and 9). Here, the Prinochori Formation is underlain by the fossiliferous Petralona limestone, which itself overlies locally transgressive with an arkosic sandstone layer the foliated Monopigadon granitoid (e.g. Kockel et al. 1977; Michard et al. 1998). The age of the latter is controversially discussed. Ricou (1965 cited in Kockel et al. 1971) presented a K–Ar biotite age of ca. 180 Ma. Younger ages of ca. 149 Ma (Kreuzer in Mussallam & Jung 1986) and 141 ± 3 Ma (Michard et al. 1998) were interpreted as a result of partial argon loss during a thermal overprint (Michard et al. 1998). Kostopoulos et al. (2001) reported a $^{207}Pb/^{206}Pb$ single-zircon evaporation age of ca. 192 ± 4 Ma that might be considered as a minimum for the age of intrusion of the Monopigadon granitoid. A much older $^{207}Pb/^{206}Pb$ single-zircon evaporation age of ca. 225 Ma was recently obtained by Himmerkus et al. (in preparation) for a part of the Monopigadon granitoid that is similar to intrusion ages of the Arnea suite from the Vertiskos Terrane of the Serbo-Macedonian Massif (Himmerkus et al. 2004b, in preparation). Here, we consider the younger K–Ar biotite ages of around 150 Ma as more reliable. The single-zircon ages probably indicate that older crustal rocks have been involved in latest Middle–Late Jurassic magma genesis in the eastern Vardar Zone. This seems plausible since Anders et al. (2005) have reported zircon xenocrysts of pre-

Jurassic age from the ca. 155–164 Ma-old granitoids of the Guevgueli ophiolite complex. Ricou et al. (1998) already considered the Monopigadon granitoid as part of the granitoid-bearing Guevgueli arc. Hence, marble and skarn inliers between the Monopigadon granitoid and the Petralona limestone (e.g. Kockel et al. 1977; Ricou et al. 1998) may have been a result due to Late Jurassic arc magmatism that effected older basement rocks and the overlying carbonate platform.

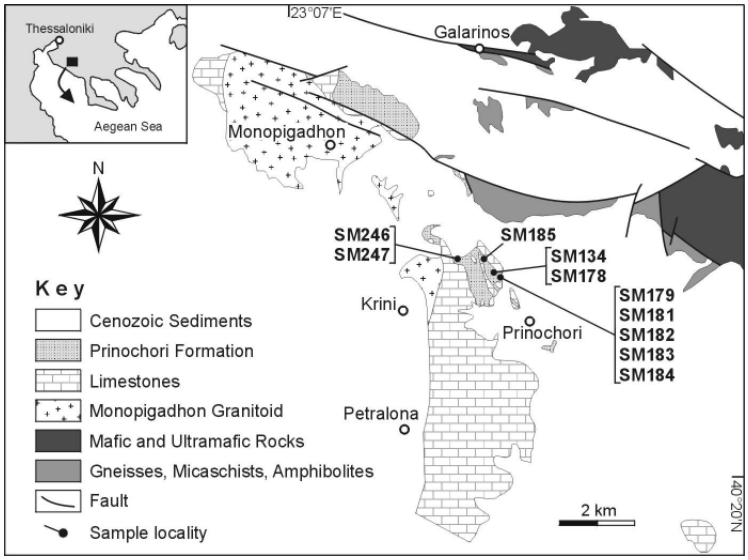

Fig. 8. Geological map of the Petralona area modified after Kockel & Mollat (1977) showing the sampling locations for samples of the Prinochori Formation.

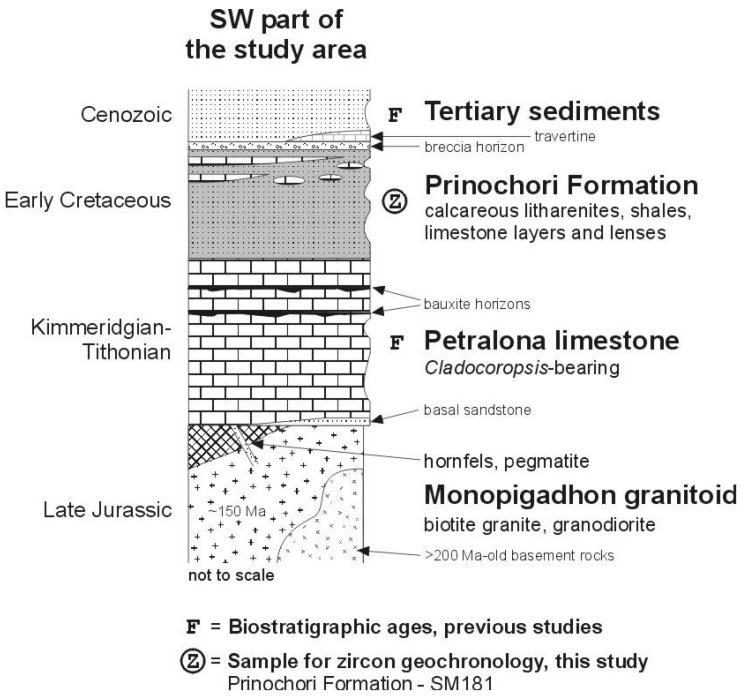

Fig. 9. Interpretive stratigraphic column of the Petralona area, compiled using data from Kockel et al. (1971, 1977), Michard et al. (1998) and own field observations (this study).

The Petralona limestone has been biostratigraphically dated as Late Jurassic (Kimmeridgian–Tithonian), based on *Pseudocyclammina* sp., *Nerinella* sp., *Ceritella* sp., *Exelissa* sp. and *Cladocoropsis* sp. (e.g. Kockel et al. 1977). Furthermore, Carras & Geogala (1998) reported *Clypeina jurassica* Favre, *Salpingoporella annulata* Carozzi, *Kurnubia palastiniensis* Henson, and *Anchispirocyclina lusitanica* Egger. The Petralona limestone was correlated with limestone beds drilled in boreholes around Epanomi town in the Western Chalkidiki peninsula (Carras & Geogala 1998).

The Prinochori Formation, well exposed in a canyon north of Prinochori village (Fig. 8), predominantly comprises calcareous litharenites and calcschists of greyish colour interbedded with thin conglomeratic layers. More to its upper part, massive limestone lenses of grey colour are intercalated (Fig. 9). Their size ranges from few decimetres up to several decametres in length. In general, the bedding planes have an intermediate dip (ca. 25–45°) towards NE (Fig. 6c). The whole succession experienced a very low-grade greenschist-facies metamorphism (Kockel et a. 1971; Michard et al. 1998). Based on stratigraphic relationships to the underlying limestones, the Prinochori Formation is accepted to be latest Jurassic–earliest Cretaceous in age (e.g. Kockel et al. 1977) although that is lacking a direct biostratigraphic control. However, based on the biostratigraphic study by Carras & Geogala (1998) on limestone beds from boreholes around Epanomi town, it seems plausible to suggest that the Prinochori Formation is Early Cretaceous in age. Along the dust road north of Prinochori, just few metres south of sample locality SM185, limestones and clastic sediments of the Prinochori Formation are exposed in small amounts at the verge (40°24´35.6´´N, 23°11´09.8´´E). Thin quartz veinlets were locally observed. The bedding surfaces of both the limestones and the clastic sediments show slickenside striations, indicating a top-to-the-SW tectonic transport. The Prinochori Formation is overlain by a thin breccia horizon followed by light-coloured karstified limestones (travertine). The breccia horizon is well exposed ca. 1.5 km NW of Prinochori village, west of the dust road (40°24´03.1´´N, 23°11´13.0´´E), consisting of reworked material of the Prinochori Formation, including clasts of litharenite, grey limestone and minor milk quartz. The latter may be derived from the quartz veins observed. The breccia horizon and the light-coloured limestones lack metamorphic overprint. They are presumably of post-Eocene age, according to time constraints for deformation and metamorphism described for rocks of the Serbo-Macedonian Massif and adjacent units by Kilias et al. (1999).

2.7. Neochorouda Unit

The Neochorouda Unit is used here as synonym for the "Konglomerat von Dubkon" of Kockel et al. (1977) and the Oreokastro Limestone breccia of Ricou et al. (1998), respectively. The Neochorouda Unit is a NW–SE-elongated conglomeratic calcareous succession, which unconformably overlies pillow lavas and gabbros east of Neochorouda village (Fig. 10, 11a), more to the north also metasedimentary rocks of the Melissochori Formation and of the Aspro Vrisi Serie (e.g. Kockel et al. 1977). The conglomeratic succession consists of limestone pebbles, partly fossiliferous, for example, coral-bearing reef-limestone, of calcareous sandstones, wackes and quartzites as well as of metabasic and meta-igneous clasts. Platy limestones of dark gray colour and sandy beds are intercalated. The clast size ranges from few centimetres up to half a metre. Some of the metasedimentary clasts are supposed to be derived from the Melissochori Formation; clasts of meta-rhyolite have been assigned to the Pirghoto Formation and clasts of gabbro may derive from the underlying ophiolite complex (Kockel et al. 1971, 1977; Mussallam & Jung 1986).

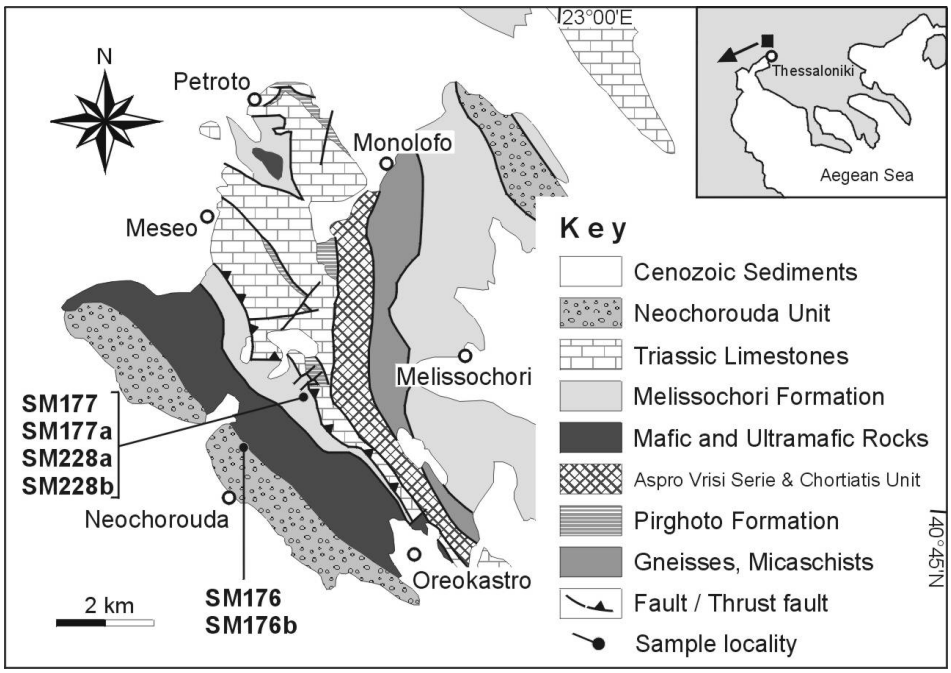

Fig. 10. Geological map of the Oreokastro area modified after Kockel & Mollat (1977) showing the sampling locations for biostratigraphy and whole-rock chemistry. Note: At least a part of the stripe between the mafic and ultramafic rocks to the west and the Triassic limestones to the east assigned in all previous studies to the Melissochori Formation is interpreted here as a single individual formation of Mid-Cretaceous age, named Oreokastro Formation (see text for discussion).

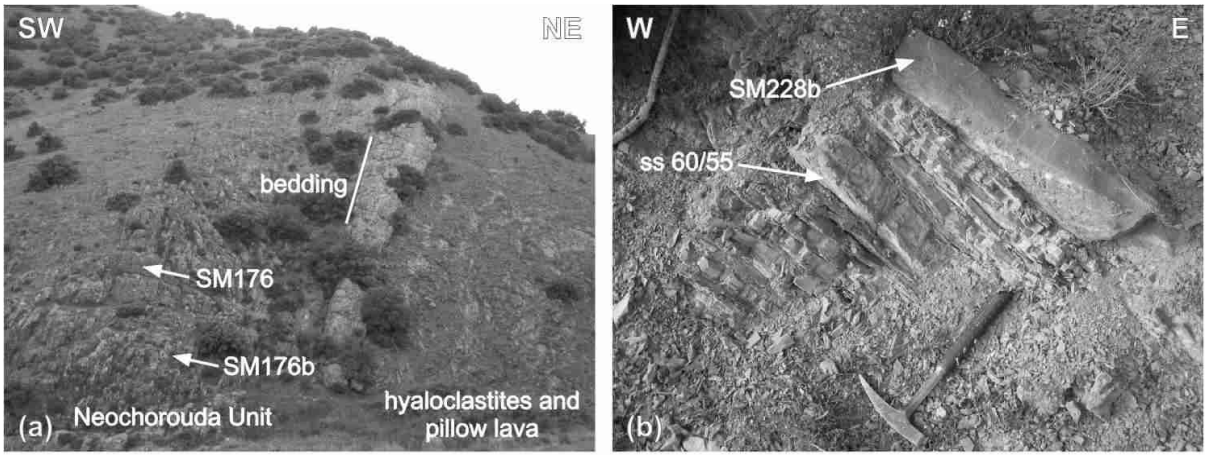

Fig. 11. (**a**) Neochorouda Unit overlying hyaloclastites and pillow lava northeast of Neochorouda village (40°44´53.3´´N, 22°52´39.0´´E); (**b**) Calcareous clastic sedimentary succession of the Oreokastro Formation (40°45´23.7´´N, 22°53´24.3´´E; see also Fig. 10).

Fossiliferous limestone lenses collected ca. 4 km NW of Neochorouda village yielded fragments of Lamellibranchiata, gastropods of genus *Nerinea*, undeterminable corals, stromatoporoids of genus *Cladocoropsis*, and undeterminable algae (Mercier 1968; Kockel et al. 1977). Mussallam & Jung (1986) described sandstones comprising the ammonoids *Berriasella ex gr. subcallisto* (Toucas) and *B. ex gr. oppeli* (Kilian) and limestone conglomerates with colonies of dasycladacea algae *Teutloporella socialis* (Praturlon). Based on the recovered fauna, the age of the Neochorouda Unit is accepted to be Late Jurassic to earliest Early Cretaceous (e.g. Mercier 1968; Kockel et al. 1977).

Cenozoic sedimentary rocks cover most of the study area in the southwest of the Chalkidiki peninsula (Fig. 2). Voluminious Cenozoic volcanic intrusions can be found on Sithonia and Athos; minor intrusions occur in the adjacent area to the NW. Isotopic investigations have suggested an Eocene age for these granitoids (e.g. De Wet et al. 1989; Christofides et al. 1990; Frei 1996).

3. Methods

To constrain the age, provenance and depositional setting of sedimentary rocks from the eastern Vardar suture zone, we have collected in total 42 samples for whole-rock geochemical analyses (major and trace elements), detrital chrome spinel chemical analyses and U–Pb zircon geochronology supplemented by biostratigraphic analyses. Sample localities

are given in the Appendix and are shown in Figures 2, 4, 8 and 10 respectively. The analytical data referred to in this chapter are included in the Appendix. Although this study mainly focuses on the clastic sedimentary rocks of the Examili, Melissochori and Prinochori Formations, the geochemistry of two calcareous samples from the Oreokasto area is also presented in some diagrams, but these two samples are only supplementary and, therefore, their geochemistry will not be discussed here in detail.

3.1. Whole-rock geochemistry

The composition of clastic sedimentary rocks is predominantly controlled by the lithology of their source area(s), and modified by several factors such as weathering, transport and sorting, redox environment and diagenesis (e.g. Johnsson 1993). If the whole-rock geochemistry is not significantly modified by secondary processes it can be used as chemostratigraphic indicator and as fingerprint for provenance and depositional setting of sedimentary rocks (e.g. Bhatia & Crook 1986; McLennan 1989; McLennan et al. 1990, 1993). With the exception of a few major-element fingerprints, we have only employed relatively immobile trace elements and rare earth elements (REE) for the characterisation of sedimentary provenance and depositional setting.

In total, 37 samples were used for whole-rock geochemical analyses. The samples were crushed into small pieces and then powdered using an agate mill. Major and trace elements of whole rock were analysed by X-ray fluorescence (XRF) spectrometry on fused glass discs and pressed powder pellets, respectively, using a Philips MagiX Pro X-ray spectrometer at the University of Mainz, following procedures outlined in Meinhold et al. (2007). Loss on ignition (LOI) was determined gravimetrically by heating the samples to 1000°C. Rare earth elements (REE), Hf, Ta, Th, and U of selected samples were analysed on fused discs by laser ablation inductively-coupled plasma mass spectrometer (LA-ICPMS) using an Agilent 7500ce equipped with a NewWave/Merchantek 213 nm Nd-YAG laser system at the University of Mainz, following procedures described in Nehring et al. (2007).

3.2. Mineral chemistry

Detrital chrome spinel in sedimentary rocks is generally taken as provenance indicator of basic and ultrabasic rocks in the source area, mostly adributed to ophiolites (e.g. Hiscott 1984; Zimmerle 1984; Pober & Faupl 1988). Chemical fingerprints such as Cr/(Cr + Al) and Mg/(Mg + Fe^{2+}) ratios, respectively, and TiO_2 abundances of chrome spinels can be used to signify the tectonic setting of source rocks from which they were derived (e.g. Dick & Bullen 1984; Pober & Faupl 1988; Cookenboo et al. 1997; Kamenetsky et al. 2001). However, use of petrogenetic discrimination diagrams in provenance studies or for interpretation of altered ophiolite complexes have also been criticised (Power et al. 2000). Nevertheless, with keeping the critics in mind, we applied the common practise for interpretation of detrital chrome spinel chemistry. Detrital chrome spinel compositions were determined on polished heavy mineral separates of four samples, obtained following procedure outlined in Meinhold et al. (2007). Mineral analyses were carried out using a Jeol JXA 8900 RL electron microprobe at the University of Mainz, Germany, operated at an accelerating voltage of 20 kV and a beam current of 12 nA, with a beam diameter of 2 μm. Natural and synthetic materials were used as standards. The PRZ procedure was applied to calculate concentration units. Cations were calculated stoichiometric based on 4 oxygens per formula unit. Following common practice for chrome spinel interpretation, the Cr-number [Cr# = Cr/(Cr+Al)] and Mg-number [Mg# = Mg/(Mg+Fe^{2+})] for each analysis were calculated assuming stoichiometry.

3.3. Zircon geochronology

U–Pb dating of detrital zircons has been proven to be a powerful tool for sedimentary provenance studies and in the absence of fossil and other stratigraphic data the youngest grain in a sedimentary rock can indicate a maximum limit for the age of deposition (e.g. Fedo et al. 2003, and references therein). U–Pb zircon geochronology was carried out on three individual samples taken from the Examili, Melissochori and Prinochori Formations. Zircons were separated from the bulk samples using standard techniques and prepared for zircon dating as described in Chapter 4 of this thesis. High-spatial resolution U–Pb dating of individual zircon grains was performed on a Thermo-Finnigan Element II sector-field inductively-coupled plasma mass spectrometer (LA-ICPMS) equipped with a NewWave/Merchantek 213 nm Nd-

YAG laser system at the Geological Survey of Denmark and Greenland (GEUS), Copenhagen, Denmark, following the methodology described in Chapter 4 of this thesis. Unless stated otherwise, $^{206}Pb/^{238}U$ ages are used for zircon grains <1.2 Ga whereas older grains are quoted using their $^{207}Pb/^{206}Pb$ ages. The latter are generally considered as minimum ages due to the effect of possible Pb loss. Concordia diagrams and probability density distribution and histogram plots were produced using the programs Isoplot/Ex (Ludwig 2003) and AgeDisplay (Sircombe 2004) respectively. Unless stated otherwise, ages reported in the text are given at the 2-sigma level. The isotopic data referred to in this chapter are included in the Appendix. The Geological Time Scale (GTS) of Gradstein et al. (2004) was used as stratigraphic reference for data interpretation.

3.4. Biostratigraphy

In total seven samples were used for biostratigraphic analyses (see Fig. 3). Five samples were taken from rock successions with macroscopic appearance of fossils (e.g. gastropods). From those, four samples come from the Oreokastro area and were investigated in thin sections using an optical microscope equipped with a digital camera system. One sample of greyish limestone was collected from the Svoula Limestone along the main road NE of Mandres village to Pirghoto village and has been disolved in acetic acid. After sieving the residue, the remaining fraction was investigated under a binocular microscope for microfossils. Two other samples come from the Melissochori Formation and were treated according to palynological standard preparation method with hydrochloric and hydrofluoric acid. The remaining residue was sieved and embedded with glycerine gelatine on standard glass slides, and the material was investigated under a light microscope using combined transmitted and reflected light.

4. Results

4.1. Whole-rock geochemistry

Examili Formation: According to the diagram of Herron (1988), the metasedimentary rocks of the Examili Formation can be chemically classified as subarkoses (Fig. 12) that is

coincident with petrographical observations. As shown in Figure 13, the rocks display high contents of SiO_2 (84–93 wt.%), moderate to low contents of Al_2O_3 (3.8–8.0 wt.%), very low contents of TiO_2 (≤0.21 wt.%), Fe_2O_3 (≤1 wt.%) and CaO (<0.3 wt.%), and variable contents of K_2O (0.8–3.7 wt.%). Very low values of CaO and LOI indicate the absence of carbonate-bearing minerals. The concentrations of trace elements are consistently low (e.g. Cr ≤14 ppm, Ni ≤7 ppm, Sr ≤36 ppm).

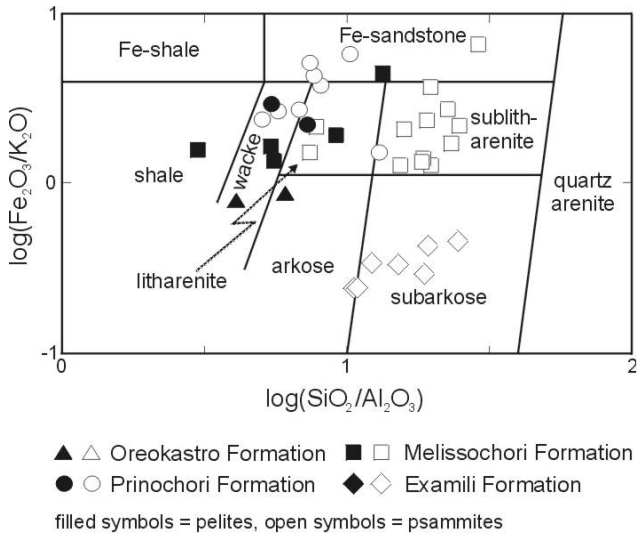

Fig. 12. Chemical classification scheme for terrigenous clastic sediments after Herron (1988).

Multi-element diagrams normalised to upper continental crust composition exhibit depletion in trace elements with characteristic negative Sr and Ti anomalies, and a strong depletion in V, Sc, Cr and Ni (Fig. 14). PAAS-normalised REE patterns of two samples are almost flat and show a strong depletion in total REE (Fig. 15), with stronger depletion of light REE (LREE) compared to heavy REE (HREE). Chondrite-normalised REE patterns (Fig. 15) show a light rare earth element (LREE) enrichment (La_N/Yb_N ~ 5.0 and 6.3) and flat heavy rare earth element (HREE) profiles (Gd_N/Yb_N ~ 1.0 and 1.2) with a negative Eu anomaly (Eu/Eu* ~ 0.6). The sedimentary rocks of the Examili Formation have Th/Sc ratios between 1.5 and 6.8 accompanied by Zr/Sc ratios between 34 and 125 that suggest, according to the McLennan et al. (1993), pronounced sediment reworking, consistent with zircon enrichment (Fig. 16). Taken collectively, petrography and geochemistry clearly point to a source area of acidic composition, presumably K-feldspar bearing granites or equivalents. Using the ternary discrimination diagrams of Bhatia & Crook (1986) the psammitic samples of the Examili Formation plot in the active and passive margin field (Fig. 18).

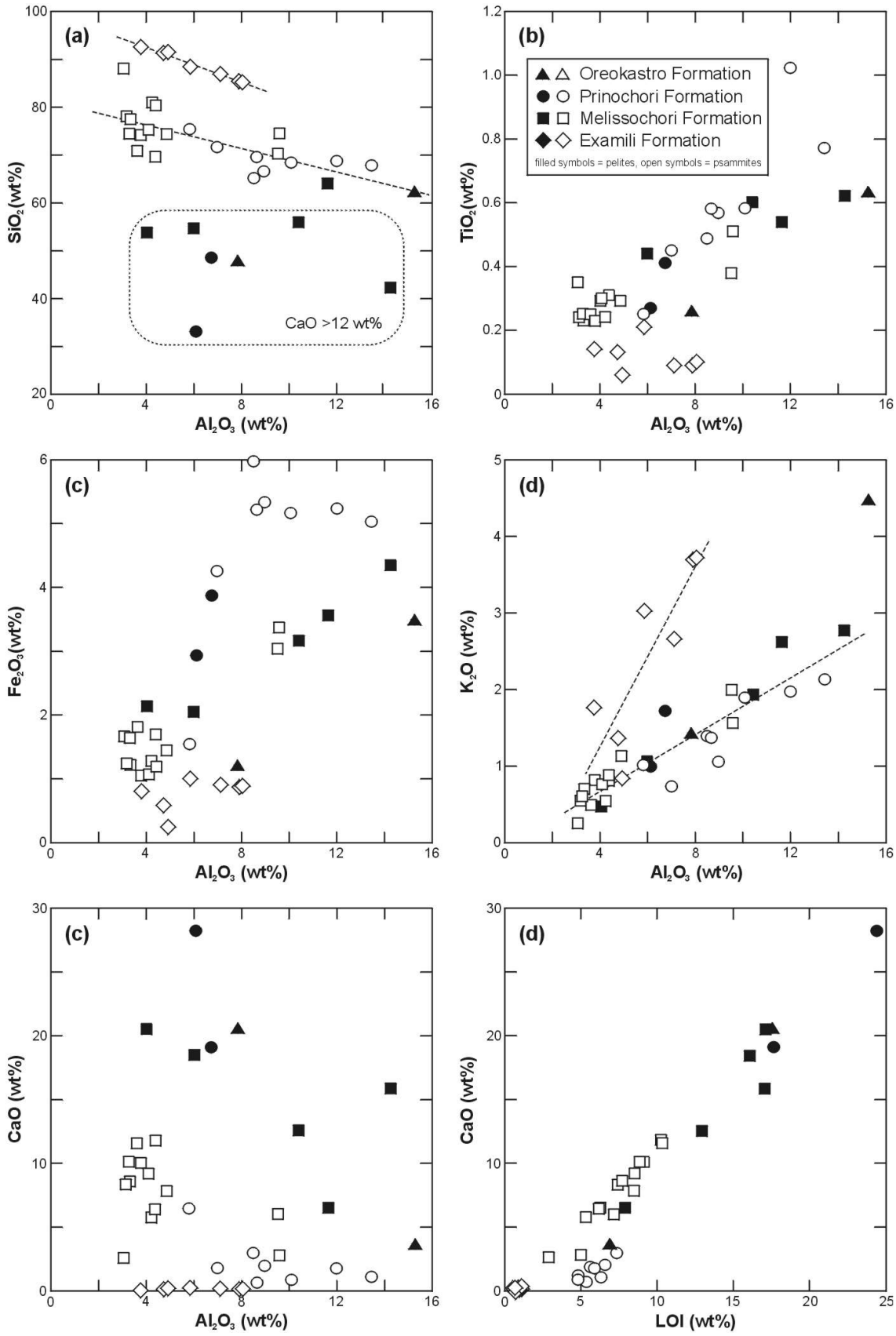

Fig. 13. Correlation diagrams of SiO_2, TiO_2, Fe_2O_3, K_2O and CaO v. Al_2O_3 and CaO v. LOI for sedimentary rocks of the eastern Vardar suture zone.

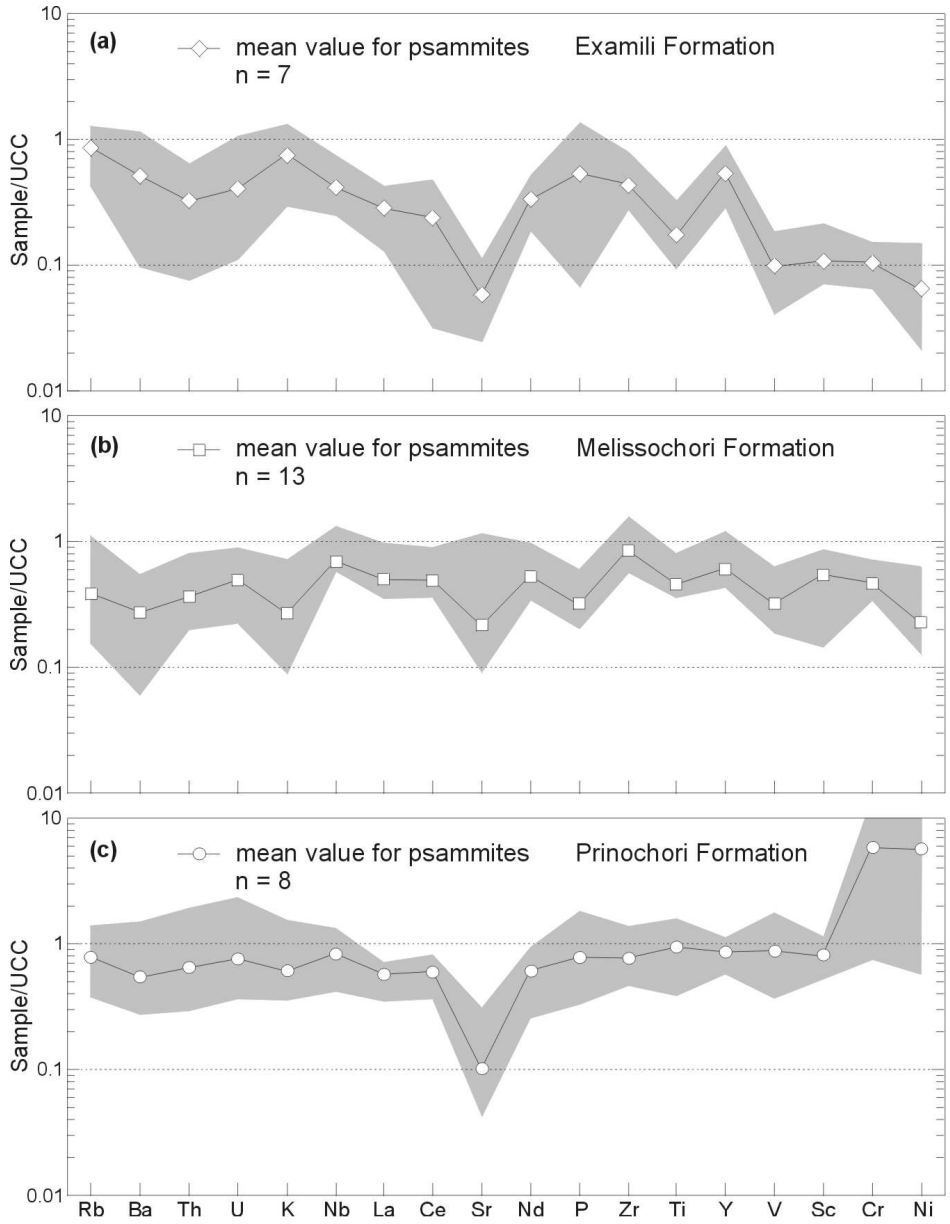

Fig. 14. Multi-element diagrams for psammitic sedimentary rocks of the eastern Vardar suture zone. Concentrations are normalised against the upper continental crust composition (UCC, Rudnick & Gao 2003). Only mean values (symbols) and the chemical range (grey fields) are given.

Melissochori Formation: Because most discrimination for identifying the provenance and tectonic setting of sedimenary rocks are only valid for siliciclastic rocks, with a preference of psammitic rocks, a differentiation between siliciclastic and more calcareous dominated rocks as well as psammitic and pelitic rocks was deemed necessary. In this study, the rocks have been distinguished according to their contents of SiO_2 and CaO. For convention, samples with SiO_2 >65 wt.% and accompanying CaO <12 wt.% have been assigned to psammites, all other samples are classified as pelites, including calcareous

sedimentary rocks such as packstones and wackestones. According to the diagram of Herron (1988), the majority of the psammitic sedimentary rocks of the Melissochori Formation can be chemically classified as sublitharenites; two samples are litharenites (Fig. 12). Five pelitic rocks plot in the fields for shale, wacke, litharenite and iron-bearing sandstone. As shown in Figure 13, the psammitic rocks display moderate to high contents of SiO_2 (70–88 wt.%), moderate to low contents of Al_2O_3 (3–10 wt.%), moderate to low contents of TiO_2 (0.2–0.5 wt.%) and Fe_2O_3 (1.0–3.4 wt.%), moderate to low contents of K_2O (0.2–2.0 wt.%), and variable elevated contents of CaO (2.6–11.7 wt.%). The pelitic rocks have low contents of SiO_2 (42–64 wt.%), moderate to high contents of Al_2O_3 (4–14 wt.%), moderate to low contents of TiO_2 (0.3–0.6 wt.%) and Fe_2O_3 (2.0–4.3 wt.%), moderate to low contents of K_2O (0.5–2.8 wt.%), and variably elevated contents of CaO (6.5–20.4 wt.%). Medium to high values of CaO and LOI in psammitic and pelitic rocks accompanied by a strong positive linear correlation between both values indicate the presence of carbonate-bearing minerals such as calcite, which is confirmed by petrography.

Multi-element diagram normalised to upper continental crust composition exhibit minor depletion in trace elements, compared to samples of the Examili Formation, with characteristic negative K and Sr anomalies, and slight enrichment in Zr (Fig. 14). PAAS-normalised REE patterns of two samples are flat, with no differences between LREE and HREE, and strong depletion in total REE (Fig. 15). The PAAS-normalised REE patterns of sample SM144 is similar but shows a slight positive Eu anomaly. Chondrite-normalised REE patterns (Fig. 15) show a LREE enrichment (La_N/Yb_N ~ 8.9 and 12.1) and flat HREE profiles (Gd_N/Yb_N ~ 1.5 and 1.6) with a negative Eu anomaly (Eu/Eu* ~ 0.6–0.7), the exception being sample SM144 with an almost indistinct Eu anomaly of ~ 0.9, presumably because of plagioclase enrichment in the sand-size fraction during sorting (e.g. McLennan et al. 1990). The metasedimentary rocks of the Melissochori Formation have Th/Sc ratios between 0.1 and 1.2 accompanied by Zr/Sc ratios between 4 and 30 that suggest, according to the McLennan et al. (1993), compositional variation within the source area (Fig. 16). One exception is sample SM241 with a Th/Sc ratio of 2 and a Zr/Sc ratio of 153 that may indicate sedimentary reworking, consistent with zircon enrichment. Taken collectively, petrography and geochemistry point to a source area of acidic and calcareous composition, presumably continental basement of granitic composition and carbonate platform deposits. Using the ternary discrimination diagrams of Bhatia & Crook (1986) the psammitic samples of the

Melissochori Formation plot in the continental island-arc field, the exception being sample SM241 that plots in the passive margin field (Fig. 18).

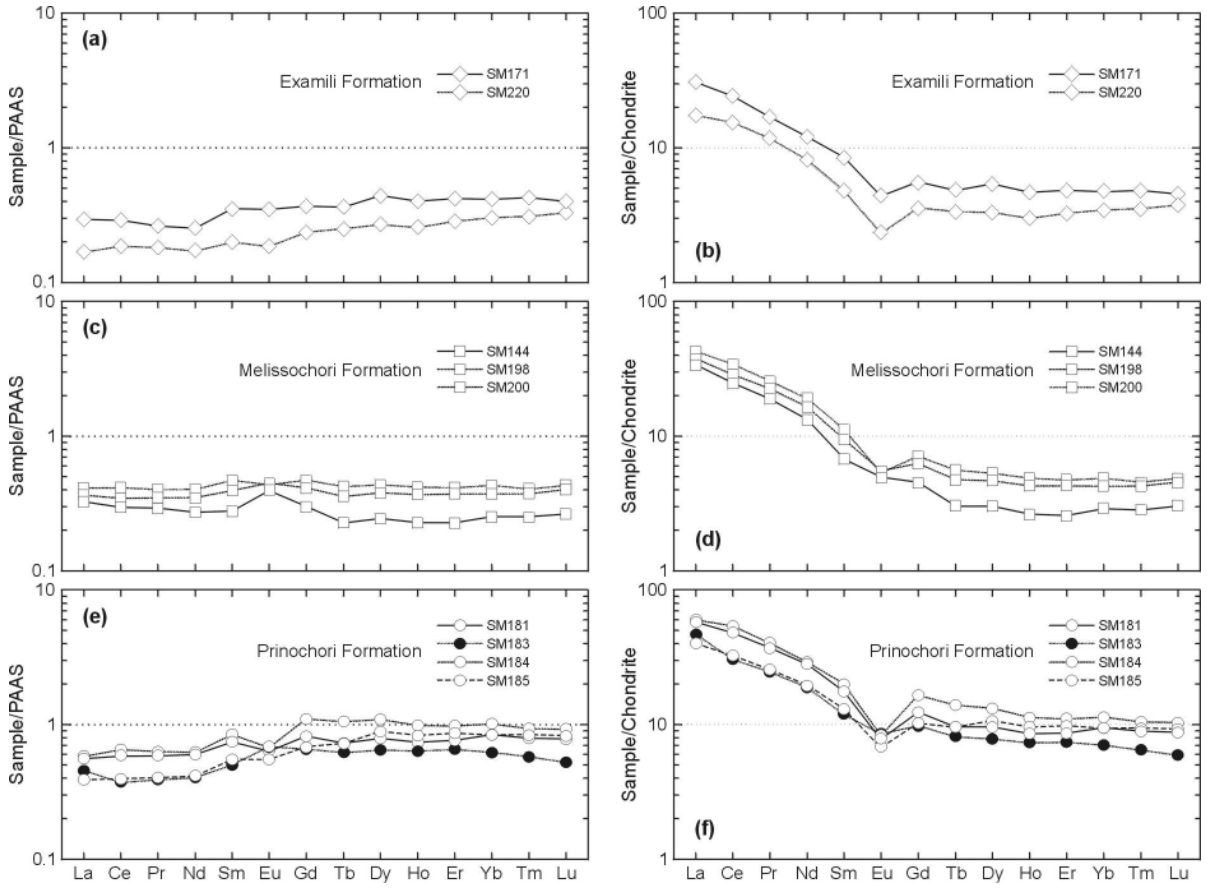

Fig. 15. (a, c, e) PAAS-normalised REE diagrams. Normalising values from McLennan (1989). **(b, d, f)** Chondrite-normalised REE diagrams. Normalising values from Taylor & McLennan (1985). Open symbols indicate psammitic sediments; full symbols, pelitic sediments.

Prinochori Formation: According to the diagram of Herron (1988), the majority of the sedimentary rocks of the Prinochori Formation can be chemically classified as wackes (i.e. greywackes), litharenites and iron-bearing sandstones; only one sample plots in the field for sublitharenites (Fig. 12). As shown in Figure 13, the psammitic rocks display moderate to low contents of SiO_2 (65–75 wt.%) and TiO_2 (0.2–1.0 wt.%), moderate contents of Al_2O_3 (6–13 wt.%) Fe_2O_3 (1.5–6.0 wt.%) and K_2O (0.7–2.1 wt.%), and low to elevated contents of CaO (0.7–6.4 wt.%). Sedimentary rocks of the Prinochori Formation are characterised by very high concentrations of the trace elements Cr (up to 1332 ppm) and Ni (up to 472 ppm), illustrated in Figure 17a. Extraordinary high Cr contents in sedimentary rocks have also been reported, for example, from Archaean shales of the Witwatersrand basin in South Africa (up to 1528

ppm Cr: Wronkiewicz & Condie 1987) and from Ordovician flysch of the Taconian orogeny in North America (up to 3950 ppm Cr: Hiscott 1984). They were interpreted as significant contribution of a basic–ultrabasic source component. Garver et al. (1996) suggested that values of Cr >150 ppm and Ni >100 ppm, Cr/Ni between 1.3–1.5 and a high correlation coefficient between Cr and Ni are diagnostic of ultrabasic rocks in the source area, whereas higher Cr/Ni ratios (around 2 and higher) typify an input of basic volcanic detritus. Cr/Ni ratios of >3.0 for sandstones suggest significant sedimentary fractionation (Garver et al. 1996). According to the high Cr and Ni concentration and Cr/Ni ratios of 2.0–3.2, the sedimentary rocks of the Prinochori Formation received basic and ultrabasic detritus from the source area. McLennan et al. (1993) used the ratios of Cr/V and Y/Ni (Fig. 17b) to illustrate the importance of ophiolitic provenance in sedimentary rocks. The Cr/V ratio monitors the enrichment of Cr over the other ferromagnesian trace elements. Cr is concentrated in high amounts in chrome spinel that is a key mineral in (ultra)basic rocks and hence in ophiolites. The Y/Ni ratio shows the general level of ferromagnesian trace elements (Ni) compared with Y, which is used as a proxy for the heavy REE (McLennan et al. 1993), typically hosted in zircon and garnet. With exception of one sample, the sedimentary rocks of the Prinochori Formation clearly tend towards an ophiolitic source.

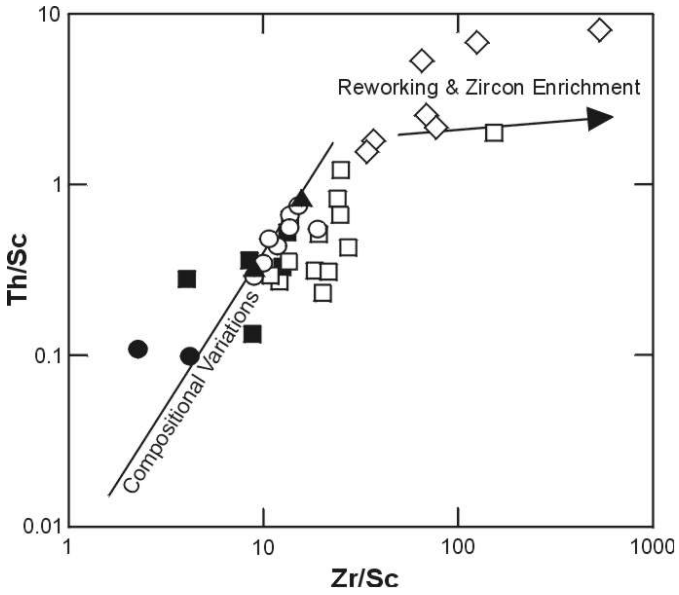

Fig. 16. Discrimination diagram after McLennan et al. (1993) illustrating sediment recycling.

The multi-element pattern is almost flat and similar to upper continental crust composition, the exception being a characteristic negative Sr anomaly, and strong enrichment in Cr and Ni (Fig. 14). The latter indicates significant input of (ultra)basic rocks. PAAS-

normalised REE patterns of three psammitic samples and one pelitic sample are similar (Fig. 15); they are almost flat and show a stronger depletion of LREE compared to HREE. The latter are similar or only slightly depleted to PAAS. Chondrite-normalised REE patterns (Fig. 15) show a LREE enrichment (La_N/Yb_N ~ 4.2 and 7.3) and flat HREE profiles (Gd_N/Yb_N ~ 1.1 and 1.6) with a varying negative Eu anomaly (Eu/Eu* ~ 0.5–0.8). The sedimentary rocks of the Prinochori Formation have Th/Sc ratios between 0.1 and 0.8 accompanied by Zr/Sc ratios between 2 and 19 that suggest, according to the McLennan et al. (1993), compositional variation within the source area (Fig. 16). Taken collectively, petrography and geochemistry clearly point to a source area of intermediate and pronounced basic to ultrabasic composition, presumably granodiorites or equivalents and ophiolitic rocks. Using the ternary discrimination diagrams of Bhatia & Crook (1986) the psammitic samples of the Prinochori Formation plot in the continental-island arc field, the exception being sample SM179 that plots in the ocean island-arc field (Fig. 18).

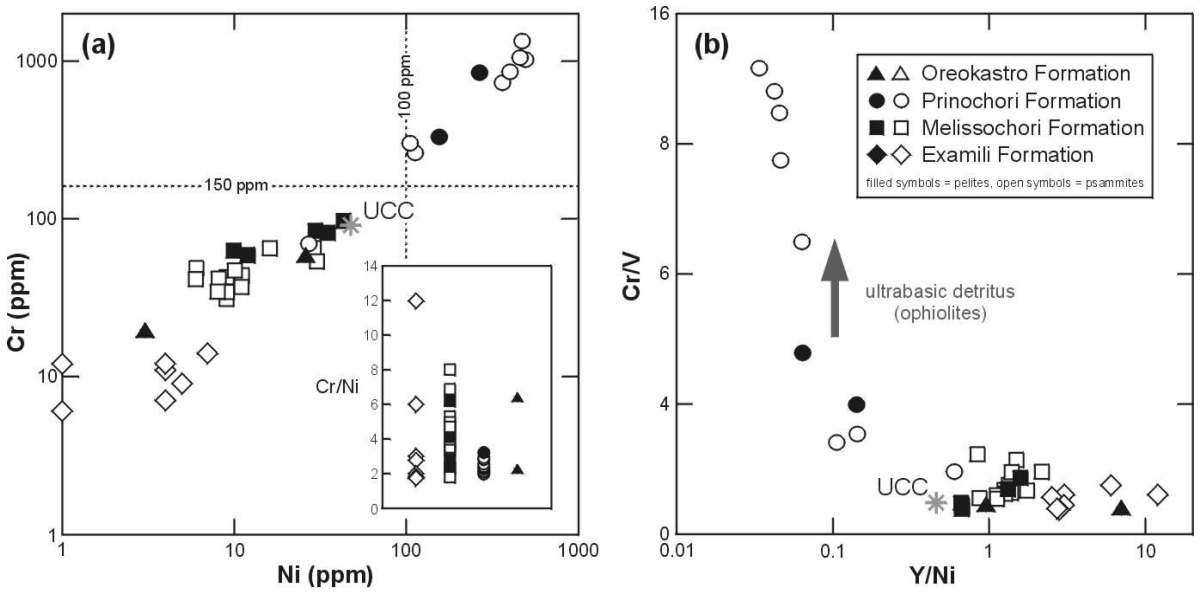

Fig. 17. Diagrams for identifying an ultramafic provenance. **(a)** Cr vs. Ni diagram. Values of Cr (>150 ppm) and Ni (>100 ppm), Cr/Ni ratios between 1.3–1.5 and a high correlation coefficient between Cr and Ni are diagnostic of ultramafic rocks in the source area; Cr/Ni ratios of 2 and greater typify an input of mafic volcanic rocks (Garver et al. 1996). **(b)** Cr/V vs. Y/Ni diagram after McLennan et al. (1993). UCC according to Rudnick & Gao (2003).

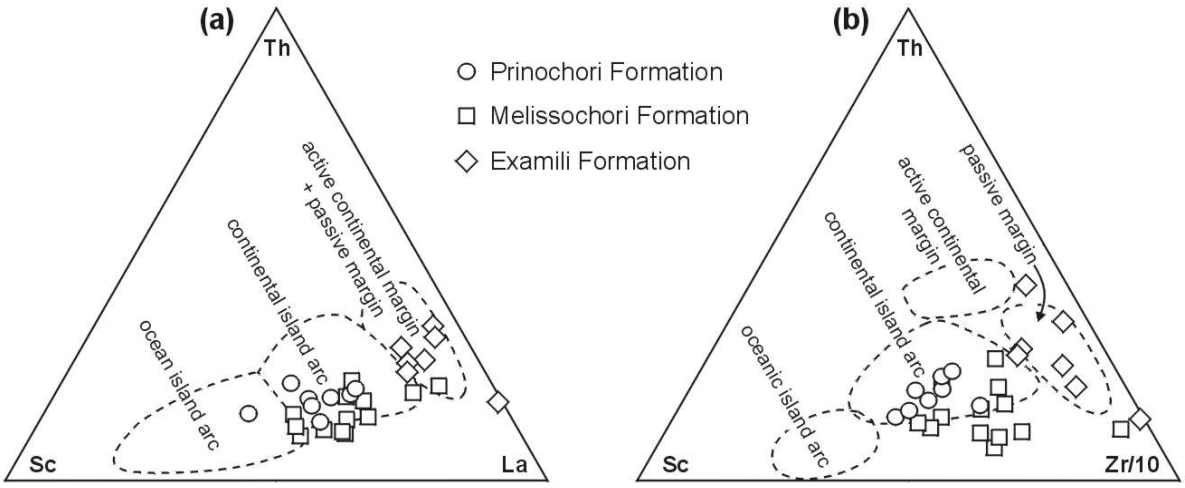

Fig. 18. (a–b) Discrimination diagrams after Bhatia & Crook (1986) illustrating the tectonic setting. Only psammites are plotted.

4.2. Mineral chemistry

Detrital chrome spinel was found in clastic sedimentary rocks of the Prinochori Formation, which confirms an input of (ultra)basic rocks from the source area as suggested by whole-rock geochemistry (see paragraph before). In thin section, it could be observed that chrome spinel is intergrown with serpentine. The chrome spinels analysed here are brown to dark reddish brown and black. Their major-element composition shows a broad range that suggests multiple source areas for the chrome spinels. Minor variation may also be through alteration or weathering processes. Trace-element concentrations are consistently low, with NiO <0.18 wt.%, V_2O_3 <0.40 wt.%, ZnO <0.70 wt.% and CoO <0.13 wt.%. Using the diagram of Pober & Faupl (1988), the observed spread in Cr-number (0.40–0.90) and Mg-number (0.25–0.70) suggests a mixed (ultra)basic source of highly depleted peridotites of mainly harzburgite and minor lherzolite composition (Fig. 19a). Few chrome spinels plot in the field for metamorphic spinel (Fig. 19a). These chrome spinels have also very low $Fe^{3+}/(Cr + Al + Fe^{3+})$ ratios that specifies their metamorphic origin as being derived from high-grade metamorphic rocks (Barnes & Roeder 2001). In general, the Fe^{3+} concentration is consistently low for all chrome spinels, with $Fe^{3+}/(Cr + Al + Fe^{3+}) \leq 0.08$, the exception being one grain with 0.12. Following Kamenetzky et al. (2001), the analysed chrome spinels can be separated into spinels derived from peridotitic and volcanic source rocks on the basis of their TiO_2 contents and Fe^{2+}/Fe^{3+} ratios. Around 84 % of all chrome spinels have TiO_2 concentrations

less than 0.2 wt.% and Fe^{2+}/Fe^{3+} ratios higher than 3.4 that suggest peridotites as source rocks. Combined with the Al_2O_3 vs. TiO_2 diagram of Kamenetzky et al. (2001), most of the detrital chrome spinels were derived from MOR-type peridotites and supra-subduction zone (SSZ) peridotites, whereas only a small fraction comes from volcanic rocks, supposedly island-arc basalts and MORB-type rocks (Fig. 19b).

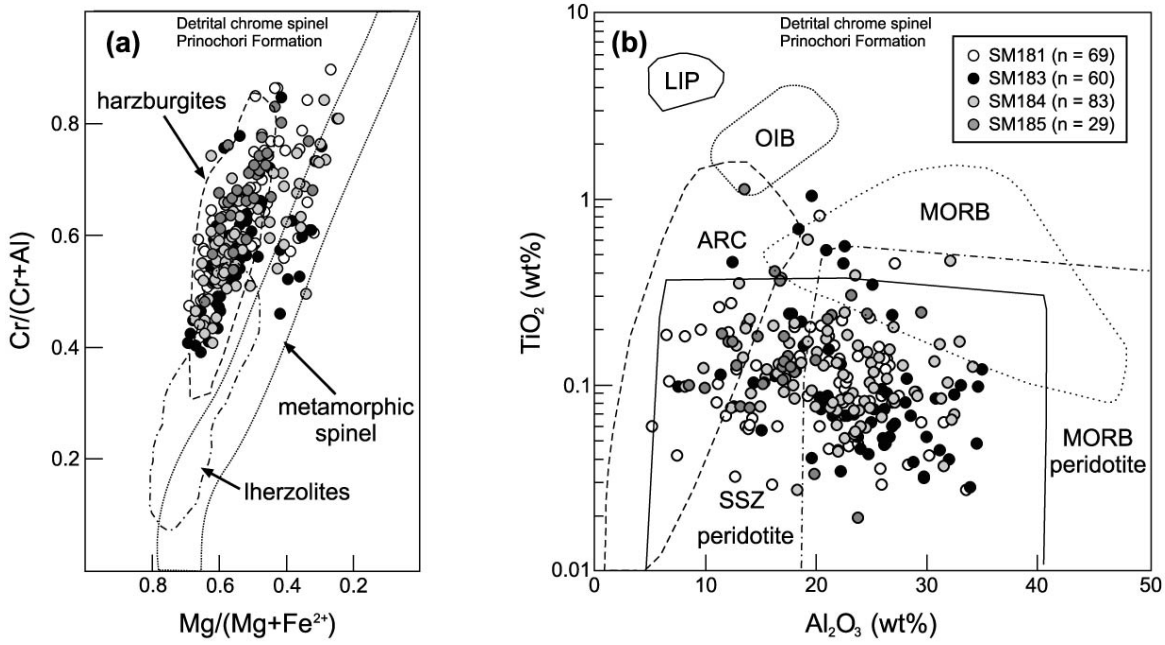

Fig. 19. Chemical composition of detrital chrome spinel grains of the Prinochori Formation. **(a)** Cr/(Cr+Al) vs. $Mg/(Mg+Fe^{2+})$ diagram showing the discrimination fields of chrome spinel derived from the two major peridotite subtypes as well as of metamorphic spinel after Pober & Faupl (1988). **(b)** TiO_2 vs. Al_2O_3 diagram showing the discrimination fields of chrome spinel derived from various types of mafic and ultramafic rocks after Kamenetsky et al. (2001). MORB – mid-ocean ridge basalt, OIB – ocean-island basalt, LIP – large igneous province, ARC – island-arc magmas, SSZ – supra-subduction zone.

4.3. Zircon geochronology

Examili Formation: Sample SM220 was collected from a quartzite successions cropping out in a quarry NW of Examili village (40°52´26.7´´N, 22°59´44.7´´E; Fig. 4). Sample SM220 consists predominantly of subangular to rounded monoquartz, minor polyquartz, and higly altered K-feldspar in a sericitic matrix with zircon, rutile and apatite as major accessory minerals. The zircon crystals are predominantly subhedral to rounded, clear colourless. The length of single zircon crystals varies between 110 and 280 µm. The majority

of the analysed zircons of the Examili Formation have clear oscillatory zonation patterns in CL images (Fig. 20) and appear to be magmatic in origin; only a few exhibit no zoning. Inherited cores are sparse. The concordance-filtered zircon ages of 60 analyses on 58 single grains show a polymodal age distribution with a prominent peak at ca. 450 Ma, minor peaks at ca. 320 and 370 Ma, and a subordinate cluster between 520 and 680 Ma (Fig. 21). The youngest grain is subhedral and has a concordant $^{206}Pb/^{238}U$ age of 311 ± 11 Ma, thus giving a maximum age of deposition for this rock and hence for the Examili Formation. The two oldest ages are from xenocrysts with $^{207}Pb/^{206}Pb$ ages of 1886 ± 9 Ma and 3012 ± 10 Ma, respectively. The presence of a Palaeoproterozoic (1800–2200 Ma) source is also demonstrated by few discordant grains that probably suffered radiogenic lead loss. Lead loss in zircons is a common phenomenon and mostly attributed to metamictisation and later recrystallisation during which Pb is removed from the zircon crystals (Williams 1992; Mezger & Krogstad 1997).

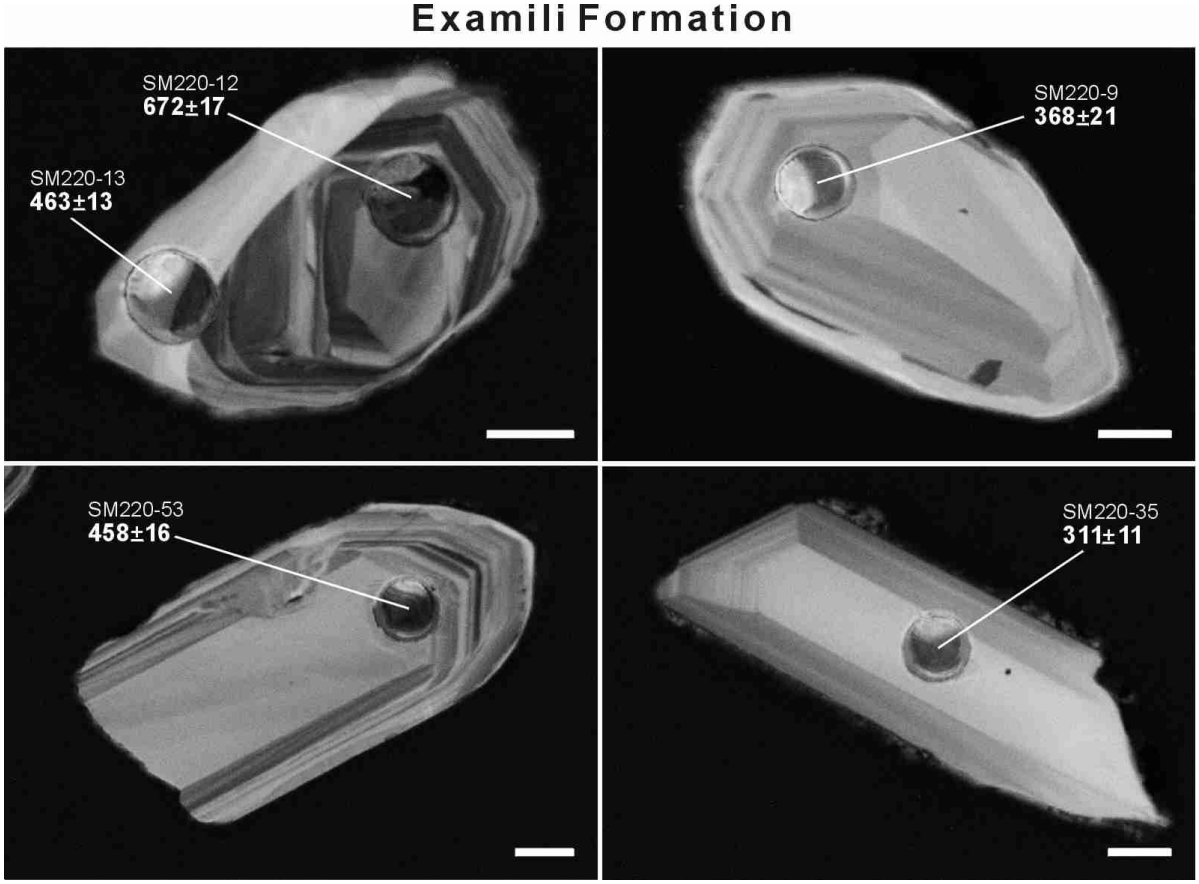

Fig. 20. CL images of representative zircon grains from analysed sample SM220 of the Examili Formation with location of the LA-ICPMS analysis spot and corresponding $^{206}U/^{238}Pb$ age (±2σ). Letter–number code above the ages: sample-spot. The scale bar represents 30 μm in all images.

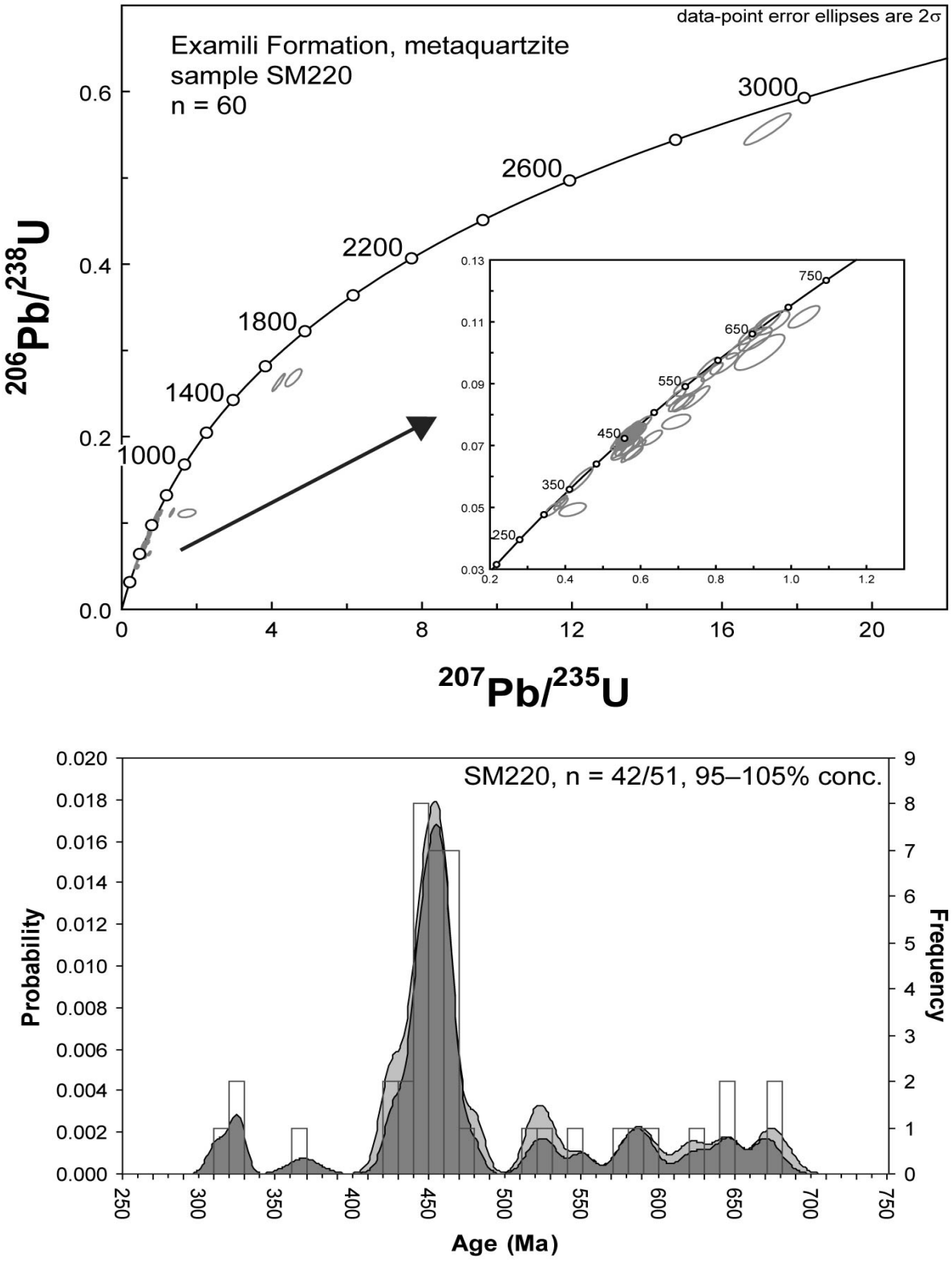

Fig. 21. Concordia diagrams (*upper*) and combined probability density distribution and histogram plots (*lower*) for the set of U–Pb analytical zircon data of the Examili Formation. Error ellipses in concordia plots represent 2σ uncertainties. Probability plot: Dark grey shaded – zircon ages with 95–105% concordance, light grey shaded – zircon ages with >5 % discordance (see text for explanation). Abbreviation: n = number of analyses.

Melissochori Formation: Sample SM198 was collected from an outcrop along the road west of Paleokastro village (40°26´27.6´´N, 23°25´31.5´´E; Fig. 2). Sample SM198 is a quartzarenite consisting predominantly of single monoquartz, minor plagioclase (albite) and single muscovite flakes floating a matrix of fine grained quartz, sericite and calcite. Accessory minerals are zircon, rutile, apatite and pyrite. The pyrites are partly or totally replaced by hematite. The zircon crystals are predominantly clear colourless to slightly pinkish, subhedral to rounded; only a few are euhedral. The length of single zircon crystals varies between 90 and 190 µm. The majority of the analysed zircons of the Melissochori Formation have clear oscillatory zonation patterns in CL images and appear to be magmatic in origin (Fig. 22); only a few exhibit no zoning. Inherited cores are minor present.

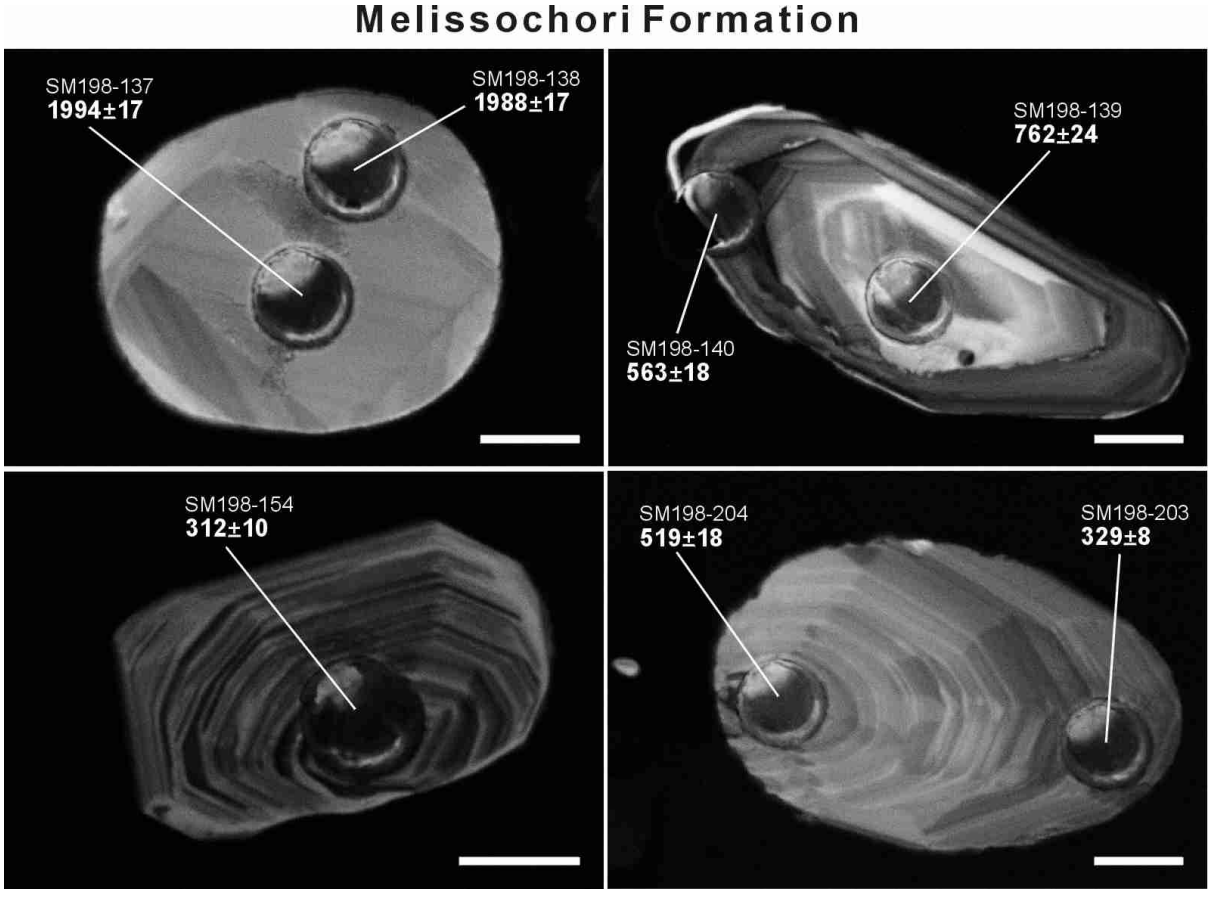

Fig. 22. CL images of representative zircon grains from analysed sample SM198 of the Melissochori Formation with location of the LA-ICPMS analysis spot and corresponding $^{206}U/^{238}Pb$ age (±2σ) for grains <1.2 Ga and $^{207}Pb/^{206}Pb$ ages (±2σ) for grains >1.2 Ga, respectively. Letter–number code above the ages: sample-spot. The scale bar represents 30 µm in all images.

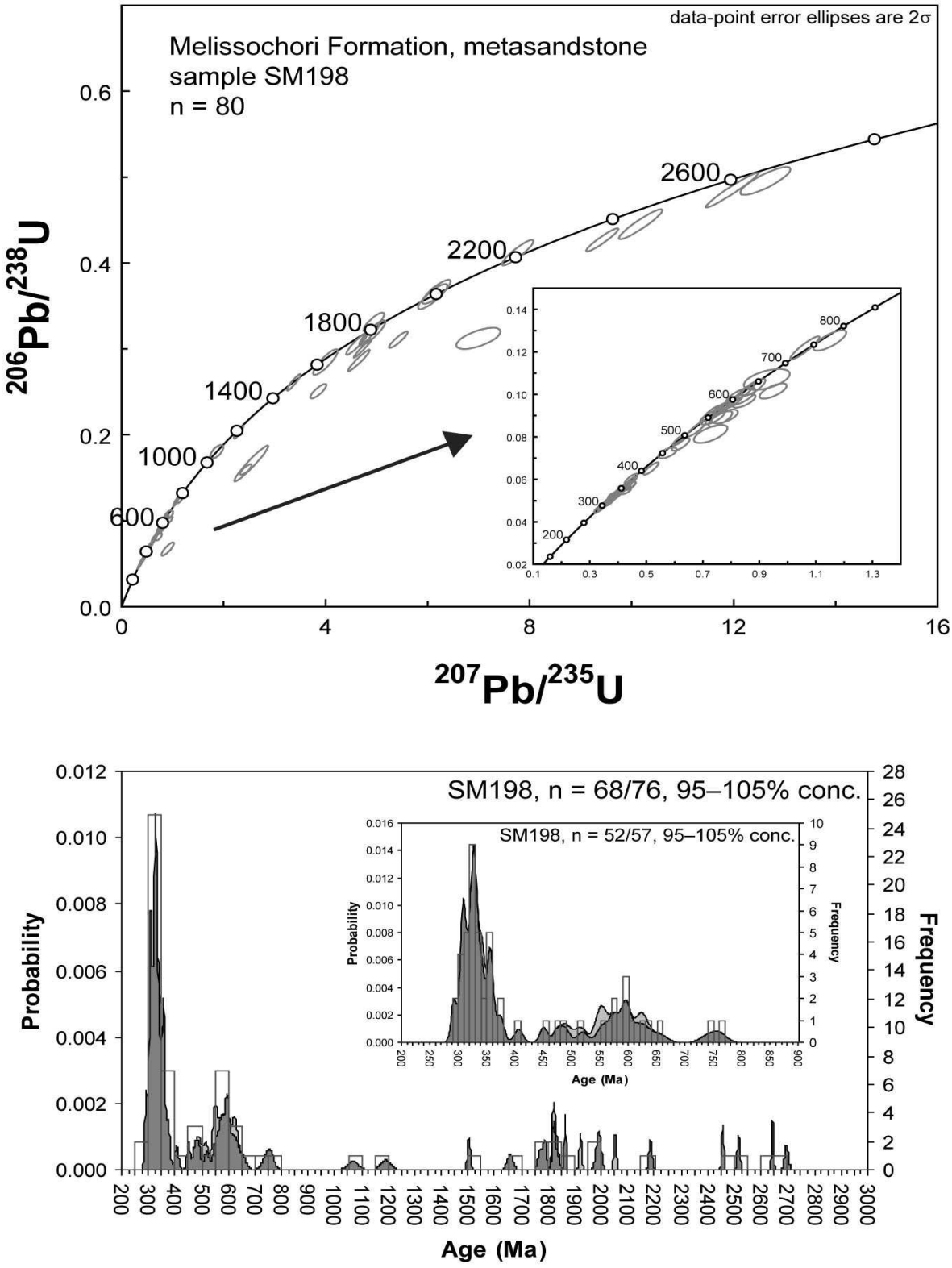

Fig. 23. Concordia diagrams (*upper*) and combined probability density distribution and histogram plots (*lower*) for the set of U–Pb analytical zircon data of the Melissochori Formation. Error ellipses in concordia plots represent 2σ uncertainties. 1.2 Ga limit is used to switch between $^{206}Pb/^{238}U$ and $^{207}Pb/^{206}Pb$ ages for the probability and histogram plots. Dark grey shaded – zircon ages with 95–105% concordance, light grey shaded – zircon ages with >5 % discordance (see text for explanation). Abbreviation: n = number of analyses.

The concordance-filtered zircon ages of 80 analyses on 63 single grains show a polymodal age distribution with a prominent cluster at ca. 290–370 Ma, and subordinate clusters at ca. 450–520, 545–655 Ma and 1780–2100 Ma. Few single Mesoproterozoic, Early Palaeoproterozoic and Late Archaean ages are also present (Fig. 23). The youngest grain is subhedral and has a concordant $^{206}Pb/^{238}U$ age of 291 ± 10 Ma, thus giving a maximum age of deposition for this rock and hence for the Melissochori Formation. The presence of a Palaeoproterozoic (1800–2200 Ma) source is also demonstrated by few discordant grains that probably suffered radiogenic lead loss. The oldest grain is rounded and has a $^{207}Pb/^{206}Pb$ age of 2696 ± 14 Ma. It is noteworthy that one grain has an inherited core with a highly discordant outer rim of around 419 Ma. In a concordia diagram a regression of the core and the rim yields a discordia with a lower intercept at 128 ± 45 Ma and an upper intercept at 1873 ± 13 Ma (not shown). In effect, lower-intercept ages do not necessarily have a geological meaning and should therefore be handled with care (Mezger & Krogstad 1997). In this case, however, the lower intercept of the zircon rim at 128 ± 45 Ma may indicate the time of lead loss due to metamorphic overprint. The upper intercept reflects the time of primary zircon crystallisation, and is interpreted as the age of formation of the magmatic protolith that survived as the inherited core.

Prinochori Formation: Sample SM181 was collected in a canyon north of Prinochori village (40°24´00.3´´N, 23°11´35.3´´E; Fig. 8). Sample SM181 is a litharenite consisting of quartz and minor plagioclase (albite) and white mica in a matrix of clay minerals, chlorite, and calcite. Accessory minerals are zircon, rutile, apatite, Fe-oxides and chrome spinel. The zircons crystals are predominantly rounded to well rounded, some are subhedral or euhedral. Most of them are clear colourless to slightly pinkish; only a few are cloudy. The length of single zircon crystals varies between 90 and 210 µm. The majority of the analysed zircons of the Prinochori Formation have clear oscillatory zonation patterns in CL images and appear to be magmatic in origin (Fig. 24); few exhibit no zoning or patchy zoning. Inherited cores are minor present. The concordance-filtered zircon ages of 79 analyses on 64 single grains show a polymodal age distribution with prominent clusters at ca. 425–465, 540–700, 750–1050 and 1800–2100 Ma, and minor peaks at ca. 1450, 2535, 2610 and 2975 Ma (Fig. 25). The latter peaks, however, are based on a very limited number of analyses only and stand out because of the relatively small errors in their $^{207}Pb/^{206}Pb$ ratios. The youngest grain is euhedral to

subhedral and has a concordant $^{206}Pb/^{238}U$ age of 258 ± 9 Ma, thus giving a maximum age of deposition for this rock and hence for the Prinochori Formation. Few discordant grains that probably suffered radiogenic lead loss also demonstrate the presence of Neoproterozoic (580–900 Ma) and Palaeoproterozoic (1950–2300 Ma) sources. The oldest grain is rounded and has a $^{207}Pb/^{206}Pb$ age of 2974 ± 15 Ma.

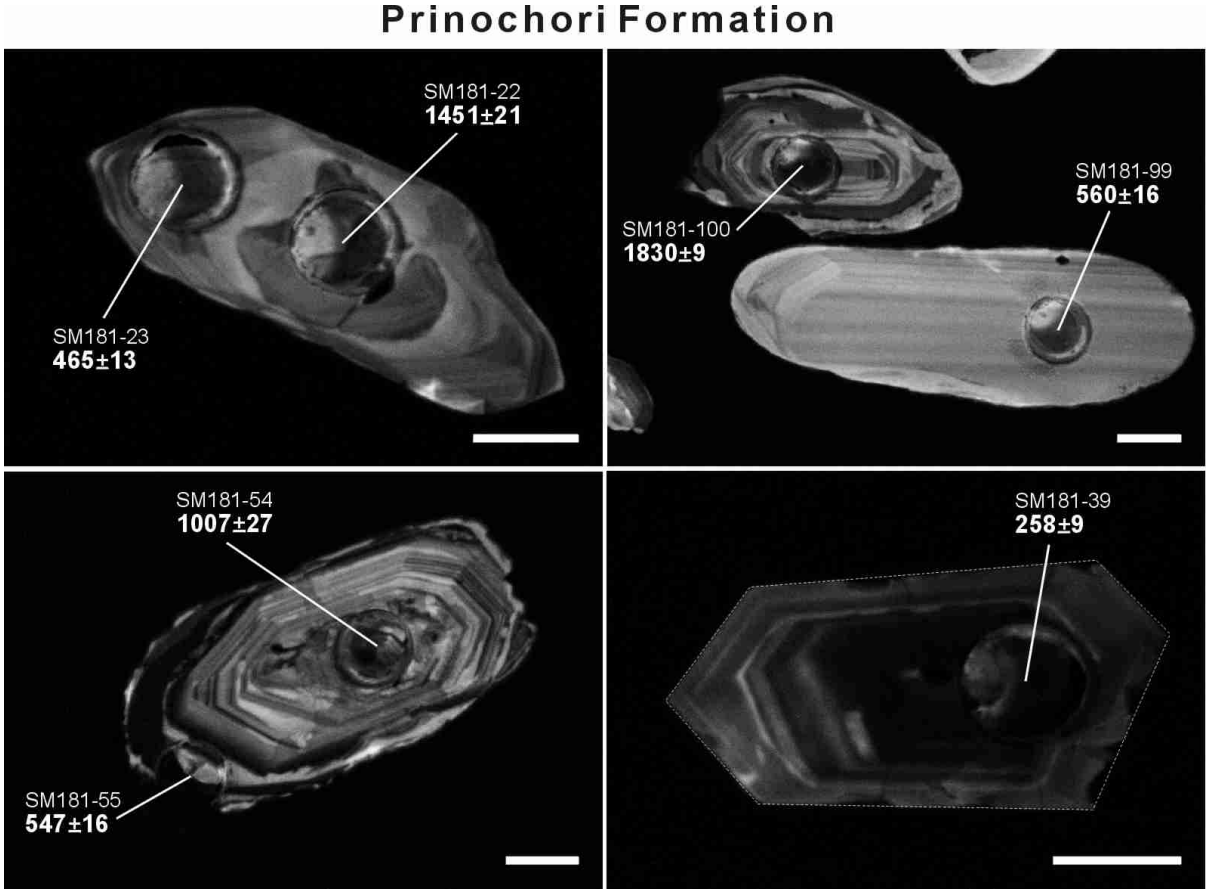

Fig. 24. CL images of representative zircon grains from analysed sample SM181 of the Prinochori Formation with location of the LA-ICPMS analysis spot and corresponding $^{206}U/^{238}Pb$ age (±2σ) for grains <1.2 Ga and $^{207}Pb/^{206}Pb$ age (±2σ) for grains >1.2 Ga, respectively. Letter–number code above the ages: sample-spot. The scale bar represents 30 μm in all images.

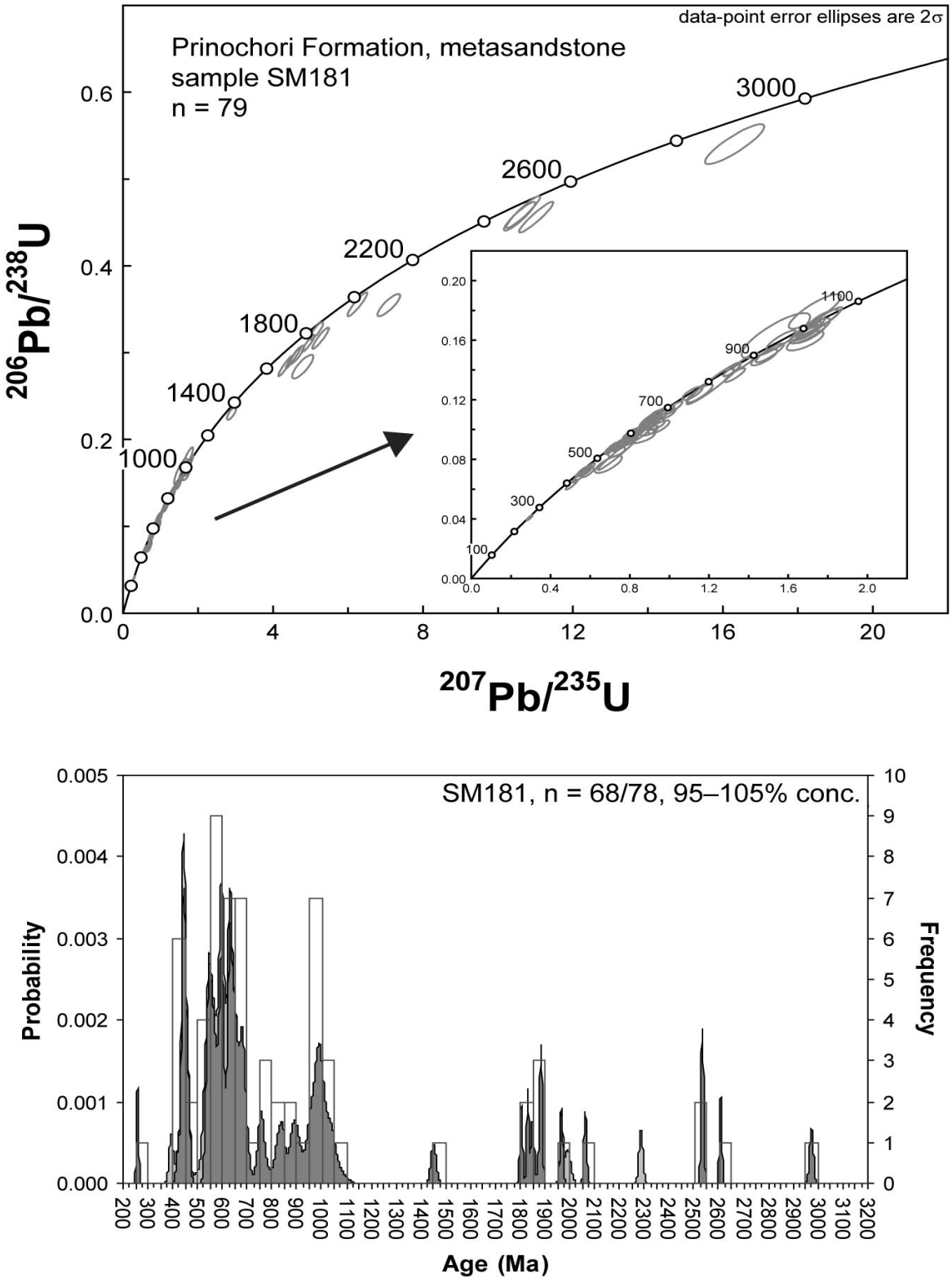

Fig. 25. Concordia diagrams (*upper*) and combined probability density distribution and histogram plots (*lower*) for the set of U–Pb analytical zircon data of the Prinochori Formation. Error ellipses in concordia plots represent 2σ uncertainties. 1.2 Ga limit is used to switch between $^{206}Pb/^{238}U$ and $^{207}Pb/^{206}Pb$ ages for the probability and histogram plot. Dark grey shaded – zircon ages with 95–105% concordance, light grey shaded – zircon ages with >5 % discordance (see text for explanation). Abbreviation: n = number of analyses.

4.4. Biostratigraphy

Samples SM160 and SM164 collected from the Melissochori Formation and prepared for a palynological study gave no results because of the absence of useful organic material. Sample SM224 collected from the Svoula Limestone west of Pirghoto village and disolved in acetic acid yielded several echinoid spines which are unfortunately of only low stratigraphic significance. Echinoid spines have already been described by Kockel et al. (1977) from calcareous rocks NNE of Mesio village for which a Middle Triassic age was suggested. Samples SM176 and SM176b come from the Neochorouda Unit and were collected at the northern side of the gorge NE of Neochorouda village. The conglomeratic calcareous succession there unconformably overlies pillow lavas and gabbros of the Oreokastro Ophiolite Complex (Fig. 11a). In sample SM176 *Trocholina* sp. could be indentified. *Trocholina* ranges from Triassic (Norian) to Cenomanian with only one species in the Triassic and all others from the Bajocian to the Cenomanian. Sample SM176b is a limestone block of about 20 cm in diameter (Fig. 26) with colonies of dasycladacea algae *Neoteutloporella socialis* (= *Teutloporella socialis* Praturlon). Bassoullet et al. (1978) and De Castro (1993) gave a detailed illustrated account of the genus and its assigned species, supported by extensive bibliography. *Neoteutloporella* is common in Upper Jurassic (Tithonian: Sartorio & Venturini 1988) shallow marine carbonates of the Tethyan realm and can be found occasionally relatively often. The limestone block is interpreted by us to be an olistolith derived from an Upper Jurassic carbonate platform and deposited in a slightly younger conglomeratic calcareous succession, which is represented by the Neochorouda Unit. The remaining two samples come from a calcareous clastic sedimentary succession cropping out between the Oreokastro Ophiolite Complex to the west and the Triassic limestones to the east (Figs. 10, 11b). All previous workers (e.g. Kockel & Mollat 1977; Ricou et al. 1998) assigned this narrow stripe of sedimentary rocks to the Melissochori Formation. At the sampling locations SM177 and SM228b the sedimentary succession comprises greyish fossiliferous wackestones and packstones intercalated with calcareous siltstone, sandstone and marls. The thickness of distinct beds varies between 2 and 35 cm. The whole succession is virtually unmetamorphosed. Only sample SM228b yielded a determinable fossil assemblage. This sample contains besides a macrofauna of gastropods and crinoids also a microfauna assemblage of *Ovalveolina* sp., *Pseudonummuloculina* sp., and dasycladacea

algae of genus *Thaumatoporella* sp. (Fig. 27). *Ovalveolina* and *Pseudonummuloculina* range from Albian to Cenomanian. *Thaumatoporellales* are widespread in Mesozoic (Upper Triassic onwards) carbonate platform facies (Barattolo 1991), and extends to the Paleocene (De Castro 1990). The genus *Thaumatoporella* is especially common in Liassic platform carbonates of the southern Tethys (Santorio & Venturini 1988; BouDagher-Fadel et al. 2001), notably, for example, the Pantokrator Limestones of Corfu in western Greece (Flügel 1983).

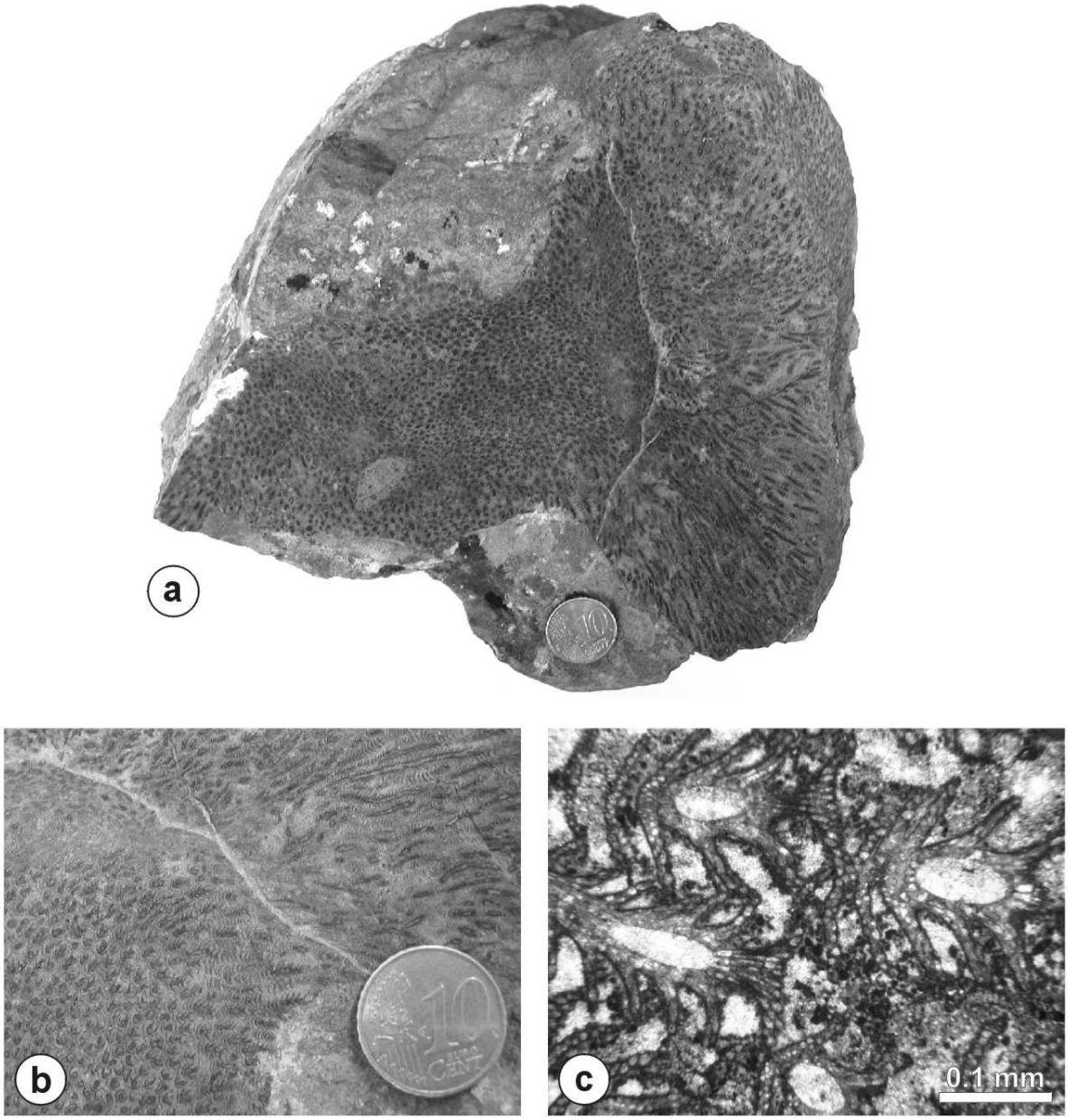

Fig. 26. Dasycladacea algae *Neoteutloporella socialis* (= *Teutloporella socialis* Praturlon) from the Neochorouda Unit northeast of Neochorouda village (sample SM176b). Sampling location is shown in Figure 10. **(a)** Limestone lens. **(b)** Macroscopic view on surface. **(c)** Photomicrograph of thin section.

Nonetheless, the occurrence of *Ovalveolina* sp. and *Pseudonummuloculina* sp. in the carbonaceous matrix of sample SM228b clearly indicates an Albian to Cenomanian age for the virtually unmetamorphosed calcareous clastic sedimentary succession investigated NW of Oreokastro town.

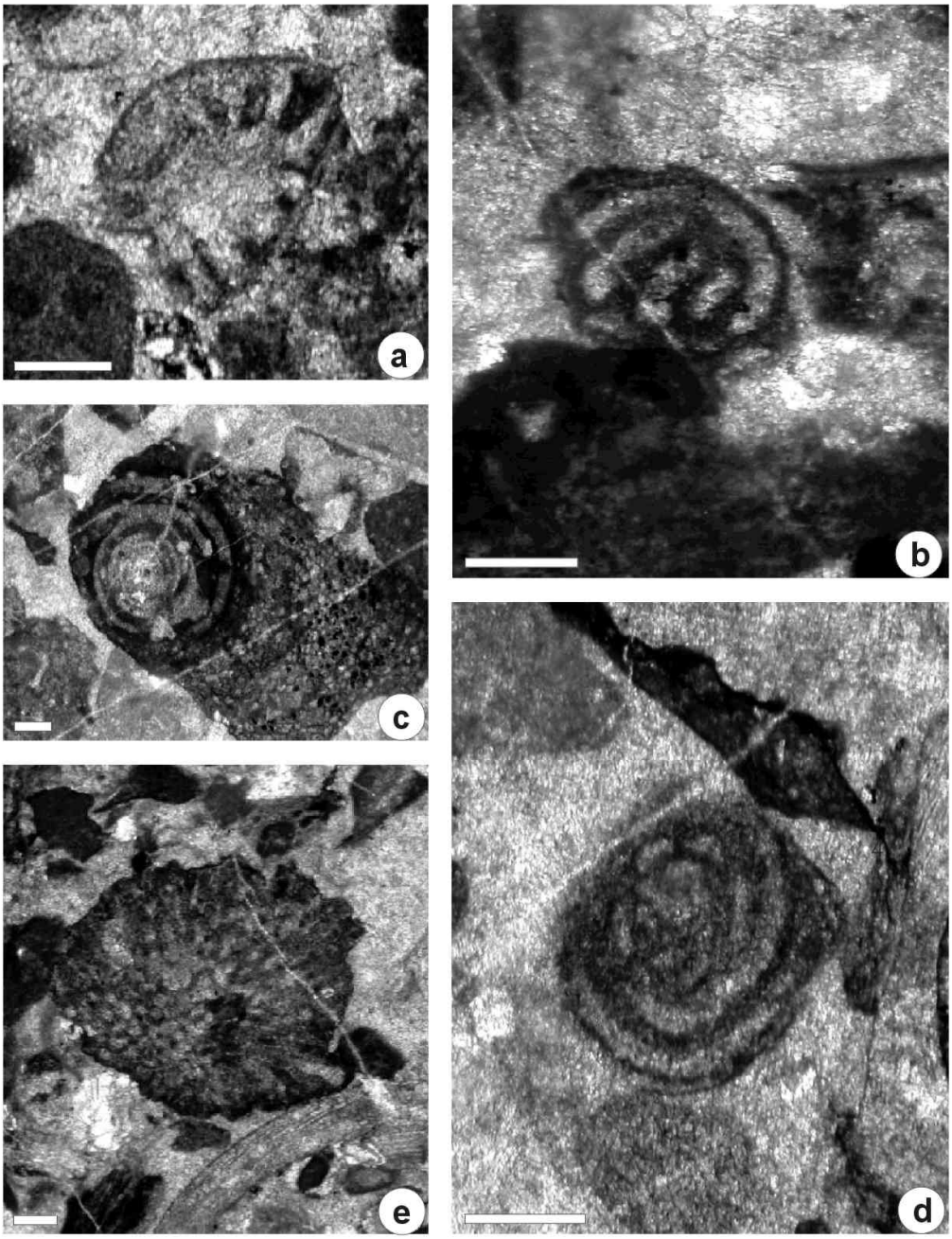

Fig. 27. Fossil assemblage from the calcareous clastic successions northwest of Oreokastro town. Scale bars equal 0.2 mm. Sampling location is shown in Figure 10. **(a)** *Trocholina* sp., sample SM176. **(b & d)** *Pseudonummuloculina* sp., sample SM228b. **(c)** *Ovalveolina* sp. encrusted on *Thaumatoporella* sp., sample SM228b. **(e)** *Thaumatoporella* sp., sample SM228b.

5. Discussion and conclusions

5.1. Examili Formation

The sedimentary rocks of the Examili Formation are predominantly composed in high amounts of quartz and in varying amounts of K-feldspar. This combined with the whole-rock geochemical signature suggest that the Examili Formation is dominated by material of acidic igneous origin (e.g. granite, syenite or equivalents) deposited on a passive margin. The enrichment of quartz, the varying amounts of K-feldspar and the depletion or absence of plagioclase and absence of biotite can be explained by weathering, transport, and sedimentation. This is also expressed in depleted multi-element and REE patterns. The rocks of the Examili Formation are heavily tectonized in many places that may have caused fluid circulation and disturbance of the primary whole-rock geochemical signature due to fractionation and mobilisation of some major and trace elements.

The prominent cluster of detrital zircon ages at ca. 420–480 Ma suggests significant input of Ordovician and Silurian magmatic rocks. Similar ages have been reported as protolith ages for the underlying orthogneisses of the Vertiskos Unit (Himmerkus et al. 2006a, 2007, submitted; Chapter 4 of this thesis). Therefore, it seems plausible to assume that orthogneisses of the Vertiskos Unit or equivalent rocks contributed significant amounts of detritus to the sedimentary rocks of the Examili Formation. A minor source is indicated by the presence of ca. 520–680 Ma-old detrital zircons. They could have been derived from clastic metasedimentary rocks of the Vertiskos Unit since these rocks contain a prominent cluster of zircon ages between 550 and 800 Ma (Chapter 4 of this thesis). Furthermore, these rocks could have supplied the few >1.8 Ga-old detitral zircons, which probably represent recycled zircons, rather than having directly been derived from Palaeoproterozoic or Archaean rocks. Another possible source for ca. 520–680 Ma-old detrital zircons could have been the orthogneisses and metaquartzites of the Pirgadikia Unit (Himmerkus et al. 2006a, 2007; Chapter 4 of this thesis), which forms tectonic inliers within the Circum-Rhodope Belt. The metaquartzites of the Pirgadikia Unit, however, also contain ca. 1–1.2 and 1.5 Ga-old detrital zircons, which are absent in the Examili Formation. Another source, but more far to the North, may have possible been the Pan-African basement rocks from western Bulgaria (ca. 544–569 Ma, U–Pb on zircon: von Quadt et al. 2000; Graf 2001; Kounov 2002). Zircon

fission-track ages from Pan-African basement rocks of the Struma Unit, for instance, indicate that the rocks were cooled below ca. 260 °C in late Carboniferous to early Permian times and exhumed to the surface before they were covered by Permian and Triassic sedimentary successions (Kounov 2002). It is noteworthy that Pan-African ages could have also been derived (but in minor amounts) from Ordovician meta-igneous rocks since one zircon grain was found yielding concordant ages of 672 ± 17 Ma for the inherited core and 463 ± 13 Ma for the magmatic rim (Fig. 20). This grain shows the involvement of a Pan-African crustal source during Ordovician magma genesis. The Carboniferous detrital zircons, which were found in the Examili Formation (ca. 311–327 Ma in sample SM220), could have been derived from basement rocks of the Pelagonian Zone (including the Attic-Cycladic Massif), from Sakarya or the Lower Tectonic Unit of the Rhodope Massif since Carboniferous ages of that range are documented for magmatic basement rocks from these areas (see Fig. 9 in Chapter 3 of this thesis). Dimitriadis & Asvesta (1993) mentioned NE to SW direction of sediment transport (present-day orientation) that would exclude supply of Carboniferous zircons from the Pelagonian Zone but points to material of pre-Permian basement rocks from northeastern Greece and Bulgaria.

The stratigraphic age of the Examili Formation is generally thought to be of Permian to Early Triassic because of the time constraints imposed by the overlying Pirghoto Formation (e.g. Ferrière & Stais 1995). The contact to the latter, however, is always tectonic; one exception might be an outcrop west of Kato Potamia village (see Kockel et al. 1977). The youngest detrital zircon grain has a concordant $^{206}Pb/^{238}U$ age of 311 ± 6 Ma which constrains the maximum depositional age of the sedimentary rocks of the Examili Formation. Its minimum age of deposition is may constrained by the absence of detrital zircons with ages of ca. 222–241 Ma (Arnea suite: Himmerkus et al. 2004b, in preparation) since the country rocks of the Arnea suite supplied significant amounts of detritus to the sedimentary rocks of the Examili Formation. Keeping in mind both the geological frame and time necessary for uplift and erosion of plutonic rocks and that necessary for weathering, transport and abrasion, we propose that the sedimentary rocks of the Examili Formation are Permo–Triassic in age, as suggested by previous studies.

Hence, the Examili Formation represents a clastic sedimentary succession that was probably deposited in an intracontinental rift-related sedimentary basin in proximity to the Vertiskos Unit in the Permo–Triassic (Fig. 28). Because the latter is lacking Carboniferous

ages, a more distal source has also been subject of erosion, which supplied in minor amounts detrital zircons of Carboniferous ages. Following previous studies, volcano-sedimentary rocks of the Pirghoto Formation, including associated rift-related volcanic rocks, overlie the Examili Formation. The Arnea suite, which comprises predominantly A-type granitoids of Middle to early Late Triassic age (Himmerkus et al. 2004b, in preparation), may represents a plutonic counterpart to the rift-related volcanic rocks of the Pirghoto Formation.

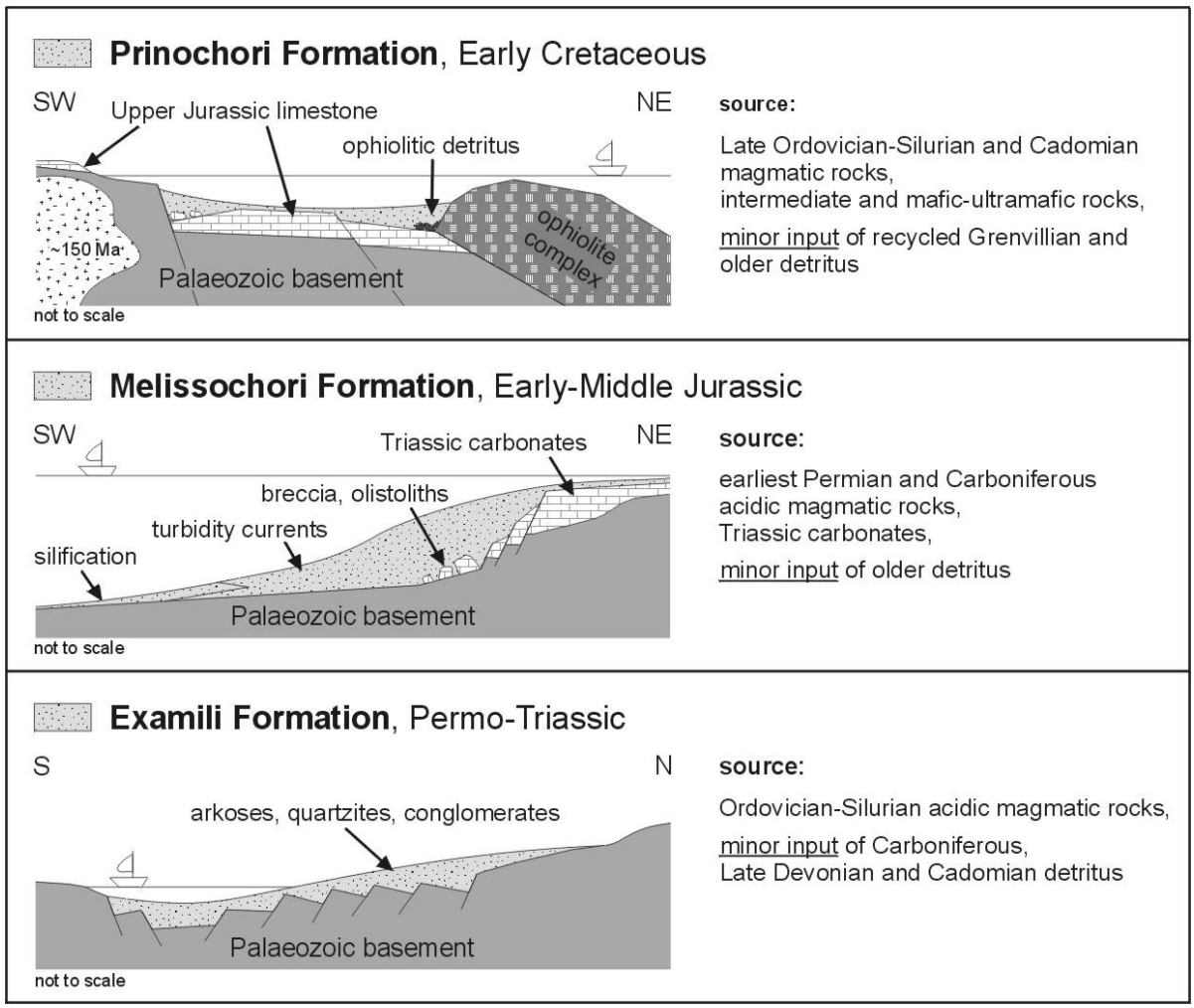

Fig. 28. Sketches illustrating palaeotectonic settings and source areas of the Examili, Melissochori and Prinochori Formations.

5.2. Melissochori Formation

The sedimentary rocks of the Melissochori Formation are predominantly composed of quartz, plagioclase, white mica and calcite. This combined with the whole-rock geochemical

signature suggest that the Melissochori Formation is dominated by material of acidic igneous origin (e.g. granite or equivalents) and carbonates. The latter may have been limestones derived from a carbonate platform.

The prominent cluster of detrital zircon ages at ca. 290–370 Ma suggests significant input of Permo-Carboniferous to Middle Devonian magmatic rocks. Early Permian and Carboniferous ages are well documented from basement rocks of the Pelagonian Zone (including the Attic-Cycladic Massif), Sakarya and the Lower Tectonic Unit of the Rhodope Massif (see Fig. 9 in Chapter 3 of this thesis). The only well documented Middle Devonian protolith ages so far are single-zircon evaporation $^{207}Pb/^{206}Pb$ ages of ca. 372 Ma obtained from granitic-granodioritic gneisses cropping out in the northern part of the Biga peninsula close to the Sea of Marmara and in the south near Edremit town (Özmen & Reischmann 1999). Basement rocks with Middle–Late Devonian protolith ages were probably exposed in larger amounts at the surface in Late Palaeozoic–Early Mesozoic times and were subject to erosion since detrital zircons of ca. 370 Ma were also reported from a Permo-Triassic sandstone of Chios Island (Meinhold et al. 2006; Chapter 3 of this thesis). The cluster of detrital zircons at ca. 450–520 Ma comprises only few single grains and is therefore of less significance only. Ordovician zircon ages were recently documented from orthogneisses of the Vertiskos Unit. This unit, however, also comprises in significant amounts magmatic zircons, with ages between 410 and 450 Ma (Himmerkus et al. 2006a, 2007, submitted; Chapter 4 of this thesis), which are absent in sample SM198 of Melissochori Formation. Therefore, it seems plausible to assume that orthogneisses of the Vertiskos Unit were either never present or not yet exposed in the source area. The clusters of detrital zircon ages at ca. 545–655 Ma and 1780–2100 Ma, and the occurrences of three concordant ages at ca. 1060, 1200 and 1500 Ma suggest that the Melissochori Formation is also dominated by material from the Pirgadikia Unit or equivalents since such ages constitute the major component in this unit (see Himmerkus et al. 2006a, 2007; Chapter 4 of this thesis). Taking collectively petrography, whole-rock geochemistry and zircon geochronology, the Melissochori Formation was deposited in front of a Variscan basement unit of volcanic-arc origin with minor input of older basement rocks, probably at the slope of a carbonate platform (Fig. 28). Limestone breccias and olistoliths such as those described by Kockel et al. (1977) are suggestive of an unstable slope setting that was probably tectonically controlled.

The stratigraphic age of the Melissochori Formation is generally accepted of being Early–Middle Jurassic (e.g. Kockel et al. 1977) or Late Triassic–early Late Jurassic (e.g. Dimitriadis & Asvesta 1993), although biostratigraphic data are very scarce. The youngest detrital zircon grain has a concordant $^{206}Pb/^{238}U$ age of 291 ± 10 Ma, which limits the maximum depositional age of the sedimentary rock of the Melissochori Formation. Keeping in mind the geological frame, a Permo–Triassic might be plausible, as proposed by Mercier (1968) and Kockel et al. (1971). Furthermore, Dixon & Dimitriadis (1984), following Kockel et al. (1971, 1977), considered that the Melissochori Formation can be traced well into the Serbo-Macedonian Massif in the southeast where the rocks have been overprinted by the same deformation and metamorphism. Kockel et al. (1977) and De Wet et al. (1989) emphasised that the Arnea granite intruded the metasedimentary rocks. If so, this would imply that metasedimentary rocks of the Melissochori Formation are older than late Middle Triassic since Himmerkus et al. (2004b, in preparation) reported $^{207}Pb/^{206}Pb$ single-zircon evaporation ages of ca. 222–241 Ma as the time of intrusion for the Arnea suite. This would constrain a Permo–Triassic age for the Melissochori Formation (see above). However, as already emphasised at the beginning (Chapter 2.3. of this study), the metasedimentary rocks in the southeast do not belong to the Melissochori Formation. They are assigned to a mélange zone, forming the border between the Vertiskos Terrane and the Kerdilion Terrane (see Himmerkus et al. 2006a, 2007).

The Melissochori Formation is most probably younger than Permo–Triassic, as suggested by few biostratigraphic data (e.g. Kauffmann et al. 1976; Kockel et al. 1977). At the present state of knowledge, however, it is not possible to give a more precise age than Early–Middle Jurassic (e.g. Kockel et al. 1977) or Late Triassic–early Late Jurassic (e.g. Dimitriadis & Asvesta 1993). The unconformably overlying Neochorouda Unit that is accepted to be Late Jurassic to earliest Cretaceous (e.g. Mercier 1968; Kockel et al. 1977) gives the maximum age of deposition. Furthermore, the rocks of the Melissochori Formation experienced metamorphism probably as old as Cretaceous since a zircon core–rim pair yielded a lower intercept age of ca. 128 ± 45 Ma (this study), which is interpreted as the time of lead loss due to metamorphic overprint after deposition of the zircon grain.

5.3. Prinochori Formation

The sedimentary rocks of the Prinochori Formation are predominantly composed of quartz, plagioclase, biotite, white mica and minor calcite. Chrome spinel is a major accessory phase. This combined with the whole-rock geochemical signature suggest that the Prinochori Formation is dominated by material of intermediate and pronounced basic and ultrabasic origin, presumably granodiorites or equivalents and ophiolitic rocks. The ophiolitic source can be specified by detrital chrome spinel chemistry, being a mixed source of highly depleted peridotites of mainly harzburgite and minor lherzolite composition. Most of the detrital chrome spinels were derived from MOR-type peridotites and supra-subduction zone (SSZ) peridotites, whereas only a small fraction points to volcanic rocks, presumably island-arc basalts and MORB-type rocks. Because of the geological frame, it seems plausible to assume supply of chrome spinels from the adjacent eastern Vardar ophiolites. The peridotites are of mainly harzburgite composition (e.g. Mussallam et al. 1981; Christofides et al. 1994), and most of the basic rocks were formed in an intraoceanic subduction zone environment or in an island-arc setting (e.g. Zachariadis 2007, and references therein). However, keeping large scale thrust tectonics and transcurrent movements in mind, the ultrabasic source might be also located somewhere else in the Vardar Zone.

The prominent cluster of detrital zircon ages at ca. 425–465 Ma suggests significant input of Silurian to Middle Ordovician magmatic rocks. The closest source is the Vertiskos Unit, which comprises orthogneisses of granodioritic to granitic composition with protolith ages between 410 and 480 Ma (Himmerkus et al. 2006a, 2007, submitted; Chapter 4 of this thesis). The age cluster between ca. 540–700 Ma exhibits peaks at ca. 550, 595, 630, and 680 Ma. This combined with the occurrences of prominent clusters at ca. 750–1050 and 1800–2100 Ma, and minor peaks at ca. 1450, 2535, 2610 and 2975 Ma suggest sediment supply from the Pirgadikia Unit or equivalents since the latter is characterised by such age spectra (see Himmerkus et al. 2006a, 2007; Chapter 4 of this thesis). Clastic metasedimentary rocks of the Vertiskos Unit may also have contributed detritus in larger amounts, the exception being ages at ca. 1.5 Ga, which are absent in these rocks (see Chapter 4 of this thesis). It is noteworthy that detrital zircons with Permo-Carboniferous ages are totally absent in the Prinochori Formation. Rocks of such ages were either never present or still at considerable depth in the source area. They may build the basement on which the Jurassic carbonate

platform was formed. Later, the basement rocks were overprinted by a magmatic/ metamorphic event in the Late Jurassic, indicated by K–Ar biotite ages of ca. 150 Ma (Kreuzer in Mussallam & Jung 1986).

The youngest detrital zircon grain reported from the Prinochori Formation has a concordant $^{206}Pb/^{238}U$ age of 258 ± 9 Ma, which gives the maximum depositional age for the sedimentary rock of the Prinochori Formation. Nonetheless, a Triassic age seems not realistic since the Prinochori Formation is generally accepted to be latest Jurassic–earliest Cretaceous because of the time constraints imposed by the underlying fossiliferous Petralona limestone (e.g. Kockel et al. 1977). At the present state of knowledge, we suggest that the Prinochori Formation is Early Cretaceous in age, whereas an younger age cannot be excluded insofar as no further geochronological or biostratigraphic data are available.

5.4. Oreokastro area

In the Oreokastra area, the study focused on two main sedimentary successions. One is the Neochorouda Unit; the other is the virtually unmetamorphosed calcareous clastic sedimentary succession cropping out in a narrow stripe NW of Oreokastro town.

The Neochorouda Unit is a conglomeratic calcareous succession unconformably overlying pillow lavas and gabbros of the Oreokastro Ophiolite Complex and therefore postdates the ages of intrusion and obduction of the Oreokastro Ophiolite Complex. Based on previous (e.g. Mercier 1968; Kockel et al. 1977) and our own biostratigraphic data, the Neochorouda Unit is younger than Late Jurassic, presumably earliest Cretaceous in age. De Wet et al. (1989) emphasised that the Neochorouda Unit was deformed and metamorphosed in the Early Cretaceous and is itself involved in thrust tectonics.

Furthermore, the new biostratigraphic data from the Oreokastro area clearly indicate that a part of the sedimentary succession in the area north of Oreokastro town, formerly seen by previous workers as belonging to the Melissochori Formation (e.g. Kockel & Mollat 1977; Ferrière & Stais 1995; Ricou et al. 1998), represents an individual formation of latest Early Cretaceous to earliest Late Cretaceous age. This, however, does not mean that we assign a Cretaceous age to the entire Melissochori Formation. We propose here that at least a part of the stripe between the Oreokastro Ophiolite Complex to the west and the Triassic limestones to the east belongs to a virtually unmetamorphosed calcareous clastic sedimentary succession

of Albian–Cenomanian age that was deposited in a shallow marine environment on a carbonate platform. The described succession is named here Oreokastro Formation. We like to note that it might be possible that the Oreokastro Formation represents the stratigraphic younger part of the Neochorouda Unit. Nonetheless, our new data clearly show that previous stratigraphic concepts for the Oreokastro area, proposing a continous stratigraphy from the Permo-Carboniferous to the Jurassic (e.g. Ferrière & Stais 1995), have to be revised. Ricou et al. (1998) assigned the sedimentary stripe north of Oreokastro town, including the Oreokastro Formation, to the Melissochori Formation. Based on field observations and mapping, the fossil-bearing Triassic limestones were considered by them as blocks floating in the Melissochori Formation. In general, we agree to the concept that olistostromes are present in the study area; at the present state of our knowledge, however, we do not correlate the Oreokastro Formation with the Melissochori Formation, meaning we do not assign a Cretaceous age to the entire Melissochori Formation. If the latter would be Cretaceous in age, it could be expected that numerous detrital zircons with post-Early Permian ages, for example, derived from the Pirghoto Formation and from the Middle–Late Jurassic acidic to basic magmatic complexes, should be present in Melissochori Formation since all these units are found as tectonic slivers and blocks adjacent to the Melissochori Formation. Furthermore, detrital chrome spinel should also be present since ophiolite complexes were already obducted and subject of erosion since the latest Jurassic. However, as the results of this study show, detrital zircons of post-Early Permian age and chrome spinel grains are absent in the investigated samples from the Melissochori Formation, and hence most of the Melissochori Formation is probably older than Cretaceous. It appears that re-mapping of the Oreokastro area and in general, of the Circum-Rhodope Belt is necessary to clarify the tectonostratigraphy of the different units and their relation to each other since these areas are key localities to understand the Mesozoic history of the eastern Vardar Zone.

5.5. Palaeogeographic model

During the Permo-Triassic, rifting and extension became dominant at the southern margin of Laurussia, forming several intracontinental basins of which some merged later on into oceanic basins (e.g. Stampfli & Borel 2002; Stampfli et al. 2003, and references therein). The Examili Formation probably represents such a rift-related sedimentary succession that

was deposited in proximity to the Vertiskos Unit. Sediment supply from a more distal source is indicated by minor amounts of Carboniferous detrital zircons. Rifting processes continued with deposition of volcano-sedimentary rocks, including associated rift-related bimodal volcanic rocks (e.g. Dimitriadis & Asvesta 1993; Stais & Ferrière 1995), expressed by the Pirghoto Formation. The Arnea suite may represent a plutonic counterpart to the rift-related volcanic rocks of the Pirghoto Formation. In a more regional frame, Triassic rift-related magmatism is also known from the Pelagonian Zone (including the Attic-Cycladic Massif) (e.g. Anders et al. 2006b, and references therein) and is generally assigned to the formation of Neotethyan oceans (e.g. Stampfli & Borel 2002; Stampfli et al. 2003). Hence, Triassic rift-related magmatism in the eastern Vardar Zone probably marks the birth of a Neotethyan ocean in Greece. Fauna and facies of the Triassic limestones (Svoula Limestones) indicate predominantly shallow marine conditions, presumably on a carbonate platform. Locally, a deeper water facies occurred (outer margin or slope), documented by reddish limestones of Hallstatt type (Fig. 3). Later, the carbonate shelf was subsided, probably rift triggered. Basalt layers and pillow lava intercalating with dark limestones of Liassic age probably indicate the beginning of ocean floor formation within the subsided basin that may belong to the formation of the Vardar Ocean. It remains speculative if the Melissochori Formation was deposited at the same palaeomargin as the Triassic and Early Jurassic limestones since all contacts to the latter are tectonic. However, it is clear that the Melissochori Formation was deposited close to a hinterland with prominent Carboniferous rocks of volcanic-arc origin as well as some older basement rocks involved at the slope of a carbonate platform probably in the Early Jurassic. The presence of carbonate even in the very fine grained beds suggests that deposition took place above the calcite compensation depth (CCD). Limestone breccias and olistoliths such as described by Kockel et al. (1977) are suggestive of an unstable slope setting that was probably tectonically controlled. Brown & Robertson (2003, 2004) suggested a deposition at the rifted passive margin bordering the Serbo-Macedonian Massif to the southwest (in present coordinates). However, based on detrital zircon ages, the Melissochori Formation was deposited either close to Pelagonia or to the Thracia Terrane; the latter corresponds to the Lower Tectonic Unit of the Rhodope Massif (see Turpaud 2006). Kauffmann et al. (1976) and Kockel et al. (1977) described turbiditic sandstones and quartzites of the Melissochori Formation intercalating the chert-bearing sedimentary succession of the Aspro Vrisi Serie. The Melissochori Formation can be interpreted either as

time equivalent to the Aspro Vrisi Serie, which would than present the more distal facies to the Melissochori Formation, or the Melissochori Formation pass gradually upwards into the presumably younger Aspro Vrisi Serie. Pelitic sedimentary rocks and cherts in the Aspro Vrisi Serie suggest deeper water conditions. Some stratigraphic deeper parts of the Melissochori Formation show features of silification. Silicified beds and cherts of the Aspro Vrisi Chortiatis Unit are free of radiolaria, the exception being presumably one location near Monolofo village. Most of the cherts intercalated with the basic rocks have probably been produced by hydrothermal activity, which is quite common in back-arc basin settings. Hydrothermal activity commonly led to sulphide and iron exhalation into the ocean water that could explain the high amounts of pyrite (nowadays partly or totally replaced by hematite) found in the Melissochori Formation and in the Aspro Vrisi Serie.

As recorded in the ophiolite complexes of the eastern Vardar Zone, the Middle–Late Jurassic was dominated by intraoceanic subduction and back-arc basin spreading (e.g. Zachariadis 2007, and references therein). Later, parts of these Vardarian ophiolites were obducted that may explain the source for detrital chrome spinel found in sedimentary rocks of the Prinochori Formation. The Petralona limestone represents the underlying succession of the latter. Based on the occurrence of the stromatoporoid *Cladocoropsis* and the bauxite horizons (e.g. Kockel et al. 1977; Carras & Geogala 1988), the Petralona limestone is interpreted by us as facies equivalent to the *Cladocoropsis* Limestone found elsewhere on Pelagonia (e.g. Jacobshagen 1986). *Cladocoropsis* is generally attributed to a lagoonal-type facies (e.g. Flügel 1974; Turnsek et al. 1981). According to that and Carras & Geogala (1988), the Petralona limestone was deposited in a shallow marine, open lagoonal environment on a carbonate platform in the Late Jurassic, perhaps at the northeastern margin of Pelagonia or in close vicinity. The bauxite horizons, which were formed under subtropical climate, are evidence for sporadic sealevel decrease that might have been related to partly uplift above sealevel due to flexural bulge in the front part of nappe units that formed during Late Jurassic to Early Cretaceous thrusting (Eohellenic event *sensu lato*: Jacobshagen et al. 1976). Bauxites are characteristic in the Late Jurassic of the Pelagonian domain (Carras & Geogala 1988). Locally, the Early Cretaceous was probably characterised by mass-flow deposits with reefal debris related to synsedimentary tectonism. One example may represent the Neochorouda Unit. The Early Cretaceous limestone beds drilled in the Western Chalkidiki peninsula (Carras & Geogala 1988) may represent a time and facies equivalent to

the Neochorouda Unit. The Oreokastro Formation probably indicates Mid-Cretaceous transgression sealing the main thrusting. Later, all units have finally been affected by the Alpine orogeny (Mesohellenic and Neohellenic phases *sensu lato*: e.g. Jacobshagen et al. 1976) during the Late Cretaceous to Mid-Cenozoic collision of the African and European plates. The whole area was modified by dextral strike-slip tectonics, syntectonic magmatism (e.g. Sithonia granite) and large-scale block rotation (e.g. Ricou et al. 1998; Brun & Sokoutis 2007, and references therein) that complicate palinspastic reconstructions. Nowadays, the eastern Vardar zone is a complex imbricated belt formed by polyphase tectonism and metamorphism, comprising high-grade metamorphic rocks, Mesozoic sedimentary and volcanic rocks, and ophiolites.

Chapter 6

Geochemistry and provenance of metasedimentary rocks in the eastern Circum-Rhodope Belt, Thrace, NE Greece

Abstract

In northeastern Greece the mid-greenschist facies Makri Unit and the virtually unmetamorphosed Melia Formation belong to the eastern Circum-Rhodope Belt that forms the uppermost tectonostratigraphic unit of the Rhodope metamorphic nappe pile. Petrology and whole-rock geochemistry of metasedimentary rocks from the Makri Unit suggest a source of intermediate to acidic composition resembling upper continental crust and/or young differentiated arc material, with varying input from a calcareous component. U–Pb LA-ICPMS and SHRIMP-II analyses of detrital zircons gave predominantly age clusters at ca. 310–290 Ma and at ca. 240 Ma for igneous zircons, which may have been derived from basement rocks of the Pelagonian Zone (including the Attic-Cycladic Massif) or equivalent rocks. The youngest detrital zircon grain found so far indicates that the metasedimentary succession of the Makri Unit, or at least parts of it, cannot be older than Late Triassic. By contrast, the petrology and whole-rock geochemistry of metasedimentary rocks from the Melia Formation suggest a uniform source of intermediate to acidic composition, which was less affected by intracrustal differentiation processes. The detrital mineral assemblage of epidote, zoisite, garnet and phengitic mica points to metamorphic rocks being the major source of the clastic sedimentary succession of the Melia Formation. U–Pb LA-ICPMS and SHRIMP-II analyses of detrital zircons gave a prominent age cluster at ca. 315–285 Ma for igneous zircons. Inherited cores indicate the involvement of Pan-African and Late Ordovician–Early Silurian crustal sources during Late Carboniferous–Early Permian magma genesis. We suggest that the Melia Formation was deposited in Cretaceous times in front of a

metamorphic nappe pile with Rhodope affinities. The Makri Unit and the Melia Formation were derived from different sources and tectonically juxtaposed during Balkan and Alpine orogenic processes.

1. Introduction

The Internal Hellenides are an integral part of the Alpine-Himalayan orogenic belt in south-eastern Europe, consisting from west to east of the Pelagonian Zone (including the Attic-Cycladic Massif), the Vardar Zone, the Serbo-Macedonian Massif, and the Rhodope Massif (Fig. 1). Kauffmann et al. (1976) described a narrow arcuate belt of metasedimentary rocks bordering the Serbo-Macedonian-Massif to the west, continuing to Samothraki Island and tectonically overlying the Rhodope Massif mainly in the south and east as Circum-Rhodope Belt. Other workers also assigned basic and ultrabasic rocks from the Chalkidiki, Evros and Samothraki ophiolites to this belt (e.g. Biggazzi et al. 1989; Magganas et al. 1991; Magganas 2002). The Circum-Rhodope Belt is thought to continue to the northwest into the region of lake Doirani in SW Bulgaria and in the northeast into the Strandza zone of SE Bulgaria (e.g. Kauffmann et al. 1976; Bonev & Stampfli 2007, and references therein). Contradicting to previous workers, Ricou et al. (1998) rejected the concept of a Mesozoic Circum-Rhodope Belt, covering the Rhodope Massif. According to those authors, the rocks of the Circum-Rhodope Belt belong to two distinct greenschist-facies belts, and the cover sequences of the Rhodope cannot be older than Late Cretaceous. For distinction purposes, we use here the term western Circum-Rhodope Belt for the western belt (equivalent to the "western greenschists" of Ricou et al. 1998) and eastern Circum-Rhodope Belt for the eastern belt (equivalent to the "roof greenschists" of Ricou et al. 1998). This study focuses on the eastern Circum-Rhodope Belt in Greece that can be subdivided into at least two tectonostratigraphic units (e.g. von Braun 1993): the mid-greenschist facies Makri Unit and the tectonically overlying virtually unmetamorphosed Melia Formation (Fig. 2). The Makri Unit comprises a lower carbonate-siliciclastic series and an overlying upper greenschist series (von Braun, 1993), and is suggested to be Triassic to earliest Cretaceous (Berriasian) in age (Dimadis & Nikolov 1997). The Melia Formation comprises a clastic sequence of probably Early Cretaceous age (Dimadis & Nikolov 1997). Kauffmann et al. (1976) interpreted limestones and calcschists of the Makri Unit as facies equivalents to the Svoula limestone,

whereas shales and greywackes of the Melia Formation were considered by them to represent the Svoula flysch of the western Circum-Rhodope Belt. In contract, Pe-Piper & Piper (2002) noted that the Makri Unit resembles the Svoula flysch. Metasedimentary rocks of the Makri Unit and the Melia Formation have been correlated with metasedimentary successions of the Mandrica and Maglenica groups of SE Bulgaria (e.g. Papadopoulos et al. 1989; von Braun 1993; Bonev & Stampfli 2007, and references therein).

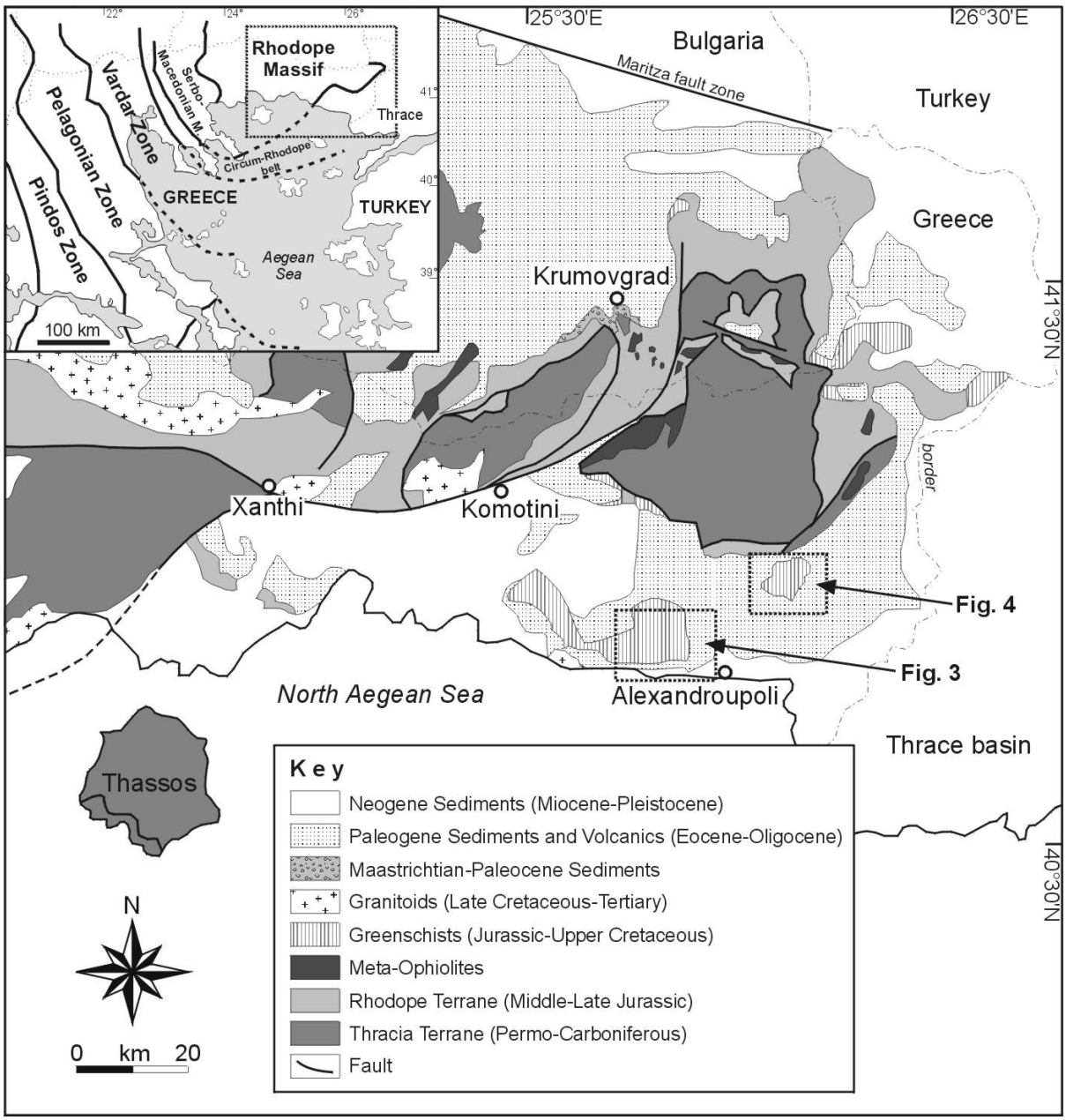

Fig. 1. Geological map of northeastern Greece (modified after Bonev et al. 2005). The inset (upper left) shows the major geotectonic zones of Greece (after Jacobshagen 1986). The locations of the study areas are indicated (see also Figs. 3 and 4).

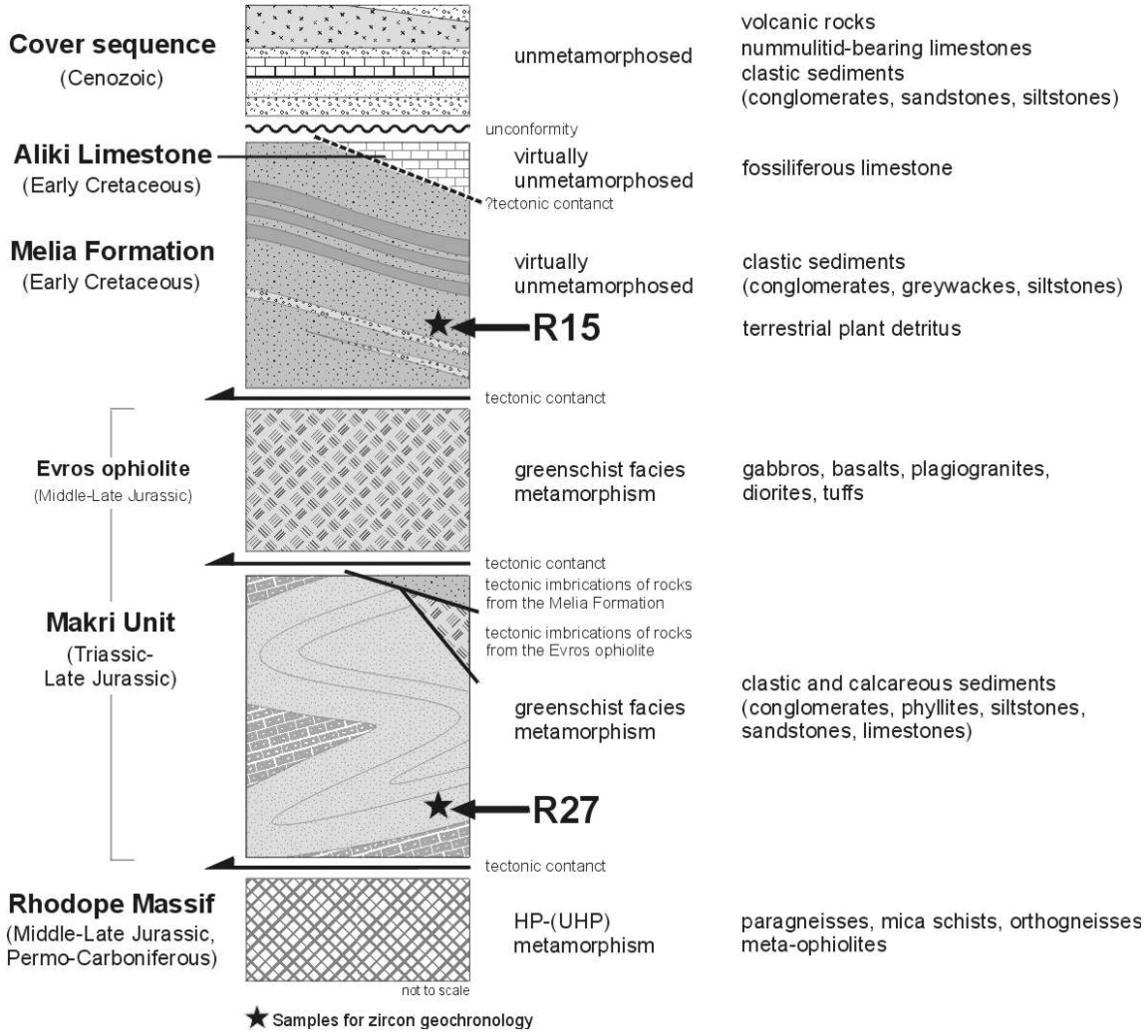

Fig. 2. Interpretative tectonostratigraphic column for the eastern Circum-Rhodope Belt compiled after data in von Braun (1993) and own field observations (this work).

Unconformably overlying Upper Cretaceous (Campanian) marine deposits (von Braun 1993) mark the upper time limit for the age of sedimentation and deformation of rocks from the eastern Circum-Rhodope Belt. Based on compilation of literature data, Pe-Piper & Piper (2002) concluded that the Makri Unit comprises Jurassic clastic sedimentary rocks and dismembered oceanic crust that have been thrust over the Upper Tectonic Unit of the Rhodope Massif. The Makri Unit was overthrusted by the Melia Formation, which includes deep-water sedimentary rocks and ophiolitic rocks, ranging in age from Early Jurassic to Middle Cretaceous (Pe-Piper & Piper 2002). Bonev & Stampfli (2003) recently interpreted the eastern Circum-Rhodope Belt as Late Jurassic–Early Cretaceous allochthonous subduction–accretion complex of Vardarian intraoceanic island-arc origin, which was strongly reworked by Cenozoic extensional and strike-slip tectonics.

All these equivocal interpretations clearly show the need to revisit the eastern Circum-Rhodope Belt. There are many uncertainties, especially the provenance and the depositional environment of metasedimentary successions of the Makri Unit and of the Melia Formation are still unknown, and their stratigraphic ages are still a matter of discussion. The age and origin of the rocks in the eastern Circum-Rhodope Belt, however, is important for palaeotectonic reconstructions of the northern Neotethyan realm. In order to reconstruct ancient source rock lithologies and tectonic settings, this study presents for the first time major- and trace-element composition of whole-rock samples, the chemical composition of detrital minerals, and U–Pb ages of detrital zircons. The latter were analysed by sensitive high-resolution ion-microprobe (SHRIMP-II) and laser ablation magnetic sector-field inductively-coupled plasma mass spectrometry (LA-ICPMS). Especially U–Pb dating of detrital zircon can be used to glean information regarding the age of potential source regions (e.g. Fedo et al. 2003, and references therein). The data of this study reveal new aspects in the origin of metasedimentary rocks of the eastern Circum-Rhodope Belt and contribute to clarify their palaeotectonic position within the Eastern Mediterranean during the Mesozoic.

2. Geological setting

The Rhodope Massif in northeastern Greece and southern Bulgaria constitutes the innermost part of the Hellenides (e.g. Jacobshagen 1986) and is considered to be an Alpine nappe stack of metamorphic units derived from continental and oceanic crust (e.g. Burg et al. 1996; Ricou et al. 1998; Barr et al. 1999). Simplified, two major tectonic units can be distinguished in the Greek part of the Rhodope, consisting mainly in varying amounts of orthogneisses, paragneisses, mica schists, marbles and amphibolites (e.g. Mposkos 1989; Burg et al. 1996; Barr et al. 1999, and references therein). Geochronological studies have shown that the Lower Tectonic Unit (Thracia Terrane) is dominated by Permo-Carboniferous orthogneisses whereas the Upper Tectonic Unit (Rhodope Terrane) predominantly consists of latest Middle–Late Jurassic and Early Cretaceous orthogneisses (e.g. Turpaud & Reischmann 2005; Turpaud 2006). The Thracia Terrane and the Rhodope Terrane are separated by a major NW–SE trending, southwest-vergent thrust fault zone (Nestos thrust: Papanikolaou & Panagopoulos 1981), which was recently interpreted as a suture zone (Nestos suture: Turpaud 2006; Reischmann & Kostopoulos 2007). It is worth mentioning that acidic rocks of similar

composition and age like those of the Thracia Terrane have been documented from the southerly Sredna Gora Terrane in Bulgaria (Carrigan et al. 2005). Structural and petrological data have shown that the rocks of the Greek Rhodope experienced polyphase deformation and up to high-pressure (HP) metamorphism (e.g. Mposkos 1989; Burg et al. 1996) during Middle Jurassic to Early Tertiary times (e.g. Liati et al. 2002; Liati 2005; Bauer et al. 2007). Evidence for ultra-high pressure (UHP) metamorphism was locally found in the Central and Eastern Rhodope (e.g. Mposkos & Kostopoulos 2001; Liati et al. 2002; Perraki et al. 2006). Parts of the Rhodope Massif are tectonically overlain by rock successions, which experienced only up to greenschist facies metamorphism (e.g. von Braun 1993), being assigned to the eastern Circum-Rhodope Belt (see above). In northeastern Greece, they include the Makri Unit and the Melia Formation, which are the focus of this study. Cenozoic sedimentary and igneous rocks, both volcanic and plutonic, occupy large parts of the study area to the south of the eastern Rhodope (Fig. 1). Isotopic investigations have suggested Oligocene to Early Miocene ages for the igneous rocks (e.g. Innocenti et al. 1984; Christofides et al. 2004). The intensive Tertiary magmatic activity was associated with crustal extension after the thickening/uplift of the Hellenic orogen and is regarded as the result of underthrusting of the African plate beneath the southern European margin (e.g. Christofides et al. 2004).

2.1. Makri Unit

The Makri Unit occupies the major part of the eastern Circum-Rhodope Belt in the Evros region of Greece and corresponds to the Phyllitserie of von Braun (1968) and the Makri Unit of Papadopoulos et al. (1989), respectively. The Makri Unit is well exposed, for instance, west of Alexandroupoli (Figs. 1 and 3). It comprises a lower, metasedimentary series and an upper, meta-volcanosedimentary series (e.g. von Braun 1968, 1993; Papadopoulos et al. 1989). The metasedimentary series consists of light grey conglomerates, light to dark grey sericite schists, calcschists and phyllites, and greyish limestones and marbles. The conglomerates contain clasts of quartz, quartzite, gneiss and limestone (von Braun 1968). Despite the metamorphic overprint, fossils could be identified in the limestone clasts. They include mainly corals, probably of the genus *Calamophyllia*, as well as rotalide and fragments of hexacorallia (von Braun 1968). Furthermore, corals similar to the genus *Oppelismilia* from the uppermost Triassic and the problematicum *Tubiphytes* have been

described (von Braun 1968). Papadopoulos et al. (1989) have seen the conglomerates as the basal part of the metasedimentary series unconformably overlying the metamorphic basement rocks of the Rhodope Massif. They interpreted the chalky and limestone (marble) dominated succession as upper part, showing a shallow marine environment. The contact to the underlying Rhodope Massif, however, is clearly tectonic (von Braun 1993).

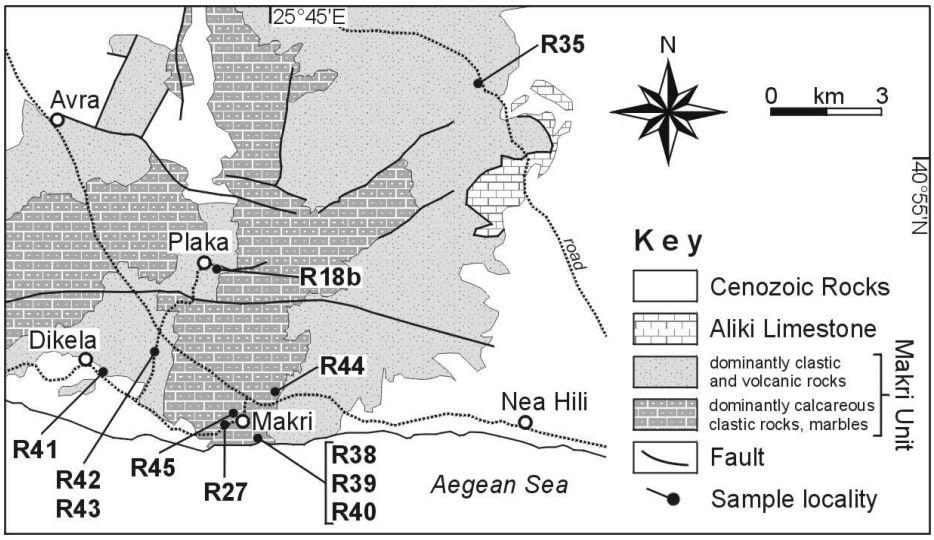

Fig. 3. Geological map of the Makri area (modified after Papadopoulos et al. 1989) showing sample localities of the Makri Unit. The Aliki limestone is always in tectonic contact to the Makri Unit (von Braun 1993). Note: Rocks of the Melia Formation may are tectonically imbricated with the Makri Unit (von Braun 1993). However, they are not shown in the map since their occurrences are not well described.

Contradicting to Kopp (1969) and Papadopoulos et al. (1989), who assumed a continuous stratigraphy, von Braun (1993) presented evidence that the Makri Unit is essentially a tectonic mélange. The tectonic overprint and the scarcity of marker horizons make an estimation of the thickness difficult. Von Braun (1968) assumed an effective thickness of around 2000 m. Dimades & Nikolov (1997) showed a general stratigraphic column with a thickness of ca. 480 m in the area of Makri village. The rocks of the Makri Unit were metamorphosed under mid-greenschist facies conditions (D1), with the development of asymmetric, sub-isoclinal folds (Ioannidis et al. 1998). D2 open folds without accompanying metamorphism overprinted the D1 structures (Ioannidis et al. 1998).

The stratigraphic age of the metasedimentary series of the Makri Unit has been debated over several decades and is still a matter of discussion. Fossil findings predominantly range from (Late Palaeozoic) Early Triassic to Late Jurassic (e.g. von Braun 1968, 1993;

Papadopoulos et al. 1989). Ioannidis et al. (1998) suggested that sedimentation of the Makri Unit started with conglomerates in Carboniferous time and continued with deposition of limestones, shales and marls into the Late Triassic–Early Jurassic. Dimadis & Nikolov (1997) described an ammonite specimen from sericite schists, ca. 1500 m north of Dikelia village that was determined by Nikolov as *Pseudosubplanites (Pseudosubplanites)* cf. *combesi* (Le Hegarat) indicating the occurrence of Early Cretaceous (Berriasian) within the metasedimentary series of the Makri Unit. Dimadis & Nikolov (1997) therefore suggested a Triassic to earliest Cretaceous age for the Makri Unit. Von Braun (1993) however emphasized tectonic imbrications of rocks from the Melia Formation with the Makri Unit that may explain the find of the Berriasian ammonite north of Dikelia (see von Braun 1993) and thus suggests a pre-Cretaceous age for the metasedimentary series of the Makri Unit, based on the remaining biostratigraphic data.

The metasedimentary series is overlain by a volcano-sedimentary series (the so called 'Greenschist Series') consisting from bottom to top of gabbroic cumulates, metagabbros and serpentinites of harzburgite composition ('Lower Metavolcanics'), followed by greenschists of volcanic origin, and pillowed or massive metavolcanic and metapyroclastic rocks ('Upper Metavolcanics'; e.g. Magganas 1988, 2002; Magganas et al. 1991). Bonev & Stampfli (2005) described also sheeted dykes and plagiogranites. Magganas (1988) considered the basic and ultrabasic rocks as parts of an incomplete and dismembered ophiolite that he named Evros ophiolite. Geochemical signatures classify the basic rocks and greenschists as mid-ocean ridge basalt (MORB) and island-arc tholeiite (IAT) whereas transitional IAT to MORB affinities also exist that is consistent with an island-arc/back-arc tectonic setting (Magganas et al. 1991; Magganas 2002; Bonev & Stampfli 2005). A volcanic (intraoceanic) island-arc tectonic setting was recently shown for basic rocks of the Bulgarian part of the eastern Circum-Rhodope Belt (Bonev & Stampfli 2003, 2007). Previous apatite fission-track ages of 140 ± 46 Ma and 161 ± 31 Ma from gabbros near Petrota (Biggazzi et al. 1989) provided cooling ages for the Evros ophiolite below the closure temperature of apatite. Recently, sensitive high-resolution ion microprobe (SHRIMP-II) analyses of zircons from a gabbroic sample near Maronia gave a precise mean $^{206}Pb/^{238}U$ age of ca. 169 ± 2 Ma that was interpreted as the age of gabbro intrusion (Koglin et al. 2007).

Middle and Upper Eocene deposits, including conglomerates, nummulitid-bearing limestones, sandstones and marls with tuffaceous layers, rest unconformably on the mid-

greenschist facies rocks of the Makri Unit (Kopp 1965; von Braun 1968), which gives the upper time limit of sedimentation and metamorphism for those rocks.

2.2. Melia Formation

The Melia Formation mainly crops out west and northwest of Melia village (Figs. 4 and 5) and corresponds to the 'terrain de transition' of Viquesnel (1868), the 'Grauwackenserie' of Wirth (1940) and the Drimos-Melia Formation of Dimadis et al. (1996), respectively. The latter authors have been the first who used the stratigraphic term Formation that we will continue here. However, we neglect the word Drimos since this refers to a small village which does not exist anymore. Papadopoulos et al. (1989) suggested that the Melia Formation covers unconformably the Makri Unit; von Braun (1993), however, provided convincing evidence that they are separated by tectonic contact. The Melia Formation is dominantly made up of ca. 1000 m thick siliciclastic rocks, including dark grey, shales, mica-rich, compact sandstones, and fine to coarse-grained greywackes and minor conglomerate layers (e.g. Kopp 1969; von Braun 1968, 1993). The sandstone and greywacke beds can reach up to almost 2 m in thicknesses that are well visible, for example, along the main road north of Loutros. The bedding has a general dip of ca. 30–40° to the south and southeast. The stratigraphic age of the Melia Formation is still a matter of discussion. Trikkalinos (1955) found a tectonically deformed ammonite (stephanoceratid or perisphinct) near Melia village that has stratigraphically been assigned to the Middle–Late Jurassic transition (Callovian–Oxfordian). Kopp (1965) reported a bivalve mollusc of the genus *Pecten* of the Early or Middle Jurassic from the well Evros 1 near Ardanion village. In the course of this study, a *Thalassinoides* ichnofossil was found west of Melia (Fig. 5b), which is usually interpreted as a burrow constructed by crustaceans or other kinds of arthropods (e.g. Ekdala & Bromley 2003). In vicinity to the former locality, layers rich in coalified terrestrial plant fragments have been found on bedding surfaces (Figs. 5c, d). A biostratigraphic age for these plant fragments could not be obtained as yet because of lack of characteristic features necessary for an accurate age determination (V. Wilde, pers. comm.). Papadopoulos et al. (1989) suggested a Late Jurassic to Early Cretaceous age for the Melia Formation. Dimadis et al. (1996), however, reported two thin-shell bivalve specimens from a locality NW of Melia identified as *Halobia superba* Mojsisovicz, which led them to conclude that at least a part of

the Melia Formation is Late Ladian–Early Carnian in age. Dimadis & Nikolov (1997) suggested contradicting that the Melia Formation cannot be older than Early Cretaceous with the upper time limit of sedimentation being Mid-Cretaceous.

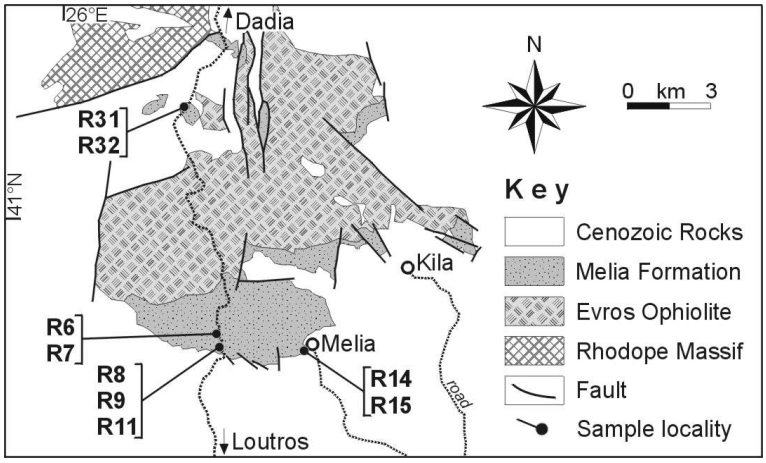

Fig. 4. Geological map of the Melia area (modified after von Braun 1993) showing sample localities of the Melia Formation.

Kopp (1969) and von Braun (1993) noted that the clastic succession of the Melia Formation is gradually overlain by the Aliki limestone. Since field relations do not allow such a gradual transition, we interpreted the Aliki limestone as a single stratigraphic unit, which is not in direct contact to the Melia Formation. Nonetheless, the micritic matrix of limestones south of Aliki contains calcalgae and foraminifera of the families Miliolidae and Textularidae (von Braun 1968). The Miliolidae have been identified as *Quinqueloculine* sp. and *Massilina* sp., the Textularidea as *Trocholina* sp., indicating an Early Cretaceous age for the Aliki limestone (von Braun 1968; Kopp 1969).

The upper time limit of sedimentation and metamorphism of the Melia Formation is clearly set by the unconformably overlying Middle Eocene clastic deposits (see Kopp 1965; von Braun 1968). A basal Middle Eocene conglomerate, cropping out west of the former village Drimos, consists of clasts of grey limestone, among others, similar to those exposed near Aliki. The limestone clasts contain foraminifera such as *Lenticulina*, Miliolidae, *Orbitolina*, *Textularia* and *Pseudocyclammina* as well as gastropod molluscs of the genus *Nerinea* (Kopp 1965; von Braun 1968). The occurrence of *Orbitolina* indicates that uppermost Lower Cretaceous–lowermost Upper Cretaceous limestones were exposed in the source area during the Paleogene. Nowadays, however, no rocks of such age are preserved in the Evros region.

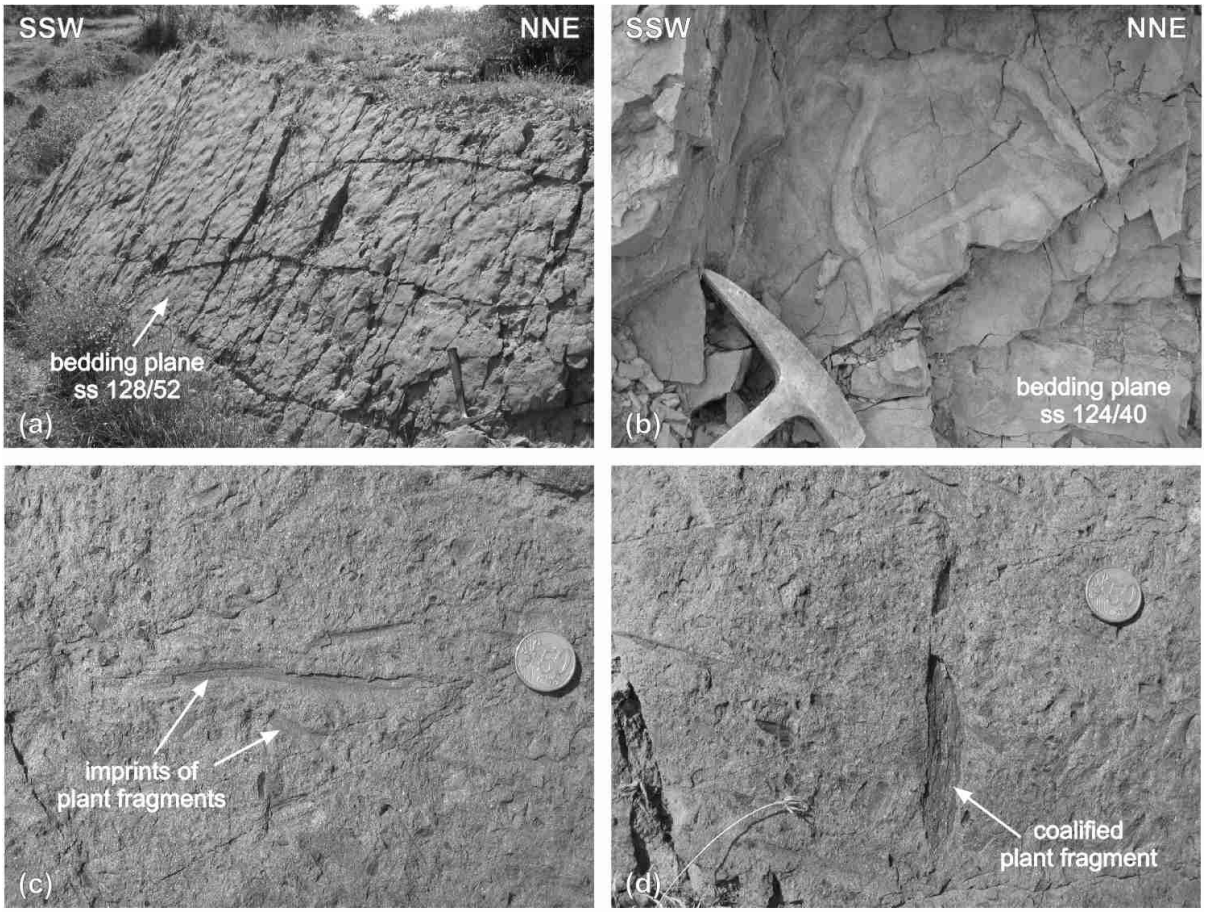

Fig. 5. Melia Formation west of Melia village (40°57'07.0''N, 26°06'12.1''E). **(a)** Sole marks (flute casts) on the sole of a greywacke bed. **(b)** *Thalassinoides* ichnofossil on the sole of a siltstone bed. **(c, d)** Terrestrial plant fragments on bedding surfaces.

3. Samples and methods

A total of twenty siliciclastic metasedimentary rocks including greywackes, sandstones, siltstones and phyllites (metapelites) were collected from the Makri Unit and from the Melia Formation for whole-rock major- and trace-element geochemical analyses, detrital mineral chemistry, zircon geochronology, and palynological investigations. Sample localities (including geographic coordinates) and the analytical data referred to in this chapter are included in the Appendix.

Psammites of the Makri Unit include metasandstones, which are poorly sorted by size and predominantly consist of angular to subangular fragments of quartz (both mono- and polycrystalline), white mica and Na-rich feldspar (albite). Furthermore, sericite, minor chlorite and hematite, and in varying amount calcite are present. Plagioclase grains often

display alteration due to sericitisation. Some samples therefore contain a secondary matrix of sericite (e.g. sample R27). Accessory minerals mainly include zircon, rutile, tourmaline and opaque minerals.

Psammites of the Melia Formation include greywackes, which are poorly sorted by size and dominated by angular to subangular fragments of quartz (both mono- and polycrystalline), feldspar (mainly albite) and white mica. Further, epidote, zoisite, garnet, chlorite (Fe-Mg rich), calcite and sericite are present. Plagioclase grains often display patchy alteration due to sericitisation and replacement by calcite. The psammites of the Melia Formation are predominantly clast-supported; primary matrix if present consists mainly of sericite. Accessory minerals dominantly include zircon, rutile, titanite and opaque minerals. It is noteworthy that in outcrops at Melia village terrestrial plant fragment are macroscopically visible at hand specimen (Figs. 5c, d). At other localities, e.g. along the main road from Loutros to Dadia, no plant fragments could be found macroscopically. However, organic material (plant cuticula) could be identified in thin section.

3.1. Whole-rock geochemistry

The composition of clastic sedimentary rocks is predominantly controlled by the lithology of their source area(s), and modified by several factors such as weathering, transport and sorting, redox environment and diagenesis (e.g. Johnsson 1993). If secondary processes do not significantly modify the whole-rock geochemistry it can be used as chemostratigraphic indicator and as fingerprint for provenance and depositional setting of sedimentary rocks (e.g. Bhatia & Crook 1986; McLennan 1989; McLennan et al. 1990, 1993).

In total, 20 samples were used for whole-rock geochemical analyses. Major and trace elements of whole rock were analysed by X-ray fluorescence (XRF) spectrometry on fused glass discs and pressed powder pellets, respectively, using a Philips MagiX Pro X-ray spectrometer at the University of Mainz, following procedures outlined in Meinhold et al. (2007). Loss on ignition (LOI) was determined gravimetrically by heating the samples to 1000°C. Rare earth elements (REE), Hf, Ta, Th, and U of selected samples were analysed on fused discs by laser ablation inductively-coupled plasma mass spectrometer (LA-ICPMS) using an Agilent 7500ce equipped with a NewWave/Merchantek 213 nm Nd-YAG laser system at the University of Mainz, following procedures described in Nehring et al. (2007).

3.2. Mineral chemistry

Beside petrography and whole-rock chemistry microprobe analysis of detrital mineral phases has great potential to determine the petrology of source rocks (e.g. von Eynatten & Gaupp 1999, and references therein). Therefore, the chemistry of detrital feldspar, mica, and garnet was determined in polished thin sections using an electron microprobe (JEOL JXA 8900RL) equipped with 5 wavelenght-dispersive spectrometers at the University of Mainz. Operating conditions were 15 kV acceleration voltages with a beam current of 8 nA and a beam diameter of 5 µm for feldspar. Mica was analysed with 15 kV acceleration voltages, a beam current of 12 nA, and a beam diameter of 2 µm. An accelerating voltage of 20 kV and a beam current of 20 nA, with a beam diameter of 2 µm was used for garnet. Natural and synthetic materials were used as standards. The PRZ procedure was applied to calculate concentration units. Cations of feldspar, mica, and garnet were calculated stoichiometric, based on 8, 11, and 12 oxygens per formula unit, respectively.

3.3. Zircon geochronology

U–Pb dating of detrital zircons has been proven to be a powerful tool for sedimentary provenance studies and in the absence of fossil and other stratigraphic data the youngest grain in a sedimentary rock can indicate a maximum limit for the age of deposition (e.g. Fedo et al. 2003, and references therein). U–Pb zircon geochronology was carried out on two individual samples taken from the Makri Unit and the Melia Formation. Zircons were separated from the bulk samples using standard techniques (hydraulic press, rotary mill, Wilfley table, Frantz isodynamic magnetic separator and heavy liquids [methylene iodide]). Final purification was done by handpicking under a binocular microscope. Zircon grains were mounted in epoxy resin, sectioned and polished. Prior to the analyses, cathodoluminescene (CL) images were obtained for all grains to expose their internal structure and to target specific areas within them, e.g. growth structures and inherited cores. Measurements were carried out in two different sessions with to different facilities: SHRIMP-II and LA-ICPMS. SHRIMP-II measurements were performed at the Centre of Isotopic Research, St. Petersburg, Russia, following the methodology described in Chapter 4 of this thesis. LA-ICPMS measurements were performed at the Geological Survey of Denmark and Greenland, Copenhagen, Denmark,

following the methodology described in Chapter 4 of this thesis. In order to test the quality of the applied method and the reproducibility of the obtained ages, U–Pb data of 6 zircon grains previously dated by SHRIMP-II were re-measured by LA-ICPMS. Furthermore, chips of the TEMORA 1 zircon standard (Black et al. 2003) were analysed as unknown sample during the analytical session. Unless otherwise stated, $^{206}Pb/^{238}U$ ages are used for zircon grains <1.2 Ga whereas older grains are quoted using their $^{207}Pb/^{206}Pb$ ages. This is because the $^{207}Pb/^{206}Pb$ ages become increasingly imprecise below <1.2 Ga due to small amounts of ^{207}Pb. The $^{207}Pb/^{206}Pb$ ages are generally considered as being minimum ages due to the effect of possible Pb loss. Concordia diagrams and probability density distribution and histogram plots were produced using the programs Isoplot/Ex (Ludwig 2003) and AgeDisplay (Sircombe 2004) respectively. Ages reported in the text are given at the 2-sigma level. The Geological Time Scale (GTS) of Gradstein et al. (2004) was used as stratigraphic reference for data interpretation.

3.4. Palynology

One siltstone from the Melia Formation (sample R8) was treated according to palynological standard preparation method with hydrochloric and hydrofluoric acid. The remaining residue was sieved and embedded with glycerine gelatine on standard glass slides, and the material was investigated under a light microscope using combined transmitted and reflected light. Because sample R8 yielded only coalified material (probably plant remains) which could not be used for further determination, and no palynomorphs have been found, sample R8 will not be further discussed here.

4. Results

4.1. Whole-rock geochemistry

Makri Unit: According to the diagram of Herron (1988), two of the psammitic rocks of the Makri Unit can be chemically classified as arkoses; one is a wacke (i.e. greywacke), and two samples plot in the field for iron-bearing shale, however, close to the field for iron-bearing sandstone (Fig. 6). The pelitic rocks plot in the field for shale. As shown in Figure 7,

the metasedimentary rocks of the Makri Unit show a wider spread in their whole-rock chemical composition than those of the Melia Formation. Two psammitic rocks of the Makri Unit display high contents of SiO_2 (79 and 83 wt.%), moderate to low contents of Al_2O_3 (9 and 10 wt.%), low contents of TiO_2 (<0.5 wt.%), low to high contents of Na_2O (0.8 and 3.3 wt.%) and K_2O (1.1 and 2.6 wt.%), and low contents of CaO (<1.3 wt.%). The remaining three psammitic samples have moderate contents of SiO_2 (59–67 wt.%), Al_2O_3 (around 13 wt.%), and TiO_2 (0.5–0.8 wt.%), high contents of Na_2O (2.4–3.6 wt.%), moderate contents of K_2O (1–2 wt.%), and elevated contents of CaO (3.8–7.6 wt.%). The pelitic rocks have higher Al_2O_3 contents because of their higher amounts of clay minerals, the exception being samples with high contents of CaO (>17 wt.%), which have Al_2O_3 contents between 6 and 11 wt.%. Medium to high values of CaO and LOI in psammitic and pelitic rocks of the Makri Unit accompanied by a strong positive linear correlation between both values indicate the presence of carbonate-bearing minerals such as calcite, which is confirmed by petrography.

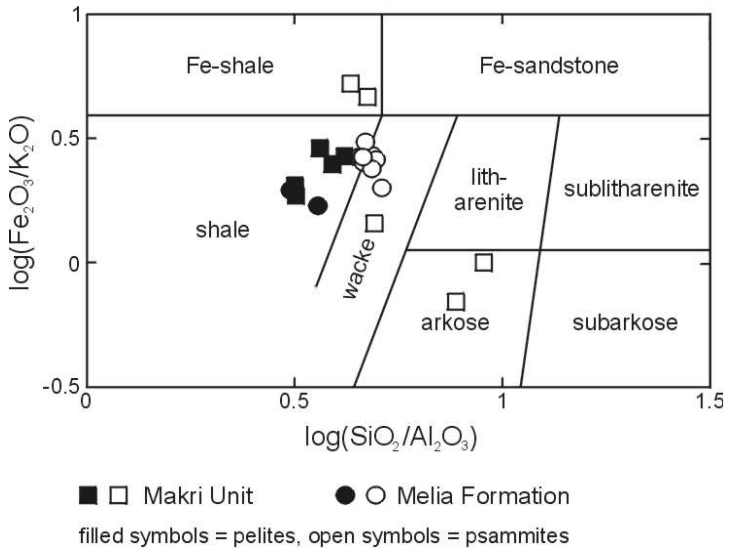

Fig. 6. Chemical classification scheme for terrigenous clastic sediments after Herron (1988).

Multi-element diagrams normalised to upper continental crust composition exhibit depletion in some trace elements, with characteristic negative Ba, U, Sr, Cr, and Ni anomalies (Fig. 8a). PAAS-normalised REE patterns of two samples (R27 and R43) are almost flat, with no differences between light rare earth element (LREE) and heavy rare earth element (HREE), and only minor depletion in total REE (Fig. 9a). Chondrite-normalised REE patterns (Fig. 9b) show LREE enriched (La_N/Yb_N ~ 9.0 and 11.4) and almost flat HREE patterns (Gd_N/Yb_N ~ 1.6 and 1.8) with negative Eu anomalies (Eu/Eu* ~ 0.6 and 0.7). These features

are characteristic for upper continental crust and young differentiated arc material and their erosional products (e.g. McLennan et al. 1990, 1993; McLennan & Taylor 1991).

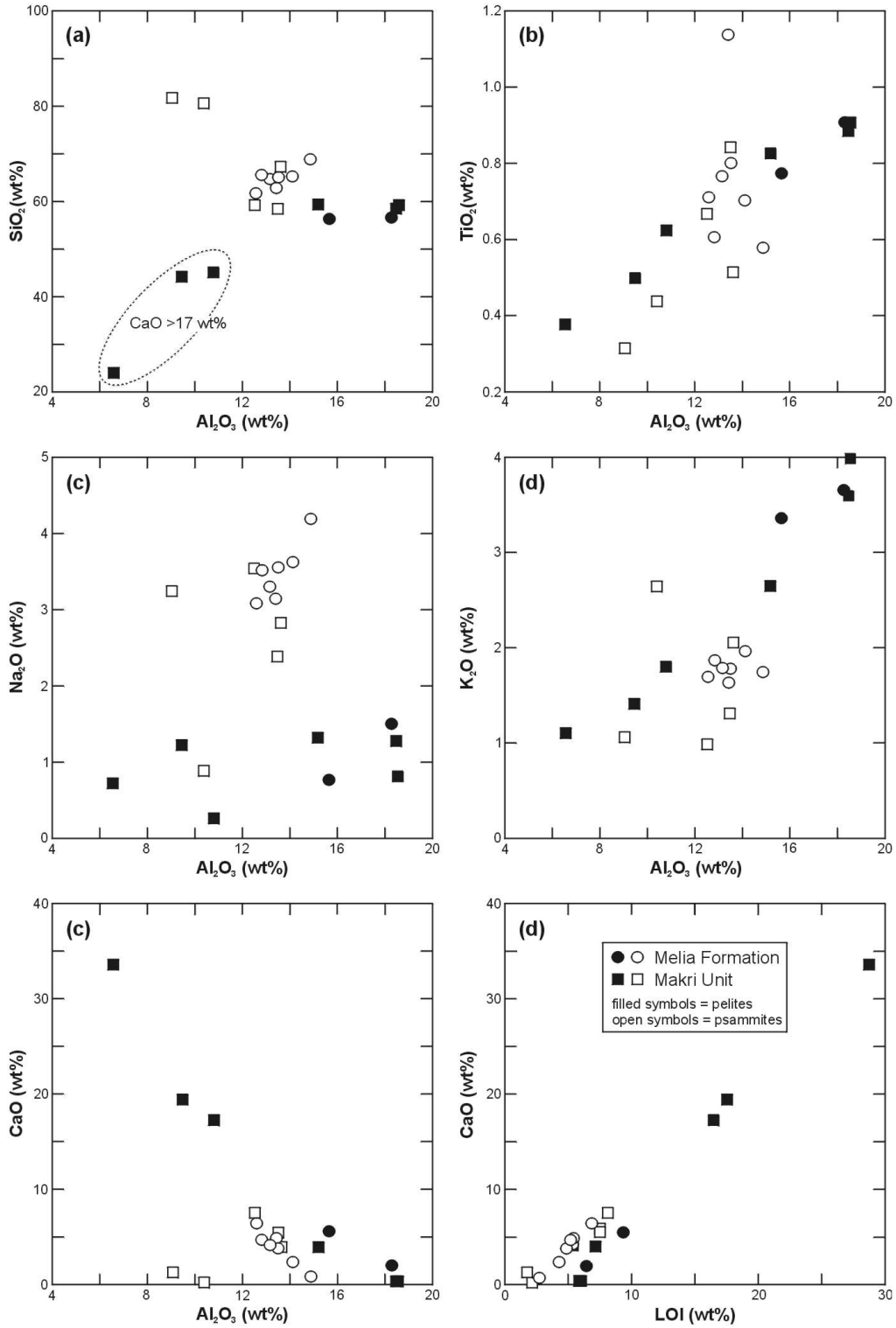

Fig. 7. Correlation diagrams of SiO_2, TiO_2, Na_2O, K_2O and CaO vs. Al_2O_3 and CaO v. LOI for metasedimentary rocks of the eastern Circum-Rhodope Belt.

Sedimentary rocks of the Makri Unit have Th/Sc ratios between 0.1 and 3.0 accompanied by Zr/Sc ratios between 2 and 29 that suggest, according to the McLennan et al. (1993), compositional variation within the source area (Fig. 10). Fractionation during transport and sedimentation may have to be considered for some pelitic samples. Since all samples are characterised by normal contents of Cr and Ni, and normal Cr/V and Y/Ni ratios, an (ultra)basic source can be safely excluded (Fig. 11). The elevated contents of Cr and Ni in some pelitic samples are not critical because these elements are commonly controlled by clay minerals, which are enriched in pelites.

Taken collectively, whole-rock geochemistry clearly points to a source area of intermediate to acidic composition, with varying input of a calcareous component. Using the ternary discrimination diagrams of Bhatia & Crook (1986) three of the psammitic samples of the Makri Unit plot in the continental-island arc field whereas two plot in the active continental margin and passive margin fields (Fig. 12).

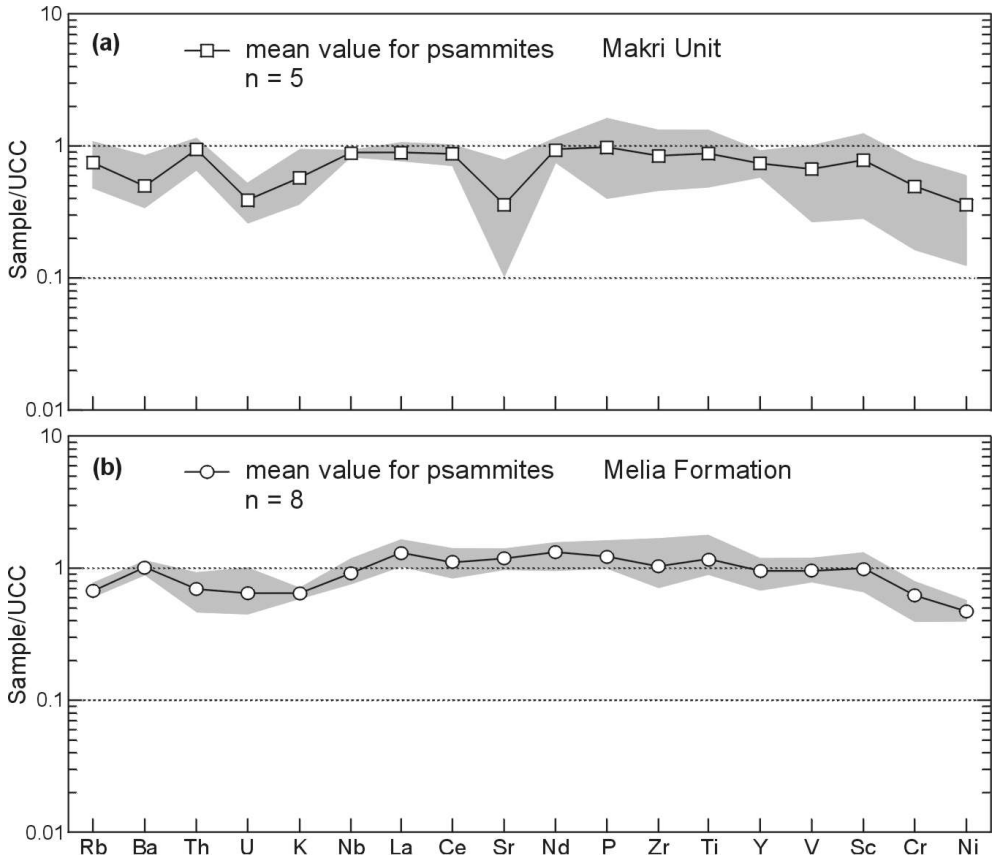

Fig. 8. Multi-element diagrams for psammitic metasedimentary rocks of the eastern Circum-Rhodope Belt. Concentrations are normalised against the upper continental crust composition (UCC, Rudnick & Gao 2003). Only mean values (symbols) and the chemical range (grey fields) are given.

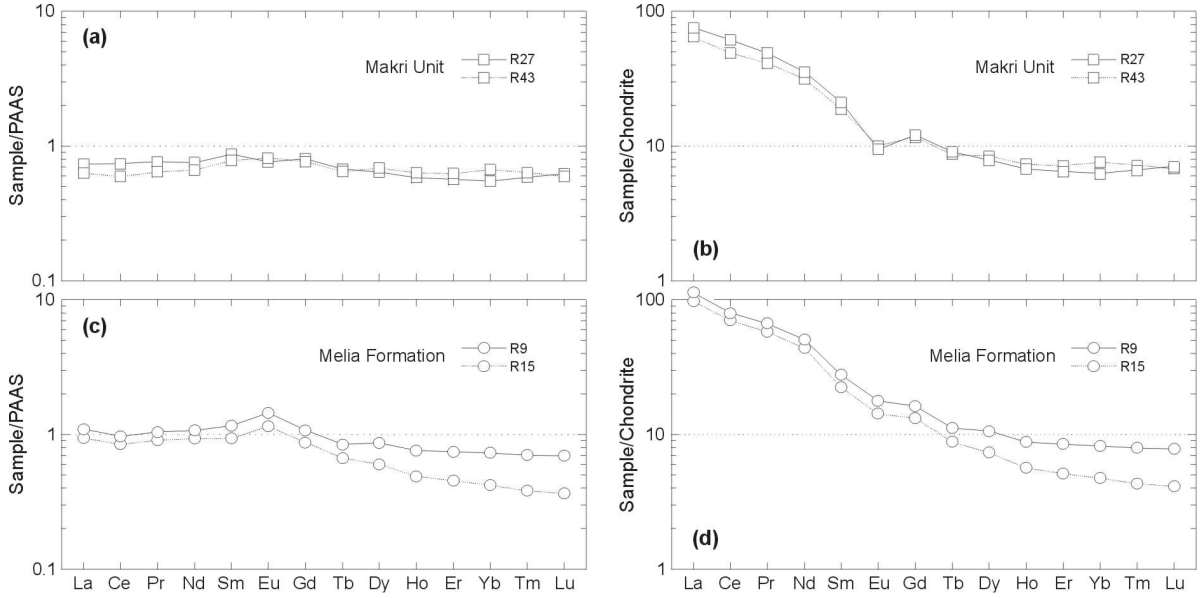

Fig. 9. (a, c) PAAS-normalised REE diagrams. Normalising values from McLennan (1989). **(b, d)** Chondrite-normalised REE diagrams. Normalising values from Taylor & McLennan (1985). Only psammites are plotted.

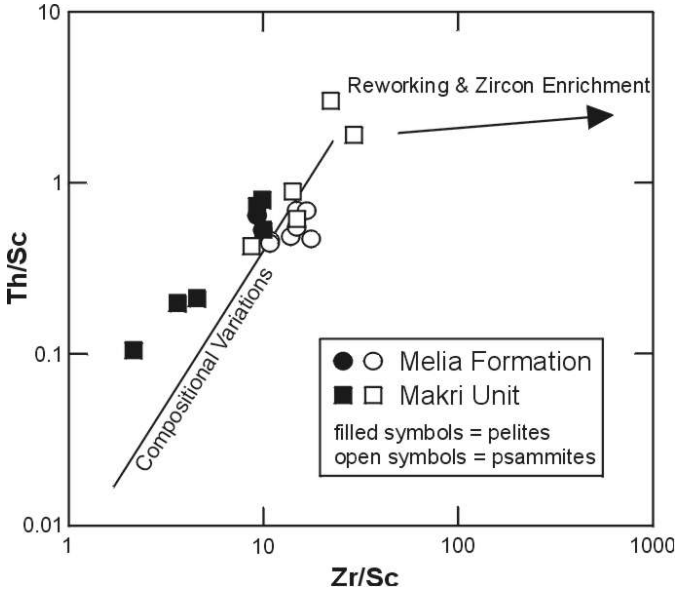

Fig. 10. Discrimination diagram after McLennan et al. (1993) illustrating sediment recycling.

Melia Formation: According to the diagram of Herron (1988), the psammitic rocks of the Melia Formation can be chemically classified as wackes (i.e. greywackes), with lying close to the field of shale (Fig. 6). The pelitic rocks plot in the field for shale. In general, metasedimentary rocks of the Melia Formation are relatively homogenous in composition, as it is expressed by their whole-rock chemistry (Fig. 7). The psammitic rocks have moderate contents of SiO_2 (60–69 wt.%), Al_2O_3 (12–15 wt.%), TiO_2 (0.6–1.1 wt.%), high contents of Na_2O (3.0–4.2 wt.%), low contents of K_2O (1.6–1.9 wt.%), and variably contents of CaO

(0.7–6.4 wt.%). The two pelitic samples have higher contents of Al_2O_3 and K_2O because of their higher amounts of clay minerals.

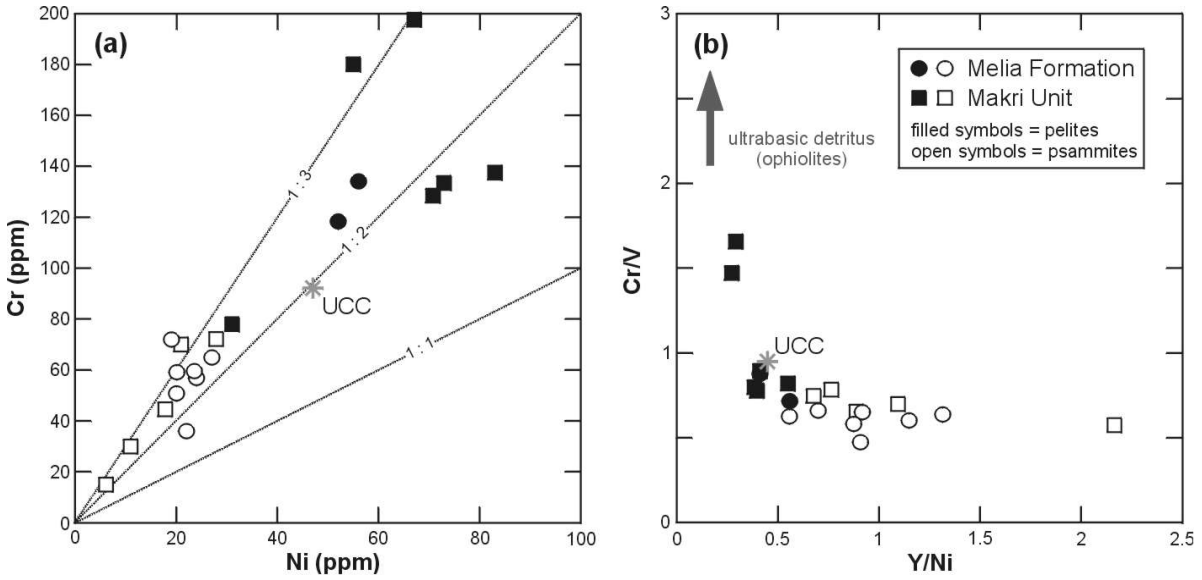

Fig. 11. Diagrams for identifying an ultrabasic provenance. **(a)** Cr vs. Ni diagram. Values of Cr (>150 ppm) and Ni (>100 ppm), Cr/Ni ratios between 1.3–1.5 and a high correlation coefficient between Cr and Ni are diagnostic of ultrabasic rocks in the source area; Cr/Ni ratios of 2 and greater typify an input of basic volcanic rocks (Garver et al. 1996). **(b)** Cr/V vs. Y/Ni diagram after McLennan et al. (1993). UCC according to Rudnick & Gao (2003).

Multi-element diagrams normalised to upper continental crust composition exhibit an almost flat pattern in trace elements, compared to samples of the Makri Unit, with only minor depletion in Rb, U, K, Cr, and Ni (Fig. 8b). No Sr anomaly occurs. PAAS-normalised REE patterns of two samples (R9 and R15) are flat and undistinguishable from PAAS for LREE, however, showing depletion of HREE, and positive Eu anomaly (Fig. 9c). Chondrite-normalised REE patterns (Fig. 9d) show strong LREE enriched (La_N/Yb_N ~ 14.2 and 22.6) and fractionated HREE patterns (Gd_N/Yb_N ~ 2.0 and 3.0) with an almost indistinct Eu anomaly (Eu/Eu^* ~ 0.8). Furthermore, the samples of the Melia Formation have higher contents of Na_2O and Sr than those of the Makri Unit. A higher Na_2O content suggests plagioclase enrichment, which is confirmed by petrography. Given the fact that Eu^{2+} and Sr^{2+} have comparable ionic sizes and that both partly substitute for Ca^{2+} in plagioclase, a higher Sr content with no concomitant negative Eu anomaly could reflect input of juvenile crustal material (McLennan 1989; Gao & Wedepohl 1995). The lack of a Eu anomaly in samples of

the Melia Formation resulted from high amounts of plagioclase derived from the source rocks. Hence, the REE patterns are characteristic for acidic igneous rocks less affected by intracrustal differentiation processes and their erosional products (e.g. McLennan 1989; McLennan & Taylor 1991). Sample R15 exhibits depletion in HREE compared to sample R9 that is probably caused by its smaller amount of detrital garnet since garnet is a major host of HREE. Sedimentary rocks of the Melia Formation have Th/Sc ratios between 0.4 and 0.7 accompanied by Zr/Sc ratios between 9 and 17 that suggest uniform composition of the source area (Fig. 10). Since all samples are characterised by normal contents of Cr and Ni, and normal Cr/V and Y/Ni ratios, an (ultra)basic source seems most unlikely (Fig. 11).

Taken collectively, whole-rock geochemistry clearly points to a uniform source area of intermediate to acidic composition, with minor input of a calcareous component. Using the ternary discrimination diagrams of Bhatia & Crook (1986) all psammitic samples of the Melia Formation plot in the continental-island arc field or close to this, respectively (Fig. 12).

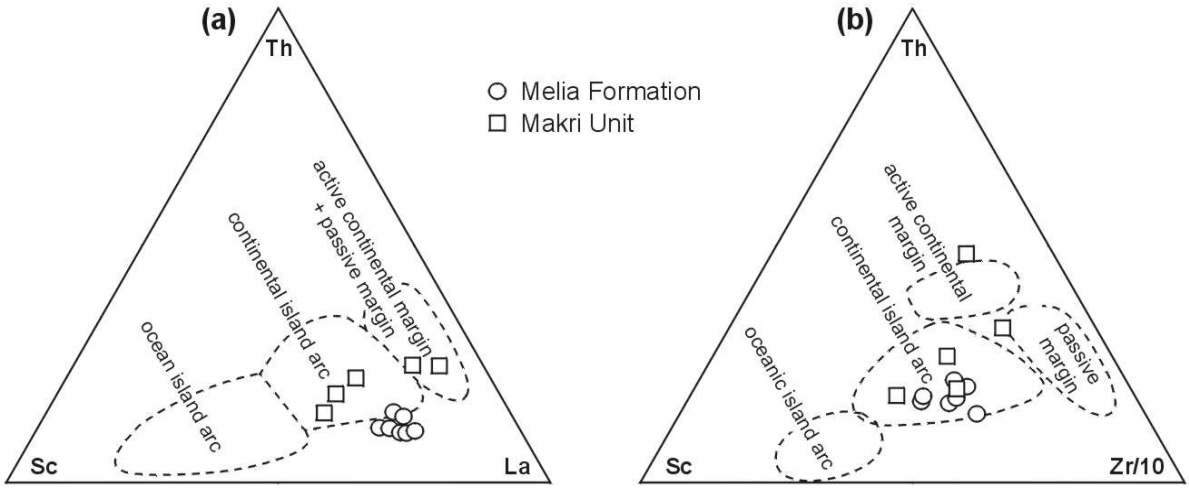

Fig. 12. Discrimination diagrams after Bhatia & Crook (1986) illustrating the tectonic setting. Only psammites are plotted.

4.2. Mineral chemistry

Feldspar: The analysed detrital feldspar grains of the Makri Unit and the Melia Formation show slightly differences in their chemistry that is illustrated in a ternary diagram showing the three end-member components $NaAlSi_3O_8$ (albite, Ab), $KAlSi_3O_8$ (orthoclase, Or) and $CaAl_2Si_2O_8$ (anorthite, An). Feldspar grains of the Makri Unit have very high Na_2O contents accompanied by very low CaO and K_2O contents, which indicate albite being the major feldspar component ($Ab_{97-100}An_{0-3}Or_{0-2}$). Feldspar grains of the Melia Formation, however, show besides high Na_2O contents also slightly elevated contents of CaO and K_2O, which indicate besides albite also a subordinate composition of oligoclase ($Ab_{5-99}An_{0-15}Or_{0-92}$). Two grains plot in the field for anorthoclase and one grain is an orthoclase (Fig. 13).

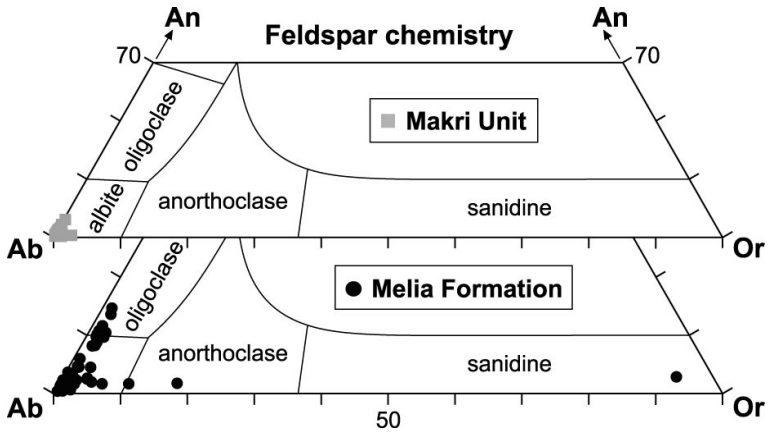

Fig. 13. Ab-An-Or ternary diagram of detrital feldspar of the Makri Unit (sample R27, n = 50) and the Melia Formation (sample R15, n = 60) analysed in thin sections.

Mica: The chemical composition of detrital white mica of the Makri Unit and the Melia Formation reveal a broad range in Si content from ca. 3.01 to 3.44 p.f.u. and in Al content from ca. 2.03 to 2.85 p.f.u. (Fig. 14a). All analysed micas are characterised by high K contents of ca. 0.70 to 0.95 p.f.u. which indicates the presence of K-rich white mica. Si contents >3.0 p.f.u. suggest the presence of phengitic mica. Si contents >3.3 of some micas suggest that these minerals were formed under medium to high pressure metamorphic conditions, depending on their primary mineral assemblage and crystallisation temperature in the source rocks (Massonne & Schreyer 1987). The deviation of some phengitic mica from the 1:1 substitution line of Si + Mg (stippled line in Fig. 14b) suggests that Fe^{2+} substitution occurs.

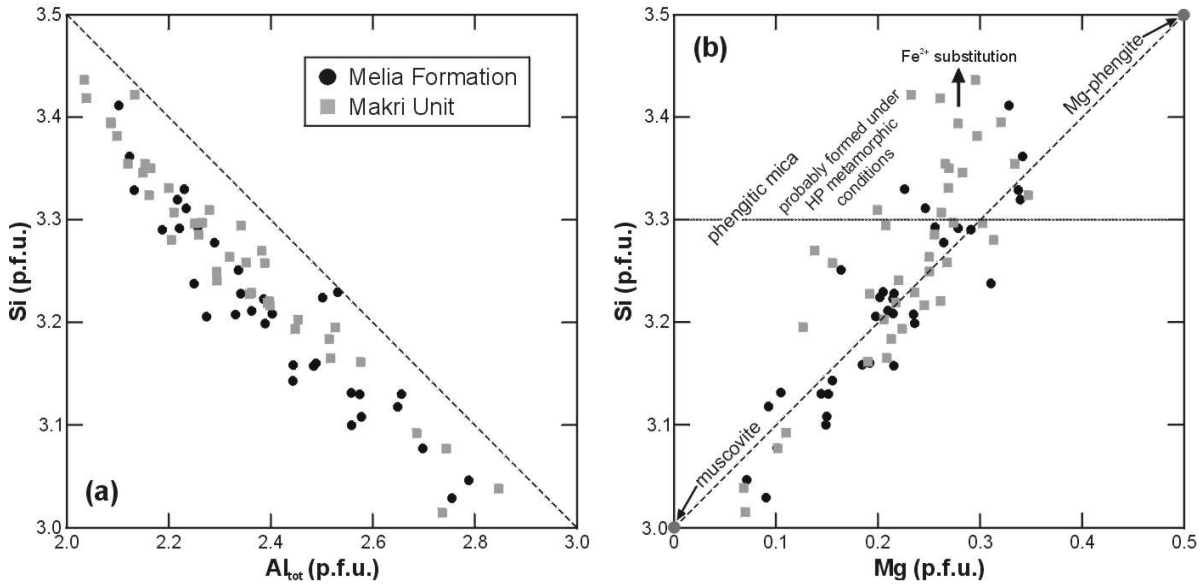

Fig. 14. Mineral chemistry of detrital mica of the Makri Unit (sample R27, n = 40) and the Melia Formation (sample R15, n = 34) analysed in thin sections. **(a)** Binary plot of Si content vs. Al content; **(b)** Binary plot of Si content vs. Mg content after von Eynatten & Gaupp (1999); the field for phengitic mica formed under HP metamorphic conditions is according to Massonne & Schreyer (1987).

Garnet: Besides epidote and zoisite, garnet is an abundant detrital heavy mineral in metasedimentary rocks of the Melia Formation. In general, the chemical variability of detrital garnet of sedimentary rocks is a very useful provenance indicator (e.g. Morton 1985, 1991; Takeuchi 1994; von Eynatten & Gaupp 1999; Morton et al. 2004). However, secondary processes can substantially modify garnet geochemistry up to total garnet dissolution that has to be considered when dealing with garnet provenance analysis (e.g. Morton 1991; Morton & Hallsworth 1999). These processes could act either at an early stage of deposition through circulation of acidic meteoric pore waters, or during burial through circulation of high-temperature pore fluids (Morton 1985, 1991; Morton & Hallsworth 1999; Morton et al. 2004). Furthermore, the stability of garnet is also controlled by its composition, with high-Ca garnets being less stable than low-Ca garnets (e.g. Morton 1987). Garnet is especially characteristic of metamorphic rocks of a wide variety of types, and it can be also found in igneous rocks such as granites, pegmatites, acidic volcanic rocks, kimberlites and some metasomatic rocks (e.g. Deer et al. 1992).

Detrital garnets in metasedimentary rocks of the Melia Formation occur generally as discrete grains and have mostly an angular shape. Most grains were analysed at the grain core. Some grains were additionally analysed at the grain rim. Calculation of end-member

garnet compositions reveals that detrital garnets of the Melia Formation are almandine-rich garnets, with 42–74 mol% of almandine (Alm, X_{Fe}), 3–39 mol% of grossular (Grs, X_{Ca}), 2–37 mol% of pyrope (Py, X_{Mg}), and 1–23 mol% of spessartine (Sp, X_{Mn}), the exception being two grains with high grossular end-member compositions (Fig. 15a). Core–rim analyses indicate an almost homogenous composition of single grains (Fig. 15b). Secondary alteration or primary zonation is negligible relative to the overall variability of garnet composition considered here. Morton et al. (2004) distinguished three major garnets types, being low-Ca, high-Mg garnets (Field A in Fig. 15), Fe–Mn-rich garnets, with variable Ca and low Mg contents (Field B in Fig. 15), and high-Ca, high-Mg garnets (Field C in Fig. 15). According to this classification, the majority of the detrital garnets of the Melia Formation (excluding the two Grs-rich grains) fall in the Fields C (60%) and B (26%). Garnets of Field A form only 14% of the population.

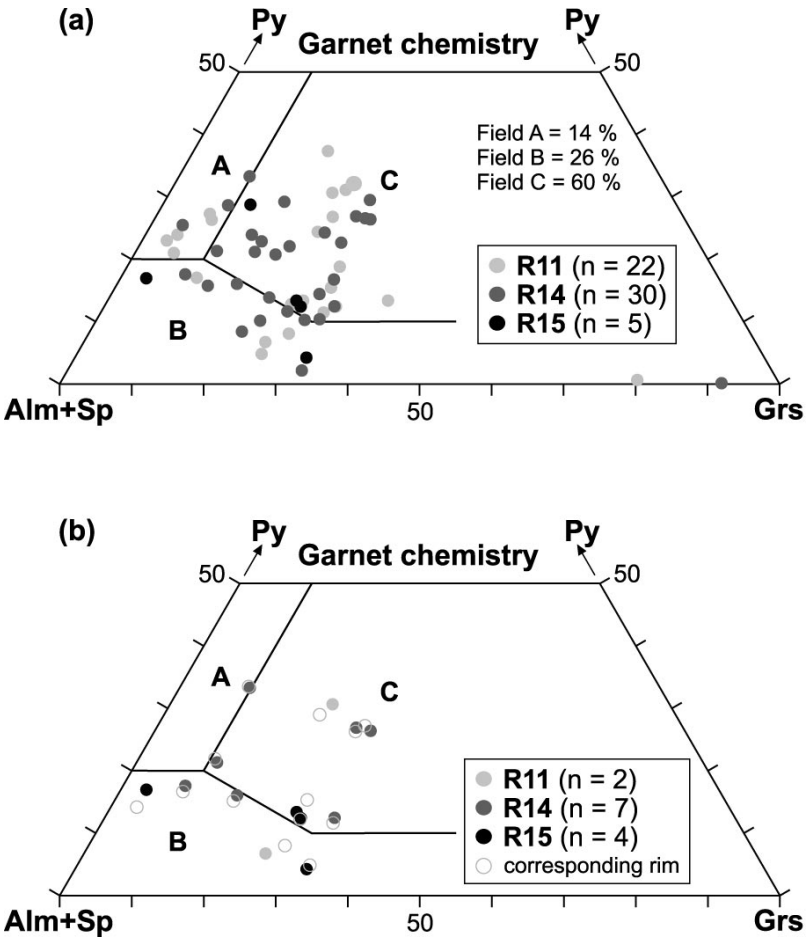

Fig. 15. Ternary diagram of the endmember proportions of detrital garnet of the Melia Formation analysed in thin sections. The main composition is $Alm_{42-74}Gr_{3-39}Py_{2-37}Sp_{1-23}$, excluding two garnet grains with a very high grossular component. **(a)** Only analyses at the grain core are shown. **(b)** Analyses of core–rim pairs are shown.

4.3. Zircon geochronology

To test the precision and accuracy of the LA-ICPMS technique applied, during the course of LA-ICPMS analytical session thirteen spots were set on chips of the TEMORA 1 zircon standard (ID-TIMS: 416.8 ± 1.1 Ma, spike uncertainty included; Black et al. 2003) and analysed as unknown samples. The results are shown in Figure 16. All measurements yielded concordant U–Pb ages and define a concordia age of 416.7 ± 3.5 Ma (2σ), which is well within the range of the ID-TIMS analyses reported by Black et al. (2003).

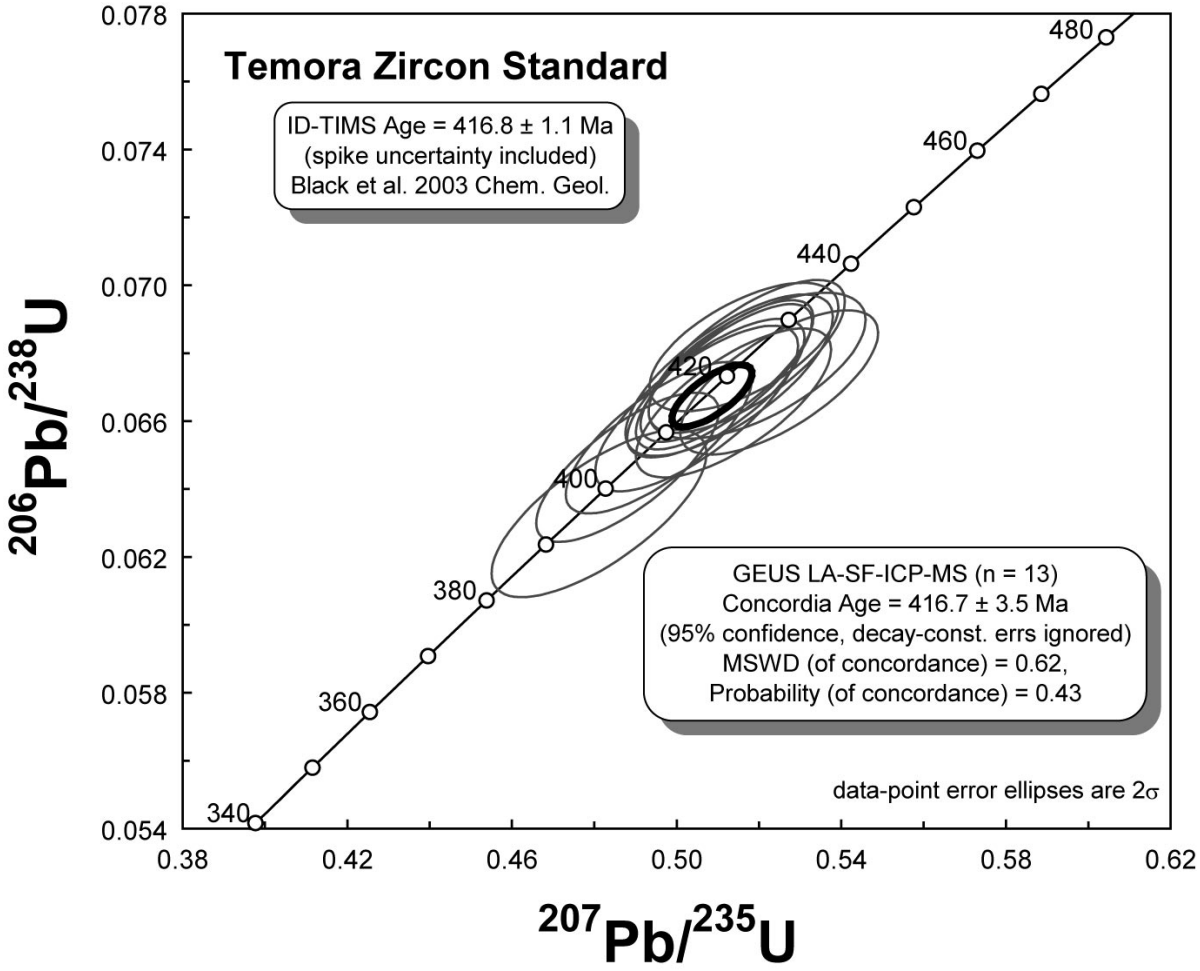

Fig. 16. Concordia diagram showing the results obtained by LA-ICPMS analyses on grains of the TEMORA 1 zircon standard.

Furthermore, Figure 17 compares the LA-ICPMS and the SHRIMP-II U–Pb ages previously analysed on the same zircon grains. Some LA-ICPMS spots were set exactly on the SHRIMP-II spots, whereas others were set on the opposite position on the same zircon

grain (Fig. 18). In general, U–Pb ages obtained by LA-ICPMS analyses are identical to those previously obtained by SHRIMP-II dating, which confirms previous studies showing the successful application of LA-ICPMS for U–Pb zircon dating (e.g. Gerdes & Zeh 2006). However, it may happen that grains dated by LA-ICPMS show ages slightly different to those obtained by SHRIMP-II, although the analysis was performed at one and the same spot (e.g. spot R15-79, Fig. 18). This might be due to the fact that during U–Pb isotope analysis the laser penetrates to depths of about 30 µm whereas during SHRIMP-II analysis the material is collected from a sample depth ≤3 µm, meaning LA-ICPMS dating is more sensitive to inhomogeneities within the zircon crystal. For convention, where both SHRIMP-II and LA-ICPMS ages are available for one and the same spot only the LA-ICPMS data were used for interpretation of the zircon ages since they form the dominant data set of this study.

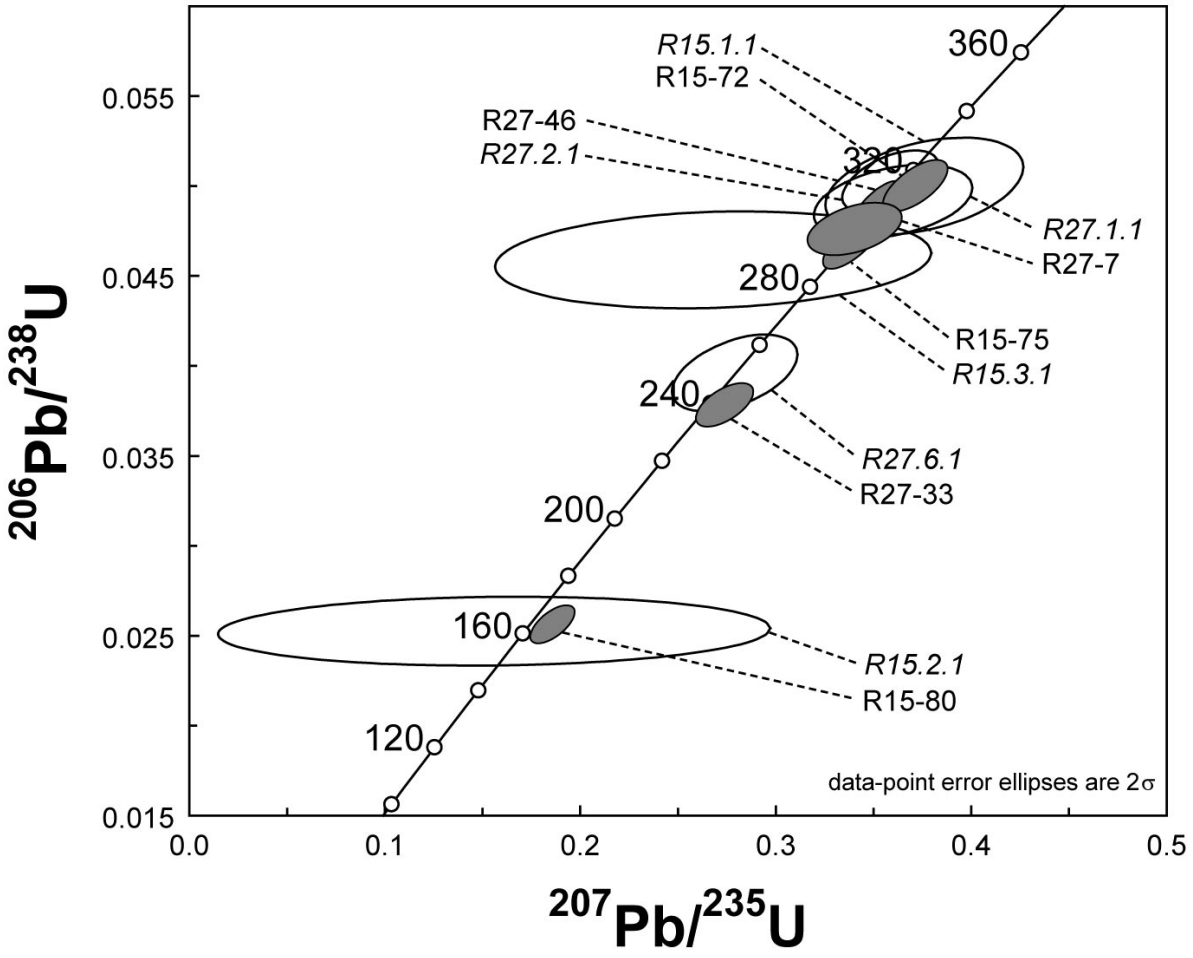

Fig. 17. Concordia diagram showing the results obtained by LA-ICPMS (filled symbols) and SHRIMP-II analyses (open symbols) on the same zircon grains. Error ellipses in concordia plot represent 2σ uncertainties. All grains are shown in CL images on Figure 18.

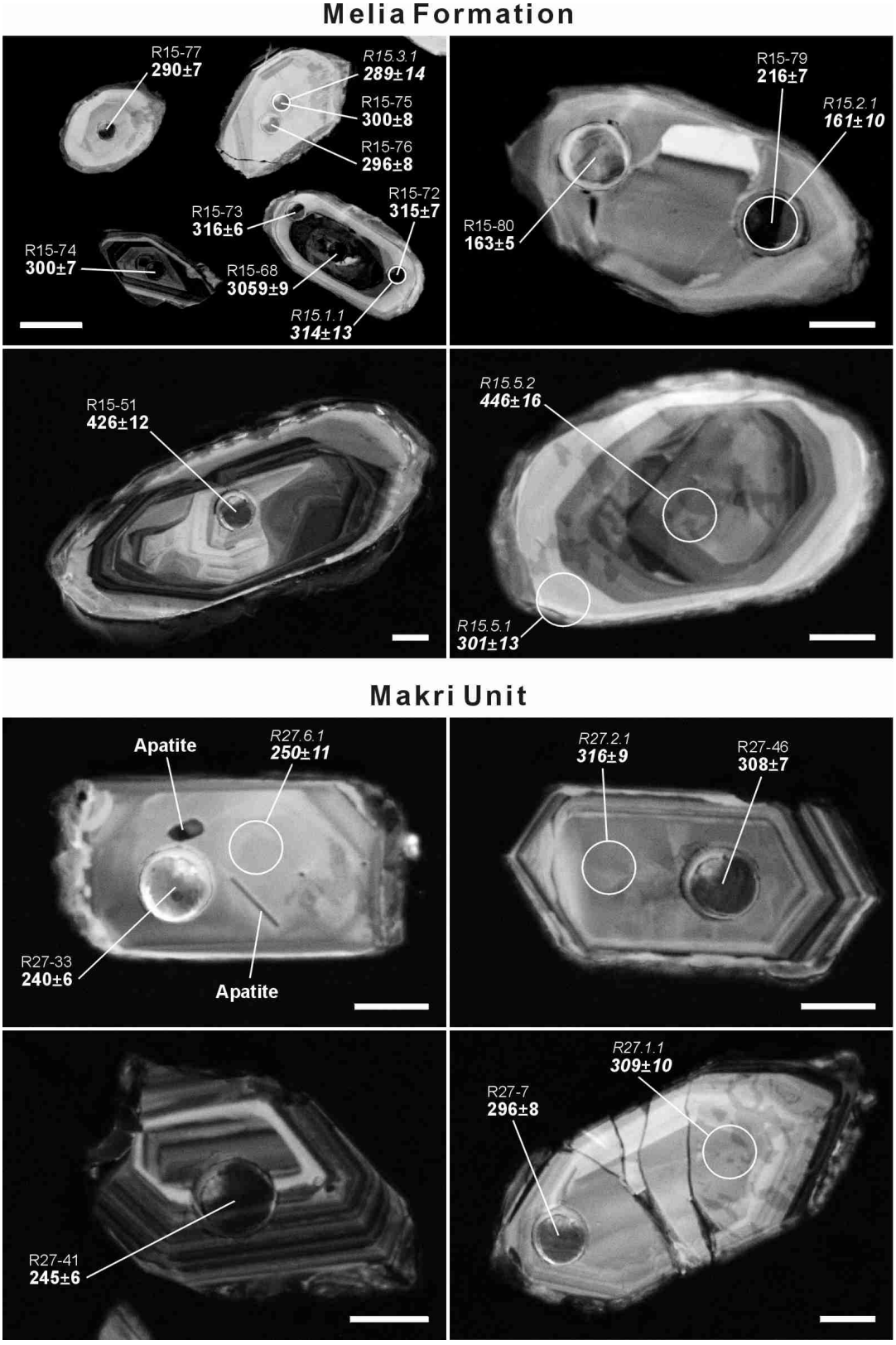

Fig. 18. CL images of representative zircon grains from analysed samples with location of analysis spot and corresponding $^{206}U/^{238}Pb$ age (± 2σ), the exception being spot R15-68 with corresponding $^{207}Pb/^{206}Pb$ age (± 2σ). Note: SHRIMP-II analyses are shown by a white circle with ages given in italics. The remaining are LA-ICPMS analyses. Letter–number code above the ages: sample-spot. The scale bar represents 30 μm in all images.

Makri Unit: Sample R27 was collected from a metasandstone succession cropping out at the main road from Makri to Dikela (40°51´10.0´´N, 25°44´25.3´´E; Fig. 3). Most detrital zircons of this sample are clear and colourless and have a subhedral shape; few are euhedral or rounded. Some zircons are rich in mineral inclusions (e.g. apatite, quartz); others are characterised by fractures filled with iron hydroxides and hence appear dirty brown in parts. Gas or melt channels similar to those illustrated by Corfu et al. (2003, fig. 15) have been found in one crystal. The length of single zircon crystals varies between 100 and 300 µm. The analysed zircons have clear oscillatory zonation patterns in CL images (Fig. 18) and appear to be magmatic in origin; few crystals exhibit weak or no zoning. Inherited cores are sparse. Altogether, 35 single zircon grains have been analysed for their U–Pb ages using SHRIMP-II (7 spots) and LA-ICPMS techniques (31 spots). Grains that were analysed by both methods are shown in Figures 17 and 18 and are indicated in the Appendix. Detrital zircons from sample R27 show a polymodal age distribution with a major cluster between 310–290 Ma, a minor cluster at ca. 240 Ma, and less prominent peaks (each peak represents one analysis) at 376, 343, 262 and 214 Ma (Fig. 19). The youngest grains are rounded (R27-23) and euhedral (R27-24) and have $^{206}Pb/^{238}U$ ages of 214 ± 6 Ma and 233 ± 6 Ma, respectively, thus giving a maximum age of deposition for the metasandstone sample R27 and hence for the Makri Unit. Zircon grains of Middle Triassic age are predominantly euhedral. The (100) prism of these zircons dominates over the (110) prism, with only the (101) bipyramid present, corresponding to the P4 and P5 zircon types of Pupin (1980). Such a morphology is typical of an igneous origin and suggests crystallisation temperatures of about 800–850°C in an alkaline magma. Only a few crystals of Carboniferous age are euhedral that could be used for determining their zircon type. There seems to be two different clusters of zircon types. In both clusters, the (101) prism of the euhedral zircons dominates over the (100) prism, or they are equal in size. In cluster I, however, the (211) bipyramid dominates over the (101) bipyramid, or the latter is subordinate, corresponding to the Q1, Q2, Q3, S6 and S11 zircon types of Pupin (1980), whereas in cluster II only the (101) bipyramid is present, corresponding to the G1, P1 and P2 zircon types of Pupin (1980). Such morphologies are typical of an igneous origin and suggests crystallisation temperatures of about 650–750°C in an aluminous magma for cluster I and in a subalkaline magma for cluster II.

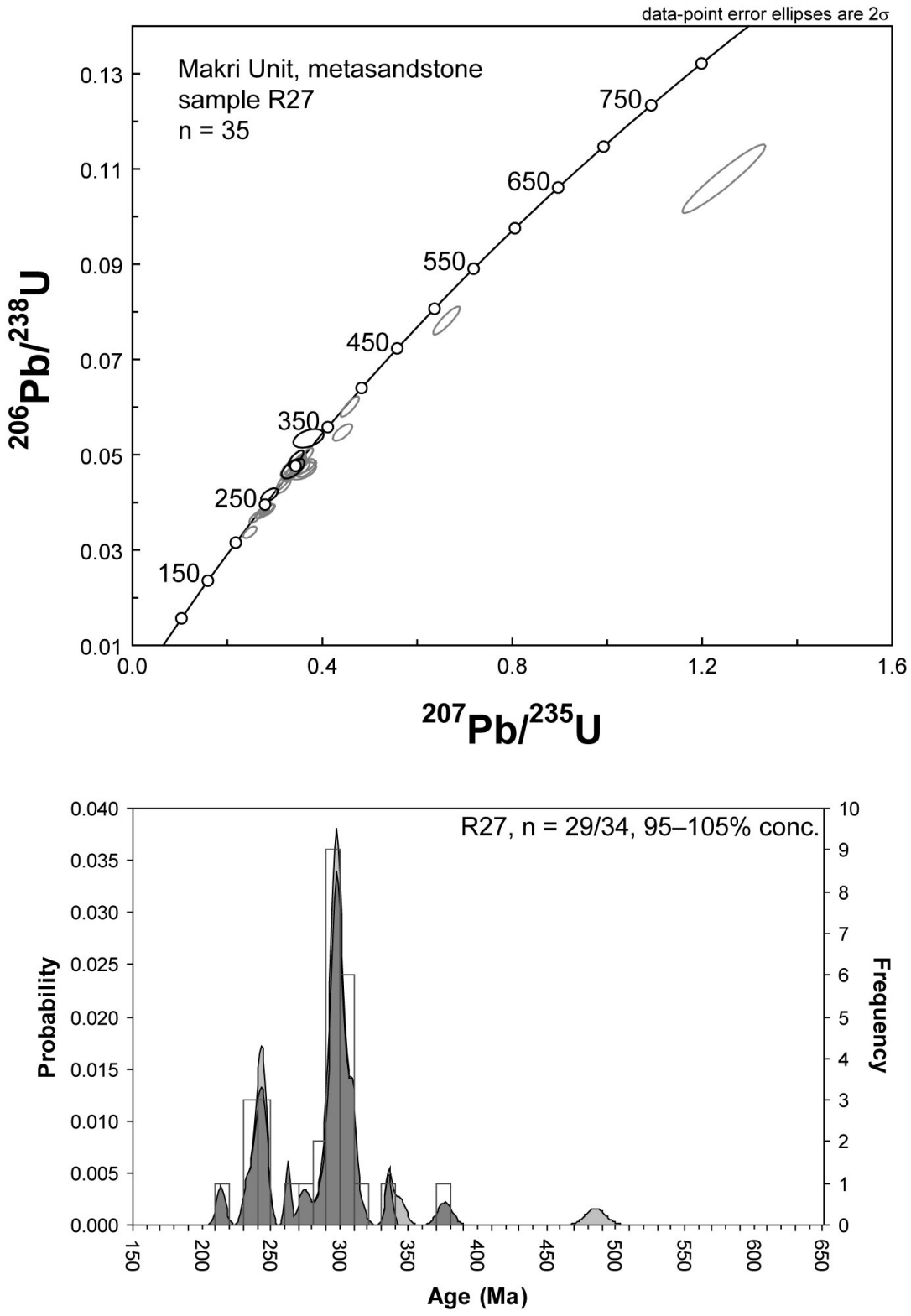

Fig. 19. Concordia diagram (*upper*) and combined probability density distribution and histogram plots (*lower*) showing the results obtained by LA-ICPMS (grey symbols) and SHRIMP-II analyses (black symbols) for detrital zircons from sample R27, Makri Unit. Error ellipses in concordia plots represent 2σ uncertainties. Probability density distribution plots: Dark grey shaded – zircon ages with 95–105% concordance, light grey shaded – zircon ages with >5 % discordance (see text for explanation). Abbreviation: n = number of analyses.

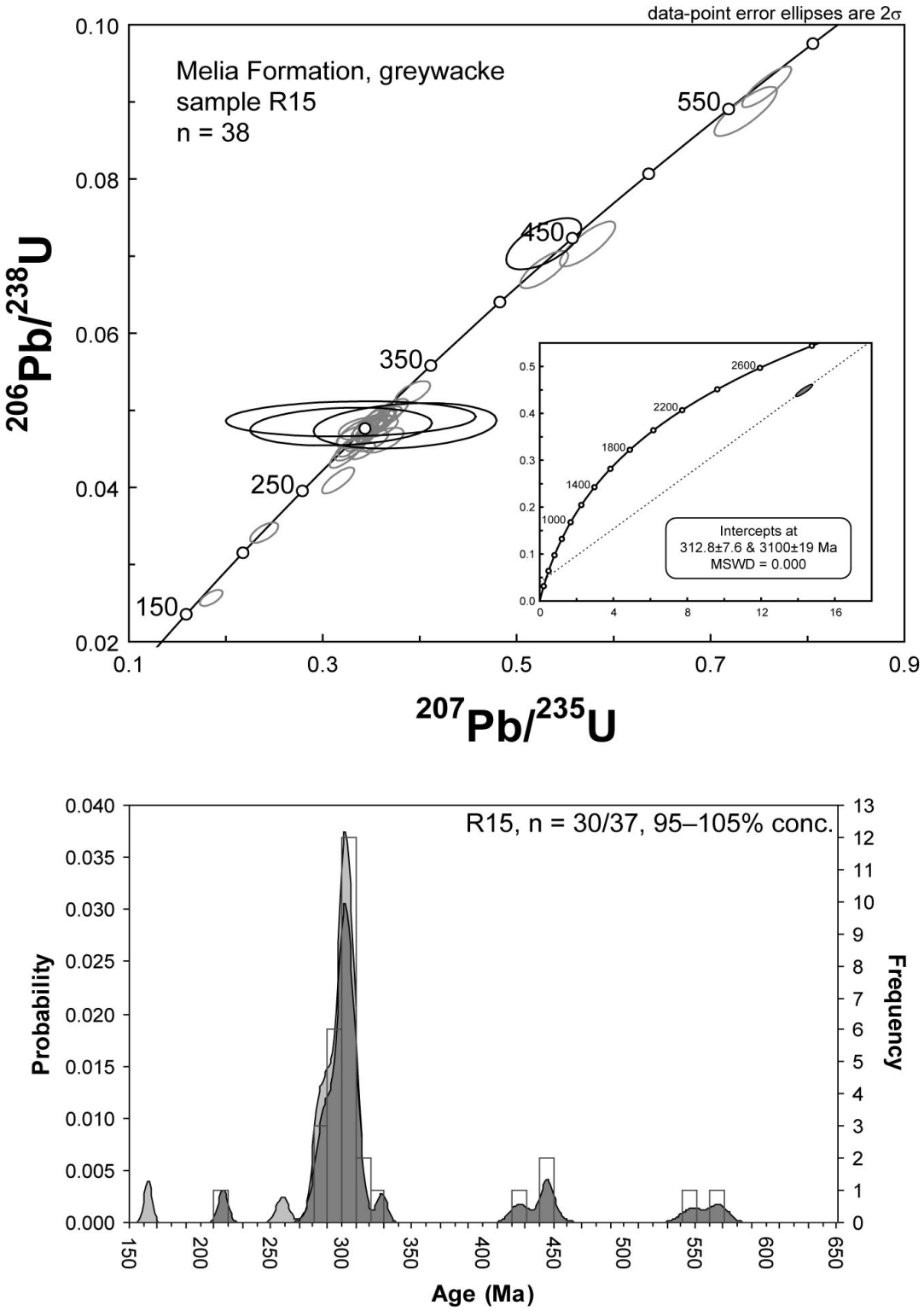

Fig. 20. Concordia diagrams (*upper*) and combined probability density distribution and histogram plots (*lower*) showing the results obtained by LA-ICPMS (grey symbols) and SHRIMP-II analyses (black symbols) for detrital zircons from sample R15, Melia Formation. Error ellipses in concordia plots represent 2σ uncertainties. Probability density distribution plots: Dark grey shaded – zircon ages with 95–105% concordance, light grey shaded – zircon ages with >5 % discordance (see text for explanation). Abbreviation: n = number of analyses.

Melia Formation: Sample R15 was collected from a greywacke successions cropping out at Melia (40°57´07.0´´N, 26°06´12.1´´E; Fig. 4). Most detrital zircons of this sample are clear and colourless and have a subhedral to rounded shape. Some zircons are characterised by fractures filled with iron hydroxides and thus appear dirty brown in parts. The length of single zircon crystals varies between 110 and 300 µm. CL images reveal two types of detrital zircons. Zircons of type I have inherited cores with clear oscillatory zonation patterns in CL images, suggesting a magmatic origin, and younger overgrowths of brighter luminescence, which exhibit no zoning (Fig. 18). Overgrowths of such appearance are commonly characteristic for recrystallisation and new growth of zircon in high-grade metamorphic rocks (e.g. Corfu et al. 2003). The zircon overgrowths in sample R15, however, have Th/U ratios of ≥0.4 that is higher than 0.1, a value that is generally accepted as the lower limit of magmatic values (e.g. Teipel et al. 2004, and references therein) and hence suggests a non-metamorphic origin. Zircons of type II do not have inherited cores. They show clear oscillatory zonation patterns in CL images or a weak zoning and appear to be magmatic in origin (Fig. 18). Altogether, 33 single zircon grains have been analysed for their U–Pb ages using SHRIMP-II (7 spots) and LA-ICPMS techniques (36 spots). Grains that were analysed by both methods are shown in Figures 17 and 18 and are indicated in the Appendix. Detrital zircons from sample R15 show a polymodal age distribution with a major cluster between 315–285 Ma and minor clusters around 550 and 450 Ma (Fig. 20). The Pan-African and Late Ordovician–Early Silurian ages belong to inherited cores. The youngest grain is subhedral and has a late Middle Jurassic age (concordant SHRIMP-II age of 161 ± 10 Ma; slightly discordant LA-ICPMS age of 163 ± 5 Ma; see Fig. 17), thus giving a maximum age of deposition for the greywacke sample R15 and hence for the Melia Formation. It is noteworthy that one grain has an inherited core with a highly discordant $^{206}Pb/^{238}U$ of ca. 2388 Ma and a magmatic rim of ca. 315 Ma (Fig. 18). In a concordia diagram, a regression of the core and the rim yields a discordia with a concordant lower intercept at 312.8 ± 7.6 Ma and an upper intercept at 3100 ± 19 Ma (Fig. 20). The latter age is in good agreement with the $^{207}Pb/^{206}Pb$ age of ca. 3059 Ma that has to be considered as minimum age due to the effect of Pb loss. In general, lower-intercept ages do not necessarily have a geological meaning and should therefore be handled with care (Mezger & Krogstad 1997). In this case, however, the lower intercept of the zircon rim is a concordant age and can be interpreted as the time of secondary zircon crystallisation (magmatic). The upper intercept reflects the time of primary zircon crystallisation, and is

interpreted as the age of formation of the magmatic protolith that survived as the inherited core and hence indicates the presence of a minor Mesoarchaean component.

5. Discussion and conclusions

5.1. Makri Unit

The petrology and whole-rock geochemistry of sedimentary rocks of the Makri Unit suggest a source of intermediate to acidic composition, probably upper continental crust and/or young differentiated arc material, with varying input of a calcareous component. Sediment supply from an ultrabasic source can be excluded. Minor differences in the composition between the samples can be explained by compositional variation within the source area. However, it has to be kept in mind that the rocks are tectonized and experienced a greenschist facies metamorphic overprint that may have caused fluid circulation and disturbance of the primary whole-rock geochemical signature due to fractionation and mobilisation of some major and trace elements.

Mineral chemistry indicates that detrital feldspar is dominated by albite. A prominent content of detrital albite could reflect sediment supply from spilites (altered submarine basalt) where it is the most characteristic mineral (Deer et al. 1992). Such a source, however, should be seen in the whole-geochemical signature (e.g. elevated Cr and Ni values), which is not the case for the analysed metasedimentary rocks of the Makri Unit. The source of detrital albite has to be sought probably in metamorphic rocks of the chlorite and biotite zones since albite is the stable plagioclase in these zones (Deer et al. 1992). Minor input may have come from magmatic albite. In general, the application of detrital feldspar composition for provenance analysis is restricted.

The erosion of rocks, which have formed under different temperature and pressure conditions, can explain the large spread of Si contents of the detrital K-rich white micas from the Makri Unit. The low-Si phengitic mica may have derived from igneous or low-pressure metamorphic rocks. The abundance of intermediate to high-Si phengitic mica points to exposed medium- to high-pressure rocks in the source area during time of deposition. Recycling of detrital mica from older sedimentary succession should also be kept in mind. The compositional range of the analysed detrital white micas could also be explained by

retrograde overprinting of white micas derived from primary high-pressure metamorphic rocks. Nevertheless, the chemistry of detrital mica clearly indicates supply of detritus derived from high-pressure metamorphic rocks during time of deposition of the Makri Unit.

The prominent cluster of detrital zircon ages at ca. 310–290 Ma suggests significant input of Upper Carboniferous and Lower Permian igneous rocks. Similar ages have been reported as protolith ages for orthogneisses of the Thracia Terrane (e.g. Turpaud & Reischmann 2005; Turpaud 2006; Cornelius et al. 2007), which constitutes the closest possible source area. Therefore, it seems plausible to assume that orthogneisses of the latter or equivalents contributed significant amounts of detritus to the clastic metasedimentary succession of the Makri Unit. The source of the second cluster of detrital zircon ages at ca. 240 Ma, however, cannot be sought in the Thracia Terrane since metagranitoid rocks of Middle Triassic age have not yet been described from there. Late Carboniferous and Early Permian together with Middle Triassic zircons have been documented from various meta-igneous rocks of the Attic-Cycladic Massif (e.g. Reischmann 1998; Tomaschek et al. 2001) and the Pelagonian Zone (e.g. Anders et al. 2006b, and references therein). Thus, they may be considered as possible source areas, although they are laying more fare to the south and west nowadays. An input of zircons from the voluminous Arnea suite, which comprises predominantly A-type granitoids of Middle to early Late Triassic age (Himmerkus et al. 2004b, in preparation), can be safely excluded since Silurian ages from the adjacent country rocks (Vertiskos Unit: Himmerkus et al. 2006a, 2007, submitted) are absent in the age spectrum of detrital zircons from the metasandstone of the Makri Unit. The youngest detrital zircon grain found so far indicates that the metasedimentary succession of the Makri Unit, or at least parts of it, cannot be older than Late Triassic.

5.2. Melia Formation

The petrology and whole-rock geochemistry of clastic metasedimentary rocks from the Melia Formation suggest a uniform source of intermediate to acidic composition, which was less affected by intracrustal differentiation processes. Input from an ultrabasic source can be excluded.

Detrital feldspar grains from the Melia Formation include besides albite also subordinate amounts of oligoclase and minor anorthoclase and orthoclase. The large range in

feldspar composition reflects the large range in possible source rock lithologies. Similar to detrital feldspar in the Makri Unit, the source of detrital albite has to be sought probably in metamorphic rocks of the chlorite and biotite zones since albite is the stable plagioclase in these zones (Deer et al. 1992). The detrital mineral assemblage of epidote, zoisite and garnet that together with phengitic mica indicates metamorphic rocks being the major source for clastic metasedimentary rocks of the Melia Formation supports this origin. The presence of oligoclase suggests derivation from acidic to intermediate igneous rocks; orthoclase and anorthoclase may have derived from acidic igneous rocks (Deer et al. 1992). Erosion of rocks that have formed under different temperature and pressure conditions can explain the large spread of Si contents of the detrital K-rich white micas from the Melia Formation. The low-Si phengitic mica may have derived from igneous or low-pressure metamorphic rocks. The abundance of intermediate to high-Si phengitic mica points to exposed medium- to high-pressure rocks in the source area during time of deposition. Recycling of detrital mica from older sedimentary succession should also be kept in mind. The compositional range of the analysed detrital white micas could also be explained by retrograde overprinting of white micas derived from primary high-pressure metamorphic rocks. Nevertheless, the chemistry of detrital mica clearly indicates supply of detritus derived from high-pressure metamorphic rocks during time of deposition of the Melia Formation. Detrital phengite could have been derived from paragneisses, mica schists (metapelites) and orthogneisses of the Rhodope Massif since phengite is present in these rocks (e.g. Mposkos 1989; Mposkos & Liati 1993).

The majority of the analysed garnets from the Melia Formation are almandine-rich with minor pyrope and grossular components. According to the classification of Morton et al. (2004), the majority of the garnets belong to Field C garnets (60%) and subordinate Field B garnets (26%). Only 14 % of the population belong to Field A garnets. The ultimate source of Field A garnets is suggested to be high-grade (granulite facies) metasedimentary rocks or charnockites (Morton et al. 2004). Field B garnets are probably derived from intermediate to acidic gneisses, together with granites or pegmatites, and Field C garnets are probably derived from high-grade basic gneisses, eclogites and quartz-biotite gneisses (Morton et al. 2004). An input of high-grade basic gneisses and eclogites, however, seems most unlikely since accompanied mineral paragenesis such as amphibole are not present as framework component in clastic metasedimentary rocks of the Melia Formation, although intensive alteration and weathering of amphibole to clay minerals cannot be excluded. In general,

almandine garnets with pyrope contents from 10 to 40 mol% occur in epidote–amphibolite to granulite facies gneisses (e.g. Takeuchi 1994). According to the accompanying heavy mineral assemblage, the detrital garnets of the Melia Formation have probably been derived from mica schists and gneisses, which experienced higher greenschist to lower amphibolite facies regional metamorphism. An input of garnet from acidic igneous rocks (e.g. granites, pegmatites) seems most unlikely, according to Morton (1991, fig. 11). The two grossular-rich garnets were probably derived from metamorphosed impure calcareous rocks, for example, skarn deposits (Deer et al. 1992).

According to the data above, metasedimentary rocks have been the main source for the Melia Formation. Therefore, it seems plausible to suggest that most of the detrital zircons have been derived from metasedimentary rocks and thus represent recycled material. The prominent cluster of detrital zircon ages at ca. 315–285 Ma suggests significant input of Upper Carboniferous and Lower Permian igneous rocks. The inherited cores indicate the involvement of Pan-African and Late Ordovician–Early Silurian crustal sources during Late Carboniferous–Early Permian magma genesis. Acidic igneous rocks of similar composition have been documented from the southerly Sredna Gora Terrane in Bulgaria (Carrigan et al. 2005). There, leucogranites of Late Carboniferous and Early Permian age contain 80–90% inherited cores with ages of ~300–400 Ma, ~450 Ma and ~600–900 Ma (Carrigan et al. 2005). Furthermore, Upper Carboniferous–Lower Permian orthogneisses with zircons containing abundant Early Palaeozoic and Pan-African inherited cores have been recently discovered in the Thracia Terrane of the Eastern Rhodope (N. Cornelius 2007, pers. comm.). Therefore, it seems plausible to assume that leucogranites of the Sredna Gora Terrane or orthogneisses of the Thracia Terrane or equivalent rocks contributed significant amounts of detritus to a clastic sedimentary succession. Later, this succession has been overprinted under higher greenschist to lower amphibolite facies metamorphic conditions before it was uplifted and exposed on the surface to supply detritus for the clastic succession of the Melia Formation. The youngest detrital zircon grain (ca. 160 Ma) found so far indicates that the rocks of the Melia Formation cannot be older than latest Middle Jurassic. This grain may have derived from orthogneisses of the Rhodope Terrane since these rocks are Middle–Late Jurassic in age (Turpaud & Reischmann 2005; Turpaud 2006).

5.3. Palaeotectonic implications

Makri Unit: In general, sedimentary provenance data do not show evidence for reworking of rocks from the Makri Unit supplying detritus to the Melia Formation. The Makri Unit and the Melia Formation had different source areas, although those are lying nowadays side by side in the Rhodope Massif. Furthermore, the Melia Formation does not transgressively overlay rocks of the Makri Unit. The contact between Makri Unit and Melia Formation is a tectonic contact, as already emphasized by von Braun (1993). The youngest detrital zircon grain indicates that at least a part of the metasedimentary succession of the Makri Unit cannot be older than Late Triassic. The conglomerates, quartz arenites, litharenites and limestones (now marble) have probably belonged to a single succession deposited under shallow marine conditions. The clastic rocks received large amounts of acidic detritus of volcanic-arc origin, with minor input of carbonates. The euhedral crystal shape of many grains and the narrow range of zircon ages and the rarity of pre-Carboniferous detritus indicate proximity to a Carboniferous source area of homogeneous composition. At the present state of knowledge, it may have been basement rocks from the Pelagonian Zone (including the Attic-Cycladic Massif) or equivalent rocks. The upper time limit of deposition is difficult to constrain. However, it may be given by the tectonically overlying Evros ophiolite. The following scenario is suggested: continental shelf sedimentation (= metasedimentary rocks of Makri Unit; Fig. 21), rifting and oceanic basin opening, intraoceanic subduction, ophiolite obduction (= Evros ophiolite) and oceanic basin closure. Therefore, we suggest that the Makri Unit is older than ca. 170 Ma (the formation age of the Evros ophiolite) but younger than ca. 214 Ma, probably latest Triassic and/or Early Jurassic in age. Younger fossil findings described from the Makri Unit (e.g. Dimadis & Nikolov 1997) may be explained by tectonic imbrications of rocks from the Melia Formation (see von Braun 1993).

Melia Formation: The clastic metasedimentary successions of the Makri Unit and the Melia Formation are quite different from each other in their age, lithology and source. U–Pb detrital zircon geochronology indicates that the Melia Formation cannot be older than latest Middle Jurassic. Dimadis & Nikolov (1997) even suggested that it cannot be older than Early Cretaceous with the upper time limit of sedimentation being Mid-Cretaceous. The upper time limit of sedimentation and metamorphism of the Melia Formation is clearly set by the

unconformably overlying Middle Eocene clastic deposits (see Kopp 1965; von Braun 1968). The new data of this study do not fit with a recently presented palaeotectonic model by Bonev & Stampfli (2003, 2007). In their model, the Melia Formation correlates with the Mandrica group of SE Bulgaria, and both were generated in a Middle–Late Jurassic intraoceanic Vardarian volcanic-arc environment. The clastic sedimentary succession of the Melia Formation, however, received large amounts of detritus of metasedimentary rocks, which probably experienced higher greenschist to lower amphibolite facies regional metamorphism. The sedimentary input of terrestrial plant fragments indicates proximity to a hinterland with vegetation (Fig. 21). The angular to subangular shape of the framework components, the poor sorting, and the high amounts of unstable lithoclasts (plagioclase) indicate rapid erosion and deposition without significant rounding or sorting. This and the narrow range of zircon ages suggest deposition in a fast-subsiding sedimentary basin accompanied by fast uplift in the hinterland, probably the Rhodope Massif. The input of metamorphic detritus indicates palaeotectonic modifications that might have corresponded to microplate reorganisation and progressive uplift of a part of the Rhodope metamorphic complex. Taken collectively, the data suggest deposition in a developing foreland basin in front of a metamorphic nappe pile with Rhodope affinities in post-Jurassic time rather than a Middle–Late Jurassic intraoceanic Vardarian volcanic-arc environment.

In order to gain a regional perspective, we would like to discuss the concept of the Circum-Rhodope Belt sensu Kaufmann et al. (1976). As already mentioned in the introduction, Ricou et al. (1998) rejected the concept of a Mesozoic Circum-Rhodope Belt, covering the Rhodope Massif. According to those authors, the rocks of the Circum-Rhodope Belt belong to two distinct greenschist-facies belts, and the cover sequences of the Rhodope are not older than Late Cretaceous. Here, we only discuss the sedimentary rocks since they have been the focus of this study. Basic and ultrabasic rocks from the Chalkidiki, Samothraki and Evros ophiolites share many similarities in age, lithology, geochemistry and tectonic setting and thus could have formed in the same arc and back-arc basin environment (e.g. Zachariadis et al. 2006; Koglin et al. 2007; Zachariadis 2007). However, such an in-depth analysis is beyond the scope of the present study and will be subject of the work of colleagues in Mainz. Nonetheless, according to the data of this study, the Circum-Rhodope belt sensu Kauffmann et al. (1976) does not exist. Only the clastic sedimentary succession of the Makri Unit resembles the Melissochori Formation (former Svoula flysch) of the western Circum-

Rhodope Belt, as already noted by Pe-Piper & Piper (2002), although the Melissochori Formation had a different source area (see Chapter 5 of this thesis). Thus, the Makri Unit may represent a time and facies equivalent to the Melissochori Formation and was deposited in distance to the latter in a Neotethyan oceanic basin to the northeast of the Pelagonian Zone.

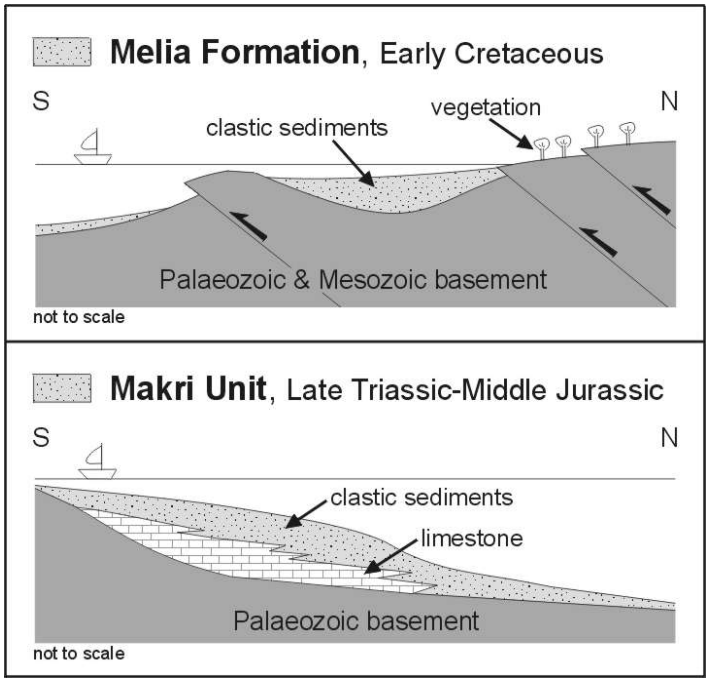

Fig. 21. Schematic sketches for the depositional settings of sedimentary rock of the eastern Circum-Rhodope Belt.

In contrast to Kaufmann et al. (1976), we want to emphasize that sedimentary rocks of the Melia Formation cannot be correlated with those of the Melissochori Formation. They had quite different source areas and sedimentation ages (see Chapter 5 of this thesis). Furthermore, the correlation between the Melia Formation of Greece and parts from the Maglenica Group of Bulgaria (e.g. von Braun 1993; Bonev & Stampfli 2003, 2007, and references therein) is still speculative and needs further verification. Structural studies provided evidence that the Makri Unit primary underwent N- to NW-directed thrusting (von Braun 1993). Similar features were described by Bonev & Stampfli (2003) from Mesozoic schists of the eastern Circum-Rhodope Belt in Bulgaria and have been assigned by those authors to a possible earlier thrusting event, which could represent deformation in a subduction–accretion complex. Following Bonev & Stampfli (2003), it seems plausible to suggest that the Makri Unit together with the Evros ophiolite have been thrust over the Rhodope promontory, probably during the Late Jurassic–Early Cretaceous. This may correspond to the collision event that was responsible for the Late Jurassic–Early Cretaceous

N-directed Balkan orogeny (e.g. Bonev & Stampfli 2003, 2007). The Melia Formation, however, does not fit in such a scenario. Its sedimentary succession was derived from a different source in post-Jurassic time, probably a metamorphic nappe pile with Rhodope affinities. Later, the rocks of the eastern Circum-Rhodope Belt and the underlying basement of the Rhodope were involved in late-orogenic extensional tectonics during Alpine orogeny in Late Cretaceous and Tertiary times (e.g. Burg et al. 1996; Bonev et al. 2005).

Synthesis

In the following, the most important results on the provenance of sedimentary successions of the Internal Hellenides are compiled (Figs. 1 and 2) and implications on palaeotectonic reconstructions are highlighted.

Serbo-Macedonian Massif: The Pirgadikia Unit appears as tectonic inliers within the Vardar suture zone bordering the Serbo-Macedonian Massif to the southwest. Its metasedimentary succession is correlated with Ordovician overlap sequences deposited at the northern margin of Gondwana on the basis of maturity and zircon age spectra. This unit can be best interpreted as a peri-Gondwana terrane of Avalonian origin situated in close proximity to Cadomian terranes by the Late Neoproterozoic–Early Palaeozoic. Detrital zircons from a garnetiferous micaschist of the Vertiskos Unit suggest a NW African source. One sample of garnet-biotite gneiss, interpreted as orthogneiss, comprises zircons of igneous origin with late Middle Ordovician to Silurian ages. The rock association of the Vertiskos Unit can be assigned to an ancient active-margin succession of the Hun superterrane.

Chios Island: Major- and trace-element data of Late Palaeozoic and Permo-Triassic clastic sediments from Chios are compatible with an acidic to intermediate source, minor input of (ultra)mafic detritus and recycling of older sedimentary components. Rutile chemistry and Zr-in-rutile thermometry indicate a change in source-rock lithology through time. Detrital zircon ages in conjunction with provenance analysis of fossiliferous olistoliths strongly suggest that the clastic succession of Chios received its detritus from basement rocks of the Sakarya microcontinent in western Turkey and time and facies equivalents of Palaeozoic units from the Istanbul Zone in northern Turkey and the Balkan region.

Eastern Vardar Zone including the western Circum-Rhodope Belt: The sediments here record a Neotethyan cycle of oceanic basin opening and closure. The clastic sediments of the Examili Formation were deposited in an intracontinental rift-related sedimentary basin in proximity to the Vertiskos Unit in the Permo-Triassic. The Melissochori Formation was deposited in front of a Permo-Carboniferous basement unit of volcanic-arc origin with minor input of older basement rocks, probably at the slope of a carbonate platform in the Early–Middle Jurassic. The Prinochori Formation was probably deposited in front of a nappe

complex in the Early Cretaceous, comprising ophiolitic rocks and basement slivers from the Vertiskos Unit or equivalent rocks. Taken collectively, the eastern Vardar Zone is a complex imbricated belt (suture zone) comprising various types of metasedimentary and meta-igneous rocks which were tectonically juxtaposed. Polyphase tectonics and metamorphism obstruct palinspastic reconstructions.

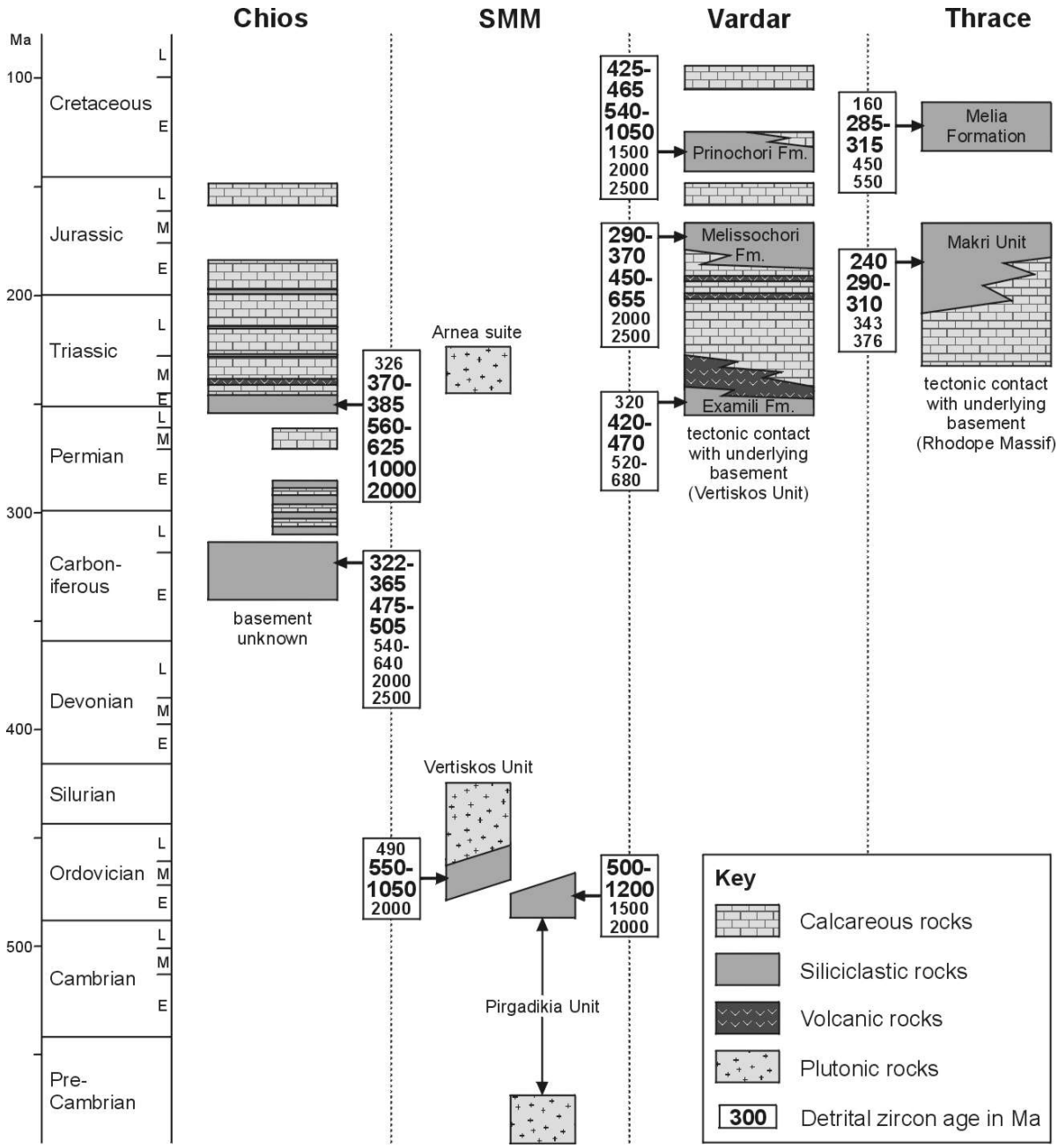

Fig. 1. Chronostratigraphic chart showing generalised stratigraphic columns of the study areas with the most significant detrital zircon ages of the sedimentary successions investigated. The font size of the detrital zircon ages is proportionate to their frequency of occurrence.

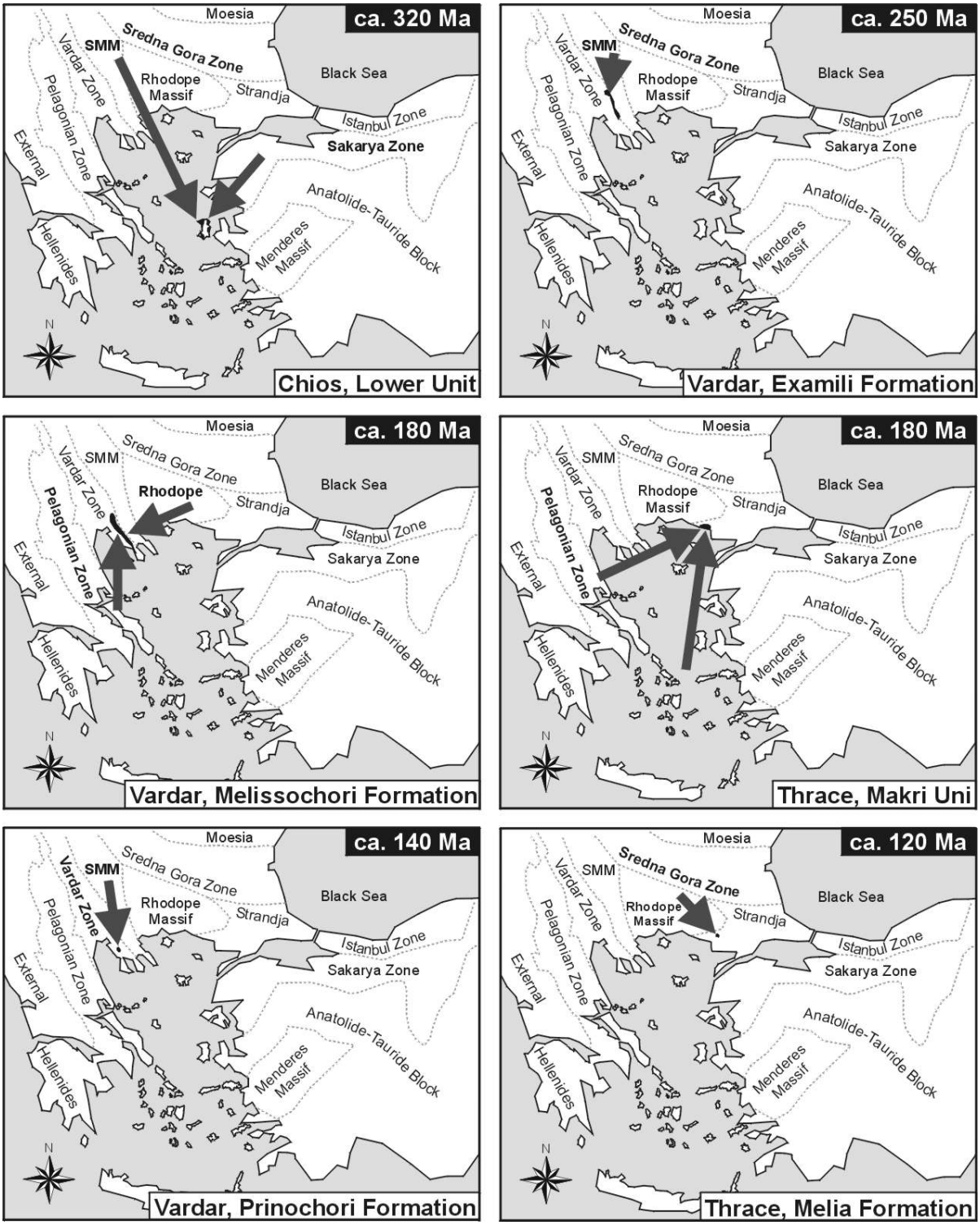

Fig. 2. Major geotectonic units in the Eastern Mediterranean. Suggested source areas for the Late Palaeozoic and Mesozoic sedimentary successions (shown in black) are highlighted in bold print and indicated by arrows.

Eastern Circum-Rhodope Belt: The Makri Unit and the Melia Formation belong to the eastern Circum-Rhodope Belt that forms the uppermost tectonostratigraphic unit of the

Rhodope metamorphic nappe pile. Metasediments from the Makri Unit had a source of intermediate to acidic composition resembling upper continental crust and/or young differentiated arc material, with varying input from a calcareous component. Detrital zircons suggest derivation from basement rocks of the Pelagonian Zone or equivalent rocks. By contrast, metasediments from the Melia Formation had a uniform source of intermediate to acidic composition, which was less affected by intracrustal differentiation processes. The detrital mineral assemblage of epidote, zoisite, garnet, and phengitic mica points to metamorphic rocks being the major source of the clastic sediments of the Melia Formation. The Melia Formation was probably deposited in Cretaceous times in front of a metamorphic nappe pile with Rhodope affinities. The Makri Unit and the Melia Formation were derived from different sources and tectonically juxtaposed during Balkan and Alpine orogenic processes.

The data of this study clearly show that subduction of a branch of the Palaeotethys Ocean in the Late Palaeozoic and the subsequent accretion of North Gondwana-derived terranes close to the southern active margin of Eurasia supplied detritus to the sedimentary successions of the Internal Hellenides. Early Mesozoic rifting marks the birth of Neotethyan oceans in Greece. Intraoceanic subduction and ophiolite obduction characterise the Jurassic. The Late Jurassic and Early Cretaceous phase of nappe tectonics was sealed by Mid-Cretaceous carbonate deposition. In the Internal Hellenides the final closure of Neotethyan oceanic basins occurred during the Late Cretaceous and Tertiary.

References

ABDELSALAM, M.G., LIÉGEOIS, J.P. & STERN, R.J., 2002. The Saharan metacraton. *Journal of African Earth Sciences*, **34**, 119–136.

AFTALION, M., BOWES, D.R. & VŘANA, S., 1989. Early Carboniferous U–Pb zircon ages for garnetiferous perpotassic granulites, Blanský les massif, Czechoslovakia. *Neues Jahrbuch für Mineralogie*, *Monatshefte*, **4**, 145–152.

ALEKSIĆ, V., DIMITRIADIS, S., KALENIĆ, M., STOJANOV, R. & ZAGORČEV, I., 1988. Precambrian in the Serbo-Macedonian Massif. *In:* ZOUBEK, V., COGNÉ, J., KOZHOUKHAROV, D. & KRÄUTNER, H.G. (eds) *Precambrian in younger fold belts; Europe and Variscides, the Carpathians and Balkans*. Wiley, 779–820.

ALTINER, D., ÖZKAN-ALTINER, S. & KOÇYIĞIT, A., 2000. Late Permian foraminiferal biofacies belts in Turkey: palaeogeographic and tectonic implications. *In:* BOZKURT, E., WINCHESTER, J.A. & PIPER, J.D.A. (eds) *Tectonics and Magmatism in Turkey and the Surrounding Area*. Geological Society, London, Special Publications, **173**, 139–161.

ANDERS, B., REISCHMANN, T., POLLER, U. & KOSTOPOULOS, D., 2005. Age and origin of granitic rocks of the eastern Vardar Zone, Greece: new constraints on the evolution of the Internal Hellenides. *Journal of the Geological Society*, *London*, **162**, 857–870.

ANDERS, B., REISCHMANN, T., KOSTOPOULOS, D. & POLLER, U., 2006a. The oldest rocks of Greece: first evidence for a Precambrian terrane within the Pelagonian Zone. *Geological Magazine*, **143**, 41–58.

ANDERS, B., REISCHMANN, T. & KOSTOPOULOS, D., 2006b. Zircon geochronology of basement rocks from the Pelagonian Zone, Greece: constraints on the pre-Alpine evolution of the westernmost Internal Hellenides. *International Journal of Earth Sciences*, doi:10.1007/s00531-006-0121-7.

ANDRIESEN, P.A.M., BANGA, G. & HEBEDA, E.H., 1987. Isotopic age study of pre-Alpine rocks in the basal units on Naxos, Sikinos, and Ios, Greek Cyclades. *Geologie en Mijnbouw*, **66**, 3–14.

ANGIOLINI, L., CARABELLI, L. & GAETANI, M., 2005. Middle Permian brachiopods from Greece and their palaeobiogeographical significance: new evidence for a Gondwanan affinity of the Chios island Upper Unit. *Journal of Systematic Palaeontology*, **3**, 169–185.

ANTHES, G. & REISCHMANN, T., 2001. Timing of granitoid magmatism in the eastern mid-German crystalline rise. *Journal of Geodynamics*, **31**, 119–143.

AVIGAD, D., KOLODNER, K., MCWILLIAMS, M., PERSING, H. & WEISSBROD, T., 2003. Origin of northern Gondwana Cambrian sandstone revealed by detrital zircon SHRIMP dating. *Geology*, **31**, 227–230.

AVIGAD, D., SANDLER, A., KOLODNER, K., STERN, R.J., MCWILLIAMS, M., MILLER, N. & BEYTH, M., 2005. Mass-production of Cambro-Ordovician quartz-rich sandstones as a consequence of chemical weathering of Pan-African terranes: Environmental implications. *Earth and Planetary Science Letters*, **240**, 818–826.

BARATTOLO, F., 1991. Mesozoic and Cenozoic marine benthic calcareous algae with particular regard to the Mesozoic dasycladaleans. *In:* RIDING, R. (ed) *Calcareous algae and stromatolites*. Springer Verlag, Berlin Heidelberg New York, 504–540.

BARNES, S.J. & ROEDER, P.L., 2001. The range of spinel composition in terrestrial mafic and ultramafic rocks. *Journal of Petrology*, **42**, 2279–2302.

BASSOULLET, J.P., BERNIER, P., DELOFFRE, R., GENOT, P., JAFFREZO, M., POIGNANT, A.F. & SEGONZAC, G., 1977. Classification criteria of fossil Dasycladales. *In:* FLÜGEL, E. (ed) *Fossil Algae*. Springer Verlag, Berlin Heidelberg New York, 154–166.

BARR, S.R., TEMPERLEY, S.T. & TARNEY, J., 1999. Lateral growth of the continental crust through deep level subduction-accretion: a re-evaluation of central Greek Rhodope. *Lithos*, **46**, 69–94.

Baud, A., Jenny, C., Papanikolaou, D., Sideris, C. & Stampfli, G., 1991. New observations on Permian stratigraphy in Greece and geodynamic interpretation. *Bulletin of the Geological Society of Greece*, **25**, 187–206.

Bauer, C., Rubatto, D., Krenn, K., Proyer, A. & Hoinkes, G., 2007. A zircon study from the Rhodope metamorphic complex, N-Greece: Time record of a multistage evolution. *Lithos*, doi:10.1016/j.lithos.2007.05.003.

Bébien, J., Dubois, R. & Gauthier, A., 1986. Example of ensialic ophiolites emplaced in a wrench zone: Innermost Hellenic ophiolite belt (Greek Macedonia). *Geology*, **14**, 1016–1019.

Belka, Z., Valverde-Vaquero, P., Dörr, W., Ahrendt, H., Wemmer, K., Franke, W. & Schäfer, J., 2002. Accretion of first Gondwana-derived terranes at the margin of Baltica. *In:* Winchester, J.A., Pharaoh, T.C. & Verniers, J. (eds) *Palaeozoic Amalgamation of Central Europe*. Geological Society, London, Special Publications, **201**, 19–36.

Besenecker, H., Dürr, S., Herget, G., Jacobshagen, V., Kauffmann, G., Lüdtke, G., Roth, W. & Tietze, K.W., 1968. Geologie von Chios (Ägäis). *Geologica et Palaeontologica*, **2**, 121–150.

Besenecker, H., Dürr, S., Herget, G., Kauffmann, G., Lüdtke, G., Roth, W. & Tietze, K.W., 1971. Geological Map of Greece, Chios sheet, 1 : 50 000 (2 sheets: Northern and Southern). *Institute for Geology and Subsurface Research*, Athens.

Bhatia, M.R., 1983. Plate tectonics and geochemical composition of sandstones. *Journal of Geology*, **91**, 611–627.

Bhatia, M.R., 1985. Rare earth element geochemistry of Australian Paleozoic graywackes and mudstones: Provenance and tectonic control. *Sedimentary Geology*, **45**, 97–113.

Bhatia, M.R. & Crook, K.A.W., 1986. Trace element characteristics of graywackes and tectonic setting discrimination of sedimentary basins. *Contributions to Mineralogy and Petrology*, **92**, 181–193.

Biggazzi, G., Del Moro, A., Innocenti, F., Kyriakopoulos, K., Manetti, P., Papadopoulos, P., Norelliti, P. & Magganas, A., 1989. The magmatic intrusive complex of Petrota, West Thrace: age and geodynamic significance. *Geologica Rhodopica*, **1**, 290–297.

Black, L.P., Kamo, S.L., Allen, C.M., Aleinikoff, J.N., Davis, D.W., Korsch, R.J. & Foudoulis, C., 2003. TEMORA 1: a new zircon standard for Phanerozoic U–Pb geochronology. *Chemical Geology*, **200**, 155–170.

Bloomer, S.H. & Hawkins, J.W., 1987. Petrology and geochemistry of boninite series rocks from the Mariana trench. *Contributions to Mineralogy and Petrology*, **97**, 361–377.

Blumenstengel, H., Hansch, W., Heuse, T., Leonhardt, D., Maletz, J., Meisel, S., Samuelsson, J., Sarmiento, G.N., Sehnert, M., Tröger, K.-A., Verniers, J. & Walter, H., 2006. Fauna und Flora im Silur Deutschlands. *In:* Deutsche Stratigraphische Kommission, Heuse, T. & Leonhardt, D. (eds) für die Subkommission Proterozoikum–Silur. *Stratigraphie von Deutschland VII, Silur*. Schriftenreihe der Deutschen Gesellschaft für Geowissenschaften, **46**, 137–139.

Bonev, N.G. & Stampfli, G.M., 2003. New structural and petrologic data on Mesozoic schists in the Rhodope (Bulgaria): geodynamic implications. *Comptes Rendus Geoscience*, **335**, 691–699.

Bonev, N.G. & Stampfli, G.M., 2005. Compositional diversity of the Evros ophiolite, Thrace, northeastern Greece: field occurrences, preliminary petrologic and geochemical data on plutonic sequences and tectonic implications. *Proceedings of the 80th Anniversary Jubilee Meeting of the Bulgarian Geological Society*, 24–27.

Bonev, N. & Stampfli, G., 2007. Petrology, geochemistry and geodynamic implications of Jurassic island arc magmatism as revealed by mafic volcanic rocks in the Mesozoic low-grade sequence, eastern Rhodope, Bulgaria. *Lithos*, doi:10.1016/j.lithos.2007.06.019.

Bonev, N., Burg, J.-P. & Ivanov, Z., 2005. Mesozoic–Tertiary structural evolution of an extensional gneiss do— the Kesebir–Kardamos dome, eastern Rhodope (Bulgaria–Greece). *International Journal of Earth Sciences*, doi:10.1007/s00531-005-0025-y.

Bonjour, J.L., Peucat, J.J., Chauvel, J.J., Paris, F. & Cornichet, J., 1988. U-Pb zircon dating of the Early Paleozoic (Arenigian) transgression in western Brittany (France): a new constraint for the Lower Paleozoic time-scale. *Chemical Geology*, **72**, 329–336.

Boudagher-Fadel, M.K., Rose, E.P.F., Bosence, D.W.J. & Lord, A.R., 2001. Lower Jurassic foraminifera and calcified microflora from Gibraltar, Western Mediterranean. *Palaeontology*, **44**, 601–621.

Brown, S.A.M. & Robertson, A.H.F., 2003. Sedimentary geology as a key to understand the tectonic evolution of the Mesozoic-Early Tertiary Paikon Massif, Vardar suture zone, N Greece. *Sedimentary Geology*, **160**, 179–212.

Brown, S.A.M. & Robertson, A.H.F., 2004. Evidence for Neotethys rooted within the Vardar suture zone from the Voras Massif, northernmost Greece. *Tectonophysics*, **381**, 143–173.

Brun, J.-P. & Sokoutis, D., 2007. Kinematics of the Southern Rhodope Core Complex (North Greece). *International Journal of Earth Sciences*, doi:10.1007/s00531-007-0174-2.

Burg, J.-P., Godfriaux, I. & Ricou, L.E., 1995. Extension of the Mesozoic Rhodope thrust units in the Vertiskos-Kerdilion Massifs (Northern Greece). *Comptes Rendus de l'Académie des Sciences*, **320**, 889–896.

Burg, J.-P., Ricou, L.-E., Ivanov, Z., Godfriaux, I., Dimor, D. & Klain, L., 1996. Syn-metamorphic nappe complex in the Rhodope Massif. Structure and Kinematics. *Terra Nova*, **8**, 6–15.

Calvez, J.Y. & Vidal, P., 1978. Two billion year old relicts in the Hercynian belt of western Europe. *Contributions to Mineralogy and Petrology*, **65**, 395–399.

Candan, O., Dora, O., Oberhänsli, R., Çetinkaplan, M., Partzsch, J., Warkus, F. & Dürr, S., 2001. Pan-African high-pressure metamorphism in the Precambrian basement of the Menderes Massif, western Anatolia, Turkey. *International Journal of Earth Sciences*, **89**, 793–811.

Carras, N. & Geogala, D., 1998. Upper Jurassic to Lower Cretaceous carbonate facies of African affinities in a peri-European area: Chalkidiki peninsula, Greece. *Facies*, **38**, 153–164.

Carrigan, C.W., Mukasa, S.B., Haydoutov, I. & Kolcheva, K., 2005. Age of Variscan magmatism from the Balkan sector of the orogen, central Bulgaria. *Lithos*, **82**, 125–147.

Carrigan, C.W., Mukasa, S.B., Haydoutov, I. & Kolcheva, K., 2006. Neoproterozoic magmatism and Carboniferous high-grade metamorphism in the Sredna Gora Zone, Bulgaria: An extension of the Gondwana-derived Avalonian-Cadomian belt?. *Precambrian Research*, **147**, 404–416.

Chen, F., Siebel, W., Satir, M., Terzioğlu, M. & Saka, K., 2002. Geochronology of the Karadere basement (NW Turkey) and implications for the geological evolution of the Istanbul zone. *International Journal of Earth Sciences*, **91**, 469–481.

Chlupáč, I., Kříž, J. & Schönlaub, H.P., 1980. Field Trip E. Silurian and Devonian conodonts of the Barrandian. *In:* Schönlaub, H.P. (ed) *Second European Conodont Symposium-ECOS II. Guidebook Abstracts*. Abhandlungen der Geologischen Bundesanstalt, **35**, 147–180.

Christofides, G., D'Amico, C., Del Moro, A., Elefteriadis, G. & Kyriakopulos, C., 1990. Rb/Sr geochronology and geochemical characters oh the Sithonia plutonic complex (Greece). *European Journal of Mineralogy*, **2**, 79–87.

Christofides, G., Thimiatis, G., Koroneos, A., Sklavounos, S. & Eleftheriadis, G., 1994. Mineralogy and chemistry of Cr-chlorites associated with chromites from Vavdos and Vasilika ophiolite complexes (Chalkidiki, Macedonia, N. Greece). *Chemie der Erde*, **54**, 151–166.

Christofides, G., Pecskay, Z., Eleftheriadis, G., Soldatos, T. & Koroneos, A., 2004. The Tertiary Evros volcanic rocks (Thrace, Northeastern Greece): Petrology and K/Ar geochronology. *Geologica Carpathica*, **55**, 397–409.

Cookenboo, H.O., Bustin, R.M. & Wilks, K.R., 1997. Detrital chromian spinel compositions used to reconstruct the tectonic setting of provenance: implications for orogeny in the Canadian Cordillera. *Journal of Sedimentary Research*, **67**, 116–123.

Corfu, F., Hanchar, J.M., Hoskin, P.W.O. & Kinny, P., 2003. Atlas of zircon textures. *In:* Hanchar, J.M. & Hoskin, P.W.O. (eds) *Zircon*. Reviews in Mineralogy and Geochemistry, **53**, 469–500.

Cornelius, N.K., Reischmann, T., Frei, D. & Kostopoulos, D., 2007. Geochronology, geochemistry and isotopes of orthogneisses from the Greek Rhodope. *Geochimica et Cosmochimica Acta, Abstracts 17th Annual Goldschmidt Conference, Cologne, Germany*, A190.

Corradini, C. & Serpagli, E., 1998. A Late Llandovery–Pridoli (Silurian) conodont biozonation in Sardinia. *Giornale di Geologia*, ser. 3, **60** (special issue – Sardinia), 85–88.

Corradini, C. & Serpagli, E., 1999. A Silurian conodont biozonation from late Llandovery to end of Přídolí in Sardinia (Italy). *In:* Sergali, E. (ed) *Studies on Conodonts: Proceedings of the Seventh European Conodont Symposium, Bologna-Modena 1998*. Bollettino della Società Paleontologica Italiana, **37**, 255–273.

Crowley, Q.G., Floyd, P.A., Winchester, J.A., Franke, W. & Holland, J.G., 2000. Early Palaeozoic rift-related magmatism in Variscan Europe: fragmentation of the Armorican Terrane Assemblage. *Terra Nova*, **12**, 171–180.

Dalziel, I.W.D., 1992. On the organization of American plates in the Neoproterozoic and the breakout of Laurentia. *GSA Today*, **2**, 237–241.

Dalziel, I.W.D., 1997. Neoproterozoic-Paleozoic geography and tectonics: Review, hypothesis, environmental speculation. *Geological Society of America Bulletin*, **109**, 16–42.

De Castro, P., 1990. Thaumatoporella: conoscenze attualli e approccio all'interpretazione. *Bollettino della Società Paleontologica Italiana*, **29**, 179–206.

De Castro, P., 1993. Observation on Campbelliella Radoicic 1959 and Neoteutloporella Bossoullet et al., 1978. *In:* Barattolo, F., De Castro, P. & Parente, M. (eds) *Studies on Fossil Benthic Algae – Proceedings of the 5th International Symposium on Fossil Algae*. Bollettino della Società Paleontologica Italiana, Special Volume **1**, 121–184.

De Wet, A.P., Miller, J.A., Bickle, M.J. & Chapman, H.J., 1989. Geology and geochronology of the Arnea, Sithonia and Ouranopolis intrusions, Chalkidiki Peninsula, northern Greece. *Tectonophysics*, **161**, 65–79.

Dean, W.T., Monod, O., Rickards, R.B., Demir, O. & Bultynck, P., 2000. Lower Palaeozoic stratigraphy and palaeontology, Karadere-Zirze area, Pontus Mountains, northern Turkey: *Geological Magazine*, **137**, 555–582.

Deer, W.A., Howie, R.A. & Zussman, J., 1992. *An introduction to rock-forming minerals*. Hong Kong: Longman Group Limited.

Dick, H.J.B. & Bullen, T., 1984. Chromian spinel as a petrogenetic indicator in abyssal and alpine-type peridotites and spatially associated lavas. *Contributions to Mineralogy and Petrology*, **86**, 54–76.

Dickinson, W.R. & Suczek, C.A., 1979. Plate tectonics and sandstone compositions. *The American Association of Petroleum Geologists, Bulletin*, **63**, 2164–2182.

Dimadis, E. & Nikolov, T., 1997. An ammonite find in the Makri unit (Berriasian, southeast Rhodopes, northeast Greece). *Comptes Rendus de l'Académie Bulgare des Sciences*, **50**, 71–74.

Dimadis, L., Papadopoulos, P., Goranov, A. & Encheva, M., 1996. First biostratigraphic evidence for the presence of Triassic at Melia (Western Thrace, Greece). *Geologica Balcanica*, **26**, 37–40.

Dimitriadis, S. & Asvesta, A., 1993. Sedimentation and magmatism related to the Triassic rifting and later events in the Vardar-Axios Zone. *Bulletin of the Geological Society of Greece*, **28**, 149–168.

Dinter, D.A. & Royden, L., 1993. Late Cenozoic extension in the northeastern Greece: Strimon Valley detachment system and Rhodope metamorphic core complex. *Geology*, **21**, 45–48.

Dixon, J.E. & Dimitriadis, S., 1984. Metamorphosed ophiolitic rocks from the Serbo-Macedonian Massif near Lake Volvi, north-east Greece. *In:* Dixon, J.E. & Robertson, A.H.F. (eds) *The geological evolution of the eastern Mediterranean*. Geological Society, London, Special Publications, **17**, 603–618.

Dojen, C., Özgül, N., Göncüoglu, Y. & Göncuoglu, M.C., 2004. Early Devonian ostracods of Thuringian ecotype from NW Anatolia (Turkey). *Neues Jahrbuch für Geologie und Paläontologie*, *Monatshefte*, **12**, 733–774.

Duncan, R.A. & Green, D.H., 1987. The genesis of refractory melts in the formation of oceanic crust. *Contributions to Mineralogy and Petrology*, **96**, 326–342.

Dürr, S. & Jacobshagen, V., 1986. Ostägäische Inseln. *In:* Jacobshagen, V. (ed) *Geologie von Griechenland*. Beiträge zur Regionalen Geologie der Erde, **19**, 169–187.

Egal, E., Thiéblemont, D., Lahondére, D., Guerrot, C., Costea, C. A., Iliescu, D., Delor, C., Goujou, J. C., Lafon, J.M., Tegyey, M., Diaby, S. & Kolié, P., 2002. Late Eburnean granitization and tectonics along the western and northwestern margin of the Archean Kénéma-Man domain (Guinea, West African Craton). *Precambrian Research*, **117**, 57–84.

Ekdale, A.A. & Bromley, R.G., 2003. Paleoethologic interpretation of complex *Thalassinoides* in shallow-marine limestones, Lower Ordovician, southern Sweden. *Palaeogeography, Palaeoclimatology, Palaeoecology*, **191**, 221–227.

Engel, M. & Reischmann, T., 1998. Single zircon geochronology of orthogneisses from Paros, Greece. *Bulletin of the Geological Society of Greece*, **32**, 91–99.

Engel, M. & Reischmann, T., 1999. Geochronology of the pre-alpine basement of the central Cyclades, Greece. *Journal of Conference Abstracts*, **4**, 806.

Ennih, N. & Liégeois, J.P., 2001. The Moroccan Anti-Atlas: the West African craton passive margin limited Pan-African activity. Implications for the Northern limit of the craton. *Precambrian Research*, **112**, 289–302.

Epstein, A.G., Epstein, J.B. & Harris, L.D., 1977. Conodont color alteration – and index to organic metamorphism. *U.S. Geological Survey Professional Paper*, **995**, 1–27.

Eren, Y., Kurt, H., Rosselet, F. & Stampfli, G.M., 2004. Palaeozoic deformation and magmatism in the northern area of the Anatolide block (Konya), witness of the Palaeotethys active margin. *Eclogae geologicae Helvetiae*, **97**, 293–306.

Faupl, P., Petrakakis, K., Migiros, G. & Pavlopoulos, A., 2002. Detrital blue amphiboles from the western Othrys Mountain and their relationship to the blueschist terrains of the Hellenides (Greece). *International Journal of Earth Sciences*, **91**, 433–444.

Fedo, C.M., Sircombe, K.N. & Rainbird, R.H., 2003. Detrital zircon analysis of the sedimentary record. *In:* Hanchar J.M. & Hoskin P.O. (eds) *Zircon*. Reviews in Mineralogy and Geochemistry, **53**, 277–303.

Fenninger, A., 1983. Codiaceen aus dem Unterdevon von Karaburun (Türkei) und Chios (Griechenland). *Mitteilungen der Österreichischen Geologischen Gesellschaft*, **76**, 273–288.

Fernández-Suárez, J., Gutiérrez-Alonso, G., Jenner, G. A. & Tubrett, M.N., 2000. New ideas on the Proterozoic–early Paleozoic evolution of NW Iberia: insights from U–Pb detrital zircon ages. *Precambrian Research*, **102**, 185–206.

Fernández-Suárez, J., Gutiérrez Alonso, G., Cox, R. & Jenner, G.A., 2002. Assembly of the Armorican microplate: a strike-slip terrane delivery? Evidence from U-Pb ages of detrital zircons. *Journal of Geology*, **110**, 619–626.

Fernández-Suárez, J., Gutiérrez Alonso, G. & Jeffries, T.E., 2002. The importance of along-margin terrane transport in northern Gondwana: insights from detrital zircon parentage in Neoproterozoic rocks from Iberia and Brittany. *Earth and Planetary Science Letters*, **204**, 75–88.

Ferrière, J. & Stais, A., 1995. Nouvelle interprétation de la suture téthysienne vardarienne d'après l'analyse des séries de Péonias (Vardar oriental, Hellénides internes). *Bulletin de la Societé géologique de France*, **166**, 327–339.

Fett, A., 1995. *Elementverteilung zwischen Granat, Klinopyroxen und Rutil in Eklogiten - Experiment und Natur*. PhD Thesis. University of Mainz, Germany.

Flajs, G., Hüssner, M., Fenninger, A. & Hubmann, G., 1996. Upper Permian Richthofeniid Buildups of Chios Island (Aegean Sea) – Preliminary Report. *Jahrbuch der Geologischen Bundesanstalt*, **139**, 21–28.

Floyd, P.A. & Leveridge, B.E., 1987. Tectonic environment of Devonian Gramscatho basin, south Cornwall: framework mode and geochemical evidence from turbiditic sandstones. *Journal of the Geological Society, London*, **144**, 531–542.

FLÜGEL, E., 1974. Fazies-Interpretation der Cladocoropsis-Kalke (Malm) auf Karaburun, W-Anatolien. *Archiv für Lagerstättenforschung in den Ostalpen*, Sonderband **2**, 79–94.

FLÜGEL, E., 1983. Mikrofazies der Pantokrator-Kalke (Lias) von Korfu, Griechenland. *Facies*, **8**, 263–300.

FORCE, E.R., 1980. The provenance of rutile. *Journal of Sedimentary Petrology*, **50**, 485–488.

FREI, D., HOLLIS, J.A., GERDES, A., HARLOV, D., KARLSSON, C., VASQUEZ, P., FRANZ, G., JOHANSSON, L. & KNUDSEN, C., 2006. Advanced *in-situ* trace element and geochronological microanalysis of geomaterials by laser ablation techniques. *Geological Survey of Denmark and Greenland Bulletin*, **10**, 25–28.

FREI, R., 1996. The extent of inter-mineral isotope equilibrium: a systematic bulk U-Pb and Pb step leaching (PbSL) isotope study of individual minerals from the Tertiary granite of Ierissos (northern Greece). *European Journal of Mineralogy*, **8**, 1175–1189.

FRIEDL, G., FINGER, F., PAQUETTE, J.-L., VON QUADT, A., MCNAUGHTON, N.J. & FLETCHER, I.R., 2004. Pre-Variscan geological events in the Austrian part of the Bohemian Massif deduced from U–Pb zircon ages. *International Journal of Earth Sciences*, **93**, 802–823.

GAETANI, M., JACOBSHAGEN, V., NICORA, A., KAUFFMANN, G., TSELEPIDES, V., FANTINI SESTINI, N., MERTMANN, D. & SKOURTSIS-CORONEOU, V., 1992. The Early-Middle Triassic Boundary at Chios (Greece). *Rivista Italiana di Paleontologia e Stratigrafia*, **98**, 181–204.

GAO, S. & WEDEPOHL, K.H., 1995. The negative Eu anomaly in Archean sedimentary rocks: implication for decomposition, age and importance of their granitic sources. *Earth and Planetary Science Letters*, **133**, 81–94.

GARCÍA-LÓPEZ, S., RODRÍGUEZ-CAÑERO, R., SANZ-LÓPEZ, J., SARMIENTO, G.N. & VALENZUELA-RÍOS, J.I., 1994. Conodontos silúricos de Europa meridional y África septentrional. *Communicaciones de las X Jornadas e Paleontología*, 84–88.

GARVER, J.I., ROYCE, P.R. & SMICK, T.A., 1996. Chromium and nickel in shale of the Taconic foreland: a case study for the provenance of fine-grained sediments with an ultramafic source. *Journal of Sedimentary Research*, **66**, 100–106.

GEBAUER, D., WILLIAMS, I.S., COMPSTON, W. & GRÜNENFELDER, M., 1989. The development of the Central European continental crust since the Early Archean based on conventional and ion-microprobe dating of up to 3.84 b.y. old detrital zircons. *Tectonophysics*, **157**, 81–96.

GERDES, A. & ZEH, A., 2006. Combined U-Pb and Hf isotope LA-(MC)-ICP-MS analyses of detrital zircons: Comparison with SHRIMP and new constraints for the provenance and age of an Armorican metasediment in Central Germany. *Earth and Planetary Science Letters*, **249**, 47–61.

GESSNER, K., RING, U., PASSCHIER, C.W. & GÜNGÖR, T., 2001. How to resist subduction: evidence for large-scale out-of-sequence thrusting during Eocene collision in western Turkey. *Journal of the Geological Society, London*, **158**, 769–784.

GESSNER, K., COLLINS, A.S., RING, U. & GÜNGÖR, T., 2004. Structural and thermal history of poly-orogenic basement: U–Pb geochronology of granitoid rocks in the southern Menderes Massif, Western Turkey. *Journal of the Geological Society, London*, **161**, 93–101.

GNOLI, M., 2003. Northern Gondwanan Siluro-Devonian palaeogeography assessed by cephalopods. *Palaeontologia Electronica*, **5**, 19 pp., 917KB.

GÖTZE, J., 1996. Genetic information of accessory minerals in clastic sediments. *Zentralblatt für Geologie und Paläontologie*, **Teil 1 1995**, 101–118.

GÖNCÜOĞLU, M.C. & KOZLU, H., 2000. Early Paleozoic evolution of the NW Gondwanaland: data from southern Turkey and surrounding regions. *Gondwana Research*, **3**, 315–323.

GÖNCÜOĞLU, M.C., DIRIK, K. & KOZLU, H., 1997. Pre-Alpine and Alpine terranes in Turkey: Explanatory Notes to the Terrane map of Turkey. *In:* PAPANIKOLAOU, D.J. &. SASSI, F.P (eds) *IGCP Project No: 276 Final Volume: Terrane Maps and Terrane Descriptions.* Annales géologiques des pays helléniques, **37**, 515–536.

GÖNCÜOĞLU, M.C., TURHAN, N., ŞENTÜRK, K., ÖZCAN, A., UYSAL, Ş. & YALINIZ, M.K., 2000. A geotraverse across northwestern Turkey: tectonic units of the Central Sakarya region and their tectonic evolution. *In:* BOZKURT, E.,

WINCHESTER, J.A. & PIPER, J.D.A. (eds) *Tectonics and Magmatism in Turkey and the Surrounding Area*. Geological Society, London, Special Publications, **173**, 139–161.

GÖNCÜOĞLU, M.C, GÖNCÜOGLU, Y., KOZLU, H. & KOZUR, H.W., 2004. Paleozoic stratigraphy of the Geyik Dagi unit in the Eastern Taurides (Turkey): New age data and implications for Gondwanan evolution. *Geologica Carpathica*, **55**, 433–447.

GORBATSCHEV, R. & BOGDANOVA, S., 1993. Frontiers in the Baltic Shield. *Precambrian Research*, **64**, 3–21.

GÖRÜR, N., MONOD, O., OKAY, A.I., ŞENGÖR, A.M.C., TÜYSÜZ, O., YIĞITBAŞ, E., SAKANÇ, M. & AKKÖK, R., 1997. Palaeogeographic and tectonic position of the Carboniferous rocks of the western Pontides (Turkey) in the frame of the Variscan belt. *Bulletin de la Société Géologique de France*, **168**, 197–205.

GRADSTEIN, F.M., OGG, J.G. & SMITH, A.G., 2004. *A Geologic Time Scale 2004*. Cambridge University Press, Cambridge.

GRAF, J., 2001. *Alpine tectonics in western Bulgaria: Cretaceous compression of the Kraište region and Cenozoic exhumation of the crystalline Osogovo-Lisec Complex*. PhD Thesis, ETH Zürich, Switzerland.

GROVES, J.R., LARGHI, C., NICORA, A. & RETTORI, R., 2003. Mississippian (Lower Carboniferous) microfossils from the Chios Mélange (Chios Island, Greece). *Geobios*, **36**, 379–389.

GUTIÉRREZ-ALONSO, G., FERNÁNDEZ-SUÁREZ, J., COLLINS, A.S., ABAD, I. & NIETO, F., 2005. Amazonian Mesoproterozoic basement in the core of the Ibero-Armorican Arc: $^{40}Ar/^{39}Ar$ detrital mica ages complement the zircon's tale. *Geology*, **33**, 637–640.

HAAS, W., 1968. Das Alt-Paläozoikum von Bithynien (Nordwest-Türkei). *Neues Jahrbuch für Geologie und Paläontologie*, *Abhandlungen*, **131**, 178–242.

HAENEL-REMY, S. & BEBIEN, J., 1985. The Oreokastro ophiolite (Greek Macedonia): an important component of the innermost Hellenic ophiolite belt. *Ofioliti*, **10**, 279–298.

HEGNER, E. & KRÖNER, A., 2000. Review of Nd isotopic data and xenocrystic and detrital zircon ages from the pre-Variscan basement in the eastern Bohemian Massif: speculations on palinspastic reconstructions. *In:* FRANKE, W., HAAK, V., ONCKEN, O. & TANNER, D. (eds) *Orogenic Processes: Quantification and Modelling in the Variscan Belt*. Geological Society, London, Special Publications, **179**, 113–129.

HENJES-KUNST, F. & KREUZER H., 1982. Isotopic dating of Pre-Alpidic rocks from the island of Ios (Cyclades, Greece). *Contributions to Mineralogy and Petrology*, **80**, 245–253.

HERGET, G., 1968. *Die Geologie von Nord-Chios (Ägäis)*. PhD Thesis, University of Marburg, Germany.

HERGET, G. & ROTH, W., 1968. Stratigraphie des Paläozoikums im Nordwest-Teil der Insel Chios (Ägäis). *Neues Jahrbuch für Geologie und Paläontologie*, *Abhandlungen*, **131**, 46–71.

HERRON, M.M., 1988. Geochemical classification of terrigenous sands and shales from core or log data. *Journal of Sedimentary Petrology*, **58**, 820–829.

HETZEL, R. & REISCHMANN, T., 1996. Intrusion age of Pan-African augen gneisses in the southern Menderes massif and the age of cooling after Alpine ductile extensional deformation. *Geological Magazine*, **133**, 565–572.

HIMMERKUS, F., REISCHMANN, T. & KOSTOPOULOS, D., 2004a. The Pirkadikia Unit, the oldest crustal segment in the Serbo-Macedonian terrane assemblage. *5th ISEMG Conference Proceedings*, **1**, 84–85.

HIMMERKUS, F., REISCHMANN, T. & KOSTOPOULOS, D., 2004b. Triassic rifting recorded in Gondwana derived Tethyan terranes, Serbo-Macedonian Massif, northern Greece. *Berichte der Deutschen Mineralogischen Gesellschaft*, *Beihefte zum European Journal of Mineralogy*, **16**, 57.

HIMMERKUS, F., REISCHMANN, T. & KOSTOPOULOS, D., 2006a. Late Proterozoic and Silurian basement units within the Serbo-Macedonian Massif, northern Greece: the significance of terrane accretion in the Hellenides. *In:* ROBERTSON, A.H.F. & MOUNTRAKIS, D. (eds) *Tectonic Development of the Eastern Mediterranean Region*. Geological Society, London, Special Publications, **260**, 35–50.

HIMMERKUS, F., REISCHMANN, T. & KOSTOPOULOS, D., 2006b. Permo-Carboniferous and upper Jurassic basement ages in the Kerdillion Unit, eastern Serbo-Macedonian Massif, northern Greece. *Geophysical Research Abstracts*, **8**, 05758.

Himmerkus, F., Anders, B., Reischmann, T. & Kostopoulos, D., 2007. Gondwana-derived terranes in the northern Hellenides. *In:* Hatcher, R.D., Jr., Carlson, M.P., McBride, J.H. & Martínez Catalán, J.R. (eds) *4-D Framework of Continental Crust*. Geological Society of America Memoir, **200**, 379–390.

Himmerkus, F., Reischmann, T. & Kostopoulos, D., submitted. Serbo-Macedonian revisited: a Silurian basement terrane from northern Gondwana in the Internal Hellenides, Greece.

Himmerkus, F., in preparation. *The Pre-Alpine to early Alpine history of the Serbo-Macedonian Massif, Northern Greece, the significance of Terrane Accretion*. PhD Thesis, University of Mainz, Germany.

Hiscott, R.N., 1984. Ophiolitic source rocks for Taconic-age flysch: Trace element evidence. *Geological Society of America Bulletin*, **95**, 1261–1276.

Holland, C.H., 1992. Orthoconic nautiloid cephalopod genera. *Geological Magazine*, **129**, 123–124.

Holland, H.D., 1978. *The chemistry of the atmosphere and oceans*. Wiley, New York.

Horstwood, M.S.A., Foster, G.L., Parrish, R.R., Noble, S.R. & Nowell, G.M., 2003. Common-Pb corrected *in situ* U–Pb accessory mineral geochronology by LA-MC-ICP-MS. *Journal of Analytical Atomic Spectrometry*, **18**, 837–846.

IGME, 1983. *Geological Map of Greece, scale 1:500 000*. Institute of Geology and Mineral Exploration, Athens.

Innocenti, F., Kolios, N., Manetti, P., Mazzuoli, R., Peccerillo, G., Rita, F. & Villari, L., 1984. Evolution and geodynamic significance of the Tertiary orogenic volcanism in Northeastern Greece. *Bulletin of Volcanology*, **47**, 25–37.

Ioannidis, N., Hatzidimitriadis, E., Mountrakis, D. & Kilias, A., 1998. Study of metasedimentary formation of upper Paleozoic to Mesozoic age from Neo Makri (Alexandroupolis area), W.Thrace/Greece. (in Greek with English abstract). *Bulletin of the Geological Society of Greece*, **32**, 79–89.

Jackson, S., Pearson, N.J., Griffin, W.L. & Belousova, E.A., 2004. The application of laser ablation – inductively coupled plasma – mass spectrometry to *in situ* U-Pb zircon geochronology. *Chemical Geology*, **211**, 47–69.

Jacobshagen, V., 1986. Geologie von Griechenland. *Beiträge zur Regionalen Geologie der Erde*, **19**, 1–363.

Jacobshagen, V. & Wallbrecher, E., 1984. Pre-Neogene nappe structure and metamorphism of the North Sporades and the southern Pelion peninsula. *In:* Dixon, J.E. & Robertson, A.H.F. (eds) *The geological evolution of the eastern Mediterranean*. Geological Society, London, Special Publications, **17**, 591–602.

Jacobshagen, V., Risch, H. & Roeder, D., 1976. Die Eohellenische Phase, Definition und Interpretation. *Zeitschrift der Deutschen Geologischen Gesellschaft*, **127**, 133–145.

Jacobshagen, V., Skala, W. & Wallbrecher, E., 1978. Alpine structure and development of the southern Pelion peninsula and the North Sporades. *In:* Closs, H., Roeder, D.H. & Schmidt, K. (eds) *Alps, Apennines, Hellenides*. E. Schweizerbart'sche, Stuttgart, 484–488.

Janoušek, V., Gerdes, A., Vrána, S., Finger, F., Erban, V., Friedl, G. & Braithwaite, C.J.R., 2006. Low-pressure Granulites of the Lišov Massif, Southern Bohemia: Viséan Metamorphism of Late Devonian Plutonic Arc Rocks. *Journal of Petrology*, **47**, 705–744.

Jenny, C. & Stampfli, G.M., 2000. Permian paleogeography of the Tethyan realm. *Permophiles*, **37**, 24–33.

Jeppsson, L., 1993. Silurian events: the theory and the conodonts. *Proceedings of the Estonian Academy of Sciences*, *Geology*, **42**, 23–27.

Jeppsson, L., 1998. Silurian oceanic events: summary of general characteristics. *In:* Landing, E. & Johnson, M.E. (eds) *Silurian Cycles: Linkages of dynamic stratigraphy with atmospheric, oceanic, and tectonic changes*. James Hall Centennial Volume. New York State Museum Bulletin, **491**, 239–257.

Jeppsson, L. & Aldridge, R.J., 2000. Ludlow (late Silurian) oceanic episodes and events. *Journal of the Geological Society*, *London*, **157**, 1137–1148.

Jeppsson, L., Eriksson, M.E. & Calner, M., 2005a. Biostratigraphy on Gotland. *In:* Eriksson, M.E. & Calner, M.H. (eds) *The Dynamic Silurian Earth. Subcommision on Silurian Stratigraphy, Field Meeting 2005*. Sveriges geologiska undersökning, Rapporter och meddelanden, **121**, 14–17.

Jeppsson, L., Eriksson, M.E. & Calner, M., 2005b. Locality descriptions. *In:* Eriksson, M.E. & Calner, M.H. (eds) *The Dynamic Silurian Earth. Subcommision on Silurian Stratigraphy, Field Meeting 2005*. Sveriges geologiska undersökning, Rapporter och meddelanden, **121**, 22–47.

Jeppsson, L., Eriksson, M.E. & Calner, M., 2006. A latest Llandovery to latest Ludlow high-resolution biostratigraphy based on the Silurian of Gotland – a summary. *Geologiska Föreningens i Stockholm Förhandlingar*, **128**, 109–114.

Johnsson, M.J., 1993. The system controlling the composition of clastic sediments. *In:* Johnsson, M.J. & Basu, A. (eds) *Processes controlling the composition of clastic sediments*. Geological Society of America, Special Papers, **284**, 1–19.

Kalvoda, J., 2003. Carboniferous foraminiferal paleobiogeography in Turkey and its implications for plate tectonic reconstructions. *Rivista Italiana di Paleontologia e Stratigrafia,* **109**, 255–266.

Kamenetsky, V., Crawford, A.J. & Meffre, S., 2001. Factors controlling chemistry of magmatic spinel: an empirical study of associated olivine, Cr-spinel and melt inclusions from primitive rocks. *Journal of Petrology*, **42**, 655–671.

Kauffmann, G., 1965. Fossil-belegtes Altpaläozoikum im Nordost-Teil der Insel Chios (Ägäis). *Neues Jahrbuch für Geologie und Paläontologie*, *Monatshefte*, **1965**, 647–659.

Kauffmann, G., 1969. *Die Geologie von Nordost-Chios (Ägäis)*. PhD Thesis, University of Marburg, Germany.

Kauffmann, G., Kockel, F. & Mollat, H., 1976. Notes on the stratigraphic and paleogeographic position of the Svoula formation in the Innermost Zone of the Hellenides (Northern Greece). *Bulletin de la Societé géologique de France*, **18**, 225–230.

Keay, S. & Lister, G., 2002. African provenance for the metasediments and metaigneous rocks of the Cyclades, Aegean Sea, Greece. *Geology*, **30**, 235–238.

Keay, S., Lister, G. & Buick, I., 2001. The timing of partial melting, Barrovian metamorphism and granite intrusion in the Naxos metamorphic core complex, Cyclades, Aegean Sea, Greece. *Tectonophysics*, **342**, 275–312.

Kelepertsis, A., Chatsidimitriadis, E. & Andrulakis, J., 1985. Geology, Geochemistry and Tectonic Setting of the Volcanosedimentary Series, Kilkis, central Macedonia, Greece. *Chemie der Erde*, **44**, 151–174.

Kemp, A.I.S., Hawkesworth, C.J., Paterson, B.A. & Kinny, P.D., 2006. Episodic growth of the Gondwana supercontinent from hafnium and oxygen isotopes in zircon. *Nature*, **439**, 580–583.

Keppie, J.D., Davis, D.W. & Krogh, T.E., 1998. U-Pb geochronological constraints on Precambrian stratified units in the Avalon Composite Terrane of Nova Scotia, Canada: tectonic implications. *Canadian Journal of Earth Sciences*, **35**, 222–236.

Kilias, A., 1987. Die Phyllit-Schiefer-Serie der Insel Oinousai: Mikrostrukturen, Kinematik und tektonische Stellung im Helleniden Orogen (Griechenland). *Geologica Balcanica*, **17**, 83–90.

Kilias, A., Falalakis, G. & Mountrakis, D., 1999. Cretaceous-Tertiary structures and kinematics of the Serbomacedonian metamorphic rocks and their relation to the exhumation of the Hellenic hinterland (Macedonia, Greece). *International Journal of Earth Sciences*, **88**, 513–531.

Kiriakidis, L. & Brooks, M., 1989. A geophysical study of the Vardar Zone ophiolite belt in Chalkidhiki, northern Greece. *Journal of the Geological Society*, *London*, **146**, 859–865.

Klapper, G. & Murphy, M.A., 1975. Silurian-Lower Devonian conodont sequence in the Roberts Mountains Formation of central Nevada. *University of California Publications in Geological Sciences*, **111**, 1–62.

Kockel, F. & Walther, H.W., 1965. Die Strimonlinie als Grenze zwischen Serbo-Mazedonischen und Rila-Rhodope-Massif in Ost-Mazedonien. *Geologisches Jahrbuch*, **83**, 575–602.

KOCKEL, F. & MOLLAT, H., 1977. *Geological map of the Chalkidiki peninsula and adjacent areas (Greece), Scale 1:100000*. Bundesanstalt für Geowissenschaften und Rohstoffe, Hannover.

KOCKEL, F., MOLLAT, H. & WALTHER, H.W., 1971. Geologie des Serbo-Mazedonischen Massivs und seines mesozoischen Rahmens (Nordgriechenland). *Geologisches Jahrbuch*, **89**, 529–551.

KOCKEL, F., MOLLAT, H. & WALTHER, H.W., 1977. *Erläuterungen zur Geologischen Karte der Chalkidiki und angrenzender Gebiete 1 : 100000 (Nord-Griechenland)*. Bundesanstalt für Geowissenschaften und Rohstoffe, Hannover.

KOGLIN, N., REISCHMANN, T., KOSTOPOULOS, D., MATUKOV, D. & SERGEEV, S., 2007. Zircon SHRIMP ages and the origin of ophiolitic rocks from the NE Aegean region, Greece. *Geophysical Research Abstracts*, **9**, 06848.

KOLODNER, K., AVIGAD, D., MCWILLIAMS, M., WOODEN, J.L., WEISSBROD, T. & FEINSTEIN, S., 2006. Provenance of north Gondwana Cambrian–Ordovician sandstone: U–Pb SHRIMP dating of detrital zircons from Israel and Jordan. *Geological Magazine*, **143**, 367–391.

KOPP, K.O., 1965. Geologie Thrakiens III: Das Tertiär zwischen Rhodope und Evros. *Annales géologiques des pays helléniques*, **16**, 315–362.

KOPP, K.O., 1969. Geologie Thrakiens VI: Der Coban Dag westlich Alexandroupolis. *Geotektonische Forschungen*, **31**, 97–116.

KORALAY, O.E., CHEN, F., OBERHÄNSLI, R., WAN, Y. & CANDAN, O., 2006. Age of granulite facies metamorphism in the Menderes Massif, Western Anatolia / Turkey: Shrimp U-Pb zircon dating. *Abstracts 59th Geological Congress Turkey*, *20–24 March 2006*, *Ankara*.

KOŠLER, J., FONNELAND, H., SYLVESTER, P., TUBRETT, M. & PEDERSEN, R.B., 2002. U–Pb dating of detrital zircons for sediment provenance studies—a comparison of laser ablation ICPMS and SIMS techniques. *Chemical Geology*, **182**, 605–618.

KOSSMAT, F., 1924. Geologie der zentralen Balkanhalbinsel: Mit einer Übersicht des dinarischen Gebirgsbaus. *Die Kriegsschauplätze 1914-1918 geologisch dargestellt*, **12**, 1–198.

KOSTOPOULOS, D.K. & MURTON, B.J., 1992. Origin and distribution of components in boninite genesis: significance of the OIB component. *In:* PARSON, L.M., MURTON, B.J. & BROWNING, P. (eds) *Ophiolites and their Modern Oceanic Analogues*. Geological Society, London, Special Publications, **60**, 133–154.

KOSTOPOULOS, D., REISCHMANN, T. & SKLAVOUNOS, S., 2001. Palaeozoic and Early Mesozoic magmatism and metamorphism in the Serbo-Macedonian Massif, Central Macedonia, Northern Greece. *Journal of Conference Abstracts*, **6**, 318.

KOUGOULIS, C., VERANIS, N. & KASSOLI-FOURNARAKI, A., 1990. Meta-volcanic rocks in the Examili formation (North Greece). *Chemie der Erde*, **50**, 67–79.

KOUNOV, A., 2002. *Thermotectonic evolution of Kraishte, western Bulgaria*. PhD Thesis, ETH Zürich, Switzerland.

KOZLU, H., GÖNCÜOĞLU, Y., SARMIENTO, G.N., GÖNCÜOĞLU, M.C., 2002. First finding of Late Silurian conodonts from the "Orthoceras Limestones", Camdag area, NW Turkey: preliminary constraints for the paleogeography. *Geologica Balcanica*, **32**, 3–12.

KOZUR, H., 1998. The age of the siliciclastic series (Karareis Formation) of the western Karaburun Peninsula, western Turkey. *In:* SZANIAWSKI, H. (ed) *Proceedings of the Sixth European Conodont Symposium (ECOS VI)*. Palaeontologia Polonica, **58**, 171–189.

KOZUR, H.W., SENEL, M. & TEKIN, K., 1998. First Evidence of Hercynian Lower Carboniferous Flyschoid Deep-water Sediments in the Lycian Nappes, Southwestern Turkey. *Geologia Croatica*, **51**, 15–22.

KRÖNER, A. & ŞENGÖR, A.M.C., 1990. Archean and Proterozoic ancestry in late Precambrian and early Paleozoic crustal elements in southern Turkey as revealed by single-zircon dating. *Geology*, **18**, 1186–1190.

KRÖNER, A., EYAL, M. & EYAL, Y., 1990. Early Pan-African evolution of the basement around Elat, Israel, and the Sinai Peninsula revealed by single-zircon evaporation dating, and implication for crustal accretion rates. *Geology*, **18**, 545–548.

KRÖNER, A., GREILING, R., REISCHMANN, T., HUSSEIN, I.M., STERN, R.G., DÜRR, S., KRÜGER, J. & ZIMMER, M., 1987. Pan-African crustal evolution in the Nubian segment of northeast Africa. *In:* KRÖNER, A. (ed) *Proterozoic lithospheric evolution*. American Geophysical Union Geodynamics Series, **17**, 235–257.

KRÖNER, A., O'BRIEN, P.J., NEMCHIN, A.A. & PIDGEON, R.T., 2000. Zircon ages for high-pressure granulites from South Bohemia, Czech Republic, and their connection to the Carboniferous high temperature processes. *Contributions to Mineralogy and Petrology*, **138**, 127–142.

KRÖNER, A., ŠTÍPSKÁ, P., SCHULMANN, K. & JAECKEL, P., 2000. Chronological constaints on the pre-Variscan evolution of the northeastern margin of the Bohemian Massif, Czech Republic. *In:* FRANKE, W., HAAK, V., ONCKEN, O. & TANNER, D. (eds) *Orogenic Processes: Quantification and Modelling in the Variscan Belt*. Geological Society, London, Special Publications, **179**, 63–86.

LAKOVA, I. & GÖNCÜOĞLU, M.C., 2005. Early Ludlovian (early Late Silurian) palynomorphs from the Palaeozoic of Camdag, NW Anatolia, Turkey. *Yerbilimleri*, *Earth Sciences*, **26**, 61–73.

LARGHI, C., CORDEY, F., CORRADINI, C., GAETANI, M. & NICORA, A., 2005. Palaeozoic (Silurian and Devonian) radiolarians and conodonts from chert olistoliths of the Volissos Turbidites, Chios island, Greece. *Eclogae geologicae Helvetiae*, **98**, 123–131.

LIATI, A., 2005. Identification of repeated Alpine (ultra) high-pressure metamorphic events by U–Pb SHRIMP geochronology and REE geochemistry of zircon: the Rhodope zone of Northern Greece. *Contributions to Mineralogy and Petrology*, **150**, 608–630.

LIATI, A. & GEBAUER, D., 1999. Constraining the prograde and retrograde P-T-t- path of Eocene HP rocks by SHRIMP dating of different zircon domains: inferred rates of heating, burial, cooling and exhumation for central Rhodope, northern Greece. *Contributions to Mineralogy and Petrology*, **135**, 340–354.

LIATI, A., GEBAUER, D. & WYSOCZANSKI, R., 2002. U–Pb SHRIMP-dating of zircon domains from UHP garnet-rich mafic rocks and late pegmatoids in the Rhodope zone (N Greece); evidence for Early Cretaceous crystallization and Late Cretaceous metamorphism. *Chemical Geology*, **184**, 281–299.

LIATI, A., GEBAUER, D. & FANNING, C.M., 2004. The age of ophiolitic rocks of the Hellenides (Vourinos, Pindos, Crete): first U–Pb ion microprobe (SHRIMP) zircon ages. *Chemical Geology*, **207**, 171–188.

LINNEMANN, U., MCNAUGHTON, N.J., ROMER, R.L., GEHMLICH, M., DROST, K. & TONK, C., 2004. West African provenance for Saxo-Thuringia (Bohemian Massif): Did Armorica ever leave pre-Pangean Gondwana? – U/Pb-SHRIMP zircon evidence and the Nd-isotopic record. *International Journal of Earth Sciences*, **93**, 683–705.

LOOS, S. & REISCHMANN, T., 1999. The evolution of the southern Menderes Massif in SW Turkey as revealed by zircon dating. *Journal of the Geological Society*, *London*, **156**, 1021–1030.

LUDWIG, K.R., 2001. *SQUID 1.02*. Berkeley Geochronological Center, Special Publications, **2**.

LUDWIG, K.R., 2003. *Isoplot/Ex 3.00. A Geochronological Toolkit for Microsoft Excel*. Berkeley Geochronological Center, Special Publications, **4**.

MAGGANAS, A.C., 1988. *Mineralogical, petrological and geochemical study on metabasic and metaultrabasic rocks of Circum-Rhodope Belt in Thrace area* (in Greek with English summary). PhD Thesis, University of Athens, Greece.

MAGGANAS, A.C., 2002. Constraints on the petrogenesis of Evros ophiolite extrusives, NE Greece. *Lithos*, **65**, 165–182.

MAGGANAS, A., SIDERIS, C. & KOKKINAKIS, A., 1991. Marginal basin-volcanic arc origin of metabasic rocks from the Circum-Rhodope Belt, Thrace, Greece. *Mineralogy and Petrology*, **44**, 235–252.

MÄNNIK, P. & MAŁKOWSKI, K., 1998. Silurian conodonts from the Gołdap core, Poland. *In:* SZANIAWSKI, H. (ed) *Proceedings of the Sixth European Conodont Symposium (ECOS VI)*. Palaeontologia Polonica, **58**, 141–151.

MARAKIS, G., 1970. Geochronology studies of some granites from Macedonia. *Annales géologiques des pays helléniques*, **21**, 121–152.

MAREELS, J., 2004. *ICP–MS analysis, geochemistry, and petrogenesis of granites from the Variscan northern Vosges (France)*. PhD Thesis, Katholieke Universiteit Leuven, Belgium.

Massonne, H-J. & Schreyer, W., 1987. Phengite geobarometry based on the limiting assemblage with K-feldspar, phlogopite, and quartz. *Contributions to Mineralogy and Petrology*, **96**, 212–224.

Matte, P., 1986. Tectonics and plate tectonic model for the Variscan belt of Europe. *Tectonophysics*, **126**, 329–374.

McLennan, S.M., 1989. Rare earth elements in sedimentary rocks: influence of provenance and sedimentary processes. *In:* Lipin, B.R. & McKay, G.A. (eds) *Geochemistry and mineralogy of rare earth elements*. Reviews in Mineralogy, **21**, 169–200.

McLennan, S.M. & Taylor, S.R., 1980. Th and U in sedimentary rocks: crustal evolution and sedimentary recycling. *Nature*, **285**, 621–624.

McLennan, S.M. & Taylor, S.R., 1991. Sedimentary rocks and crustal evolution: Tectonic setting and secular trends. *Journal of Geology*, **99**, 1–21.

McLennan, S.M., Taylor, S.R., McCulloch, M.T. & Maynard, J.B., 1990. Geochemical and Nd–Sr isotopic composition of deep-sea turbidites: Crustal evolution and plate tectonic associations. *Geochimica et Cosmochimica Acta*, **54**, 2015–2050.

McLennan, S.M., Hemming, S., McDaniel, D.K. & Hanson, G.N., 1993. Geochemical approaches to sedimentation, provenance, and tectonics. *In:* Johnsson, M.J. & Basu, A. (eds) *Processes controlling the composition of clastic sediments*. Geological Society of America, Special Papers, **284**, 21–40.

Meinhold, G., Kostopoulos, D. & Reischmann, T., 2007. Geochemical constraints on the provenance and depositional setting of sedimentary rocks from the islands of Chios, Inousses and Psara, Aegean Sea, Greece: implications for the evolution of Palaeotethys. *Journal of the Geological Society*, *London*, **164**, 1145–1163.

Meinhold, G., Kostopoulos, D., Reischmann, T., Matukov, D. & Sergeev, S., 2006. Provenance of Permo-Triassic clastic sediments from Chios Island, Greece, using detrital zircon ages. *Geophysical Research Abstracts*, **8**, 04496.

Mercier, J., 1968. Étude géologique des zones internes des Hellénides en Macédoine centrale (Grèce). Contribution a l'étude du métamorphisme et de l'évolution magmatique des zones internes des Hellénides. *Annales géologiques des pays helléniques*, **20**, 1–792.

Mezger, K. & Krogstad, E.J., 1997. Interpretation of discordant U–Pb zircon ages: An evaluation. *Journal of metamorphic Geology*, **15**, 127–140.

Michard, A., Goffé, B., Liati, A. & Mountrakis, D., 1994a. Blueschist-facies assemblage in the Peri-Rhodopian zone and hints for an eohellenic HP-LT belt in northern Greece. *Bulletin of the Geological Society of Greece*, **30**, 185–192.

Michard, A., Goffé, B., Liati, A. & Mountrakis, D., 1994b. Découverte du faciès schists bleu dans les nappes du Circum–Rhodope: un élément d'une ceinture HP–BT éohellénique en Grèce septentrionale?. *Comptes Rendus de l'Académie des Sciences de Paris*, **318**, 1535–1542.

Michard, A., Feinberg, H. & Montigny, R., 1998. Supra-ophiolitic formations from the Thessaloniki nappe (Greece), and associated magmatism: an intra-oceanic subduction predates the Vardar obduction. *Comptes Rendus de l'Académie des Sciences de Paris*, **327**, 493–499.

Milodowski A.E. & Zalasiewicz, J.A., 1991. Redistribution of rare earth elements during diagenesis of turbidite/hemipelagite mudrock sequences of Llandovery age from central Wales. *In:* Morton, A.C., Todd, S.P. & Haughton, P.D.W. (eds) *Developments in Sedimentary Provenance Studies*. Geological Society, London, Special Publications, **57**, 101–124.

Mingram, B., Kröner, A., Hegner, E. & Krentz, O., 2004. Zircon ages, geochemistry, and Nd isotopic systematics of pre-Variscan orthogneisses from the Erzgebirge, Saxony (Germany), and geodynamic interpretation. *International Journal of Earth Sciences*, **93**, 706–727.

Morton, A.C., 1985. Heavy minerals in provenance studies. *In:* Zuffa, G.G. (ed) *Provenance of arenites*. Reidel, Dordrecht, 249–277.

Morton, A.C., 1985. A new approach to provenance studies: electron microprobe analysis of detrital garnets from Middle Jurassic sandstones of the North Sea. *Sedimentoloy*, **32**, 553–566.

Morton, A.C., 1987. Influence of provenance and diagenesis on detrital garnet suites in the Forties sandstone, Paleocene, central North Sea. *Journal of Sedimentary Petrology*, **57**, 1027–1032.

Morton, A.C., 1991. Geochemical studies of detrital heavy minerals and their application to provenance research. *In:* Morton, A.C., Todd, S.P. & Haughton, P.D.W. (eds) *Developments in Sedimentary Provenance Studies*. Geological Society, London, Special Publications, **57**, 31–45.

Morton, A.C. & Hallsworth, C.R., 1999. Processes controlling the composition of detrital heavy mineral assemblages in sandstones. Sedimentary Geologie, **124**, 3–29.

Morton, A., Hallsworth, C. & Chalton, B., 2004. Garnet compositions in Scottish and Norwegian basement terrains: a framework for interpretation of North Sea sandstone provenance. *Marine and Petroleum Geology*, **21**, 393–410.

Mountrakis, D., Sapountzis, E., Kilias, A., Eleftheriadis, G. & Christofides, G., 1983. Paleogeographic conditions in the western Pelagonian margin in Greece during the initial rifting of the continental area. *Canadian Journal of Earth Sciences*, **20**, 1673–1681.

Mposkos, E., 1989. High-pressure metamorphism in gneisses and pelitic schists in the East Rhodope Zone (N. Greece). *Mineralogy and Petrology*, **41**, 25–39.

Mposkos, E. & Liati, A., 1993. Metamorphic evolution of metapelites in the high pressure terrain of the Rhodope Zone, Northern Greece. *Canadian Mineralogist*, **31**, 401–424.

Mposkos, E.D. & Kostopolous, D.K., 2001. Diamonds, former coesite and supersilic garnet in metasedimentary rocks from the Greek Rhodope: a new ultrahigh-pressure metamorphic province established. *Earth and Planetary Science Letters*, **192**, 497–506.

Mposkos, E., Kostopoulos, D.K. & Krohe, A., 2001. Low-P / high-T pre-Alpine metamorphism and medium-P Alpine overprint of the Pelagonian Zone documented in high-alumina metapelites from the Vernon Massif, western Macedonia, northern Greece. *Bulletin of the Geological Society of Greece*, **34**, 949–958.

Murphy, J.B., Fernández-Suárez, J., Keppie, J.D. & Jeffries, T.E., 2004. Continuous rather than discrete Paleozoic histories for the Avalon and Meguma terranes based on detrital zircon data. *Geology*, **32**, 585–588.

Mussallam, K., 1991. Geology, Geochemistry, and the Evolution of an Oceanic Crustal Rift at Sithonia, NE Greece. *In:* Peters, T., Nicolas, A. & Coleman, R.G. (eds) *Ophiolite Genesis and Evolution of the Oceanic Lithosphere*. Kluwer, 685–704.

Mussallam, K. & Jung, D., 1986. Geologie und Bau des Sithonia-Ophioliths (Chalkidiki, NE-Griechenland: Anmerkungen zur Bildung ozeanischer Krusten). *Geologische Rundschau*, **75**, 383–409.

Mussallam, K., Jung, D. & Burgath, K., 1981. Textural features and chemical characteristics of chromites in ultramafic rocks, Chalkidiki Complex (Northern Greece). *Tschermaks Mineralogische und Petrographische Mitteilungen*, **29**, 75–101.

Nance, R.D. & Murphy, J.B., 1994. Contrasting basement isotopic signatures and the palinspastic restoration of peripheral orogens; example from the Neoproterozoic Avalonian-Cadomian belt. *Geology*, **22**, 617–620.

Nance, R.D. & Murphy, J.B., 1996. Basement isotopic signatures and Neoproterozoic paleogeography of Avalonian-Cadomian and related terranes in the circum–North Atlantic. *In:* Nance R.D. & Thompson M.D. (eds) *Avalonian and related peri-Gondwana terranes of the circum-North Atlantic*. Geological Society of America, Special Papers, **304**, 333–345.

Nehring, F., Jacob, D.E., Barth, M.G. & Foley, S.F., 2007. Laser-ablation ICP-MS analysis of siliceous rock glasses fused on an Iridium strip heater using MgO dilution. *Microchimica Acta*, doi:10.1007/s00604-007-0819-7.

Nesbitt, H.W., 1979. Mobility and fractionation of REE during weathering of a granodiorite. *Nature*, **279**, 206–210.

Nesbitt, H.W., Markovics, G. & Price, R.C., 1980. Chemical processes affecting alkalis and alkaline earths during continental weathering. *Geochimica et Cosmochimica Acta*, **44**, 1659–1666.

Nesbitt, H.W., MacRae, N.D. & Kronberg, B.I., 1990. Amazon deep-sea fan muds: light REE enriched products of extreme chemical weathering. *Earth and Planetary Science Letters*, **100**, 118–123.

Neubauer, F., 2002. Evolution of late Neoproterozoic to early Paleozoic tectonic elements in Central and Southeast European Alpine mountain belts: review and synthesis. *Tectonophysics*, **352**, 87–103.

Neubauer, F. & Stattegger, K., 1995. Composition and geodynamic significance of Palaeozoic sandstones from Chios island, Greece. *Geological Society of Greece*, *Special Publications*, **4**, 367–371.

Noblet, C. & Lefort, J.P., 1990. Sedimentological evidence for a limited separation between Armorica and Gondwana during the Early Ordovician. *Geology*, **18**, 303–306.

Ohsaka, T., Izumi, F. & Fujiki, Y., 1978. Raman spectrum of anatase, TiO_2. *Journal of Raman Spectroscopy*, **7**, 321–324.

Okay, A.I., Şengör, A.M.C. & Görür, N., 1994. Kinematic history of the opening of the Black Sea and its effect on the surrounding regions. *Geology*, **22**, 267–270.

Okay, A.I., Satir, M. & Siebel, W., 2006. Pre-Alpine Palaeozoic and Mesozoic orogenic events in the Eastern Mediterranean region. *In:* Gee, D. & Stephenson, R. (eds) *European Lithosphere Dynamics*. Geological Society, London, Memoir, **32**, 389–405.

Okay, A.I., Satir, M., Tüysüz, O., Akyüz, S. & Chen, F., 2001. The tectonics of the Strandja Massif: late-Variscan and mid-Mesozoic deformation and metamorphism in the northern Aegean. *Interntational Journal of Earth Sciences*, **90**, 217–233.

Okay, A.I., Satir, M., Maluski, H., Siyako, M., Monie, P., Metzger, R. & Akyüz, S., 1996. Palaeo- and Neo-Tethyan events in northwestern Turkey: Geologic and geochronologic constraints. *In:* Yin, A. & Harrison, T.M. (eds) *The Tectonic Evolution of Asia*. Cambridge University Press, Cambridge, 420–441.

Okrusch, M., Hock, R., Schüssler, U., Brummer, A., Baier, M. & Theisinger, H., 2003. Intergrown niobian rutile phases with Sc- and W-rich ferrocolumbite: An electron-microprobe and Rietveld study. *American Mineralogist*, **88**, 986–995.

Ovtcharova, M., Cherneva, Z., von Quadt, A. & Peytcheva, I., 2002. Migmatitic geochronology and geochemistry – a key to understanding the exhumation of the Madan dome (Bulgaria). *Geochimica et Cosmochimica Acta, Abstracts 12th Annual Goldschmidt Conference, Davos, Switzerland*, A573.

Özmen, F. & Reischmann, T., 1999. The age of the Sakarya continent in W Anatolia: implications for the evolution of the Aegean region. *Journal of Conference Abstracts*, **4**, 805.

Paeckelmann, W. & Sieverts, H., 1932. Obersilurische und devonische Faunen der Prinzeninseln, Bithyniens und Thraziens. *Abhandlungen der Preußischen Geologischen Landesanstalt*, **142**, 1–79.

Papadopoulos, P., Arvanitides, N.D. & Zanas, I., 1989. Some preliminary geological aspects on the Makri unit (phyllite series); peri-Rhodopian zone. *Geologica Rhodopica*, **1**, 34–42.

Papanikolaou, D.J., 1984. The three metamorphic belts of the Hellenides: a review and a kinematic interpretation. *In:* Dixon, J.E. & Robertson, A.H.F. (eds) *The geological evolution of the eastern Mediterranean*. Geological Society, London, Special Publications, **17**, 551–561.

Papanikolaou, D.J., 1997. The tectonostratigraphic terranes of the Hellenides. *In:* Papanikolaou, D.J. &. Sassi, F.P (eds) *IGCP Project No: 276 Final Volume: Terrane Maps and Terrane Descriptions*. Annales géologiques des pays helléniques, **37**, 495–514.

Papanikolaou, D. & Panagopoulos, A., 1981. On the structural style of Southern Rhodope, Greece. *Geologica Balcanica*, **11**, 13–22.

Papanikolaou, D. & Sideris, C., 1983. Le Paléozoïque de l'autochtone de Chios: une formation à bloc de type wildflysch d'âge Permien (pré parte). *Comptes Rendus de l'Académie des Sciences*, **297**, 603–606.

Passchier, C.W. & Trouw, R.A.J., 2005. *Microtectonics*. 2nd edition, Springer-Verlag, Berlin.

Pearce, J.A., Harris, N.B.W. & Tindle, A.G., 1984. Trace element discrimination diagrams for the tectonic interpretation of granitic rocks. *Journal of Petrology*, **25**, 956–983.

Pe-Piper, G. & Kotopouli, C.N., 1994. Palaeozoic volcanic rocks of Chios, Greece: Record of a Palaeotethyan suture. *Neues Jahrbuch für Mineralogie*, *Monatshefte*, **1**, 23–39.

Pe-Piper, G. & Piper, D.J.W., 2002. The igneous rocks of Greece. *Beiträge zur Regionalen Geologie der Erde*, **30**, 1–573.

Perraki, M., Proyer, A., Mposkos, E., Kaindl, R. & Hoinkes, G., 2006. Raman micro-spectroscopy on diamond, graphite and other carbon polymorphs from the ultrahigh-pressure metamorphic Kimi Complex of the Rhodope Metamorphic Province, NE Greece. *Earth and Planetary Science Letters*, **241**, 672–685.

Pettijohn, F., Potter, P.E. & Siever, R., 1972. *Sand and Sandstone*. Springer, Berlin Heidelberg New York.

Peytcheva, I. & von Quadt, A., 1995. U-Pb Zircon dating of metagranites from Byala Reka region in the East Rhodopes, Bulgaria. *Geological Society of Greece*, *Special Publications*, **4**, 637–642.

Peytcheva, I. & von Quadt, A., 2004. The Palaeozoic protoliths of the Central Srednogorie, Bulgaria: records in zircons from basement rocks and Cretaceous magmatites. *5th ISEMG Conference Proceedings*, **1**, 392–395.

Pober, E. & Faupl, P., 1988. The chemistry of detrital chromian spinels and its implications for the geodynamic evolution of the Eastern Alps. *Geologische Rundschau*, **77**, 641–670.

Porto, S.P.S., Fleury, P.A. & Damen, T.C., 1967. Raman spectra of TiO_2, MgF_2, ZnF_2, FeF_2, and MnF_2. *Physical Review*, **154**, 522–526.

Power, M.R., Pirrie, D., Andersen, J.C.Ø. & Wheeler, P.D., 2000. Testing the validity of chrome spinel chemistry as a provenance and petrogenetic indicator. *Geology*, **28**, 1027–1030.

Preston, J., Hartley, A., Mange-Rajetzky, M., Hole, M., May, G. & Buck, S., 2002. The provenance of Triassic continental sandstones from the Beryl field, Northern North Sea: Mineralogical, geochemical, and sedimentological constraints. *Journal of Sedimentary Research*, **72**, 18–29.

Pupin, J.P., 1980. Zircon and granite petrology. *Contributions to Mineralogy and Petrology*, **73**, 207–220.

Reischmann, T., 1998. Pre-alpine origin of tectonic units from the metamorphic complex of Naxos, Greece, identified by single zircon Pb/Pb dating. *Bulletin of the Geological Society of Greece*, **32**, 101–111.

Reischmann, T. & Kostopoulos, D., 2007. Terrane accretion in the internal Hellenides. *Geophysical Research Abstracts*, **9**, 05337.

Reischmann, T., Kostopoulos, D., Loos, S., Anders, B., Avgerinas, A. & Sklavounos, S., 2001. Late Palaeozoic magmatism in the basement rocks southwest of Mt. Olympos, Central Pelagonian Zone, Greece: Remnants of a Permo-Carboniferous Magmatic Arc. *Bulletin of the Geological Society of Greece*, **34**, 985–993.

Rejebian, V.A., Harris, A.G. & Huebner, J.S., 1987. Conodont color and textural alteration: An index to regional metamophism, and hydrothermal alteration. *Geological Society of America Bulletin*, **99**, 471–479.

Ricou, L.-E. & Godfriaux, I., 1994. The Thessaloniki klippe. A nappe of Vertiskos origin emplaced upon the Mesozoic flysches of the Vardar basin. *Bulletin of the Geological Society of Greece*, **30**, 69–78.

Ricou, L.-E., Burg, J.-P., Godfriaux, I. & Ivanov, Z., 1998. Rhodope and Vardar: the metamorphic and olistostromic paired belts related to the Cretaceous subduction under Europe. *Geodinamica Acta*, **11**, 285–309.

Ring, U., Laws, S. & Bernet, M., 1999a. Structural analysis of a complex nappe sequence and late-orogenic basins from the Aegean Island of Samos, Greece. *Journal of Structural Geology*, **21**, 1575–1601.

Ring, U., Gessner, K., Güngör, T. & Passchier, C.W., 1999b. The Menderes Massif of western Turkey and the Cycladic Massif in the Aegean – do they really correlate?. *Journal of the Geological Society*, *London*, **156**, 3–6.

Robertson, A.H.F. & Pickett, E.A., 2000. Palaeozoic – Early Tertiary Tethyan evolution of mélanges, rift and passive margin units in the Karaburun Peninsula (western Turkey) and Chios Island (Greece). *In:* Bozkurt, E., Winchester J.A. & Piper J.D.A. (eds) *Tectonics and Magmatism in Turkey and the Surrounding Area*. Geological Society, London, Special Publications, **173**, 43–82.

Robertson, A.H.F., Dixon, J.E., Brown, S., Collins, A., Morris, A., Pickett, E., Sharp, I. & Ustaömer, T., 1996. Alternative tectonic models for the Late Paleozoic – Early Tertiary development of Tethys in the Eastern Mediterranean region. *In:* Morris, A. & Tarling, D.H. (eds) *Palaeomagnetism and Tectonics of the Mediterranean Region*. Geological Society, London, Special Publications, **105**, 239–263.

Robertson, A.H.F., Ustaömer, T., Pickett, E.A., Collins, A.S., Andrew, T. & Dixon, J.E., 2004. Testing models of Late Palaeozoic–Early Mesozoic orogeny in Western Turkey: support for an evolving open-Tethys model. *Journal of the Geological Society*, *London*, **161**, 501–511.

Romano, S.S., Dörr, W. & Zulauf, G., 2004. Cambrian granitoids in pre-Alpine basement of Crete (Greece): evidence from U-Pb dating of zircon. *International Journal of Earth Sciences*, **93**, 844–859.

Romano, S.S., Brix, M., Dörr, W., Krenn, E. & Zulauf, G., 2005. The evolution of the Cretan pre-Alpine basement. *In:* Freiwald, A., Röhling, H.-G. & Löffler, S.-B. (eds) *GeoErlangen 2005. System Erde – Biosphere Coupling. Regional Geology of Central Europe. Program and Abstracts*. Schriftenreihe der Deutschen Gesellschaft für Geowissenschaften, **39**, 317.

Romano, S.S., Brix, M., Dörr, W., Fiala, J., Krenn, E. & Zulauf, G., 2006. The Carboniferous to Jurassic evolution of the pre-Alpine basement of Crete: constraints from U–Pb and Th–(U)–Pb dating of orthogneisses, fission track dating of zircon, structural and petrological data. *In:* Robertson, A.H.F. & Mountrakis D. (eds) *Tectonic Development of the Eastern Mediterranean Region*. Geological Society, London, Special Publications, **260**, 69–90.

Roser, B.P. & Korsch, R.J., 1988. Provenance signatures of sandstone-mudstone suites determined using discriminant function analysis of major-element data. *Chemical Geology*, **67**, 119–139.

Rosselet, F. & Stampfli, G.M., 2003. The Paleotethys siliciclastic sequence in Karaburun, a remnant of the Paleotethys fore-arc basin in western Turkey. *Geophysical Research Abstracts*, **5**, 09770.

Rudnick, R.L. & Gao, S., 2003. Composition of the continental crust. *In:* Holland, H.D. & Turekian, K.K. (eds) *Treatise on Geochemistry*. Elsevier-Pergamon, Oxford, 1–64.

Rudnick, R.L., Barth, M., Horn, I. & McDonough, W.F., 2000. Rutile-bearing refractory eclogites: missing link between continents and depleted mantle. *Science*, **287**, 278–281.

Samson, S.D. & D'Lemos, R.S., 1998. U-Pb geochronology and Sm-Nd isotopic composition of Proterozoic gneisses, Channel Island, UK. *Journal of the Geological Society*, *London*, **155**, 609–618.

Samson, S.D., D'Lemos, R.S., Miller, B.V. & Hamilton, M.A., 2005. Neoproterozoic palaeogeography of the Cadomia and Avalon terranes: constraints from detrital zircon U–Pb ages. *Journal of the Geological Society*, *London*, **162**, 65–71.

Sarmiento, G.N., Sanz-López, J., García-López, S. & Hamoumi, N., 1997. La Biozona de *Polygnathoides siluricus* (Conodonta, Ludlow superior) en las "calizas con ortocerátidos" del Tafilalt, Anti-Atlas oriental, Marruecos. *Actas XIII Jornadas Paleontología y V Reunión Internacional Proyecto 351 PICG*, 257–259.

Sartorio, D. & Venturini, S., 1988. *Southern Tethys biofacies*. Agip, Milan.

Savov, I., Ryan, J., Haydutov, I. & Schijf, J., 2001. Late Precambrian Balkan-Carpathian ophiolite – a slice of the Pan-African ocean crust?: geochemical and tectonic insights from the Tcherni Vrah and Deli Jovan massifs, Bulgaria and Serbia. *Journal of Volcanology and Geothermal Research*, **110**, 299–318.

Seidel, M., Zacher, W., Schwarz, W.H., Jaeckel, P. & Reischmann, T., 2006. A Late Carboniferous age of the gneiss of Potamos (Kythira Island, Greece) and new considerations on geodynamic interpretations of the Western Hellenides. *Neues Jahrbuch für Geologie und Paläontologie*, *Abhandlungen*, **241**, 325–344.

Şengör, A.M.C., Yilmaz, Y. & Sungurlu, O., 1984. Tectonics of the Mediterranean Cimmerides: Nature and evolution of the western termination of Palaeo-Tethys. *In:* Dixon, J.E. & Robertson, A.H.F. (eds) *The geological evolution of the eastern Mediterranean*. Geological Society, London, Special Publications, **17**, 77–112

Serpagli, E. & Corradini, C., 1998. New Taxa of *Kockelella* (Conodonta) from late Wenlock–Ludlow (Silurian of Sardinia). *Giornale di Geologia*, ser. 3, **60** (special issue – Sardinia), 79–83.

Sideris, C., 1989. Late Paleozoic in Greece. *Geologické práce*, *Správy*, **88**, 191–202.

Sircombe, K.N., 1999. Tracing provenance through the isotope ages of littoral and sedimentary detrital zircon, eastern Australia. *Sedimentary Geology*, **124**, 47–67.

Sircombe, K.N., 2004. AgeDisplay: an EXCEL workbook to evaluate and display univariate geochronological data using binned frequency histograms and probability density distributions. *Computers & Geosciences*, **30**, 21–31.

Spear, F.S., Wark, D.A., Cheney, J.T., Schumacher, J.C. & Watson, B., 2006. Zr-in-rutile thermometry in blueschists from Sifnos, Greece. *Contributions to Mineralogy and Petrology*, **152**, 375–385.

Spiegel, C., Siebel, W. & Frisch, W., 2002. Sr and Nd isotope ratios of detrital epidote as provenance indicator and their significance for the reconstruction of the exhumation history of the Central Alps. *Chemical Geology*, **189**, 231–250.

Spray, J.G., Bébien, J., Rex, D.C. & Roddick, J.C., 1984. Age constraints on the igneous and metamorphic evolution of the Hellenic–Dinaric ophiolites. *In:* Dixon, J.E. & Robertson, A.H.F. (eds) *The geological evolution of the eastern Mediterranean*. Geological Society, London, Special Publications, **17**, 619–627.

Stacey, J.S. & Kramers, J.D., 1975. Approximation of terrestrial lead-isotope evolution by a two stage model. *Earth and Planetary Science Letters*, 2**6**, 359–362.

Stampfli, G.M., 2000. Tethyan oceans. *In:* Bozkurt, E., Winchester, J.A. & Piper, J.D.A. (eds) *Tectonics and Magmatism in Turkey and the Surrounding Area*. Geological Society, London, Special Publications, **173**, 1–23.

Stampfli, G.M. & Borel, G.D., 2002. A plate tectonic model for the Paleozoic and Mesozoic constrained by dynamic plate boundaries and restored synthetic oceanic isochrones. *Earth and Planetary Science Letters*, **196**, 17–33.

Stampfli, G.M., Marcoux, J. & Baud, A., 1991. Tethyan margins in space and time. *Palaeogeography Palaeoclimatology Palaeoecology*, **87**, 337–409.

Stampfli, G.M., von Raumer, J. & Borel, G.D., 2002. Palaeozoic evolution of pre-Variscan terranes: From Gondwana to the Variscan collision. *In:* Martínez-Catalán, J.R., Hatcher, R.D., Arenas, R. & Díaz García, F. (eds) *Variscan-Appalachian dynamics: The building of the late Paleozoic basement*. Geological Society of America, Special Papers, **364**, 263–280.

Stampfli, G.M., Borel, G., Cavazza, W., Mosar, J. & Ziegler, P.A., 2001. The Paleotectonic Atlas of the PeriTethyan Domain. European Geophysical Society (CD-ROM), Katlenburg-Lindau.

Stampfli, G.M., Vavassis, I., De Bono, A., Rosselet, F., Matti, B., & Bellini, M., 2003. Remnants of the Paleotethys oceanic suture-zone in the western Tethyan area. *In:* Cassinis, G. & Decandia, F.A. (eds) *Stratigraphic and Structural Evolution on the Late Carboniferous to Triassic Continental and Marine Successions in Tuscany (Italy): Regional Reports and General Correlation*. Bolletino della Società Geologica Italiana, Volume speciale, **2**, 1–23.

Stattegger, K., 1984. Chromspinell im klastischen Karbon von Chios, Ägäis (Vorbericht). *Anzeiger der Österreichischen Akademie der Wissenschaften*, *Mathematisch-Naturwissenschaftliche Klasse*, **1983**/1, 1–2.

Steiger, R.H. & Jäger, E., 1977. Subcommission on geochronology: convention on the use of decay constants in geo- and cosmochronology. *Earth and Planetary Science Letters*, **36**, 359–362.

Stendal, H., Toteu, S.F., Frei, R., Penaye, J., Njel, U.O., Bassahak, J., Nni, J., Kankeu, B., Ngako, V. & Hell, J.V., 2006. Derivation of detrital rutile in the Yaoundé region from the Neoproterozoic Pan-African belt in southern Cameroon (Central Africa). *Journal of African Earth Sciences*, **44**, 443–458.

Takeuchi, M., 1994. Changes in garnet chemistry show a progressive denudation of the source areas for Permian–Jurassic sandstones, Southern Kitakami Terrane, Japan. *Sedimentary Geology*, **93**, 85–105.

Talent, J.A. & Mawson, R., 1999. North-eastern Molong Arch and adjacent Hill End Trough (eastern Australia): mid-Palaeozoic conodont data and implications. *In:* Feist, R., Talent, J.A. & Daurer, A. (eds) *North Gondwana: Mid-Palaeozoic terranes, stratigraphy and biota*. Abhandlungen der Geologischen Bundesanstalt Wien, **54**, 49–105.

Taylor, S.R. & McLennan, S.M., 1985. *The Continental Crust: Its Composition and Evolution*. Blackwell, Oxford.

Teipel, U., Eichhorn, R., Loth, G., Rohrmüller, J., Höll, R. & Kennedy, A., 2004. U-Pb SHRIMP and Nd isotopic data from the western Bohemian Massif (Bayerischer Wald, Germany): Implications for Upper Vendian and Lower Ordovician magmatism. *International Journal of Earth Sciences*, **93**, 782–801.

Timmermann, H., Parrish, R.P., Noble, S.R. & Kryza, R., 2000. New U–Pb monazite and zircon data from the Sudetes Mountains in SW Poland: evidence for a single-cycle Variscan orogeny. *Journal of the Geological Society*, *London*, **157**, 265–268.

Timmermann, H., Štedrá, V., Gerdes, A., Noble, S.N., Parrish, R.R. & Dörr, W., 2004. The problem of dating high-pressure metamorphism: a U–Pb isotope and geochemical study on eclogites and related rocks of the Mariánské Lázne Complex, Czech Republic. *Journal of Petrology*, **45**, 1311–1338.

Titorenkova, R., Macheva, L., Zidarov, N., von Quadt, A. & Peytcheva, I., 2003. Metagranites from SW Bulgaria as a part of the Neoproterozoic to early Paleozoic system in Europe: New insight from zircon typology, U-Pb isotope data and Hf-tracing. *Geophysical Research Abstracts*, **5**, 08963.

Tomaschek, F., Kennedy, A., Keay, S. & Ballhaus, C., 2001. Geochronological constraints on Carboniferous and Triassic magmatism in the Cyclades: SHRIMP U–Pb ages of zircons from Syros, Greece. *Journal of Conference Abstracts*, **6**, 315.

Tompsett, G.A., Bowmaker, G.A., Cooney, R.P., Metson, J.B., Rodgers, K.A. & Seakins, J.M., 1995. The Raman spectrum of brookite, TiO_2 (*Pbca*, $Z = 8$). *Journal of Raman Spectroscopy*, **26**, 57–62.

Topuz, G., Altherr, R., Kalt, A., Satir, M., Werner, O. & Schwarz, W.H., 2004. Aluminous granulites from the Pulur Complex, NE Turkey: a case of partial melting, efficient melt extraction and crystallisation. *Lithos*, **72**, 183–207.

Trikkalinos, J., 1955. Beiträge zur Erforschung des tektonischen Baues Griechenland. Über das Alter der vortertiären Schichten des Gebietes von Alexandroupolis-Didymotichon, Westthrazien. *Annales géologiques des pays helléniques*, **6**, 81–82.

Turnsek, D., Buser, S. & Ogorelec, B., 1981. An Upper Jurassic reef complex from Slovenia, Yugoslavia. *In:* Toomey, D.F. (ed) *European fossil reef models*. SEPM Special Publication, **30**, 361–369.

Turpaud, P., 2006. *Characterisation of igneous terranes by zircon dating: implications for UHP relicts occurrences and suture identification in the Central Rhodope, Northern Greece*. PhD Thesis, University of Mainz, Germany.

Turpaud, P. & Reischmann, T., 2005. Relationships between crustal blocks and UHP relics, an example from Northern Greece. *Geophysical Research Abstracts*, **8**, 04353.

Turhan, N., Okuyucu, C. & Göncüoğlu, C.M., 2004. Autochthonous Upper Permian (Midian) Carbonates in the Western Sakarya Composite Terrane, Geyve Area, Turkey: Preliminary Data. *Turkish Journal of Earth Sciences*, **13**, 215–229.

Triebold, S., von Eynatten, H. & Zack, T., 2005. Trace elements in detrital rutile as provenance indicator: A case study from the Erzgebirge, Germany. *In:* Haas, H., Ramseyer, K. & Schlunegger, F. (eds) *Sediment 2005, Abstracts*. Schriftenreihe der Deutschen Gesellschaft für Geowissenschaften, **38**, 144–145.

Triebold, S., von Eynatten, H., Luvizotto, G.L. & Zack, T., 2007. Deducing source rock lithology from detrital rutile geochemistry: An example from the Erzgebirge, Germany. *Chemical Geology*, doi: 10.1016/j.chemgeo.2007.06.033.

Uher, P., Černý, P., Chapman, R., Határ, J. & Miko, O., 1998. Evolution of Nb, Ta-oxide minerals in the Prašivá granitic pegmatites, Slovakia. I. Primary Fe, Ti-rich assemblage. *Canadian Mineralogist*, **36**, 525–534.

Ustaömer, P.A., Mundil, R. & Renne, P.R., 2005. U/Pb and Pb/Pb zircon ages for arc-related intrusions of the Bolu Massif (W Pontides, NW Turkey): evidence for Late Precambrian (Cadomian) age. *Terra Nova*, **17**, 215–223.

Uyeno, T.T., 1980. Stratigraphy and conodonts of Upper Silurian and Lower Devonian rocks in the environs of the Boothia Uplift, Canadian Archipelago. Part II. Systematic study of conodonts. *Geological Survey of Canada Bulletin*, **292**, 39–75.

VAVASSIS, I., DE BONO, A., STAMPFLI, G.M., GIORGIS, D., VALLOTON, A. & AMELIN, Y., 2000. U-Pb and Ar-Ar geochronological data from the Pelagonian Basement in Evia (Greece): geodynamic implications for the evolution of Paleotethys. *Schweizerische Mineralogische und Petrographische Mitteilungen*, **80**, 21–43.

VIQUESNEL, A., 1868. Voyage dans la Turquie d'Europe: Description physique et géologique de la Thrace. Tome II, Paris.

VON BRAUN, E., 1968. Die mesozoischen Hüllgesteine der SE-Rhodopen in Westthrazien (Griechenland). *Geologisches Jahrbuch*, **85**, 565–584.

VON BRAUN, E., 1993. The Rhodope Question viewed from Eastern Greece. *Zeitschrift der Deutschen Geologischen Gesellschaft*, **144**, 406–418.

VON EYNATTEN, H. & GAUPP, R., 1999. Provenance of Cretaceous synorogenic sandstones from the Eastern Alps: constraints from framework petrography, heavy mineral analysis, and mineral chemistry. *Sedimentary Geology*, **124**, 81–111.

VON EYNATTEN, H., TOLOSANA-DELGADO, R., TRIEBOLD, S. & ZACK, T., 2005. Interactions between grain size and composition of sediments: two examples. *Proceedings 2nd CoDaWork, 19–21 October 2005, Girona, Spain*.

VON QUADT, A., GRAF, J. & BERNOULLI, D., 2000. Pre-Variscan and Tertiary magmatism in western Bulgaria (Kraiste) based on U-Pb single zircon analyses, trace and REE element distribution and Sm/Nd – Rb/Sr investigation. *Terra Nostra*, **2000/1**, 87.

VON RAUMER, J., STAMPFLI, G.M., BOREL, G. & BUSSY, F., 2002. Organization of pre-Variscan basement areas at the north-Gondwanan margin. *International Journal of Earth Sciences*, **91**, 35–52.

VON RAUMER, J.F., STAMPFLI, G.M. & BUSSY, F., 2003. Gondwana-derived microcontinents - the constituents of the Variscan and Alpine collisional orogens. *Tectonophysics*, **365**, 7–22.

WALLISER, O., 1964. Conodonten des Silurs. *Abhandlungen des Hessischen Landesamtes für Bodenforschung*, **41**, 1–106.

WALSH, G.J., ALEINIKOFF, J.N., BENZIANE, F., YAZIDI, A. & ARMSTRONG, T.R., 2002. U–Pb zircon geochronology of the Paleoproterozoic Tagragra de Tata inlier and its Neoproterozoic cover, western Anti-Atlas, Morocco. *Precambrian Research*, **117**, 1–20.

WATSON, E.B., WARK, D.A. & THOMAS, J.B., 2006. Crystallization thermometers for zircon and rutile. *Contributions to Mineralogy and Petrology*, **151**, 413–433.

WIEDENBECK, M., ALLÉ, P., CORFU, F., GRIFFIN, W.L., MEIER, M., OBERLI, F., VON QUADT, A., RODDICK, J.C. & SPIEGEL, W., 1995. Three natural zircon standards for U-Th-Pb, Lu-Hf, trace element and REE analyses. *Geostandard Newsletter*, **19**, 1–23.

WILLIAMS, I.S., 1992. Some observations on the use of zircon U–Pb geochronology in the study of granitic rocks. *Transactions of the Royal Society of Edinburgh, Earth Sciences*, **83**, 447–458.

WINCHESTER, J.A., PHARAOH, T.C., VERNIERS, J., IOANE, D. & SEGHEDI, A., 2006. Palaeozoic accretion of Gondwana-derived terranes to the East European Craton: recognition of terrane fragments dispersed after collision with promontories. *In:* GEE, D. & STEPHENSON, R. (eds) *European Lithosphere Dynamics*. Geological Society, London, Memoir, **32**, 323–332.

WIRTH, E., 1940. Das Erdölhoffnungsgebiet Westthrazien (Griechenland). *Oel und Kohle*, **36**, 433–456.

WRONKIEWICZ, D.J. & CONDIE, K.C., 1987. Geochemistry of Archaean shales from the Witwatersrand Supergroup, South Africa: Source-area weathering and provenance. *Geochimica et Cosmochimica Acta*, **51**, 2401–2416.

XYPOLIAS, P., DÖRR, W., ZULAUF, G., 2006. Late Carboniferous plutonism within the pre-Alpine basement of the External Hellenides (Kithira, Greece): evidence from U–Pb zircon dating. *Journal of the Geological Society, London*, **163**, 539–547.

YANEV, S., GÖNCÜOGLU, M.C., GEDIK, I., LAKOVA, I., BONCHEVA, I., SACHANSKI, V., OKUYUCU, C., ÖZGÜL, N., TIMUR, E., MALIAKOV, Y. & SAYDAM, G., 2006. Stratigraphy, correlations and palaeogeography of Palaeozoic terranes of Bulgaria and NW Turkey: a review of recent data. *In:* ROBERTSON, A.H.F. & MOUNTRAKIS, D. (eds) *Tectonic*

Development of the Eastern Mediterranean Region. Geological Society, London, Special Publications, 260, 51–67.

YARWOOD, G.A. & AFTALION, M., 1976. Field relations and U-Pb geochronology of a granite from the Pelagonian zone of the Hellenides (High Pieria, Greece). *Bulletin de la Société Géologique de France*, **18**, 259–264.

YIĞITBAŞ, E., KERRICH, R., YILMAZ, Y., ELMAS, A. & XIE, Q., 2004. Characteristics and geochemistry of Precambrian ophiolites and related volcanics from the Istanbul- Zonguldak Unit, Northwestern Anatolia, Turkey: following the missing chain of the Precambrian South European suture zone to the east. *Precambrian Research*, **132**, 179–206.

ZACHARIADIS, P., 2007. *Ophiolites of the eastern Vardar Zone, N. Greece*. PhD Thesis, University of Mainz, Germany.

ZACHARIADIS, P., KOSTOPOULOS, D., REISCHMANN, T., HIMMERKUS, F., MATUKOV, D. & SERGEEV, S., 2006. U–Pb ion-microprobe zircon dating of subduction - related magmatism from northern Greece: The ages of the Guevgueli, Thessaloniki and Chalkidiki igneous complexes. *Geophysical Research Abstracts*, **8**, 05560.

ZACK, T. & LUVIZOTTO, G.L., 2006. Application of rutile thermometry to eclogites. *Mineralogy and Petrology*, **88**, 69–85.

ZACK, T., KRONZ, A., FOLEY, S.F. & RIVERS, T., 2002. Trace element abundances in rutiles from eclogites and associated garnet mica schists. *Chemical Geology*, **184**, 97–122.

ZACK, T., MORAES, R. & KRONZ, A., 2004a. Temperature dependence of Zr in rutile: empirical calibration of a rutile thermometer. Contrib. *Mineralogy and Petrology*, **148**, 471–488.

ZACK, T., VON EYNATTEN, H. & KRONZ, A., 2004b. Rutile geochemistry and its potential use in quantitative provenance studies. *Sedimentary Geology*, **171**, 37–58.

ZANCHI, A., GARZANTI, E., LARGHI, C., ANGIOLINI, L. & GAETANI, M., 2003. The Variscan orogeny in Chios (Greece): Carboniferous accretion along a Palaeotethyan active margin. *Terra Nova*, **15**, 213–223.

ZEH, A., BRÄTZ, H., MILLAR, I.L. & WILLIAMS, I.S., 2001. A combined zircon SHRIMP and Sm-Nd isotope study on high-grade paragneisses from the Mid-German Crystalline Rise: Evidence for northern Gondwanan and Grenvillian provenance. *Journal of the Geological Society*, *London*, **158**, 983–994.

ZIMMERLE, W., 1984. The geotectonic significance of detrital brown spinel in sediments. *Mitteilungen aus dem Geologisch-Paläontologischen Institut der Universität Hamburg*, **56**, 337–360.

Appendix

Appendix A. Sample list

Appendix B. Whole-rock geochemical data

Appendix C-1. Mineral chemical data – Chrome spinel

Appendix C-2a. Mineral chemical data – Rutile (single measurements)

Appendix C-2b. Mineral chemical data – Rutile (multiple measurements)

Appendix C-3. Mineral chemical data – Feldspar

Appendix C-4. Mineral chemical data – Mica

Appendix C-5. Mineral chemical data – Garnet

Appendix D-1. U–Pb SHRIMP-II zircon data

Appendix D-2. U–Pb LA-ICPMS zircon data

Appendix E. Magmatic zircon ages for pre-Triassic rocks from the Aegean and the surrounding region

Appendix A. Sample list

Chapter(s)	Sample	Rock type	Locality	Latitude	Longitude
	Chios Island				
	Lower Unit (Carboniferous)				
1, 2	CH9	greywacke	ESE' Volissos	38°28'12.6''	25°57'33.7''
1	CH12	sandstone	NNW' Langada	38°30'47.6''	26°06'12.3''
1	CH31	greywacke	N' Langada	38°31'47.2''	26°06'42.1''
1	CH46	siltstone	SE' Metochi bay	38°24'37.6''	25°58'18.9''
1, 2	CH51	greywacke	NE' Volissos	38°30'24.5''	25°56'58.3''
1, 2, 3	CH52	greywacke	E' Volissos	38°28'58.0''	25°56'05.1''
1	CH56	greywacke	W' Parparia	38°31'16.8''	25°52'52.3''
1, 2	CH61	greywacke	W' Nenitouria	38°34'05.1''	25°52'23.5''
1	CH63	siltstone	S' Afrodisia	38°32'25.4''	25°56'19.7''
1, 2	CH65	greywacke	N' Pispilounta	38°32'28.2''	25°57'42.0''
1, 2	CH66	greywacke	N' Pispilounta	38°32'28.2''	25°57'42.0''
1, 2	CH70	greywacke	W' Chios	38°23'08.1''	26°06'10.1''
3	CH13	limestone (olistolith)	S' Ano Kardamilia	38°30'48.5''	26°06'04.0''
	Lower Unit (Permo-Triassic)				
1, 3	CH11	sandstone	NNW' Langada	38°30'14.2''	26°06'31.7''
1	CH34	sandstone	N' Langada	38°32'00.8''	26°06'57.2''
1	CH47	siltstone	SE' Metochi bay	38°24'50.0''	25°57'59.4''
1, 2	CH48	quarzitic sandstone	SE' Metochi bay	38°24'53.2''	25°57'52.2''
1	CH71	sandstone	NNW' Langada	38°30'14.2''	26°06'31.5''
	Upper Unit (Permo-Carboniferous)				
1, 2	CH26	greywacke	NE' Pantoukios	38°27'50.7''	26°08'01.6''
1	CH27	sandstone	W' Langada	38°28'40.1''	26°07'02.0''
1, 2	CH36	greywacke	W' Pirgi	38°14'12.1''	25°57'52.1''
1	CH39	greywacke	S' Olimbi	38°13'39.2''	25°56'32.1''
1, 2	CH42	greywacke	NE' Limenas	38°17'20.9''	25°56'21.1''
	Inousses Island				
1	IN1	meta-litharenite	NW' Inousses	38°31'57.8''	26°11'37.1''
1	IN2	phyllite	N' Inousses	38°31'36.0''	26°13'30.3''
1	IN3	phyllite	N' Inousses	38°31'36.0''	26°13'30.3''
1	IN5	meta-litharenite	E' Inousses	38°31'04.3''	26°16'07.2''
1	IN6	meta-litharenite	E' Inousses	38°31'04.3''	26°16'07.2''
1	IN7	phyllite	N' Inousses	38°31'06.2''	26°13'16.7''
1	IN8	meta-litharenite	N' Inousses	38°31'17.2''	26°12'59.6''
	Psara Island				
	Upper Unit				
1	CH16	garnet-mica schist	N' Psara	see Fig. 5a in Chapter 1	
1	CH18	garnet-mica schist	N' Psara	see Fig. 5a in Chapter 1	
1	CH19	garnet-mica schist	N' Psara	38°35'36.4''	25°35'00.3''
	Lower Unit				
1	CH20	phyllite	N' Psara	38°35'19.8''	25°34'44.1''
1	CH21	phyllite	N' Psara	see Fig. 5a in Chapter 1	
1	CH25	meta-litharenite	S' Psara	38°32'35.8''	25°34'02.0''

Appendix A. Continued

Chapter(s)	Sample	Rock type	Locality	Latitude	Longitude
	Serbo-Macedonian Massif				
	Pirgadikia Unit				
4	SM201	metaquartzite	NE' Taxiarchis	40°26'00.7''	23°30'58.1''
4	SM202	metasiltstone	NE' Taxiarchis	40°26'04.0''	23°31'02.3''
4	SM204	metaquartzite	NE' Taxiarchis	40°25'45.6''	23°30'57.6''
4	SM205	metaquartzite	NE' Taxiarchis	40°25'39.1''	23°30'51.8''
4	SM208	metaquartzite	E' Taxiarchis	40°25'36.1''	23°30'44.4''
4	SM209	metaquartzite	E' Taxiarchis	40°25'36.1''	23°30'44.4''
4	SM250	metasiltstone	E' Taxiarchis	40°25'25.6''	23°30'39.3''
4	SM251	metaquartzite	E' Taxiarchis	40°25'36.1''	23°30'44.5''
4	SM252	metaquartzite	NE' Taxiarchis	40°25'58.3''	23°30'58.2''
4	*Vertiskos Unit*				
4	SM151	garnet-biotite gneiss	W' Agh. Iraklio	41°07'44.4''	23'12'13.7''
4	SM157	garnetiferous micaschist	N' Ano Poroia	41°17'27.3''	23°02'00.0''
	Vardar Zone				
	Examili Formation				
5	SM171	arkosic quartzite	E' Evangelismos	40°41'39.8''	23°13'22.7''
5	SM220	quartzite	NW' Examili	40°52'26.7''	22°59'44.7''
5	SM254	arkosic quartzite	E' Evangelismos	40°41'40.2''	23°13'19.8''
5	SM256	arkosic quartzite	W' Evangelismos	40°42'10.4''	23°12'29.3''
5	SM257	quartzite	E' Drakondio	40°44'11.9''	23°09'40.2''
5	SM258	quartzite	W' Polidentri	40°43'51.0''	23°05'32.9''
5	SM261	arkosic quartzite	N' Examili	40°52'27.3''	23°00'14.7''
	'Svoula limestone'				
5	SM224	limestone	W' Pirghoto	40°52'23.9''	22°55'50.6''
	Melissochori Formation				
5	SM143	phyllite	ESE' Galatista	40°27'37.1''	23°17'51.5''
5	SM144	litharenite	ESE' Galatista	40°27'37.1''	23°17'51.5''
5	SM160	phyllite	W' Exochi	40°38'11.4''	23°00'56.9''
5	SM164	litharenite	Ardameri	40°35'50.7''	23°10'52.1''
5	SM165	litharenite	S' Zangliveri	40°33'30.2''	23°16'56.4''
5	SM166	litharenite	S' Zangliveri	40°33'08.8''	23°17'06.0''
5	SM167	phyllite	NW' Petrokerasa	40°31'44.0''	23°16'38.5''
5	SM195	litharenite	N' Vavdos	40°27'07.3''	23°19'56.1''
5	SM197	litharenite	W' Agh. Prodromos	40°27'52.0''	23°21'19.5''
5	SM198	litharenite	Paleokastro	40°26'27.6''	23°25'31.5''
5	SM199	litharenite	S' Paleokastro	40°25'13.2''	23°25'51.7''
5	SM200	litharenite	SE' Poligiros	40°21'07.2''	23°29'10.5''
5	SM213	phyllite	NNW' Poligiros	40°25'00.5''	23°25'16.6''
5	SM214	litharenite	NNE' Metamorfosi	40°16'45.9''	23°36'22.1''
5	SM227	litharenite	SE' Monolofo	40°47'29.8''	22°56'47.1''
5	SM231	litharenite	S' Agh. Haralambos	40°22'30.1''	23°15'58.5''
5	SM241	litharenite	N' B. Lagomandra	40°08'17.7''	23°44'41.8''
5	SM242	phyllite	Marmaras	40°06'19.8''	23°46'39.3''

Appendix A. Continued

Chapter(s)	Sample	Rock type	Locality	Latitude	Longitude
	Prinochori Formation				
5	SM134	litharenite	N' Prinochori	40°24'04.9''	23°11'28.8''
5	SM178	litharenite	N' Prinochori	40°24'04.9''	23°11'28.8''
5	SM179	litharenite	N' Prinochori	40°24'00.3''	23°11'35.3''
5	SM181	litharenite	N' Prinochori	40°24'00.3''	23°11'35.3''
5	SM182	chalky litharenite	N' Prinochori	40°24'00.3''	23°11'35.3''
5	SM183	litharenite	N' Prinochori	40°24'00.3''	23°11'35.3''
5	SM184	litharenite	N' Prinochori	40°24'00.3''	23°11'35.3''
5	SM185	litharenite	N' Prinochori	40°24'35.6''	23°11'09.8''
5	SM246	chalky litharenite	N' Prinochori	40°24'26.2''	23°10'34.1''
5	SM247	chalky litharenite	N' Prinochori	40°24'26.2''	23°10'34.1''
	Neochorouda Unit				
5	SM176	packstone	E' Neochorouda	40°44'53.3''	22°52'39.0''
5	SM176b	limestone olistolith	E' Neochorouda	40°44'53.3''	22°52'39.0''
	Oreokastro Formation				
5	SM177	wackstone	E' Neochorouda	40°45'21.6''	22°53'25.7''
5	SM177a	packstone	E' Neochorouda	40°45'21.6''	22°53'25.7''
5	SM228a	marly siltstone	E' Neochorouda	40°45'23.7''	22°53'24.3''
5	SM228b	packstone	E' Neochorouda	40°45'23.7''	22°53'24.3''
	Thrace				
	Makri Unit				
6	R18b	litharenite	W' Plaka	40°53'08.3''	25°44'11.0''
6	R27	litharenite	Makri	40°51'10.0''	25°44'25.3''
6	R35	siltstone	SE' Kirki	40°55'05.1''	25°48'28.1''
6	R38	phyllite	Makri	40°50'54.0''	25°44'57.0''
6	R39	phyllite	Makri	40°50'54.0''	25°44'57.0''
6	R40	siltstone	Makri	40°50'54.0''	25°44'57.0''
6	R41	phyllite	NE' Dikela	40°51'55.7''	25°42'05.0''
6	R42	litharenite	NE' Dikela	40°52'16.6''	25°42'31.3''
6	R43	litharenite	NE' Dikela	40°52'16.6''	25°42'31.3''
6	R44	litharenite	N' Makri	40°51'39.7''	25°44'31.8''
6	R45	siltstone	Makri	40°51'18.1''	25°44'27.1''
	Melia Formation				
6	R6	litharenite	NW' Melia	40°57'20.4''	26°03'58.1''
6	R7	litharenite	NW' Melia	40°57'20.4''	26°03'58.1''
6	R8	siltstone	NW' Melia	40°57'12.5''	26°04'00.4''
6	R9	litharenite	NW' Melia	40°57'12.5''	26°04'00.4''
6	R11	litharenite	NW' Melia	40°57'12.5''	26°04'00.4''
6	R14	litharenite	Melia	40°57'07.0''	26°06'12.1''
6	R15	litharenite	Melia	40°57'07.0''	26°06'12.1''
6	R31	siltstone	NNW' Melia	41°01'44.5''	26°03'08.4''
6	R32	litharenite	NNW' Melia	41°01'44.5''	26°03'08.4''

Appendix B. Whole-rock geochemical data

Chapter no.	1	1	1	1	1	1	1	1	1
Sample no.	CH9	CH12	CH31	CH46	CH51	CH52	CH56	CH61	CH63
SiO_2 (wt%)	70.48	74.12	71.08	60.59	70.82	68.77	73.06	73.43	60.31
TiO_2	0.78	0.69	0.67	0.87	0.77	0.9	0.95	0.67	0.83
Al_2O_3	12.4	12.17	12.07	18.14	13.97	13.7	11.95	12.64	17.06
Fe_2O_3	3.77	4.15	5.18	7.35	5.05	5.38	5.09	4.31	6.85
MnO	0.04	0.02	0.08	0.03	0.04	0.07	0.05	0.06	0.06
MgO	1.15	1.12	2.32	1.76	1.3	2	1.31	1.33	2.63
CaO	1.46	0.21	0.96	0.88	0.27	0.77	0.4	0.11	1.65
Na_2O	1.56	1.15	2.99	1.31	2.2	2.32	1.68	2.07	1.39
K_2O	2.53	2.4	1.33	2.79	2.21	1.99	1.88	1.88	3.38
P_2O_5	0.07	0.1	0.1	0.13	0.12	0.15	0.14	0.08	0.13
LOI	5.45	3.68	3.44	6.15	3.53	3.65	3.42	3.46	5.60
Total	99.7	99.8	100.2	100.0	100.3	99.7	99.9	100.0	99.9
Sc (ppm)	12	9	17	21	12	14	11	11	20
V	77	76	113	158	95	103	84	79	140
Cr	108	59	130	117	69	75	83	62	109
Co	13	8	11	16	7	10	5	10	18
Ni	42	23	47	50	28	32	31	24	49
Cu	13	16	19	46	17	17	14	18	35
Zn	61	71	63	86	70	76	65	60	102
Ga	14	14	14	19	16	16	14	14	20
Rb	94	93	54	111	87	79	75	75	142
Sr	86	58	101	91	66	74	57	65	71
Y	20	27	20	27	26	29	29	27	29
Zr	180	234	135	166	176	215	267	166	164
Nb	15	13	9	12	13	13	14	11	14
Ba	337	235	200	414	413	409	373	442	553
Hf	*5.74*	*7.85*	*3.74*	n.d.	*5.74*	*6.94*	n.d.	*5.20*	n.d.
Ta	*1.07*	*1.04*	*0.61*	n.d.	*1.01*	*1.05*	n.d.	*0.92*	n.d.
Th	*8.63*	*11.43*	*6.39*	11.5	*9.57*	*9.57*	10.9	*7.74*	11.6
U	*3.35*	*3.95*	*2.40*	3.2	*3.22*	*3.36*	2.4	*3.06*	2.4
La	*26.85*	*31.57*	*19.33*	33	*29.15*	*30.92*	32	*28.00*	36
Ce	*53.94*	*61.97*	*41.51*	65	*59.78*	*64.64*	72	*58.20*	77
Pr	*5.76*	*6.84*	*4.52*	6	*6.69*	*7.25*	6	*6.56*	10
Nd	*23.34*	*27.31*	*18.35*	32	*27.31*	*29.69*	32	*27.09*	34
Sm	*4.41*	*5.21*	*3.70*	5	*5.34*	*6.01*	8	*5.60*	7
Eu	*0.81*	*1.03*	*0.90*	n.d.	*1.09*	*1.22*	n.d.	*1.16*	n.d.
Gd	*3.74*	*4.54*	*3.32*	n.d.	*4.75*	*5.43*	n.d.	*5.08*	n.d.
Tb	*0.63*	*0.79*	*0.57*	n.d.	*0.80*	*0.93*	n.d.	*0.86*	n.d.
Dy	*3.49*	*4.42*	*3.23*	n.d.	*4.50*	*5.09*	n.d.	*4.63*	n.d.
Ho	*0.73*	*0.90*	*0.67*	n.d.	*0.93*	*1.03*	n.d.	*0.92*	n.d.
Er	*2.05*	*2.58*	*1.88*	n.d.	*2.63*	*2.91*	n.d.	*2.61*	n.d.
Tm	n.d.	n.d.	n.d.	n.d.	n.d.	n.d.	n.d.	n.d.	n.d.
Yb	*1.99*	*2.54*	*1.82*	n.d.	*2.53*	*2.73*	n.d.	*2.50*	n.d.
Lu	*0.31*	*0.39*	*0.28*	n.d.	*0.39*	*0.42*	n.d.	*0.38*	n.d.

n.d. = not determined; b.d. = below detection limit; LOI = loss on ignition; Data analysed by ICPMS appear in italics.

Appendix B. Continued

Chapter no.	1	1	1	1	1	1	1	1	1
Sample no.	CH65	CH66	CH70	CH26	CH27	CH36	CH39	CH42	CH11
SiO_2 (wt%)	70.58	74.19	72.56	71.15	73.23	70.4	72.43	76.91	84.81
TiO_2	0.82	0.78	0.75	0.62	0.25	0.68	0.63	0.64	0.5
Al_2O_3	13.8	11.92	12.38	10.12	4.87	12.45	9.02	10.36	7.75
Fe_2O_3	5.25	4.34	3.9	4.67	2.93	4.65	3.42	3.71	1.93
MnO	0.04	0.03	0.06	0.07	0.06	0.07	0.11	0.03	0.01
MgO	1.52	1.24	1.35	1.74	0.4	1.33	0.96	1.5	0.55
CaO	0.28	0.24	1.23	3.12	8.36	2.09	4.53	0.57	0.1
Na_2O	2.12	2.38	2.19	1.57	0.74	2	1.95	0.96	0.41
K_2O	2.17	1.64	1.92	1.51	0.75	1.96	1.19	1.84	1.31
P_2O_5	0.14	0.13	0.13	0.11	0.04	0.12	0.11	0.11	0.07
LOI	3.31	2.59	3.60	4.96	8.37	4.40	5.54	3.52	2.60
Total	100.0	99.5	100.1	99.6	100.0	100.1	99.9	100.2	100.0
Sc (ppm)	13	11	9	12	8	13	12	9	7
V	100	82	80	95	30	87	75	79	56
Cr	77	66	70	130	73	65	60	104	97
Co	12	6	9	12	5	5	6	9	3
Ni	29	27	23	53	27	23	19	40	22
Cu	18	15	16	17	3	16	15	11	6
Zn	79	62	54	62	51	62	48	61	34
Ga	16	13	14	11	6	14	10	12	9
Rb	87	66	76	62	28	78	46	74	49
Sr	67	60	76	86	87	121	163	64	44
Y	28	27	25	20	16	24	26	23	16
Zr	210	216	188	161	130	171	164	218	198
Nb	13	11	12	11	5	13	9	11	8
Ba	389	297	439	232	169	417	242	276	129
Hf	n.d.	*6.88*	*6.36*	*4.80*	*3.83*	*5.43*	*5.06*	*7.19*	*5.76*
Ta	n.d.	*0.94*	*1.07*	*0.77*	*0.36*	*0.95*	*0.67*	*0.82*	*0.55*
Th	8.6	*7.94*	*8.53*	*7.58*	*3.39*	*9.86*	*6.19*	*8.56*	*6.07*
U	3.2	*3.24*	*3.53*	*2.76*	*1.81*	*3.24*	*2.40*	*2.88*	*2.22*
La	29	*27.50*	*32.58*	*22.57*	*12.13*	*28.49*	*20.97*	*22.79*	*16.41*
Ce	62	*56.44*	*66.02*	*47.19*	*25.43*	*58.67*	*43.15*	*48.53*	*32.94*
Pr	5	*6.26*	*7.27*	*5.15*	*2.83*	*6.57*	*4.80*	*5.31*	*3.61*
Nd	29	*25.74*	*29.18*	*20.91*	*11.45*	*26.83*	*20.06*	*21.66*	*14.76*
Sm	7	*5.07*	*5.60*	*4.03*	*2.31*	*5.24*	*4.14*	*4.18*	*2.91*
Eu	n.d.	*0.98*	*1.02*	*0.87*	*0.48*	*1.04*	*0.90*	*0.85*	*0.65*
Gd	n.d.	*4.62*	*4.83*	*3.64*	*2.23*	*4.67*	*3.97*	*3.76*	*2.63*
Tb	n.d.	*0.81*	*0.78*	*0.61*	*0.39*	*0.79*	*0.70*	*0.64*	*0.45*
Dy	n.d.	*4.64*	*4.30*	*3.33*	*2.23*	*4.25*	*4.08*	*3.56*	*2.54*
Ho	n.d.	*0.96*	*0.88*	*0.68*	*0.46*	*0.86*	*0.86*	*0.72*	*0.54*
Er	n.d.	*2.74*	*2.47*	*1.91*	*1.31*	*2.37*	*2.48*	*2.13*	*1.52*
Tm	n.d.	n.d.	n.d.	n.d.	n.d.	n.d.	n.d.	n.d.	n.d.
Yb	n.d.	*2.69*	*2.38*	*1.86*	*1.26*	*2.23*	*2.43*	*2.09*	*1.55*
Lu	n.d.	*0.40*	*0.36*	*0.28*	*0.21*	*0.33*	*0.37*	*0.33*	*0.24*

n.d. = not determined; b.d. = below detection limit; LOI = loss on ignition; Data analysed by ICPMS appear in italics.

Appendix B. Continued

Chapter no.	1	1	1, 2	1	1	1	1	1	1
Sample no.	CH34	CH47	CH48	CH71	IN1	IN2	IN3	IN5	IN6
SiO_2 (wt%)	76.77	47.49	74.44	63.71	75.15	56.7	62.89	81.92	84.83
TiO_2	0.2	0.71	0.69	0.66	0.76	0.93	0.92	0.49	0.39
Al_2O_3	5.01	13.97	12.13	11.63	12.4	21.18	17.77	8.59	7.14
Fe_2O_3	1.28	5.91	4.27	3.73	3.83	6.85	6.14	2.75	2.76
MnO	0.1	0.07	0.03	0.04	0.04	0.03	0.03	0.02	0.04
MgO	3.52	1.96	1.71	1.26	0.79	2.35	2.06	0.71	0.53
CaO	4.2	12.01	0.22	6.76	0.12	0.12	0.18	0.12	0.14
Na_2O	1.29	0.7	0.68	0.41	2.72	1.3	1.26	1.85	1.58
K_2O	0.4	2.24	2.22	2.12	1.83	4.35	3.62	1.2	1.02
P_2O_5	0.02	0.08	0.11	0.12	0.13	0.12	0.16	0.08	0.08
LOI	7.62	14.92	3.47	9.19	2.29	5.34	4.07	1.58	1.48
Total	100.4	100.1	100.0	99.6	100.1	99.3	99.1	99.3	100.0
Sc (ppm)	7	29	11	18	11	21	17	6	5
V	39	161	105	102	76	157	121	46	43
Cr	46	154	99	108	70	131	96	41	34
Co	6	13	10	9	5	9	9	4	7
Ni	12	61	45	38	21	37	39	11	13
Cu	7	30	10	20	16	16	28	9	12
Zn	25	79	71	59	54	99	90	41	38
Ga	5	16	15	13	13	27	22	10	8
Rb	17	84	85	79	72	177	145	46	40
Sr	68	352	66	87	49	55	55	38	36
Y	16	21	22	24	29	34	35	18	19
Zr	70	130	185	204	198	157	214	120	112
Nb	5	9	11	11	13	17	16	8	7
Ba	65	317	314	290	357	814	697	255	225
Hf	n.d.	n.d.	*6.34*	*6.65*	*6.99*	*4.44*	*6.57*	*3.81*	*3.24*
Ta	n.d.	n.d.	*0.87*	*0.84*	*1.07*	*1.40*	*1.36*	*0.66*	*0.51*
Th	3.8	7.5	*8.89*	*9.25*	*7.30*	*11.14*	*9.35*	*5.97*	*3.95*
U	0.6	3.5	*2.80*	*3.75*	*2.20*	*2.37*	*2.76*	*1.36*	*1.25*
La	17	30	*24.96*	*27.69*	*30.60*	*44.39*	*37.54*	*18.02*	*22.73*
Ce	24	54	*51.84*	*52.61*	*64.00*	*90.71*	*77.04*	*37.35*	*36.73*
Pr	4	3	*5.62*	*5.59*	*7.24*	*10.29*	*8.83*	*4.08*	*4.12*
Nd	14	27	*22.90*	*22.94*	*29.57*	*40.16*	*34.45*	*16.56*	*16.69*
Sm	5	6	*4.50*	*4.70*	*6.06*	*7.89*	*7.00*	*3.21*	*3.20*
Eu	n.d.	n.d.	*1.02*	*0.95*	*1.18*	*1.49*	*1.38*	*0.62*	*0.61*
Gd	n.d.	n.d.	*4.10*	*4.25*	*5.55*	*6.76*	*6.61*	*3.05*	*2.99*
Tb	n.d.	n.d.	*0.69*	*0.74*	*0.98*	*1.03*	*1.04*	*0.50*	*0.49*
Dy	n.d.	n.d.	*3.92*	*4.05*	*5.23*	*6.00*	*6.30*	*2.81*	*2.75*
Ho	n.d.	n.d.	*0.82*	*0.85*	*1.04*	*1.23*	*1.32*	*0.58*	*0.57*
Er	n.d.	n.d.	*2.25*	*2.35*	*2.88*	*3.44*	*3.67*	*1.66*	*1.59*
Tm	n.d.	n.d.	n.d.	n.d.	n.d.	n.d.	n.d.	n.d.	n.d.
Yb	n.d.	n.d.	*2.19*	*2.27*	*2.67*	*3.29*	*3.42*	*1.63*	*1.54*
Lu	n.d.	n.d.	*0.32*	*0.35*	*0.41*	*0.51*	*0.52*	*0.23*	*0.23*

n.d. = not determined; b.d. = below detection limit; LOI = loss on ignition; Data analysed by ICPMS appear in italics.

Appendix B. Continued

Chapter no.	1	1	1	1	1	1	1	1	4
Sample no.	IN7	IN8	CH16	CH18	CH19	CH20	CH21	CH25	SM201
SiO_2 (wt%)	56.89	79.32	60.48	56	53.39	61.06	61.75	74.71	84.28
TiO_2	0.97	0.65	0.81	0.8	0.8	0.47	0.91	0.42	0.6
Al_2O_3	20.39	10.23	15.03	16.18	17.71	11.32	19.68	11.5	5.5
Fe_2O_3	8.12	3.5	6.05	6.65	5.56	4.1	6.42	3.74	4.46
MnO	0.04	0.05	0.07	0.16	0.07	0.09	0.03	0.07	0.07
MgO	2.31	0.25	2.38	2.47	1.43	0.43	0.5	0.41	1.08
CaO	0.09	0.18	4.79	6.33	6.89	9.43	0.4	1.61	0.18
Na_2O	1.23	1.81	1.56	1.41	0.9	0.62	0.59	1.55	1.06
K_2O	3.86	1.69	2.81	3.11	4.17	2.19	4.01	2.07	0.45
P_2O_5	0.1	0.12	0.13	0.13	0.14	0.1	0.16	0.09	0.03
LOI	5.63	2.19	5.84	6.83	8.74	10.26	5.60	4.41	1.65
Total	99.6	100.0	100.0	100.1	99.8	100.1	100.0	100.6	99.4
Sc (ppm)	22	8	18	20	22	18	20	9	7
V	185	62	113	133	134	103	148	53	64
Cr	128	63	88	94	102	68	135	76	46
Co	12	3	19	17	17	9	14	6	8
Ni	48	19	33	45	37	28	41	27	13
Cu	42	12	40	43	23	17	24	9	5
Zn	121	49	106	104	128	66	92	58	40
Ga	25	12	18	22	21	14	25	13	6
Rb	160	69	113	136	171	89	170	81	16
Sr	48	40	310	329	240	216	225	89	31
Y	32	22	19	30	23	27	30	18	17
Zr	152	208	175	178	160	111	211	157	221
Nb	14	12	15	15	14	9	15	10	9
Ba	742	315	603	650	652	467	756	435	144
Hf	*4.28*	*6.69*	*5.03*	n.d.	*5.05*	*3.26*	*6.23*	*5.71*	*5.79*
Ta	*1.14*	*0.85*	*1.20*	n.d.	*1.29*	*0.79*	*1.38*	*0.81*	*0.47*
Th	*12.07*	*9.07*	*12.62*	12.8	*15.62*	*9.35*	*14.80*	*10.41*	*6.17*
U	*2.48*	*2.15*	*2.03*	1.3	*2.86*	*1.96*	*2.85*	*2.93*	*0.96*
La	*38.39*	*25.36*	*32.57*	46	*41.61*	*26.79*	*41.17*	*23.65*	*18.02*
Ce	*81.47*	*54.51*	*68.42*	92	*82.01*	*46.61*	*86.77*	*51.12*	*39.95*
Pr	*9.20*	*6.05*	*7.54*	8	*9.33*	*5.89*	*9.61*	*5.57*	*4.47*
Nd	*36.38*	*24.71*	*29.15*	41	*35.90*	*23.47*	*37.47*	*22.81*	*17.33*
Sm	*7.28*	*4.92*	*5.42*	6	*6.76*	*4.90*	*7.33*	*4.49*	*3.35*
Eu	*1.51*	*0.95*	*1.07*	n.d.	*1.15*	*1.02*	*1.44*	*0.81*	*0.69*
Gd	*6.89*	*4.32*	*4.84*	n.d.	*5.96*	*4.82*	*6.52*	*3.97*	*2.86*
Tb	*1.03*	*0.71*	*0.69*	n.d.	*0.84*	*0.75*	*0.96*	*0.67*	*0.43*
Dy	*5.96*	*3.92*	*3.84*	n.d.	*4.66*	*4.40*	*5.51*	*3.51*	*2.59*
Ho	*1.21*	*0.80*	*0.75*	n.d.	*0.91*	*0.94*	*1.10*	*0.69*	*0.51*
Er	*3.45*	*2.25*	*2.18*	n.d.	*2.48*	*2.73*	*2.99*	*1.94*	*1.43*
Tm	n.d.	n.d.	n.d.	n.d.	n.d.	n.d.	n.d.	n.d.	*0.23*
Yb	*3.30*	*2.16*	*2.26*	n.d.	*2.31*	*2.75*	*2.50*	*1.94*	*1.69*
Lu	*0.52*	*0.33*	*0.35*	n.d.	*0.36*	*0.44*	*0.35*	*0.30*	*0.24*

n.d. = not determined; b.d. = below detection limit; LOI = loss on ignition; Data analysed by ICPMS appear in italics.

Appendix B. Continued

Chapter no.	4	4	4	4	4	4	4	4	4
Sample no.	SM202	SM204	SM205	SM208	SM209	SM250	SM251	SM252	SM151
SiO_2 (wt%)	63.42	94.73	96.54	85.18	92.55	59.74	86.22	72.91	67.41
TiO_2	1.08	0.06	0.27	0.47	0.78	1.23	0.26	0.64	0.59
Al_2O_3	15.91	1.68	1.56	5.82	1.89	17.86	4.78	10.73	15.57
Fe_2O_3	7.7	1.21	0.61	3.57	2.49	7.84	4.5	6.7	4.5
MnO	0.09	0.01	0.00	0.05	0.02	0.11	0.05	0.07	0.06
MgO	2.47	0.18	0.00	0.88	0.35	2.25	0.91	1.64	1.36
CaO	0.76	0.04	0.02	0.26	0.2	0.38	0.09	0.38	3.27
Na_2O	1.68	0.38	b.d.	1.34	0.26	0.77	0.26	1.28	3.24
K_2O	3.23	0.12	0.49	0.56	0.21	4.5	0.59	1.76	2.9
P_2O_5	0.09	0.01	0.00	0.05	0.11	0.07	0.06	0.06	0.17
LOI	3.83	0.73	0.46	1.47	0.71	3.62	1.82	3.47	0.79
Total	100.3	99.1	99.9	99.7	99.6	98.4	99.5	99.6	99.8
Sc (ppm)	21	1	b.d.	6	4	28	7	17	10
V	129	12	15	49	44	150	53	89	60
Cr	96	7	12	45	35	114	27	77	27
Co	14	2	b.d.	8	2	13	8	10	7
Ni	35	2	1	11	7	34	14	26	11
Cu	5	4	20	5	2	20	10	6	10
Zn	89	16	7	36	19	93	40	76	66
Ga	19	2	2	6	3	20	6	12	20
Rb	99	5	17	21	8	140	21	60	92
Sr	48	10	9	47	17	98	15	68	236
Y	31	10	9	19	38	24	26	35	32
Zr	237	42	136	167	177	348	90	156	177
Nb	25	2	5	7	9	20	5	12	13
Ba	703	67	133	223	70	765	160	418	850
Hf	n.d.	n.d.	n.d.	n.d.	n.d.	n.d.	*2.16*	n.d.	*5.23*
Ta	n.d.	n.d.	n.d.	n.d.	n.d.	n.d.	*0.23*	n.d.	*0.97*
Th	7.6	1	0.4	2.6	2.3	13.2	*3.18*	4.9	*15.13*
U	3.5	1.5	0.8	1.3	1.2	3.6	*0.60*	0.5	*2.47*
La	24	9	10	25	10	24	*13.69*	28	*44.12*
Ce	40	20	6	42	20	42	*14.71*	49	*87.19*
Pr	6	2	2	3	3	10	*4.00*	6	*10.22*
Nd	22	10	7	22	10	23	*16.05*	27	*40.52*
Sm	4	4	3	6	4	4	*3.95*	7	*7.96*
Eu	n.d.	n.d.	n.d.	n.d.	n.d.	n.d.	*0.86*	n.d.	*1.28*
Gd	n.d.	n.d.	n.d.	n.d.	n.d.	n.d.	*4.20*	n.d.	*7.11*
Tb	n.d.	n.d.	n.d.	n.d.	n.d.	n.d.	*0.59*	n.d.	*1.02*
Dy	n.d.	n.d.	n.d.	n.d.	n.d.	n.d.	*4.03*	n.d.	*6.26*
Ho	n.d.	n.d.	n.d.	n.d.	n.d.	n.d.	*0.78*	n.d.	*1.20*
Er	n.d.	n.d.	n.d.	n.d.	n.d.	n.d.	*2.19*	n.d.	*3.38*
Tm	n.d.	n.d.	n.d.	n.d.	n.d.	n.d.	*0.29*	n.d.	*0.50*
Yb	n.d.	n.d.	n.d.	n.d.	n.d.	n.d.	*1.77*	n.d.	*3.14*
Lu	n.d.	n.d.	n.d.	n.d.	n.d.	n.d.	*0.24*	n.d.	*0.47*

n.d. = not determined; b.d. = below detection limit; LOI = loss on ignition; Data analysed by ICPMS appear in italics.

Appendix B. Continued

Chapter no.	4	5	5	5	5	5	5	5	5
Sample no.	SM157	SM171	SM220	SM254	SM256	SM257	SM258	SM261	SM143
SiO_2 (wt%)	69.29	85.06	92.59	84.45	86.45	90.24	90.98	87.83	55.85
TiO_2	0.72	0.09	0.14	0.1	0.09	0.13	0.06	0.21	0.6
Al_2O_3	13.87	7.87	3.76	7.95	7.07	4.68	4.88	5.82	10.37
Fe_2O_3	4.94	0.87	0.8	0.88	0.9	0.58	0.24	1	3.15
MnO	0.07	0.01	0	0	0.01	0.01	0.01	0.01	0.06
MgO	2.12	0.28	0.09	0.22	0.27	0.34	0.13	0.21	1.36
CaO	1.36	0.1	0.01	0.19	0.19	0.12	0.16	0.26	12.51
Na_2O	2.39	0.57	b.d.	0.47	0.79	0.66	1.57	b.d.	0.89
K_2O	3.33	3.68	1.76	3.68	2.65	1.35	0.83	3.01	1.92
P_2O_5	0.21	0.07	0.01	0.14	0.13	0.09	0.1	0.2	0.1
LOI	1.41	1.05	0.67	0.98	0.96	0.81	0.54	0.86	12.88
Total	99.7	99.7	99.8	99.1	99.5	99.0	99.5	99.4	99.7
Sc (ppm)	11	1	1	2	3	1	b.d.	2	22
V	86	10	10	8	12	10	4	18	89
Cr	68	12	11	7	9	12	6	14	84
Co	14	1	b.d.	1	b.d.	b.d.	b.d.	1	11
Ni	28	1	4	4	5	4	1	7	30
Cu	21	4	3	4	3	1	2	5	24
Zn	80	9	8	12	13	20	9	11	63
Ga	17	6	4	8	7	4	5	6	12
Rb	119	100	59	109	99	44	36	97	74
Sr	170	23	8	25	36	20	15	14	53
Y	28	12	10	12	14	12	6	19	20
Zr	188	65	69	74	102	125	53	153	187
Nb	13	4	3	9	5	4	6	6	15
Ba	755	510	172	556	418	379	61	703	346
Hf	*5.42*	*1.94*	*1.49*	n.d.	n.d.	n.d.	n.d.	n.d.	n.d.
Ta	*1.15*	*0.82*	*0.31*	n.d.	n.d.	n.d.	n.d.	n.d.	n.d.
Th	*11.62*	*5.30*	*2.53*	3.6	4.7	6.8	0.8	4.3	7.9
U	*3.00*	*1.28*	*0.53*	2.9	2	1.1	1.5	0.3	1
La	*31.24*	*11.25*	*6.44*	9	13	13	4	9	35
Ce	*66.66*	*23.11*	*14.86*	15	24	30	2	24	63
Pr	*7.63*	*2.33*	*1.62*	3	2	b.d.	b.d.	2	6
Nd	*29.80*	*8.62*	*5.83*	10	11	14	5	12	32
Sm	*6.00*	*1.97*	*1.11*	3	3	3	2	4	5
Eu	*1.24*	*0.38*	*0.20*	n.d.	n.d.	n.d.	n.d.	n.d.	n.d.
Gd	*5.35*	*1.72*	*1.10*	n.d.	n.d.	n.d.	n.d.	n.d.	n.d.
Tb	*0.82*	*0.28*	*0.19*	n.d.	n.d.	n.d.	n.d.	n.d.	n.d.
Dy	*5.26*	*2.07*	*1.26*	n.d.	n.d.	n.d.	n.d.	n.d.	n.d.
Ho	*1.05*	*0.40*	*0.26*	n.d.	n.d.	n.d.	n.d.	n.d.	n.d.
Er	*2.89*	*1.21*	*0.82*	n.d.	n.d.	n.d.	n.d.	n.d.	n.d.
Tm	*0.43*	*0.17*	*0.12*	n.d.	n.d.	n.d.	n.d.	n.d.	n.d.
Yb	*2.80*	*1.20*	*0.88*	n.d.	n.d.	n.d.	n.d.	n.d.	n.d.
Lu	*0.46*	*0.17*	*0.14*	n.d.	n.d.	n.d.	n.d.	n.d.	n.d.

n.d. = not determined; b.d. = below detection limit; LOI = loss on ignition; Data analysed by ICPMS appear in italics.

Appendix B. Continued

Chapter no.	5	5	5	5	5	5	5	5	5
Sample no.	SM144	SM160	SM164	SM165	SM166	SM167	SM195	SM197	SM198
SiO_2 (wt%)	80.61	64.1	74.41	77.05	74.47	42.25	70.21	75.33	80.23
TiO_2	0.24	0.54	0.51	0.23	0.25	0.62	0.38	0.3	0.31
Al_2O_3	4.21	11.63	9.56	3.3	3.29	14.2	9.49	4.1	4.38
Fe_2O_3	1.27	3.56	3.36	1.21	1.64	4.34	3.03	1.07	1.18
MnO	0.05	0.08	0.03	0.02	0.03	0.1	0.05	0.02	0.02
MgO	0.49	1.92	1.18	0.36	0.34	1.68	0.65	0.31	0.13
CaO	5.76	6.54	2.75	8.57	10.13	15.8	6.03	9.19	6.41
Na_2O	1.08	1.13	1.38	0.42	0.3	0.82	0.77	0.39	0.32
K_2O	0.54	2.62	1.56	0.7	0.6	2.76	1.99	0.76	0.87
P_2O_5	0.04	0.07	0.09	0.04	0.04	0.09	0.06	0.05	0.05
LOI	5.37	7.87	5.00	7.62	9.09	16.98	7.15	8.50	6.16
Total	99.6	100.1	99.8	99.5	100.2	99.7	99.8	100.0	100.0
Sc (ppm)	6	13	7	8	9	28	12	9	7
V	18	91	59	27	29	130	61	25	32
Cr	41	81	65	31	43	97	53	48	42
Co	3	15	11	5	1	13	9	1	3
Ni	6	35	29	9	9	43	30	6	8
Cu	4	23	21	7	7	34	29	6	6
Zn	14	63	54	18	26	83	48	20	25
Ga	4	13	11	3	4	16	11	4	5
Rb	22	96	68	27	25	125	93	32	39
Sr	48	46	48	88	32	87	55	47	29
Y	9	23	25	10	12	29	20	13	14
Zr	143	171	175	147	183	114	163	192	172
Nb	8	12	16	7	7	14	10	8	9
Ba	106	411	334	228	142	480	247	195	149
Hf	*3.3*	n.d.	n.d.	n.d.	n.d.	n.d.	n.d.	n.d.	*4.00*
Ta	*0.45*	n.d.	n.d.	n.d.	n.d.	n.d.	n.d.	n.d.	*0.52*
Th	*4.95*	6.9	8.5	2.5	2.1	7.9	7.5	2.8	*4.65*
U	*0.64*	1.8	1.1	1.5	1.5	0.7	2.4	0.6	*1.36*
La	*12.54*	16	30	14	11	30	23	16	*15.74*
Ce	*23.62*	40	46	28	33	57	56	39	*33.09*
Pr	*2.56*	5	8	2	b.d.	7	6	5	*3.55*
Nd	*9.25*	18	26	14	13	30	23	19	*13.68*
Sm	*1.54*	4	6	1	2	6	4	5	*2.61*
Eu	*0.43*	n.d.	n.d.	n.d.	n.d.	n.d.	n.d.	n.d.	*0.47*
Gd	*1.40*	n.d.	n.d.	n.d.	n.d.	n.d.	n.d.	n.d.	*2.20*
Tb	*0.18*	n.d.	n.d.	n.d.	n.d.	n.d.	n.d.	n.d.	*0.33*
Dy	*1.16*	n.d.	n.d.	n.d.	n.d.	n.d.	n.d.	n.d.	*2.04*
Ho	*0.23*	n.d.	n.d.	n.d.	n.d.	n.d.	n.d.	n.d.	*0.42*
Er	*0.65*	n.d.	n.d.	n.d.	n.d.	n.d.	n.d.	n.d.	*1.18*
Tm	*0.10*	n.d.	n.d.	n.d.	n.d.	n.d.	n.d.	n.d.	*0.18*
Yb	*0.70*	n.d.	n.d.	n.d.	n.d.	n.d.	n.d.	n.d.	*1.14*
Lu	*0.11*	n.d.	n.d.	n.d.	n.d.	n.d.	n.d.	n.d.	*0.19*

n.d. = not determined; b.d. = below detection limit; LOI = loss on ignition; Data analysed by ICPMS appear in italics.

Appendix B. Continued

Chapter no.	5	5	5	5	5	5	5	5	5
Sample no.	SM199	SM200	SM213	SM214	SM227	SM231	SM241	SM242	SM134
SiO_2 (wt%)	74.01	69.64	53.66	74.22	70.89	78.12	87.65	54.42	48.26
TiO_2	0.23	0.31	0.29	0.29	0.25	0.24	0.35	0.44	0.41
Al_2O_3	3.78	4.38	4.02	4.86	3.61	3.16	3.04	5.95	6.7
Fe_2O_3	1.04	1.69	2.13	1.43	1.81	1.23	1.65	2.04	3.86
MnO	0.02	0.03	0.09	0.02	0.04	0.02	0.02	0.06	0.3
MgO	0.52	0.39	0.55	0.97	0.4	0.34	0.51	0.39	1.04
CaO	10.02	11.72	20.43	7.82	11.55	8.35	2.58	18.38	19.03
Na_2O	0.45	0.75	0.95	0.65	0.5	0.39	0.58	0.75	0.6
K_2O	0.81	0.81	0.48	1.13	0.49	0.56	0.25	1.06	1.72
P_2O_5	0.04	0.05	0.05	0.05	0.05	0.04	0.03	0.07	0.14
LOI	8.87	10.26	17.07	8.43	10.32	7.46	2.83	16.00	17.57
Total	99.8	100.0	99.7	99.9	99.9	99.9	99.5	99.6	99.6
Sc (ppm)	10	12	21	7	12	7	2	17	26
V	27	33	36	33	32	25	24	48	153
Cr	34	44	62	34	37	47	59	65	854
Co	3	2	3	1	4	3	4	6	29
Ni	8	11	10	9	11	10	12	16	266
Cu	7	7	7	6	8	7	7	10	9
Zn	18	26	25	18	21	19	31	37	38
Ga	5	5	4	5	4	4	3	7	8
Rb	32	32	22	43	23	25	13	46	57
Sr	365	130	369	239	68	54	34	77	51
Y	11	14	16	10	14	14	10	21	17
Zr	108	158	184	134	145	191	306	211	109
Nb	7	10	8	9	7	7	8	10	7
Ba	224	165	99	280	121	259	37	192	956
Hf	n.d.	*3.80*	n.d.	n.d.	n.d.	n.d.	n.d.	n.d.	n.d.
Ta	n.d.	*0.55*	n.d.	n.d.	n.d.	n.d.	n.d.	n.d.	n.d.
Th	2.9	*4.20*	2.8	3.6	3.3	3	4	5.6	2.6
U	1.8	*1.06*	2.1	2.4	1.6	1.3	1.5	2.3	1.7
La	15	*13.93*	20	16	14	13	14	27	16
Ce	26	*27.63*	37	26	23	26	31	49	25
Pr	b.d.	*3.10*	1	2	2	6	4	2	6
Nd	12	*11.84*	15	14	11	15	14	25	13
Sm	2	*2.20*	4	3	2	2	1	b.d.	b.d.
Eu	n.d.	*0.48*	n.d.	n.d.	n.d.	n.d.	n.d.	n.d.	n.d.
Gd	n.d.	*1.93*	n.d.	n.d.	n.d.	n.d.	n.d.	n.d.	n.d.
Tb	n.d.	*0.28*	n.d.	n.d.	n.d.	n.d.	n.d.	n.d.	n.d.
Dy	n.d.	*1.79*	n.d.	n.d.	n.d.	n.d.	n.d.	n.d.	n.d.
Ho	n.d.	*0.36*	n.d.	n.d.	n.d.	n.d.	n.d.	n.d.	n.d.
Er	n.d.	*1.06*	n.d.	n.d.	n.d.	n.d.	n.d.	n.d.	n.d.
Tm	n.d.	*0.15*	n.d.	n.d.	n.d.	n.d.	n.d.	n.d.	n.d.
Yb	n.d.	*1.06*	n.d.	n.d.	n.d.	n.d.	n.d.	n.d.	n.d.
Lu	n.d.	*0.17*	n.d.	n.d.	n.d.	n.d.	n.d.	n.d.	n.d.

n.d. = not determined; b.d. = below detection limit; LOI = loss on ignition; Data analysed by ICPMS appear in italics.

Appendix B. Continued

Chapter no.	5	5	5	5	5	5	5	5	5
Sample no.	SM178	SM179	SM181	SM182	SM183	SM184	SM185	SM246	SM247
SiO_2 (wt%)	66.63	65.09	68.16	75.24	33.07	69.39	71.47	67.63	68.61
TiO_2	0.57	0.49	0.58	0.25	0.27	0.58	0.45	0.77	1.02
Al_2O_3	8.96	8.49	10.04	5.79	6.1	8.61	6.96	13.38	11.95
Fe_2O_3	5.35	5.98	5.15	1.54	2.94	5.21	4.25	5.02	5.23
MnO	0.04	0.09	0.04	0.15	0.7	0.04	0.03	0.04	0.05
MgO	8.54	8	7.12	1.21	2.58	8.18	8.25	2.89	3.05
CaO	2	2.94	0.85	6.43	28.25	0.67	1.8	1.15	1.76
Na_2O	0.26	b.d.	0.91	1.8	0.64	0.23	0.08	1.71	0.1
K_2O	1.06	1.39	1.9	1.01	1	1.37	0.73	2.12	1.98
P_2O_5	0.11	0.09	0.12	0.05	0.08	0.11	0.09	0.13	0.16
LOI	6.58	7.30	4.78	6.16	24.43	5.31	5.65	4.81	5.85
Total	100.1	99.7	99.7	99.6	100.1	99.7	99.8	99.6	99.8
Sc (ppm)	11	14	10	9	30	11	11	16	14
V	87	93	81	36	83	82	63	94	97
Cr	1002	1332	728	69	330	1062	858	261	298
Co	18	31	24	5	17	22	23	9	8
Ni	493	472	365	27	155	460	398	113	105
Cu	7	9	8	6	8	5	4	17	13
Zn	54	69	55	20	36	53	47	72	71
Ga	11	11	11	5	7	10	9	15	14
Rb	41	71	89	32	38	60	30	82	76
Sr	21	79	22	99	192	18	16	36	34
Y	23	16	23	16	22	21	17	12	15
Zr	149	125	152	90	68	150	117	190	267
Nb	9	8	11	5	6	10	9	13	16
Ba	226	178	296	477	1400	198	149	418	380
Hf	n.d.	n.d.	*4.99*	n.d.	*1.64*	*4.76*	*3.02*	n.d.	n.d.
Ta	n.d.	n.d.	*0.89*	n.d.	*0.35*	*0.81*	*0.72*	n.d.	n.d.
Th	6.2	4.1	*7.50*	3.1	*3.26*	*7.32*	*5.35*	7.1	7.7
U	3.6	1	*1.36*	1.6	*0.71*	*1.83*	*0.91*	3.1	6.2
La	18	11	*21.31*	13	*17.41*	*22.06*	*14.75*	22	16
Ce	34	24	*46.31*	23	*29.52*	*51.70*	*31.33*	42	45
Pr	2	b.d.	*5.14*	5	*3.43*	*5.54*	*3.55*	6	7
Nd	15	7	*20.10*	15	*13.63*	*21.02*	*14.02*	18	19
Sm	5	2	*4.10*	6	*2.78*	*4.68*	*3.04*	3	4
Eu	n.d.	n.d.	*0.68*	n.d.	*0.74*	*0.73*	*0.59*	n.d.	n.d.
Gd	n.d.	n.d.	*3.81*	n.d.	*3.05*	*5.09*	*3.17*	n.d.	n.d.
Tb	n.d.	n.d.	*0.56*	n.d.	*0.48*	*0.81*	*0.55*	n.d.	n.d.
Dy	n.d.	n.d.	*3.69*	n.d.	*3.01*	*5.08*	*4.13*	n.d.	n.d.
Ho	n.d.	n.d.	*0.73*	n.d.	*0.63*	*0.97*	*0.82*	n.d.	n.d.
Er	n.d.	n.d.	*2.17*	n.d.	*1.86*	*2.76*	*2.45*	n.d.	n.d.
Tm	n.d.	n.d.	*0.34*	n.d.	*0.25*	*0.41*	*0.34*	n.d.	n.d.
Yb	n.d.	n.d.	*2.22*	n.d.	*1.62*	*2.61*	*2.37*	n.d.	n.d.
Lu	n.d.	n.d.	*0.34*	n.d.	*0.23*	*0.40*	*0.36*	n.d.	n.d.

n.d. = not determined; b.d. = below detection limit; LOI = loss on ignition; Data analysed by ICPMS appear in italics.

Appendix B. Continued

Chapter no.	5	5	6	6	6	6	6	6	6
Sample no.	SM177	SM228a	R18b	R27	R35	R38	R39	R40	R41
SiO_2 (wt%)	47.95	61.84	79.42	66.65	45.38	59	59.21	59.62	24.16
TiO_2	0.26	0.63	0.43	0.51	0.63	0.89	0.91	0.83	0.38
Al_2O_3	7.89	15.21	10.23	13.49	10.87	18.6	18.59	15.27	6.63
Fe_2O_3	1.21	3.46	1.81	2.91	4.82	7.34	7.36	6.58	3.19
MnO	0.08	0.02	0.02	0.05	0.15	0.05	0.03	0.16	0.22
MgO	0.58	1.68	0.6	1.45	2.72	3.34	3.11	2.76	1.5
CaO	20.57	3.64	0.18	3.85	17.36	0.31	0.31	4.02	33.93
Na_2O	2.23	1.2	0.87	2.8	0.26	1.29	0.82	1.33	0.73
K_2O	1.43	4.45	2.6	2.03	1.81	3.62	3.99	2.66	1.12
P_2O_5	0.03	0.07	0.12	0.16	0.1	0.13	0.14	0.15	0.08
LOI	17.65	6.94	2.18	5.18	16.62	6.12	5.82	7.21	29.08
Total	99.9	99.2	98.5	99.1	100.7	100.7	100.3	100.6	101.0
Sc (ppm)	19	15	5	13	29	17	20	20	37
V	25	68	43	68	134	170	173	144	96
Cr	19	57	30	44	197	133	137	128	78
Co	b.d.	6	6	9	13	16	23	20	11
Ni	3	26	11	18	67	73	83	71	31
Cu	12	34	5	8	23	61	64	32	27
Zn	25	84	30	54	68	111	112	99	50
Ga	8	18	10	15	13	23	24	18	9
Rb	51	160	90	89	76	159	174	114	50
Sr	875	125	33	49	396	42	35	46	684
Y	21	25	12	16	18	29	32	29	17
Zr	170	234	145	184	132	168	184	198	80
Nb	8	16	11	11	10	19	18	15	7
Ba	204	548	521	332	301	547	596	469	260
Hf	n.d.	n.d.	n.d.	*5.37*	n.d.	n.d.	n.d.	n.d.	n.d.
Ta	n.d.	n.d.	n.d.	*0.88*	n.d.	n.d.	n.d.	n.d.	n.d.
Th	5.9	12	9.5	*11.47*	6.1	13.6	14.8	10.6	3.9
U	2.5	3.5	0.7	*1.06*	1.6	2.3	2.6	2.7	0.9
La	20	31	24	*27.94*	26	32	33	27	25
Ce	38	74	44	*59.00*	50	56	66	59	47
Pr	4	7	2	*6.75*	9	8	13	4	12
Nd	19	31	20	*25.44*	21	28	31	24	22
Sm	6	4	4	*4.87*	8	7	4	3	7
Eu	n.d.	n.d.	n.d.	*0.83*	n.d.	n.d.	n.d.	n.d.	n.d.
Gd	n.d.	n.d.	n.d.	*3.75*	n.d.	n.d.	n.d.	n.d.	n.d.
Tb	n.d.	n.d.	n.d.	*0.52*	n.d.	n.d.	n.d.	n.d.	n.d.
Dy	n.d.	n.d.	n.d.	*3.01*	n.d.	n.d.	n.d.	n.d.	n.d.
Ho	n.d.	n.d.	n.d.	*0.58*	n.d.	n.d.	n.d.	n.d.	n.d.
Er	n.d.	n.d.	n.d.	*1.62*	n.d.	n.d.	n.d.	n.d.	n.d.
Tm	n.d.	n.d.	n.d.	*0.22*	n.d.	n.d.	n.d.	n.d.	n.d.
Yb	n.d.	n.d.	n.d.	*1.66*	n.d.	n.d.	n.d.	n.d.	n.d.
Lu	n.d.	n.d.	n.d.	*0.27*	n.d.	n.d.	n.d.	n.d.	n.d.

n.d. = not determined; b.d. = below detection limit; LOI = loss on ignition; Data analysed by ICPMS appear in italics.

Appendix B. Continued

Chapter no.	6	6	6	6	6	6	6	6	6
Sample no.	R42	R43	R44	R45	R6	R7	R8	R9	R11
SiO_2 (wt%)	58.93	59.6	82.9	44.35	62.4	64.18	56	64.11	60.88
TiO_2	0.85	0.67	0.32	0.5	1.13	0.79	0.77	0.76	0.7
Al_2O_3	13.62	12.58	9.17	9.5	13.3	13.3	15.57	13.05	12.4
Fe_2O_3	6.9	4.62	1.08	3.71	4.97	4.18	5.66	4.65	4.47
MnO	0.11	0.25	0.02	0.08	0.08	0.06	0.05	0.06	0.07
MgO	3.56	2.33	0.46	2.44	2.22	1.99	2.54	1.92	2.06
CaO	5.46	7.57	1.22	19.5	4.83	3.75	5.53	4.08	6.42
Na_2O	2.41	3.56	3.29	1.22	3.12	3.5	0.76	3.27	3.03
K_2O	1.33	1	1.08	1.41	1.62	1.75	3.34	1.77	1.67
P_2O_5	0.24	0.15	0.06	0.08	0.24	0.2	0.1	0.17	0.17
LOI	7.59	8.19	1.78	17.61	5.36	4.77	9.26	5.33	6.76
Total	101.0	100.5	101.4	100.4	99.3	98.5	99.6	99.2	98.6
Sc (ppm)	17	16	4	31	18	14	19	14	16
V	97	90	26	109	113	98	153	98	91
Cr	72	70	15	180	72	59	134	57	59
Co	10	9	2	11	13	9	14	12	12
Ni	28	21	6	55	19	20	56	24	24
Cu	27	13	3	17	7	7	62	9	9
Zn	91	59	23	49	57	49	98	51	54
Ga	16	14	8	11	15	16	21	14	14
Rb	57	42	41	62	52	56	146	59	54
Sr	156	251	94	494	409	371	107	375	447
Y	19	16	13	16	25	23	23	21	22
Zr	254	139	89	112	316	193	177	208	173
Nb	11	10	10	8	14	12	16	12	10
Ba	233	210	240	268	562	612	516	607	718
Hf	n.d.	*4.72*	n.d.	n.d.	n.d.	n.d.	n.d.	*9.59*	n.d.
Ta	n.d.	*0.67*	n.d.	n.d.	n.d.	n.d.	n.d.	*0.64*	n.d.
Th	10.4	*6.81*	12	6.2	8.5	6.8	12.1	*9.69*	7
U	1.4	*0.93*	1.2	1.7	2.7	1.2	4.1	*1.48*	1.6
La	29	*23.94*	33	16	49	45	25	*41.75*	39
Ce	64	*47.13*	61	41	79	54	46	*76.86*	70
Pr	5	*5.69*	5	6	12	12	7	*9.18*	5
Nd	31	*22.56*	26	17	40	37	28	*36.26*	37
Sm	5	*4.33*	3	5	5	9	5	*6.42*	7
Eu	n.d.	*0.88*	n.d.	n.d.	n.d.	n.d.	n.d.	*1.56*	n.d.
Gd	n.d.	*3.59*	n.d.	n.d.	n.d.	n.d.	n.d.	*5.00*	n.d.
Tb	n.d.	*0.50*	n.d.	n.d.	n.d.	n.d.	n.d.	*0.65*	n.d.
Dy	n.d.	*3.22*	n.d.	n.d.	n.d.	n.d.	n.d.	*4.06*	n.d.
Ho	n.d.	*0.63*	n.d.	n.d.	n.d.	n.d.	n.d.	*0.75*	n.d.
Er	n.d.	*1.78*	n.d.	n.d.	n.d.	n.d.	n.d.	*2.12*	n.d.
Tm	n.d.	*0.27*	n.d.	n.d.	n.d.	n.d.	n.d.	*0.29*	n.d.
Yb	n.d.	*1.79*	n.d.	n.d.	n.d.	n.d.	n.d.	*1.98*	n.d.
Lu	n.d.	*0.26*	n.d.	n.d.	n.d.	n.d.	n.d.	*0.30*	n.d.

n.d. = not determined; b.d. = below detection limit; LOI = loss on ignition; Data analysed by ICPMS appear in italics.

Appendix B. Continued

Chapter no.	6	6	6	6
Sample no.	R14	R15	R31	R32
SiO_2 (wt%)	64.87	65.12	56.8	68.91
TiO_2	0.7	0.6	0.91	0.58
Al_2O_3	14.03	12.71	18.33	14.88
Fe_2O_3	5.14	3.75	7.11	4.37
MnO	0.05	0.05	0.1	0.06
MgO	2.35	1.66	3.36	1.77
CaO	2.31	4.69	1.91	0.72
Na_2O	3.6	3.49	1.51	4.2
K_2O	1.95	1.85	3.66	1.75
P_2O_5	0.17	0.16	0.16	0.15
LOI	4.27	5.15	6.46	2.72
Total	99.4	99.2	100.3	100.1
Sc (ppm)	15	11	21	9
V	104	78	166	76
Cr	65	51	118	36
Co	13	9	12	11
Ni	27	20	52	22
Cu	80	13	68	10
Zn	44	32	118	64
Ga	16	14	25	17
Rb	62	54	161	62
Sr	320	344	130	397
Y	15	14	29	20
Zr	164	183	208	133
Nb	10	10	17	9
Ba	650	653	702	692
Hf	n.d.	*4.69*	n.d.	n.d.
Ta	n.d.	*0.45*	n.d.	n.d.
Th	7	*7.51*	11.1	4.9
U	2.3	*1.53*	3	1.3
La	45	*36.03*	50	32
Ce	88	*67.26*	72	52
Pr	9	*7.98*	11	5
Nd	39	*31.58*	34	26
Sm	6	*5.20*	8	6
Eu	n.d.	*1.25*	n.d.	n.d.
Gd	n.d.	*4.07*	n.d.	n.d.
Tb	n.d.	*0.52*	n.d.	n.d.
Dy	n.d.	*2.82*	n.d.	n.d.
Ho	n.d.	*0.49*	n.d.	n.d.
Er	n.d.	*1.29*	n.d.	n.d.
Tm	n.d.	*0.17*	n.d.	n.d.
Yb	n.d.	*1.08*	n.d.	n.d.
Lu	n.d.	*0.16*	n.d.	n.d.

n.d. = not determined; b.d. = below detection limit; LOI = loss on ignition; Data analysed by ICPMS appear in italics.

Appendix C-1. Mineral chemical data – Chrome spinel

No.	Sample	TiO_2	Al_2O_3	Cr_2O_3	Fe_2O_3	MnO	MgO	NiO	V_2O_3	ZnO	CoO	Total
1	SM181	0.12	18.09	52.03	17.39	0.20	12.44	0.04	0.24	0.17	0.07	100.79
2	SM181	0.05	21.11	48.21	17.54	0.15	13.70	0.11	0.29	0.03	0.08	101.26
3	SM181	0.07	11.88	58.45	20.93	0.23	9.14	0.01	0.24	0.21	0.07	101.23
4	SM181	0.04	30.12	40.16	13.86	0.10	15.80	0.13	0.17	0.09	0.05	100.52
5	SM181	0.03	33.39	35.38	16.07	0.15	15.29	0.13	0.25	0.15	0.09	100.93
6	SM181	0.13	21.12	47.89	19.33	0.29	10.06	0.07	0.33	0.34	0.07	99.64
7	SM181	0.10	22.05	47.98	17.72	0.21	12.07	0.08	0.27	0.15	0.05	100.68
8	SM181	0.13	14.56	50.38	25.11	0.25	9.82	0.06	0.19	0.16	0.09	100.75
9	SM181	0.12	12.75	56.64	20.05	0.23	10.15	0.04	0.22	0.29	0.11	100.59
10	SM181	0.16	21.62	46.18	20.92	0.23	11.43	0.10	0.28	0.23	0.06	101.21
11	SM181	0.13	25.43	42.90	19.26	0.19	12.51	0.08	0.27	0.23	0.07	101.06
12	SM181	0.06	13.68	55.73	20.57	0.22	9.89	0.04	0.29	0.17	0.08	100.73
13	SM181	0.03	25.87	43.90	17.71	0.15	12.57	0.08	0.24	0.27	0.10	100.92
14	SM181	0.20	19.48	49.92	17.70	0.17	12.75	0.09	0.25	0.08	0.08	100.71
15	SM181	0.10	6.73	63.13	21.26	0.28	8.39	0.01	0.20	0.22	0.06	100.38
16	SM181	0.08	10.97	57.83	20.94	0.30	9.51	0.03	0.20	0.23	0.06	100.14
17	SM181	0.03	16.01	51.78	21.59	0.27	10.21	0.07	0.19	0.28	0.12	100.54
18	SM181	0.06	13.88	56.35	18.72	0.23	9.63	0.04	0.36	0.20	0.08	99.54
19	SM181	0.03	12.66	56.95	19.84	0.23	9.42	0.05	0.31	0.19	0.07	99.75
20	SM181	0.16	25.63	44.35	16.52	0.08	13.91	0.06	0.20	0.14	0.05	101.10
21	SM181	0.23	24.71	46.47	15.59	0.16	12.42	0.11	0.23	0.13	0.09	100.12
22	SM181	0.09	25.85	43.37	16.74	0.16	13.44	0.10	0.19	0.15	0.04	100.12
23	SM181	0.07	14.16	55.42	20.69	0.20	9.86	b.d.	0.28	0.20	0.10	100.97
24	SM181	0.05	22.90	46.07	16.94	0.18	14.38	0.08	0.28	0.13	0.05	101.06
25	SM181	0.08	24.76	44.23	18.07	0.15	12.36	0.11	0.26	0.20	0.09	100.31
26	SM181	0.06	29.36	40.64	14.85	0.16	14.79	0.15	0.24	0.16	0.07	100.47
27	SM181	0.09	22.46	47.70	16.89	0.15	13.22	0.07	0.25	0.12	0.06	101.02
28	SM181	0.18	6.48	60.09	24.27	0.28	8.60	0.02	0.15	0.18	0.08	100.34
29	SM181	0.14	17.60	49.82	22.77	0.24	9.57	0.07	0.35	0.25	0.09	100.89
30	SM181	0.04	7.52	62.87	19.53	0.27	9.87	0.05	0.27	0.14	0.10	100.67
31	SM181	0.21	20.37	50.58	15.71	0.18	13.51	0.06	0.16	0.17	0.06	101.00
32	SM181	0.20	18.02	51.59	18.63	0.17	10.48	0.04	0.28	0.18	0.06	99.66
33	SM181	0.09	27.37	41.76	16.67	0.14	14.28	0.12	0.19	0.11	0.05	100.77
34	SM181	0.14	26.30	43.48	15.91	0.14	14.33	0.09	0.21	0.19	0.06	100.83
35	SM181	0.14	18.45	49.43	20.92	0.20	9.73	0.11	0.27	0.13	0.08	99.46
36	SM181	0.04	28.21	40.31	18.33	0.19	13.57	0.10	0.22	0.20	0.11	101.27
37	SM181	0.05	26.21	42.94	18.44	0.18	12.43	0.15	0.27	0.20	0.03	100.89
38	SM181	0.10	22.64	47.45	16.88	0.21	13.50	0.08	0.18	0.17	0.07	101.28
39	SM181	0.10	11.14	61.26	16.40	0.24	10.29	0.01	0.18	0.18	0.07	99.87
40	SM181	0.04	21.93	47.68	18.95	0.26	11.04	0.06	0.27	0.17	0.09	100.49
41	SM181	0.08	22.34	46.70	19.94	0.20	10.99	0.08	0.25	0.18	0.07	100.83
42	SM181	0.13	26.49	43.90	16.02	0.13	13.51	0.12	0.29	0.13	0.03	100.74
43	SM181	0.06	5.27	66.56	18.75	0.25	7.92	b.d.	0.28	0.25	0.09	99.43
44	SM181	0.26	11.26	55.44	23.38	0.24	8.48	0.07	0.16	0.13	0.12	99.54
45	SM181	0.06	14.04	56.38	19.71	0.21	9.74	0.01	0.29	0.17	0.13	100.74
46	SM181	0.12	26.24	43.73	15.69	0.11	14.89	0.07	0.17	0.15	0.05	101.23
47	SM181	0.17	19.06	48.82	21.26	0.20	10.31	0.09	0.08	0.19	0.07	100.24
48	SM181	0.18	21.11	48.87	19.05	0.22	10.30	0.09	0.26	0.27	0.08	100.43
49	SM181	0.20	9.54	60.17	20.96	0.36	7.75	0.07	0.32	0.18	0.10	99.64
50	SM181	0.14	21.99	46.10	20.96	0.31	10.51	0.05	0.30	0.31	0.07	100.74
51	SM181	0.22	22.30	46.06	19.48	0.15	12.57	0.07	0.21	0.20	0.08	101.34

Data in wt.%; b.d. = below detection limit; Total iron is expressed as Fe_2O_3

Appendix C-1. Continued

No.	Sample	TiO_2	Al_2O_3	Cr_2O_3	Fe_2O_3	MnO	MgO	NiO	V_2O_3	ZnO	CoO	Total
52	SM181	0.11	22.80	46.70	19.66	0.19	10.88	0.02	0.21	0.25	0.10	100.92
54	SM181	0.44	26.97	42.36	15.74	0.12	13.89	0.11	0.18	0.14	0.03	99.97
55	SM181	0.09	28.96	40.46	16.21	0.18	14.69	0.11	0.16	0.06	0.05	100.96
56	SM181	0.06	16.51	53.25	19.61	0.25	10.61	0.06	0.21	0.13	0.07	100.76
57	SM181	0.05	23.73	46.72	15.46	0.15	14.34	0.07	0.28	0.12	0.06	100.97
58	SM181	0.19	12.08	55.06	23.90	0.30	7.11	0.07	0.15	0.21	0.09	99.15
59	SM181	0.09	19.25	51.67	15.55	0.16	13.52	0.08	0.28	0.10	0.09	100.78
61	SM181	0.07	22.52	48.73	14.08	0.10	14.65	0.15	0.26	0.11	0.05	100.72
62	SM181	0.81	20.21	43.86	25.66	0.20	7.59	0.15	0.31	0.18	0.10	99.06
63	SM181	0.08	23.68	46.83	17.19	0.15	12.11	0.08	0.28	0.20	0.07	100.67
64	SM181	0.14	23.68	46.32	17.47	0.17	12.33	0.07	0.27	0.23	0.09	100.76
65	SM181	0.18	8.19	64.12	16.67	0.24	9.84	0.03	0.12	0.18	0.08	99.65
66	SM181	0.06	20.27	48.81	19.03	0.17	11.60	0.04	0.32	0.14	0.08	100.51
67	SM181	0.04	25.76	43.64	17.87	0.15	13.28	0.03	0.26	0.18	0.07	101.26
69	SM181	0.09	22.74	44.98	19.84	0.16	11.91	0.09	0.33	0.17	0.04	100.34
70	SM181	0.14	26.06	43.84	17.40	0.22	12.94	0.05	0.24	0.19	0.07	101.15
71	SM181	0.27	12.38	55.48	22.29	0.27	8.06	0.05	0.11	0.14	0.05	99.10
73	SM181	0.06	31.37	37.16	17.60	0.18	14.44	0.08	0.20	0.22	0.07	101.38
75	SM183	0.10	7.58	62.44	21.63	0.31	8.24	0.03	0.30	0.16	0.05	100.84
77	SM183	0.05	23.70	45.89	17.59	0.18	13.10	0.11	0.26	0.19	0.06	101.13
78	SM183	0.13	22.14	42.61	23.71	0.28	11.19	0.14	0.21	0.22	0.08	100.71
79	SM183	0.04	19.59	50.54	18.65	0.23	11.68	0.08	0.29	0.24	0.06	101.41
80	SM183	0.06	24.89	40.89	26.36	0.32	7.59	0.09	0.15	0.53	0.10	100.98
81	SM183	0.04	28.66	40.82	17.02	0.24	13.59	0.10	0.28	0.29	0.06	101.10
82	SM183	0.08	30.63	39.25	15.22	0.10	15.04	0.08	0.18	0.17	0.08	100.85
83	SM183	0.44	22.45	42.62	23.27	0.25	10.45	0.10	0.28	0.24	0.07	100.17
84	SM183	0.03	29.65	38.02	18.38	0.21	13.39	0.09	0.23	0.24	0.11	100.35
85	SM183	0.11	11.39	59.16	18.06	0.23	11.10	0.03	0.26	0.20	0.10	100.64
86	SM183	0.05	26.11	42.32	19.00	0.15	12.66	0.09	0.26	0.29	0.07	100.99
87	SM183	0.09	32.40	36.63	17.57	0.14	13.89	0.12	0.19	0.26	0.08	101.36
88	SM183	0.07	20.38	49.16	18.51	0.22	11.57	0.08	0.34	0.21	0.09	100.63
89	SM183	0.05	25.96	44.42	16.80	0.13	13.29	0.08	0.30	0.18	0.06	101.27
91	SM183	0.03	29.64	40.38	16.45	0.16	13.71	0.10	0.23	0.16	0.07	100.93
92	SM183	0.11	28.05	38.98	18.57	0.15	13.66	0.13	0.17	0.10	0.05	99.97
93	SM183	0.03	33.76	34.75	17.05	0.20	14.55	0.12	0.22	0.26	0.09	101.02
94	SM183	0.07	21.73	48.39	17.44	0.18	12.05	0.10	0.29	0.10	0.05	100.40
96	SM183	0.08	20.54	46.93	21.91	0.22	10.80	0.08	0.31	0.24	0.07	101.18
97	SM183	0.06	14.99	54.66	19.33	0.22	9.91	0.03	0.33	0.16	0.09	99.78
98	SM183	0.10	32.96	35.97	15.48	0.20	15.99	0.14	0.16	0.15	0.04	101.18
99	SM183	0.08	12.53	58.56	19.51	0.32	9.10	0.05	0.23	0.23	0.11	100.71
100	SM183	0.04	24.66	45.15	17.56	0.19	13.18	0.09	0.21	0.18	0.07	101.33
101	SM183	0.07	22.78	45.75	19.15	0.21	12.13	0.05	0.27	0.18	0.05	100.65
102	SM183	0.07	21.40	47.67	18.75	0.20	12.39	0.10	0.25	0.12	0.06	101.02
103	SM183	0.06	26.74	43.30	16.72	0.24	12.16	0.07	0.28	0.69	0.07	100.33
104	SM183	0.53	20.88	41.72	26.76	0.27	8.83	0.13	0.35	0.12	0.05	99.64
105	SM183	0.09	21.03	48.87	18.79	0.20	10.40	0.01	0.27	0.24	0.07	99.96
106	SM183	0.45	12.44	57.37	17.58	0.20	12.32	0.08	0.22	0.09	0.04	100.79
107	SM183	0.34	24.96	44.20	16.45	0.13	14.10	0.15	0.31	0.10	0.04	100.77
108	SM183	0.07	28.43	40.25	17.94	0.19	13.60	0.09	0.14	0.19	0.06	100.96
109	SM183	0.10	14.35	54.64	21.27	0.27	9.25	0.06	0.24	0.17	0.09	100.44
110	SM183	0.16	18.89	46.77	23.18	0.25	11.09	0.11	0.18	0.18	0.07	100.89

Data in wt.%; b.d. = below detection limit; Total iron is expressed as Fe_2O_3

Appendix C-1. Continued

No.	Sample	TiO_2	Al_2O_3	Cr_2O_3	Fe_2O_3	MnO	MgO	NiO	V_2O_3	ZnO	CoO	Total
111	SM183	0.24	26.82	42.66	16.39	0.11	13.81	0.10	0.18	0.17	0.09	100.57
112	SM183	0.05	23.99	45.24	18.41	0.22	12.82	0.09	0.22	0.15	0.07	101.25
113	SM183	0.07	23.40	45.34	18.89	0.20	12.41	0.09	0.22	0.16	0.07	100.85
114	SM183	0.12	34.79	33.01	17.46	0.19	15.27	0.12	0.13	0.13	0.07	101.28
118	SM183	0.06	26.99	41.90	18.44	0.14	13.09	0.09	0.22	0.19	0.10	101.22
119	SM183	0.08	27.91	39.99	18.65	0.18	13.35	0.09	0.14	0.23	0.11	100.73
120	SM183	0.55	22.47	41.94	23.12	0.16	11.87	0.14	0.25	0.16	0.09	100.75
122	SM183	0.05	29.84	39.52	17.31	0.19	13.64	0.06	0.25	0.20	0.06	101.13
123	SM183	0.09	20.31	50.63	16.81	0.20	11.71	0.08	0.25	0.11	0.09	100.28
124	SM183	0.05	34.41	34.44	15.87	0.11	15.66	0.13	0.19	0.23	0.03	101.12
125	SM183	0.15	21.12	50.34	15.18	0.14	13.26	0.11	0.19	0.14	0.06	100.69
126	SM183	0.24	17.54	51.32	19.42	0.19	11.91	0.12	0.13	0.08	0.06	101.00
128	SM183	0.24	17.72	51.45	19.72	0.30	9.91	0.10	0.16	0.18	0.06	99.84
129	SM183	0.07	25.16	43.94	19.31	0.26	11.79	0.11	0.26	0.30	0.07	101.28
130	SM183	0.04	31.91	38.46	14.60	0.13	15.67	0.07	0.16	0.13	0.06	101.24
131	SM183	0.05	26.01	43.40	18.31	0.20	12.46	0.09	0.20	0.21	0.04	100.97
132	SM183	1.03	19.54	42.89	27.11	0.32	7.37	0.14	0.39	0.19	0.05	99.02
133	SM183	0.05	26.54	43.10	17.14	0.16	12.69	0.09	0.23	0.22	0.06	100.27
134	SM183	0.68	18.38	48.02	21.07	0.20	11.16	0.07	0.23	0.12	0.05	99.98
135	SM183	0.04	31.01	38.97	16.42	0.17	13.15	0.08	0.25	0.22	0.10	100.41
136	SM183	0.07	26.08	42.63	19.05	0.16	12.71	0.07	0.15	0.20	0.08	101.20
137	SM183	0.09	25.79	44.16	17.63	0.16	12.66	0.10	0.23	0.16	0.04	101.04
138	SM183	0.03	22.12	47.87	16.49	0.19	13.53	0.11	0.26	0.12	0.05	100.77
139	SM183	0.22	18.58	50.97	19.61	0.27	9.94	0.07	0.21	0.26	0.09	100.22
140	SM183	0.09	26.33	43.68	17.98	0.27	12.19	0.05	0.21	0.18	0.06	101.04
142	SM183	0.10	34.49	35.04	14.53	0.10	16.23	0.16	0.17	0.18	0.06	101.05
143	SM183	0.11	16.26	51.00	21.08	0.22	10.82	0.06	0.20	0.17	0.07	100.00
144	SM184	0.09	28.79	41.84	16.68	0.41	10.50	0.09	0.23	0.20	0.08	98.91
145	SM184	0.37	16.80	50.01	20.67	0.19	10.44	0.10	0.17	0.13	0.07	98.94
146	SM184	0.07	21.81	47.92	18.22	0.22	11.38	0.04	0.32	0.23	0.06	100.26
147	SM184	0.18	20.88	47.72	19.47	0.17	11.90	0.08	0.17	0.15	0.06	100.77
148	SM184	0.21	13.77	56.36	19.74	0.28	8.78	0.05	0.34	0.20	0.09	99.82
149	SM184	0.08	19.87	50.72	17.54	0.12	11.02	0.07	0.32	0.14	0.08	99.96
150	SM184	0.24	22.47	49.10	15.03	0.08	13.57	0.09	0.28	0.13	0.03	101.02
152	SM184	0.13	21.83	47.06	18.30	0.21	11.48	0.04	0.17	0.25	0.09	99.55
153	SM184	0.09	29.08	40.67	16.23	0.20	14.28	0.09	0.24	0.27	0.07	101.22
154	SM184	0.06	21.80	48.82	16.40	0.21	13.50	0.06	0.21	0.15	0.02	101.22
155	SM184	0.17	17.50	54.28	17.06	0.28	11.28	0.04	0.18	0.19	0.06	101.03
156	SM184	0.22	14.03	56.72	18.91	0.24	9.53	0.02	0.28	0.26	0.10	100.31
158	SM184	0.10	8.17	64.36	17.66	0.33	8.33	0.03	0.28	0.35	0.09	99.69
159	SM184	0.12	9.78	61.08	19.40	0.37	7.38	b.d.	0.26	0.27	0.12	98.78
160	SM184	0.16	23.71	46.54	17.24	0.19	12.80	0.09	0.25	0.20	0.08	101.25
161	SM184	0.15	26.59	41.06	20.87	0.18	11.10	0.14	0.21	0.22	0.08	100.60
162	SM184	0.11	15.42	54.06	19.13	0.22	11.86	0.06	0.21	0.20	0.07	101.33
163	SM184	0.07	25.84	45.12	15.98	0.21	13.19	0.08	0.22	0.15	0.10	100.95
165	SM184	0.07	12.34	59.11	18.92	0.29	9.18	0.02	0.24	0.22	0.12	100.51
166	SM184	0.20	13.58	57.99	14.80	0.10	13.16	0.10	0.09	0.08	0.07	100.17
167	SM184	0.07	23.77	45.91	17.94	0.16	12.70	0.07	0.32	0.22	0.07	101.22
168	SM184	0.46	32.03	37.28	15.42	0.15	14.79	0.13	0.20	0.12	0.07	100.65
169	SM184	0.05	22.53	47.83	17.49	0.18	12.53	0.10	0.19	0.18	0.05	101.13
170	SM184	0.19	20.96	49.51	17.97	0.25	11.09	0.03	0.34	0.21	0.05	100.60

Data in wt.%; b.d. = below detection limit; Total iron is expressed as Fe_2O_3

Appendix C-1. Continued

No.	Sample	TiO_2	Al_2O_3	Cr_2O_3	Fe_2O_3	MnO	MgO	NiO	V_2O_3	ZnO	CoO	Total
171	SM184	0.18	22.79	47.36	16.13	0.17	13.48	0.08	0.20	0.15	0.07	100.61
172	SM184	0.08	26.80	42.14	17.47	0.16	13.50	0.12	0.19	0.17	0.08	100.72
173	SM184	0.17	19.19	51.00	17.27	0.20	11.92	0.02	0.23	0.19	0.05	100.24
174	SM184	0.03	18.23	49.61	22.00	0.21	10.12	0.09	0.12	0.23	0.04	100.67
175	SM184	0.08	31.22	38.10	15.39	0.15	15.47	0.08	0.16	0.17	0.09	100.90
177	SM184	0.09	23.17	48.22	16.26	0.24	12.57	0.08	0.18	0.18	0.07	101.05
179	SM184	0.38	23.42	47.22	16.47	0.12	12.88	0.07	0.18	0.18	0.06	100.97
180	SM184	0.13	20.65	50.53	16.24	0.19	12.11	0.10	0.31	0.19	0.11	100.56
181	SM184	0.20	26.85	41.31	18.43	0.17	12.03	0.07	0.28	0.35	0.09	99.79
183	SM184	0.11	17.21	52.07	19.08	0.24	10.64	0.06	0.27	0.12	0.06	99.85
184	SM184	0.08	27.03	43.20	16.69	0.15	13.20	0.10	0.24	0.16	0.07	100.93
185	SM184	0.07	21.26	48.89	15.68	0.10	13.61	0.12	0.22	0.08	0.05	100.09
186	SM184	0.10	31.72	38.00	15.48	0.16	14.67	0.09	0.17	0.23	0.06	100.68
187	SM184	0.12	15.54	56.47	14.83	0.19	11.93	0.05	0.23	0.15	0.09	99.59
188	SM184	0.11	26.25	42.62	16.92	0.18	13.53	0.11	0.18	0.14	0.05	100.08
189	SM184	0.10	24.72	44.80	17.04	0.18	13.43	0.06	0.17	0.18	0.07	100.75
190	SM184	0.08	24.23	44.28	18.98	0.20	12.55	0.09	0.23	0.20	0.10	100.94
191	SM184	b.d.	25.63	43.29	17.09	0.21	13.27	0.08	0.24	0.23	0.09	100.13
192	SM184	0.05	23.38	44.85	17.82	0.18	12.92	0.12	0.23	0.17	0.06	99.77
193	SM184	0.15	20.00	49.15	20.19	0.25	10.13	0.03	0.33	0.36	0.09	100.67
194	SM184	0.13	18.65	52.40	16.30	0.17	12.42	0.09	0.09	0.16	0.08	100.49
195	SM184	0.13	24.88	44.94	15.30	0.13	14.48	0.08	0.16	0.17	0.05	100.31
196	SM184	0.06	24.46	45.22	16.64	0.15	13.36	0.06	0.23	0.28	0.08	100.53
197	SM184	0.09	14.09	56.57	18.55	0.25	9.24	0.05	0.31	0.24	0.08	99.47
198	SM184	0.06	23.95	43.81	19.46	0.20	12.70	0.10	0.14	0.16	0.07	100.64
199	SM184	0.10	17.95	51.75	17.53	0.14	12.55	0.10	0.22	0.17	0.08	100.58
200	SM184	0.15	24.50	43.80	18.63	0.20	11.96	0.08	0.16	0.22	0.09	99.80
201	SM184	0.08	17.96	52.05	17.80	0.17	11.50	0.07	0.23	0.16	0.08	100.09
202	SM184	0.60	19.21	47.39	22.00	0.26	9.44	0.02	0.18	0.12	0.07	99.29
203	SM184	0.14	13.44	59.00	15.87	0.22	10.76	0.05	0.22	0.18	0.06	99.93
204	SM184	0.04	31.41	36.49	16.86	0.09	14.69	0.11	0.18	0.22	0.09	100.17
205	SM184	0.09	17.09	53.32	17.73	0.25	11.50	0.04	0.27	0.19	0.06	100.53
206	SM184	0.16	12.80	54.92	21.95	0.27	9.26	0.05	0.29	0.18	0.08	99.95
207	SM184	0.13	27.68	41.99	16.69	0.20	12.79	0.07	0.20	0.16	0.07	99.98
208	SM184	0.07	24.74	42.94	20.00	0.20	12.13	0.10	0.30	0.20	0.08	100.74
209	SM184	0.16	31.07	38.21	16.86	0.12	13.89	0.12	0.24	0.20	0.05	100.92
210	SM184	0.07	32.38	36.81	16.80	0.14	14.15	0.09	0.19	0.28	0.09	101.00
211	SM184	0.21	18.01	51.27	19.27	0.18	10.77	0.08	0.27	0.18	0.08	100.32
212	SM184	0.06	23.44	46.89	16.50	0.13	12.84	0.10	0.24	0.14	0.05	100.39
213	SM184	0.13	30.60	39.31	14.81	0.11	15.35	0.11	0.17	0.17	0.06	100.83
215	SM184	0.11	16.46	53.77	18.12	0.30	10.58	0.07	0.31	0.18	0.07	99.97
216	SM184	0.08	22.17	47.75	18.04	0.18	11.52	0.08	0.28	0.20	0.05	100.35
217	SM184	0.04	21.91	48.45	17.34	0.14	12.19	0.09	0.21	0.10	0.07	100.55
218	SM184	0.08	14.91	55.58	18.74	0.21	10.44	0.04	0.23	0.23	0.05	100.50
219	SM184	0.13	16.56	55.12	17.45	0.22	11.08	0.05	0.27	0.19	0.08	101.15
220	SM184	0.11	22.42	47.98	16.26	0.14	13.14	0.06	0.29	0.14	0.05	100.59
221	SM184	0.20	16.06	52.57	21.73	0.20	8.35	0.05	0.33	0.20	0.09	99.78
222	SM184	0.14	25.65	42.51	18.44	0.15	13.05	0.10	0.34	0.20	0.05	100.64
223	SM184	0.12	34.06	34.90	16.12	0.11	14.25	0.16	0.16	0.18	0.06	100.13
224	SM184	0.06	32.05	37.41	15.74	0.15	15.19	0.11	0.25	0.16	0.08	101.19
225	SM184	0.08	26.91	42.94	15.96	0.18	14.62	0.12	0.19	0.17	0.06	101.24

Data in wt.%; b.d. = below detection limit; Total iron is expressed as Fe_2O_3

Appendix C-1. Continued

No.	Sample	TiO_2	Al_2O_3	Cr_2O_3	Fe_2O_3	MnO	MgO	NiO	V_2O_3	ZnO	CoO	Total
227	SM184	0.08	22.88	45.58	19.93	0.15	11.55	0.10	0.25	0.17	0.10	100.79
228	SM184	0.07	23.37	45.48	18.50	0.23	12.42	0.11	0.17	0.24	0.06	100.66
229	SM184	0.35	13.00	47.64	29.26	0.31	8.90	0.08	0.17	0.18	0.10	99.99
230	SM184	0.09	19.52	49.76	17.85	0.19	11.39	0.04	0.40	0.19	0.05	99.48
231	SM184	0.08	21.39	48.01	17.89	0.15	11.87	0.07	0.23	0.19	0.06	99.93
232	SM184	0.17	32.86	35.96	16.05	0.12	14.77	0.15	0.12	0.20	0.03	100.42
233	SM184	0.10	25.11	43.86	18.22	0.14	12.97	0.10	0.20	0.15	0.07	100.91
234	SM184	0.12	25.09	42.47	18.72	0.21	12.77	0.10	0.22	0.22	0.06	99.97
236	SM185	0.19	11.54	58.85	19.51	0.32	9.66	0.04	0.30	0.16	0.09	100.65
240	SM185	0.24	29.41	40.48	15.40	0.17	14.66	0.12	0.19	0.18	0.07	100.92
242	SM185	0.10	15.23	54.96	18.97	0.28	10.05	0.05	0.23	0.15	0.05	100.07
244	SM185	0.23	21.31	45.83	20.94	0.27	11.19	0.08	0.32	0.25	0.05	100.48
245	SM185	0.08	13.17	56.27	20.87	0.25	9.93	0.05	0.27	0.18	0.07	101.14
248	SM185	0.10	9.92	59.76	20.98	0.31	8.24	0.02	0.29	0.27	0.11	100.00
250	SM185	0.12	16.91	53.46	18.90	0.24	10.07	0.05	0.20	0.22	0.09	100.27
252	SM185	0.12	17.97	51.72	17.65	0.19	12.22	0.05	0.29	0.12	0.07	100.39
253	SM185	0.41	16.25	51.56	20.98	0.26	10.92	0.08	0.12	0.09	0.07	100.72
254	SM185	0.11	16.95	50.93	22.18	0.26	9.27	0.02	0.33	0.27	0.07	100.38
255	SM185	0.18	14.74	55.21	20.25	0.23	10.00	0.05	0.25	0.17	0.04	101.12
256	SM185	0.17	12.07	59.31	18.18	0.25	10.18	0.05	0.21	0.20	0.05	100.68
258	SM185	0.02	23.67	45.96	16.80	0.17	13.63	0.09	0.21	0.17	0.06	100.78
259	SM185	0.10	8.59	62.28	20.15	0.33	8.63	0.01	0.21	0.15	0.05	100.50
260	SM185	1.11	13.55	53.16	21.41	0.17	9.66	0.18	0.30	0.06	0.04	99.63
262	SM185	0.13	12.74	55.58	22.06	0.29	9.40	0.04	0.33	0.16	0.09	100.81
264	SM185	0.24	24.51	42.17	21.48	0.23	12.30	0.06	0.10	0.15	0.04	101.28
265	SM185	0.10	15.16	55.39	19.21	0.23	10.79	0.05	0.25	0.16	0.06	101.39
266	SM185	0.14	17.42	51.64	19.17	0.22	12.03	0.10	0.28	0.13	0.07	101.20
267	SM185	0.36	16.73	51.53	18.80	0.20	12.89	0.11	0.09	0.03	0.03	100.77
269	SM185	0.17	12.41	58.88	17.00	0.18	11.98	0.05	0.24	0.19	0.08	101.18
270	SM185	0.13	17.06	53.62	17.56	0.17	11.56	0.06	0.24	0.17	0.05	100.61
272	SM185	0.12	17.70	51.20	20.36	0.24	10.99	0.07	0.22	0.16	0.06	101.12
276	SM185	0.30	23.15	45.54	18.37	0.17	12.17	0.07	0.31	0.22	0.07	100.37
277	SM185	0.22	21.03	49.31	16.75	0.20	13.02	0.03	0.23	0.20	0.06	101.05
278	SM185	0.08	14.02	55.10	20.80	0.25	10.27	0.07	0.34	0.26	0.10	101.29
279	SM185	0.14	19.86	50.38	17.21	0.21	12.98	0.07	0.23	0.11	0.08	101.26
284	SM185	0.18	17.01	50.40	22.50	0.24	10.46	0.04	0.23	0.18	0.08	101.33
285	SM185	0.03	19.74	50.78	17.86	0.19	12.18	0.04	0.29	0.22	0.07	101.41

Data in wt.%; b.d. = below detection limit; Total iron is expressed as Fe_2O_3

Electron microprobe data for detrital chrome spinel grains referred to in Chapter 1 of this thesis are available online at http://www.geolsoc.org.uk/SUP18270.

Appendix C-2a. Mineral chemical data – Rutile (single measurements)

No.	Sample / Grain	TiO_2	Cr	Al	Fe	Nb	Zr	Si	V	Total
3	CH9 / 1*	96.40	452	1302	210	993	281	1117	1285	97.35
4	CH9 / 2	97.62	568	53	5853	510	133	103	143	98.60
5	CH9 / 3	97.94	664	74	4749	573	74	122	b.d.	98.78
6	CH9 / 4	96.76	376	217	2526	2468	111	79	918	97.70
7	CH9 / 5	97.87	390	175	2542	2677	111	108	687	98.81
8	CH9 / 6	97.55	2155	53	4726	713	b.d.	103	292	98.65
10	CH9 / 8	97.19	3791	53	575	811	74	117	503	98.05
11	CH9 / 9	97.20	6603	53	257	308	207	93	245	98.34
12	CH9 / 10	95.25	2532	95	4967	426	74	79	761	96.48
13	CH9 / 11	96.92	417	217	2449	2517	89	89	659	97.83
14	CH9 / 12	98.75	397	127	2767	2852	104	79	299	99.67
15	CH9 / 13*	97.29	1238	69	1368	1475	2561	145	2243	98.58
16	CH9 / 14	97.59	349	228	2814	3034	104	98	421	98.58
17	CH9 / 15	98.54	281	169	2868	2789	111	108	306	99.46
18	CH9 / 16	98.79	1095	64	5130	426	163	192	211	99.78
36	CH51 / 1	97.19	b.d.	74	1998	559	459	122	1305	97.82
37	CH51 / 2	95.38	438	90	1912	2391	185	131	1305	96.30
38	CH51 / 3	97.85	192	58	5037	692	192	112	1332	98.88
39	CH51 / 4	99.39	103	116	2410	112	118	154	421	99.86
40	CH51 / 5	96.61	4201	64	707	2013	703	131	1767	98.00
41	CH51 / 6	95.66	636	95	1539	266	111	229	1040	96.22
42	CH51 / 7	96.94	68	74	3265	357	311	93	1040	97.65
43	CH51 / 8	98.11	807	582	3490	8081	459	93	857	100.15
44	CH51 / 9	99.37	452	74	2573	252	496	136	829	100.04
45	CH51 / 10	97.13	2025	53	567	692	392	140	2386	98.04
46	CH51 / 11	94.28	1047	79	3094	5306	304	145	1400	95.88
47	CH51 / 12	99.76	684	111	2456	4013	311	164	1292	101.04
48	CH51 / 13	99.54	903	138	2145	133	289	117	795	100.17
49	CH51 / 14	95.96	1635	74	715	776	178	150	2875	96.89
50	CH51 / 15	95.56	b.d.	101	3754	475	363	126	1761	96.47
51	CH51 / 16	96.88	493	164	2441	4117	170	126	727	98.04
52	CH51 / 17	94.65	972	122	2324	245	600	117	836	95.38
53	CH51 / 18	95.11	1950	1784	1119	2209	577	150	714	96.41
54	CH51 / 19	96.67	1451	85	1422	84	155	126	1026	97.29
55	CH51 / 20	97.50	369	201	2542	2684	96	131	816	98.46
62	CH52 / 1	97.54	671	95	2340	839	422	112	795	98.28
63	CH52 / 2	100.18	301	111	1827	909	503	112	1686	100.95
64	CH52 / 3	97.25	2080	79	2573	1643	244	150	510	98.27
65	CH52 / 4	95.27	561	69	1205	140	555	79	2230	95.96
66	CH52 / 5	97.08	438	106	1842	496	437	112	1550	97.78
67	CH52 / 6	98.92	876	127	3490	259	111	136	693	99.70
68	CH52 / 7	95.35	1437	74	1150	538	948	112	1387	96.16
69	CH52 / 8	96.28	1676	95	1337	377	429	187	1278	97.06
70	CH52 / 9	97.59	1019	101	1586	811	289	136	585	98.23
71	CH52 / 10	97.78	787	85	1959	1894	104	145	455	98.55
72	CH52 / 11	100.09	1013	175	1897	252	326	126	1162	100.79
73	CH52 / 12	95.35	746	111	1834	685	489	154	2536	96.29
74	CH52 / 13	99.12	985	566	1842	301	118	131	571	99.78
75	CH52 / 14*	98.92	698	101	1391	643	1118	122	1706	99.74
76	CH52 / 15	96.03	b.d.	212	1726	727	622	215	999	96.67
77	CH52 / 16	98.90	438	206	1842	1489	111	108	1550	99.72

Data in wt.% (TiO_2, Total) and ppm (Cr, Al, Fe, Nb, Zr, Si, V); b.d. = below detection limit; * Raman spectroscopy

Appendix C-2a. Continued

No.	Sample / Grain	TiO_2	Cr	Al	Fe	Nb	Zr	Si	V	Total
78	CH52 / 17	98.00	1026	79	606	329	192	136	2202	98.67
79	CH52 / 18	98.69	1649	79	1321	482	244	117	1394	99.45
80	CH52 / 19	98.54	1416	74	1438	273	496	122	632	99.17
81	CH52 / 20	99.03	944	159	2868	364	267	136	421	99.75
27	CH52 / 21	99.91	1471	116	1586	1021	459	201	795	100.72
28	CH52 / 22	99.92	801	138	2239	1342	355	136	1659	100.87
29	CH52 / 23	98.89	759	58	1244	175	311	126	1332	99.46
30	CH52 / 24	101.03	725	79	1702	329	289	103	1298	101.67
31	CH52 / 25	98.77	308	116	4190	3915	126	159	428	100.05
32	CH52 / 26	98.94	2046	74	1011	678	126	126	1156	99.69
33	CH52 / 27	100.74	944	101	762	350	962	103	1251	101.38
34	CH52 / 28	99.20	924	74	1205	b.d.	363	93	918	99.72
35	CH52 / 29	96.86	1149	180	738	937	185	89	1529	97.56
36	CH52 / 30	96.62	876	74	1562	266	185	108	1543	97.28
37	CH52 / 31	97.82	828	228	2752	741	503	98	2502	98.90
38	CH52 / 32	98.02	1594	127	1492	440	141	108	775	98.69
39	CH52 / 33	99.87	349	286	3047	98	133	89	455	100.49
82	CH61 / 1	98.31	b.d.	381	2402	433	407	224	755	98.97
83	CH61 / 2	99.41	889	53	645	699	703	145	789	99.98
84	CH61 / 3	96.66	68	106	1267	b.d.	363	122	2318	97.27
85	CH61 / 4*	95.26	848	201	948	133	81	425	1285	95.86
86	CH61 / 5	99.31	568	90	2005	405	400	131	299	99.85
87	CH61 / 6	98.95	356	85	1329	245	644	173	415	99.41
88	CH61 / 7	98.04	931	180	1096	566	274	103	442	98.56
89	CH61 / 8	98.42	438	69	902	112	348	126	1196	98.88
90	CH61 / 9	96.91	1122	148	1236	1132	267	108	557	97.57
91	CH61 / 10	97.77	226	169	1376	790	141	112	1040	98.32
92	CH61 / 11	98.43	1211	101	1275	454	318	159	639	99.03
93	CH61 / 12	96.70	616	90	1710	2957	244	112	1101	97.67
94	CH61 / 13	99.12	438	85	933	1202	763	103	2311	99.96
95	CH61 / 14	98.84	677	90	2293	308	185	103	408	99.40
96	CH61 / 15	98.58	123	79	1096	2447	311	154	748	99.29
97	CH61 / 16	98.61	1163	69	956	280	192	122	510	99.08
98	CH61 / 17	99.06	1375	201	2130	377	178	98	231	99.71
99	CH61 / 18	96.04	424	116	2581	3286	126	103	741	97.07
100	CH61 / 19	96.84	1409	85	1026	231	222	117	1115	97.45
101	CH61 / 20	99.17	151	79	3513	140	281	112	673	99.84
108	CH65 / 1	99.20	417	175	1834	1000	81	93	659	99.80
109	CH65 / 2	99.87	609	169	2728	1566	178	108	1149	100.78
110	CH65 / 3	97.07	595	95	2013	189	215	103	829	97.63
111	CH65 / 4	100.46	643	138	1321	804	385	126	1353	101.14
112	CH65 / 5	95.87	992	58	1827	776	296	98	1733	96.69
113	CH65 / 6	100.01	1259	53	840	182	74	93	2128	100.68
114	CH65 / 7	98.61	267	164	1687	189	429	93	1482	99.22
115	CH65 / 8	98.11	239	122	2573	161	392	103	2338	98.94
116	CH65 / 9	97.49	185	111	3537	559	215	89	2508	98.49
117	CH65 / 10	98.71	335	450	2169	3586	170	108	1067	99.84
118	CH65 / 11	99.07	b.d.	201	2425	210	533	108	870	99.67
119	CH65 / 12	98.52	1895	79	645	433	267	112	2332	99.36
120	CH65 / 13	99.72	554	259	1088	2545	726	122	1652	100.72
121	CH65 / 14	100.39	2696	169	1065	266	452	112	1033	101.23
122	CH65 / 15	98.44	294	69	2410	1838	104	93	877	99.23

Data in wt.% (TiO_2, Total) and ppm (Cr, Al, Fe, Nb, Zr, Si, V); b.d. = below detection limit; * Raman spectroscopy

Appendix C-2a. Continued

No.	Sample / Grain	TiO_2	Cr	Al	Fe	Nb	Zr	Si	V	Total
123	CH65 / 16	96.75	513	64	2798	2111	607	122	924	97.74
124	CH65 / 17	100.51	89	101	2192	154	333	98	945	101.05
125	CH65 / 18	100.05	b.d.	58	2713	650	666	117	999	100.77
126	CH65 / 19	97.82	253	328	1174	825	511	103	1203	98.46
127	CH65 / 20*	98.97	1936	693	1656	1181	229	1159	326	100.09
43	CH65 / 21	100.10	417	159	1827	1111	200	103	1013	100.78
44	CH65 / 22	98.11	1581	138	1477	454	163	103	1047	98.82
45	CH65 / 23	97.56	1457	64	1314	217	207	108	1224	98.22
46	CH65 / 24	96.87	725	185	777	881	429	112	2624	97.71
47	CH65 / 25	98.36	821	143	1625	986	267	131	1339	99.12
48	CH65 / 26	96.47	89	111	1866	133	355	154	2522	97.22
49	CH65 / 27	99.99	848	148	1267	622	800	117	836	100.65
50	CH65 / 28	96.26	424	138	2161	1943	222	117	1060	97.12
51	CH65 / 29	98.63	534	196	1718	1237	370	117	1264	99.40
52	CH65 / 30	97.33	1067	143	1749	860	207	112	1101	98.08
53	CH65 / 31	98.69	2018	53	2635	1629	163	98	204	99.64
54	CH65 / 32	97.89	965	143	1189	713	229	89	1319	98.56
55	CH65 / 33	96.00	205	90	2954	594	466	108	1761	96.86
56	CH65 / 34	99.74	1013	153	2013	357	326	122	462	100.37
57	CH65 / 35	96.62	828	90	933	398	304	103	1298	97.19
58	CH65 / 36	99.51	383	101	1158	252	118	136	3045	100.26
59	CH65 / 37	99.02	561	460	1298	70	326	140	1441	99.65
60	CH65 / 38	97.36	479	228	2604	2195	163	98	1339	98.36
61	CH65 / 39	99.05	2737	106	1143	559	289	98	2474	100.12
62	CH65 / 40	100.59	376	74	1757	496	392	126	911	101.17
63	CH65 / 41	98.70	623	106	2861	238	148	117	734	99.37
128	CH66 / 1	99.42	951	127	1485	315	785	108	1332	100.14
129	CH66 / 2	97.52	931	127	1158	266	407	108	1937	98.23
130	CH66 / 3	99.84	1868	69	326	419	392	112	3331	100.80
131	CH66 / 4	101.02	1218	159	606	315	281	112	4208	102.03
132	CH66 / 5	100.43	376	64	1640	b.d.	89	98	1319	100.94
133	CH66 / 6	99.76	848	64	1391	b.d.	141	98	1360	100.32
134	CH66 / 7	100.03	1457	164	1446	308	178	122	360	100.61
135	CH66 / 8	97.95	499	116	1780	182	207	117	911	98.49
136	CH66 / 9	99.94	718	101	1726	2461	244	145	1965	100.99
137	CH66 / 10*	97.76	869	164	1866	1419	1022	93	884	98.65
138	CH66 / 11	98.54	828	74	474	1258	977	93	2236	99.40
139	CH66 / 12	96.10	1156	69	964	266	118	112	2964	96.92
140	CH66 / 13	97.99	185	64	2005	168	400	93	585	98.47
141	CH66 / 14	96.54	2326	69	1143	419	526	103	1563	97.42
142	CH66 / 15	96.56	780	90	2107	266	133	112	1917	97.32
143	CH66 / 16	99.66	1581	95	1780	433	407	108	1781	100.54
144	CH66 / 17	96.54	253	53	1640	287	348	117	1332	97.11
145	CH66 / 18	98.84	301	127	1850	447	548	201	1543	99.55
146	CH66 / 19	101.32	705	53	1283	1419	304	150	1489	102.09
147	CH70 / 1	96.89	308	503	2557	1978	141	117	1196	97.86
148	CH70 / 2	97.78	1478	243	1555	3817	304	108	999	99.00
149	CH70 / 3*	97.53	294	402	2130	1971	96	117	455	98.31
150	CH70 / 4	97.26	1197	85	2200	566	459	108	761	98.01
151	CH70 / 5	100.14	609	90	840	154	311	79	884	100.57
152	CH70 / 6	98.01	1026	101	591	217	400	103	1142	98.53
153	CH70 / 7	100.66	137	349	1469	447	207	117	870	101.18

Data in wt.% (TiO_2, Total) and ppm (Cr, Al, Fe, Nb, Zr, Si, V); b.d. = below detection limit; * Raman spectroscopy

Appendix C-2a. Continued

No.	Sample / Grain	TiO_2	Cr	Al	Fe	Nb	Zr	Si	V	Total
154	CH70 / 8	97.66	1334	53	1345	587	111	117	1523	98.39
155	CH70 / 9	100.60	233	85	2099	1321	74	136	1033	101.30
156	CH70 / 10	98.70	582	281	3490	5432	274	112	952	100.27
157	CH70 / 11	101.36	1108	95	886	364	207	122	836	101.88
158	CH70 / 12	98.14	328	122	2783	2733	348	112	1196	99.21
159	CH70 / 13	99.13	828	143	1454	594	178	178	1835	99.88
160	CH70 / 14	98.97	68	74	2169	231	244	103	1169	99.53
161	CH70 / 15	100.43	1355	64	513	224	429	117	1448	101.03
162	CH70 / 16*	100.63	2614	201	591	412	740	430	1394	101.58
163	CH70 / 17	99.65	889	191	4998	2363	237	117	1081	101.01
164	CH70 / 18	99.10	151	58	1391	734	296	103	999	99.63
165	CH70 / 19*	98.17	8703	53	194	419	1229	112	1597	99.96
166	CH70 / 20	96.85	623	201	2410	1195	540	103	2739	97.96
67	CH70 / 21	99.87	1095	122	466	273	370	93	904	100.35
68	CH70 / 22	98.27	226	127	2355	2538	940	131	1516	99.37
69	CH70 / 23	96.85	896	344	2449	3614	289	117	1754	98.20
70	CH70 / 24	97.63	383	302	3972	4271	274	103	653	99.02
71	CH70 / 25	99.40	178	69	2309	545	274	154	999	100.03
72	CH70 / 26	97.47	185	69	2837	552	229	93	1162	98.18
73	CH70 / 27	98.77	595	85	2021	2083	133	112	775	99.59
74	CH70 / 28	97.82	1635	138	1150	762	444	79	1251	98.60
75	CH70 / 29	99.19	513	513	2728	4991	192	98	918	100.61
76	CH70 / 30	97.59	3106	58	2099	384	126	136	1081	98.58
77	CH70 / 31	99.68	1451	222	1625	3383	333	108	1781	100.96
78	CH70 / 32	99.43	1197	79	1353	126	148	112	306	99.90
20	CH11 / 1	98.51	123	53	404	881	674	122	3922	99.41
21	CH11 / 2	98.80	417	111	1353	2447	163	79	2658	99.84
22	CH11 / 3	96.96	356	53	490	657	207	84	3678	97.77
23	CH11 / 4	97.95	1067	53	808	2013	207	75	3304	99.04
24	CH11 / 5	97.36	1061	95	404	2265	259	75	3181	98.44
25	CH11 / 6	94.50	6972	53	770	7354	800	75	3113	97.27
26	CH11 / 7	98.58	137	85	1446	1328	200	75	1088	99.20
27	CH11 / 8	97.68	1642	116	2114	1167	155	75	646	98.52
28	CH11 / 9	95.96	1054	74	995	2314	200	75	3093	97.11
29	CH11 / 10	96.46	b.d.	180	1780	846	548	75	2100	97.24
30	CH11 / 11	97.51	1834	58	1166	2097	118	75	2359	98.62
31	CH11 / 12*	99.08	1423	53	225	790	2391	75	4371	100.43
32	CH11 / 13	97.73	103	53	1384	1622	192	75	2977	98.65
33	CH11 / 14	98.32	2593	53	2270	2691	378	75	918	99.59
34	CH11 / 15	97.73	1813	69	2573	881	126	75	1190	98.68
35	CH11 / 16	96.80	1642	90	1524	2957	888	75	4024	98.41
36	CH11 / 17	96.51	294	1228	2021	315	b.d.	75	693	97.57
37	CH11 / 18*	96.87	328	228	1321	3873	437	75	1604	98.01
38	CH11 / 19	97.71	499	79	4213	3237	481	75	782	99.00
39	CH11 / 20	95.57	1348	217	3560	741	637	75	843	96.60
84	CH11 / 21	98.08	465	259	4291	8794	644	93	1298	100.31
85	CH11 / 22	99.14	1095	53	428	1223	644	145	3372	100.15
86	CH11 / 23	98.51	b.d.	58	3972	4516	570	112	1332	99.98
87	CH11 / 24	98.39	246	370	2425	1349	415	495	1965	99.45
88	CH11 / 25	99.72	164	95	3451	468	281	108	693	100.44
89	CH11 / 26	99.52	281	106	2114	734	392	79	653	100.12
91	CH11 / 28	94.38	910	153	1834	2090	333	252	2128	95.49

Data in wt.% (TiO_2, Total) and ppm (Cr, Al, Fe, Nb, Zr, Si, V); b.d. = below detection limit; * Raman spectroscopy

Appendix C-2a. Continued

No.	Sample / Grain	TiO_2	Cr	Al	Fe	Nb	Zr	Si	V	Total
92	CH11 / 29	99.16	458	79	1174	979	274	98	2474	99.96
93	CH11 / 30	99.67	356	74	1547	2062	1473	108	1788	100.72
94	CH11 / 31	99.70	575	101	1788	3341	407	98	1835	100.86
95	CH11 / 32	97.33	5918	1249	2526	1384	304	1744	734	99.48
96	CH11 / 33	99.17	513	296	2231	3432	259	117	1224	100.32
97	CH11 / 34	100.18	116	699	1337	1153	b.d.	150	b.d.	100.70
98	CH11 / 35	99.00	712	116	2899	5830	800	126	1047	100.62
99	CH11 / 36	100.96	616	58	5371	2845	192	98	2264	102.54
100	CH11 / 37	99.28	1074	53	474	657	89	112	1849	99.91
101	CH11 / 38	99.74	116	64	2938	1433	459	93	1883	100.71
102	CH11 / 39	101.94	807	53	1866	1797	67	112	673	102.70
104	CH11 / 41	98.54	547	53	272	224	659	89	6036	99.69
106	CH11 / 43	101.60	616	53	288	147	59	84	2073	102.09
107	CH11 / 44	98.51	1711	74	785	916	1584	89	3813	99.80
108	CH11 / 45	101.04	568	196	2021	1978	304	79	1278	101.95
109	CH11 / 46	98.11	1758	90	373	783	555	126	2359	98.99
110	CH11 / 47	99.29	766	127	808	1014	1022	234	2733	100.27
111	CH11 / 48	97.60	417	238	2254	4411	289	79	1597	98.92
112	CH11 / 49	99.12	1122	53	1135	1384	740	98	2773	100.17
113	CH11 / 50	99.79	513	101	1562	1748	644	103	1937	100.73
53	CH11 / 51	97.28	6589	53	762	643	207	126	3664	99.04
16	CH48 / 1	100.24	458	127	1477	273	304	126	442	100.69
17	CH48 / 2	99.32	445	206	1384	2167	141	117	1271	100.14
18	CH48 / 3	99.78	b.d.	53	4299	231	622	112	483	100.56
19	CH48 / 4	99.96	486	64	1197	1146	481	93	1128	100.61
20	CH48 / 5	98.95	1273	58	964	2286	770	103	2291	100.06
21	CH48 / 6	96.88	4748	64	808	2083	1621	108	1842	98.50
22	CH48 / 7	99.33	965	180	2441	1160	555	126	1965	100.38
23	CH48 / 8	96.39	458	53	2161	2461	133	103	979	97.28
24	CH48 / 9*	99.38	3168	69	1026	678	67	351	979	100.31
25	CH48 / 10	99.73	677	222	1345	1475	429	112	1203	100.51
26	CH48 / 11*	98.90	144	85	1710	2761	5256	122	1516	100.51
27	CH48 / 12*	96.57	2306	101	1182	1762	1259	112	2345	97.87
28	CH48 / 13	95.12	595	74	2215	3055	711	108	2270	96.40
29	CH48 / 14	97.14	472	53	1733	2698	59	145	2277	98.20
30	CH48 / 15	99.88	2846	53	1384	1174	67	112	1339	100.88
31	CH48 / 16	99.35	712	58	4345	706	96	122	170	100.19
32	CH48 / 17	97.59	1279	148	2192	3845	304	154	2107	99.02
33	CH48 / 18	97.19	588	95	2169	3894	400	131	1523	98.44
34	CH48 / 19	96.58	1382	79	1500	3712	651	117	2073	97.94
35	CH48 / 20	94.40	328	79	707	748	837	112	2719	95.20
1	CH48 / 21*	98.39	342	79	692	2272	777	271	2066	99.34
2	CH48 / 22	96.66	397	333	3195	5865	503	103	1033	98.27
3	CH48 / 23	98.72	1772	53	1073	2572	281	168	2604	99.95
4	CH48 / 24	95.18	452	85	4462	6222	222	117	680	96.88
5	CH48 / 25	98.15	4885	74	404	3950	444	192	1543	99.82
6	CH48 / 26	98.15	855	90	1578	70	52	178	911	98.69
7	CH48 / 27	98.22	1437	106	2176	1496	326	187	333	99.08
8	CH48 / 28	98.55	1820	53	2215	5418	703	150	1468	100.23
9	CH48 / 29	97.34	b.d.	79	1632	944	614	126	789	97.93
10	CH48 / 30	97.89	171	116	4400	594	244	131	761	98.76
11	CH48 / 31	99.17	629	69	1881	1216	296	103	727	99.86

Data in wt.% (TiO_2, Total) and ppm (Cr, Al, Fe, Nb, Zr, Si, V); b.d. = below detection limit; * Raman spectroscopy

Appendix C-2a. Continued

No.	Sample / Grain	TiO_2	Cr	Al	Fe	Nb	Zr	Si	V	Total
12	CH48 / 32	96.20	b.d.	116	3397	4879	503	108	897	97.58
13	CH48 / 33	96.54	192	79	1539	168	96	98	2005	97.14
14	CH48 / 34*	99.04	1498	180	505	2405	1125	108	911	100.01
15	CH48 / 35	100.90	794	90	832	1202	792	103	1733	101.70
16	CH48 / 36	99.15	123	191	3669	965	437	108	863	100.02
17	CH48 / 37	98.34	609	101	777	1167	259	182	3168	99.25
18	CH48 / 38	98.11	281	53	326	531	474	117	2529	98.74
19	CH48 / 39	96.46	164	95	1912	692	155	140	843	97.02
20	CH48 / 40*	98.50	226	201	2480	678	318	304	605	99.18
40	CH26 / 1*	98.25	1758	153	404	2188	1806	75	2631	99.55
41	CH26 / 2	98.11	260	53	972	384	555	75	1958	98.72
42	CH26 / 3	98.95	821	180	785	280	59	75	2080	99.58
43	CH26 / 4*	96.37	2833	74	770	1000	2339	75	2284	97.72
44	CH26 / 5	97.48	2682	79	482	1084	711	75	3956	98.81
45	CH26 / 6	97.46	212	53	5029	287	318	75	1278	98.44
46	CH26 / 7	96.06	2025	69	1182	2614	178	75	1489	97.16
47	CH26 / 8*	95.70	4632	53	365	1873	3220	75	2746	97.78
48	CH26 / 9	98.82	1964	191	1049	1727	2228	75	2909	100.28
49	CH26 / 10	99.79	554	95	917	930	592	75	3399	100.74
50	CH26 / 11	97.97	1690	53	1842	3782	207	75	2162	99.38
51	CH26 / 12	97.10	164	53	4959	3216	170	75	523	98.35
52	CH26 / 13	100.03	1170	95	4431	1845	363	75	190	101.15
53	CH26 / 14	98.06	458	53	964	972	1266	75	1863	98.87
54	CH26 / 15*	99.64	185	122	933	280	1984	75	1332	100.33
55	CH26 / 16	96.44	855	69	1873	944	67	75	1448	97.20
56	CH26 / 17	99.59	151	53	3218	4187	688	75	1176	100.92
59	CH26 / 18	96.59	1115	53	482	2510	651	75	2726	97.69
60	CH26 / 19	96.89	274	64	2713	1957	925	75	2162	98.03
61	CH26 / 20	97.31	123	106	4058	412	126	75	353	98.02
47	CH26 / 21	100.37	2429	74	847	1440	1118	108	1502	101.45
48	CH26 / 22	98.45	103	90	2876	1314	2036	84	1468	99.55
49	CH26 / 23	99.72	671	58	894	2027	1688	98	4167	101.10
50	CH26 / 24	100.06	1204	79	1345	2831	474	98	1502	101.13
51	CH26 / 25	99.28	3421	85	2285	3034	415	108	924	100.74
52	CH26 / 26	100.11	595	53	567	944	666	108	1584	100.76
53	CH26 / 27	99.43	766	74	1011	1629	1199	117	2950	100.54
54	CH26 / 28	100.51	465	69	715	1125	674	136	1917	101.25
55	CH26 / 29	97.55	759	85	2853	5767	718	89	2502	99.35
56	CH26 / 30	100.87	328	254	2091	811	666	84	1285	101.65
57	CH26 / 31	98.03	458	95	2293	4907	1036	89	1869	99.55
58	CH26 / 32	98.85	588	688	1384	1957	141	916	2012	100.04
59	CH26 / 33	100.20	411	201	2604	3579	385	98	945	101.36
60	CH26 / 34	97.47	1820	53	218	2405	1903	89	5615	99.22
61	CH26 / 35	100.47	623	101	1943	2873	503	84	1020	101.48
63	CH26 / 37	100.13	96	175	3902	608	400	89	775	100.95
64	CH26 / 38	97.90	910	164	933	2293	1688	84	2468	99.12
65	CH26 / 39	100.08	315	53	2107	1922	89	93	673	100.81
66	CH26 / 40	97.85	2381	64	1718	1475	333	98	4962	99.44
67	CH26 / 41	98.42	1088	127	2340	4166	363	103	1631	99.81
68	CH26 / 42	97.81	541	212	1570	2300	363	196	2216	98.88
69	CH26 / 43	100.53	1765	111	824	489	962	98	1563	101.37
70	CH26 / 44	99.55	1300	138	420	2349	651	192	3113	100.74

Data in wt.% (TiO_2, Total) and ppm (Cr, Al, Fe, Nb, Zr, Si, V); b.d. = below detection limit; * Raman spectroscopy

Appendix C-2a. Continued

No.	Sample / Grain	TiO_2	Cr	Al	Fe	Nb	Zr	Si	V	Total
71	CH26 / 45	96.73	1115	53	878	1056	59	103	2128	97.51
72	CH26 / 46	97.04	1478	85	1158	2419	800	154	1944	98.20
73	CH26 / 47	99.49	1321	58	692	2838	607	103	2352	100.64
74	CH26 / 48	97.95	1765	53	583	1342	96	98	2338	98.86
75	CH26 / 49	98.35	3332	116	311	1028	2339	103	2155	99.70
76	CH26 / 50	99.36	1067	159	1632	3817	400	93	1597	100.61
77	CH26 / 51	98.28	2196	101	785	1433	341	140	1509	99.23
78	CH26 / 52	99.11	328	69	1088	776	67	126	2087	99.77
79	CH26 / 53	99.47	1266	116	785	112	355	89	2298	100.20
80	CH26 / 54	99.51	520	79	3234	210	415	70	612	100.21
81	CH26 / 55	99.10	274	138	3094	1783	74	98	863	99.98
82	CH26 / 56	101.03	328	148	754	1056	970	79	1788	101.77
83	CH26 / 57	98.65	931	64	1733	1629	637	108	2128	99.68
62	CH36 / 1	98.18	b.d.	101	1368	1272	237	75	1414	98.82
63	CH36 / 2	99.14	96	153	2651	308	52	75	b.d.	99.59
64	CH36 / 3	100.59	1471	74	1819	2649	89	75	1183	101.63
65	CH36 / 4	97.85	1546	153	1112	2055	304	75	4847	99.32
66	CH36 / 5	97.18	855	138	3327	3677	222	75	1183	98.51
67	CH36 / 6	99.77	999	53	1213	1678	289	75	952	100.52
68	CH36 / 7	97.60	999	191	2060	4243	252	75	1747	98.97
69	CH36 / 8	98.01	1362	85	2262	3481	511	75	1754	99.36
70	CH36 / 9	99.23	965	64	1104	1475	629	75	2270	100.18
71	CH36 / 10	97.28	458	423	3296	5571	229	75	734	98.81
72	CH36 / 11	98.69	554	185	2340	1964	67	75	1108	99.58
73	CH36 / 12	97.49	1348	402	295	2447	355	75	2658	98.74
74	CH36 / 13	97.06	561	153	2184	2838	237	75	2406	98.27
75	CH36 / 14	98.37	383	58	3506	2349	74	75	1081	99.42
76	CH36 / 15	98.21	773	333	2635	5956	289	75	1529	99.87
77	CH36 / 16	98.31	1430	74	1182	720	141	75	1258	99.02
78	CH36 / 17	98.01	445	159	1391	384	289	75	1407	98.61
79	CH36 / 18	99.42	814	101	1866	203	244	75	979	100.03
80	CH36 / 19	97.51	1019	333	1834	2705	141	75	986	98.53
81	CH36 / 20	99.46	431	365	2169	1790	141	75	687	100.27
120	CH36 / 21	99.96	1225	392	1959	2971	281	79	1747	101.20
121	CH36 / 22	99.75	1423	53	3195	168	333	103	1230	100.65
122	CH36 / 23	99.32	1170	153	1189	350	415	79	1645	100.04
123	CH36 / 24	98.44	616	206	2899	2992	244	112	1550	99.66
124	CH36 / 25	97.90	1102	79	3879	853	363	84	517	98.84
125	CH36 / 26	98.08	773	132	1990	475	118	89	1081	98.74
126	CH36 / 27	100.65	452	191	2658	391	452	103	897	101.36
127	CH36 / 28	99.97	657	572	2977	4900	281	238	958	101.49
128	CH36 / 29	97.96	643	566	3008	4628	215	131	680	99.37
129	CH36 / 30	98.88	2703	85	451	1167	155	112	1054	99.72
130	CH36 / 31	97.93	972	101	1866	608	185	98	1421	98.67
131	CH36 / 32	100.83	602	291	3055	4089	252	89	843	102.13
132	CH36 / 33	101.33	705	169	902	175	207	84	2155	101.97
133	CH36 / 34	100.99	1074	111	1936	2034	141	103	1795	102.01
134	CH36 / 35	101.08	520	143	2254	846	429	93	884	101.80
135	CH36 / 36	97.31	294	582	3117	4054	274	75	1122	98.66
136	CH36 / 37	99.53	1156	228	1718	2440	304	89	1720	100.63
137	CH36 / 38	99.49	2258	122	1943	2845	252	103	1815	100.82
138	CH36 / 39	98.99	1423	111	1959	2936	281	89	1740	100.20

Data in wt.% (TiO_2, Total) and ppm (Cr, Al, Fe, Nb, Zr, Si, V); b.d. = below detection limit; * Raman spectroscopy

Appendix C-2a. Continued

No.	Sample / Grain	TiO_2	Cr	Al	Fe	Nb	Zr	Si	V	Total
139	CH36 / 40	98.34	883	249	2013	3782	237	290	1563	99.64
140	CH36 / 41	100.34	301	127	2285	1685	304	98	1883	101.28
141	CH36 / 42	99.17	1088	95	1593	2978	229	75	1516	100.25
142	CH36 / 43	97.76	513	434	1772	1021	200	103	1482	98.56
143	CH36 / 44	98.08	1382	74	1920	3104	185	112	2284	99.37
144	CH36 / 45	99.58	178	127	2433	196	267	98	1298	100.22
145	CH36 / 46	99.11	308	434	2363	2579	111	89	292	99.99
146	CH36 / 47	97.85	876	132	1904	2691	289	103	2033	98.99
147	CH36 / 48	100.39	48	79	1819	329	207	98	965	100.89
148	CH36 / 49	100.29	2039	69	637	706	237	136	1502	101.07
149	CH36 / 50	99.44	2244	53	925	245	118	89	1631	100.21
150	CH36 / 51	100.91	780	408	396	98	274	70	4357	101.86
151	CH36 / 52	99.52	267	132	707	804	148	84	2250	100.16
152	CH36 / 53	99.81	2073	328	560	1063	252	84	714	100.56
153	CH36 / 54	99.74	493	106	1220	1643	415	117	2087	100.61
154	CH36 / 55	99.22	376	212	2930	2873	163	154	870	100.29
84	CH42 / 1	98.84	82	74	3389	1377	200	75	394	99.60
85	CH42 / 2*	96.38	2135	64	1430	1084	1866	75	2012	97.61
86	CH42 / 3	99.88	486	265	2456	1314	355	75	170	100.60
87	CH42 / 4	97.82	144	752	3615	4600	407	75	755	99.29
88	CH42 / 5	100.19	267	169	2868	916	466	75	190	100.87
89	CH42 / 6	97.72	438	58	824	1433	415	75	1665	98.44
90	CH42 / 7	98.49	1211	53	1220	2698	163	75	1563	99.49
91	CH42 / 8	99.18	753	106	2596	3216	207	75	918	100.29
92	CH42 / 9	98.93	417	64	1936	1845	267	75	387	99.63
93	CH42 / 10	98.31	274	180	2588	4082	415	75	687	99.48
94	CH42 / 11	97.35	657	53	762	1594	392	75	3508	98.38
95	CH42 / 12	97.49	1115	53	1011	2188	592	75	999	98.36
96	CH42 / 13	98.05	226	95	2021	1489	192	75	1074	98.78
97	CH42 / 14	97.71	246	64	1648	2139	207	75	653	98.42
98	CH42 / 15	97.80	575	53	1049	664	89	75	1353	98.36
11	CH42 / 16	98.24	534	58	1842	1132	126	126	1332	98.97
12	CH42 / 17	99.07	397	143	1337	1084	940	108	2121	99.95
13	CH42 / 18	97.60	356	127	2495	364	163	136	673	98.20
14	CH42 / 19	97.49	1061	58	1531	972	133	126	904	98.17
15	CH42 / 20*	99.67	1451	101	855	832	118	276	1740	100.46

Data in wt.% (TiO_2, Total) and ppm (Cr, Al, Fe, Nb, Zr, Si, V); b.d. = below detection limit; * Raman spectroscopy

Appendix C-2b. Mineral chemical data – Rutile (multiple measurements)

No.	Sample / Grain	TiO_2	Cr	Al	Fe	Nb	Zr	Si	V	Total
107	CH52 / 31	96.82	807	217	2783	699	503	108	2481	97.89
108	CH52 / 31	96.13	848	243	2861	741	496	84	2542	97.23
109	CH52 / 31	96.25	814	217	3047	776	459	79	2529	97.36
110	CH52 / 31	97.44	814	259	2208	615	437	108	2454	98.42
111	CH52 / 31	96.13	828	201	2192	706	466	98	2556	97.13
112	CH52 / 31	97.00	842	196	2534	678	466	79	2502	98.03
113	CH52 / 31	96.56	835	201	2721	664	481	93	2508	97.62
114	CH52 / 31	97.00	814	222	2487	783	444	89	2447	98.03
115	CH52 / 31	96.67	842	228	3109	727	496	122	2522	97.80
116	CH52 / 31	96.29	828	180	2270	706	459	93	2502	97.29
96	CH65 / 5	96.39	1054	74	1873	601	341	103	1638	97.19
97	CH65 / 5	99.97	1040	74	1803	629	333	108	1394	100.73
98	CH65 / 5	96.75	999	122	1765	692	252	122	1611	97.54
99	CH65 / 5	96.33	1218	74	1834	797	348	89	1672	97.18
100	CH65 / 5	96.34	1197	69	1718	853	252	117	1693	97.18
101	CH65 / 5	97.79	1026	58	1508	797	281	93	1645	98.56
102	CH65 / 5	99.64	1129	69	1726	1000	222	122	1570	100.47
103	CH65 / 5	97.21	1108	95	1749	664	289	108	1618	98.01
104	CH65 / 5	96.27	1019	79	1749	1042	259	98	1618	97.10
105	CH65 / 5	96.64	1492	106	1718	1111	318	98	1625	97.56
106	CH65 / 5	96.70	1129	58	1695	741	296	98	1747	97.52
137*	CH66 / 10	97.76	869	164	1866	1419	1022	93	884	98.65
36	CH66 / 10	97.75	931	132	2013	1650	999	112	863	98.69
37	CH66 / 10	98.59	869	101	2029	1314	1014	89	870	99.47
38	CH66 / 10	99.00	903	132	1982	1699	1014	122	897	99.95
85	CH70 / 1	96.67	301	296	3140	2104	155	98	1292	97.71
86	CH70 / 1	97.14	294	630	2417	2097	163	93	1319	98.15
87	CH70 / 1	97.13	267	1154	2301	2104	178	257	1305	98.26
88	CH70 / 1	97.15	281	445	2697	2062	185	93	1339	98.16
89	CH70 / 1	97.99	281	455	2682	2174	185	112	1258	99.01
90	CH70 / 1	97.25	287	397	2697	2020	148	89	1312	98.24
91	CH70 / 1	96.95	260	524	2417	1992	178	103	1278	97.92
92	CH70 / 1	96.73	335	445	2604	1964	163	108	1271	97.71
93	CH70 / 1	96.81	246	439	2798	2090	141	117	1312	97.82
94	CH70 / 1	96.28	301	609	2433	2132	178	98	1312	97.30
95	CH70 / 1	97.36	287	545	2620	2055	141	93	1319	98.37
7	CH70 / 5	98.07	541	58	925	70	422	150	952	98.52
8	CH70 / 5	98.12	541	69	1158	112	355	122	945	98.59
9	CH70 / 5	98.14	588	53	1135	98	348	89	952	98.60
10	CH70 / 5	98.10	520	64	956	77	385	182	999	98.56
11	CH70 / 5	97.35	561	74	956	140	341	201	958	97.82
12	CH70 / 5	98.28	623	101	925	70	333	112	972	98.73
13	CH70 / 5	98.30	602	53	1034	70	341	84	958	98.75
14	CH70 / 5	97.53	629	69	979	98	392	70	986	97.99
15	CH70 / 5	98.34	650	53	1011	147	385	89	911	98.80
16	CH70 / 5	99.07	568	64	1042	b.d.	378	103	958	99.51
17	CH70 / 5	98.08	588	79	909	b.d.	304	65	945	98.49
18	CH70 / 5	98.76	623	58	1003	119	363	215	911	99.24
19	CH70 / 5	98.21	636	69	933	98	355	117	890	98.65
20	CH70 / 5	99.27	636	90	894	140	348	108	911	99.72
21	CH70 / 5	99.01	636	90	816	133	296	65	904	99.43

Data in wt.% (TiO_2, Total) and ppm (Cr, Al, Fe, Nb, Zr, Si, V); b.d. = below detection limit; * included in Appendix C-2a

Appendix C-2b. Continued

No.	Sample / Grain	TiO_2	Cr	Al	Fe	Nb	Zr	Si	V	Total
22	CH70 / 5	98.66	582	58	917	b.d.	341	89	897	99.07
23	CH70 / 5	98.18	616	85	855	147	437	89	931	98.63
24	CH70 / 5	98.42	616	85	777	133	385	89	992	98.86
25	CH70 / 5	98.65	623	74	933	133	333	89	924	99.10
26	CH70 / 5	99.03	609	85	894	70	267	108	938	99.46
27	CH70 / 5	98.80	588	164	816	154	304	75	897	99.23
28	CH70 / 5	98.56	616	64	591	119	333	84	890	98.95
29	CH70 / 5	99.15	575	69	731	77	385	103	870	99.56
30	CH70 / 5	99.11	609	64	700	b.d.	326	93	890	99.50
31	CH70 / 5	99.03	650	74	816	77	296	89	924	99.45
32	CH70 / 5	99.02	629	95	871	84	296	75	924	99.45
33	CH70 / 5	99.27	636	74	723	147	370	103	904	99.70
34	CH70 / 5	97.69	602	69	738	b.d.	355	103	958	98.10
35	CH70 / 5	98.41	582	90	840	154	296	79	931	98.84
36	CH70 / 5	98.80	643	64	614	98	281	79	1006	99.20
37	CH70 / 5	98.70	616	90	847	84	341	103	938	99.13
38	CH70 / 5	98.93	568	90	917	182	355	79	857	99.36
39	CH70 / 5	98.26	602	101	956	147	341	93	918	98.71
40	CH70 / 5	98.66	657	90	832	133	311	89	836	99.08
41	CH70 / 5	98.94	568	64	622	133	333	75	911	99.33
42	CH70 / 5	98.88	609	69	863	140	422	220	870	99.35
43	CH70 / 5	98.04	650	58	941	112	437	257	931	98.54
44	CH70 / 5	98.26	561	58	754	147	400	346	952	98.74
45	CH70 / 5	98.54	629	53	933	140	311	56	884	98.97
46	CH70 / 5	99.16	602	95	925	140	326	79	850	99.59
47	CH70 / 5	97.68	588	85	871	161	348	108	836	98.11
48	CH70 / 5	98.50	588	85	933	133	355	140	870	98.95
165*	CH70 / 19	98.17	8703	53	194	419	1229	112	1597	99.96
39	CH70 / 19	98.42	8888	53	194	419	1222	112	1611	100.24
40	CH70 / 19	98.36	8518	58	241	440	1236	98	1686	100.15
31*	CH11 / 12	99.08	1423	53	225	790	2391	75	4371	100.43
27	CH11 / 12	98.86	1444	344	505	804	2280	453	4466	100.38
28	CH11 / 12	99.95	1375	572	1003	930	2421	827	4480	101.68
29	CH11 / 12	99.53	1451	53	342	846	2295	126	4432	100.91
53*	CH11 / 51	97.28	6589	53	762	643	207	126	3664	99.04
54	CH11 / 51	98.16	6842	69	933	727	192	154	3637	99.99
55	CH11 / 51	97.36	6685	53	645	664	178	112	4038	99.17
56	CH11 / 51	97.58	5953	53	637	720	178	103	3739	99.24
57	CH11 / 51	97.19	5481	1530	1011	601	148	2323	3596	99.54
58	CH11 / 51	96.81	6343	58	583	559	178	93	4174	98.56
59	CH11 / 51	96.48	6671	53	591	755	178	145	4167	98.32
60	CH11 / 51	97.60	6609	53	630	937	185	103	3922	99.42
61	CH11 / 51	97.84	5494	58	754	1181	148	136	3392	99.47
62	CH11 / 51	97.56	6609	85	715	818	163	145	3610	99.34
63	CH11 / 51	97.21	6377	53	591	650	192	117	4085	98.97
64	CH11 / 51	97.45	5241	296	676	811	185	439	3378	99.09
65	CH11 / 51	97.01	6733	53	529	769	111	89	4215	98.84
66	CH11 / 51	97.78	6753	53	560	713	200	112	4174	99.62
67	CH11 / 51	97.38	6418	53	832	811	215	117	4045	99.20
68	CH11 / 51	97.97	4988	53	738	1307	170	117	3256	99.52
69	CH11 / 51	97.81	4933	53	622	1181	148	98	3304	99.32
70	CH11 / 51	96.95	6466	53	575	825	200	84	4208	98.76

Data in wt.% (TiO_2, Total) and ppm (Cr, Al, Fe, Nb, Zr, Si, V); b.d. = below detection limit; * included in Appendix C-2a

Appendix C-2b. Continued

No.	Sample / Grain	TiO_2	Cr	Al	Fe	Nb	Zr	Si	V	Total
71	CH11 / 51	98.62	6637	53	560	902	148	89	4235	100.46
72	CH11 / 51	97.68	6199	53	614	769	222	108	4051	99.43
73	CH11 / 51	98.08	5186	53	591	790	192	126	3535	99.61
74	CH11 / 51	97.54	6240	53	567	825	163	98	4099	99.30
75	CH11 / 51	98.00	6609	53	591	790	222	89	4208	99.83
76	CH11 / 51	98.33	6042	53	599	874	200	98	3800	100.03
77	CH11 / 51	96.43	5351	53	567	1139	148	108	3562	98.03
78	CH11 / 51	96.80	6452	349	676	720	200	510	4133	98.74
79	CH11 / 51	98.07	6568	53	544	755	178	84	4031	99.85
80	CH11 / 51	97.91	5686	64	614	1139	170	108	3637	99.58
81	CH11 / 51	96.58	5802	53	567	734	178	93	3467	98.17
82	CH11 / 51	97.91	6254	53	575	1091	178	89	4004	99.70
83	CH11 / 51	97.34	6603	53	606	1042	170	150	4208	99.22
84	CH11 / 51	98.26	6609	53	622	1181	192	98	3983	100.12
85	CH11 / 51	97.94	5309	58	521	1286	126	122	3236	99.50
86	CH11 / 51	97.66	6760	53	606	993	148	103	3854	99.49
87	CH11 / 51	97.22	6596	53	599	909	178	79	4153	99.05
88	CH11 / 51	98.57	6541	498	746	979	200	622	4072	100.62
89	CH11 / 51	97.35	6042	53	606	825	192	136	3426	99.00
90	CH11 / 51	98.11	6404	53	816	790	207	131	3854	99.90
91	CH11 / 51	97.90	6822	53	785	1042	163	98	3956	99.78
26*	CH48 / 11	98.90	144	85	1710	2761	5256	122	1516	100.51
7	CH48 / 11	99.59	137	79	1866	2684	5241	112	1516	101.20
8	CH48 / 11	100.40	109	90	1765	2852	5241	89	1625	102.04
27*	CH48 / 12	96.57	2306	101	1182	1762	1259	112	2345	97.87
9	CH48 / 12	99.01	2299	64	381	1727	1222	108	2393	100.19
10	CH48 / 12	99.67	2251	58	474	1748	1103	79	2338	100.83
11	CH48 / 12	98.13	2340	111	257	1720	1096	164	2393	99.31
14*	CH48 / 34	99.04	1498	180	505	2405	1125	108	911	100.01
12	CH48 / 34	99.34	1533	228	560	2531	1014	187	938	100.36
13	CH48 / 34	100.30	1539	217	637	2524	940	103	890	101.32
14	CH26 / 1	99.11	1765	138	389	2307	1777	150	2787	100.46
15	CH26 / 1	98.32	1758	153	303	1755	1695	117	2705	99.55
16	CH26 / 1	99.55	1765	243	567	2188	1621	215	2726	100.91
43*	CH26 / 4	96.37	2833	74	770	1000	2339	75	2284	97.72
17	CH26 / 4	97.27	2908	74	738	1132	2317	75	2502	98.66
18	CH26 / 4	98.50	2915	79	793	1118	2265	65	2536	99.90
54*	CH26 / 15	99.64	185	122	933	280	1984	75	1332	100.33
23	CH26 / 15	100.30	198	143	1011	377	2014	84	1394	101.07
24	CH26 / 15	99.77	185	143	979	287	1806	79	1387	100.46
25	CH26 / 15	101.10	219	138	1026	357	1762	89	1366	101.79
56*	CH26 / 17	99.59	151	53	3218	4187	688	75	1176	100.92
57	CH26 / 17	98.46	164	53	4003	4921	777	75	1258	100.02
58	CH26 / 17	96.66	157	53	4174	5697	770	75	1502	98.38
85*	CH42 / 2	96.38	2135	64	1430	1084	1866	75	2012	97.61
30	CH42 / 2	97.24	2169	64	1275	1160	1917	131	1931	98.47
31	CH42 / 2	96.07	2142	58	1562	1035	1836	84	1795	97.27
32	CH42 / 2	97.76	2183	69	1609	1098	1895	84	2121	99.04

Data in wt.% (TiO_2, Total) and ppm (Cr, Al, Fe, Nb, Zr, Si, V); b.d. = below detection limit; * included in Appendix C-2a

Appendix C-3. Mineral chemical data – Feldspar

No.	Sample	SiO_2	Al_2O3	Fe_2O_3	CaO	Na_2O	K_2O	BaO	MgO	Total
3	R15	67.74	18.69	0.12	0.10	11.82	0.20	0.04	0.01	98.72
8	R15	63.98	21.59	0.29	0.34	9.69	1.73	0.07	0.27	97.95
9	R15	67.25	18.50	0.06	0.49	11.29	0.04	0.03	0.00	97.65
10	R15	67.87	18.38	0.06	0.15	11.56	0.11	0.00	0.00	98.13
11	R15	66.19	20.03	0.00	0.41	10.58	0.80	0.03	0.02	98.07
12	R15	66.73	18.77	0.06	0.53	11.34	0.12	0.03	0.00	97.57
13	R15	65.53	19.82	0.13	0.93	10.42	0.56	0.02	0.08	97.49
14	R15	65.47	19.96	0.17	2.05	10.19	0.47	0.02	0.00	98.33
15	R15	66.81	18.74	0.05	0.46	11.37	0.11	0.03	0.00	97.57
16	R15	66.04	19.12	0.04	0.48	10.98	0.39	0.06	0.02	97.14
17	R15	66.65	19.27	0.03	0.64	11.00	0.23	0.01	0.00	97.83
18	R15	66.32	19.41	0.09	1.00	10.99	0.22	0.00	0.00	98.03
19	R15	65.41	20.01	0.08	2.09	10.38	0.27	0.05	0.01	98.30
21	R15	66.38	19.31	0.13	0.55	10.60	0.64	0.06	0.05	97.72
30	R15	67.52	18.69	0.01	0.30	11.37	0.08	0.08	0.00	98.05
31	R15	67.82	18.70	0.06	0.23	11.74	0.09	0.03	0.01	98.67
37	R15	67.07	18.78	0.13	0.37	11.30	0.15	0.05	0.00	97.85
38	R15	65.82	20.11	0.09	0.52	10.72	0.65	0.00	0.02	97.93
39	R15	64.74	20.54	0.14	2.14	10.25	0.25	0.00	0.00	98.06
40	R15	67.41	18.78	0.04	0.40	11.27	0.28	0.03	0.00	98.21
43	R15	68.24	18.28	0.06	0.09	11.66	0.06	0.03	0.00	98.42
46	R15	65.59	19.87	0.22	1.74	10.51	0.30	0.03	0.00	98.25
47	R15	63.79	21.31	0.09	3.02	9.58	0.24	0.00	0.00	98.03
49	R15	65.87	19.63	0.06	1.25	10.70	0.17	0.03	0.01	97.72
50	R15	66.73	18.86	0.01	0.36	11.14	0.12	0.10	0.01	97.33
51	R15	67.16	18.94	0.01	0.38	11.45	0.08	0.00	0.00	98.02
52	R15	67.04	19.21	0.01	0.42	11.32	0.10	0.03	0.00	98.14
53	R15	67.15	19.51	0.00	0.14	11.28	0.39	0.00	0.01	98.48
55	R15	65.47	20.27	0.09	1.74	10.41	0.36	0.00	0.00	98.34
57	R15	65.24	20.76	0.15	0.34	10.36	1.10	0.08	0.04	98.08
59	R15	65.00	20.33	0.07	2.27	10.17	0.25	0.00	0.00	98.09
60	R15	64.48	20.36	0.00	2.29	10.15	0.27	0.00	0.01	97.56
63	R15	61.64	23.13	0.13	0.35	8.82	2.92	0.02	0.11	97.12
65	R15	64.05	19.39	2.72	0.33	10.43	0.37	0.05	0.93	98.28
66	R15	67.04	18.74	0.03	0.36	11.32	0.06	0.03	0.00	97.58
67	R15	67.34	19.21	0.08	0.41	11.32	0.07	0.00	0.00	98.44
75	R15	62.37	17.74	0.12	0.57	0.60	15.29	0.94	0.00	97.63
77	R15	66.46	19.15	0.05	0.50	11.11	0.13	0.02	0.00	97.42
78	R15	67.09	18.97	0.02	0.39	11.32	0.06	0.06	0.00	97.92
81	R15	66.80	18.82	0.02	0.33	11.17	0.08	0.02	0.00	97.23
82	R15	67.22	18.95	0.09	0.60	11.39	0.16	0.02	0.02	98.45
83	R15	67.04	18.69	0.06	0.21	11.59	0.10	0.04	0.00	97.73
84	R15	64.81	20.66	0.04	2.42	9.96	0.26	0.00	0.01	98.16
88	R15	67.50	18.87	0.04	0.26	11.66	0.06	0.09	0.00	98.48
90	R15	66.26	19.48	0.09	0.98	11.08	0.27	0.04	0.00	98.19
91	R15	66.45	19.27	0.01	0.77	11.10	0.06	0.02	0.00	97.68
92	R15	66.69	18.99	0.09	0.43	11.15	0.12	0.05	0.00	97.51
93	R15	67.23	18.84	0.09	0.33	11.51	0.16	0.05	0.00	98.21
97	R15	65.93	19.61	0.11	0.97	11.12	0.24	0.00	0.01	97.99
98	R15	66.55	18.87	0.09	0.21	11.46	0.11	0.03	0.00	97.31
101	R15	66.93	18.78	0.10	0.25	11.38	0.22	0.05	0.01	97.72

Data in wt.%; Total iron is expressed as Fe_2O_3

Appendix C-3. Continued

No.	Sample	SiO_2	Al_2O3	Fe_2O_3	CaO	Na_2O	K_2O	BaO	MgO	Total
106	R15	67.28	18.87	0.13	0.29	11.62	0.07	0.00	0.01	98.27
108	R15	64.41	20.47	0.10	2.21	10.17	0.46	0.01	0.02	97.86
109	R15	66.82	18.67	0.07	0.26	11.53	0.12	0.02	0.00	97.49
113	R15	64.79	20.32	0.01	2.00	10.31	0.38	0.00	0.01	97.82
118	R15	65.39	20.19	0.02	1.84	10.35	0.36	0.05	0.00	98.20
119	R15	67.58	18.48	0.04	0.11	11.50	0.17	0.06	0.01	97.96
120	R15	64.10	20.90	0.09	2.84	9.76	0.31	0.04	0.00	98.04
121	R15	65.00	20.31	0.11	2.04	10.21	0.26	0.06	0.00	97.98
122	R15	67.31	18.43	0.00	0.31	11.27	0.06	0.01	0.02	97.40
157	R27	67.53	18.77	0.04	0.10	11.75	0.06	0.00	0.00	98.25
158	R27	67.12	18.65	0.00	0.12	11.86	0.03	0.07	0.00	97.86
173	R27	66.58	18.61	0.03	0.18	11.79	0.03	0.05	0.01	97.27
175	R27	67.05	19.06	0.01	0.36	11.58	0.04	0.04	0.00	98.14
176	R27	68.00	18.56	0.03	0.14	11.91	0.02	0.06	0.00	98.72
179	R27	67.93	18.39	0.08	0.08	11.77	0.00	0.09	0.00	98.35
180	R27	67.67	18.49	0.02	0.17	11.79	0.04	0.00	0.00	98.18
186	R27	67.68	18.63	0.09	0.18	11.65	0.03	0.01	0.01	98.27
187	R27	67.46	18.44	0.08	0.13	11.75	0.03	0.02	0.01	97.92
190	R27	67.22	18.71	0.00	0.17	11.50	0.07	0.02	0.00	97.70
191	R27	67.46	18.48	0.06	0.07	11.73	0.02	0.04	0.00	97.86
192	R27	67.16	18.38	0.00	0.29	11.50	0.02	0.00	0.02	97.37
194	R27	67.94	18.27	0.07	0.29	11.75	0.01	0.00	0.00	98.33
195	R27	68.16	18.55	0.07	0.05	11.63	0.03	0.00	0.00	98.49
198	R27	67.83	18.73	0.03	0.06	11.87	0.01	0.06	0.00	98.58
200	R27	67.86	18.67	0.01	0.10	11.69	0.01	0.00	0.00	98.34
207	R27	67.76	18.44	0.11	0.08	11.67	0.00	0.02	0.00	98.07
213	R27	67.88	18.71	0.00	0.14	11.84	0.02	0.00	0.00	98.60
220	R27	67.20	18.71	0.00	0.16	11.54	0.02	0.01	0.00	97.65
227	R27	66.88	18.46	0.10	0.15	11.64	0.03	0.00	0.01	97.27
232	R27	67.35	18.65	0.03	0.16	11.63	0.02	0.00	0.00	97.84
233	R27	67.81	18.59	0.06	0.17	11.62	0.02	0.00	0.00	98.28
239	R27	67.15	18.87	0.09	0.27	11.61	0.04	0.00	0.00	98.03
240	R27	67.29	18.67	0.00	0.23	11.40	0.01	0.05	0.01	97.65
251	R27	66.84	18.89	0.01	0.15	11.35	0.01	0.00	0.01	97.26
257	R27	67.70	18.62	0.06	0.17	11.58	0.00	0.00	0.00	98.13
263	R27	67.29	18.89	0.05	0.25	11.46	0.02	0.00	0.00	97.97
270	R27	67.24	18.36	0.03	0.66	11.45	0.04	0.01	0.00	97.80
271	R27	67.00	19.06	0.02	0.47	11.41	0.02	0.03	0.00	98.01
272	R27	67.77	18.63	0.10	0.15	11.72	0.02	0.04	0.00	98.42
274	R27	67.66	18.75	0.04	0.22	11.60	0.04	0.00	0.01	98.32
275	R27	66.24	19.28	0.27	0.07	10.91	0.43	0.05	0.17	97.41
276	R27	66.90	18.71	0.08	0.14	11.56	0.04	0.00	0.00	97.42
281	R27	67.39	18.52	0.07	0.07	11.81	0.02	0.04	0.00	97.92
282	R27	67.90	18.30	0.34	0.06	11.65	0.05	0.00	0.00	98.30
297	R27	67.20	18.59	0.18	0.05	11.76	0.02	0.10	0.00	97.91
298	R27	67.79	18.57	0.00	0.09	11.73	0.02	0.01	0.00	98.22
306	R27	67.72	18.60	0.03	0.08	11.82	0.01	0.03	0.00	98.29
311	R27	68.67	18.70	0.00	0.09	11.55	0.02	0.06	0.01	99.11
312	R27	68.09	18.77	0.06	0.07	11.48	0.09	0.00	0.00	98.56
313	R27	66.69	18.53	0.00	0.44	11.69	0.03	0.02	0.00	97.40
314	R27	67.23	18.79	0.09	0.07	11.58	0.02	0.00	0.00	97.78
315	R27	67.78	18.67	0.04	0.10	11.46	0.01	0.00	0.00	98.06

Data in wt.%; Total iron is expressed as Fe_2O_3

Appendix C-3. Continued

No.	Sample	SiO_2	Al_2O3	Fe_2O_3	CaO	Na_2O	K_2O	BaO	MgO	Total
317	R27	67.36	18.86	0.11	0.09	11.76	0.02	0.00	0.00	98.20
318	R27	67.25	18.53	0.01	0.05	11.61	0.04	0.00	0.00	97.49
321	R27	66.88	18.90	0.08	0.05	11.32	0.18	0.00	0.06	97.46
322	R27	67.33	18.84	0.13	0.16	11.54	0.04	0.03	0.00	98.08
324	R27	67.47	18.64	0.11	0.31	11.88	0.03	0.00	0.00	98.44
327	R27	67.66	18.88	0.13	0.15	11.73	0.06	0.04	0.00	98.64
330	R27	68.02	18.55	0.06	0.27	11.44	0.02	0.05	0.00	98.40

Data in wt.%; Total iron is expressed as Fe_2O_3

Appendix C-4. Mineral chemical data – Mica

No.	Sample	SiO_2	TiO_2	Al_2O_3	Fe_2O_3	MnO	MgO	CaO	Na_2O	K_2O	Cl	F	Cr_2O_3	BaO	Total
2	R15	50.94	0.22	26.63	3.43	0.00	3.29	0.00	0.05	10.74	0.00	0.09	0.11	0.44	95.94
6	R15	47.68	0.33	29.95	4.53	0.01	2.13	0.00	0.50	9.87	0.01	0.24	0.06	0.32	95.62
7	R15	47.38	0.54	27.93	4.81	0.16	3.05	0.00	0.16	10.75	0.00	0.00	0.03	0.67	95.49
26	R15	45.93	0.55	33.07	1.49	0.00	1.42	0.00	0.61	9.68	0.00	0.04	0.03	0.24	93.06
27	R15	44.74	0.49	33.28	2.76	0.00	0.99	0.00	1.11	8.72	0.01	0.05	0.08	0.94	93.17
28	R15	46.11	1.39	30.41	4.89	0.03	1.53	0.00	0.36	10.03	0.00	0.10	0.00	0.44	95.29
33	R15	44.74	0.57	31.48	4.26	0.00	1.45	0.00	0.32	9.30	0.01	0.00	0.09	0.74	92.95
34	R15	46.87	1.82	28.21	5.28	0.05	1.94	0.00	0.12	10.78	0.00	0.07	0.01	0.36	95.50
36	R15	47.68	0.90	30.21	3.48	0.00	2.36	0.00	0.28	10.73	0.01	0.06	0.04	0.65	96.39
41	R15	45.60	0.36	35.41	2.41	0.03	0.72	0.00	1.33	9.08	0.00	0.12	0.03	0.27	95.34
44	R15	48.78	0.54	28.91	3.68	0.00	2.64	0.00	0.22	10.52	0.00	0.00	0.05	0.60	95.94
45	R15	49.70	0.48	28.16	3.00	0.06	3.41	0.00	0.19	10.70	0.01	0.04	0.02	0.27	96.05
58	R15	48.35	0.60	27.27	5.39	0.06	2.87	0.00	0.21	9.90	0.01	0.02	0.06	1.05	95.79
61	R15	48.91	0.53	28.44	4.09	0.07	2.55	0.00	0.18	10.55	0.00	0.06	0.04	0.69	96.11
64	R15	47.16	0.92	31.51	3.48	0.11	1.92	0.00	0.21	10.23	0.01	0.08	0.05	0.23	95.90
69	R15	46.85	0.39	33.77	2.97	0.06	0.94	0.00	0.41	10.77	0.00	0.36	0.04	0.20	96.74
70	R15	48.58	0.38	31.98	1.56	0.04	2.04	0.00	0.37	10.20	0.00	0.15	0.08	0.38	95.75
72	R15	45.17	0.45	34.86	3.07	0.02	0.90	0.00	1.22	8.68	0.00	0.05	0.02	1.87	96.31
73	R15	46.78	0.97	32.42	3.79	0.00	1.05	0.00	0.41	10.70	0.00	0.16	0.03	0.04	96.34
76	R15	46.93	2.48	30.81	1.90	0.02	1.84	0.00	0.30	10.26	0.01	0.06	0.09	0.26	94.96
85	R15	49.07	0.15	32.63	1.81	0.04	2.09	0.09	0.30	9.12	0.01	0.12	0.10	0.24	95.77
99	R15	48.26	2.06	32.21	1.22	0.00	2.21	0.00	0.40	10.50	0.01	0.14	0.05	0.28	97.33
100	R15	49.28	0.63	28.21	4.36	0.11	2.46	0.00	0.26	10.21	0.00	0.25	0.04	0.30	96.11
102	R15	49.26	0.44	26.77	4.94	0.06	3.35	0.00	0.10	10.56	0.01	0.02	0.03	0.58	96.11
103	R15	47.47	0.46	29.63	4.83	0.09	2.08	0.00	0.24	11.03	0.00	0.07	0.00	0.27	96.17
104	R15	47.04	0.48	29.00	5.20	0.12	2.31	0.00	0.19	10.93	0.00	0.09	0.06	0.34	95.76
105	R15	48.25	0.47	27.62	4.51	0.06	2.74	0.00	0.14	11.03	0.01	0.10	0.02	0.26	95.21
112	R15	48.05	0.97	29.30	4.77	0.02	1.62	0.00	0.27	10.03	0.00	0.53	0.07	0.15	95.78
114	R15	49.62	0.60	28.20	4.49	0.13	2.26	0.00	0.19	10.04	0.00	0.30	0.00	0.27	96.10
115	R15	49.85	0.28	26.71	4.02	0.04	3.40	0.00	0.09	10.92	0.00	0.00	0.01	0.62	95.95
116	R15	47.64	0.84	30.27	3.53	0.00	2.14	0.00	0.24	10.45	0.00	0.01	0.02	0.57	95.70
117	R15	46.90	1.10	32.73	2.38	0.06	1.52	0.00	0.29	10.49	0.01	0.10	0.01	0.58	96.16
128	R15	45.67	0.61	31.98	4.34	0.01	1.47	0.00	0.32	10.67	0.00	0.05	0.04	0.71	95.87
138	R15	47.73	0.15	29.37	5.38	0.07	2.14	0.00	0.24	10.53	0.02	0.09	0.02	0.84	96.57
145	R27	48.34	0.38	24.28	5.36	0.12	2.79	0.08	0.11	8.73	0.02	0.26	0.05	0.01	90.52
146	R27	48.62	0.32	29.31	4.10	0.10	2.50	0.00	0.18	10.73	0.00	0.10	0.01	0.14	96.11
147	R27	47.65	0.43	29.54	5.23	0.02	1.90	0.07	0.20	10.43	0.01	0.22	0.02	0.16	95.87
148	R27	48.33	0.42	30.52	2.92	0.03	2.63	0.00	0.18	11.15	0.01	0.30	0.06	0.22	96.76
149	R27	49.38	0.36	26.91	5.34	0.08	2.80	0.00	0.09	10.35	0.00	0.20	0.01	0.14	95.67
150	R27	48.02	0.43	31.21	3.04	0.03	2.07	0.00	0.59	10.38	0.00	0.18	0.08	0.34	96.36
151	R27	48.30	0.57	31.41	3.07	0.00	2.27	0.00	1.23	9.41	0.00	0.19	0.07	0.38	96.90
152	R27	49.48	0.27	27.12	5.10	0.18	2.67	0.00	0.14	10.22	0.01	0.17	0.03	0.15	95.53
153	R27	48.99	0.39	28.63	5.26	0.05	1.98	0.01	0.12	9.45	0.00	0.16	0.02	0.20	95.26
154	R27	48.53	0.34	27.52	5.31	0.05	2.58	0.00	0.09	10.47	0.00	0.21	0.02	0.21	95.33
155	R27	46.11	0.69	31.11	2.16	0.08	2.04	0.00	1.02	9.26	0.01	0.13	0.07	0.24	92.91
159	R27	50.17	0.40	25.38	6.52	0.13	2.57	0.00	0.04	9.67	0.01	0.28	0.03	0.00	95.19
160	R27	46.15	0.07	36.69	1.45	0.02	0.70	0.00	1.33	9.72	0.00	0.05	0.00	0.17	96.34
161	R27	49.16	0.91	28.04	4.13	0.10	3.15	0.00	0.32	10.72	0.00	0.29	0.08	0.27	97.17
163	R27	47.83	0.57	28.73	5.50	0.09	2.18	0.00	0.14	10.78	0.00	0.08	0.02	0.19	96.11
164	R27	48.15	0.19	29.95	4.48	0.21	1.54	0.06	0.14	10.18	0.02	0.09	0.03	0.27	95.31
165	R27	49.71	0.29	26.17	4.89	0.12	2.93	0.00	0.10	10.54	0.01	0.25	0.08	0.29	95.37

Data in wt.%; Total iron is expressed as Fe_2O_3

Appendix C-4. Continued

No.	Sample	SiO_2	TiO_2	Al_2O_3	Fe_2O_3	MnO	MgO	CaO	Na_2O	K_2O	Cl	F	Cr_2O_3	BaO	Total
166	R27	49.49	0.34	27.73	4.50	0.08	2.68	0.00	0.12	10.76	0.00	0.20	0.04	0.20	96.13
167	R27	48.54	0.40	28.31	4.67	0.08	2.53	0.01	0.16	10.36	0.01	0.25	0.05	0.51	95.88
168	R27	47.90	0.41	32.10	2.06	0.00	2.15	0.00	0.60	10.52	0.00	0.11	0.00	0.29	96.15
169	R27	49.20	0.69	29.67	3.33	0.08	2.08	0.01	0.27	9.59	0.01	0.08	0.01	0.11	95.13
170	R27	49.55	0.54	28.70	3.25	0.08	3.05	0.00	0.45	10.36	0.00	0.21	0.07	0.60	96.85
171	R27	46.89	0.43	32.42	2.28	0.04	1.89	0.00	0.45	9.44	0.02	0.11	0.04	0.34	94.35
174	R27	50.36	0.30	26.25	4.75	0.17	3.19	0.01	0.11	10.24	0.00	0.11	0.03	0.08	95.60
177	R27	48.19	0.74	28.86	4.37	0.01	2.49	0.00	0.17	10.90	0.00	0.06	0.05	0.17	96.01
181	R27	50.48	0.22	26.70	4.79	0.09	2.30	0.03	0.09	9.48	0.02	0.17	0.04	0.15	94.56
182	R27	49.50	0.40	27.31	4.05	0.12	3.47	0.00	0.17	10.92	0.00	0.21	0.01	0.29	96.46
183	R27	49.17	0.42	28.67	3.78	0.10	2.74	0.04	0.17	10.50	0.00	0.24	0.03	0.31	96.17
184	R27	48.16	0.45	29.89	4.36	0.00	2.36	0.00	0.20	10.53	0.01	0.17	0.04	0.25	96.42
185	R27	46.22	0.34	34.97	2.12	0.03	1.03	0.00	1.49	8.21	0.01	0.05	0.11	0.84	95.41
188	R27	48.03	0.52	32.22	3.14	0.00	1.28	0.00	0.26	10.49	0.00	0.15	0.00	0.21	96.29
189	R27	48.86	0.41	30.20	4.27	0.08	1.38	0.00	0.33	10.01	0.01	0.10	0.00	0.61	96.26
193	R27	46.63	0.39	34.37	2.47	0.04	1.11	0.00	0.64	10.52	0.01	0.00	0.05	0.34	96.56
196	R27	48.10	0.48	30.34	3.79	0.01	2.18	0.00	0.22	11.05	0.00	0.12	0.03	0.21	96.53
197	R27	50.16	0.27	26.17	5.18	0.08	2.76	0.00	0.08	10.73	0.00	0.24	0.01	0.35	96.03
201	R27	45.20	1.28	34.81	2.92	0.09	0.70	0.00	0.62	10.40	0.00	0.00	0.08	0.44	96.53
202	R27	50.14	0.31	27.31	3.76	0.00	3.35	0.00	0.12	11.05	0.00	0.08	0.03	0.14	96.29
203	R27	48.70	0.35	26.11	5.72	0.06	2.59	0.00	0.07	10.56	0.00	0.29	0.04	0.15	94.64
204	R27	46.92	0.52	29.68	3.33	0.00	2.40	0.00	0.33	10.20	0.01	0.19	0.00	0.49	94.05
205	R27	48.62	0.29	29.77	3.01	0.07	2.68	0.00	0.32	10.59	0.00	0.23	0.08	0.26	95.92

Data in wt.%; Total iron is expressed as Fe_2O_3

Appendix C-5. Mineral chemical data – Garnet

No.	Sample / grain	SiO_2	TiO_2	Al_2O_3	Fe_2O_3	MnO	MgO	CaO	Cr_2O_3	Total
37	R11 / 3	39.54	0.07	21.98	20.59	0.42	9.99	6.92	0.11	99.61
40	R11 / 6	38.34	0.17	21.51	26.30	0.83	3.42	9.66	0.05	100.28
42	R11 / 8	37.73	0.17	26.76	6.97	0.04	0.13	22.47	0.06	94.34
43	R11 / 9	37.98	0.24	21.56	24.07	1.61	2.87	10.76	0.12	99.21
46	R11 / 12	37.97	0.18	21.22	28.38	0.44	2.04	9.75	0.09	100.07
47	R11 / 13	39.16	0.10	22.22	20.38	0.49	8.15	8.81	0.02	99.33
48	R11 / 14	37.90	0.00	21.85	29.87	2.12	4.23	3.62	0.07	99.66
51	R11 / 17	38.62	0.04	21.72	29.56	0.90	6.85	2.88	0.02	100.59
52	R11 / 18	38.35	0.10	21.64	24.10	1.08	4.01	10.81	0.04	100.14
53	R11 / 19	38.50	0.08	21.74	27.85	0.37	3.30	9.24	0.04	101.11
54	R11 / 20	38.52	0.04	22.10	29.50	0.89	7.10	2.61	0.06	100.81
55	R11 / 21	37.75	0.15	21.31	24.13	7.06	1.22	9.00	0.07	100.69
56	R11 / 22	39.02	0.07	22.04	22.21	0.83	7.13	9.06	0.02	100.39
57	R11 / 23	38.69	0.11	21.99	23.31	0.81	4.93	10.76	0.04	100.64
58	R11 / 24	38.42	0.16	21.47	23.95	1.34	3.19	11.47	0.03	100.03
59	R11 / 25	38.18	0.02	21.83	31.01	2.54	5.38	1.90	0.08	100.94
60	R11 / 26	38.77	0.11	21.59	21.41	0.81	3.50	14.16	0.05	100.40
61	R11 / 27	38.86	0.07	22.05	23.76	0.72	6.45	8.70	0.03	100.64
62	R11 / 28	38.28	0.01	21.74	31.59	2.24	5.94	1.21	0.04	101.06
63	R11 / 29	38.54	0.03	21.86	30.77	2.03	6.16	1.57	0.07	101.03
64	R11 / 30 core	37.82	0.13	21.25	28.74	1.79	1.69	8.83	0.05	100.29
238	R11 / 30 rim	37.71	0.11	21.53	28.55	0.55	2.02	9.57	0.02	100.06
65	R11 / 31 core	39.62	0.05	22.32	21.63	0.57	8.17	8.36	0.04	100.76
239	R11 / 31 rim	39.16	0.08	22.25	22.24	0.72	7.57	7.82	0.06	99.89
72	R14 / 7 core	38.28	0.14	21.67	24.65	0.96	3.22	11.49	0.04	100.44
253	R14 / 7 rim	37.99	0.15	21.56	24.16	1.71	3.01	11.54	0.04	100.16
73	R14 / 8 core	38.98	0.07	22.21	20.04	0.61	7.01	11.08	0.05	100.05
254	R14 / 8 rim	39.30	0.07	21.79	20.25	0.61	7.22	10.61	0.07	99.91
74	R14 / 10	37.84	0.11	21.55	26.42	1.81	2.95	9.11	0.07	99.86
75	R14 / 11 core	38.96	0.02	22.23	26.39	0.35	8.77	3.57	0.06	100.35
255	R14 / 11 rim	38.97	0.02	22.10	26.44	0.38	8.84	3.50	0.06	100.32
77	R14 / 13	37.60	0.11	21.61	28.71	1.68	2.58	8.06	0.04	100.39
78	R14 / 14	37.80	0.12	21.53	27.33	0.63	2.65	10.37	0.08	100.50
79	R14 / 15	38.37	0.02	22.03	30.60	1.66	6.58	1.56	0.03	100.85
80	R14 / 16	37.73	0.06	21.24	21.84	10.26	2.16	7.54	0.09	100.91
82	R14 / 18	39.24	0.25	21.83	19.94	0.29	7.94	10.62	0.06	100.17
84	R14 / 20	38.53	0.12	21.60	23.45	2.85	3.76	10.46	0.06	100.83
85	R14 / 21	38.28	0.04	21.85	27.75	1.04	5.50	5.97	0.04	100.48
86	R14 / 22	38.98	0.05	21.57	22.87	1.17	6.42	9.08	0.07	100.21
87	R14 / 23	38.43	0.19	21.64	23.08	1.72	4.36	10.75	0.04	100.21
88	R14 / 24	37.49	0.22	21.30	20.49	8.81	0.55	11.45	0.03	100.34
89	R14 / 25	38.38	0.08	21.82	22.49	6.70	3.56	7.92	0.12	101.07
90	R14 / 26	38.87	0.02	22.21	27.33	1.60	7.48	3.29	0.05	100.84
91	R14 / 27	38.86	0.18	21.97	22.40	0.81	5.96	10.16	0.04	100.38
92	R14 / 28 core	37.88	0.04	21.63	29.90	3.69	4.50	3.08	0.04	100.75
256	R14 / 28 rim	37.82	0.04	21.61	29.66	4.11	4.24	3.13	0.05	100.66
93	R14 / 29	38.21	0.04	21.53	28.29	4.22	4.03	4.51	0.07	100.90
94	R14 / 30	38.93	0.09	22.30	24.90	0.52	7.70	6.08	0.14	100.65
95	R14 / 31 core	39.27	0.09	22.11	20.86	0.73	7.18	10.29	0.07	100.59
257	R14 / 31 rim	38.41	0.11	22.56	20.76	0.77	6.95	10.25	0.10	99.91
97	R14 / 34	38.67	0.03	22.06	27.16	1.00	5.98	6.04	0.05	100.99

Data in wt.%; Total iron is expressed as Fe_2O_3

Appendix C-5. Continued

No.	Sample / grain	SiO_2	TiO_2	Al_2O_3	Fe_2O_3	MnO	MgO	CaO	Cr_2O_3	Total
98	R14 / 35	38.72	0.87	19.21	3.81	0.30	0.04	36.86	0.06	99.86
99	R14 / 36	39.46	0.04	22.13	20.66	0.41	7.10	10.84	0.03	100.68
100	R14 / 37	38.48	0.03	22.01	27.44	0.91	6.21	5.32	0.05	100.45
101	R14 / 38 core	37.77	0.00	21.87	29.37	1.45	4.13	5.93	0.04	100.56
258	R14 / 38 rim	37.46	0.03	22.18	29.38	1.59	3.87	5.87	0.05	100.43
102	R14 / 39 core	38.27	0.02	21.76	29.99	1.03	5.50	4.01	0.03	100.61
259	R14 / 39 rim	38.15	0.03	21.68	30.14	1.04	5.69	3.82	0.04	100.58
103	R14 / 40	38.61	0.04	22.08	25.19	1.40	5.78	7.61	0.10	100.81
104	R14 / 42	38.40	0.14	21.63	26.41	0.46	2.67	11.05	0.04	100.79
105	R14 / 43	38.62	0.07	21.82	26.53	1.09	5.40	7.09	0.08	100.69
145	R15 / 1 core	38.00	0.16	21.46	28.27	0.71	1.08	11.44	0.01	101.14
145	R15 / 1 rim	38.00	0.14	21.56	28.11	0.32	1.24	11.42	0.01	100.81
146	R15 / 2 core	38.59	0.12	21.84	27.38	0.36	3.21	9.79	0.04	101.33
146	R15 / 2 rim	38.41	0.12	21.65	27.53	0.31	3.16	9.79	0.05	101.02
148	R15 / 4	39.12	0.05	22.22	26.52	1.31	7.60	4.46	0.02	101.30
149	R15 / 5 core	38.38	0.06	21.79	26.95	0.99	3.47	9.46	0.03	101.12
149	R15 / 5 rim	38.60	0.04	21.78	25.88	0.85	3.96	9.61	0.03	100.75
150	R15 / 6 core	38.08	0.00	21.83	33.36	2.42	4.29	1.25	0.05	101.28
150	R15 / 6 rim	37.87	0.04	21.59	33.93	2.85	3.57	1.26	0.06	101.16
25	SM151 / 1	38.31	0.03	21.62	23.80	1.61	1.47	13.72	0.06	100.62
34	SM151 / 2	37.78	0.10	21.68	20.95	4.66	0.87	14.42	0.02	100.48
38	SM151 / 3	38.16	0.05	21.61	23.22	2.28	1.25	13.93	0.06	100.55
40	SM151 / 4	38.33	0.06	21.69	22.36	3.24	1.24	13.95	0.05	100.91

Data in wt.%; Total iron is expressed as Fe_2O_3

Appendix D-1. U–Pb SHRIMP-II zircon data

Sample CH52, Chios Island

						Isotopic ratios						Apparent ages (Ma)			
Analysis label	$^{206}Pb_c$ %	U ppm	Th ppm	$^{232}Th/^{238}U$	$^{206}Pb^*$ ppm	$^{207}Pb^*/^{206}Pb^*$	± %	$^{207}Pb^*/^{235}U$	± %	$^{206}U/^{238}Pb^*$	± %	$^{206}Pb/^{238}U$	± 1σ	$^{207}Pb/^{206}Pb$	± 1σ
CH52.1.1	0.08	638	122	0.20	263	0.1684	0.68	11.148	0.78	0.4801	0.38	2528	9	2542	11
CH52.2.1	29.11	2942	2016	0.71	116	0.059	82	0.26	83	0.0325	4.9	206	10	560	1800
CH52.3.1	0.02	1098	197	0.19	360	0.12646	0.39	6.651	0.49	0.3814	0.3	2083	5	2049	6.9
CH52.4.1	24.99	3453	1385	0.41	171	0.047	35	0.282	35	0.04323	2	273	5	66	830
CH52.5.1	0.27	415	476	1.19	37.2	0.0609	2.2	0.875	2.3	0.10424	0.65	639	4	636	46
CH52.6.1	0.69	661	191	0.30	32	0.0545	4	0.421	4	0.05604	0.57	352	2	390	89
CH52.10.1	3.95	909	370	0.42	34.7	0.0414	15	0.243	15	0.0426	1.1	269	3	-267	390
CH52.12.1	1.15	338	139	0.42	117	0.1066	6.5	5.83	6.7	0.397	1.9	2155	35	1740	120
CH52.13.1	--	243	45	0.19	22.9	0.0882	10	1.36	11	0.1116	3.5	682	23	1387	200
CH52.14.1	1.71	526	522	1.02	24.3	0.0515	8.1	0.376	8.2	0.05289	0.74	332	2	265	190
CH52.15.1	1.83	111	39	0.36	7.9	0.0652	11	0.729	11	0.0812	1.4	503	7	780	230
CH52.16.1	1.25	260	114	0.45	13.1	0.0548	7.1	0.438	7.1	0.05798	0.95	363	3	405	160
CH52.17.1	0.55	253	53	0.22	17.4	0.0638	5.3	0.703	5.4	0.07992	0.9	496	4	736	110
CH52.18.1	3.15	120	73	0.63	6.13	0.056	22	0.44	22	0.0574	2	360	7	435	490
CH52.19.1	0.70	323	92	0.29	25.3	0.0595	3.6	0.742	3.7	0.09045	0.74	558	4	585	79
CH52.20.1	0.29	319	109	0.35	67.8	0.1156	1	3.936	1.2	0.2469	0.62	1422	8	1890	18
CH52.21.1	6.36	1831	1279	0.72	69.6	0.0525	7.8	0.299	7.8	0.04139	0.64	261	2	306	180
CH52.22.1	0.72	312	216	0.72	13.8	0.0544	4.7	0.384	4.8	0.0512	0.86	322	3	386	110
CH52.23.1	0.42	94	46	0.50	31.2	0.1304	1.3	6.87	1.7	0.3822	1	2086	18	2104	23
CH52.24.1	1.20	554	142	0.27	59.3	0.0563	5.7	0.954	5.8	0.1229	0.9	747	6	464	130
CH52.25.1	0.80	413	77	0.19	28	0.0544	4.5	0.588	4.5	0.07835	0.77	486	4	389	100
CH52.26.1	0.41	799	30	0.04	57.5	0.0563	2.6	0.647	2.6	0.08336	0.6	516	3	464	57
CH52.27.1	9.58	157	18	0.12	13.1	0.071	23	0.85	23	0.0875	1.9	541	10	952	470
CH52.28.1	0.97	133	86	0.67	10.1	0.0635	6.8	0.767	6.9	0.0875	1.3	541	7	726	140
CH52.29.1	1.28	167	141	0.87	11.1	0.0582	6.9	0.614	7	0.07653	1.1	475	5	537	150
CH52.30.1	0.99	302	17	0.06	21.3	0.0551	6.2	0.618	6.2	0.08143	0.93	505	5	415	140
CH52.31.1	0.35	429	34	0.08	29.2	0.0564	2.9	0.615	3	0.07902	0.66	490	3	470	64

Note: Pb_c and Pb^* indicate the common and radiogenic Pb portions, respectively. Horizontal line separates two analytical sessions, with standard calibration errors (1σ) of 0.19% (upper data) and 0.40% (lower data); not included in the above errors.

Appendix D-1. Continued

Sample CH11, Chios Island

Analysis label	$^{206}Pb_c$ %	U ppm	Th ppm	$^{232}Th/^{238}U$	$^{206}Pb^*$ ppm	$^{207}Pb^*/^{206}Pb^*$	± %	$^{207}Pb^*/^{235}U$	± %	$^{206}U/^{238}Pb^*$	± %	$^{206}Pb/^{238}U$ Apparent ages (Ma)	± 1σ	$^{207}Pb/^{206}Pb$ Apparent ages (Ma)	± 1σ
CH-11.1.1	0.14	365	92	0.26	19.3	0.0527	2.5	0.448	2.6	0.06161	0.67	385	3	316	58
CH-11.2.1	--	224	63	0.29	29.3	0.07093	1.3	1.491	1.5	0.1524	0.66	915	6	955	27
CH-11.3.1	--	518	174	0.35	26.8	0.05618	1.7	0.4664	1.8	0.0602	0.57	377	2	460	37
CH-11.4.1	--	382	231	0.63	19.4	0.0536	2.2	0.437	2.3	0.05905	0.62	370	2	355	50
CH-11.5.1	0.19	549	320	0.60	46.7	0.06100	1.3	0.832	1.4	0.09887	0.41	608	2	639	28
CH-11.6.1	--	397	33	0.09	94.2	0.11322	0.85	4.31	2.4	0.276	2.3	1571	31	1852	15
CH-11.6.2	0.10	548	56	0.11	36.0	0.05625	1.5	0.5926	1.6	0.07641	0.54	475	3	462	34
CH-11.7.1	0.27	92	126	1.41	13.9	0.0723	2.9	1.737	3.1	0.1743	1.1	1036	10	994	58
CH-11.8.1	--	35	49	1.45	5.29	0.0764	4.7	1.862	4.9	0.1768	1.5	1049	15	1105	93
CH-11.9.1	0.04	35	26	0.77	4.82	0.0730	4.5	1.628	4.7	0.1617	1.6	966	14	1014	91
CH-11.10.1	0.22	175	44	0.26	22.8	0.0719	1.8	1.504	2	0.1517	0.72	910	6	984	37
CH-11.11.1	0.01	334	256	0.79	111	0.13437	0.55	7.182	0.73	0.3877	0.48	2112	8	2156	10
CH-11.12.1	0.15	96	101	1.08	29.3	0.1126	1.6	5.48	2.8	0.353	2.3	1949	38	1842	29
CH-11.13.1	--	113	77	0.70	36.3	0.1266	0.86	6.556	1.5	0.3755	1.2	2055	21	2052	15
CH-11.14.1	1.51	40	22	0.57	3.86	0.0539	8.4	0.82	8.8	0.1104	2.6	675	17	366	190
CH-11.15.1	0.08	286	92	0.33	25.0	0.0615	1.8	0.861	1.9	0.10152	0.57	623	3	657	39
CH11.1.1	0.17	354	233	0.68	108	0.1315	0.86	6.441	1	0.3553	0.59	1960	10	2118	15
CH11.2.1	0.08	659	198	0.31	198	0.1204	0.45	5.796	0.63	0.3491	0.44	1930	7	1962	8
CH11.3.1	1.82	104	41	0.40	8.34	0.0563	11	0.709	11	0.0913	1.3	563	7	463	240
CH11.4.1	0.52	275	164	0.62	30.1	0.0649	3.2	1.137	3.3	0.12705	0.68	771	5	771	68
CH11.5.1	0.32	336	308	0.95	98	0.11407	0.8	5.315	1.3	0.338	0.97	1877	16	1865	14
CH11.6.1	0.66	181	183	1.04	28.7	0.071	4	1.791	4.1	0.183	0.94	1083	10	957	82
CH11.7.1	1.95	635	378	0.61	55.3	0.0633	4.2	0.868	4.3	0.09948	0.62	611	4	719	90
CH11.8.1	0.09	745	580	0.80	253	0.1381	0.44	7.519	0.57	0.3949	0.37	2146	7	2204	8
CH11.9.1	0.49	522	229	0.45	23.4	0.0541	6.8	0.387	6.8	0.05191	0.74	326	2	375	150
CH11.1.1b	0.41	223	143	0.66	11.8	0.0563	3.9	0.475	4.5	0.0612	2.1	383	8	464	87
CH11.2.1b	2.72	103	84	0.84	8.78	0.0517	11	0.687	11	0.0963	1.5	593	9	273	260
CH11.3.1b	2.78	132	69	0.55	7.09	0.0544	18	0.457	18	0.0609	2.9	381	11	387	410

Note: Pb_c and Pb^* indicate the common and radiogenic Pb portions, respectively. Horizontal lines separate three analytical sessions, with standard calibration errors (1σ) of 0.23% (upper data), 0.19% (middle data) and 0.40% (lower data); not included in the above errors.

Appendix D-1. Continued

Sample R27, Makri Unit

				Isotopic ratios								Apparent ages (Ma)				
Analysis label	$^{206}Pb_c$ %	U ppm	Th ppm	$^{232}Th/^{238}U$	$^{206}Pb^*$ ppm	$^{207}Pb^*/^{206}Pb^*$	± %	$^{207}Pb^*/^{235}U$	± %	$^{206}U/^{238}Pb^*$	± %	$^{206}Pb/^{238}U$	± 1σ	$^{207}Pb/^{206}Pb$	± 1σ	
R27.1.1	0.19	127	111	0.90	5.38	0.0531	4.3	0.36	4.6	0.04914	1.7	309	5	333	97	#
R27.2.1	0.17	693	317	0.47	30	0.0518	2.4	0.3586	2.8	0.05026	1.4	316	4	275	54	#
R27.3.1	0.24	834	457	0.57	29.8	0.0504	2	0.2887	2.5	0.04154	1.4	262	4	214	47	
R27.4.1	0.13	1604	522	0.34	67.9	0.05072	1.2	0.3441	1.9	0.0492	1.4	310	4	228	28	
R27.5.1	0.09	419	79	0.19	17	0.0521	2.3	0.3383	2.9	0.04709	1.8	297	5	290	53	
R27.6.1	0.15	153	144	0.97	5.21	0.051	4.1	0.279	4.7	0.03961	2.2	250	6	242	95	#
R27.7.1	0.45	749	39	0.05	34.6	0.0504	3.2	0.371	3.5	0.05344	1.5	336	5	214	75	

Note: Pb_c and Pb^* indicate the common and radiogenic Pb portions, respectively. Standard calibration error (1σ) of 0.55%; not included in the above errors; #, also analysed with LA-ICPMS.

Sample R15, Melia Formation

				Isotopic ratios								Apparent ages (Ma)				
Analysis label	$^{206}Pb_c$ %	U ppm	Th ppm	$^{232}Th/^{238}U$	$^{206}Pb^*$ ppm	$^{207}Pb^*/^{206}Pb^*$	± %	$^{207}Pb^*/^{235}U$	± %	$^{206}U/^{238}Pb^*$	± %	$^{206}Pb/^{238}U$	± 1σ	$^{207}Pb/^{206}Pb$	± 1σ	
R15.1.1	--	33	30	0.94	1.42	0.0546	5.1	0.376	5.5	0.05	2.2	314	7	398	110	#
R15.2.	2.03	35	1	0.02	0.78	0.045	37	0.156	37	0.02525	3.1	161	5	-64	910	#
R15.3.1	2	57	79	1.43	2.29	0.0423	17	0.268	17	0.0459	2.4	289	7	-208	430	#
R15.4.1	0.93	68	48	0.73	2.89	0.0488	15	0.329	16	0.0489	1.9	308	6	137	360	
R15.5.1	0.81	61	25	0.42	2.53	0.0484	11	0.319	12	0.0479	2.1	301	6	117	270	rim
R15.5.2	0.22	237	12	0.05	14.6	0.0535	2.4	0.528	3	0.0716	1.9	446	8	350	54	core
R15.6.1	0.61	23	19	0.83	0.96	0.0582	10	0.385	10	0.048	2.5	302	7	539	220	

Note: Pb_c and Pb^* indicate the common and radiogenic Pb portions, respectively. Standard calibration error (1σ) of 0.55%; not included in the above errors; #, also analysed with LA-ICPMS.

Appendix D-2. U–Pb LA-ICPMS data

Sample SM201, Pirgadikia Unit

no.	Isotopic ratios										Apparent ages (Ma)							
	$^{207}Pb^{a}$ cps	U^{b} ppm	Pb^{b} ppm	Th/U	$^{207}Pb/^{235}U^{c}$	±1σ %	$^{206}Pb/^{238}U^{c}$	±1σ %	$^{207}Pb/^{206}Pb^{d}$	±1σ %	$^{207}Pb/^{235}U$	± 2σ	$^{206}Pb/^{238}U$	± 2σ	$^{207}Pb/^{206}Pb$	± 2σ	C ^{e} %	
07	8724	86	10	1.53	0.770	2.4	0.0920	2.1	0.0607	1.1	580	28	568	24	627	24	98	
08	87627	119	54	1.11	6.848	2.7	0.3653	2.3	0.1360	1.5	2092	115	2007	92	2176	26	96	
09	12215	23	9	1.64	4.538	2.8	0.3018	2.3	0.1091	1.6	1738	97	1700	79	1784	29	98	
10	12606	108	14	0.90	0.966	2.5	0.1104	2.3	0.0635	1.1	687	35	675	31	725	24	98	
11	8682	98	11	1.64	0.724	2.1	0.0891	1.7	0.0589	1.2	553	23	550	19	563	26	100	core
12	11350	129	13	1.15	0.694	2.6	0.0859	2.1	0.0586	1.4	535	27	531	22	551	32	99	rim
13	6833	79	7	0.65	0.716	2.2	0.0880	1.8	0.0590	1.3	548	24	544	19	568	28	99	
14	32552	212	30	0.19	1.462	2.0	0.1428	1.7	0.0743	0.9	915	36	860	30	1049	18	94	
15	31487	417	35	0.48	0.655	1.9	0.0808	1.8	0.0588	0.7	511	20	501	18	558	16	98	
16	3436	28	3	1.08	0.744	2.2	0.0903	1.7	0.0597	1.5	564	25	557	19	593	32	99	
20	4666	49	4	0.59	0.662	2.0	0.0821	1.6	0.0585	1.2	516	21	509	17	548	25	99	
21	8105	101	11	1.38	0.692	2.4	0.0850	2.0	0.0590	1.4	534	26	526	21	566	31	99	
22	1682	8	1	1.68	0.786	3.8	0.0971	2.3	0.0586	3.0	589	44	598	28	554	65	102	
23	15255	181	19	1.37	0.701	3.2	0.0844	2.5	0.0603	2.0	539	34	522	26	614	44	97	
24	22502	51	16	1.00	3.858	2.8	0.2557	2.5	0.1094	1.3	1605	90	1468	73	1790	24	91	
25	4621	38	4	1.02	0.758	3.1	0.0927	2.1	0.0593	2.2	573	35	571	24	578	48	100	
26	6012	7	3	0.56	5.627	2.9	0.3325	2.5	0.1227	1.5	1920	112	1851	93	1996	26	96	
27	5037	49	5	1.13	0.718	2.4	0.0876	1.9	0.0595	1.5	550	26	541	21	585	32	98	
28	4954	38	4	0.87	0.794	2.9	0.0923	2.3	0.0623	1.8	593	34	569	26	686	38	96	
29	15581	162	18	0.91	0.799	2.0	0.0963	1.7	0.0602	1.0	596	23	593	20	610	22	99	
33	6050	59	6	1.08	0.725	2.5	0.0854	1.7	0.0616	1.8	553	27	528	18	659	39	95	
34	4803	38	4	1.12	0.785	3.3	0.0943	2.6	0.0604	1.9	588	38	581	31	616	41	99	
35	3225	18	2	1.07	0.841	3.3	0.1008	2.5	0.0605	2.2	619	41	619	30	621	47	100	
36	15865	172	19	0.99	0.823	2.6	0.0959	2.2	0.0622	1.4	609	31	590	26	681	29	97	
37	16264	210	18	0.52	0.662	2.9	0.0810	2.3	0.0593	1.7	516	30	502	23	580	36	97	
38	9046	72	9	0.80	0.973	2.3	0.1113	2.0	0.0634	1.1	690	32	680	28	722	23	99	
39	45299	324	54	0.46	1.799	3.3	0.1642	2.1	0.0794	2.5	1045	68	980	41	1183	50	94	
40	20822	183	20	0.12	1.037	2.6	0.1150	1.9	0.0654	1.8	722	38	702	27	786	38	97	
41	6168	64	7	1.59	0.693	2.8	0.0847	2.2	0.0594	1.7	535	29	524	23	580	37	98	
42	3616	22	3	1.79	0.791	3.5	0.0930	2.0	0.0617	2.9	592	41	573	22	662	61	97	
46	36827	50	28	3.19	5.506	3.2	0.3071	2.2	0.1300	2.3	1902	121	1727	75	2098	40	91	
47	19153	74	16	0.57	2.251	2.0	0.1986	1.7	0.0822	1.1	1197	48	1168	40	1251	21	98	
48	38914	131	34	0.95	2.639	1.6	0.2194	1.5	0.0872	0.7	1312	43	1279	38	1366	14	98	
49	6280	65	8	1.15	0.820	2.0	0.0991	1.7	0.0600	1.1	608	25	609	21	604	25	100	
50	3141	36	4	1.35	0.670	2.3	0.0837	1.5	0.0580	1.7	521	24	518	16	530	36	100	
51	60481	57	30	0.96	9.779	2.0	0.4253	1.7	0.1667	1.0	2414	95	2285	77	2525	17	95	
52	9768	119	11	0.84	0.707	1.7	0.0867	1.4	0.0591	0.9	543	18	536	15	571	20	99	
53	53633	87	35	0.90	5.871	1.8	0.3461	1.6	0.1230	0.7	1957	69	1916	61	2001	13	98	
54	1408	2	0	2.73	0.830	5.1	0.1008	2.2	0.0597	4.6	614	63	619	28	594	99	101	
55	3164	24	3	1.05	0.816	2.4	0.1005	1.6	0.0589	1.9	606	29	617	19	565	40	102	
59	11278	138	13	0.71	0.675	1.5	0.0819	1.3	0.0598	0.7	524	15	507	13	597	16	97	
60	25584	41	16	0.55	5.690	1.7	0.3429	1.5	0.1203	0.7	1930	65	1901	58	1961	13	98	
61	24954	67	17	0.21	3.311	1.4	0.2523	1.3	0.0952	0.5	1484	42	1450	39	1532	9	98	
62	6246	60	7	1.19	0.799	2.0	0.0950	1.5	0.0610	1.2	596	23	585	18	639	27	98	
63	15736	199	27	1.28	0.693	1.6	0.0844	1.4	0.0595	0.7	535	17	523	15	587	15	98	
64	226889	223	109	0.47	9.778	1.6	0.4426	1.3	0.1602	1.0	2414	79	2362	63	2458	16	98	
65	6542	72	7	0.75	0.724	1.7	0.0885	1.5	0.0594	0.9	553	19	547	16	580	20	99	
66	80143	77	46	0.57	14.501	2.0	0.5276	1.5	0.1993	1.4	2783	112	2731	81	2821	22	98	
67	10056	95	11	1.45	0.806	2.7	0.0888	2.1	0.0658	1.6	600	32	549	23	799	33	91	

Appendix D-2. Continued

no.	Isotopic ratios										Apparent ages (Ma)							
	^{207}Pb[a] cps	U[b] ppm	Pb[b] ppm	Th/U	$^{207}Pb/^{235}U$[c]	±1σ %	$^{206}Pb/^{238}U$[c]	±1σ %	$^{207}Pb/^{206}Pb$[d]	±1σ %	$^{207}Pb/^{235}U$	± 2σ	$^{206}Pb/^{238}U$	± 2σ	$^{207}Pb/^{206}Pb$	± 2σ	C[e] %	
68	9943	120	12	0.89	0.700	1.9	0.0854	1.6	0.0595	1.0	539	21	528	17	586	21	98	
72	8421	31	7	0.79	2.029	3.0	0.1858	2.4	0.0792	1.9	1125	68	1099	52	1177	38	98	
73	36476	189	43	1.83	1.661	3.4	0.1578	3.0	0.0763	1.7	994	68	945	57	1104	33	95	
74	9285	99	11	1.06	0.793	2.8	0.0950	2.3	0.0605	1.7	593	33	585	26	622	37	99	
75	1735	7	1	1.31	0.786	3.9	0.0982	2.5	0.0581	3.0	589	46	604	30	533	66	102	
76	20917	59	17	1.09	3.128	2.9	0.2416	2.4	0.0939	1.7	1440	85	1395	67	1506	32	97	
77	49462	80	27	0.51	5.614	2.4	0.3130	2.0	0.1301	1.4	1918	94	1755	71	2099	24	92	
78	19303	44	14	0.85	3.938	2.4	0.2820	1.9	0.1013	1.4	1622	77	1601	61	1648	27	99	
79	22224	286	24	0.28	0.699	2.1	0.0854	1.6	0.0594	1.3	538	22	528	17	580	29	98	
80	13082	88	14	1.90	1.016	2.9	0.1132	2.2	0.0651	1.9	712	42	691	30	779	41	97	
81	3714	29	4	2.41	0.808	2.4	0.0969	1.6	0.0605	1.8	601	29	596	19	622	40	99	

Sample SM205, Pirgadikia Unit

no.	Isotopic ratios										Apparent ages (Ma)							
	^{207}Pb[a] cps	U[b] ppm	Pb[b] ppm	Th/U	$^{207}Pb/^{235}U$[c]	±1σ %	$^{206}Pb/^{238}U$[c]	±1σ %	$^{207}Pb/^{206}Pb$[d]	±1σ %	$^{207}Pb/^{235}U$	± 2σ	$^{206}Pb/^{238}U$	± 2σ	$^{207}Pb/^{206}Pb$	± 2σ	C[e] %	
205	2997	23	3	1.39	0.701	2.4	0.0866	1.7	0.0587	1.8	539	26	535	18	556	39	99	
206	2424	10	1	1.80	0.845	3.7	0.0969	2.8	0.0633	2.4	622	46	596	33	717	52	96	core
207	2824	13	2	2.09	0.871	2.7	0.1029	1.7	0.0614	2.0	636	34	631	21	654	44	99	rim
208	6832	84	9	1.20	0.734	2.5	0.0876	2.1	0.0607	1.3	559	28	542	23	630	28	97	
209	4956	53	5	0.70	0.722	1.9	0.0864	1.6	0.0606	1.1	552	21	534	17	627	25	97	
210	3741	31	3	0.75	0.820	2.1	0.0978	1.4	0.0608	1.5	608	26	602	17	632	33	99	core
211	7105	73	7	0.58	0.796	1.9	0.0952	1.5	0.0606	1.2	594	23	586	18	624	26	99	rim
212	17607	236	25	1.21	0.722	1.9	0.0874	1.6	0.0599	1.0	552	21	540	17	600	22	98	
213	3879	37	4	0.62	0.725	2.9	0.0883	2.1	0.0596	2.0	554	32	545	23	588	43	99	
214	3115	26	3	1.09	0.822	3.0	0.0974	2.2	0.0612	1.9	609	36	599	27	647	42	98	core
218	14972	177	21	1.22	0.800	2.5	0.0963	2.0	0.0603	1.4	597	29	593	24	613	30	99	rim
219	8848	120	10	0.80	0.585	2.8	0.0728	2.4	0.0583	1.4	468	26	453	22	541	31	97	
220	29666	86	24	0.47	3.497	2.2	0.2682	1.8	0.0946	1.2	1527	66	1532	54	1519	23	100	
221	4771	32	4	0.75	0.940	2.5	0.1100	1.9	0.0620	1.5	673	33	673	26	674	33	100	
222	11514	39	10	0.78	2.605	2.5	0.2190	1.9	0.0863	1.5	1302	64	1277	49	1344	30	98	core
223	29439	262	27	0.06	1.051	2.7	0.1115	2.2	0.0684	1.5	729	39	681	30	879	31	93	rim
224	5594	59	7	1.72	0.736	2.0	0.0906	1.5	0.0589	1.3	560	23	559	17	564	29	100	
225	2101	10	1	1.49	0.640	3.2	0.0793	1.7	0.0585	2.6	502	32	492	17	548	58	98	
226	31865	79	20	0.22	3.798	1.8	0.2568	1.6	0.1073	0.8	1592	57	1473	47	1754	15	93	
227	12786	154	17	0.96	0.795	2.4	0.0968	1.9	0.0596	1.5	594	28	596	22	588	32	100	core
231	10557	126	12	0.45	0.727	2.5	0.0890	2.1	0.0592	1.4	555	28	550	23	575	31	99	rim
232	1897	2	1	2.81	1.134	5.6	0.1163	2.8	0.0707	4.9	770	86	709	39	950	99	92	
233	8113	110	10	0.74	0.638	1.7	0.0810	1.3	0.0571	1.1	501	17	502	13	497	25	100	
234	4040	33	4	1.10	0.765	2.3	0.0944	1.4	0.0588	1.8	577	26	582	16	559	39	101	
235	3874	27	3	0.97	0.828	2.3	0.0983	1.3	0.0611	1.8	612	28	604	16	643	39	99	
236	22677	65	22	1.22	3.573	1.4	0.2761	1.3	0.0939	0.7	1544	45	1572	40	1505	13	102	
237	2607	10	2	1.96	0.869	2.7	0.1001	1.5	0.0630	2.2	635	34	615	19	707	47	97	
238	10073	115	13	1.24	0.745	1.5	0.0911	1.3	0.0593	0.7	565	17	562	14	577	16	99	
239	6038	49	6	1.36	0.776	2.1	0.0910	1.3	0.0618	1.7	583	25	562	14	669	36	96	
240	5343	58	6	0.95	0.768	1.7	0.0928	1.3	0.0600	1.0	579	19	572	15	604	22	99	
244	9053	104	12	1.05	0.783	1.7	0.0940	1.5	0.0604	0.8	587	20	579	17	617	18	99	
247	4438	29	4	1.27	1.099	2.0	0.1254	1.4	0.0636	1.5	753	31	761	21	729	31	101	
248	7542	84	9	1.08	0.684	1.7	0.0846	1.4	0.0587	1.0	529	18	523	15	554	22	99	
249	2454	11	2	2.07	0.824	2.9	0.0965	1.8	0.0620	2.3	610	36	594	22	673	49	97	

Appendix D-2. Continued

no.	Isotopic ratios										Apparent ages (Ma)						
	$^{207}Pb^{a}$ cps	U^{b} ppm	Pb^{b} ppm	Th/U	$^{207}Pb/^{235}U^{c}$	±1σ %	$^{206}Pb/^{238}U^{c}$	±1σ %	$^{207}Pb/^{206}Pb^{d}$	±1σ %	$^{207}Pb/^{235}U$	± 2σ	$^{206}Pb/^{238}U$	± 2σ	$^{207}Pb/^{206}Pb$	± 2σ	C [e] %
250	5075	46	5	1.04	0.768	1.9	0.0924	1.4	0.0602	1.3	578	23	570	16	611	29	99
251	6041	59	6	0.80	0.757	1.8	0.0926	1.4	0.0592	1.0	572	20	571	16	576	22	100
252	2994	19	2	1.16	0.744	2.2	0.0917	1.5	0.0589	1.6	565	25	565	17	562	35	100
253	3050	21	2	0.93	0.815	2.6	0.0973	1.8	0.0608	2.0	606	32	599	21	632	42	99
257	2215	5	1	1.89	0.973	4.4	0.1042	2.1	0.0677	3.8	690	60	639	27	861	79	93
258	14169	183	16	0.37	0.664	1.5	0.0834	1.3	0.0578	0.7	517	15	516	13	522	15	100
259	8387	93	9	0.62	0.727	2.7	0.0888	2.2	0.0594	1.5	555	30	548	24	582	34	99
260	6835	78	8	0.98	0.720	2.4	0.0878	1.9	0.0595	1.4	551	26	543	20	585	31	99
261	5754	49	5	0.91	0.715	2.6	0.0884	2.0	0.0587	1.7	548	29	546	22	555	37	100
262	12575	137	17	1.44	0.798	2.4	0.0967	2.1	0.0598	1.3	595	29	595	25	597	27	100
263	9775	115	13	1.39	0.766	2.2	0.0937	1.8	0.0593	1.3	577	26	577	21	578	28	100
264	3687	37	4	1.14	0.711	2.8	0.0887	2.1	0.0581	1.9	545	31	548	23	534	42	101
265	16399	235	21	0.76	0.639	1.8	0.0804	1.5	0.0576	1.1	502	18	499	15	516	23	99
266	4596	46	5	1.57	0.725	2.0	0.0907	1.5	0.0579	1.3	554	22	560	17	527	28	101

Sample SM157, Vertiskos Unit

no.	Isotopic ratios										Apparent ages (Ma)						
	$^{207}Pb^{a}$ cps	U^{b} ppm	Pb^{b} ppm	Th/U	$^{207}Pb/^{235}U^{c}$	±1σ %	$^{206}Pb/^{238}U^{c}$	±1σ %	$^{207}Pb/^{206}Pb^{d}$	±1σ %	$^{207}Pb/^{235}U$	± 2σ	$^{206}Pb/^{238}U$	± 2σ	$^{207}Pb/^{206}Pb$	± 2σ	C [e] %
07	7081	41	6	0.84	1.368	2.8	0.1323	1.8	0.0750	2.1	875	48	801	29	1069	42	91
08	8988	99	8	0.20	0.635	2.2	0.0761	2.0	0.0605	0.9	499	22	473	19	622	20	95
09	*19478*	*42*	*11*	*0.51*	*3.906*	*1.9*	*0.2256*	*1.8*	*0.1256*	*0.8*	*1615*	*63*	*1311*	*47*	*2037*	*13*	*81*
10	60039	123	43	0.68	4.439	1.7	0.2990	1.7	0.1077	0.4	1720	58	1686	56	1760	7	98
11	33450	350	34	0.17	0.853	1.8	0.1009	1.7	0.0613	0.5	626	22	620	21	650	11	99
12	27279	281	27	0.09	0.873	1.8	0.1024	1.7	0.0618	0.6	637	23	628	22	669	14	99
13	175866	85	61	0.28	20.954	1.9	0.6277	1.8	0.2421	0.8	3136	121	3141	110	3134	13	100
14	286793	287	132	0.44	10.048	2.1	0.4107	2.0	0.1774	0.7	2439	101	2218	87	2629	11	91
15	6572	54	6	0.71	0.933	2.1	0.1065	1.8	0.0635	1.1	669	28	652	23	726	24	97
16	61251	691	79	0.13	0.810	1.8	0.0968	1.7	0.0607	0.7	602	22	596	20	628	14	99
20	*100210*	*127*	*49*	*0.36*	*7.889*	*2.2*	*0.3557*	*2.1*	*0.1609*	*0.7*	*2218*	*97*	*1962*	*81*	*2465*	*12*	*88*
21	8738	89	11	1.24	0.815	1.9	0.0985	1.7	0.0600	0.8	605	23	606	20	605	18	100
22	20354	156	20	0.26	1.158	1.9	0.1273	1.7	0.0659	0.7	781	29	773	27	804	15	99
23	42076	63	27	0.83	6.306	1.7	0.3610	1.7	0.1267	0.5	2019	70	1987	67	2053	8	98
24	7977	71	10	1.70	0.878	2.0	0.1022	1.7	0.0623	1.2	640	26	627	21	684	25	98
25	9771	97	11	0.89	0.789	1.9	0.0926	1.7	0.0618	0.9	591	23	571	19	666	20	97
26	14684	128	15	0.54	0.947	1.9	0.1093	1.7	0.0629	0.8	677	26	668	23	704	17	99
27	*19609*	*196*	*19*	*0.73*	*0.793*	*2.4*	*0.0819*	*1.7*	*0.0702*	*1.7*	*593*	*28*	*508*	*17*	*934*	*34*	*86*
28	5012	27	4	0.87	1.253	2.3	0.1349	2.0	0.0674	1.1	825	38	816	33	849	24	99
29	29843	302	31	0.16	0.903	1.8	0.1049	1.7	0.0624	0.5	653	24	643	22	689	11	98
33	15781	147	18	0.75	0.935	1.8	0.1085	1.7	0.0625	0.7	670	24	664	22	691	15	99
34	9865	91	11	1.17	0.911	2.0	0.1015	1.7	0.0651	1.1	658	26	623	21	778	23	95
35	9294	92	15	2.84	0.778	2.3	0.0924	2.0	0.0611	1.1	585	27	570	23	642	24	97
36	40505	415	44	0.21	0.939	2.3	0.1092	2.2	0.0623	0.8	672	31	668	29	686	17	99
37	5676	43	5	0.63	0.950	2.1	0.1093	1.8	0.0630	1.1	678	28	669	24	710	23	99
38	13922	110	13	0.42	1.042	2.3	0.1162	2.1	0.0651	1.1	725	34	709	29	776	23	98
39	52086	446	54	0.43	1.027	2.1	0.1152	1.9	0.0647	0.7	718	29	703	27	763	16	98
40	21921	131	23	0.61	1.605	2.0	0.1639	1.8	0.0710	0.9	972	39	979	35	958	19	101
41	53515	597	58	0.21	0.849	2.1	0.0998	2.0	0.0617	0.6	624	26	613	25	663	12	98
42	150199	150	76	0.64	9.602	1.8	0.4406	1.7	0.1581	0.6	2397	87	2353	80	2435	11	98
46	9632	94	11	0.99	0.857	1.7	0.1001	1.5	0.0621	0.8	629	21	615	18	678	18	98

Appendix D-2. Continued

no.	Isotopic ratios										Apparent ages (Ma)						
	^{207}Pb[a] cps	U[b] ppm	Pb[b] ppm	Th/U	$^{207}Pb/^{235}U$[c]	±1σ %	$^{206}Pb/^{238}U$[c]	±1σ %	$^{207}Pb/^{206}Pb$[d]	±1σ %	$^{207}Pb/^{235}U$	± 2σ	$^{206}Pb/^{238}U$	± 2σ	$^{207}Pb/^{206}Pb$	± 2σ	C[e] %
47	*20479*	*40*	*13*	*0.65*	*4.564*	*2.5*	*0.2647*	*2.2*	*0.1250*	*1.2*	*1743*	*88*	*1514*	*68*	*2029*	*20*	*87*
48	52722	574	57	0.05	0.905	1.6	0.1070	1.5	0.0613	0.4	654	21	655	20	650	8	100
49	13973	105	13	0.16	1.162	1.8	0.1210	1.6	0.0697	0.9	783	29	736	24	919	18	94
50	184848	346	129	0.51	5.562	1.8	0.3372	1.7	0.1196	0.4	1910	68	1873	65	1951	7	98
51	54514	86	38	1.03	6.235	1.6	0.3509	1.5	0.1289	0.4	2009	62	1939	58	2083	8	96
52	77911	563	80	0.06	1.449	1.5	0.1507	1.5	0.0697	0.5	909	28	905	27	920	10	100
53	16135	157	17	0.34	0.910	1.7	0.1043	1.5	0.0633	0.8	657	23	640	19	718	17	97
54	8967	64	9	0.50	1.293	2.3	0.1415	2.1	0.0663	0.8	843	38	853	36	815	17	101
55	60473	751	92	0.17	0.805	1.5	0.0983	1.5	0.0594	0.4	600	18	604	18	583	8	101
59	34811	314	40	0.42	1.162	1.6	0.1261	1.5	0.0668	0.6	783	25	766	23	832	12	98
60	*6831*	*30*	*4*	*1.06*	*0.992*	*5.0*	*0.0985*	*4.0*	*0.0731*	*2.9*	*700*	*70*	*605*	*48*	*1016*	*60*	*87*
61	10878	85	11	0.49	1.165	1.9	0.1281	1.6	0.0660	1.1	784	30	777	25	806	23	99
62	7165	62	7	0.48	1.017	2.6	0.1149	2.0	0.0642	1.6	713	37	701	28	749	33	98
63	29271	302	27	0.14	0.856	2.9	0.0949	2.1	0.0654	2.1	628	37	584	24	788	44	93
64	7162	80	9	1.02	0.792	2.3	0.0954	2.0	0.0602	1.1	592	27	587	23	611	24	99
65	24277	326	25	0.19	0.651	1.9	0.0794	1.7	0.0595	0.7	509	19	493	17	584	15	97
66	57591	975	74	-3.16	0.587	2.2	0.0737	2.1	0.0578	0.5	469	21	459	20	522	11	98
67	23993	281	31	0.72	0.828	1.6	0.0998	1.5	0.0602	0.7	613	20	613	18	610	15	100
68	14029	147	15	0.24	0.875	1.8	0.1017	1.6	0.0624	0.9	638	23	625	20	686	19	98
72	9378	79	10	0.59	0.962	1.8	0.1106	1.5	0.0631	0.8	684	24	677	21	710	18	99
73	18155	219	20	0.38	0.771	2.3	0.0895	1.8	0.0625	1.5	580	27	552	19	691	32	95
74	66743	794	84	0.44	0.831	1.5	0.1000	1.5	0.0602	0.4	614	19	614	18	612	9	100
75	*35662*	*280*	*32*	*0.24*	*1.367*	*2.2*	*0.1132*	*1.5*	*0.0876*	*1.6*	*875*	*39*	*691*	*21*	*1374*	*31*	*79*
76	18828	117	21	0.72	1.591	1.6	0.1624	1.5	0.0711	0.7	967	32	970	28	959	15	100
77	31013	324	34	0.33	0.894	1.6	0.1023	1.5	0.0634	0.7	649	21	628	19	722	14	97
78	20091	113	25	1.43	1.744	1.8	0.1725	1.6	0.0734	0.8	1025	37	1026	33	1024	17	100
79	35531	378	41	0.19	0.952	1.7	0.1112	1.5	0.0621	0.6	679	22	680	21	678	12	100
80	23021	138	21	0.21	1.566	1.6	0.1574	1.5	0.0722	0.6	957	31	942	28	991	12	98
81	*35031*	*109*	*23*	*0.32*	*3.032*	*2.4*	*0.2023*	*2.3*	*0.1087*	*0.9*	*1416*	*69*	*1188*	*54*	*1778*	*17*	*84*

Sample SM151, Vertiskos Unit

no.	Isotopic ratios										Apparent ages (Ma)						
	^{207}Pb[a] cps	U[b] ppm	Pb[b] ppm	Th/U	$^{207}Pb/^{235}U$[c]	±1σ %	$^{206}Pb/^{238}U$[c]	±1σ %	$^{207}Pb/^{206}Pb$[d]	±1σ %	$^{207}Pb/^{235}U$	± 2σ	$^{206}Pb/^{238}U$	± 2σ	$^{207}Pb/^{206}Pb$	± 2σ	C[e] %
07	14295	250	18	0.29	0.578	2.1	0.0738	1.8	0.0568	1.0	463	19	459	17	483	23	99
08	10060	161	12	0.54	0.580	2.4	0.0740	1.9	0.0569	1.6	465	23	460	17	486	35	99
09	6529	93	7	0.73	0.566	1.9	0.0725	1.5	0.0567	1.1	456	17	451	14	478	24	99
10	7267	104	8	0.76	0.573	2.0	0.0741	1.7	0.0561	1.0	460	19	461	16	455	23	100
11	29954	592	40	0.20	0.547	1.5	0.0702	1.4	0.0565	0.6	443	14	437	13	472	12	99
12	9340	142	11	0.66	0.555	1.6	0.0719	1.4	0.0560	0.8	448	14	448	12	452	19	100
13	6758	104	8	0.79	0.546	2.0	0.0696	1.5	0.0569	1.3	443	18	434	13	489	29	98
14	6221	81	6	0.78	0.568	2.2	0.0697	1.4	0.0591	1.7	457	20	434	12	572	37	95
15	7929	118	10	1.06	0.546	1.9	0.0706	1.5	0.0562	1.2	443	16	440	13	459	26	99
16	13646	234	17	0.38	0.560	1.5	0.0719	1.3	0.0565	0.8	452	14	448	12	470	18	99
20	5531	83	6	0.76	0.529	1.8	0.0683	1.5	0.0562	1.1	431	16	426	12	460	23	99
21	7060	83	6	0.64	0.553	1.9	0.0699	1.4	0.0573	1.2	447	17	436	12	504	27	98
22	10766	188	14	0.59	0.571	1.7	0.0730	1.4	0.0567	1.0	459	16	454	13	481	21	99
23	19456	344	23	0.19	0.532	1.7	0.0689	1.5	0.0560	0.8	433	14	429	13	453	17	99
24	3383	35	3	0.90	0.574	2.3	0.0734	1.8	0.0567	1.4	460	21	457	16	479	31	99
25	11203	188	14	0.45	0.563	2.0	0.0710	1.5	0.0575	1.4	454	19	442	13	512	31	97

Appendix D-2. Continued

no.	Isotopic ratios										Apparent ages (Ma)						
	^{207}Pb[a] cps	U[b] ppm	Pb[b] ppm	Th/U	$^{207}Pb/^{235}U$[c]	±1σ %	$^{206}Pb/^{238}U$[c]	±1σ %	$^{207}Pb/^{206}Pb$[d]	±1σ %	$^{207}Pb/^{235}U$	± 2σ	$^{206}Pb/^{238}U$	± 2σ	$^{207}Pb/^{206}Pb$	± 2σ	C[e] %
26	5183	70	6	0.85	0.563	1.9	0.0728	1.4	0.0561	1.4	454	17	453	12	456	30	100
27	8231	101	8	0.69	0.557	2.4	0.0713	2.0	0.0567	1.4	450	22	444	18	479	30	99
28	9148	162	13	0.72	0.572	1.8	0.0741	1.4	0.0560	1.2	459	17	461	13	452	26	100
29	24465	456	31	0.25	0.536	1.9	0.0685	1.6	0.0567	1.0	436	17	427	14	481	22	98
33	9250	164	10	0.30	0.508	3.7	0.0635	2.9	0.0581	2.3	417	31	397	23	532	50	95
34	18155	299	23	0.37	0.613	2.9	0.0759	2.3	0.0586	1.7	485	28	471	22	551	37	97
35	10566	181	14	0.82	0.539	2.8	0.0687	2.4	0.0569	1.5	438	25	428	20	489	33	98
36	10078	180	13	0.38	0.560	2.1	0.0726	1.9	0.0560	1.0	452	19	452	17	452	23	100
37	*25339*	*102*	*17*	*0.65*	*2.045*	*3.7*	*0.1366*	*3.0*	*0.1086*	*2.3*	*1131*	*85*	*825*	*49*	*1776*	*42*	*73*
38	5849	102	6	0.25	0.443	2.4	0.0612	1.9	0.0525	1.6	372	18	383	14	307	36	103
39	6927	111	9	0.73	0.568	2.3	0.0752	1.9	0.0548	1.4	457	21	468	17	404	31	102
40	4991	68	6	0.98	0.561	2.0	0.0721	1.7	0.0565	1.1	452	18	449	15	471	24	99
41	4909	83	7	0.58	0.611	3.1	0.0795	2.2	0.0557	2.1	484	30	493	22	441	47	102
42	3307	47	4	0.68	0.567	3.5	0.0698	2.3	0.0589	2.6	456	32	435	20	563	57	95
46	6607	100	8	0.53	0.577	2.7	0.0737	2.3	0.0568	1.3	463	25	458	21	484	29	99
47	25276	503	33	0.13	0.538	2.2	0.0699	1.8	0.0558	1.2	437	19	436	16	445	26	100
48	14500	251	19	0.51	0.577	2.8	0.0740	2.5	0.0566	1.3	463	26	460	23	475	28	99
49	9167	169	12	0.20	0.560	2.5	0.0713	2.0	0.0570	1.4	452	22	444	18	492	32	98
50	66243	1172	94	0.24	0.622	3.3	0.0776	2.6	0.0582	2.1	491	33	481	25	536	45	98
51	8580	148	11	0.50	0.579	2.4	0.0748	1.9	0.0561	1.5	464	22	465	17	458	33	100
52	14908	288	22	0.44	0.566	2.2	0.0735	1.8	0.0559	1.2	456	20	457	17	449	27	100
53	3961	56	4	0.62	0.510	3.3	0.0680	2.4	0.0545	2.3	419	28	424	20	390	51	101
54	5879	91	7	0.64	0.547	2.5	0.0694	2.0	0.0572	1.5	443	22	433	17	499	33	98
55	10114	151	10	0.41	0.504	2.5	0.0649	2.0	0.0563	1.5	414	21	405	17	465	33	98
59	14308	268	22	1.18	0.517	2.5	0.0669	2.2	0.0560	1.3	423	21	418	18	452	29	99
60	7150	110	8	0.53	0.557	2.6	0.0723	1.9	0.0559	1.7	450	23	450	17	448	39	100
61	9665	173	13	0.43	0.557	3.0	0.0734	2.4	0.0550	1.8	449	27	457	22	412	41	102
62	20974	389	29	0.30	0.587	2.1	0.0754	1.6	0.0564	1.3	469	20	469	15	469	30	100
63	6637	86	7	1.03	0.527	3.1	0.0693	2.4	0.0552	1.9	430	26	432	21	421	41	100
66	4971	63	5	0.73	0.509	2.9	0.0658	2.1	0.0560	2.0	417	24	411	17	454	45	98
67	4815	78	6	0.72	0.531	2.3	0.0706	2.0	0.0545	1.3	432	20	440	17	392	29	102
68	8830	155	12	0.45	0.575	1.9	0.0742	1.4	0.0562	1.2	461	17	461	13	459	28	100
72	5887	71	6	0.92	0.615	2.2	0.0772	1.8	0.0578	1.3	487	22	479	17	523	28	98
73	7738	136	9	0.43	0.520	1.8	0.0655	1.6	0.0576	0.8	425	15	409	13	514	18	96
74	6981	102	8	0.52	0.578	1.7	0.0741	1.4	0.0566	1.0	463	16	461	13	475	21	99
75	*69878*	*78*	*31*	*0.38*	*8.980*	*1.9*	*0.3485*	*1.6*	*0.1869*	*1.0*	*2336*	*89*	*1927*	*63*	*2715*	*16*	*83*
76	5305	69	6	0.85	0.617	1.7	0.0789	1.3	0.0567	1.1	488	17	490	12	479	25	100
77	21422	420	31	0.35	0.576	1.3	0.0754	1.1	0.0554	0.7	462	12	468	10	429	16	101
78	12928	229	18	0.36	0.598	1.4	0.0772	1.0	0.0562	0.9	476	13	479	10	461	19	101
79	11114	184	14	0.41	0.565	1.6	0.0737	1.4	0.0556	0.8	455	14	458	13	436	17	101
80	7235	95	8	0.86	0.542	1.8	0.0702	1.3	0.0560	1.2	440	15	438	11	451	27	100
81	17094	346	25	0.30	0.555	1.4	0.0723	1.2	0.0556	0.8	448	13	450	11	437	17	100

Appendix D-2. Continued

Sample SM220, Examili Formation

no.	Isotopic ratios										Apparent Ages (Ma)							
	^{207}Pb[a] cps	U[b] ppm	Pb[b] ppm	Th/U	$^{207}Pb/^{235}U$[c]	±1σ %	$^{206}Pb/^{238}U$[c]	±1σ %	$^{207}Pb/^{206}Pb$[d]	±1σ %	$^{207}Pb/^{235}U$	± 2σ	$^{206}Pb/^{238}U$	± 2σ	$^{207}Pb/^{206}Pb$	± 2σ	C[e] %	
07	30436	337	28	0.08	0.747	2.0	0.0855	1.8	0.0634	0.9	567	22	529	19	721	18	93	
08	7758	102	7	0.21	0.557	1.6	0.0706	1.3	0.0572	1.0	449	15	440	11	498	23	98	
09	4665	59	4	0.49	0.439	3.2	0.0588	2.8	0.0541	1.4	369	23	368	21	375	31	100	
10	6929	83	7	0.64	0.570	2.0	0.0717	1.5	0.0577	1.3	458	18	447	13	517	29	97	
11	*43404*	*290*	*38*	*0.98*	*1.337*	*1.9*	*0.1122*	*1.7*	*0.0864*	*0.8*	*862*	*33*	*685*	*24*	*1348*	*15*	*80*	
12	20122	187	24	0.76	0.938	1.5	0.1098	1.3	0.0620	0.7	672	20	672	17	673	14	100	core
13	6848	77	6	0.47	0.576	2.0	0.0745	1.4	0.0560	1.4	462	18	463	13	453	31	100	rim
14	4135	28	3	0.51	0.729	2.2	0.0891	1.4	0.0593	1.7	556	25	550	16	580	37	99	
15	15345	179	17	0.56	0.694	1.5	0.0855	1.3	0.0589	0.8	535	16	529	14	562	17	99	
16	4450	46	4	0.60	0.563	2.1	0.0730	1.4	0.0560	1.6	453	19	454	12	451	35	100	
20	13500	138	15	0.80	0.790	1.5	0.0937	1.3	0.0611	0.7	591	17	578	15	644	15	98	
21	15054	221	16	0.28	0.557	1.5	0.0711	1.3	0.0568	0.8	449	14	443	11	485	18	98	
22	12076	131	12	0.42	0.703	1.6	0.0838	1.3	0.0608	0.9	541	18	519	14	633	20	96	
23	70585	38	24	0.21	17.211	1.5	0.5566	1.3	0.2243	0.6	2947	87	2853	76	3012	10	97	
24	14565	199	13	0.14	0.576	2.0	0.0700	1.6	0.0597	1.2	462	18	436	14	594	25	94	
25	15675	153	16	0.32	0.860	1.5	0.1013	1.3	0.0615	0.7	630	19	622	17	658	15	99	
26	12602	185	14	0.46	0.556	1.6	0.0722	1.3	0.0559	0.8	449	14	449	12	447	18	100	
27	14114	202	13	0.15	0.544	1.6	0.0682	1.4	0.0578	0.7	441	14	426	12	524	16	96	
28	31430	469	33	0.16	0.631	1.7	0.0725	1.3	0.0631	1.1	497	17	451	12	712	23	91	
29	6049	50	6	1.22	0.822	1.8	0.0965	1.5	0.0618	1.1	609	22	594	17	668	24	97	
33	14435	101	7	0.21	0.560	2.8	0.0691	2.3	0.0588	1.6	452	25	431	19	559	34	95	
34	14649	224	18	0.67	0.543	1.7	0.0710	1.4	0.0555	0.9	441	15	442	12	433	20	100	
35	4051	62	4	0.83	0.367	2.3	0.0494	1.8	0.0539	1.4	318	14	311	11	366	32	98	
36	8789	122	9	0.17	0.578	1.7	0.0735	1.4	0.0571	0.9	463	15	457	12	495	21	99	
37	7454	162	10	0.82	0.389	1.9	0.0511	1.5	0.0552	1.1	333	13	321	10	419	24	96	
38	8444	123	10	0.49	0.565	1.7	0.0722	1.5	0.0568	0.9	455	16	450	13	482	21	99	
39	*23563*	*258*	*18*	*0.44*	*0.739*	*1.9*	*0.0648*	*1.4*	*0.0827*	*1.3*	*562*	*21*	*405*	*11*	*1262*	*25*	*72*	
40	6006	67	6	0.98	0.582	2.3	0.0741	1.7	0.0570	1.6	466	22	461	16	490	35	99	
41	15052	232	16	0.22	0.563	1.7	0.0715	1.6	0.0571	0.7	454	16	445	14	495	15	98	
42	8651	124	9	0.26	0.560	1.6	0.0726	1.3	0.0559	1.0	452	15	452	12	450	22	100	
46	*24349*	*176*	*24*	*0.89*	*1.740*	*5.4*	*0.1113*	*1.7*	*0.1134*	*5.1*	*1023*	*111*	*680*	*23*	*1855*	*93*	*66*	
47	8992	131	9	0.23	0.559	2.3	0.0716	1.5	0.0566	1.7	451	21	446	13	476	39	99	
48	4647	55	5	0.67	0.568	2.2	0.0733	1.5	0.0563	1.6	457	20	456	13	463	36	100	
49	*15460*	*26*	*10*	*1.25*	*4.578*	*2.0*	*0.2684*	*1.5*	*0.1237*	*1.2*	*1745*	*68*	*1532*	*47*	*2011*	*22*	*88*	
50	10368	126	11	0.53	0.714	1.6	0.0838	1.4	0.0617	0.9	547	18	519	14	665	20	95	core
51	*25642*	*494*	*24*	*0.33*	*0.420*	*3.4*	*0.0493*	*1.8*	*0.0618*	*3.0*	*356*	*25*	*310*	*11*	*665*	*63*	*87*	rim
52	64304	164	43	0.13	4.181	1.6	0.2628	1.6	0.1154	0.5	1670	55	1504	47	1886	9	90	
53	9658	138	10	0.19	0.574	1.9	0.0736	1.7	0.0566	0.8	461	18	458	16	475	18	99	
54	11047	168	12	0.13	0.582	1.6	0.0742	1.3	0.0569	0.9	465	15	461	12	487	20	99	
55	7663	110	9	0.43	0.577	1.8	0.0747	1.4	0.0560	1.1	463	16	464	13	454	24	100	
59	*9871*	*136*	*9*	*0.91*	*0.616*	*1.8*	*0.0610*	*1.2*	*0.0733*	*1.3*	*488*	*18*	*382*	*9*	*1021*	*27*	*78*	
60	18350	220	20	0.18	0.779	1.4	0.0955	1.3	0.0592	0.6	585	16	588	15	573	13	101	
61	15688	208	14	0.31	0.581	1.7	0.0676	1.4	0.0624	1.0	465	16	422	11	688	22	91	
62	4183	27	3	0.65	0.948	2.1	0.1097	1.5	0.0627	1.4	677	28	671	20	697	31	99	
63	5656	34	5	0.80	1.034	1.6	0.1116	1.3	0.0672	1.0	721	24	682	18	844	21	95	
64	13682	208	15	0.20	0.573	1.4	0.0735	1.2	0.0565	0.7	460	13	457	11	473	15	99	
65	17099	176	19	0.38	0.894	1.5	0.1057	1.2	0.0613	0.9	648	19	648	15	650	19	100	
66	30893	278	29	0.22	0.916	3.0	0.1002	2.4	0.0663	1.8	660	39	615	29	817	37	93	
67	11751	174	12	0.16	0.584	1.6	0.0740	1.3	0.0572	1.0	467	15	460	12	501	22	99	
68	13599	205	15	0.16	0.575	1.6	0.0752	1.5	0.0555	0.7	462	15	467	14	433	16	101	

Appendix D-2. Continued

no.	Isotopic ratios										Apparent ages (Ma)							
	$^{207}Pb^{a}$ cps	U^{b} ppm	Pb^{b} ppm	Th/U	$^{207}Pb/^{235}U^{c}$	±1σ %	$^{206}Pb/^{238}U^{c}$	±1σ %	$^{207}Pb/^{206}Pb^{d}$	±1σ %	$^{207}Pb/^{235}U$	± 2σ	$^{206}Pb/^{238}U$	± 2σ	$^{207}Pb/^{206}Pb$	± 2σ	C [e] %	
72	9717	139	11	0.38	0.581	1.9	0.0742	1.5	0.0568	1.1	465	18	462	14	482	25	99	
73	11562	244	12	0.11	0.390	1.5	0.0521	1.3	0.0543	0.7	334	10	327	9	385	16	98	
74	8789	117	9	0.33	0.606	1.5	0.0772	1.2	0.0569	0.9	481	14	480	11	489	20	100	
75	26853	337	22	0.09	0.582	2.3	0.0682	2.1	0.0619	0.8	466	21	425	18	670	17	91	
76	9328	85	10	0.72	0.905	2.0	0.1044	1.5	0.0629	1.3	654	26	640	19	704	27	98	
77	7157	96	7	0.28	0.571	1.6	0.0735	1.3	0.0564	1.0	459	15	457	12	466	23	100	
78	5689	55	6	1.32	0.695	2.2	0.0777	1.2	0.0648	1.8	536	24	482	12	769	38	90	
79	*9174*	*127*	*8*	*0.59*	*0.624*	*2.4*	*0.0619*	*1.4*	*0.0731*	*1.9*	*493*	*24*	*387*	*11*	*1018*	*39*	*79*	
80	9209	120	8	0.18	0.558	1.8	0.0689	1.4	0.0587	1.1	450	16	429	12	557	25	95	
81	7394	98	7	0.28	0.563	1.5	0.0721	1.1	0.0566	1.0	454	14	449	10	477	22	99	

Sample SM198, Melissochori Formation

no.	Isotopic ratios										Apparent ages (Ma)							
	$^{207}Pb^{a}$ cps	U^{b} ppm	Pb^{b} ppm	Th/U	$^{207}Pb/^{235}U^{c}$	±1σ %	$^{206}Pb/^{238}U^{c}$	±1σ %	$^{207}Pb/^{206}Pb^{d}$	±1σ %	$^{207}Pb/^{235}U$	± 2σ	$^{206}Pb/^{238}U$	± 2σ	$^{207}Pb/^{206}Pb$	± 2σ	C [f] %	
111	*187785*	*473*	*160*	*0.44*	*6.996*	*2.5*	*0.3123*	*1.6*	*0.1625*	*1.9*	*2111*	*106*	*1752*	*57*	*2482*	*33*	*83*	
112	9246	135	11	0.50	0.620	1.7	0.0788	1.5	0.0571	0.8	490	17	489	15	494	19	100	
113	27612	938	52	0.46	0.391	1.7	0.0533	1.6	0.0532	0.6	335	11	335	11	337	13	100	
114	11779	300	17	0.22	0.427	1.7	0.0569	1.5	0.0544	0.7	361	12	357	11	388	16	99	
115	8046	130	12	0.83	0.622	2.0	0.0764	1.6	0.0590	1.3	491	20	475	15	568	28	97	
116	6759	143	8	0.83	0.369	1.9	0.0493	1.5	0.0542	1.1	319	12	310	9	379	25	97	
117	6354	163	10	1.06	0.352	2.0	0.0481	1.6	0.0530	1.3	306	12	303	9	329	29	99	
118	200250	257	146	0.64	11.965	1.7	0.4848	1.7	0.1790	0.4	2602	91	2548	86	2644	7	98	
119	20244	311	37	0.75	0.762	2.2	0.0884	1.7	0.0625	1.5	575	26	546	18	691	32	95	
120	12618	198	20	0.49	0.773	1.7	0.0937	1.5	0.0598	0.8	582	20	577	18	598	17	99	
124	11812	333	17	0.11	0.399	1.7	0.0540	1.5	0.0536	0.8	341	12	339	10	355	18	99	core
125	20060	603	33	0.23	0.419	1.7	0.0564	1.6	0.0539	0.6	355	12	354	11	366	15	100	rim
126	8489	199	11	0.57	0.393	1.9	0.0523	1.6	0.0546	1.0	337	13	328	10	395	23	98	core
127	23771	732	40	0.41	0.395	1.6	0.0529	1.5	0.0542	0.6	338	11	332	10	378	13	98	rim
128	9193	254	16	1.12	0.374	1.8	0.0502	1.5	0.0540	0.9	322	11	316	10	370	20	98	core
129	14283	421	27	1.00	0.387	1.7	0.0520	1.5	0.0540	0.7	332	11	327	10	370	15	98	rim
130	7028	158	10	1.20	0.366	1.9	0.0493	1.5	0.0539	1.2	317	12	310	9	368	26	98	
131	25548	69	26	0.77	4.863	1.6	0.3168	1.5	0.1113	0.5	1796	57	1774	54	1821	9	99	
132	*62575*	*338*	*56*	*0.20*	*2.437*	*1.9*	*0.1597*	*1.5*	*0.1107*	*1.1*	*1254*	*47*	*955*	*29*	*1811*	*19*	*76*	
133	12854	66	14	0.44	2.295	1.7	0.2030	1.5	0.0820	0.7	1211	40	1191	36	1245	14	98	
137	7951	14	6	0.83	6.101	1.9	0.3610	1.7	0.1226	1.0	1990	76	1987	66	1994	17	100	core
138	8986	16	7	0.87	6.173	1.8	0.3665	1.6	0.1222	1.0	2001	73	2013	62	1988	17	101	rim
139	3777	21	3	0.95	1.150	2.1	0.1254	1.6	0.0665	1.3	777	32	762	24	821	28	98	core
140	12146	198	19	0.35	0.734	1.9	0.0912	1.6	0.0583	1.0	559	21	563	18	542	22	101	rim
141	6279	67	8	0.95	0.879	2.0	0.1033	1.6	0.0617	1.2	640	25	634	20	664	25	99	core
142	3567	28	3	1.59	0.728	3.3	0.0814	2.1	0.0648	2.6	555	37	504	21	769	54	91	rim
143	23490	91	30	1.11	3.375	1.6	0.2611	1.5	0.0938	0.6	1499	48	1495	44	1503	11	100	
144	*13396*	*169*	*12*	*0.22*	*0.904*	*5.5*	*0.0671*	*4.7*	*0.0978*	*2.9*	*654*	*72*	*419*	*39*	*1582*	*54*	*64*	rim
145	99348	296	99	0.53	4.729	1.5	0.3007	1.5	0.1141	0.3	1772	54	1695	50	1865	6	96	core
146	3401	9	2	1.47	1.867	2.8	0.1803	1.8	0.0751	2.1	1070	59	1069	39	1072	42	100	
150	*8906*	*43*	*8*	*0.50*	*2.542*	*5.3*	*0.1665*	*5.1*	*0.1107*	*1.5*	*1284*	*137*	*993*	*102*	*1811*	*27*	*77*	core
151	6917	150	9	0.77	0.382	2.0	0.0517	1.6	0.0536	1.1	328	13	325	10	352	25	99	rim
152	30577	92	33	0.72	4.609	1.8	0.3056	1.7	0.1094	0.7	1751	63	1719	57	1789	13	98	
153	7997	246	14	0.74	0.360	2.1	0.0489	1.7	0.0534	1.2	312	13	308	11	344	26	99	
154	10209	327	19	0.83	0.360	1.8	0.0495	1.6	0.0527	0.8	312	11	312	10	314	19	100	

Appendix D-2. Continued

no.	Isotopic ratios										Apparent ages (Ma)						
	^{207}Pb[a] cps	U[b] ppm	Pb[b] ppm	Th/U	$^{207}Pb/^{235}U$[c]	±1σ %	$^{206}Pb/^{238}U$[c]	±1σ %	$^{207}Pb/^{206}Pb$[d]	±1σ %	$^{207}Pb/^{235}U$	± 2σ	$^{206}Pb/^{238}U$	± 2σ	$^{207}Pb/^{206}Pb$	± 2σ	C[e] %	
155	12819	177	23	1.38	0.847	1.7	0.1010	1.6	0.0608	0.7	623	21	620	19	633	15	100	
156	3988	26	3	1.41	0.734	2.4	0.0893	1.6	0.0596	1.8	559	27	551	18	589	39	99	
157	12634	144	20	0.77	1.061	2.0	0.1219	1.8	0.0631	0.8	734	29	741	27	713	17	101	
158	7872	177	15	1.75	0.446	1.9	0.0591	1.7	0.0547	0.9	375	14	370	12	401	20	99	
159	52090	163	48	0.17	4.653	1.8	0.2866	1.8	0.1178	0.5	1759	65	1624	57	1923	10	92	
163	11056	279	15	0.28	0.386	1.8	0.0514	1.6	0.0545	0.9	331	12	323	10	390	19	97	
164	8392	235	15	1.27	0.342	1.6	0.0466	1.3	0.0532	0.8	299	9	294	8	338	18	98	
165	4937	40	5	1.05	0.949	2.1	0.1016	1.4	0.0677	1.5	677	28	624	18	860	31	92	
166	39137	67	31	0.58	7.768	1.6	0.4121	1.5	0.1367	0.7	2205	71	2225	65	2186	12	101	
167	4808	78	5	1.25	0.384	2.0	0.0524	1.3	0.0531	1.5	330	13	329	8	335	35	100	
168	6443	92	6	0.44	0.517	2.1	0.0651	1.8	0.0576	1.0	423	18	407	15	514	22	96	
169	6213	168	9	0.67	0.333	2.1	0.0461	1.7	0.0523	1.3	292	12	291	10	300	29	100	
170	7569	150	9	0.54	0.430	1.7	0.0567	1.4	0.0549	1.0	363	12	356	10	410	23	98	
171	41587	109	39	0.62	4.919	2.1	0.3186	1.9	0.1120	1.0	1806	76	1783	67	1832	18	99	
172	8141	196	13	1.17	0.391	1.7	0.0531	1.4	0.0534	0.9	335	11	334	9	346	21	100	
176	3727	27	3	1.06	0.833	2.6	0.0990	1.8	0.0611	1.9	616	32	609	21	642	40	99	core
177	3351	8	1	1.57	0.926	3.6	0.1070	1.9	0.0628	3.0	666	48	656	25	701	65	98	rim
178	12476	34	12	0.86	3.998	2.5	0.2847	2.1	0.1018	1.2	1634	80	1615	69	1658	22	99	
179	89690	116	56	0.30	10.178	1.7	0.4452	1.6	0.1658	0.6	2451	84	2374	76	2516	10	97	
180	183503	199	112	0.42	12.624	1.6	0.4955	1.3	0.1848	0.9	2652	84	2595	69	2696	14	98	
181	23202	631	40	0.42	0.445	2.0	0.0602	1.6	0.0536	1.1	374	15	377	12	356	25	101	core
182	6997	121	7	0.46	0.443	1.8	0.0569	1.4	0.0564	1.2	372	14	357	10	468	27	96	rim
183	13651	384	20	0.23	0.395	1.7	0.0539	1.5	0.0532	0.8	338	12	338	10	337	17	100	
184	7138	170	10	0.61	0.384	1.7	0.0520	1.4	0.0536	0.9	330	11	327	9	353	20	99	
185	20960	452	29	0.91	0.443	1.7	0.0572	1.3	0.0562	1.1	372	13	358	9	460	25	96	
189	15271	37	14	0.68	4.946	1.7	0.3311	1.4	0.1083	0.9	1810	60	1844	50	1772	17	102	
190	27302	97	25	0.34	3.859	1.7	0.2509	1.4	0.1116	0.9	1605	53	1443	39	1825	17	90	core
191	17480	257	26	0.41	0.796	1.4	0.0963	1.3	0.0600	0.6	595	17	593	15	603	13	100	rim
192	3717	15	2	2.02	0.778	2.4	0.0896	1.5	0.0629	1.9	584	28	553	16	706	41	95	
193	6632	152	10	1.14	0.379	1.7	0.0512	1.4	0.0537	1.0	327	11	322	9	359	23	99	
194	15366	233	24	0.61	0.814	1.5	0.0969	1.3	0.0610	0.7	605	18	596	16	638	15	99	rim
195	9091	119	12	0.70	0.764	1.5	0.0934	1.3	0.0594	0.9	576	18	575	15	580	19	100	core
196	44961	106	34	0.20	5.427	1.4	0.3108	1.3	0.1267	0.6	1889	52	1744	44	2052	10	92	
197	6774	153	9	0.70	0.427	1.8	0.0547	1.2	0.0567	1.4	361	13	343	9	480	30	95	core
198	8971	206	12	0.53	0.405	1.6	0.0546	1.2	0.0538	1.0	345	11	343	9	361	23	99	rim
202	98144	135	67	0.55	9.425	1.4	0.4269	1.3	0.1601	0.5	2380	65	2292	59	2457	8	96	
203	7856	207	11	0.36	0.385	1.5	0.0523	1.2	0.0534	0.9	331	10	329	8	345	20	99	rim
204	21916	358	32	0.53	0.678	2.0	0.0839	1.8	0.0586	1.0	526	21	519	18	553	21	99	core
205	9412	262	15	0.92	0.374	1.7	0.0505	1.3	0.0537	1.1	322	11	317	8	358	25	98	rim
206	15047	475	32	0.21	0.357	1.5	0.0490	1.2	0.0529	0.9	310	9	308	8	324	19	99	core
207	4706	93	6	0.61	0.414	1.9	0.0552	1.3	0.0544	1.3	352	13	346	9	389	30	98	
208	8276	58	8	1.60	0.845	2.0	0.0969	1.3	0.0632	1.4	622	24	596	16	717	31	96	core
209	21611	664	34	0.30	0.384	1.4	0.0518	1.2	0.0538	0.7	330	9	326	8	362	15	99	rim
210	5963	137	8	1.01	0.358	1.6	0.0489	1.2	0.0530	1.0	311	10	308	8	331	24	99	
211	3242	25	2	1.51	0.575	2.3	0.0724	1.4	0.0576	1.8	461	21	451	13	514	39	98	

Appendix D-2. Continued

Sample SM181, Prinochori Formation

no.	Isotopic ratios										Apparent ages (Ma)							
	^{207}Pb[a] cps	U[b] ppm	Pb[b] ppm	Th/U	$^{207}Pb/^{235}U$[c]	±1σ %	$^{206}Pb/^{238}U$[c]	±1σ %	$^{207}Pb/^{206}Pb$[d]	±1σ %	$^{207}Pb/^{235}U$	± 2σ	$^{206}Pb/^{238}U$	± 2σ	$^{207}Pb/^{206}Pb$	± 2σ	C[e] %	
07	7249	58	8	0.86	0.964	1.5	0.1120	1.2	0.0625	0.9	685	21	684	17	690	20	100	core
08	10059	85	10	0.56	0.985	1.9	0.1107	1.3	0.0645	1.3	696	26	677	18	759	28	97	rim
09	34105	78	33	1.28	4.945	1.4	0.3108	1.3	0.1154	0.5	1810	50	1745	45	1886	9	96	core
10	13462	25	10	0.89	5.156	1.4	0.3251	1.2	0.1150	0.7	1845	53	1814	45	1881	13	98	rim
11	11856	129	14	0.44	0.860	1.4	0.1016	1.1	0.0614	0.8	630	17	624	14	654	16	99	core
12	28513	382	40	0.35	0.863	1.2	0.1027	1.1	0.0610	0.5	632	16	630	14	639	10	100	rim
13	9072	121	9	0.54	0.582	1.8	0.0734	1.5	0.0575	1.1	466	17	457	13	511	24	98	
14	3317	13	2	1.49	0.921	2.4	0.1034	1.4	0.0646	2.0	663	32	634	18	762	42	96	
15	19427	125	23	0.63	1.696	1.4	0.1658	1.2	0.0742	0.6	1007	27	989	24	1048	13	98	
20	18491	155	25	0.77	1.315	1.3	0.1398	1.2	0.0682	0.6	852	22	843	20	875	12	99	
21	13486	246	18	0.42	0.547	1.4	0.0705	1.2	0.0563	0.7	443	13	439	11	466	16	99	
22	25057	96	24	0.45	2.896	1.7	0.2302	1.3	0.0912	1.1	1381	47	1336	35	1451	21	97	core
23	7938	108	9	0.49	0.599	1.6	0.0749	1.4	0.0580	0.9	477	16	465	13	531	20	98	rim
24	23702	50	17	0.42	5.268	1.7	0.3167	1.6	0.1207	0.7	1864	63	1773	56	1966	12	95	
25	7192	87	7	0.62	0.562	1.8	0.0710	1.3	0.0574	1.3	453	16	442	11	507	28	98	
26	24168	195	32	0.91	1.330	1.6	0.1365	1.4	0.0707	0.7	859	27	825	23	947	15	96	core
27	21124	278	27	0.30	0.809	1.6	0.0975	1.4	0.0602	0.7	602	19	600	17	612	16	100	rim
28	11075	167	13	0.64	0.563	1.9	0.0722	1.6	0.0566	1.0	454	17	450	15	475	21	99	core
29	12351	192	15	0.58	0.556	1.7	0.0715	1.4	0.0564	0.9	449	15	445	13	467	20	99	rim
33	33269	85	26	0.24	4.641	1.6	0.2976	1.5	0.1131	0.7	1757	58	1679	49	1850	14	96	
34	53331	630	83	0.35	1.023	1.7	0.1147	1.5	0.0647	0.8	715	24	700	21	763	17	98	
35	17812	12	9	1.02	16.315	2.0	0.5402	1.7	0.2190	0.9	2895	114	2784	97	2974	15	96	
36	10089	56	11	1.01	1.709	2.5	0.1663	2.1	0.0746	1.3	1012	50	992	41	1057	26	98	
37	8268	105	8	0.63	0.506	2.4	0.0631	2.1	0.0582	1.1	416	20	394	17	539	24	95	core
38	18879	387	26	0.26	0.545	2.5	0.0684	2.3	0.0578	1.1	442	22	426	20	524	23	96	rim
39	18242	689	31	0.51	0.295	1.9	0.0409	1.7	0.0523	0.9	262	10	258	9	300	20	98	
40	42239	290	52	0.37	1.768	2.4	0.1726	2.3	0.0743	0.8	1034	50	1027	46	1049	17	99	
41	43420	428	54	0.30	1.153	2.3	0.1243	2.0	0.0673	1.2	779	36	755	30	846	25	97	
42	17553	205	21	0.15	0.913	1.6	0.1062	1.4	0.0623	0.8	659	21	651	18	686	18	99	
46	97041	252	73	0.16	4.791	2.4	0.2839	2.0	0.1224	1.4	1783	86	1611	63	1991	25	90	
47	92231	107	63	1.10	10.576	1.6	0.4571	1.5	0.1678	0.7	2487	80	2427	71	2536	11	98	
48	14585	120	17	0.53	1.224	4.6	0.1311	4.4	0.0677	1.3	812	74	794	70	861	27	98	
49	8058	41	9	1.19	1.734	3.1	0.1793	2.6	0.0701	1.6	1021	63	1063	56	932	33	104	
50	8663	93	11	1.05	0.790	2.5	0.0928	1.8	0.0617	1.8	591	30	572	20	665	39	97	core
51	*13536*	*181*	*14*	*0.46*	*0.692*	*4.0*	*0.0767*	*3.1*	*0.0655*	*2.6*	*534*	*43*	*476*	*29*	*790*	*54*	*89*	rim
52	8903	82	10	0.81	0.947	2.3	0.1018	1.8	0.0675	1.4	677	31	625	22	854	30	92	core
53	11731	113	13	0.63	0.898	2.0	0.0992	1.4	0.0657	1.4	651	26	610	17	795	30	94	rim
54	24563	173	33	0.80	1.719	1.5	0.1691	1.3	0.0737	0.7	1016	31	1007	27	1034	14	99	core
55	34693	523	44	0.11	0.751	1.7	0.0885	1.5	0.0615	0.8	569	19	547	16	658	18	96	rim
59	25032	212	34	0.26	1.537	4.6	0.1631	3.8	0.0684	2.6	945	87	974	74	880	54	103	
60	13715	82	16	0.85	1.565	1.9	0.1600	1.7	0.0709	1.0	956	37	957	32	955	21	100	
61	27460	402	38	0.14	0.813	1.6	0.0972	1.4	0.0607	0.8	604	19	598	17	629	16	99	core
62	11522	130	15	0.99	0.799	1.8	0.0968	1.5	0.0598	0.9	596	21	596	18	598	20	100	rim
63	6225	49	7	0.94	1.116	1.9	0.1244	1.5	0.0651	1.1	761	28	756	22	777	24	99	
64	7503	85	10	0.87	0.837	2.2	0.0979	1.8	0.0620	1.2	617	27	602	22	673	26	98	
65	11952	131	15	0.47	0.918	1.8	0.1049	1.6	0.0635	0.9	661	24	643	20	725	19	97	
66	7592	82	7	0.91	0.578	1.9	0.0720	1.5	0.0582	1.1	463	17	448	14	539	24	97	
67	4875	15	3	1.29	1.685	2.3	0.1596	1.7	0.0766	1.5	1003	45	955	32	1109	30	95	
68	9806	120	12	0.81	0.707	1.9	0.0870	1.7	0.0590	0.9	543	20	538	18	566	19	99	
72	7968	47	9	0.93	1.694	1.9	0.1660	1.5	0.0740	1.1	1006	37	990	30	1042	21	98	

Appendix D-2. Continued

no.	Isotopic ratios										Apparent ages (Ma)							
	^{207}Pb[a] cps	U[b] ppm	Pb[b] ppm	Th/U	$^{207}Pb/^{235}U$[c]	±1σ %	$^{206}Pb/^{238}U$[c]	±1σ %	$^{207}Pb/^{206}Pb$[d]	±1σ %	$^{207}Pb/^{235}U$	± 2σ	$^{206}Pb/^{238}U$	± 2σ	$^{207}Pb/^{206}Pb$	± 2σ	C[e] %	
73	13986	89	14	0.45	1.507	1.9	0.1515	1.7	0.0722	0.9	933	36	909	31	990	18	97	core
74	23115	181	25	0.12	1.384	1.8	0.1456	1.7	0.0689	0.7	882	32	876	29	897	15	99	rim
75	6521	56	6	0.61	0.739	5.5	0.0837	5.3	0.0640	1.1	562	61	518	55	741	24	92	
76	7821	84	9	0.66	0.821	2.0	0.0959	1.6	0.0621	1.2	609	24	590	19	678	25	97	rim
77	24746	370	37	0.52	0.797	2.3	0.0943	2.2	0.0613	0.7	595	28	581	26	649	15	98	core
78	14828	163	19	0.48	0.919	1.7	0.1091	1.5	0.0611	0.8	662	23	668	20	643	18	101	
79	118886	371	136	0.67	4.327	1.8	0.2845	1.6	0.1103	0.6	1699	60	1614	53	1805	11	95	
80	31392	505	45	0.34	0.705	1.7	0.0878	1.6	0.0582	0.6	542	19	542	18	539	13	100	rim
81	11477	148	14	0.63	0.734	2.4	0.0850	1.5	0.0626	1.8	559	26	526	16	696	38	94	core
85	8420	53	11	0.75	1.781	1.8	0.1746	1.4	0.0740	1.0	1039	36	1037	29	1041	21	100	
86	5741	47	6	0.76	0.896	1.8	0.1032	1.3	0.0630	1.1	649	23	633	17	707	24	97	core
87	16582	213	21	0.33	0.863	2.2	0.0973	2.0	0.0643	0.8	632	27	599	24	752	17	95	rim
88	102011	187	68	0.14	7.088	1.7	0.3548	1.5	0.1449	0.9	2123	74	1957	58	2287	16	92	
89	11777	191	14	0.35	0.589	2.1	0.0711	1.7	0.0601	1.2	470	20	443	15	606	25	94	
90	9215	68	11	0.49	1.479	1.8	0.1485	1.5	0.0722	1.1	922	34	892	26	993	22	97	
91	5123	44	5	1.18	0.736	2.1	0.0886	1.4	0.0603	1.5	560	23	547	15	614	33	98	
92	7153	69	9	0.92	0.890	1.9	0.1030	1.5	0.0627	1.1	646	24	632	19	698	24	98	
93	35721	511	55	0.39	0.886	1.6	0.1063	1.5	0.0604	0.6	644	21	651	19	619	14	101	
94	60540	107	43	0.53	6.249	1.7	0.3558	1.6	0.1274	0.7	2011	69	1962	62	2062	11	98	
98	12816	90	17	0.83	1.709	1.9	0.1644	1.6	0.0754	1.0	1012	38	981	31	1080	21	97	
99	5978	72	9	1.55	0.758	2.0	0.0907	1.4	0.0606	1.4	573	23	560	16	625	30	98	
100	98741	281	125	0.53	4.539	1.8	0.2942	1.7	0.1119	0.5	1738	61	1663	56	1830	9	96	
101	106372	129	73	0.86	10.672	1.7	0.4620	1.6	0.1675	0.6	2495	86	2449	79	2533	10	98	
102	8325	74	9	0.60	0.918	1.9	0.1076	1.6	0.0619	1.1	662	25	659	21	672	23	100	
103	18022	227	24	0.07	0.983	1.8	0.1117	1.6	0.0638	0.8	695	25	683	21	735	17	98	
104	160961	199	107	0.69	11.021	1.7	0.4562	1.6	0.1752	0.6	2525	85	2423	77	2608	10	96	
105	15559	231	22	0.50	0.742	1.8	0.0903	1.6	0.0596	0.7	564	20	557	18	588	16	99	
106	5232	40	5	1.54	0.790	2.3	0.0924	1.7	0.0620	1.5	591	27	570	19	674	33	96	
107	4286	13	2	2.17	0.853	3.6	0.0954	2.0	0.0649	3.0	626	46	587	23	770	64	94	

Sample R27, Makri Unit

no.	Isotopic ratios										Apparent ages (Ma)							
	^{207}Pb[a] cps	U[b] ppm	Pb[b] ppm	Th/U	$^{207}Pb/^{235}U$[c]	±1σ %	$^{206}Pb/^{238}U$[c]	±1σ %	$^{207}Pb/^{206}Pb$[d]	±1σ %	$^{207}Pb/^{235}U$	± 2σ	$^{206}Pb/^{238}U$	± 2σ	$^{207}Pb/^{206}Pb$	± 2σ	C[e] %	
07	5245	87	5	1.49	0.340	1.8	0.0470	1.3	0.0524	1.3	297	11	296	8	305	29	100	#
08	3732	40	2	1.27	0.331	2.3	0.0472	1.6	0.0509	1.7	290	14	297	10	238	38	102	
09	15951	369	17	0.45	0.325	2.8	0.0453	2.5	0.0521	1.2	286	16	286	14	290	27	100	
10	5294	70	4	0.81	0.318	1.9	0.0434	1.4	0.0532	1.3	281	11	274	8	338	29	98	
11	6045	89	5	0.73	0.365	1.8	0.0498	1.3	0.0531	1.2	316	11	313	8	335	26	99	
12	6992	136	8	0.41	0.443	1.9	0.0547	1.3	0.0587	1.4	372	14	343	9	555	30	92	
13	10215	220	10	0.31	0.348	1.9	0.0472	1.4	0.0535	1.2	303	11	297	9	349	26	98	
14	13871	324	18	0.80	0.345	1.5	0.0471	1.2	0.0530	0.8	301	9	297	7	330	19	99	
15	19584	494	23	0.29	0.346	1.3	0.0474	1.2	0.0530	0.6	302	8	298	7	329	14	99	
16	10745	250	12	0.48	0.339	1.7	0.0470	1.3	0.0523	1.1	296	10	296	8	300	26	100	
20	12007	258	15	0.96	0.352	1.6	0.0481	1.4	0.0531	0.8	306	10	303	8	333	19	99	
21	8461	210	9	0.78	0.273	1.8	0.0379	1.3	0.0522	1.2	245	9	240	6	292	28	98	
22	7465	165	7	0.64	0.288	1.7	0.0384	1.2	0.0544	1.1	257	9	243	6	387	26	95	
23	3288	49	2	1.20	0.248	2.3	0.0337	1.5	0.0533	1.8	225	10	214	6	340	40	95	
24	6169	141	6	0.69	0.258	1.8	0.0368	1.2	0.0509	1.3	233	8	233	6	236	30	100	
25	6702	151	7	0.69	0.285	1.8	0.0385	1.3	0.0537	1.3	255	9	243	6	358	29	96	

Appendix D-2. Continued

no.					Isotopic ratios						Apparent ages (Ma)							
	$^{207}Pb^{a}$ cps	U^{b} ppm	Pb^{b} ppm	Th/U	$^{207}Pb/^{235}U^{c}$	±1σ %	$^{206}Pb/^{238}U^{c}$	±1σ %	$^{207}Pb/^{206}Pb^{d}$	±1σ %	$^{207}Pb/^{235}U$	± 2σ	$^{206}Pb/^{238}U$	± 2σ	$^{207}Pb/^{206}Pb$	± 2σ	C [e] %	
26	4698	81	6	1.91	0.364	2.2	0.0477	1.3	0.0554	1.8	315	14	300	8	429	41	95	
27	2553	33	2	0.77	0.333	2.2	0.0459	1.3	0.0526	1.7	292	13	290	8	314	40	99	
28	1683	18	1	1.18	0.360	3.1	0.0466	1.6	0.0559	2.7	312	20	294	9	450	60	94	
29	6981	124	6	0.64	0.354	2.2	0.0471	1.3	0.0545	1.7	308	13	297	8	391	39	96	
33	3772	84	4	1.04	0.274	2.2	0.0379	1.3	0.0524	1.7	246	11	240	6	304	40	98	#
34	4125	73	4	1.30	0.366	2.4	0.0471	1.6	0.0563	1.8	316	15	297	9	463	40	94	
35	9558	284	12	0.59	0.280	1.6	0.0389	1.2	0.0521	1.0	250	8	246	6	291	22	98	
36	9187	195	10	0.43	0.351	1.7	0.0476	1.2	0.0534	1.2	305	10	300	7	347	27	98	
37	7475	103	7	0.59	0.458	1.7	0.0601	1.4	0.0553	1.0	383	13	376	11	423	21	98	
38	6725	131	8	1.50	0.349	1.7	0.0484	1.3	0.0523	1.1	304	11	305	8	300	25	100	
39	25347	308	23	0.17	0.662	1.7	0.0782	1.5	0.0614	0.8	516	18	485	15	652	18	94	
40	4394	62	3	0.78	0.351	2.1	0.0478	1.4	0.0532	1.6	305	13	301	8	339	37	99	
41	16044	463	18	0.38	0.275	1.5	0.0388	1.3	0.0514	0.7	247	7	245	6	260	16	99	
42	26587	196	23	0.41	1.246	2.9	0.1080	2.7	0.0837	0.9	822	47	661	36	1285	17	80	
46	10686	223	12	0.65	0.352	1.5	0.0490	1.1	0.0522	1.0	306	9	308	7	292	22	101	#

Sample R15, Melia Formation

no.					Isotopic ratios						Apparent ages (Ma)							
	$^{207}Pb^{a}$ cps	U^{b} ppm	Pb^{b} ppm	Th/U	$^{207}Pb/^{235}U^{c}$	±1σ %	$^{206}Pb/^{238}U^{c}$	±1σ %	$^{207}Pb/^{206}Pb^{d}$	±1σ %	$^{207}Pb/^{235}U$	± 2σ	$^{206}Pb/^{238}U$	± 2σ	$^{207}Pb/^{206}Pb$	± 2σ	C [e] %	
47	3170	28	2	1.32	0.335	2.5	0.0470	1.6	0.0518	1.9	294	15	296	10	275	43	101	
48	19259	506	31	0.65	0.325	2.3	0.0445	1.8	0.0530	1.4	286	13	281	10	329	31	98	
49	16090	237	18	0.43	0.573	2.0	0.0716	1.7	0.0581	1.2	460	19	446	15	533	26	97	
50	5780	116	7	1.15	0.349	2.1	0.0479	1.4	0.0528	1.6	304	13	302	8	318	36	99	
51	4842	56	4	0.74	0.528	1.9	0.0683	1.5	0.0562	1.2	431	16	426	12	458	27	99	
52	7351	151	10	1.66	0.361	1.5	0.0489	1.1	0.0535	1.0	313	10	308	7	352	23	98	
53	6125	119	6	0.57	0.351	1.6	0.0481	1.1	0.0529	1.2	305	10	303	6	325	28	99	
54	3926	59	3	0.88	0.362	2.4	0.0461	1.4	0.0570	1.9	314	15	291	8	490	41	93	
55	15164	385	17	0.36	0.329	1.6	0.0453	1.2	0.0527	1.1	289	9	286	7	314	24	99	
59	7220	157	8	0.82	0.338	1.7	0.0461	1.3	0.0532	1.1	296	10	291	7	337	26	98	
60	5241	81	4	0.25	0.393	1.9	0.0523	1.2	0.0545	1.4	336	13	328	8	392	33	98	
61	17838	206	23	1.21	0.758	1.4	0.0920	1.2	0.0598	0.7	573	16	567	13	596	15	99	core
62	5857	98	4	0.48	0.316	2.2	0.0409	1.7	0.0560	1.3	279	12	258	9	453	30	93	rim
63	7641	72	8	1.07	0.736	1.8	0.0888	1.5	0.0602	1.0	560	20	548	16	609	22	98	
64	4531	72	3	0.54	0.329	2.1	0.0451	1.5	0.0529	1.4	289	12	284	8	323	33	99	
65	4104	59	4	1.62	0.366	1.7	0.0492	1.1	0.0540	1.3	317	11	310	7	370	30	98	
66	3128	39	2	1.51	0.335	2.5	0.0466	1.3	0.0521	2.2	293	15	293	8	292	49	100	
67	8825	197	10	0.99	0.340	1.6	0.0448	1.0	0.0552	1.3	297	10	282	6	418	29	95	
68	386967	298	150	0.31	14.280	1.3	0.4484	1.2	0.2310	0.6	2768	72	2388	56	3059	9	86	core
72	4876	84	4	0.40	0.372	1.8	0.0500	1.2	0.0539	1.3	321	11	315	7	367	30	98	rim, #
73	6251	99	5	0.39	0.366	1.5	0.0502	1.0	0.0528	1.1	316	9	316	6	322	25	100	opposite rim
74	10080	231	13	0.97	0.347	1.4	0.0476	1.1	0.0528	0.8	303	8	300	7	322	19	99	
75	2326	23	2	2.12	0.341	2.9	0.0476	1.3	0.0518	2.6	298	17	300	8	278	60	101	#
76	2915	22	2	2.26	0.343	2.4	0.0470	1.3	0.0529	2.1	300	15	296	8	326	47	99	close by 75
77	2997	30	2	1.23	0.351	2.0	0.0461	1.2	0.0552	1.6	305	12	290	7	420	35	95	
78	4080	59	3	0.77	0.358	2.2	0.0479	1.2	0.0543	1.9	311	14	301	7	383	42	97	
79	1976	19	1	3.51	0.240	2.5	0.0341	1.6	0.0509	1.9	218	11	216	7	237	44	99	rim, #
80	2737	24	1	1.50	0.185	2.6	0.0257	1.7	0.0523	2.0	172	9	163	5	297	45	95	opposite rim, #
81	6201	117	6	0.85	0.342	1.6	0.0474	1.0	0.0524	1.2	299	9	299	6	303	26	100	
85	10264	222	13	1.10	0.361	1.4	0.0486	1.1	0.0538	0.9	313	9	306	7	364	21	98	

Appendix D-2. Continued

no.	Isotopic ratios										Apparent ages (Ma)							
	^{207}Pb[a] cps	U[b] ppm	Pb[b] ppm	Th/U	$^{207}Pb/^{235}U$[c]	±1σ %	$^{206}Pb/^{238}U$[c]	±1σ %	$^{207}Pb/^{206}Pb$[d]	±1σ %	$^{207}Pb/^{235}U$	± 2σ	$^{206}Pb/^{238}U$	± 2σ	$^{207}Pb/^{206}Pb$	± 2σ	C[e] %	
86	5754	107	6	0.76	0.348	1.8	0.0473	1.2	0.0534	1.3	303	11	298	7	344	29	98	
87	4672	78	5	0.92	0.357	1.5	0.0494	1.1	0.0525	1.0	310	9	311	7	305	24	100	
88	4459	77	5	1.71	0.356	1.7	0.0482	1.1	0.0536	1.4	309	11	303	7	355	31	98	core
89	4207	60	3	0.71	0.357	1.7	0.0482	1.0	0.0537	1.3	310	10	304	6	359	30	98	rim
90	11819	274	13	0.25	0.351	1.7	0.0487	1.3	0.0523	1.1	306	10	306	8	299	24	100	
91	3041	32	2	1.59	0.356	2.2	0.0487	1.4	0.0531	1.7	309	14	306	9	331	39	99	

Temora

no.	Isotopic ratios										Apparent ages (Ma)							
	^{207}Pb[a] cps	U[b] ppm	Pb[b] ppm	Th/U	$^{207}Pb/^{235}U$[c]	±1σ %	$^{206}Pb/^{238}U$[c]	±1σ %	$^{207}Pb/^{206}Pb$[d]	±1σ %	$^{207}Pb/^{235}U$	± 2σ	$^{206}Pb/^{238}U$	± 2σ	$^{207}Pb/^{206}Pb$	± 2σ	C[e] %	
92	6957	113	8	0.51	0.481	2.2	0.0633	1.6	0.0551	1.5	399	18	396	13	418	34	99	
93	7970	124	9	0.57	0.512	1.7	0.0675	1.3	0.0551	1.1	420	14	421	11	414	25	100	
94	7972	118	8	0.45	0.516	1.8	0.0682	1.1	0.0549	1.4	423	15	425	10	409	32	101	
98	4195	49	4	0.62	0.496	1.9	0.0655	1.4	0.0549	1.2	409	15	409	11	407	28	100	
99	5496	72	5	0.59	0.488	1.9	0.0646	1.4	0.0548	1.2	404	15	404	11	402	28	100	
100	4283	51	4	0.65	0.520	2.1	0.0676	1.3	0.0557	1.6	425	18	422	11	441	36	99	
101	8992	133	10	0.62	0.505	2.0	0.0664	1.5	0.0552	1.3	415	17	414	12	419	29	100	
102	5852	78	6	0.72	0.514	1.9	0.0665	1.3	0.0560	1.3	421	16	415	11	453	29	99	
103	5422	61	5	0.74	0.510	1.7	0.0670	1.2	0.0552	1.2	418	14	418	10	419	27	100	
104	5448	53	4	0.78	0.525	1.9	0.0671	1.3	0.0567	1.4	428	16	419	11	480	30	98	
105	4360	43	3	0.72	0.517	1.9	0.0679	1.4	0.0552	1.3	423	16	424	11	421	29	100	
106	5586	60	4	0.72	0.513	2.0	0.0674	1.4	0.0552	1.4	420	17	420	12	421	31	100	
107	5439	59	4	0.74	0.511	1.7	0.0673	1.3	0.0551	1.1	419	14	420	11	417	25	100	

Note: [a] Within-run background-corrected mean ^{207}Pb signal. [b] U and Pb content and Th/U ratio were calculated relative to GJ-1 reference material. [c] corrected for background and within-run Pb/U or Pb/Th fractionation and normalized to GJ-1 (ID-TIMS value/measured value); $^{207}Pb/^{235}U$ calculated using $^{207}Pb/^{206}Pb/(^{238}U/^{206}Pb \times 1/137.88)$. [d] mass bias corrected by normalizing to GJ-1 (ca. 0.5% per amu). [e] degree of concordance = 100 × ($^{206}Pb/^{238}U$ age/$^{207}Pb/^{235}U$ age). Analyses that have been excluded from further consideration are shown in italics (see corresponding chapters for explanation). #, also analysed with SHRIMP.

Appendix E. Magmatic zircon ages for pre-Triassic rocks from the Aegean and the surrounding region

Locality	Age (Ma)	Method	Reference and comments
External Hellenides			
E' Crete	514±14*; 511±16*	U–Pb	Romano et al. (2004), *upper intercept
Kithira	324±2; 323±3; 302±12*	U–Pb	Seidel et al. (2006), *upper intercept; Xypolias et al. (2006)
Attic-Cycladic Massif			
Delos	327–295	Pb–Pb	Engel & Reischmann (1999)
Ios	311–302	Pb–Pb	Engel & Reischmann (1999)
Naxos	372±28*; 322–306; 316±4; 275±3	Pb–Pb; U–Pb	Andriessen et al. (1987), *upper intercept; Reischmann (1998); Keay et al. (2001)
Paros	325–302	Pb–Pb	Engel & Reischmann (1998, 1999)
Antiparos	308–292	Pb–Pb	Engel & Reischmann (1999)
Samos	302	Pb–Pb	Ring et al. (1999a)
Sikinos	325–301	Pb–Pb	Engel & Reischmann (1999)
Syros	315±3	U–Pb	Tomaschek et al. (2001)
Pelagonia			
Florina	713±18; 710±5; 298±7	Pb–Pb; U–Pb	Anders et al. (2006a)
Kastoria	302±5; 292±5	Pb–Pb; U–Pb	Mountrakis (1984); Anders et al. (2006a)
Deskati	699±7	U–Pb	Anders et al. (2006a)
Fotino	710±13	U–Pb	Anders et al. (2006a)
High Pieria	302±5	U–Pb	Yarwood & Aftalion (1976)
Mt. Olympos	290–280; 271±3	Pb–Pb; U–Pb	Reischmann et al. (2001); Anders et al. (2006b)
Evia	319–303	U–Pb	Vavassis et al. (2000); Anders et al. (2006b)
Voras Mts.	293±9; 285±2; 276±9	Pb–Pb; U–Pb	Anders et al. (2006b)
Varnous Mts.	296–282	Pb–Pb; U–Pb	Anders et al. (2006b)
Driovouno	307±11; 300±2; 272±16	U–Pb	Anders et al. (2006b)
Mt. Ossa	312±2; 266±2	U–Pb	Anders et al. (2006b)
Mavrovouni	280±2	U–Pb	Anders et al. (2006b)
Pilion	546±10*; 309±13; 281±3; 279±14	Pb–Pb; U–Pb	Anders et al. (2006b), *upper intercept
Skiathos	289±14; 287±12; 264±14	U–Pb	Anders et al. (2006b)
Vardar Zone			
Pigi	319±4	U–Pb	Anders et al. (2005)
Serbo-Macedonian Massif			
Bulgaria	459.9±7.6; 451±18	U–Pb	Titorenkova et al. (2003)
Greece	587–555; 433–428	Pb–Pb	Himmerkus et al. (2004a, 2006a)
Kraište	569–544	U–Pb	von Quadt et al. (2000); Graf (2001); Kounov (2002)
Rhodope			
Bulgaria	319±9; 310±5.5; 310.7±4.6; 305±52; 300±11	U–Pb	Peytcheva & von Quadt (1995); Ovtcharova et al. (2002); Peytcheva et al. (2004)
Greece	357±20*; 345±40#; 294±8; 294.3±2.4; 300–270	Pb–Pb; U–Pb	*Wawrzenitz (1997) cited in Liati & Gebauer (1999); #Kokkinakis (1978) cited in Vavassis et al. (2000); Liati & Gebauer (1999); Turpaud & Reischmann (2005); Turpaud (2006)
Sredna Gora Zone including Balkan terrane	616.9±9.5; 595±23; 563±3; 406±30*; 480±30*; 485±50*; 443±1.5; 316–285	U–Pb	*Arnaudov et al. (1989) cited in Peytcheva & von Quadt (2004); Peytcheva & von Quadt (2004); Carrigan et al. (2003, 2005, 2006)
Strandja Massif	309±24; 271±11; 271±2	Pb–Pb	Okay et al. (2001)
Istanbul Zone	590–559; 262±19	Pb–Pb; U–Pb	Chen et al. (2002); Ustaömer et al. (2005)
Sakarya Zone	462±6; 399±13; 397±1.4*; 370–373; 319.2±1.5*; 313–293	Pb–Pb	Okay et al. (1996, *2006); Özmen & Reischmann (1999)
Anatolide-Tauride Block			
Sandıklı	543±7	Pb–Pb	Kröner & Şengör (1990)
Cine submassif of the Menderes Massif	572–521; 566±9; 541±14; 522±15	Pb–Pb; U–Pb	Hetzel & Reischmann (1996); Loos & Reischmann (1999); Gessner et al. (2004)
Ödemis submassif of the Menderes Massif	551±1.4	U–Pb	Hetzel et al. (1998)